NEW TRENDS
IN HIGH-ENERGY PHYSICS

Proceedings of the 21-th International conference
organized by the Bogolyubov Institute for Theoretical Physics,
National Academy of Sciences of Ukraine,
held in Odessa (Ukraine) on May 12–18, 2019
https://incico.bitp.kiev.ua/event/1/

Edited by
László Jenkovszky, Rainer Schicker and Jolán Turóci

Printed by “OUTDOOR-SHARK”
Kiev–Uzhhorod (Ungvár), 2020

EDITORIAL FOREWORD

The present Proceedings contain contributions presented at the 21-th International conference on New Trends in High-Energy Physics, organized by the Bogolyubov Institute for Theoretical Physics, National Academy of Sciences of Ukraine and held in Odessa (Ukraine) on May 12–18, 2019.

The Conference brought together 95 leading scientists and student from all over the world, who presented 71 contributions on new experimental data and on their theoretical interpretation. We selected the best 20 experimental and 20 theoretical presentations included in the present Book. Some of them have been published also in the Ukrainian Journal of Physics. We thank all writers for their ingenious contributions.

The next conference of this series will be held in Kiev on June 26–July 2, 2022. It was planned for 2021, but has been postponed because of the COVID quarantine.

The editorial work and print of the present Book was supported by the grant HR-17/2020 of the Hungarian Academy of Sciences extended to the Ukrainian-Hungarian Workshop via the 2020 DOMUS program.

CONTENTS

https://doi.org/10.15407/ujpe64.7.543

V. AUSHEV
On behalf of the ZEUS and H1 collaborations
Taras Shevchenko Kyiv National University
(60, Volodymyrs'ka Str., Kyiv, Ukraine, 01033; e-mail: volodymyr.aushev@gmail.com)

CHARM AND BEAUTY PRODUCTION CROSS-SECTION MEASUREMENTS IN DEEP INELASTIC ELECTRON-PROTON SCATTERING AT HERA

The open charm and beauty production cross-sections in the deep inelastic ep scattering (DIS) at HERA from the H1 and ZEUS Collaborations are combined. Reduced cross-sections are obtained in the kinematic range of negative four-momentum transfer squared of a photon $2.5 \leq Q^2 \leq 2000$ *GeV*^{2} *and the Bjorken scaling variable* $3\times10^{-5} \leq x_{Bj} \leq 5\times10^{-2}$. *The different charm- and beauty-tagging methods are used for the heavy-flavor production study in DIS. The combined method accounts for the correlations of systematic uncertainties, as well as statistical uncertainties among the different datasets. Perturbative QCD (pQCD) calculations are compared to the measured combined data. A NLO QCD analysis is performed using these data together with the combined inclusive deep inelastic scattering cross-sections from HERA. The running charm- and beauty-quark masses are determined as* $m_c(m_c) = 1.290^{+0.046}_{-0.041}(exp/fit)^{+0.062}_{-0.014}(model)^{+0.03}_{-0.031}(parametrization)$ *GeV and* $m_b(m_b) = 4.049^{+0.104}_{-0.109}(exp/fit)^{+0.090}_{-0.032}(model)^{+0.001}_{-0.031}(parametrization)$ *GeV.*

Keywords: charm and beauty production, deep inelastic interaction, electron-proton scattering, quark mass, perturbative QCD, combined cross-sections.

1. Introduction

Measurements of open charm and beauty productions in the deep inelastic ep-scattering at HERA provide the important input for tests of quantum chromodynamics (QCD). HERA collected about 0.5 fb^{-1} of the integrated luminosity by each experiment. Measurements at HERA have shown that the heavy-flavor (HFL) production in DIS proceeds predominantly via the boson-gluon-fusion process, i.e. $\gamma g \rightarrow q\bar{q}$. Therefore, the cross-section depends on the gluon distribution in the proton, as well as the heavy-quark mass. This mass provides a hard scale for the applicability of pQCD. At the same time, other hard scales are also present in this process such as the transverse momenta of the outgoing quarks and the virtuality, Q^2, of the exchanged photon. The presence of several hard scales complicates the calculation of the HFL production in pQCD. We used different approaches to cope with the multiple scale problem. In our study, the massive fixed-flavor-number scheme (FFNS) and the variable-flavor-number scheme (VFNS) are used.

The ZEUS and H1 detector systems at the HERA electron-proton collider were general purpose detectors. They have a similar structure and consist of tracking systems (including high-resolution silicon vertex detectors) surrounded by electromagnetic and hadronic calorimeters and muon detectors. This provides almost 4π coverage of the collision region.

In this report, a H1 and ZEUS combination of the charm and beauty quark productions is presented

[4]. This analysis is an extension of the previous combination of charm cross-section measurements in DIS, including new charm and beauty data. A single consistent dataset of reduced charm and beauty cross-sections from both detectors is obtained. All correlations are included. This dataset covers the kinematic range of boson (photon) virtualities $2.5 \leq Q^2 \leq$ ≤ 2000 GeV^2 and the Bjorken scaling variable in the region $3 \times 10^{-5} \leq x_{Bj} \leq 5 \times 10^{-2}$.

For these measurements, different flavor tagging methods are used: the full reconstruction of D or $D^{\star\pm}$ mesons, which is sensitive to the charm production; the lifetime of heavy-flavored hadrons and their semileptonic decays. This allows the measurement of charm and beauty cross-sections simultaneously. These methods show the dependences on sources of systematic uncertainties for different regions of the heavy-quark phase space. The simultaneous combination of charm and beauty cross-section measurements reduces all uncertainties. The combined charm cross-sections of the previous analysis [1] are superseded by the new results presented in this paper. The measured combined beauty cross-sections are presented for the first time. In general, this paper sums up almost 20 years of HFL researches at HERA.

The new data are analyzed using QCD methods for determining the running charm and beauty quark masses at the NLO calculations in the minimum-subtraction (MS) scheme. The FFNS is used for pQCD calculations for the corrections of measurements to the full phase space and in the QCD fits. In this scheme, heavy quarks are always treated as massive. The number of active flavors in the PDFs, n_f, is set equal to 3. In this model, heavy quarks are produced only in the hard-scattering ep process. In all FFNS heavy-quark calculations presented in this paper, the default renormalization scale μ_r and factorization scale μ_f are set to $\mu_r = \mu_f = \sqrt{(Q^2 + 4m_Q^2)}$, where m_Q is a pole or running mass. Predictions from different variants of the VFNS are also compared to the data. In the VFNS, heavy quarks are treated as massive at small Q^2 up to $Q^2 \approx O(m_Q^2)$ and as massless at $Q^2 \gg m_Q^2$, with interpolation prescriptions between the two regimes.

2. Combined Cross-Sections and QCD Analysis

The data have been obtained from both the HERA I (in the years 1992–2000) and HERA II (in the years 2003–2007) data-taking periods. The combination includes measurements based on using different HFL-tagging techniques: the reconstruction of particular decaying D mesons, the inclusive analysis of tracks exploiting the lifetime information and the reconstruction of electrons and muons from heavy-quark semileptonic decays.

A total of 209 charm and 57 beauty data points are combined simultaneously to obtain 52 charm and 27 beauty cross-section data-sets. A χ^2 value of 149 for 187 degrees of freedom is obtained in the combination, indicating a good consistency of the input data. There are 167 sources of correlated uncertainties in total. These are 71 experimental systematic sources, 16 sources due to the extrapolation procedure (including the uncertainties on the fragmentation fractions and branching ratios), and 80 statistical charm and beauty correlations.

The experiments at HERA typically measure the so-called reduced cross-section,$\sigma_{\rm red}$, which is closely related to the double-differential cross-section in the kinematic quantities Q^2 and x. The combined reduced cross-sections $\sigma_{\rm red}^{\rm cc}$ are shown as functions of x_{Bj} in bins of Q^2 together with the input H1 and ZEUS data in Fig. 1. As we can see, the combined cross-sections are significantly more precise than any of the individual input data-sets for the charm and beauty productions. This is illustrated in Fig. 2, where the charm measurements for $Q^2 = 32$ GeV^2 are shown. The uncertainty of the combined charm cross-section is 9% on the average and reaches values of about 5% or better in the region 12 GeV$^2 \leq$ $\leq Q^2 \leq 60$ GeV^2. The uncertainty of the combined beauty cross-section is about 25% on the average and reaches about 15% at small x_{Bj} and 12 GeV$^2 \leq Q^2 \leq$ ≤ 200 GeV^2.

Theoretical predictions of the FFNS in the MS running mass scheme are compared to the combined reduced cross-sections $\sigma_{\rm red}^{\rm cc}$ and $\sigma_{\rm red}^{\rm bb}$, as we can see in Figs. 3 and 4, respectively. In these calculations, the running quark masses are set to the world average values [2] of $m_c(m_c) = 1.27 \pm 0.03$ GeV and $m_b(m_b) = 4.18 \pm 0.03$ GeV.

The charm cross-sections of the current analysis agree well with the previous measurements, but have considerably smaller uncertainties. The observed changes in the χ^2 values are consistent with an improvement in the data precision. The tension observed between the central theory predictions and

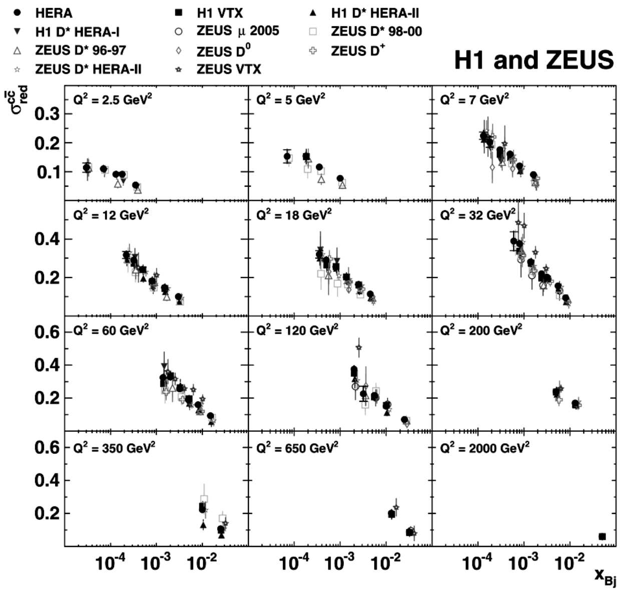

Fig. 1. Combined measurements of the charm production cross-sections, σ_{red}, (full circles) as functions of x_{Bj} for different values of Q^2. The inner error bars indicate the uncorrelated part of the uncertainties, and the outer error bars represent the total uncertainties. The input measurements with their total uncertainties are also shown by different markers. For a better visibility, the individual input data are slightly displaced in x_{Bj} toward larger values

the charm data ranges from $\sim 3\sigma$ to more than 6σ, depending on the prediction. The NLO FFNS calculations provide the best description of the charm data. For the beauty cross-sections, a good agreement of theory and data is observed within the larger experimental uncertainties. The effect of the PDF uncertainties on the χ^2 values is negligible.

The combined charm and beauty data are used together with the combined HERA inclusive DIS data [3] to perform a QCD analysis. In our QCD analysis, we determined simultaneously the running heavy-quark masses $m_c(m_c)$ and $m_b(m_b)$. We investigated the x_{Bj} dependence of the reduced charm cross-sections. We used the XFITTER programme, in which the scale evolution of partons is calculated through DGLAP equations at NLO (using the QCDNUM programme). The theoretical FFNS predictions for the HERA data are obtained using the OPENQCDRAD programme interfaced in the XFITTER framework. The number of active flavors is set to $n_f = 3$ at all scales. For the heavy-quark contributions, the scales are set to $\mu_r = \mu_f = \sqrt{(Q^2 + 4m_Q^2)}$.

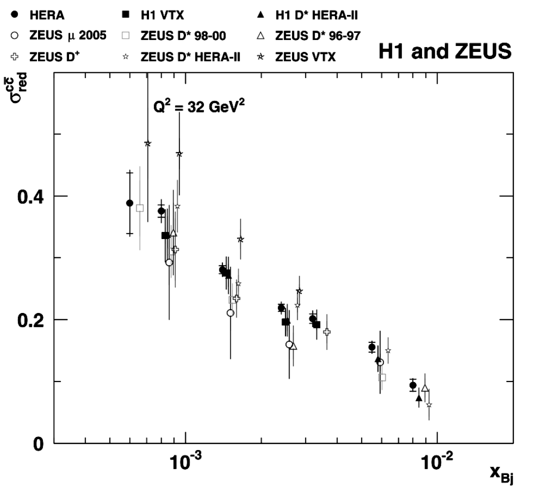

Fig. 2. Reduced cross-sections as a function of x_{Bj} at $Q^2 = 32$ GeV^2 for the charm production. The combined cross-sections (full circles) are compared to the input measurements shown by different markers. For the combined measurements, the inner error bars indicate the uncorrelated part of the uncertainties and the outer error bars represent the total uncertainties

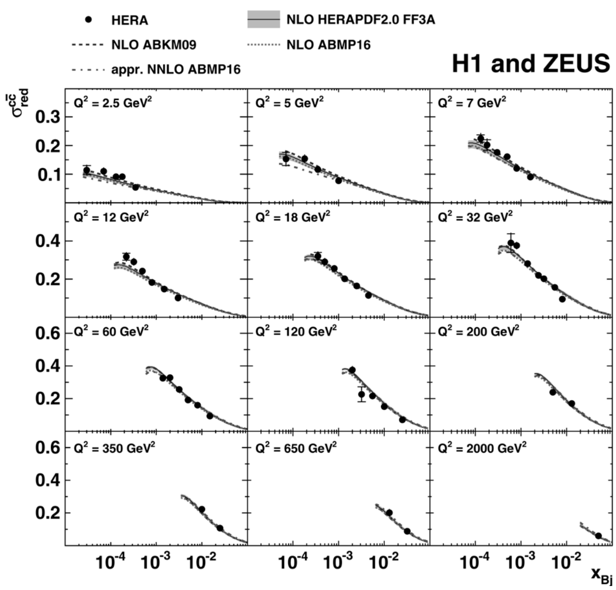

Fig. 3. Combined reduced charm cross-sections, $\sigma_{\text{red}}^{\text{cc}}$ (full circles) as functions of x_{Bj} for given values of Q^2 , compared to the NLO QCD FFNS predictions based on the HERAPDF2.0 FF3A (solid lines), ABKM09 (dashed lines), and ABMP16 (dotted lines) PDF sets. The approximate NNLO prediction using ABMP16 (dash-dotted lines) is also shown. The shaded bands on the HERAPDF2.0 FF3A predictions show the theory uncertainties obtained by adding PDF, scale, and charm-quark mass uncertainties in quadrature

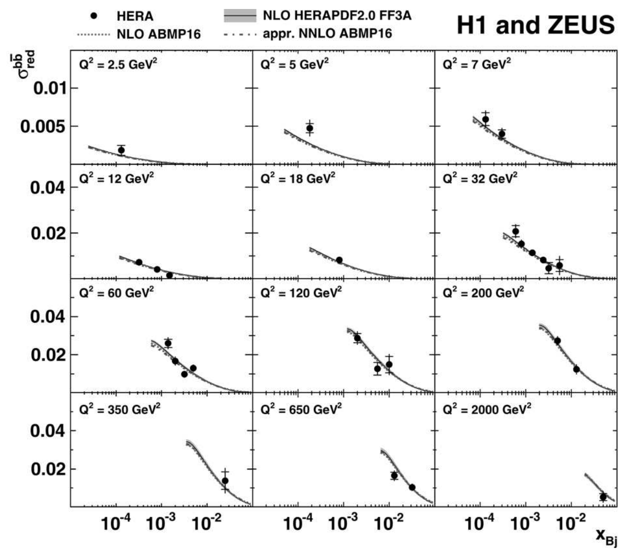

Fig. 4. Combined reduced beauty cross-sections $\sigma_{\rm red}^{\rm bb}$ (full circles) as functions of x_{Bj} for the given values of Q^2 , compared to the NLO QCD FFNS predictions based on the HERAPDF2.0 FF3A (solid lines), ABKM09 (dashed lines), and ABMP16 (dotted lines) PDF sets. The approximate NNLO prediction using ABMP16 (dashed-dotted lines) is shown as well. The shaded bands on the HERAPDF2.0 FF3A predictions show the theory uncertainties obtained by adding PDF, scale, and beauty-quark mass uncertainties in quadrature

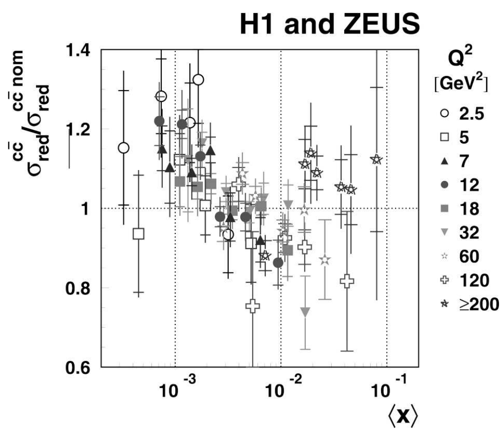

Fig. 5. Ratio of the combined reduced cross-sections, $\sigma_{\rm red}^{\rm cc}$, to the respective NLO FFNS cross-section predictions, $\sigma_{\rm red}^{\rm nom}$ based on HERAPDF-HQMASS, as a function of the partonic average x for different values of Q^2

The c and b-quark masses are left free by fitting. The running heavy-quark masses are fitted simultaneously with the PDF parameters. The fit yields a total $\chi^2 = 1435$ for 1208 degrees of freedom. The smaller uncertainties of the new combination reduce the uncertainty of the charm-quark mass determination with respect to the previous result. The beauty quark mass determination improves the previous result based on a single dataset. The running quark masses are determined (in GeV) as:

$$m_c(m_c) = 1.290^{+0.046}_{-0.041}(\exp/\mathrm{fit})^{+0.062}_{-0.014}(\mathrm{model})^{+0.03}_{-0.031}(\mathrm{param}),$$

$$m_b(m_b) = 4.049^{+0.104}_{-0.109}(\exp/\mathrm{fit})^{+0.090}_{-0.032}(\mathrm{model})^{+0.001}_{-0.031}(\mathrm{param}).$$

The model uncertainties are dominated. A better description of the charm data can be achieved, if $x_{Bj} \leq 0.01$ are excluded from the fit. Alternative NLO and NNLO QCD calculations, including those with low-x resummation, do not provide a better description of the combined heavy-quark data.

Since, in LO QCD, the heavy-quark production proceeds via the photon-gluon-fusion, at least two partons are present in the final state. The x of the incoming parton is different from x_{Bj} measured at the photon vertex. The x of the gluon is equal to

$$x = x_{Bj}\left(1 + \frac{\hat{s}}{Q^2}\right),$$

where $\hat{s}$ is the invariant mass of the heavy-quark pair. In Fig. 5, the ratio of the measured reduced cross-sections to the NLO FFNS predictions based on HERAPDF-HQMASS is shown. More detailed studies of the x slope tension showed that it can not be solved by varying the gluon density, or adding higher orders, or resumming $\log(\frac{1}{x}$ terms, within the respective pQCD frameworks.

3. Conclusions

The results of measurements of charm and beauty production reduced cross-sections in the deep inelastic ep scattering by the H1 and ZEUS experiments at the HERA collider are combined for the first time (beauty) and significantly reduced uncertainties (charm) than those previously published. Next-to-leading and approximate next-to-next-to-leading order QCD predictions are compared to the data. Calculations are found to be in a good agreement with the charm data. The NLO calculations in the fixed-flavor-number scheme provide the best description of the heavy-flavor data. The beauty data have larger experimental uncertainties. These data are well described by all QCD predictions. The new combined data are subjected to a NLO QCD analysis in the fixed-flavor-number scheme using the MS running-mass definition. The running heavy-quark masses are determined from combined data. The simultaneously determined parton density functions are found to agree well with HERA-PDF2.0 FF3A. The QCD analysis reveals some tensions, at the level of 3σ, in describing simultaneously the inclusive and heavy-quark HERA DIS data. The measured reduced charm cross-sections show a stronger x_{Bj} dependence than that obtained in the combined QCD fit of charm and inclusive data, in which the PDFs are dominated by the fit of the inclusive data.

The work was supported by the Ministry of Education and Science of Ukraine

1. H. Abramowicz *et al.* [H1 and ZEUS Collaborations]. Combination and QCD analysis of charm production cross section measurements in deep-inelastic ep scattering at HERA *Eur. Phys. J. C* **73**, 2311 (2013) [arXiv:1211.1182].
2. C. Patrignani *et al.* Particle Data Group. Review of particle physics. *Chin. Phys. C* **40**, 100001 (2016).
3. H. Abramowicz *et al.* [H1 and ZEUS Collaborations]. Combination of measurements of inclusive deep inelastic $e^{\pm}p$ scattering cross sections and QCD analysis of HERA data. *Eur. Phys. J. C* **75**, 580 (2015) [arXiv:1506.06042].
4. H. Abramowicz *et al.* [H1 and ZEUS Collaborations]. Combination and QCD analysis of charm and beauty production cross-section measurements in deep inelastic ep scattering at HERA *Eur. Phys. J. C* **78**, 473 (2018).

Received 08.07.19

В. Аушев

ВИМІРЮВАННЯ ПОПЕРЕЧНИХ ПЕРЕРІЗІВ УТВОРЕННЯ КВАРКІВ CHARM ТА BEAUTY В ЕЛЕКТРОН-ПРОТОННИХ ЗІТКНЕННЯХ НА HERA

Р е з ю м е

Наведено комбіновані значення перерізів утворення c та b кварків в глибоко-непружних електрон-протонних взаємодіях на колайдері HERA, виміряних колабораціями ZEUS і H1. Параметри визначено в діапазоні віртуальності обмінного фотона $2{,}5 \leq Q^2 \leq 2000$ ГеВ^2 та значення змінної Бйоркена $3 \cdot 10^{-5} \leq x_{Bj} \leq 5 \cdot 10^{-2}$. Використано різні методи тагування c та b кварків, які спираються на всебічне дослідження важких ароматів. При комбінуванні обчислювались статистичні та систематичні невизначеності для різних наборів даних. Для обчислень використовувалась пертурбативна КХД в різних порядках наближення і результати обчислень порівнювались з виміряними даними. Визначено поточні значення мас c та b кварків, які становлять: $m_c(m_c) = 1{,}290^{+0{,}046}_{-0{,}041}(\exp/\mathrm{fit})^{+0{,}062}_{-0{,}014}(\mathrm{model})^{+0{,}03}_{-0{,}031}(\mathrm{param})$, $m_b(m_b) = 4{,}049^{+0{,}104}_{-0{,}109}(\exp/\mathrm{fit})^{+0{,}090}_{-0{,}032}(\mathrm{model})^{+0{,}001}_{-0{,}031}(\mathrm{param})$.

https://doi.org/10.15407/ujpe64.7.548

E. BOZZO,[1] L. AMATI,[2] P. O'BRIEN,[3] D. GÖTZ[4]

[1] Department of Astronomy, University of Geneva
(16, chemin d'Ecogia, 1290 Versoix, Switzerland; e-mail: enrico.bozzo@unige.ch)
[2] INAF-OAS Bologna
(101, via P. Gobetti, I-40129 Bologna, Italy)
[3] Department of Physics and Astronomy, University of Leicester
(Leicester LE1 7RH, United Kingdom)
[4] CEA, UniversitΓ© Paris-Saclay
(F-91191 Gif-sur-Yvette, France)

THE TRANSIENT HIGH-ENERGY SKY AND EARLY UNIVERSE SURVEYOR

The Transient High-Energy Sky and Early Universe Surveyor (THESEUS) is a mission concept developed in the last years by a large European consortium and currently under study by the European Space Agency (ESA) as one of the three candidates for next M5 mission (launch in 2032). THESEUS aims at exploiting high-redshift GRBs for getting unique clues to the early Universe and, being an unprecedentedly powerful machine for the detection, accurate location (down to ∼arcsec) and redshift determination of all types of GRBs (long, short, high-z, under-luminous, ultra-long) and many other classes of transient sources and phenomena, at providing a substantial contribution to multi-messenger time-domain astrophysics. Under these respects, THESEUS will show a strong synergy with the large observing facilities of the future, like E-ELT, TMT, SKA, CTA, ATHENA, in the electromagnetic domain, as well as with next-generation gravitational-waves and neutrino detectors, thus greatly enhancing their scientific return.

Keywords: THESEUS, space mission concept, ESA, M5, gamma-ray bursts, cosmology, gravitational waves, multi-messenger astrophysics.

1. Introduction

The main feature of the modern astrophysics is the rapid development of multi-messenger astronomy. At the same time, relevant open issues still affect our understanding of the cosmological epoch (a few millions years after the "big-bang"), at which first stars and galaxies start illuminating the Universe and reionizing the inter-galactic medium.

In this context, a substantial contribution is expected from the Transient High Energy Sky and Early Universe Surveyor (THESEUS [1]), a space mission concept developed by a large European consortium including Italy, UK, France, Germany, Switzerland, Spain, Poland, Denmark, Czech Republic, Ireland, Hungary, Slovenia, ESA, with Lorenzo Amati (INAF-OAS Bologna, Italy) as a lead proposer. In May 2018, THESEUS was selected by ESA for a Phase 0/A study as one of the three candidates for the M5 mission within the Cosmic Vision programme. The end of phase A and a down-selection to one mission to be implemented is expected for mid-2021. The launch of the selected M5 mission is planned for 2032. Details on the THESEUS science objectives, mission concept, and expected performances are reported in [1] and [2].

2. Scientific Objectives

THESEUS is designed to vastly increase the discovery space of high energy transient phenomena over the entirety of cosmic history (see Fig. 1).

Because of their huge luminosities, mostly emitted in the X and gamma-rays, their redshift distribution extending at least to $z \sim 9$ and their association with explosive death of massive stars and star forming regions, GRBs are unique and powerful tools for investigating the early Universe: SFR evolution,

[1] https://www.isdc.unige.ch/theseus

physics of re-ionization, galaxies metallicity evolution and luminosity function, first generation (pop III) stars. THESEUS will obtain a statistical sample of high-z GRBs, which allow us, in turn, to [1]:

• measure independently the cosmic star-formation rate, even beyond the limits of current and future galaxy surveys;

• directly (or indirectly) detect the first population of stars (pop III);

• obtain the number density and properties of low-mass galaxies (even JWST and ELTs surveys will be not able to probe the faint end of the galaxy luminosity function at $z > 8$–10);

• evaluate the neutral hydrogen fraction;

• measure the escape fraction of UV photons from high-z galaxies;

• study the early metallicity of ISM and IGM and its evolution.

Through a carefull design optimization, a mission capable to substantially increase the rate of identification and characterization of high-z GRBs can also provide a survey of the high-energy sky from soft X-rays to gamma-rays with an unprecedented combination of a wide Field of View (FoV), source location accuracy, and sensitivity below 10 keV. For this reason, THESEUS will provide a substantial contribution also to the time-domain astrophysics, in general, and, in particular, to the newly born and fastly growing field of multi-messenger astrophysics. For instance, THESEUS will be able to provide the detection, accurate location, characterization, and redshift measurements of the electromagnetic emission (short GRBs, possible soft X-ray transient emission, kilonova emission in the near-infrared) from gravitational-wave sources like NS-NS or NS-blackhole (BH) mergers [2].

THESEUS will be an unprecedentedly powerful machine for the detection, accurate localization (down to ∼arcsec), and redshift determination of all types of GRBs (long, short, high-z, under-luminous, ultra-long) and many other classes of transient sources and phenomena. THESEUS will also provide a substantial contribution to the multi-messenger time-domain astrophysics. The mission capabilities in exploring the multi-messenger transient sky can be summarized as follow:

• Localize and identify the electromagnetic counterparts to sources of gravitational radiation and neutrinos, which may be routinely detected in the late '20s/early '30s by next generation facilities like aLIGO/aVirgo, eLISA, ET, or Km3NET;

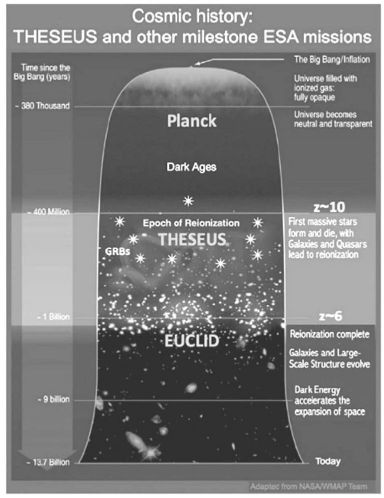

Fig. 1. Gamma-ray bursts in the cosmological context and the role of THESEUS (adapted from a picture by the NASA/WMAP Science team)

• Provide real-time triggers and accurate (∼1 arcmin within a few seconds, ∼1 arcsec within a few minutes) localizations of both high-energy transients for follow-up with next-generation optical-NIR (E-ELT, JWST, if still operating), radio (SKA), X-rays (ATHENA), TeV (CTA) telescopes, as well as to LSST sources;

• Provide a fundamental step forward in the comprehension of the physics of various classes of transients and fill the present gap in the discovery space of new classes of transient events.

In the field of gravitational wave source, THESEUS capabilities will permit us to:

• detect short GRBs over a large FoV with arcmin localization;

• detect the kilonovae and provide their arcsec localization and characterization;

• detect weaker isotropic X-ray emissions.

3. Mission Concept and Payload

THESEUS will be capable to achieve the exceptional scientific objectives summarized above thanks to a smart combination of the instrumentation and mission profile. On its board, the mission will carry two large-FoV monitors, a 1-sr FoV in the region of soft X-rays (0.3–5 keV) with unprecedented sensitivity and arcmin location accuracy and a several-sr FoV from

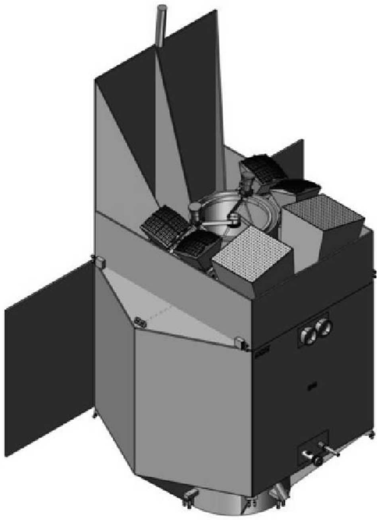

Fig. 2. Sketch of the THESEUS spacecraft and payload accommodation. The IRT is placed in the middle of the optical bench and is clearly visible with 4 SXI squared cameras, as well as the two XGIS rectangular cameras (credits: ESA)

Fig. 3. Sketch of THESEUS inside the VEGA fairing (credits: ESA)

2 keV up to 20 MeV, with additional source location capabilities of a few arcmin from 2 to 30 keV. Once a GRB or a transient of interest is detected by one or both the monitors, the THESEUS spacecraft will autonomously slew quickly to point, within a few minutes, an on-board near infra-red telescope (70 cm class operating from 0.7 to 1.8 μm) toward the direction of the transient, so to catch the fading NIR afterglow or, e.g., the kilonova emission, localizing it at a 1 arcsec accuracy and measuring its redshift through photometry and moderate resoluton spectroscopy.

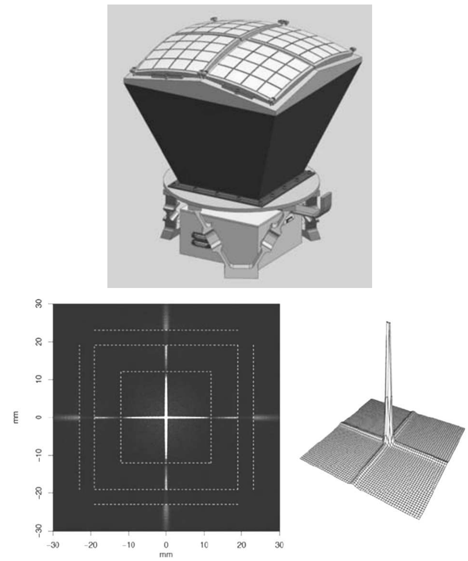

Fig. 4. Top: sketch of one SXI camera. Left: the SXI point spread function

The detailed description of THESEUS can be found in [1]. A sketch of the THESEUS spacecraft, showing also the accommodation of all payload elements, is presented in Fig. 2. This sketch is a result of the Concurrent Design Facility (CDF) study performed by ESA at the end of the phase 0 before the kick-off of phase A (end of 2018). It is expected that THESEUS will be injected into a low equatorial orbit (<6 deg. inclination, $\sim$600 km altitude) with a VEGA-C launcher (see Fig. 3). We provide a short description of the THESEUS payload, comprising the SXI, XGIS, and the IRT instruments, in the following subsections.

3.1. The soft X-ray imager

The soft X-ray Imager (SXI) comprises a set of four sensitive lobster-eye telescopes observing in the 0.3–5 keV energy band and providing a FoV of $\sim$1sr. The expected source location accuracy is 0.5–1 arcmin. A few details of the instrument are provided in Fig. 4. The SXI is being developed by a UK-led consortium.

3.2. X- and gamma-ray imaging spectrometer

The X- and Gamma-rays Imaging Spectrometer (XGIS) comprises 2 coded-mask cameras using bars of Silicon diodes coupled with CsI crystal scintillators (see Fig. 5). The instrument is operating in the 2 keV–10 MeV energy band, providing the imaging capabilities only in the 2–30 keV energy range. It operates as a collimated instrument between 30–150 keV and as an all-sky monitor at higher energies. Depending on the operating mode, the XGIS can achieve a FoV as large as ∼2–4 sr and provides a source location accuracy of about 5 arcmin. In order to optimize the detection of high-energy transients and GRBs, in particular, the FoV of the XGIS partly overlaps with that of the SXI (see Fig. 6). The XGIS is being developed by an Italy-led consortium.

3.3. Infrared telescope

The InfraRed Telescope (IRT) is a 0.7 m class IR telescope operating between 0.7–1.8 μm. A design based on a off-axis Korsch model is presently (see Fig. 7) assumed, resulting in a FoV of 15×15 arcmin and providing both imaging and moderate resolution spectroscopy capabilities (up to $R = 500$). The IRT is being developed by a France-led consortium.

4. THESEUS Performances

4.1. Early Universe with GRBs

THESEUS will have the ideal combination of the instrumentation and the mission profile for detecting all types of GRBs (long, short/hard, weak/soft, high-redshift), localizing them from a few arcmin down to arsec, and measuring the redshift for a large fraction of them (see Fig. 8).

In addition to the GRB prompt emission, THESEUS will also detect and localize, down to 0.5–1 arcmin, the soft X-ray short/long GRB afterglows, NS-NS (BH) mergers, and many classes of galactic and extra-galactic transients. For several of these sources, the IRT will provide a characterization of the associated IR counterpart, including a location within 1 arcsec and, possibly, the redshift.

The impact of the THESEUS measurements for shedding light on the study of the early Universe exploiting GRBs is represented in Fig. 9, where we show the expected number per year of GRBs detected, localized, and such, for which a redshift measurement is achieved. The THESEUS expected performance is compared to the present situation, which is a result of the large efforts coordinated between Swift, Konus-WIND, Fermi/GBM, and several on-ground robotic/large telescopes.

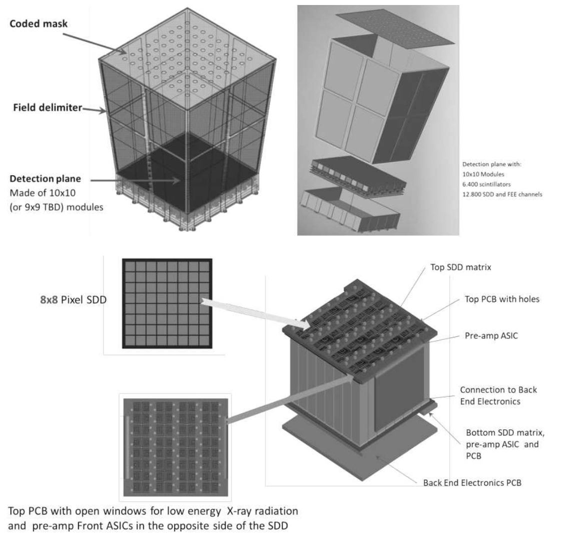

Fig. 5. Top: sketch of one XGIS camera. Bottom: details of one of the 100 modules comprised within the focal plane of each XGIS camera

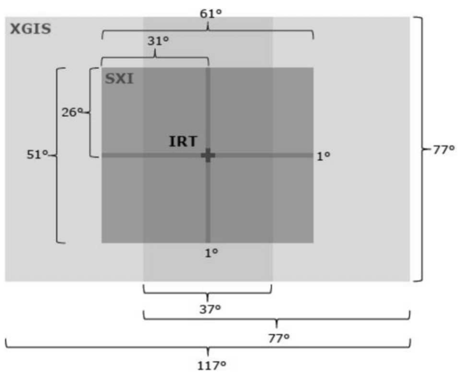

Fig. 6. Combined THESEUS instruments FoV (credits: ESA)

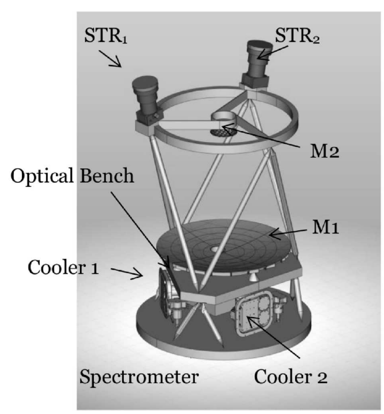

Fig. 7. The IRT assembly (credits: ESA)

4.2. Multi-messenger and time-domain astrophysics

As anticipated in a few of the previous sections, THESEUS will be capable of monitoring a number of different expected gravitational wave source counterparts in the electromagnetic (EM) domain, including:

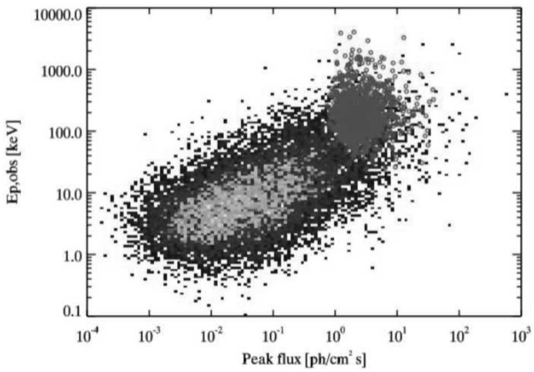

Fig. 8. GRB distribution in the peak flux – spectral peak energy ($E_{\rm P}$) plane according to the most recent population synthesis models and measurements ([1]). For all shown GRBs, THESEUS will be able to provide the detection, accurate location, characterization, and measurement of the redshift. The low-$E_{\rm P}$ – low peak flux region is populated by high-redhsift GRBs (shown in dark blue, blue, ligt blue, green, yellow), a population unaccessible by current facilities, while the high $E_{\rm P}$ region highlighted with red points shows, where the shortest GRBs will lay

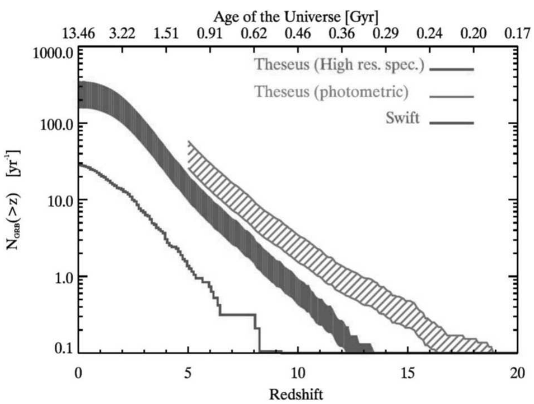

Fig. 9. Yearly cumulative distribution of GRBs with redshift determination vs. redshift for Swift and THESEUS. These predictions are conservative, as they reproduce the current GRB rate as a function of the redshift. However, thanks to its improved sensitivity, THESEUS can detect a GRB of $E_{\rm iso} = 10^{53}$ erg (corresponding to the median of the GRB radiated energy distribution) up to $z = 12$. Our currently poor knowledge of the GRB rate-star formation rate connection does not preclude the existence of a sizable number of GRBs at such high redshifts, in agreement with recent expectations on Pop III stars

• NS-NS/NS-BH mergers: for these events, THESEUS is expected to detect the collimated EM emission from short GRBs, as well as their afterglows (the currently estimated event rate is of $\lesssim$1 yr^{-1} for the GW detectors of the second generation, but up to $\sim$20 yr^{-1} for the third generation detectors such as the Einstein Telescope). THESEUS is also expected to detect the NIR and soft X-ray isotropic emissions from macronovae, as well as from off-axis afterglows and, for NS-NS, to identify newly born magnetars spinning down in the millisecond domain (the rate of GW detectable NS-NS or NS-BH systems is estimated at dozens-hundreds yr^{-1}).

• Core collapse of massive stars: for these events, THESEUS is expected to detect the emission from long GRBs, LLGRBs, as well as ccSNe (in these cases, the prediction on the energy released in GWs is much more uncertain, and the estimated rate of events is of $\sim$1 yr^{-1}).

• Flares from isolated NSs: for these events, THESEUS is expected to be able to detect the typical emission from, e.g., the Soft Gamma Repeaters (although the associated GW energy content is estimated to be only $\sim$0.01%–1% of the EM emission).

THESEUS will be able to detect, localize, characterize, and measure the redshift for NS-NS/NS-BH mergers thorugh the following channels:

• collimated on-axis and off-axis prompt gamma-ray emission from short GRBs;

• NIR and soft X-ray isotropic emissions from kilonovae, off-axis afterglows, and, for NS-NS, from newly born ms magnetar spindown.

THESEUS will thus beautifully complement the capabilities of the next generation of GW detectors (e.g., Einstein Telescope, Cosmic Explorer, further advanced LIGO and Virgo, KAGRA, *etc.*) by promptly and accurately localizing e.m. counterparts to GW signals from NS-NS and NS-BH mergers and measuring their redshift. These combined measurements will provide unique clues on the nature of the progenitors, on the extreme physics of the emission and, by exploiting the simultaneous redshift (from e.m. counterpart) and luminosity distance (from the GW signal modeling) of tens of sources, fully exploit the potentialities of the multi-messenger astrophysics for cosmology.

4.3. Time-domain astronomy and GRB physics

The unique capabilities of THESEUS will also allow us to provide relevant contributions to the more general field of the time-domain astronomy and, of course, to the GRB science. As a few examples, THESEUS will provide the astrophysical community with:

• survey capabilities of transient phenomena similar to the Large Synoptic Survey Telescope (LSST) in the optical range: a remarkable scientific sinergy can be anticipated;

• substantially increased detection rate and characterization of subenergetic GRBs and X-ray flashes;

• unprecedented insights in the physics and progenitors of GRBs and their connection with peculiar core-collapse SNe.

5. Conclusions

THESEUS, under study by ESA and a large European collaboration with strong interest by international partners (e.g., US) will fully exploit GRBs as powerful and unique tools to investigate the early Universe and will provide us with unprecedented clues to the GRB physics and subclasses. This mission will also play a fundamental role for the GW/multi-messenger and time domain astrophysics at the end of the next decade, also by providing a flexible follow-up observatory for fast transient events with multi-wavelength ToO capabilities. THESEUS observations will thus impact on several fields of astrophysics, cosmology, and even fundamental physics and will enhance importantly the scientific return of next-generation multi-messenger (aLIGO/aVirgo, LISA, ET, or Km3NET) and e.m. facilities (e.g., LSST, E-ELT, SKA, CTA, ATHENA)

In addition, the THESEUS scientific return will include the significant observatory science, e.g., studying thousands of faint to bright X-ray sources through the unique simultaneous availability of broad band X-ray and NIR observations.

THESEUS will be a really unique and superbly capable facility, one that will do the amazing science on its own, but also will add a huge value to the currently planned new photon and multi-messenger astrophysics infrastructures in the 2020 s to >2030 s.

1. L. Amati, P. O'Brien, D. Götz, *et al.* The THESEUS space mission concept: Science case, design and expected performances. *Adv. in Space Research* **62**, 191 (2018).
2. G. Stratta, R. Ciolfi, L. Amati, *et al.* THESEUS: A key space mission concept for multi-messenger astrophysics. *Adv. in Space Research* **62**, 662 (2018).

Received 01.07.19

Е. Боццо, Л. Аматі, П. Обраєн, Д. Гьотц

ПЕРЕХІДНЕ ВИСОКОЕНЕРГЕТИЧНЕ
НЕБО І ТОПОГРАФІЯ РАННЬОГО ВСЕСВІТУ

Р е з ю м е

Перехідне високоенергетичне небо та топографія раннього Всесвіту (THESEUS) – це концепція космічної місії, яка розроблена в останні роки великим європейським консорціумом і наразі вивчається Європейським космічним агентством (ЄКА) як один з трьох можливих кандидатів на чергову місію M5 (запуск у 2032 р.). THESEUS має на меті експлуатувати GRB з високим червоним зміщенням для отримання унікальних підказок від раннього Всесвіту і, будучи безпрецедентною потужною машиною для виявлення точного розташування (до ∼арксекунди) і визначення червоного зміщення всіх типів GRB (довге, коротке, з високим z, нижче світлових, наддовге) та багато інших класів перехідних джерел і явищ, має на меті зробити істотний внесок у багаточастотну астрофізику часової області. У цьому відношенні THESEUS покаже сильну синергію з великими проектами спостереження майбутнього, такими як E-ELT, TMT, SKA, CTA, ATHENA в електромагнітній області, а також з детекторами нового покоління для спостереження гравітаційних хвиль і нейтрино, що значно підвищує їхню наукову результативність.

https://doi.org/10.15407/ujpe64.7.554

K. CIEŚLA, R. STASZEWSKI, J.J. CHWASTOWSKI

The Henryk Niewodniczański Institute of Nuclear Physics, Polish Academy of Sciences
(152, Radzikowskiego, 31-342 Kraków, Poland; e-mail: krzysztof.ciesla@ifj.edu.pl, rafal.staszeski@ifj.edu.pl, janusz.chwastowski@ifj.edu.pl)

ON THE CENTRALITY DETERMINATION WITH FORWARD PROTON DETECTORS

The forward proton detectors, already installed at the Large Hadron Collider, are studied in the context of heavy-ion collisions. The potential of such detectors in measuring the nuclear debris coming from the spectator fragments is presented. The geometric acceptance of the forward proton detectors for different debris is estimated. The impact of experimental conditions and the Fermi motion on the acceptance is studied. A possibility of the collision impact parameter reconstruction from the measurement of nuclear fragments is discussed.

Keywords: heavy-ion physics, impact parameter, forward detectors.

1. Introduction

The Large Hardon Collider [1] is equipped with forward proton detectors designed to register protons scattered in diffractive or electromagnetic interactions. Such protons are scattered at very low angles, and this requires detectors to be installed very far away from the interaction point. In addition, with the use of the Roman Pot technology, they can be placed very close to the beam. The LHC physics programme is not entirely devoted to studies of proton-proton interactions. The machine may also accelerate the heavy-ion beams. This resulted in many measurements of proton-lead and lead-lead collisions [2].

A sketch of an typical heavy-ion collision is shown in Fig. 1. It is quite obvious that the impact parameter of a collision has usually a non-zero value. This means that only a part of nucleons belonging to the one nucleus interacts with a part of nucleons of the other one. Nucleons actively participating in the interactions are called participants, in contrary to the spectators.

The time scale of a ultrarelativistic heavy-ion collision is much shorter than the time scale of the interactions within the nuclei. The spectators are mostly left intact and are scattered into the beampipe escaping the central detector acceptance, similar to the forward protons. This paper tries to answer whether and to what extent the forward proton detectors installed at the LHC can be used with heavy-ion beams.

2. Forward Proton Detectors

Several systems of forward proton detectors are currently installed at the LHC, including: AFP [3], ALFA [4], CT-PPS [5], and TOTEM [6]. All of them are installed about 200 m away from their corresponding interaction points. The ALFA detectors approach the beams vertically, the AFP and CT-PPS horizontally, while TOTEM has both types of the detectors. This work takes the AFP detectors as an example. However, similar results could also be expected for other horizontal detectors.

The AFP (ATLAS Forward Proton) detectors [3] are a subsystem of the ATLAS experiment. They consist of four detector stations – two on each outgoing beam, with the near stations placed at 205 m and the far stations at 217 m away from the interaction point. Each AFP station includes four planes of 3D

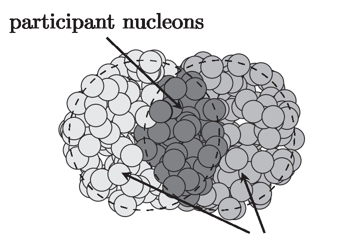

Fig. 1. Schematic diagram of an ultrarelativistic collision of two heavy nuclei (a view along the motion axis)

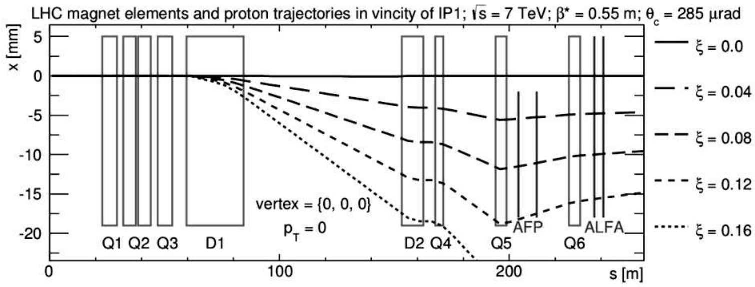

Fig. 2. Trajectories of forward protons in the LHC magnetic lattice. s is the distance from the interaction point along the nominal optics, x is the horizontal coordinate of a trajectory with respect to the nominal orbit, ξ is the relative energy loss of a forward proton

Silicon pixel tracker sensors [7], the far stations are additionally equipped with quartz Cherenkov time-of-flight detector [8] (not important in the current study). The use of the Roman Pot mechanism allows the AFP detectors to be horizontally inserted into the accelerator beampipe.

Since the AFP detectors are located at some distance from the interaction point, the scattered protons, before being registered by them, travel through magnetic fields of several LHC magnets, confront Fig. 2. The Q1–Q3 quadrupole magnets are responsible for the final focusing of a beam, providing the high luminosity of the collisions. As for two dipole magnets, D1 separates the outgoing and the incoming beams, and D2 accommodates them within the beampipes. The Q4 and Q5 quadrupole magnets are used to match the interaction region optics to the optics of the rest of the machine.

As a result of the interaction, the forward protons produced in pp interactions (e.g., in diffractive processes) have slightly different kinematics, than the beam protons. They are scattered at a very small angle and often lose some part of their energy. Small scattering angles mean a very steep distribution of forward proton transverse momenta. Thus, the forward proton trajectory and the position in the detectors are primarily determined by the proton energy. The transverse momentum leads to a moderate smearing of the scattered proton position at the detector. The forward proton relative energy loss is defined as $\xi = 1 - E_{\text{proton}}/E_{\text{beam}}$. The higher its value, the larger is the forward proton trajectory curvature in the magnetic fields. An example of various trajectories is illustrated in Fig. 2, where also the positions of the LHC magnets and AFP detectors are

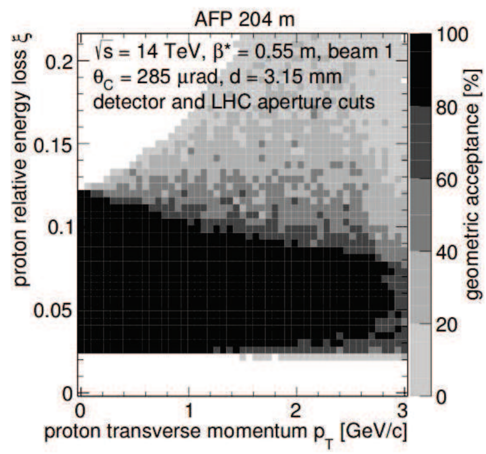

Fig. 3. Geometric acceptance of the AFP detectors for forward protons

shown. The kinematic range in which the measurements are possible can be described by the value of the geometric acceptance treated as a function of the relative energy loss and transverse momentum of the forward proton, p_T. The acceptance calculated using the MAD-X program [9] for the design LHC optics [10] is shown in Fig. 3. One can see that the AFP detectors can register protons with relative energy loss between 2% and 12% and less than 3 GeV of the transverse momentum.

3. Acceptance for Nuclear Spectator Fragments

Before the ultrarelativistic heavy-ion collision, both participating and spectating nucleons are parts of the nucleus, interacting with each other. During an interaction, the spectators are, in a sense, peeled away from participants, and their ensemble is left in a very

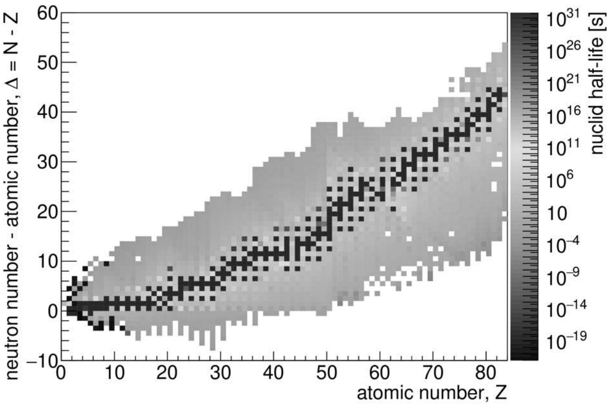

Fig. 4. Half-life time of the known nuclei

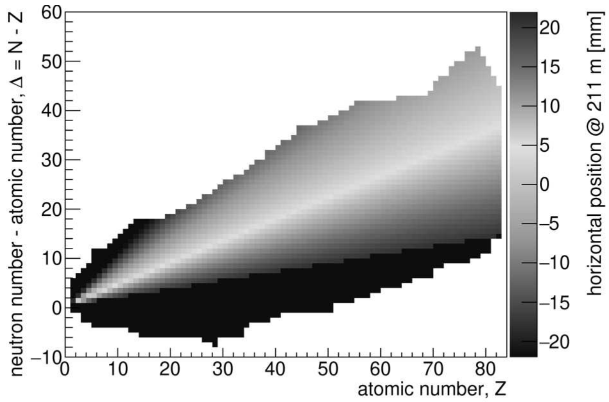

Fig. 5. Horizontal position of the nuclei at the distance of 211 m from the ATLAS interaction point

peculiar state which subsequently decays into lighter fragments. In the calculations of the geometric acceptance of the detectors for the spectator fragments, it is assumed that all nuclei lighter than the projectiles can possibly be produced.

Since the AFP detectors are positioned far away from the interaction point, it is necessary to check whether and which produced fragments can hit a detector before the decay. For a Pb beam at the LHC with magnets set as for 6.5 TeV proton optics, the proper time between the production and reaching a detector is about 0.3 ns. The half-life time of the known nuclei, as a function of the atomic number Z and the difference between the number of neutrons and the atomic number Δ is shown in Fig. 4. We can see that a vast majority of known nuclei could reach the detectors before the decay.

The nuclear fragment transport simulation was preformed using the MAD-X program, assuming the beam of fully ionized ^{208}Pb ions accelerated to the energy of 2.56 TeV per nucleon. The LHC optics corresponding to the LHC Run 2 heavy-ion operations [10] was used. Trajectories of ions different from Pb were simulated by scaling their momenta to the momentum of a lead ion that would have same trajectory in the magnetic filed as the tracked one. This scaling procedure is possible due to the dependence of the trajectory observed in the magnetic field on the ratio of the particle momentum to its charge.

Without introducing the spreads originating from the beam emittance and internal motion of nucleons, a nucleus with a given A and Z will hit the AFP detectors at a well-defined position. Dipole magnets bend the beam trajectory in the horizontal direction, so the x-coordinate of a fragment trajectory plays the major role in this consideration. It should also be noted that, for the safety reasons, the detectors are positioned at some distance with respect to the beam. An additional dead material of the Roman Pot floor has also been taken into account in the calculations.

Predicted horizontal positions of all nuclei at 211 m from the interaction point (in the middle between the near and far stations) are shown in Fig. 5. The position of ^{208}Pb ($\Delta = 44$) and all nuclei with the same Δ/Z ratio is equal to zero. Nuclei containing less neutrons per proton are deflected outside the LHC ring, similarly as the forward protons, and can be registered in the AFP detectors. Nuclei with more neutrons per proton are deflected toward the LHC center and escape the detection. Nuclei with Δ/Z ratio very different from that of lead can be lost in the LHC and not reach the AFP detectors.

Neglecting the internal motion of the nucleons within a nucleus, the energy of each nucleon is the same and equal to the energy of the beam divided by the mass number of the beam particles: $E_N = E_{\text{beam}}/A_{\text{beam}}$. Assuming that the spectator fragments are left intact during the collision, the energy of a spectator with mass number A will be equal to $A \cdot E_N$. The internal motion of nucleons is introduced by applying the Fermi-gas model of a nucleus. In the rest frame of a nucleus, the density of nucleon states is given by $dn \sim p^2 dp$. In the simulation, the absolute value of the momentum of each nucleon was randomly drawn from a quadratic distribution between zero and the Fermi momentum of 250 MeV. Then the momentum of a given fragment was calculated as a vector sum of the momenta of all its nucleons and the Lorentz-transformed into the laboratory frame.

For the beam emittance value of 1.233 μm [10], the lead beam angular spread is 24 μrad at the interaction point, and the interaction vertex distribution has the transverse and longitudinal spreads of 13 μm and 5.5 cm, respectively. The horizontal width of the beam at 211 m from the interaction point, σ_x, is 134 μm. This width is an usual unit of distance between the detector and the beam. The distance between the edge of a sensor and the center of the beam is assumed to be 3 mm. It covers about 19 σ_x and a 0.5-mm-long distance between the active sensor edge and the outer wall of the Roman Pot floor.

The result of studies of the influence of various factors on the positions of the selected ions at the distance of 211 m away from the interaction point is shown in Fig. 6. One can observe that the effects of the beam spreads and those due to the transverse component of the Fermi motion are small. The position smearing is dominated by the longitudinal Fermi motion magnified by the Lorentz boost. This effect is stronger for the lighter nuclei.

Figure 7 shows the acceptance to detect a given nuclear fragment as a function of its Z and Δ at a distance of 211 m away from the interaction point. The results were averaged over the distributions of the momenta and the Gaussian spatial and angular spreads of the LHC beam. However, the AFP detectors were not designed for measurement of the nuclear debris, and their acceptance covers a significant part of the nuclei spectrum. As one can observe, for a given Z, especially for heavier nuclei, more than a half of known nuclei can be potentially detected. This range of accepted masses decreases linearly with decreasing value of Z.

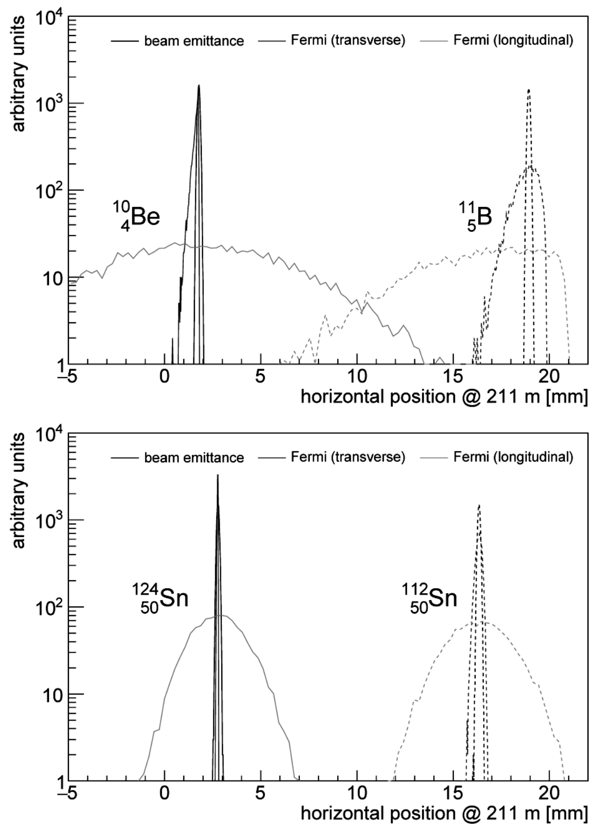

Fig. 6. Effects of the beam emittance and the Fermi motion on the fragment position in the AFP for selected light (top) and heavy (bottom) nuclei

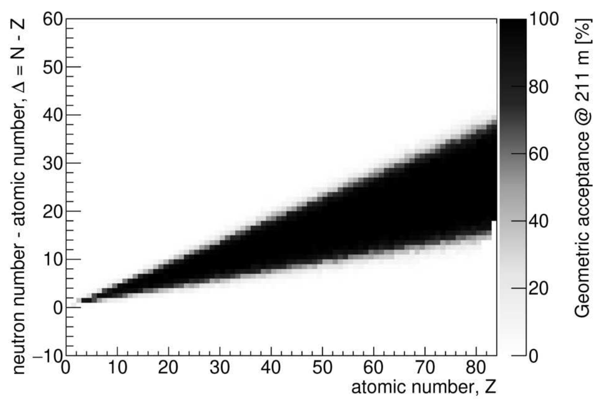

Fig. 7. AFP acceptance for nuclear fragments

4. Centrality Determination

To study how the measurements of fragments can be used to retrieve information about a central state, a simulation of Pb–Pb collisions using the DPMJET Monte Carlo generator [11] was performed. For each event, the generator reports a list of produced particles, including the spectators. Figure 8 shows the distribution of produced fragments.

Each event is generated with a known random value of the impact parameter. Figure 9, *a* shows the correlation between the impact parameter value and the sum of the mass numbers of all produced frag-

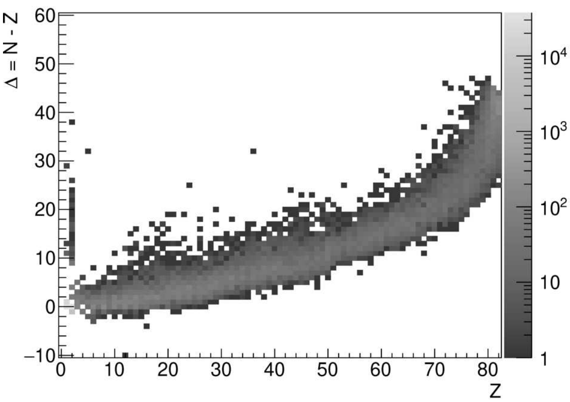

Fig. 8. Multiplicity of the nuclear fragments produced in Pb–Pb collisions simulated using DPMJET

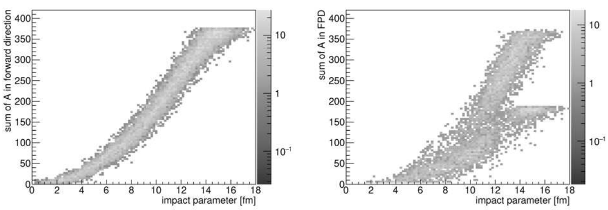

Fig. 9. Correlation between the collision impact parameter and the sum of mass numbers of: all produced fragments (left), fragments produced within the acceptance of forward proton detectors (right)

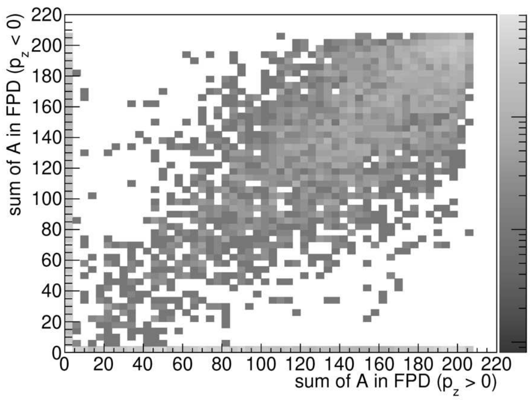

Fig. 10. Correlation between the sum of masses of fragments produced within the acceptance of forward proton detectors on the sides with positive and negative longitudinal momenta

ments. One can observe a strong dependence between these two variables – the more peripheral the event, the more the spectators are produced. Calculating this plot, the acceptance of forward proton detectors was not considered. Figure 9, *b* shows the same correlation. But here, the sum runs only over the fragments within the acceptance of the forward proton detectors[1]. One can notice that the correlation persists. However, it is not as strong as in the previous case. The correlation has two components – one similar to the original one and the another one with ΣA scaled down.

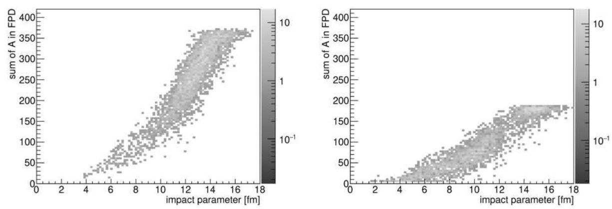

Fig. 11. Correlation between the collision impact parameter and the sum of mass numbers of fragments produced within the acceptance of forward proton detectors for double-tag (left) and single-tag (right) (see text)

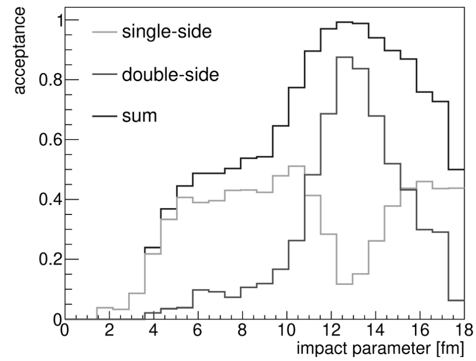

Fig. 12. Acceptance for events with nuclear fragments measured in forward proton detectors

The initial state of the Pb–Pb collision is, in the first approximation, symmetric with respect to the p_z sign. In a particular event, fluctuations of the shape of ions and those related to the spectator fragmentation can break this symmetry leading to a two-component picture. Indeed, this can be observed from Fig. 10 showing the correlation between the sum of A measured on the two sides. Two types of events can be distinguished – events with fragments on both sides (double-tag) and only one side (single-tag). For double-tag events, the ΣA of the fragments measured on both sides are correlated. The width of this correlation reflects the correlation between the impact parameter and the measurements on each side.

[1] For the results based on the DPMJET simulation, the acceptance of the forward proton detectors is taken into account in an approximate way based on their A/Z ratio.

Figure 11 shows the correlations between the collision impact parameter and the sum of A for measured fragments of the two types of events separately. A correlation between the two variables is visible in both cases, which shows that the proposed method can be used for the centrality determination.

Figure 12 shows the probability that a given event will be of either type as a function of the impact parameter. For the most central events (small impact parameter), the probability of observing any fragment in the forward detectors is zero. In such collisions, only the lightest fragments can be produced, which will escape the detection. With increasing value of the impact parameter, the probability of observing the single-tag events increases. However, at about 12–14 fm it drops down, which corresponds to a peak in the probability for double-tag events.

5. Conclusions

The presented study shows that the existing forward proton detectors at the LHC provide an interesting possibility of detecting the nuclear debris originating from the collision of two heavy ions. One of the possibility is a measurement of the centrality of Pb–Pb collisions. Different centralities result in different signals generated by the produced nuclear fragments. Such measurement would be independent of and complementary to the other commonly used methods. A direct measurement of the number of spectator fragments and, hence, the determination of the number of participants could be possible, if several forward detectors providing thus a much larger acceptance are used [12]. The present work shows that one can get information about the centrality even with the limited acceptance of the already existing detectors. More details can be found in [13].

The measurements of spectators using the Roman Pot detectors could be considered also for proton-ion and lepton-ion interactions. However, this topic requires dedicated studies.

This work was supported in part by a Polish National Science Center grant No. 2015/19/B/ST2/00989.

1. L. Evans, P. Bryant. LHC machine. *JINST* **3**, S08001 (2008).
2. F. Antinori, A. Dainese, P. Giubellino, V. Greco, M.P. Lombardo, E. Scomparin. *Proc., 27th International Conference on Ultrarelativistic Nucleus-Nucleus Collisions (Quark Matter 2018): Venice, Italy, May 14–19, 2018. Nucl. Phys. A* **982**, 1 (2019).
3. ATLAS Collaboration. *Technical Design Report for the ATLAS Forward Proton Detector.* CERN-LHCC-2015-009, ATLAS-TDR-024.
4. ATLAS Collaboration. *ATLAS Forward Detectors for Measurement of Elastic Scattering and Luminosity.* CERN-LHCC-2008-004, ATLAS-TDR-018.
5. CMS-TOTEM Collaboration. *CMS-TOTEM Precision Proton Spectrometer.* CERN-LHCC-2014-021, TOTEM-TDR-003, CMS-TDR-13.
6. TOTEM Collaboration. *The TOTEM experiment at the CERN Large Hadron Collider. JINST* **3**, S08007 (2008).
7. S. Grinstein, M. Baselga, M. Boscardin, M. Christophersen, C. Da Via *et al.* Beam test studies of 3D pixel sensors irradiated non-uniformly for the ATLAS forward physics detector. *Nucl. Instrum. Meth. A* **730**, 28 (2013).
8. J. Lange *et al.*. Beam tests of an integrated prototype of the ATLAS forward proton detector. *JINST* **11**, P09005 (2016).
9. *MAD – Methodical Accelerator Design.* https://mad.web.cern.ch/mad/.
10. *LHC Optics Web Home.* http://cern.ch/lhcoptics.
11. S. Roesler, R. Engel, J. Ranft. The Monte Carlo event generator DPMJET-III. In: *Advanced Monte Carlo for Radiation Physics, Particle Transport Simulation and Applications.* Edit. by A. Kling, F.J.C. Barão, M. Nakagawa, L. Távora, P. Vaz (Springer, 2001).
12. S. Tarafdar, Z. Citron, A. Milov. A centrality detector concept. *Nucl. Instrum. Meth. A* **768**, 170 (2014).
13. R. Staszewski, K. Cieśla, J. J. Chwastowski. Forward proton detectors in heavy ion physics. In: *XXV Cracow EPIPHANY Conference on Advances in Heavy Ion Physics, 8–11 January* (2019).

Received 08.07.19

К. Чешла, Р. Сташевскі, Й.Й. Хвастовскі

ПРО ВИЗНАЧЕННЯ ЦЕНТРАЛЬНОСТІ
ЗА ДОПОМОГОЮ ДЕТЕКТОРІВ ПРОТОНІВ,
ЩО ВИЛІТАЮТЬ УПЕРЕД

Р е з ю м е

Вивчаються детектори протонів, що вилітають уперед, які вже встановлені на великому Адронному Колайдері, для дослідження зіткнень важких іонів. Демонструються можливості таких детекторів для вивчення продуктів поділу ядер – фрагментів спектаторів. Дана оцінка геометричного аксептансу детекторів протонів, що вилітають уперед, у випадку різних продуктів поділу. Вивчається вплив на аксептанс умов експерименту та руху Фермі. Обговорюється можливість реконструкції параметра зіткнень за допомогою вимірювання ядерних фрагментів.

https://doi.org/10.15407/ujpe64.7.560

D. DITTERT
for the HADES Collaboration
Institut für Kernphysik, Technische Universiät Darmstadt
(Darmstadt, Germany; e-mail: d.dittert@gsi.de)

ELECTROMAGNETIC RADIATION FROM Au + Au COLLISIONS AT $\sqrt{s_{NN}} = 2.4$ GeV MEASURED WITH HADES

We present results of low-mass dielectron measurements from Au + Au collisions at $\sqrt{s_{NN}} = 2.4$ GeV *with HADES. The focus lies on the extraction of the effective temperature from the differential dilepton spectra and the analysis of the azimuthal anisotropy of virtual photons.*

Keywords: HADES, dielectrons, effective temperature, azimuthal anisotropy.

1. Introduction

The matter created in heavy-ion collisions at relativistic energies is rather compressed than heated, reaching net baryon densities of a few times normal nuclear matter density and moderate temperatures below 70 MeV/$k_{\rm B}$. Such matter is commonly described as the resonance matter consisting of a gas of nucleons and excited baryonic states, as well as contributions from mesonic excitations. Due to the compression in the inital phase of the collision, the hadron properties are substantialy modified. To understand the microscopic structure of baryon-dominated matter, HADES systematically measures virtual photons, that decay into dileptons, from elementary and heavy-ion collisions. These electromagnetic probes access the entire space-time evolution of a fireball and leave the collision zone without further interactions. Moreover, in contrast to real photons, they carry an additional information through their invariant mass. Thus, they provide the unique information about the various stages of the collision.

In Au + Au at $\sqrt{s_{NN}} = 2.4$ GeV, HADES observed a strong excess radiation which is remarkably well described assuming the emission out of a thermalized system [1]. Thus, the results imply strong medium effects beyond a pure superposition of individual nucleon-nucleon (pp, np) collisions.

The total yield of dileptons in the low-mass region up to 1 GeV/c^2 is related to the fireball lifetime [2]. The inverse slope of the invariant mass spectra provides information about the temperature in the system averaged over the whole space-time evolution of the collision [3, 4]. To gain a further insight, the dependence of those temperatures on the virtual photon transverse momentum and rapidity and on the event centrality can be studied. Furthermore, the shapes of the spectra can be confronted with model calculations to obtain the understanding of the processes occurring in low-energy heavy-ion collisions such as the establishment of a local thermal equilibrium and the restoration of the chiral symmetry at high densities leading to modifications in the low-mass in-medium vector meson spectral function [2,5–8]. Using a coarse-grained transport calculation to describe the fireball evolution leads to a good agreement with the experimental data in the region $M_{ee} > 0.3$ GeV/c^2 [9, 10].

This approach implies a locally equilibrated system for which the corresponding thermodynamic parameters can be extracted [2]. However, non-equilibrated transport-calculations also describe the data points without significant deviations.

In addition, the observables related to the collectivity of a system, e.g., the flow, are used to describe the macroscopic properties of nuclear matter. The collective flow consists of a radial flow, which affects the thermal spectra of the outgoing particles, and anisotropic flow, which affects the spatial orientation of the particle momenta. The azimuthal anisotropy is especially useful to disentangle early and late emission sources, because the effective temperature results from the superposition of all fireball stages with decreasing the temperature T, but increasing the flow β_T over time (see Eq. 4). The azimuthal anisotropies, on the other hand, are actually small in the early phases of the fireball evolution, where the flow is not yet fully developed and grow larger for the later phases. Thus, the elliptic flow does not show this implicit time dependence, and the combined dependence of the elliptic flow of dileptons on their transverse momentum and their invariant mass provides a rich landscape of structures, which allows one to set the observational window on specific stages of the fireball evolution [11].

2. Data Analysis and Signal Extraction

HADES at SIS18 (GSI, Darmstadt, Germany) is a fixed-target experiment. The spectrometer provides a large acceptance between 18° and 85° in the polar angle, as well as a nearly full azimuthal coverage. Figure 1 shows a 3D view of HADES with the main components of the detector. The Ring Imaging CHerenkov detector (RICH), the Time of Flight (TOF) and RPC detector, as well as the Pre-Shower detector, are mainly used for the particle identification, while four planes of low-mass MDCs in combination with a superconducting toroidal magnet are used to determine the particle tracks and momenta. In order to reduce the background from the photon conversion in a detector material, all tracking detectors are designed as light as possible. About 7 m behind the spectrometer, the Forward Wall is placed. It is used to reconstruct the event plane and to determine the centrality of a collision by measuring the spectator nucleons.

In twelve runs between 2002 and 2019, HADES collected data from various experiments at beam energies of 1–3.5 GeV. The size of the collision system ranged from elementary $p + p$ collisions over light- (C + C) and medium-sized (Ar + KCl) collision systems to the large Au + Au system. In the two runs performed in 2014, also the pion-induced reactions were investigated. Before the most recent run (Ag + Ag @ $\sqrt{s_{NN}} = 2.55$ GeV completed in March 2019), the major detector upgrades including the RICH detector and a new electromagnetic calorimeter were conducted. In this work, the results of analysis of the data taken from the Au + Au run at

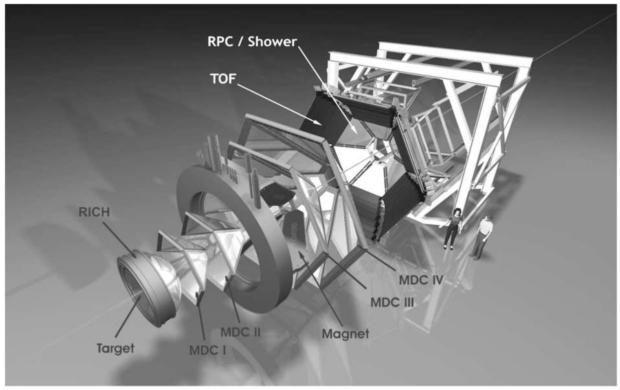

Fig. 1. 3D view of the HADES setup

2.4 GeV [1] in 2012 will be presented. In the five-week beamtime (overall 557 hours) with beam intensities between 1.2–1.5 $\times 10^6$ ions/s, the total of 7.3 billion events were collected and stored in 138 TB of data [13, 14].

After choosing only the events with a reaction vertex inside the target, rejecting the pile-up events and using a high-multiplicity trigger that selects 47% of the most central events along with event quality selection criteria, a clean sample of about 2.6×10^9 events were left to analyze.

Dileptons are very rare due to low branching ratios, e.g., $\Gamma_{ee}/\Gamma = (4.72 \pm 0.05) \times 10^{-5}$ in the case of a ρ-meson [15]. Thus, a very precise particle identification is crucial for reliable measurements. To separate the leptons from the hadronic background, the hard cuts in one or two dimensions can be applied on various observables. However, a better performance can be achieved, by considering the correlations between all the observables simultaneously, i.e., by using Multivariate Analysis (MVA) methods. They allowed us to identify single leptons with a very high purity of at least 98% and a good efficiency. In order to take the step from the reconstructed single electron signal to the dilepton spectra, the electron-positron pairs have to be build. It is not possible to identify electrons and protons from the same vertex. Instead, all possible unlike-sign pair combinations are calculated event-by-event (Fig. 2, black circles). This leads to a large contribution of wrong pair-

[1] A center-of-mass energy of $\sqrt{s_{NN}} = 2.42$ GeV corresponds to a beam energy of $E_{\mathrm{beam}} = 1.23A$ GeV and a center-of-mass rapidity of $y_{\mathrm{mid}} = 0.74$.

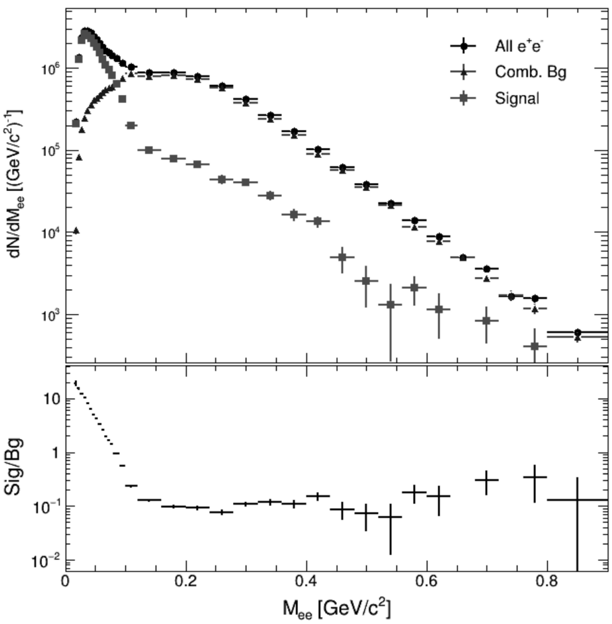

Fig. 2. Resulting dilepton spectrum and signal-to-background ratio

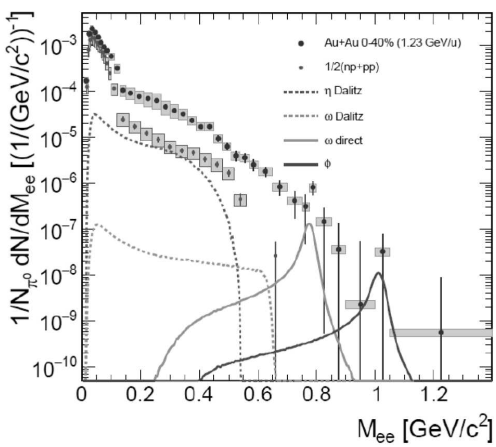

Fig. 3. Efficiency corrected dilepton spectrum is shown alongside a simulated cocktail of contributions from first chance collisions and the freeze-out stage [17]

ings to the final spectra. This so-called combinatorial background has to be subtracted from all pairs to obtain the true signal pairs (Fig. 2, blue triangles). As usual, two types of fake lepton pairs are distinguished, namely, the uncorrelated and correlated backgrounds. The former one stems from the pairing of leptons, originating from different mother particles, which is the largest contribution to the combinatorial background. Due to the random combination of two different decays, it is structureless. In the case of a two-photon decay or a Dalitz decay with the subsequent photon conversion of a neutral meson, it can happen that the paired leptons have different mother particles, but share their grandparent. The correlation of these pairs leads to a background contribution with a bump-like structure. While the uncorrelated background can be reproduced using the event mixing, the correlated background, which is dominant in the low-mass region, is handled using a same-event like-sign technique. The signal is a result of subtracting the combinatorial background from all e^+e^- combinations (Fig. 2, red squares). The signal-to-background ratio (bottom panel of Fig. 2) is $\sim 10\%$ for the invariant masses above 0.15 GeV/c^2.

3. Anisotropy Analysis

The flow coefficients v_1 (directed flow), v_2 (elliptic flow), v_3 (triangular flow), *etc.* are defined as the Fourier coefficients of the azimuthal angle expansion [16]:

$$\frac{dN}{d\Delta\Phi} \propto 1 + 2\sum_{n=1}^{\infty} v_n \cos(n\Delta\Phi), \quad \Delta\Phi = \Phi_{ee} - \Psi_{\mathrm{EP}}. \tag{1}$$

To extract the $\Delta\Phi$ of dileptons, the difference of the azimuthal angle of the dilepton pair (Φ_{ee}) and the angle of the event plane (Ψ_{EP}), which is determined using the information of the spectator hits in the Forward Wall, is calculated. This subtraction is necessary due to the correlation between the directed and elliptic flow components and the collision geometry. Furthermore, a correction factor accounting for the event plane angle resolution has to be applied [18]. The anisotropy coefficient v_2^{sig} of the signal pairs is then calculated from [19]:

$$v_2^{\mathrm{sig}} = \frac{1}{r} v_2^{\mathrm{tot}} - \frac{1-r}{r} v_2^{\mathrm{bg}}, \tag{2}$$

where r is the mass-dependent signal-to-background ratio, and v_2^{sig}, v_2^{tot}, and v_2^{bg} represent the flow coefficients for the signal pairs, all pairs, and the combinatorial background pairs. The latter ones are determined using different methods, namely, the same-event like-sign geometric mean background, mixed-event unlike-sign background and making an assumption that the combinatorial pairs, being built from the same single particles as signal pairs, have also the same orientation with respect to the reaction plane. To obtain a final value for the azimuthal anisotropy, the mean of the different methods is calculated. Their standard deviation is used to determine the systematic uncertainty. The statistical uncertainties are taken from the same-event like-sign geometric mean background for the lowest mass region, where the correlated background from π^0-Dalitz decays is dominant, and from the mixed-event background in the mass regions above.

4. Results

Figure 4 shows the effective slope parameter T_{slope} as a function of the invariant mass of the dielectron pairs, resulting from the fit:

$$\frac{1}{p_T}\frac{dN}{dp_T} \propto m_T K_1\left(\frac{m_T c^2}{k_{\text{B}}T_{\text{slope}}}\right), \tag{3}$$

with $m_T = \sqrt{M_{ee}^2 + p_T^2 c^2}$ and the assumption of a pure Boltzmann nature of the source. Since only a small fraction of the dilepton yield is lying outside of the HADES acceptance, which can be verified by comparing the rapidity spectra to different model calculations, this assumption is justified and is valid to apply a thermal fit without prior extrapolation to the unmeasured rapidity. Utilizing the good agreement between the shapes of the model fits and the experimental p_T spectra, a parametrization of the slopes from the model provides a further quantitative information. From

$$k_{\text{B}}T_{\text{slope}} = k_{\text{B}}T_{\text{kin}} + \frac{1}{2}M_{ee}c^2\langle\beta_T\rangle^2, \tag{4}$$

where T_{kin} and $\langle\beta_T\rangle$ in the case of dileptons can be interpreted as the properties of their source averaged over four-volume, rather than of the freeze-out hypersurface, the values $T_{\text{kin}} = 65$ MeV$/k_{\text{B}}$, $\langle\beta_T\rangle = 0.19$ for the coarse-grained (CG) approach plus cocktail and $T_{\text{kin}} = 74$ MeV$/k_{\text{B}}$, $\langle\beta_T\rangle = 0.05$ for Hadron String Dynamics (HSD) can be extracted. Extrapolating those model fits to the zero invariant mass results in $T_{\min} = 61$ MeV$/k_{\text{B}}$ and $T_{\min} = 69$ MeV$/k_{\text{B}}$, respectively. However, more precise experimental data are needed to decide for one model or another one. Contrary to hadrons [22, 23], the slope parameter is not dependent on the invariant mass, but stays rather constant over the whole mass range. This is due to the very low transverse velocity $\langle\beta_T\rangle$, indicating that the majority of dileptons is emitted at an early phase, thus not carrying the full $\langle\beta_T\rangle$ established at the freeze-out.

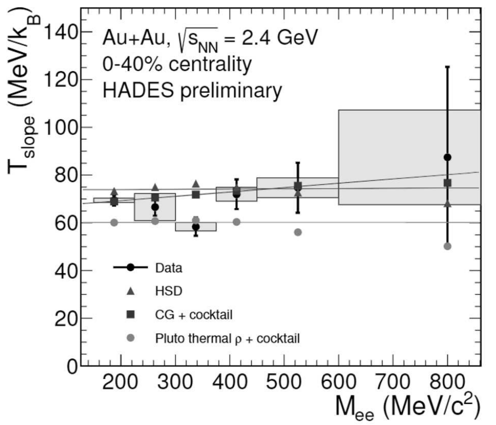

Fig. 4. Fitted slope parameters of the p_T-spectra in experimental data and model calculations of HSD [20], freeze-out meson cocktail combined with the in-medium ρ-spectral function [2] (denoted as CG), and the same cocktail combined with simple thermal ρ simulated using the Pluto event generator [21]. Solid curves represent the parametrization in Eq. 4, fitted to the model points [24]

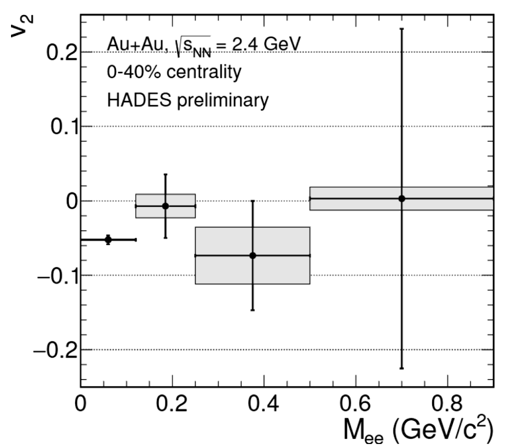

Fig. 5. v_2 coefficient of signal dileptons as a function of the invariant mass [24]

The second Fourier harmonic of the azimuthal anisotropy as a function of the invariant mass is shown in Fig. 5. The value in the lowest mass region $\left(0 \le M_{ee}\ [\text{GeV}/c^2] \le 0.12\right)$, where the dilepton spectrum is dominated by π^0-Dalitz decays, is in a good agreement with the elliptic flow seen in charged pions (see Fig. 6). A negative sign of v_2

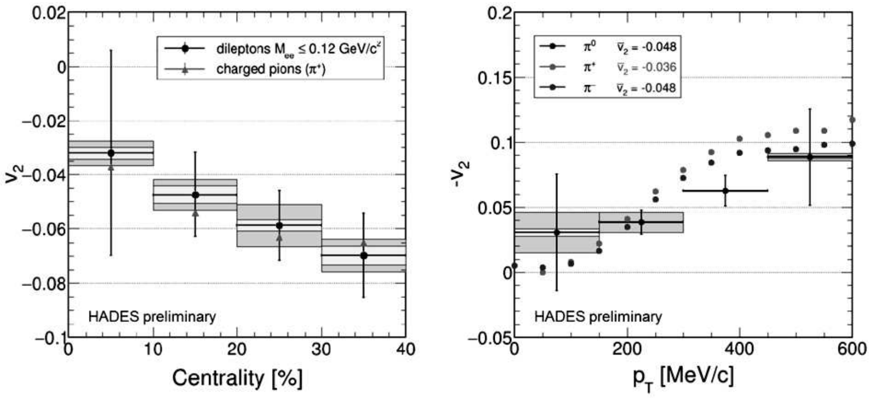

Fig. 6. v_2 of dileptons below 0.12 GeV/c^2 and charged pions as functions of the centrality and transverse momentum

means that the majority of the particles is ejected perpendicularly to the event plane. This out-of-plane flow can be explained by the passing spectator nuclei shadowing the collision center. This shadowing effect reduces the mean free path of particles that are emitted into the reaction plane, which leads to a squeeze-out of ejectiles perpendicularly to the reaction plane. At masses above the π^0-region, the azimuthal anisotropy seems to decrease and indeed is consistent with zero. Recalling the cocktail contributions shown in Fig. 3, it becomes apparent that the physics background contribution in those mass regions is at the level of at most 10% from η-decays, thus much lower than the 90% pion contribution in the first mass bin, meaning that those dileptons are mostly stemming from an early phase before the build-up of the flow. This is consistent with the observed very low transverse velocity discussed above. An alternative explanation of the vanishing azimuthal anisotropy is given by the penetrating nature of dileptons, which therefore do not experience the shadowing effect of the spectator matter [25]. More insights will be provided with the new set of data collected in March 2019, and that data are awaiting for theory interpretations. Figure 6 shows a comparison between v_2 of dileptons below 0.12 GeV/c^2 and charged pions. In the left panel, the centrality-dependent elliptic flow is plotted. As the collision gets more peripheral, more spectator nucleons are shielding the collision zone resulting in a stronger, i.e. more negative, flow. The values from the dileptons from π^0-decays and the charged pions are in a very good agreement. The same is true for the transverse-momentum-dependent flow coefficients shown in the right panel.

5. Conclusions

The results from the dilepton analysis in Au + Au collisions at 2.4 GeV show a clear evidence for the penetrating nature of the electromagnetic probes. The very low transverse velocity indicates that the majority of dileptons is ejected before the freeze-out, where the full transverse velocity seen in hadrons would have build up. The same is true for the creation of a flow in the system. Thus, the dileptons, which do not stem from hadronic decays show little or no azimuthal anisotropy. However, both methods would profit from higher statistics, as it is not possible up to now to definitely rule out one of the models with the inverse slope analysis or extract the azimuthal anisotropy with higher precision. In the most recent HADES beamtime with Ag + Ag at $\sqrt{s_{NN}} =$ = 2.55 GeV, conducted in March 2019, ∼15 billion events were collected, and the first low-level analysis promises high statistics and a very good data quality. Moreover, a newly installed electromagnetic calorimeter allows one to directly detect neutral mesons, making it possible to further determine the physics background in the dilepton spectra. In addition, the effects of the system size can be investigated. Combining the presented Au + Au data with the recently measured Ag + Ag run, as well as Ar + KCl at $\sqrt{s_{NN}} = 2.6$ GeV, will help one to draw a more complete picture.

This work was supported by BMBF:05P18RDFC1.

1. J. Adamczewski-Musch *et al.* for the HADES Collaboration. Probing dense baryon-rich matter with virtual photons. *Nature Physics* (2019) [DOI: https://doi.org/10.1038/s41567-019-0583-8].
2. T. Galatyuk, P. Hohler, R. Rapp, F. Seck, J. Stroth. Thermal dileptons from coarse-grained transport as fireball probes at SIS energies. *Eur. Phys. J. A* **52**, 131 (2016).
3. H. Specht. Thermal dileptons from hot and dense strongly interacting matter. *AIP Conf. Proceed.* **1322**, 1 (2010).
4. R. Rapp, H. van Hees. Thermal dileptons as fireball thermometer and chronometer. *Phys. Lett. B* **753**, 586 (2016).
5. R. Rapp, J. Wambach, H. van Hees. The chiral restoration transition of QCD and low mass dileptons. *Landolt-Bornstein* **23**, 134 (2010).
6. S. Endres, H. van Hees, J. Weil, M. Bleicher. Dilepton production and reaction dynamics in heavy-ion collisions at SIS energies from coarse-grained transport simulations. *Phys. Rev. C* **92**, 014911 (2015).
7. S. Endres, H. van Hees, J. Weil, M. Bleicher. Coarse-graining approach for dilepton production at energies available at the CERN Super Proton Synchrotron. *Phys. Rev. C* **91**, 054911 (2015).
8. J. Staudenmaier, J. Weil, V. Steinberg, S. Endres, H. Petersen. Dilepton production and resonance properties within a new hadronic transport approach in the context of the GSI-HADES experimental data. *Phys. Rev. C* **98** (5), 054908 (2018).
9. S. Harabasz, (HADES Collaboration). Exploring barion rich matter with heavy-ion collisions. *Ukr. Phys. J.* **64**, 563 (2019).
10. F. Seck, T. Galatyuk, R. Rapp, J. Stroth. Probing the fireball at SIS-18 energies with thermal dilepton radiadtion. *Acta Phys. Polon. Supp.* **10**, 717 (2017).
11. R. Rapp. Dilepton spectroscopy of QCD matter at collider energies. *Adv. High Energy Phys.* **2013**, Article ID 148253 (2013).
12. C. Müntz *et al.* for the HADES-MDC Collaboration. The HADES tracking system. *Nucl. Instrum. Meth. A* **535**, 242 (2004).
13. T. Galatyuk. HADES overview. *Nucl. Phys. A*, **931**, 41 (2014).
14. List of all HADES beamtimes [URL:https://www-hades.gsi.de/?q=node/5].
15. C. Patrignani *et al.* (Particle Data Group). Review of particle physics. *Chinese Phys. C* **40**, 10 (2016).
16. G. Vujanovic, C. Young, B. Schenke, R. Rapp, S. Jeon, C. Gale. Dilepton emission in high-energy heavy-ion collisions with viscous hydrodynamics. *Phys. Rev. C* **89**, 034904 (2014).
17. P. Sellheim. Reconstruction of the low-mass dielectron signal in 1.23A GeV Au + Au collisions. *PhD thesis* (Johann Wolfgang Goethe-Universitet, 2017).
18. J.-Y. Ollitrault. Flow systematics from SIS to SPS energies. *Nucl. Phys. A* **638** (1–2), 195 (1998).
19. L. Adamczyk, *et al.* Dielectron azimuthal anisotropy at mid-rapidity in Au + Au collisions at $\sqrt{s_{NN}} = 200$ GeV. *Phys. Rev. C* **90**, 064904 (2014).
20. E. Bratkovskaya, J. Aichelin, M. Thomere, S. Vogel, M. Bleicher. System size and energy dependence of dilepton production in heavy-ion collisions at 1–2 GeV/nucleon energies. *Phys. Rev. C* **87**, 064907 (2013).
21. I. Fröhlich, T. Galatyuk, R. Holzmann, J. Markert, B. Ramstein, P. Salabura, J. Stroth. Design of the Pluto event generator. *J. Phys. Conf. Ser.* **219**, 032039 (2010).
22. J. Adamczewski-Musch *et al.* for the HADES Collaboration. Deep sub-threshold Φ production in Au + Au collisions. *Phys. Lett. B* **778**, 403 (2018).
23. J. Adamczewski-Musch *et al.* for the HADES Collaboration. Sub-threshold production of K^0_s mesons and Λ hyperons in Au + Au collisions at $\sqrt{s_{NN}} = 2.4$ GeV. *Phys. Lett. B* **793**, 457 (2019).
24. S. Harabasz. Multi-differential pattern of low-mass e^+e^- excess from $\sqrt{s_{NN}} = 2.4$ GeV Au + Au collisions with HADES. *Nucl. Phys. A* **982**, 771 (2019).
25. A. Wagner *et al.* The emission pattern of high-energy pions: A new probe for the early phase of heavy ion collisions. *Phys. Rev. Lett.* **85** 18 (2000).

Received 08.07.19

Д. Діттерт
від імені Колаборації HADES

ЕЛЕКТРОМАГНІТНЕ ВИПРОМІНЮВАННЯ
В ЗІТКНЕННЯХ Au + Au ПРИ ЕНЕРГІЇ 2,4 ГеВ,
В ДОСЛІДАХ НА HADES

Р е з ю м е

Представляємо результати вимірювання діелектронів малих мас у зіткненнях Au + Au при енергії 2,4 ГеВ у дослідах на HADES з метою отримання ефективної температури з диференційного спектра ділептонів, а також для аналізу азимутальної анізотропії віртуальних фотонів.

https://doi.org/10.15407/ujpe64.7.566

F. FIONDA
on behalf of the ALICE Collaboration
Department of Physics and Technology, University of Bergen
(55, Allegaten, Bergen 5007, Norway; e-mail: fiorella.fionda@cern.ch)

QUARKONIUM PRODUCTION MEASUREMENTS WITH THE ALICE DETECTOR AT THE LHC

In (ultra-)relativistic heavy-ion collisions, the strongly interacting matter is predicted to undergo a phase transition into a plasma of deconfined quarks and gluons (QGP), and quarkonia probe different aspects of this medium. However, the medium modification of the quarkonium production includes also the contribution of cold nuclear matter effects (CNM), such as the shadowing or nuclear break-up in addition to QGP effects. Proton–nucleus collisions, where no QGP is expected, are used to measure cold nuclear matter effects on the quarkonium production. The vacuum production of quarkonia is modeled in proton–proton (pp) collisions, which are used as the reference for both heavy-ion and proton–nucleus collisions. Besides serving as a reference, the results in pp collisions represent a benchmark test of QCD-based models in both perturbative and non-perturbative regimes. The ALICE detector has unique capabilities at the LHC for measuring quarkonia down to the zero transverse momentum. Measurements are carried out at both central and forward rapidities in the dielectron and dimuon decay channels, respectively. In this contribution, the latest quarkonium measurements performed by the ALICE Collaboration during the LHC Run-2 period for various energies and colliding systems will be discussed.

K e y w o r d s: QGP, quarkonium,relativistic heavy-ion collisions, cold nuclear matter effects.

1. Physics Motivations

Quarkonium measurements represent an important tool for the investigation of the interaction of heavy quarks with the hot and energy-dense medium created in heavy-ion collisions, known as Quark–Gluon Plasma (QGP) [1], and provide an important insight about its properties. In the original prediction by Matsui and Satz [2], it was argued that quarkonium states could melt in a deconfined medium, since the binding energy between the quark and antiquark is screened due to the presence of free color charges. This implies that the quarkonium production in heavy-ion collisions should be suppressed as compared to binary-scaled *pp* collisions. However, it is also argued that the large production cross-section of heavy quarks in the hot thermalized medium leads to the (re)generation of quarkonia via the statistical recombination at the phase boundary [3] or through the coalescence of charm quarks [4]. Models including (re)generation describe the majority of charmonium measurements from LHC Run-1 (2009–2013), showing already the evidence that the (re)generation is the dominant production mechanism of J/ψ in heavy-ion collisions at LHC energies [5]. Measurements of the bottomonium production, for which the contribution from the (re)generation could be small due to the much smaller beauty production cross-section, and the comparison with the corresponding charmonium results can further shed light on the quarkonium production mechanisms in large systems. Furthermore, if heavy-flavor quarks thermalize in the QGP, regenerated quarkonium states could inherit their flow and then participate in the collective motion of the QGP.

The study of the quarkonium production in proton–nucleus collisions is relevant to quantify cold nuclear matter (CNM) effects. Mechanisms such as a modification of the parton distribution functions in nuclei, the presence of a Color Glass Condensate (CGC), and coherent energy loss of the $c\bar{c}$ or $b\bar{b}$ pair in the medium have been employed to describe the

J/ψ and Υ production obtained in proton–nucleus collisions from the LHC Run-1 [6–8].

In elementary pp collisions, the production of a quarkonium state can be understood as the creation of a heavy-quark pair ($q\bar{q}$) followed by its binding into a state with given quantum numbers. The first step is well described by perturbative quantum chromodynamics (QCD), while the second step is inherently non-perturbative. Currently, none of the existing models is able to satisfactorily describe simultaneously all aspects of the quarkonium production in pp collisions. Therefore, more differential measurements represent a powerful tool for adding further constraints to quarkonium production models, improving significantly our understanding of quarkonium production mechanisms in elementary hadronic collisions.

2. Quarkonium Measurements in ALICE

The ALICE detector [9] has unique capabilities to measure the quarkonium production down to the zero transverse momentum (p_{T}) in two rapidity ranges [1]: at mid-rapidity ($|y| < 0.9$) with the central barrel through the dielectron decay channel and at forward rapidity ($2.5 < y < 4$) with the muon arm through the dimuon decay channel.

The main tracking detectors in the central barrel are the Inner Tracking System (ITS) and the Time Projection Chamber (TPC). The ITS provides the primary and secondary vertex information, the latter is useful to separate the non-prompt J/ψ contribution (from beauty-hadron decays). The TPC provides the excellent particle identification for particles with intermediate momenta, in particular, for electrons up to about 10 GeV/c, based on the measurement of their specific energy loss.

The forward muon spectrometer includes a dipole magnet with an integrated field of 3 T·m, five tracking stations comprising two planes of cathode pad chambers each, and two trigger stations consisting of two planes of resistive plate chambers each. The latter allows one to trigger on events with at least a pair of opposite-sign track segments in the muon trigger system, each with a p_{T} above a specific threshold. A system of absorbers is used for filtering out hadrons.

[1] The rapidity ranges are quoted in the "laboratory" reference frame ($y = y_{\mathrm{lab}}$) which is coincident with the center-of-mass reference frame (y_{cms}) in pp and Pb–Pb collisions, but not in p-Pb collisions because of the asymmetric beam conditions.

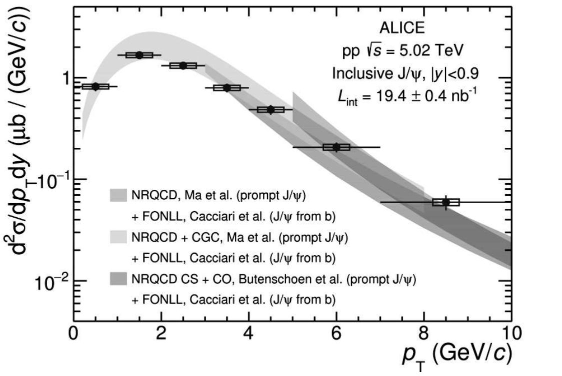

Fig. 1. p_{T}-differential inclusive J/ψ cross-section measured at mid-rapidity in pp collisions at $\sqrt{s} = 5$ TeV compared to prompt J/ψ NRQCD calculations added to predictions of non-prompt J/ψ from FONLL (see [10] and references therein)

3. Results: Selected Highlights

3.1. pp collisions

An extensive study of quarkonium production cross-sections in pp collisions has been performed by the ALICE Collaboration at several center-of-mass energies.

In Fig. 1, the inclusive J/ψ cross-section measured at mid-rapidity at $\sqrt{s} = 5$ TeV (see [10] and references therein) is compared to different sets of Non-Relativistic QCD (NRQCD) calculations of the prompt J/ψ production.

The model from Ma *et al.* is coupled to a CGC description of the low-x gluons in the proton and can predict the prompt J/ψ cross-sections down to $p_{\mathrm{T}} = 0$. In all cases, the non-prompt J/ψ component calculated from Fixed-Order Next-To-Leading-Logarithm (FONLL) predictions is added to the prompt J/ψ contribution.

The agreement between all models and data is good in the measured p_{T} range. It is worth noting that the uncertainties on the data points are significantly smaller than the model uncertainties, especially at low p_{T}. The ψ(2S)-to-J/ψ cross-section ratio, measured at the forward rapidity as a function of p_{T} in pp collisions at $\sqrt{s} = 13$ TeV, is compared to NLO NRQCD calculations in Fig. 2 (see [11] and references therein). In the ratio, many of the systematic uncertainties cancel for both data and model.

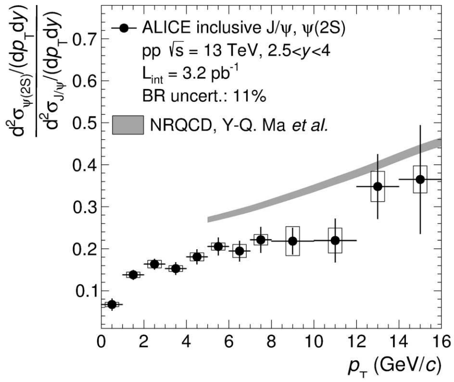

Fig. 2. ψ(2S)-to-J/ψ cross-section ratio as a function of $p_{\rm T}$ in *pp* collisions at $\sqrt{s}$ = 13 TeV measured at the forward rapidity as compared to NLO NRQCD calculations (see [11] and references therein)

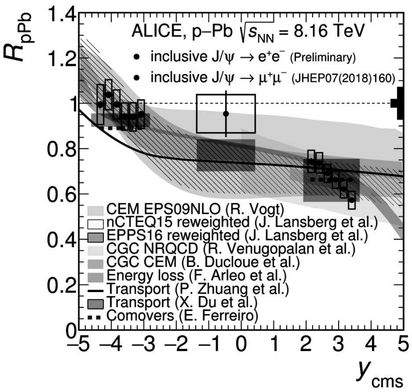

Fig. 3. $R_{p\text{-Pb}}$ as a function of $y_{\rm cms}$ of the J/ψ in p-Pb collisions at $\sqrt{s}_{\rm NN}$ = 8.16 TeV. The results are compared to several theoretical predictions (see [13] and references therein; for the model of Du *et al.* see [14])

From the comparison, it is clear that there are still tensions between data and models. Similarly, discrepancies are observed for polarization measurements performed in *pp* collisions at $\sqrt{s}$ = 8 TeV at the forward rapidity [12].

3.2. p-Pb collisions

The nuclear effects on the quarkonium production in p-Pb collisions are estimated via the $p_{\rm T}$ and rapidity differential nuclear modification factor defined as

$$R_{p\text{-Pb}}(y_{\rm cms}, p_{\rm T}) = \frac{{\rm d}^2\sigma^{\rm onium}_{p\text{-Pb}}/{\rm d}y_{\rm cms}{\rm d}p_{\rm T}}{A_{\rm Pb}\,{\rm d}^2\sigma^{\rm onium}_{pp}/{\rm d}y_{\rm cms}{\rm d}p_{\rm T}},$$

where the p-Pb production cross-section of a given quarkonium state, ${\rm d}^2\sigma^{\rm onium}_{p\text{-Pb}}/{\rm d}y_{\rm cms}{\rm d}p_{\rm T}$, is normalized to the corresponding quantity for *pp* collisions times the atomic mass number of a Pb nucleus ($A_{\rm Pb}$ = = 208). The $p_{\rm T}$-integrated $R_{p\text{-Pb}}$ of inclusive J/ψ, measured in p-Pb collisions at $\sqrt{s_{\rm NN}}$ = 8.16 TeV, is shown in Fig. 3 as a function of the center-of-mass rapidity, $y_{\rm cms}$. Measurements in the dimuon channel are performed by taking data in two configurations of the beams with either protons or Pb ions going toward the muon spectrometer, corresponding to forward and backward rapidities, respectively. For the mid-rapidity measurement, the data corresponding to the two configurations can be combined due to the symmetry of the central barrel detector. The nuclear modification factor is compatible with unity at backward and mid-rapidities. In contrast, a suppression is visible at the forward rapidity. It is compared to several theoretical models which attempt to describe the prompt J/ψ production (see [13] and references therein; for the model of Du *et al.* see [14]). The results of calculations based on shadowing only show a good agreement with data, when the nCTEQ15 or EPPS16 set of nuclear parton distribution functions (nPDF) are adopted (Lansberg *et al.*), while using the EPS09 set of nPDF leads to a slightly worse agreement at the forward $y_{\rm cms}$ (Vogt). Calculations based on a CGC approach coupled with various quarkonium vacuum production models are able to reproduce the data in their domain of validity, corresponding to the forward-$y_{\rm cms}$ region (Venugopalan *et al.*; Ducloue *et al.*). The model of Arleo *et al.*, based on the calculation of the effects of parton coherent energy loss, gives a good description of the results for both backward-$y_{\rm cms}$ and forward-$y_{\rm cms}$ rapidities. Finally, models including a contribution from the final state interactions of the $c\bar{c}$ pair with the partonic/hadronic system created in the collision (Zhuang *et al.*; Du *et al.*; Ferreiro) can also reproduce the trend observed in the data. In the latter set of models, the nuclear shadowing is included, and it is the mechanism that plays a dominant role in determining the values of the nuclear modification factors.

The $R_{p\text{-Pb}}$ for ψ(2S) as a function of $y_{\rm cms}$ is shown in Fig. 4, where it is compared to the corresponding J/ψ result. At the forward rapidity, J/ψ and ψ(2S) show a similar suppression, while, at the backward rapidity, ψ(2S) is significantly more suppressed than J/ψ. Contrary to the J/ψ case, only models that include final state interactions with the surrounding medium are able to reproduce ψ(2S) results.

The ALICE Collaboration has also measured long-range correlations between forward-$y_{\rm cms}$ and backward-$y_{\rm cms}$ inclusive J/ψ and mid-rapidity charged hadrons, in p-Pb collisions at both $\sqrt{s}_{\rm NN} = 5.02$ and 8.16 TeV [15]. The data indicate persisting long-range correlation structures at $\Delta\phi \sim 0$ and $\Delta\phi \sim \pi$, reminiscent of the double ridge previously found in charged-particle correlations at mid- and forward rapidities [16]. The corresponding $v_2^{J/\psi}$, obtained by combining data of the two collision energies, is shown in Fig. 5. In heavy-ion collisions, this coefficient is related to the azimuthal anisotropy of the final-state particle momentum distribution and is sensitive to the geometry and the dynamics of the early stages of the collision. The results in p-Pb collisions are compared to $v_2^{J/\psi}$ measurements performed in Pb–Pb collisions at $\sqrt{s_{\rm NN}} = 5.02$ TeV [17]. The positive v_2 coefficients observed in Pb–Pb collisions for ${p_{\rm T}}^{J/\psi}$ below 3–4 GeV/c are believed to originate from the recombination of charm quarks thermalized in the medium and are described fairly well by the transport model. In p-Pb collisions, the $v_2^{J/\psi}$ is compatible with zero at low $p_{\rm T}$, and this is in line with expectations, since no QGP is expected to be produced in which charm quarks could thermalize. Even assuming such scenario, the amount of produced charm quarks is small compared to that in heavy-ion collisions. Therefore, the contribution from the recombination should be negligible. However, at high-$p_{\rm T}$, J/ψ v_2 is comparable to the magnitude of the flow observed in central Pb–Pb collisions. It is worth noting that, in Pb–Pb collisions, the measured $v_2^{J/\psi}$ coefficients exceed substantially the theoretical predictions for $p_{\rm T}^{J/\psi} > 4$ GeV/c, where the main contribution to $v_2^{J/\psi}$ is expected to come from the path-length dependent suppression inside the medium. These intriguing results point to a common underlying mechanism, not included in current calculations, at the origin of the comparable magnitude of the $v_2^{J/\psi}$ at a high transverse momentum in both systems.

3.3. Pb–Pb collisions

The nuclear modification factor, for a quarkonium state in a given centrality class i of the Pb–Pb collision, is calculated as

$$R^1_{\rm Pb-Pb}(y, p_{\rm T}) = \frac{{\rm d}^2 N^{\rm onium}_{{\rm Pb-Pb},i}/{\rm d}y{\rm d}p_{\rm T}}{\langle T^i_{\rm AA}\rangle \, {\rm d}^2\sigma^{\rm onium}_{pp}/{\rm d}y{\rm d}p_{\rm T}},$$

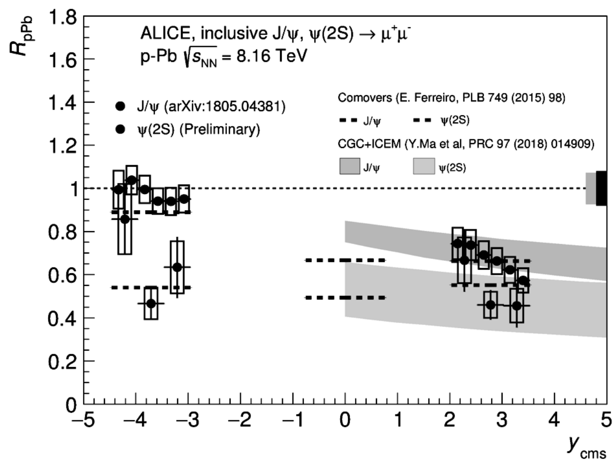

Fig. 4. $R_{p\text{-Pb}}$ as a function of $y_{\rm cms}$ for ψ(2S) and J/ψ in p-Pb collisions at $\sqrt{s}_{\rm NN} = 8.16$ TeV. The results are compared to different theoretical models (see references on the plot)

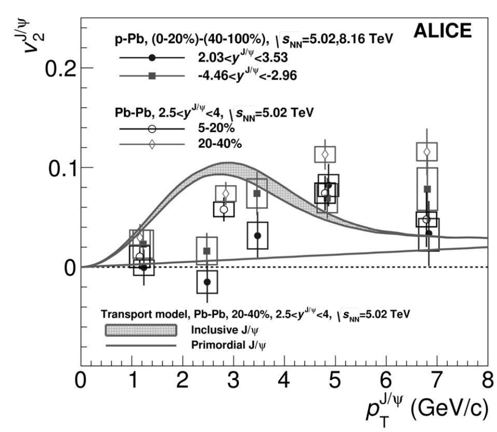

Fig. 5. Combined $v_2^{J/\psi}$ coefficients in p-Pb collisions at $\sqrt{s_{\rm NN}} = 5.02$ and 8.16 TeV compared to results in central and semicentral Pb–Pb collisions at $\sqrt{s_{\rm NN}} = 5.02$ TeV and to the transport model calculations for semicentral Pb–Pb collisions (see [15] and references therein).

where ${\rm d}^2 N^{\rm onium}_{{\rm Pb-Pb},i}/{\rm d}y{\rm d}p_{\rm T}$ is the corrected yield of the studied quarkonium state in Pb–Pb collisions, $\langle T^i_{\rm AA}\rangle$ is the nuclear overlap function, and ${\rm d}^2\sigma^{\rm onium}_{\rm pp}/{\rm d}y{\rm d}p_{\rm T}$ is the corresponding cross-section in pp collisions at the same center-of-mass energy. Figure 6 shows $R_{\rm AA}$ as a function of the centrality, for J/ψ measured at the forward rapidity in Pb–Pb collisions at $\sqrt{s_{\rm NN}} = 5.02$ TeV, in the transverse momentum range $0.3 < p_{\rm T} < < 8$ GeV/c [18]. The $p_{\rm T}$ region below 0.3 GeV/c was excluded in order to reduce significantly the contribution from the photo-production

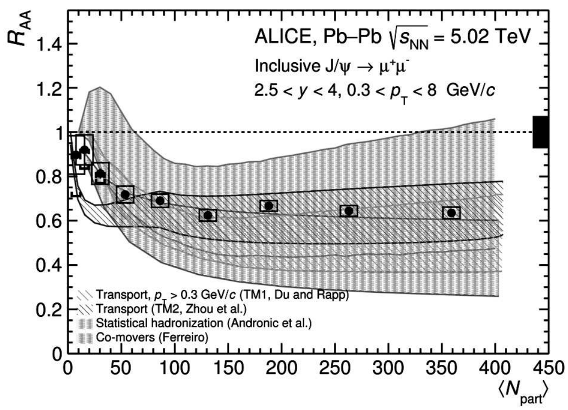

Fig. 6. Centrality dependence of inclusive J/ψ R_{AA} for $0.3 <$ $< p_{\mathrm{T}} < 8$ GeV/c measured in Pb–Pb collisions at $\sqrt{s_{\mathrm{NN}}} =$ $= 5.02$ TeV and comparison with theoretical models (see [18] and references therein)

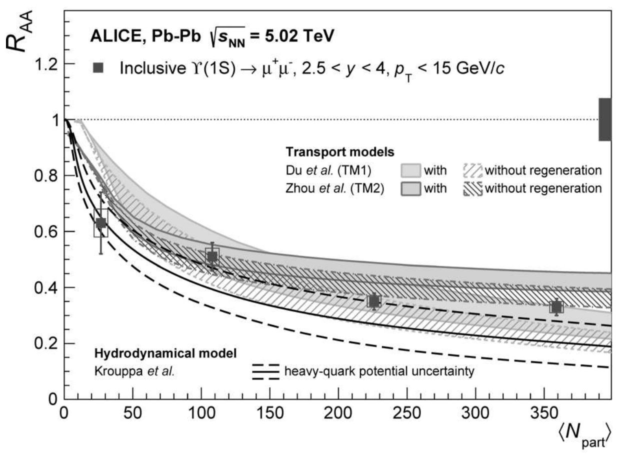

Fig. 7. Inclusive $\Upsilon(1\mathrm{S})$ R_{AA} as a function of the centrality measured at the forward rapidity in Pb–Pb collisions at $\sqrt{s_{\mathrm{NN}}} = 5.02$ TeV, compared to theoretical model calculations (see [20] and references therein)

of J/ψ, which could influence the R_{AA} in peripheral collisions [19]. The results are compared to several theoretical models. The statistical hadronization model assumes that J/ψ are created, like all other hadrons, only at the chemical freeze-out according to their statistical weights. Transport models are based on a thermal rate equation, which includes the continuous dissociation and regeneration of J/ψ, both in the QGP and in the hadronic phase. Finally, in the "co-mover" model, J/ψ are dissociated via interactions with the partons/hadrons produced in the same rapidity range, and the regeneration term is included

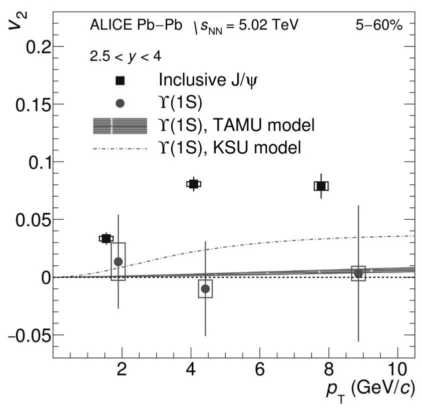

Fig. 8. The $\Upsilon(1S)$ v_2 coefficient as a function of p_{T} measured in Pb–Pb collisions at $\sqrt{s_{\mathrm{NN}}} = 5.02$ TeV in the 5–60% centrality interval compared to that of inclusive J/ψ and to theoretical calculations (see [21] and references therein)

as well. The data are described by the various calculations, the latter having rather large uncertainties. These are related to the choice of the corresponding input parameters, and in particular, the nucleon-nucleon $c\bar{c}$ production cross-section ($\mathrm{d}\sigma_{c\bar{c}}/\mathrm{d}y$), as well as the set of nPDF.

The centrality dependence of the nuclear modification factor for $\Upsilon(1\mathrm{S})$ measured in Pb–Pb collisions at $\sqrt{s_{\mathrm{NN}}} = 5.02$ TeV is shown in Fig. 7 along with several theoretical model calculations [20]. Both transport and dynamical model calculations reproduce qualitatively the observed centrality dependence. However, current uncertainties on both model and data prevent a firm conclusion regarding the contribution from the regeneration in the bottomonium sector. Furthermore, more precise measurements of the feed-down contribution from higher-mass bottomonia to the $\Upsilon(1\mathrm{S})$ are needed for a correct interpretation of results. Further information about the interplay between the regeneration and suppression in the bottomonium sector can be provided by elliptic flow measurements. The v_2 of $\Upsilon(1\mathrm{S})$, obtained by combining data samples recorded by ALICE during the 2015 and 2018 LHC Pb–Pb runs at $\sqrt{s_{\mathrm{NN}}} = 5.02$ TeV, is shown in Fig. 8 in three p_{T} intervals [21] and is compared to the inclusive J/ψ v_2, measured in the same centrality and rapidity ranges. The $\Upsilon(1\mathrm{S})$ results are compatible with zero and with the small positive values predicted by the available theoretical models within uncertainties. Furthermore, the $\Upsilon(1\mathrm{S})$ v_2 is found to be lower by about 2.6σ compared to the one of the inclusive J/ψ in the centrality 5–60% and for $2 < p_{\rm T} < 15$ GeV/c. This observation, coupled to the different measured centrality and $p_{\rm T}$ dependences of the Υ(1S) and J/ψ suppression, provides a further evidence that, unlike Υ(1S), the J/ψ production has a significant regeneration component.

4. Conclusions and Future Perspectives

Selected quarkonium measurements in *pp*, *p*-Pb, and Pb–Pb collisions performed by the ALICE Collaboration are presented. In *pp* collisions, NRQCD predictions coupled with CGC fairly describe the data in a wide range of momentum and rapidity. However, some tensions between data and models are still present. In *p*-Pb collisions, theoretical models are in fair agreement with quarkonium results, in particular, for ψ(2S), models that include final state effects are able to describe the data. The positive v_2 measured for J/ψ is comparable with a similar measurement in Pb–Pb collisions for $p_{\rm T} > 44$ GeV/c. The latter exceeds theoretical predictions in Pb–Pb collisions at high $p_{\rm T}$, where the v_2 originates from the path-length suppression inside the medium. This intriguing observation points to a common mechanism at the origin of v_2 in both systems at high transverse momentum, besides what is currently included in the models. An extensive y and $p_{\rm T}$-differential studies of the J/ψ suppression in Pb–Pb collisions indicate that, at LHC energies, a significant contribution to the J/ψ yields originates from the regeneration mechanism. However, for a better discrimination among the models, an improved precision is needed for both data and theoretical predictions. $\Upsilon(1S)$ is found to be more suppressed than J/ψ. Currently, the comparison with models does not allow us to quantify the contribution from the regeneration. A large elliptic flow for J/ψ, measured at low $p_{\rm T}$, suggests the thermalization of charm quarks within the medium. On the contrary, the Υ(1S) v_2 is found to be compatible with zero and with values predicted by models, suggesting a negligible contribution from the regeneration mechanism in the bottonomium sector.

A significant improvement regarding the quarkonium measurements is expected for Run-3 (starting in 2021) and Run-4, when a major upgrade of the ALICE detector is foreseen [22]. A high-statistics minimum bias sample ($L_{\rm int} = 10$ nb^{-1}) will improve significantly mid-rapidity quarkonium measurements at low transverse momenta. Furthermore, a new Muon Forward Tracker (MFT) will be installed at the forward rapidity enabling the reconstruction of secondary vertices in this rapidity range, needed to measure the contribution of charmonia coming from beauty-hadron decays.

1. N. Cabibbo, G. Parisi. Exponential hadronic spectrum and quark liberation. *Phys. Lett. B* **59**, 67 (1975).
2. T. Matsui, H. Satz. J/ψ suppression by quark-gluon plasma formation. *Phys. Lett. B* **178**, 416 (1986).
3. P. Braun-Munzinger, J. Stachel. (Non)thermal aspects of charmonium production and a new look at J/ψ suppression. *Phys. Lett. B* **490**, 196 (2000).
4. R.L. Thews, M. Schroedter, J. Rafelski. Enhanced J/ψ production in deconfined quark matter. *Phys. Rev. C* **63**, 054905 (2001).
5. B. Abelev *et al.*, ALICE Coll. J/ψ Suppression at Forward Rapidity in Pb–Pb Collisions at $\sqrt{s_{\rm NN}} = 2.76$ TeV. *Phys. Rev. Lett.* **109**, 072301 (2012).
6. B. Abelev *et al.*, ALICE Coll. $J\psi$ production and nuclear effects in *p*-Pb collisions at $\sqrt{s_{\rm NN}} = 5.02$ TeV. *JHEP* **02**, 73 (2014).
7. J. Adam *et al.*, ALICE Coll. Centrality dependence of inclusive $J\psi$ production in *p*-Pb collisions at $\sqrt{s_{\rm NN}} = 5.02$ TeV. *JHEP* **11**, 127 (2015).
8. B. Abelev *et al.*, ALICE Coll. Production of inclusive Υ(1S) and Υ(2S) in *p*-Pb collisions at $\sqrt{s_{\rm NN}} = 5.02$ TeV. *Phys. Lett. B* **740**, 105 (2015).
9. K. Aamodt *et al.*, ALICE Coll. The ALICE experiment at the CERN LHC. *JINST* **3**, S08002 (2008).
10. S. Acharya *et al.*, ALICE Coll. Inclusive J/ψ production at mid-rapidity in *pp* collisions at $\sqrt{s} = 5.02$ TeV. arXiv:1905.07211 [nucl-ex] (2019).
11. S. Acharya *et al.*, ALICE Coll. Energy dependence of forward-rapidity J/ψ and ψ(2S) production in *pp* collisions at the LHC. *Eur. Phys. J. C* **77**, 392 (2017).
12. S. Acharya *et al.*, ALICE Coll. Measurement of the inclusive J/ψ polarization at forward rapidity in *pp* collisions at $\sqrt{\mathbf{s}} = \mathbf{8}$ TeV. *Eur. Phys. J. C* **78**, 562 (2018).
13. S. Acharya *et al.*, ALICE Coll. Inclusive J/ψ production at forward and backward rapidity in *p*-Pb collisions at $\sqrt{s_{\rm NN}} = 8.16$ TeV. *JHEP* **07**, 160 (2018).
14. X. Du, R. Rapp. In-medium charmonium production in proton–nucleus collisions. *JHEP* **03**, 15 (2019).
15. S. Acharya *et al.*, ALICE Coll. Search for collectivity with azimuthal J/ψ-hadron correlations in high multiplicity *p*-Pb collisions at and $\sqrt{\mathbf{s}_{\rm NN}} = \mathbf{5.02}$ and 8.16 TeV. *Phys. Lett. B* **780**, 7 (2018).
16. V. Khachatryan *et al.*, CMS Coll. Observation of long-range near-side angular correlations in proton-lead collisions at the LHC. *Phys. Lett. B* **718**, 795 (2013).
17. S. Acharya *et al.*, ALICE Coll. J/ψ elliptic flow in Pb–Pb collisions at $\sqrt{\mathbf{s}_{\rm NN}} = \mathbf{5.02}$ TeV. *Phys. Rev. Lett.* **119**, 242301 (2017).
18. J. Adam *et al.*, ALICE Coll. J/ψ suppression at forward rapidity in Pb–Pb collisions at $\sqrt{\mathbf{s}_{\rm NN}} = \mathbf{5.02}$ TeV. *Phys. Lett. B* **766**, 212 (2017).

19. J. Adam *et al.*, ALICE Coll. Measurement of an excess in the yield of J/ψ at very low p_T in Pb–Pb Collisions at $\sqrt{s_{\rm NN}} = 2.76$ TeV. *Phys. Rev. Lett.* **116**, 222301 (2016).
20. S. Acharya *et al.*, ALICE Coll. $\Upsilon(1S)$ suppression at forward rapidity in Pb–Pb collisions at $\sqrt{\mathbf{s}_{\rm NN}} = \mathbf{5.02}$ TeV. *Phys. Lett. B* **790**, 89 (2019).
21. S. Acharya *et al.*, ALICE Coll. Measurement of $\Upsilon(1S)$ elliptic flow at forward rapidity in Pb–Pb collisions at $\sqrt{\mathbf{s}_{\rm NN}} = \mathbf{5.02}$ TeV. *arXiv:1907.03169 [nucl-ex]* (2019).
22. Z. Citron *et al.* Future physics opportunities for high-density QCD at the LHC with heavy-ion and proton beams. *arXiv:1812.06772 [hep-ph]* (2018).

Received 08.07.19

Ф. Фіонда, від імені Колаборації ALICE

ВИМІРЮВАННЯ ПРОДУКУВАННЯ КВАРКОНІЯ ЗА ДОПОМОГОЮ ДЕТЕКТОРА ALICE НА LHC

Р е з ю м е

Передбачається, що в (ультра)релятивістських зіткненнях важких іонів сильно взаємодіюча речовина проходить фазовий перехід до плазми кварків та глюонів (КГП), а кварконій може бути джерелом інформації щодо властивостей цієї матерії. Проте модифікація середовища, де продукується кварконій, включає також вплив холодної ядерної речовини (CNM) як екранування ядерного (брейкап) розвалу на додаток до ефектів КГП. Протон-ядерні зіткнення, в яких не очікуються утворення КГП, служать для визначення впливу холодної ядерної речовини на продукування кварконія. Вакуумне продукування кварконія моделюється в протон-протонних зіткненнях, які служать еталоном як для зіткнень важких іонів, так і для протон-ядерних зіткнень. Окрім калібровки, результати зіткнень протонів служать також орієнтиром для моделей, основаних на КХД як в пертурбативній, так і в непертурбативній областях. Детектор ALICE має унікальні для LHC можливості для вимірювання кварконіїв аж до нульового значення поперечного імпульсу. Вимірювання було виконано як для центральних, так і для передніх бистрот в каналах розпаду, відповідно, діелектрона та дімюона. В даній роботі представлено новітні вимірювання продукування кварконія Колаборацією ALICE на LHC під час Сеансу-2 при різних енергіях та для різних систем.

https://doi.org/10.15407/ujpe64.7.573

F.M. FRAENKLE
for the KATRIN collaboration
Institute for Nuclear Physics (IKP), Karlsruhe Institute of Technology (KIT)
(1, Hermann-von-Helmholtz-Platz, 76344 Eggenstein-Leopoldshafen, Germany;
e-mail: florian.fraenkle@kit.edu)

THE NEUTRINO MASS EXPERIMENT KATRIN

The KArlsruhe TRItium Neutrino (KATRIN) experiment is a large-scale experiment with the objective to determine the effective electron antineutrino mass in a model-independent way with an unprecedented sensitivity of 0.2 eV/c^2 at 90% C.L. The measurement method is based on the precision β-decay spectroscopy of molecular tritium. The experimental setup consists of a high-luminosity windowless gaseous tritium source, a magnetic electron transport system with differential cryogenic pumping for the tritium retention, and an electrostatic spectrometer section for the energy analysis, followed by a segmented detector system for the counting of transmitted β-electrons. The first KATRIN neutrino mass measurement phase started in March 2019. Here, we will give an overview of the KATRIN experiment and its current status.

Keywords: neutrino mass, tritium β-decay, spectrometers.

1. Introduction

The absolute neutrino mass scale is one of the big open questions in particle physics, astrophysics, and cosmology. Cosmological observations and neutrinoless double β-decay experiments provide an indirect access to the absolute neutrino mass scale, but are model-dependent. A model-independent direct method to determine the neutrino mass is the precise investigation of weak decays such as the β-decay.

In the nuclear β-decay, the neutron in an atomic nucleus decays into a proton, thereby emitting an electron (e^-) and an electron antineutrino ($\overline{\nu}_e$). The energy released in the decay is divided between the e^- and $\overline{\nu}_e$ in a statistical way. The energy spectra of the electron is given by the well-known Fermi theory of β-decay [1]:

$$\frac{dN}{dE} \propto p(E+m_e c^2)(E_0-E)\sqrt{(E_0-E)^2 - m^2_{\overline{\nu}_e} c^4} \quad (1)$$

with the electron energy E, the endpoint energy E_0, the electron mass m_e, and the effective electron antineutrino mass $m^2_{\overline{\nu}_e} = \sum |U_{ei}|^2\ m(\nu_i)^2$. This is the incoherent sum of neutrino mass eigenstates and is therefore insensitive to the phases of the neutrino mixing matrix (in contrast to the neutrinoless double β-decay). As one can see in Eq. 1, it is the square of the neutrino mass $m^2_{\overline{\nu}_e}$ that enters, as a parameter. Its effect on the shape of the spectrum is significant only in a very narrow region close to E_0. The current upper limit on the neutrino mass of 2 eV/c^2 [2] was determined from investigating the tritium β-spectrum near the endpoint of 18.6 keV by the experiments in Mainz [3] and Troitsk [4].

2. KATRIN Experiment

The **KA**rlsruhe **TRI**tium **N**eutrino (KATRIN) experiment [5] is a next-generation, large-scale experiment to determine the effective mass of an electron antineutrino by investigating the tritium β-decay kinematics with a sensitivity of 0.2 eV/c^2. The experiment was executed at the Karlsruhe Institute of Technology (KIT) in Germany. The measurement setup (see Figure 1) has an overall length of $\approx$ 70 m. Molecular tritium is injected into a windowless gaseous tritium source (b), where it decays with an activity of 10^{11} Bq, thus providing a sufficient number of β-decay electrons close to the endpoint energy E_0. The activity of the source is monitored at the rear section (a). Tritium is removed from the beamline in the differential pumping section (c) and the cryogenic pumping section (d), while electrons from the source are magnetically guided toward the spectrometer section. Both a pre-spectrometer and a main spectrometer are operated as electrostatic retarding high

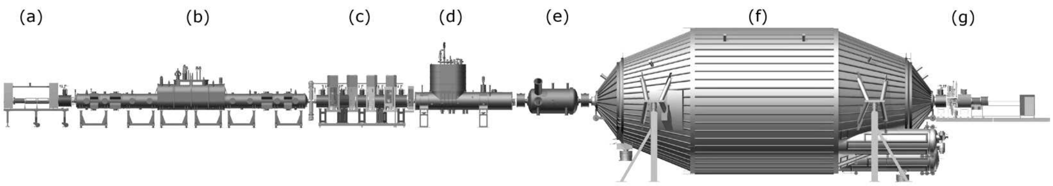

Fig. 1. The KATRIN experimental setup with its main components: rear section (*a*); windowless gaseous tritium source (WGTS) (*b*); differential pumping section (DPS) (*c*); cryogenic pumping section (CPS) (*d*); pre-spectrometer; (*f*) main spectrometer (*e*); focal plane detector (*g*)

pass filters of the MAC-E filter (**M**agnetic **A**diabatic **C**ollimation combined with an **E**lectrostatic Filter) type [6]. The pre-spectrometer (*e*) is operated as a pre-filter in order to reduce the flux of electrons into the main spectrometer (*f*) which performs the energy analysis of the β-decay electrons near the endpoint with the energy resolution $\Delta E = 0.93$ eV at 18.6 keV. The main spectrometer is equipped with a dual-layer wire electrode system for electrostatically shielding secondary electrons from the inner vessel surface and for the fine-tuning of a retarding potential. The transmitted β-decay electrons are counted in the detector system (*g*) with a segmented silicon detector [7].

2.1. Windowless gaseous tritium source

The windowless gaseous tritium source (WGTS) consists of a 10 m long tube 90 mm in diameter and is operated at a temperature of about 30 K by the circulation of two-phase neon. Molecular tritium (T_2) is injected into the center of the source tube and decays with an activity of 10^{11} Bq to provide a sufficient number of electrons close to the tritium endpoint energy E_0. The β-electrons are guided via an axial magnetic field of up to 3.6 T toward the spectrometer section. T_2 is collected via turbo-molecular pumps at both ends of the WGTS and is recirculated via an "inner loop" which removes contaminants (particularly, ^{3}He) and is capable to process 40 g of T_2 per day. A prototype system to investigate the performance of the temperature stabilization of a beam tube showed that the stringent thermal performance specifications (temperature stability ± 30 mK) could be met, and the temperature stability better by a factor of twenty was achieved [8]. The WGTS was delivered to KIT in September 2015 and integrated into the KATRIN beam line. The magnet system was successfully tested to the maximum field. Initial tests of the temperature stabilization confirmed the performance better than the specified one already observed at the prototype system.

2.2. Differential cryogenic pumping section

The task of the Differential Pumping Section (DPS) is to reduce the T_2 partial pressure by a factor of $>10^5$ and to guide β-electrons via a strong magnetic field of up to 5.6 T. The beam tube has four bends to avoid the beaming of T_2 molecules toward the spectrometers. In order to remove tritium ions, the DPS is equipped with electric dipole electrodes. The magnet system was successfully commissioned, and the installation of the beam tube is complete.

Any remaining T_2 that passes the DPS is trapped in the Cryogenic Pumping Section (CPS) by argon frost frozen on the 4 K cold beam tube. The argon frost forms a highly efficient, large-area, and radiation-immune surface. The feasibility of this approach was successfully tested in a test experiment called TRAP [9] which achieved a T_2 reduction factor of about 10^7. The CPS was delivered to KIT in July 2015 and was successfully cooled to the operational temperature of about 4 K. Simulations based on the performance of the initial cool-down indicate that the T_2 reduction factor could be two or more orders of magnitude better than specified.

2.3. Spectrometer section

The spectrometer section consists of two spectrometers of the MAC-E filter type: a pre-spectrometer and a much larger main spectrometer.

The pre-spectrometer is intended to be used as a pre-filter on a potential a few hundred Volts below E_0. The pre-filtering reduces the flux of β-electrons into the main spectrometer by many orders of magnitude and minimizes β-electron-induced background processes in the main spectrometer.

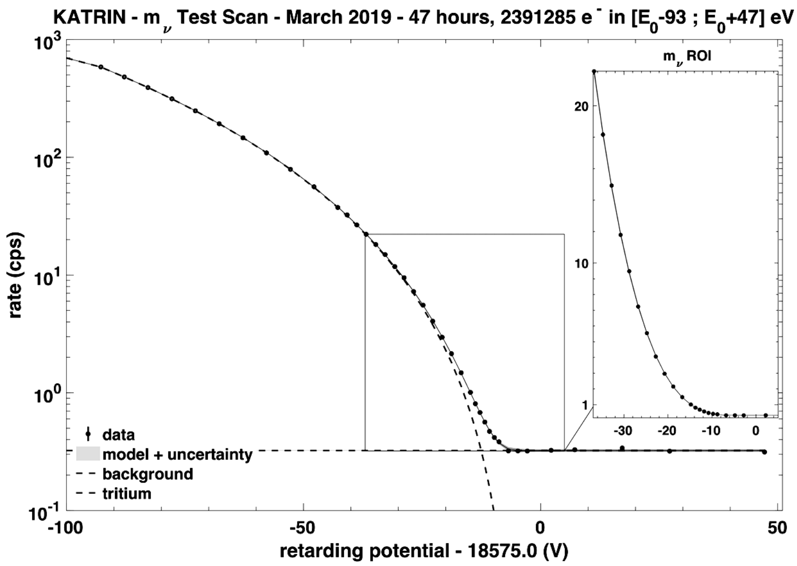

Fig. 2. Test scan of the tritium β-spectrum close to the endpoint

The purpose of the 10-m-diameter and 24-m-long main spectrometer is to analyze the energy of the β-decay electrons. It has an energy resolution of 0.93 eV at 18.6 keV. In order to reduce the spectrometer background rate, a double layer inner electrode system made of thin wires – mounted with submillimeter precision – is installed. The wire layers are put on a more negative potential with respect to the tank voltage in order to shield secondary electrons produced in the vessel wall. The absolute voltage of -18.6 kV needs to be stable on the 1 ppm level and is monitored with a high-precision voltage divider an independent calibration beam line [10]. The vacuum system of the main spectrometer is capable of reaching a pressure of about 10^{-10} mbar with one active non-evaporable getter pump [11]. After a recent baking of the spectrometer, a second getter pump was activated, and a pressure on the order of 10^{-11} mbar was achieved inside the main spectrometer.

2.4. Detector

Electrons that are able to overcome the potential barriers of the spectrometers are detected in a monolithic 148 pixel silicon PIN diode [7]. The energy resolution of the detector system is 1.4 keV (FWHM). The selection of materials, shielding, and an active veto are used to keep the intrinsic detector background at a low level of 1.2 mcps/keV.

3. Tritium Commissioning Measurements

The official inauguration of the KATRIN experiment took place on June 11th, 2018. In the following months, the tritium activity was increased step-by-step. The results of an initial test scan of the β-spectrum close to the endpoint are shown in Fig. 2. The plot shows the integral rate at the detector as a function of the main spectrometer retarding voltage. The spectrum is composed of two components: a voltage-independent background and the tail of the β-spectrum close to the endpoint.

The first KATRIN neutrino mass measurement phase started in March 2019 and concluded in May. The first results of this measurement phase are expected to be announced in September of this year.

4. Conclusions

Direct neutrino mass measurements are a model-independent way to determine the neutrino mass. A major improvement of the neutrino mass sensitivity by one order of magnitude is expected of the KATRIN experiment, which has completed its first neutrino mass measurement following its construction phase.

We acknowledge the support of Helmholtz Association (HGF), Ministry for Education and Research BMBF (05A17PM3, 05A17PX3, 05A17VK2, and 05A17WO3), Helmholtz Alliance for Astropar-

ticle Physics (HAP), and Helmholtz Young Investigator Group (VH-NG-1055) in Germany; Ministry of Education, Youth and Sport (CANAM-LM2011019, LTT18021), in cooperation with JINR Dubna (3 + 3 grants), in the Czech Republic; and the Department of Energy through grants DE-FG02-97ER41020, DE-FG02-94ER40818, DE-SC0004036, DE-FG02-97ER41033, DE-FG02-97ER41041, DE-AC02-05CH11231, and DE-SC0011091 in the United States.

1. E. Fermi. Versuch einer Theorie der β-Strahlen. *Zeitschrift für Phys.* **88**, 161 (1934)
2. C. Patrignani *et al.* (Particle Data Group). Review of particle physics. *Chin. Phys. C* **40**, 100001 (2016).
3. C. Kraus *et al.* Final results from phase II of the Mainz neutrino mass search in tritium β decay. *Europ. Phys. J. C* **40**, 447 (2005).
4. V.N. Aseev *et al.* Upper limit on the electron antineutrino mass from the Troitsk experiment. *Phys. Rev. D* **84**, 112003 (2011).
5. K. Collaboration. KATRIN design report. *FZKA scientific report, 7090* (2005).
6. G. Beamson it et al. The collimating and magnifying properties of a superconducting field photoelectron spectrometer. *J. Phys. E: Sci. Inst.* **13**, 64 (1980).
7. J.F. Amsbaugh *et al.* Focal-plane detector system for the KATRIN experiment. *Nucl. Instr. Methods in Phys. Res. Section A* **778**, 40 (2015).
8. S. Grohmann *et al.* The thermal behaviour of the tritium source in KATRIN. *Cryogenics* **55–56**, 5 (2013).
9. F. Eichelhardt *et al.*, The cryogenic pumping section of KATRIN and the test experiment TRAP. *Nucl. Phys. B – Proc. Suppl.* **221**, 342 (2011).
10. M. Erhard it et al. High-voltage monitoring with a solenoid retarding spectrometer at the KATRIN experiment. *J. Instrum.* **9**, P06022 (2014).
11. K. Collaboration. Commissioning of the vacuum system of the KATRIN Main Spectrometer. *J. Instrum.* **11**, 1 (2016).

Received 08.07.19

Ф.М. Френкле, від імені Колаборації KATRIN

ЕКСПЕРИМЕНТ KATRIN ДЛЯ ВИМІРЮВАННЯ МАСИ НЕЙТРИНО

Р е з ю м е

Karlsruhe Tritium Neutrino (KATRIN) є широкомасштабним експериментом, метою якого є визначення маси електронного антинейтрино модельно-незалежним шляхом з безпрецедентною точністю 0,2 еВ/c^2. Метод вимірювання базується на точній спектроскопії бета-розпаду молекулярного тритія. Експериментальна установка складається з безвіконного газовидного джерела молекулярного тритія високої світимості, магнітної електронної транспортної системи з диференційованою кріогенною помпою для затримки тритію, а також електростатичною спектрометричною секцією для контролю за енергією, за якою слідує сегментована система детекторів для підрахунку переданих бета-електронів. Перша фаза вимірювання маси нейтрино почалася у березні 2019 року. В роботі ми даємо огляд експерименту KATRIN та його сучасного стану.

https://doi.org/10.15407/ujpe64.7.577

YU. GORNUSHKIN
on behalf of the DsTau Collaboration
Joint Institute for Nuclear Research
(6, Joliot-Curie Str., Dubna, 141980, Russia; e-mail: gornshk@yandex.ru)

STUDY OF TAU NEUTRINO PRODUCTION IN PROTON NUCLEUS INTERACTIONS

In the DsTau experiment at the CERN SPS, an independent direct way to study the tau neutrino production in high energy proton-nucleous interactions was proposed. Since the main source of tau neutrinos is a decay of D_s mesons, the project aims at measuring the differential cross-section of this reaction. The experimental method is based on the use of high-resolution emulsion detectors for the efficient registration of events with short-lived particle decays. The motivation of the project, details of the experimental technique, and the first results of the analysis of the data collected during test runs, which prove the feasibility of the study are presented.

Keywords: tau neutrino, cross-section, nuclear emulsions.

1. Introduction

Tau neutrino is eventually the least studied elementary particle. Although its existence was predicted after the tau lepton discovery in 1975 [1], the first tau neutrinos were detected in the DONuT experiment 25 years later [2]. In 2015, somewhat more ν_τ appeared through $\nu_\mu \leftarrow \nu_\tau$ oscillations were detected by OPERA [3]. Super-Kamiokande (SK) and IceCube [4] also reported an evidence of the ν_τ presence in their data.

Given a poor statistics of registered tau neutrinos, their properties are not well studied. In particular, the cross-section of the tau neutrino charge current (CC) interaction is known [5] with much larger statistical and systematic uncertainties compared to the other neutrino flavors, as shown in Fig. 1. However, a precise measurement of this cross-section would allow testing of the Lepton Flavor Universality (LFU) in the neutrino scattering. LFU is a principal assumption of the Standard Model (SM) of particle physics, but its validity was questioned by recent results on the B decay asymmetry [6–8]. There is the expectation of a possible deviation of the cross-section of the ν_τ interaction as well [9]. The measurement of the ν_τ CC cross-section has impact on the current and future neutrino oscillation experiments. In the mass hierarchy measurements in the atmospheric Super-Kamiokande (SK) [10] and accelerator neutrino experiments (e.g., in DUNE [11] and HyperKamiokande [12]), ν_e flux measurement will have a background due to $\tau \to e$ decays. So, the systematic uncertainty of the ν_τ interaction cross-section will be a limiting factor in the oscillation analyses in these experiments [13, 14].

So far, the tau neutrino interaction cross-section was only measured in the DONuT [5], OPERA [18], and SK [17] experiments, though under rather different conditions. All the measurements have large statistical and/or systematic errors of 30–50% due to low statistics and experimental uncertainties. In a future experiment at CERN, SHiP [19], a rich neutrino program [20] is proposed with thousands of tau neutrino interactions detected, hence, providing a negligible statistical error of the cross-section measurement. The overall accuracy of the cross-section will be determined by the systematic errors, and, in particular, by the ν_τ flux uncertainty, which is to be studied by the DsTau experiment [34].

The dominant source (>90%) of ν_τ in an accelerator-based neutrino beam is leptonic decays of $D_s^\pm$ mesons produced in proton-nucleus interactions:

$$D_s^- \to \tau^- \overline{\nu}_\tau,$$
$$\tau^- \to X \nu_\tau,$$

producing ν_τ and $\overline{\nu}_\tau$ in every decay.

Conventionally, the differential production cross-section of charmed particles is approximated by a

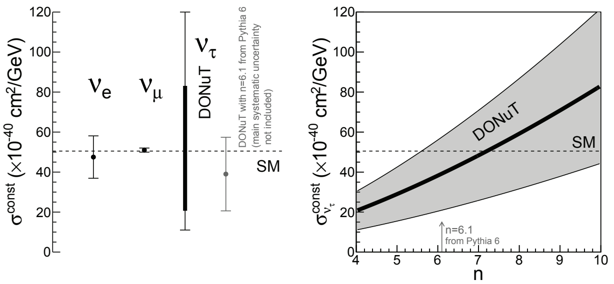

Fig. 1. Left: ν, $\overline{\nu}$ averaged energy-independent cross-section of the three neutrino flavors ([15] for ν_e, [16] for ν_μ, and for ν_τ [5]). The SM LFU prediction is indicated as a dashed horizontal line. For the DONuT result, since there is no measurement of the parameter n concerning the D_s double differential production cross-section (Eq. 1), the value is plotted in the empirical range of a parameter n given by the DONuT paper as in the right plot

phenomenological formula

$$\frac{d^2\sigma}{dx_{\mathrm{F}} \cdot dp_T^2} \propto (1- \mid x_F \mid)^n \cdot e^{-b \cdot p_T^2}, \tag{1}$$

where x_{F} is the Feynman x ($x_{\mathrm{F}} = 2p_Z^{\mathrm{CM}} \sqrt{s}$) and p_T is the transverse momentum, n and b are the parameters controlling the longitudinal and transverse dependences of the differential production cross-section, respectively. Although there were several measurements on charm particles [21–25], there is a lack of measurements on the D_s differential production cross-section in the proton interactions, especially concerning the longitudinal dependence represented by the parameter n. This has been the main source of the systematic uncertainty of the ν_τ cross-section measurements in DONuT [5].

Thus, a new measurement of the differential production cross-section of D_s is necessary for future precise tau neutrino measurements, as well as for the reevaluation of the DONuT result. In the DsTau experiment, a direct study of the tau neutrino production, namely, the measurement of $D_s \to \tau \to X$ decays following high-energy proton-nucleus interactions, is proposed. DsTau will provide an independent ν_τ flux prediction for future neutrino beams with accuracy under 10%. Then the systematic uncertainty of the ν_τ CC cross-section measurement can be made sufficiently low to test LFU in the neutrino scattering by future experiments [20].

In addition to the primary aim of measuring the D_s differential production cross-section in 2.3×10^8 proton interactions, a high yield of $\mathcal{O}(10^5)$ charmed particle pairs is expected. The analysis of those events can provide valuable by-products.

2. Overview of the Project

DsTau exploits a simple setup consisting of a segmented high-resolution nuclear emulsion vertex detector (a module) capable to recognize $D_s \to \tau \to X$ by their very peculiar double-kink topology as shown in the bottom part of Fig. 2. In addition, because charm quarks are created in pairs, another decay of a charged/neutral charmed particle from the same vertex will be observed with a flight length of a few millimeters. Such a “double-kink plus decay” topology in a short distance has a marginal background.

However, to register the events is a challenge. First, all the decays take place on a scale of millimeters: the mean flight lengths of D_s, τ, and pair-charms are 3.6, 2.1, and 4.2 mm, respectively. Second, although the kink angle at the τ decay vertex is easily recognizable (mean kink angle of 96 mrad), the one at $D_s \to \tau$ decays is rather small, 6.2 mrad. The expected signal features were studied making use of Pythia 8.1 [29]. The project aims to detect $\sim$1000 $D_s \to \tau \to X$ decays in 2.3×10^8 proton interactions with a tungsten target. State-of-the-art nuclear emulsion detectors with a nanometric-precision readout will be used to achieve this goal. The modern use of the emulsion detection technology is based on the high-speed high-precision automatic readout of emulsions developed during the last two decades and available today [26–28].

The DsTau module structure is shown in Fig. 2. The upstream part is named the *decay module*. The basic unit is made of a 500 μm-thick tungsten plate (target) followed by 10 emulsion films interleaved with 9 200 μm-thick plastic sheets which act as a decay volume for short-lived particles, as well as high-precision particle trackers. This structure (thickness of 5.4 mm) is repeated 10 times. Five additional emulsion films are placed most upstream of the module to tag the incoming beam protons. It is followed by the downstream part made of a repeated structure of emulsion films and 1-mm-thick lead plates for the measurement of the momenta of daughter particles through their Multiple Coulomb Scattering (MCS) measurement [30]. The entire detector module is 12.5 cm wide, 10 cm high, and 8.6 cm thick and consists of a total of 131 emulsion films.

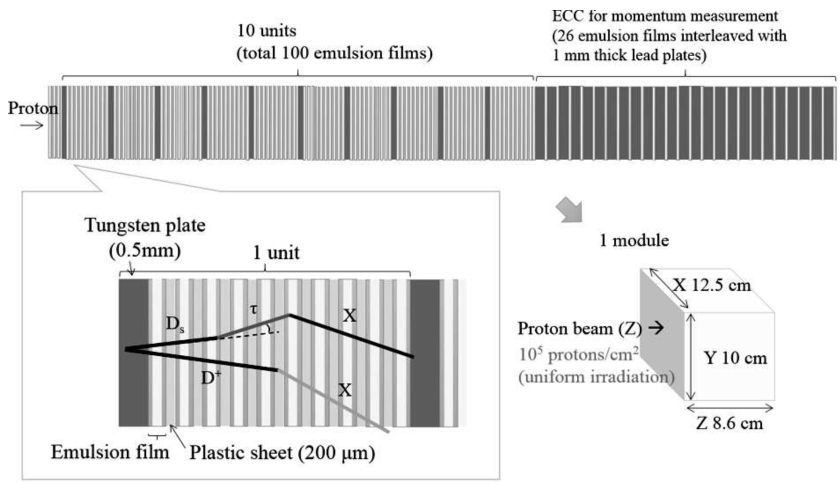

Fig. 2. Schematic view of the module structure. A tungsten target plate is followed by 10 emulsion films alternated by 9 plastic sheets acting as a tracker and a decay volume of 5.4 mm. The sensitive layers of emulsion detectors are indicated by green color. This basic structure is repeated 10 times, and then followed by a lead-emulsion structure for the measurement of the momenta of daughter particles. In the bottom part, the "double kink" topology of $D_s \to \tau \to X$ is shown

Once a charged particle passes through the emulsion layer, the ionization is recorded quasipermanently and then amplified and fixed by the chemical process. The trajectory of a charged particle can be observed on an optical microscope. The emulsion detector with 200 nm-diameter AgBr crystals and a 210 μm-thick base has a track position resolution of 50 nm [32] and an angular resolution of 0.34 mrad (projection). With this angular resolution, one can detect 2-mrad kink with 4σ confidence.

A key feature of the modern emulsion technique is the use of fast readout instruments, which allow extracting and digitizing the information on the tracks fully automatically. Emulsion detectors and automated readout systems have been successfully employed in several neutrino experiments such as CHORUS [33], DONuT [2, 5] and OPERA [3]. The latest scanning system, HTS [26, 27], allows the scanning of emulsion films at a speed of 5,000 cm^2 per hour per emulsion layer, which is $\mathcal{O}(100)$ faster than those used in OPERA.

The detection efficiency for the $D_s \to \tau \to 1$ prong events (85% of τ decays) was estimated by the PYTHIA 8.1 [29] simulation.

The following criteria were requested to be fulfilled: (1) the parent particle has to pass through at least one emulsion film (two sensitive layers), (2) the first kink daughter has to pass through at least two sensitive layers, and the kink angle is $\geq$2 mrad, (3) the flight length of the parent and the first kink daughter has to be <5 mm, (4) the second kink angle is $\geq$15 mrad and (5) the partner of the charm pair is detected with 0.1 mm $\leq$ flight length <5 mm (they can be charged decays with a kink angle >15 mrad or neutral decays). With these selection criteria, the detection efficiency was estimated to be 20%.

The main background to $D_s \to \tau \to 1$ prong events is hadron interactions that can mimic the decays of short-lived particles. Its probability was obtained by simulating 3×10^5 protons on the detector with the FLUKA [35] simulation. The criteria used for the charged charm or tau decay topology selection are applied to the interactions of secondary hadrons with only one charged daughter particle ($P > 2$ GeV/c). In addition to high-energy particles, a large part of interactions has associated nuclear fragments, which is a strong evidence of hadron interactions. Those are effectively rejected by requesting only one charged daughter. The total probabilities to account for background events such as a double kink with charged pair charm or with neutral pair charm are $1.3 \pm 0.4 \times 10^{-9}$ and $2.7 \pm 0.8 \times 10^{-9}$ per incident proton, respectively. The expected numbers of background events in the full statistics of DsTau (4.6×10^9 p.o.t.) are 6.0 ± 1.8 and 12.4 ± 3.7 for these 2-signal channels, respectively.

DsTau will provide the differential cross-section of D_s meson production and the following decay to a

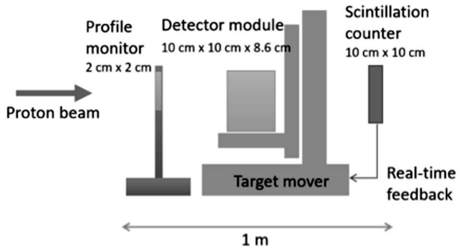

Fig. 3. Schematic of the DsTau setup. The detector module was moved in the plane perpendicular to the beam to provide uniform exposure at a density of 10^5 protons/cm^2

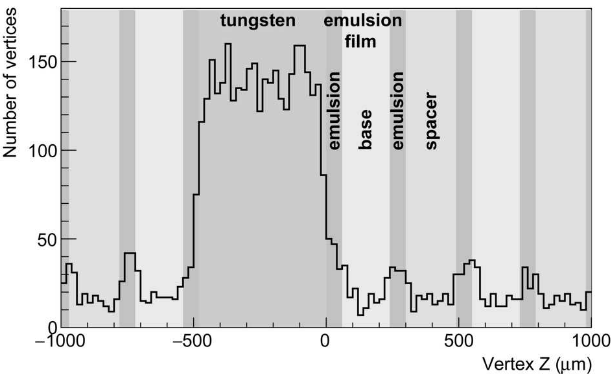

Fig. 4. Reconstructed vertex position distribution in Z. The correspondence with the detector structure is clearly visible

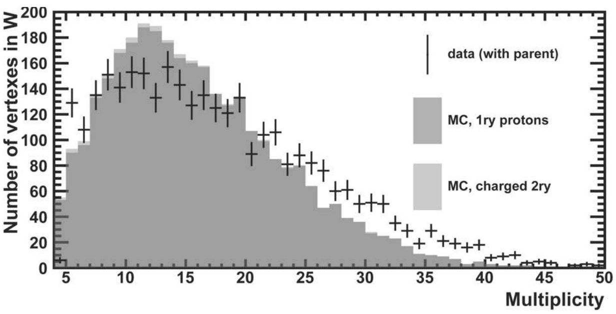

Fig. 5. Measured multiplicity of charged particles at the proton interaction vertices compared with the prediction from FLUKA simulations

tau lepton in the 400-GeV proton-nucleus interaction. It may be fit with the phenomenological formula, Eq. (1), and get the parameter n estimated, which is relevant for a re-evaluation of the tau neutrino cross-section measurement by the DONuT experiment. At the statistics of 1000 $D_s \to \tau \to X$ detected events, the relative uncertainty of the ν_τ flux will be reduced to below 10% [34].

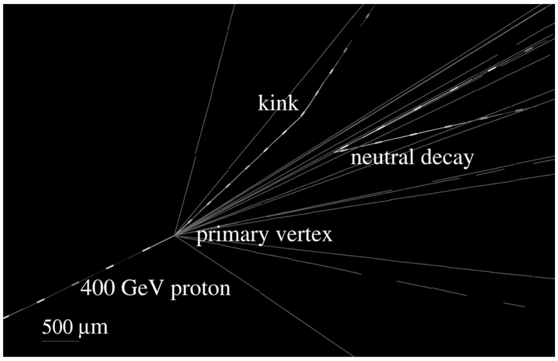

Fig. 6. A double charm candidate event with neutral 2-prong (vee) and charged 1-prong (kink) topologies. (tilted view) See the text about the details of event features

In order to collect 1000 $D_s \to \tau$ events, 230 millions of proton interactions are to be analyzed, which is another challenge from the point of view of the track density and the amount of data to be processed. The high proton density of 10^5 cm^2 at the upstream surface of an emulsion detector was chosen to maximize the number of interactions in a single module. The track density will then increase in the detector, yet not exceeding 10^6 cm^2 at the downstream part of the decay module, which is affordable for the emulsion detector readout and reconstruction. With this density, 6.25×10^5 proton interactions are expected in the tungsten target in a decay module. To accumulate 2.3×10^8 proton interactions in the tungsten plates, 4.6×10^9 protons on the target are needed. About 370 modules with a total film area of 593 m^2 will be employed for this measurement.

3. Beam Exposure and Analysis Scheme

Two test beam campaigns were held at CERN SPS in 2016 and in 2017. In 2018, a pilot run was conducted aiming at the recording of 10% of the experimental data. A schematic view of the detector setup is shown in Fig. 3.

The proton beam profile was measured by a silicon pixel telescope. Each emulsion detector module was mounted on a motorized X-Y stage (target mover) to change the position of the module with respect to the proton beam, so to make the detector surface uniformly irradiated at a density of 10^5 tracks/cm^2.

The emulsion detector is both a detector and the data storage media at the same time. The automatic scanning systems read out the track information accumulated in the emulsion films during the exposure, digitize it, and transfer to the computers for the pattern recognition and track analysis like in case of any electronic detector. The output of the readout is the information on the track segments recorded in the top and bottom layers of a film (*microtracks*). A segment made by linking the microtracks on two layers in a film is called a *basetrack*, which is a basic unit of the track information from each emulsion film for the later processing. Each basetrack provides 3D coordinates $\mathbf{X} = (x, y, z)$, 3D vector $\mathbf{V} = (\tan\theta_x, \tan\theta_y, 1)$, and dE/dx parameter. The tracks are reconstructed by linking basetracks on different films making use of their position and direction.

The average basetrack efficiency measured with tracks is higher than 95%, which provides the track detection with efficiency >99%. The reconstructed tracks are then used to find vertices. To provide the efficient detection of small kinks of $D_s \to \tau$ decays, the analysis is performed in two stages: (1) scan the full module by a fast HTS system with relatively coarse angular resolution (2.5 mrad) and detect events that have two decays in a short distance, namely, the decays of τ and partner charm ($D^{\pm}$ and D^0); (2) perform a high-precision measurement around the τ decay candidates to find $D_s \to \tau$ small kinks. For this, the dedicated stations with a piezo-based Z axis are used providing a reproducibility of a single hit position measurement of 8 nm and angular measurements of 0.16 mrad (RMS).

Here, the first results acheaved at the first stage of the analysis are presented. Figure 4 shows the distribution of the Z coordinate (along the beam) of the vertices reconstructed in the detector. An enhancement of the vertices in the tungsten target is evident. One can even see the microstructure corresponding to the emulsion layers (of higher density) and plastic bases/spacers. Figure 5 shows the measured multiplicity of charged particles at proton interactions, compared with the prediction by FLUKA. A good agreement of the numbers of observed tracks and expected ones demonstrates a good efficiency of the track reconstruction.

With the data analyzed so far, several events with short-lived particle decays have been already recognized (See an example in Figure 6).

4. Conclusion and Outlook

The DsTau experiment is going to study the tau neutrino production following the high-energy proton interactions, which will provide necessary information for future ν_τ experiments. CERN SPSC recommended approving DsTau in April 2019.

The test of a beam in 2016–2017 and the pilot run in August 2018 were performed, and over 20 million proton interactions in the detector were registered. The emulsion scanning and analysis of these samples are ongoing, which would allow confirming the Ds detection feasibility and the re-evaluation of the ν_τ cross-section by refining the ν_τ flux. The full scale study scheduled for the next physics run at CERN SPS in 2021 and 2022. A large amount of the decays of charmed particles is expected to be recorded, as well providing a possibility of interesting by-product results.

1. M. Perl *et al.* Evidence for anomalous lepton production in e^+e^- annihilation. *Phys. Rev. Lett.* **35**, 1489 (1975).
2. K. Kodama *et al.* Observation of tau neutrino interactions. *Phys. Lett. B* **504**, 218 (2001).
3. N. Agafonova *et al.* Discovery of τ neutrino appearance in the CNGS neutrino beam with the OPERA experiment. *Phys. Rev. Lett.* **115**, 121802 (2015).
4. M.G. Aartsen *et al.* [IceCube Collaboration]. Measurement of atmospheric tau neutrino appearance with IceCube DeepCore. *Phys. Rev. D* **99**, No. 3, 032007 (2019).
5. K. Kodama *et al.* [DONuT Collaboration]. Final tau-neutrino results from the DONuT experiment. *Phys. Rev. D* **78**, 052002 (2008).
6. J.P. Lees *et al.* [BABAR Collaboration]. Evidence for an excess of $\bar{B} \to D^{(*)}\tau^-\bar{\nu}_\tau$ decays. *Phys. Rev. Lett.* **109**, 101802 (2012).
7. R. Aaij *et al.* [LHCb Collaboration]. Test of lepton universality using $B^+ \to K^+l^+l^-$ decays. *Phys. Rev. Lett.* **113**, 151601 (2014).
8. R. Aaij *et al.* [LHCb Collaboration]. Measurement of the ratio of branching fractions $B(\bar{B}^0 \to D^{*+}\tau^-\bar{\nu}_\tau)/B(\bar{B}^0 \to$ $\to D^{*+}\mu^-\bar{\nu}_\mu)$. *Phys. Rev. Lett.* **115**, No. 11, 111803 (2015).
9. H. Liu, A. Rashed, A. Datta. Probing lepton nonuniversality in tau neutrino scattering. *Phys. Rev. D* **92**, 073016 (2015).
10. Y. Fukuda *et al.* [Super-Kamiokande Collaboration]. Measurement of a small atmospheric ν_μ/ν_e ratio. *Phys. Let. B* **433**, Iss. 1, 9 (1998).
11. R. Acciarri *et al.* [DUNE Collaboration]. Long-Baseline Neutrino Facility (LBNF) and Deep Underground Neutrino Experiment (DUNE). Vol. 1. The LBNF and DUNE Projects, FERMILAB-DESIGN-2016-01 (2016).
12. K. Abe *et al.* [Hyper-Kamiokande Proto-Collaboration]. Physics potential of a long-baseline neutrino oscillation experiment using a J-PARC neutrino beam and Hyper-Kamiokande. *PTEP* **2015**, 053C02 (2015).

13. R. Wendell, K. Okumura. Recent progress and future prospects with atmospheric neutrinos. *New J. Phys.* **17**, 025006 (2015).
14. D. Meloni. On the systematic uncertainties in DUNE and their role in New Physics studies. *JHEP* **1808**, 028 (2018). e-Print: arXiv:1805.01747 [hep-ph].
15. J. Blietschau *et al.* [Gargamelle Collaboration]. Total cross sections for ν_e and $\bar{\nu}_e$ interactions and search for neutrino oscillations and decay. *Nucl. Phys. B* **133**, 205 (1978).
16. K.A. Olive *et al.* [Particle Data Group]. Review of Particle Physics. *Chin. Phys. C* **38**, 090001 (2014).
17. Z. Li *et al.* [SuperKamiokande Collaboration], Measurement of the tau neutrino cross-section in atmospheric neutrino oscillations with Super-Kamiokande. *Phys. Rev. D* **98**, No. 5, 052006 (2018); arXiv:1711.09436 [hep-ex].
18. N. Agafonova *et al.* [OPERA Collaboration]. Final results of the OPERA experiment on ν_τ appearance in the CNGS neutrino beam. *Phys. Rev. Lett.* **120**, No. 21, 211801 (2018). Erratum: [*Phys. Rev. Lett.* **121**, No. 13, 139901 (2018).] [arXiv:1804.04912 [hep-ex]].
19. M. Anelli *et al.* [SHiP Collaboration]. A facility to search for hidden particles (SHiP) at the CERN SPS, CERN-SPSC-2015-016, SPSC-P-350 (2015).
20. M. De Serio [SHiP Collaboration]. Neutrino physics with the SHiP experiment at CERN, PoS EPS-HEP2017 (2017) 101,
21. I. Abt *et al.* [HERA-B Collaboration]. Measurement of D^0, D^+, Ds^+ and D^{*+} production in fixed target 920 GeV proton-nucleus collisions. *Eur. Phys. J. C* **52**, 531 (2007).
22. K. Kodama *et al.* [Fermilab E653 Collaboration]. Charm meson production in 800-GeV/c proton – emulsion interactions. *Phys. Lett. B* **263**, 573 (1991).
23. R. Ammar *et al.* [LEBC-MPS Collaboration]. D-Meson Production in 800-GeV/c pp interactions. *Phys. Rev. Lett.* **61**, 2185 (1988).
24. G.A. Alves *et al.* [E769 Collaboration]. Feynman-x and transverse momentum dependence of D meson production in 250 GeV p, K, and p interactions with nuclei. *Phys. Rev. Lett.* **77**, 2392 (1996).
25. M. Kaya *et al.* [SELEX Collaboration], Production asymmetry of D(s) from 600-GeV/c Sigma- and pi-beam. *Phys. Lett. B* **558**, 34 (2003).
26. T. Nakano, M. Yoshimoto, R. Komatani. The Newest Technique for Nuclear Emulsion Readout. *J. of Society of Photographic Sci. and Techn. of Japan* **79**, 54 (2016).
27. M. Yoshimoto, T. Nakano, R. Komatani, H. Kawahara. Hyper-track selector nuclear emulsion readout system aimed at scanning an area of one thousand square meters. *PTEP* **10**, 103 (2017).
28. A. Ariga, T. Ariga. Fast 4π track reconstruction in nuclear emulsion detectors based on GPU technology. *JINST* **9**, P04002 (2014).
29. T. Sjostrand *et al.* A brief introduction to PYTHIA 8.1. *Comput. Phys. Commun.* **178**, 852 (2008).
30. N. Agafonova *et al.* [OPERA Collaboration]. Momentum measurement by the multiple Coulomb scattering method in the OPERA lead emulsion target. *New J. Phys.* **14**, 013026 (2012).
31. T. Nakamura, *et al.* The OPERA film: New nuclear emulsion for large-scale, high-precision experiments. *Nucl. Instrum. Meth. A* **556**, 80 (2006).
32. S. Aghion *et al.* Prospects for measuring the gravitational free-fall of antihydrogen with emulsion detectors. *JINST* **8**, P08013 (2013).
33. E. Eskut *et al.* New results from a search for $\nu_\mu \to \nu_\tau$ and $\nu_e \to \nu_\tau$ oscillation. *Phys. Lett. B* **497**, 8 (2001).
34. S. Aoki, *et al.* Experimental proposal, study of tau-neutrino production at the CERN-SPS, CERN-SPSC-2017-029, SPSC-P-354, arXiv:1708.08700.
35. T.T. Böhlen, F. Cerutti, M.P. W. Chin, A. Fasso, A. Ferrari, P.G. Ortega, A. Mairani, P.R. Sala, G. Smirnov, V. Vlachoudis. The FLUKA code: developments and challenges for high energy and medical applications. *Nucl. Data Sheets* **1 20**, 211 (2014).

Received 08.07.19

Ю. Горнушкін

ДОСЛІДЖЕННЯ ПРОДУКУВАННЯ
ТАУ-НЕЙТРИНО В ПРОТОН-ЯДЕРНІЙ ВЗАЄМОДІЇ

Р е з ю м е

В рамках експерименту DsTau на прискорювачі SPS в ЦЕРНі нами запропоновано незалежний та прямий спосіб дослідження продукування тау-нейтрино в високоенергетичних зіткненнях протонів з ядрами. Зважаючи не те, що основним джерелом нейтрино є розпад Ds-мезонів, в проекті будуть вимірюватись диференційні перерізи цього процесу. Методика експерименту базується на застосуванні емульсійних детекторів для ефективної реєстрації подій розпаду короткоживучих частинок. Нами представлено мотивацію проекту, деталі експериментальної техніки, а також перші результати аналізу даних з перших пробних сеансів, що показали ефективність нашого експерименту.

https://doi.org/10.15407/ujpe64.7.583

S. HARABASZ
for the HADES Collaboration
Institut für Kernphysik, Technische Universität Darmstadt/GSI
(9, Schlossgartenstr., 64289 Darmstadt, Germany; e-mail: s.harabasz@gsi.de)

EXPLORING BARYON RICH MATTER WITH HEAVY-ION COLLISIONS

Collisions of heavy nuclei at (ultra-)relativistic energies provide a fascinating opportunity to re-create various forms of matter in the laboratory. For a short extent of time (10^{-22} s), matter under extreme conditions of temperature and density can exist. In dedicated experiments, one explores the microscopic structure of strongly interacting matter and its phase diagram. In heavy-ion reactions at SIS18 collision energies, matter is substantially compressed (2–3 times ground-state density), while moderate temperatures are reached ($T < 70$ MeV). The conditions closely resemble those that prevail, e.g., in neutron star mergers. Matter under such conditions is currently being studied at the High Acceptance DiElecton Spectrometer (HADES). Important topics of the research program are the mechanisms of strangeness production, the emissivity of matter, and the role of baryonic resonances herein. In this contribution, we will focus on the important experimental results obtained by HADES in Au + Au collisions at 2.4 GeV center-of-mass energy. We will also present perspectives for future experiments with HADES and CBM at SIS100, where higher beam energies and intensities will allow for the studies of the first-order deconfinement phase transition and its critical endpoint.

Keywords: heavy-ion collisions, HADES, vector meson dominance, dileptons, strangeness.

1. Introduction

When two heavy ions collide at relativistic energies, they form matter of high temperature (10^{12} K) and density ($< 3\rho_0$). The exact values and, thus, the detailed properties of the matter depend on the kinetic energy of the collision. While, at $\sqrt{s_{\rm NN}}$ of the order of hundreds GeV or of TeV, the properties of the matter resemble that, which prevailed in the Universe shortly after the Big Bang, with energies of few GeVs, thermodynamic conditions are similar to neutron star mergers (see, e.g., [1]). The scan of beam energies in between probes the phase diagram of a strongly interacting matter (search for a first-order phase transition and a critical point). Through the relation between a phase structure and symmetry patterns, it sheds light on the problems of quark confinement and hadron mass generation.

In this paper, we will present the results on the production of strange hadrons and dileptons in Au + Au collisions at $\sqrt{s_{\rm NN}} = 2.4$ GeV obtained by HADES. We will put them in context of earlier results on the dilepton production in nucleon-nucleon (*pp* and *np*) reactions at the same collision energy (per nucleon).

2. Experimental Setup

HADES is a fixed-target setup installed at SIS18 (*Schwerionen-Synchrotron* with rigidity 18 Tm) accelerator in Darmstadt, Germany [2]. It possess a six-fold symmetry defined by identical sectors covering nearly 60 degrees of the azimuthal angle each. Within the sectors, the particle tracking and momentum reconstruction are provided by the toroidal magnetic field generated by compact superconducting coils located between sectors and by four Multiwire Drift Chambers (MDCs): two upstream and two downstream to the magnetic field region. The tracking resolution for lepton pair invariant masses close to vector meson poles is of the order of few % ($\delta M = 15$ MeV/c^2 at $M = 780$ MeV/c^2).

Behind the tracking system, time-of-flight detectors are located. Above the polar angle of about 45 degree, a wall of plastic scintillator bars is mounted, at lower polar angles, Resistive Plate Chambers

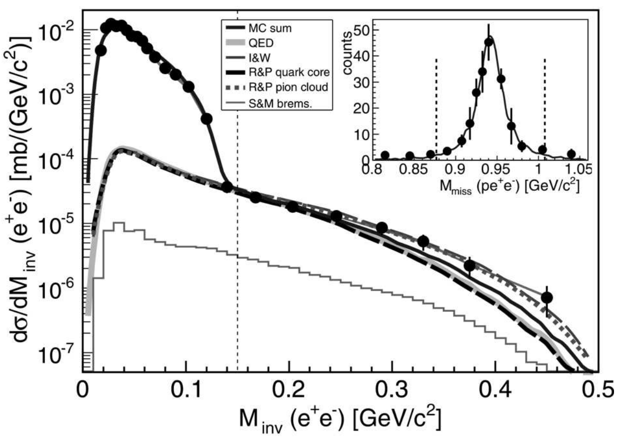

Fig. 1. e^+e^- invariant mass within the HADES acceptance. Experimental data (black dots) are corrected for the detection and reconstruction inefficiencies. Curves represent models, as discussed in the text

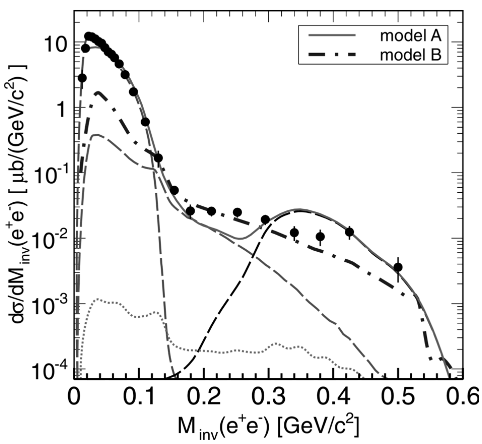

Fig. 2. Dielectron differential cross section as a function of the invariant mass of e^+e^- within the HADES acceptance. The data (black dots) are corrected for the detection and reconstruction inefficiencies. The simulated cocktail (curves) of the π^0 (dashed violet), η (dotted magenta), Δ (dashed red) Dalitz decays, ρ from the $\Delta - \Delta$ interaction process (dashed black) according to the model [4] and the sum (contributions from π^0, η, Δ and ρ – solid green curve) are displayed – model A. The dotted-dashed blue curve shows the bremsstrahlung contribution from [6] – model B

(RPCs) are installed, which have granularity necessary for high-multiplicity Au + Au events. After the proper calibration, the intrinsic time resolution of the scintillator wall is 150 ps and that of RPC – below 70 ps. Behind the RPC, an electromagnetic PreShower detector is located, which contributes to the lepton identification. In each sector, it consists of two lead converter plates sandwiched between three wire chambers in the streamer mode.

The main role in the lepton identification task is played by a Ring Imaging Cherenkov (RICH) detector. It is placed in front of the tracking system in the field-free region. It consists of a single chamber filled with C_4F_{10} radiator gas, closed by a spherical mirror in the forward direction and separated from the photon detector by a CaF_2 window in the backward direction. The photon detector is an MWPC with aa planar CsI photocathode divided into pads in such a way that Cherenkov light emitted in the radiator and reflected from the mirror forms rings on the cathode plane, whose radii in terms of the number of pads are independent of the location. For C_4F_{10}, the threshold Lorentz γ for Cherenkov emission is 18. This translates to the threshold momenta for electrons of 0.01 GeV/c, for muons of 1.9 GeV/c, and for pions of 2.4 GeV/c. With the energy available for the particle production at $\sqrt{s_{\mathrm{NN}}} = 2.4$ GeV collisions, the very fact of the Cherenkov radiation emission discriminates between electrons and other particles.

The spectrometer is also equipped with a CVD (chemical vapor deposition) diamond t_0 detector placed in front of and a VETO detector behind the target. About 7 m downstream the target, a Forward Wall hodoscope is located. The Au target was split into 15 segments, each 20 μm thick, in order to reduce the conversion probability of real photons in the target.

3. Dileptons in $p + p$ and $n + p$

Collisions of single hadrons (nucleon-nucleon and pion-nucleon) allow for determining various resonance properties in elementary collisions, in particular the electromagnetic transition form factors. Via the Dalitz decays, they can be studied in the kinematic region $0 < q^2 < 4m_p^2$ (m_p is the proton mass), which is not accessible in annihilation experiments.

The analysis of the exclusive channel $pp \to ppe^+e^-$ with a kinetic energy of 1.25 GeV of the beam allowed HADES to measure, for the first time, the branching ratio of the decay $\Delta \to pe^+e^-$. It equals $(4.19 \pm 0.62 \pm 0.34) \times 10^{-5}$, where the former uncertainty is systematic, including the model dependence, and the latter is statistical [12].

Figure 1 shows the invariant mass distribution of dileptons from $p + p$ collisions after the cut on the

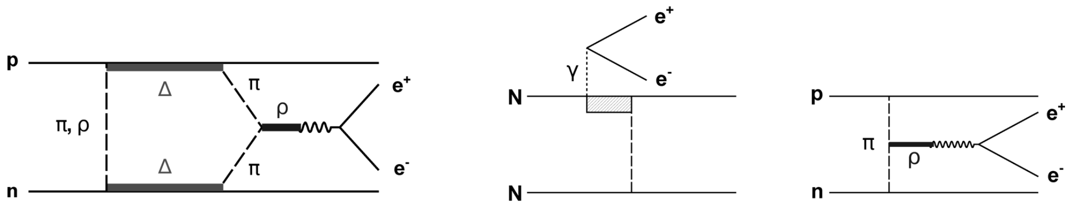

Fig. 3. Left: one of the diagrams contributing to the $\Delta - \Delta$ interaction in model A [4] of Fig. 2. Middle and right: diagrams contributing to the coherent sum in the bremsstrahlung description of [6]

proton missing mass indicated in the inset, compared to different models of the Δ form factor. The blue curve represents the sum of the following contributions: π^0 Dalitz decay, Δ Dalitz decay according to [5], and bremsstrahlung according to [6]. The cyan curve is the Δ Dalitz contribution in a description with a point-like $\gamma^* NR$ coupling ("QED-model") [7, 8], fixed from reactions with $q^2 = 0$. The two-component Iachello–Wan model [9–11], depicted with the dashed dark green curve, has the largest contribution. It parametrizes the electromagnetic interaction by a direct coupling and a coupling via a vector meson with dressed ρ propagator. The constituent quark model by Ramalho and Peña [5] describes the dominant G_M^* form factor with two contributions: quark core (quark-diquark S-wave) and pion cloud (photon directly coupling to a pion or to an intermediate baryon state). The two components are shown after scaling each of them up to the same yield as in the full model: quark core (dashed black curve) and pion cloud (dashed red curve). All model contributions are supplemented with the bremsstrahlung (shown also separately as a green histogram).

It should be noted that the quark-core contribution of the Ramalho–Peña model nearly coincides with the "QED-model," and both are not sufficient to describe the experimental data. An additional coupling in terms of the pion could/intermediate ρ meson seems to be necessary.

The role of a ρ meson is also highlighted by the np measurement [13]. It was performed by colliding a deuterium beam with a kinetic energy $1.25A$ GeV and selecting events with a quasifree neutron through the proton detection in a forward hodoscope. The cross-section distribution for the e^+e^- production over the pair invariant mass is shown in Fig. 2. It is compared to two model calculations. Model A includes hadronic sources, as well as $\Delta - \Delta$ interaction, as shown in the left-most panel of Fig. 3 (other

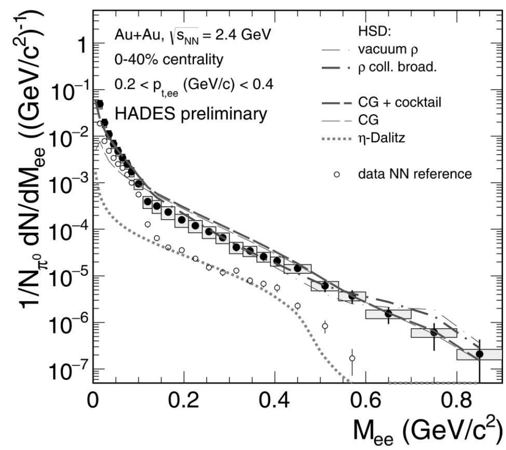

Fig. 4. Invariant mass distribution of e^+e^- from Au + Au collisions at $\sqrt{s_{\mathrm{NN}}} = 2.4$ GeV. It was corrected for the detection efficiency, extrapolated to 4π and the zero single-lepton momentum and normalized to the π^0 multiplicity. Similarly, the corrected normalized distribution from the reference pp and np reactions is shown as well. Curves represent theoretical model calculations: [18] (HSD), [16] (CG). The latter is accompanied by a cocktail of hadronic sources at the freeze-out (these sources are already included in the HSD calculation). The largest contribution to the cocktail above the π^0 mass, $\eta \to \gamma e^+e^-$, is shown separately

diagrams permuting incoming and outgoing propagators are also included). Model B contains only bremsstrahlung, described in [6] in terms of diagrams like shown in the middle and the right panel of Fig. 3 (with appropriate permutations). Model A underestimates the cross-section in the invariant mass region of 0.15–0.3 GeV/c^2. The bremsstrahlung contribution goes though the experimental points here. A full model adding all the contributions, perhaps coherently, would be needed. But the results indicate that the interaction via the pion exchange or annihilation of virtual pions with the subsequent emission of a ρ meson plays an important role in hadronic interactions.

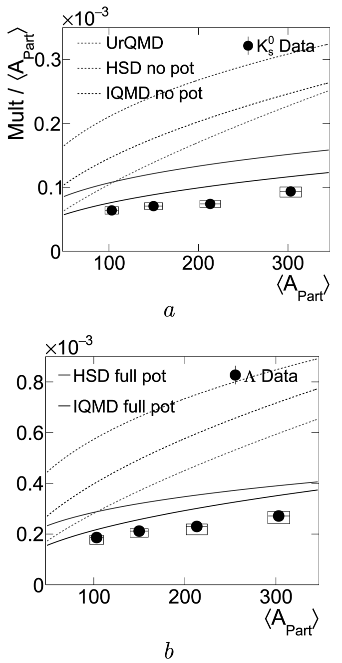

Fig. 5. Multiplicities per mean number of participants Mult/$\langle A_{\rm part}\rangle$, as a function of $\langle A_{\rm part}\rangle$ for K^0_s (a) and Λ (b) compared to various transport model calculations

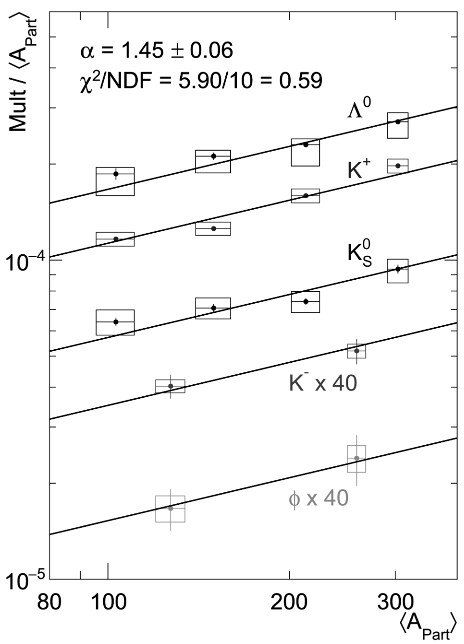

Fig. 6. Multiplicities per mean number of participants Mult/$\langle A_{\rm part}\rangle$ as a function of $\langle A_{\rm part}\rangle$. All hadron yields are fitted simultaneously with a function of the form Mult $\propto \langle A_{\rm part}\rangle^\alpha$ with the result: $\alpha = 1.45 \pm 0.06$

4. Dileptons in Heavy-Ion Collisions

In heavy-ion collisions, the dileptons are not scattered or reabsorbed through the strong interaction with hadronic matter. Thus, they can probe the interior and early stages of the evolution of a hot dense fireball. Their multiplicity will be ever-increasing with fireball's lifetime, and the spectra will take exponential shape with the slope reflecting the effective temperature of the system, which should be higher than the freeze-out temperature extracted from the spectra of hadrons that decouple in the late stage of the collision.

Figure 4 shows the invariant mass distribution of the radiation of dileptons at $\sqrt{s_{\rm NN}} = 2.4$ GeV, for a pair transverse momentum $p_{\rm t,ee}$ range of 0.2–0.4 GeV/c. It is compared to the spectrum from pp and np reactions which represents, after a proper normalization, first-chance collisions between nucleons participating in a heavy-ion reaction ("NN reference"). The excess amounts to the factor of 8–10 in the mass range above the π^0 mass, see also [14]. By comparing to the ρ spectra from the transport model HSD [18], where a ρ meson is treated as free or subject to the collisional broadening, one can note that the resonant structure completely disappears ("melts") in the experiment. This feature is captured by different implementations of the relatively novel approach of coarse-graining (CG) [15–17], where the explicit assumption of local thermal equilibrium is made. It is used to calculate the temperature and density of small space-time cells of a fireball (with transport models as the input). These are used to calculate the thermal dilepton emission using a vector meson (ρ dominating) spectral function. Coarse-graining approaches also make use of the vector meson dominance (VMD) assumption, according to which all the dilepton emission proceeds through an intermediate vector meson. Their validity is strengthened by the aforementioned findings in NN collisions.

At lower values of the invariant mass, all the models leave room for an improvement, and the higher statistics data with a higher signal-to-background ratio (main source of the systematic uncertainty) would be of great importance.

5. Strangeness Production in Heavy-Ion Collisions

Collision energies at SIS18 are below the strangeness production threshold in NN collisions. Therefore, the multiplicities and spectra of strange particles in heavy-ion reactions are sensitive to the mechanisms of energy accumulation and possibly to the equation of state of the strongly interacting matter.

Figure 5 shows the multiplicities of K_s^0 and Λ as functions of the mean number of nucleons participating in the collision, $\langle A_{\rm part}\rangle$ in Au + Au at $\sqrt{s_{\rm NN}} = 2.4$ GeV [19]. It is compared to a number of transport models: UrQMD [21], IQMD [22], and HSD [23]. For HSD and IQMD, two versions of a simulation were done: with a repulsive K-N potential of 40 MeV at the nuclear ground state density ρ_0, which increases linearly with the density, and without such a potential. Turning on the potential brings the theory predictions closer to the experimental data, both in terms of the multiplicity values and of the α exponent in the power law Mult $\propto \langle A_{\rm part}\rangle^\alpha$. The large spread between the models themselves would result in the value of the potential strongly model-dependent.

The $\langle A_{\rm part}\rangle$ dependence of the multiplicities of all strange particles reconstructed in HADES (K^+, K^-, ϕ [20], K_s^0, and Λ [19]) is displayed in Fig. 6. Data for all the particles can be described by the power law with the same exponent. This does not reflect the hierarchy in NN thresholds for different strange particles and is not expected, if the energy for their production is accumulated in a sequence of isolated nucleon-nucleon collisions. Instead, we suggested in [19] that the total amount of strange quarks in a collision is produced according to the system size determined by the number of participating nucleons. Their distribution between hadrons is fixed at the freeze-out.

6. Conclusions

HADES provides the high-statistics and high-precision data on the particle production in Au + Au collisions at the relatively low energy $\sqrt{s_{\rm NN}} = 2.4$ GeV. In this contribution, a selection of results was presented, which suggests that the hot dense fireball created in such collisions is a much stronger correlated system, than it was assumed up to now. These correlations might allow for a faster thermalization of the system, a statistical redistribution of strange quarks among hadrons, and the melting of a ρ meson. These cannot be exactly reproduced by the conventional hadronic transport models. It remains to be rigorously studied on the ground of theory and phenomenology, if the correlations can be attributed to a "pion cloud" of hadron (or another formalism), whose effect is clearly visible in NN collisions. If the density-dependent repulsive effective K-N potential can be regarded as a proxy for the nontrivial hadron structure, then the improvement in the description of the Mult($\langle A_{\rm part}\rangle$) dependence for K_s^0 and Λ could also be a manifestation of this structure.

7. Outlook

On the experimental side, the understanding of the effects observed in heavy-ion collisions requires more data with various colliding systems and beam energies. To this end, HADES measured Ag + Ag collisions at $\sqrt{s_{\rm NN}} = 2.4$ GeV and $\sqrt{s_{\rm NN}} = 2.55$ GeV in March 2019. The statistics of events at the former energy is slightly lower as in Au + Au at $\sqrt{s_{\rm NN}} = 2.4$ GeV, while it is a few times higher at the latter energy. Moreover, in Ag + Ag, the combinatorial background in the reconstruction of unstable particles is expected to be smaller, than in Au + Au. Therefore, it will very likely that the main physical results of Au + Au can be extended to Ag + Ag at both collision energies.

In the future FAIR (Facility for Antiproton and Ion Research) in Darmstadt, currently under the construction, the CBM (Compressed Baryonic Matter) experiment will collide heavy ions at energies of $\sqrt{s_{\rm NN}}$ from roughly 3 to 6 GeV. This will fill the gap in energy between the existing data of HADES and STAR at Relativistic Heavy-Ion Collider in Brookhaven. It will collect data with an unprecedented interaction rate of 10 MHz (0.5 MHz from day 1), which will allow for the studies of rare and penetrating probes, in particular, dileptons and multistrange particles and for the search of the critical point of the deconfinement phase transition. HADES at SIS100 will focus mainly on the e^+e^- and strangeness production in pp and pA collisions.

We gratefully acknowledge the support by the grants SIP JUC Cracow (Poland), 2013/10/M/ST2/00042; TU Darmstadt (Germany), VH-NG-823; GU Frankfurt, (Germany), BMBF:05P15RFFCA, HIC for FAIR, ExtreMe Matter Institute EMMI; TU MΓjnchen, Garching (Germany), MLL MΓjnchen, DFG EClust 153, DFG FAB898/2-1, BmBF 05P15WOFCA; JLU Giessen (Germany), *BMBF:05P12RGGHM; IPN, IN2P3/CNRS (France); NPI CAS Rez (Czech Republic), GACR 13-06759S, MSMT LM2015049.*

1. M. Hanauske *et al.* Neutron star mergers: Probing the EoS of hot, dense matter by gravitational waves. *Particles* **2**, 44 (2019).
2. G. Agakichiev *et al.* (HADES). The high-acceptance dielectron spectrometer HADES. *Eur. Phys. J. A* **41**, 243 (2009).
3. G. Ramalho, M.T. Peña, J. Weil, H. van Hees, U. Mosel. Role of the pion electromagnetic form factor in the $\Delta(1232) \rightarrow \gamma^* N$ timelike transition. *Phys. Rev. D* **93**, 033004 (2016).
4. M. Bashkanov, H. Clement. On a Possible Explanation of the DLS Puzzle. *Eur. Phys. J. A* **50**, 107 (2014).
5. G. Ramalho, M.T. Peña, J. Weil, H. van Hees, U. Mosel. The high-acceptance dielectron spectrometer HADES. *Phys. Rev. D* **93**, 033004 (2016).
6. R. Shyam, U. Mosel. Dilepton production in proton-proton and quasi-free proton-neutron reactions at 1.25 GeV. *Phys. Rev. C* **82**, 062201 (2010).
7. M. Zétényi, Gy. Wolf. Dilepton decays of baryon resonances. *Heavy Ion Phys.* **17**, 27 (2003).
8. F. Dohrmann *et al.* A versatile method for simulating $\mathrm{pp} \rightarrow \mathrm{pp}\ \mathrm{e}^+\mathrm{e}^-$ and $\mathrm{dp} \rightarrow \mathrm{pn}\ \mathrm{e}^+\mathrm{e}^-\ \mathrm{p(spec)}$ reactions. *Eur. Phys. J. A* **45**, 401 (2010).
9. F. Iachello and Q. Wan. Structure of the nucleon from electromagnetic timelike form factors. *Phys. Rev. C* **69**, 055204 (2004).
10. Q. Wan, F. Iachello. A unified description of baryon electromagnetic form factors. *Int. J. Mod. Phys. A* **20**, 1846 (2005).
11. Q. Wan, PhD Thesis. A Unified Approach to Baryon Electromagnetic Form Factors (Yale University, New Haven, 2007).
12. J. Adamczewski-Musch *et al.* (HADES Collaboration). $\Delta(1232)$ Dalitz decay in proton-proton collisions at $T = 1.25$ GeV measured with HADES at GSI. *Phys. Rev. C* **95**, 065205 (2017).
13. J. Adamczewski-Musch *et al.* (HADES Collaboration). entrality determination of Au + Au collisions at 1.23 A GeV with HADES. *Eur. Phys. J. A* **53**, 149 (2017).
14. J. Adamczewski-Musch *et al.* (HADES Collaboration). Probing dense baryon-rich matter with virtual photons. *Nature Physics.* https://doi.org/10.1038/s41567-019-0583-8.
15. S. Endres *et al.*. Dilepton production and reaction dynamics in heavy-ion collisions at SIS energies from coarse-grained transport simulations. *Phys. Rev. C* **92**, 014911 (2015).
16. T. Galatyuk *et al.* Thermal dileptons from coarse-grained transport as fireball probes at SIS energies. *Eur. Phys. J. A* **52**, 131 (2016).
17. J. Staudenmaier *et al.* Dilepton production and resonance properties within a new hadronic transport approach in the context of the GSI-HADES experimental data. *Phys. Rev. C* **98**, 054908 (2018).
18. E. L. Bratkovskaya *et al.* System size and energy dependence of dilepton production in heavy-ion collisions at 1–2 GeV/nucleon energies. *Phys. Rev. C* **87**, 064907 (2013).
19. J. Adamczewski-Musch *et al.* (HADES Collaboration). Sub-threshold production of K_0^s mesons and Λ hyperons in Au + Au collisions at $\sqrt{s_{NN}} = 2.4$ GeV. *Phys. Lett. B* **793**, 457 (2019).
20. J. Adamczewski-Musch *et al.* (HADES Collaboration). Deep sub-threshold ϕ production in Au + Au collisions. *Phys. Lett. B* **778**, 403 (2018).
21. S.A. Bass *et al.* Microscopic models for ultrarelativistic heavy ion collisions. *Prog. Part. Nucl. Phys.* **41**, 225 (1998).
22. C. Hartnack. *et al.* Modeling the many body dynamics of heavy ion collisions: Present status and future perspective. *Eur. Phys. J. A* **1**, 151 (1998).
23. W. Cassing, E.L. Bratkovskaya. Hadronic and electromagnetic probes of hot and dense nuclear matter. *Phys. Rept.* **308**, 65 (1999).

Received 08.07.19

С. Гарабаш

ДОСЛІДЖЕННЯ БАРІОННОЇ
МАТЕРІЇ В ЗІТКНЕННЯХ ВАЖКИХ ІОНІВ

Р е з ю м е

Зіткнення важких іонів при (ультра-)релятивістських енергіях дають чудову можливість для створення різних форм речовини в лабораторії. Короткий час (10^{-22} сек) може існувати речовина з екстремальними температурою та щільністю. В спеціальних експериментах вивчається мікроскопічна структура сильновзаємодіючої речовини і її фазова діаграма. В реакціях з важкими іонами при енергіях SIS18 речовина значно стискається (в 2–3 рази порівняно зі щільністю основного стану) при помірних температурах ($T < 70$ МеВ). Ці умови нагадують, наприклад, стан колапсу нейтронних зірок. Речовина при таких умовах власне вивчається на HADES (High Acceptance DIElectron Spectrometer). Важливими в рамках цієї програми є дослідження механізму продукування дивності, випромінювання матерії та роль в цьому баріонних резонансів. В даній роботі ми звертаємо увагу на важливі експериментальні результати, отримані на HADES у зіткненнях Au+Au при енергії в системі центра мас 2,4 ГеВ. Ми також представимо перспективи майбутніх експериментів з HADES та CBM при SIS100, де більш високі енергії та інтенсивності дозволять вивчати фазовий перехід першого роду деконфайнменту та відповідну йому критичну точку.

https://doi.org/10.15407/ujpe64.7.589

D. HORVÁTH

Wigner Research Centre for Physics, Budapest, Hungary;
and Institute of Nuclear Research (Atomki), Debrecen, Hungary
(H-1121 Budapest, Konkoly-Thege 29-33, Hungary; e-mail: horvath.dezso@wigner.mta.hu, dezso.horvath@cern.ch)

TESTS OF *CPT* INVARIANCE AT THE ANTIPROTON DECELERATOR OF CERN

The Standard Model, the theory of particle physics is based on symmetries: both the structure of the composite particles and their interactions are derived using gauge invariance principles. Some of these are violated by the weak interaction like parity and CP symmetry, and even masses are created via spontaneous symmetry breaking. CPT invariance, the most essential symmetry of the Standard Model, states the equivalency of matter and antimatter. However, because of the lack of antimatter in our Universe it is continuously tested at CERN. We overview these experiments: measuring the properties of antiprotons as compared to those of the proton at the Antiproton Decelerator and also searching for antimatter in cosmic rays.

Keywords: Standard Model, CPT invariance, antiproton mass, antihydrogen, cosmic antimatter.

1. Introduction

The theory behind particle physics, called for historic reasons *the Standard Model*, developed half a century ago, is based on *gauge symmetries* [1]. Some of those, however, are violated, like the maximally broken parity symmetry or the tiny little CP-violation. And of course, there is the spontaneous symmetry breaking mechanism necessary to create masses for the elementary particles.

The fundamental particles of the Standard Model are fermions with half-integer and bosons with integer spins. The elementary fermions have three families, each consisting of a pair of quarks and a pair of leptons and all of them have antiparticles of opposite charges, but otherwise identical properties. The leptons can propagate, but the quarks are bound in hadrons: the baryons (like the proton and neutron) consist of three quarks and the antibaryons of three antiquarks, and the mesons (like the pion) are bound states of a quark and an antiquark.

The three basic interactions in the Standard Model are derived from local gauge invariances: the strong interaction from a local SU(3) and the electroweak one from a local U(1)⊗SU(2) gauge invariance with the *spontaneous symmetry breaking*. These interactions are mediated by elementary bosons, the strong interaction by the eight gluons carrying the colour charges of the quarks and antiquarks, the weak interaction by the three heavy weak bosons, $W^{\pm}$ and Z^0 and the electromagnetism by the γ photon. These bosons are virtual when they mediate the interactions, but they can also be emitted and observed experimentally, even the heavy weak bosons and the coloured gluons in high-energy collisions.

2. CPT Invariance

According to the well-known theorem of Emmy Noether, continuous symmetries of the Lagrangian lead to conservation laws. The conservation of the electric charge and of the fermion number is connected to the U(1) symmetry of the Dirac Lagrangian: that is a valid, non-breaking symmetry. The colour-SU(3) symmetry of quantum chromodynamics leads to the conservation of the colour charge. The ultimate symmetry of matter and antimatter is manifested by the CPT invariance, which makes it possible to treat free antiparticles as particles moving backward in space and time. This is a most important symmetry of Nature: the physical laws do not change when charge (C), space (P) and time (T) are simultaneously inverted:

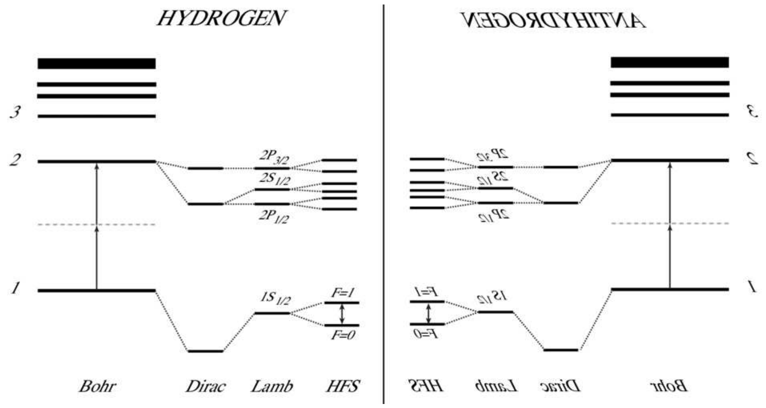

Fig. 1. Energy levels of hydrogen and antihydrogen. The 2S–1S transition offers extremely precise two-photon spectroscopy [3]

- charge conjugation (i.e. changing particles into antiparticles), $C\psi(r,t) = \overline{\psi}(r,t)$;
- parity change (i.e. mirror reflection), $P\psi(r,t) = \psi(-r,t)$, and
- time reversal, $T\psi(r,t) = \psi(r,-t)K$ where K denotes complex conjugation.

Time reversal is an *anti-unitary* operation due to the phase factor connecting time and energy in the state function. As a result, CPT is also anti-unitary, it conjugates the phase of the system while not changing the measurable properties. Using CPT invariance positron annihilation can be described as if an electron arrived, irradiated two or three photons and left backward in space and time.

CPT invariance is supported by all known theoretical and experimental evidence. Its role is so fundamental in quantum field theory that it is almost impossible to test experimentally: in the case of observing a small deviation one should suspect the violation of a conservation law rather than CPT violation. Giving up CPT invariance brings dire consequences: one may lose causality, unitarity or Lorentz invariance. Nevertheless, it seems to be grossly violated: according to the generally accepted Big Bang theory of cosmology, at the end of the radiation period particles and antiparticles should have been produced in exactly the same amounts, but we cannot see antimatter galaxies anywhere [2]. This badly necessitates testing the CPT invariance experimentally. To date the most precise one of such tests is the mass difference between the neutral kaon and anti-kaon as measured using kaon oscillation: the relative difference is less than 10^{-18}.

3. Antimatter Problems

In 1928 Paul M. Dirac tried to produce a linear equation for the hydrogen atom and got two solutions for the electron: an ordinary one and another one with positive charge and negative mass. Dirac first assumed the latter non-physical, but three years later Carl Anderson observed positively charged electrons, positrons in cosmic rays (both of them were awarded the Nobel Prize).

In addition to the mysterious lack of antimatter in our Universe, there are some other questions for antiparticles. Is it really true that particles and their antiparticles have exactly the same properties except for the sign of their charges? Could there be a tiny difference between particle and antiparticle to cause the lack of antimatter galaxies? Are there particles which are their own antiparticles (called Majorana particles)? In principle, the neutrinos can be Majorana-particles, although there are no signs of this in experiment. Could the dark matter of the Universe consist of such particles?

The above problems may point to a possible CPT violation, and so we are obliged – in spite of our belief in its validity – to test CPT invariance. The easiest way is to compare the properties of particles and antiparticles. In addition to the kaon-anti-kaon mass difference one can compare the spectroscopic properties of atoms and anti-atoms. It was shown [3] that the simplest and most precise such measurement with antiprotons should be to perform two-photon spectroscopy on antihydrogen atoms, $\overline{\mathrm{H}} = [\overline{\mathrm{p}}\mathrm{e}^+]$, the bound state of an antiproton and a positron, and that antihydrogen can be produced and confined in electromagnetic traps. The 1S–2S transition of antihydrogen (Fig. 1) seemed to be most eligible as it can be excited with two photons only and as a result of that it has a very long lifetime and consequently very narrow line width. Moreover, when applying two counter-propagating laser pulses one excludes the longitudinal Doppler-broadening of the line width, significantly increasing the precision of the measurement.

4. The Antiproton Decelerator of CERN

Antihydrogen atoms were first produced at the Low Energy Antiproton Ring (LEAR) at CERN and later also at Fermilab [4, 5]. Relativistic antiprotons collide in the storage ring with Xe atoms and produce electron-positron pairs. With a low probability the antiproton can pick up a fast positron forming an antihydrogen atom which is neutral and leaves the ring along a straight beam line. The positron and the antiproton of the antihydrogen atom are then separated and identified: the positron annihilates to two photons and the antiproton to several charged pions.

CERN, the joint European Particle Physics Laboratory has built the *Antiproton Decelerator, AD* facility (it is now called Antimatter Factory) in 1997-99 to study antimatter physics and to test the CPT invariance, mainly via producing and studying antihydrogen. At the moment there are six experiments: three to test CPT and another three to check antigravity, i.e. to measure the gravitational mass of the antiproton.

The Antiproton Decelerator works the following way. The Proton Synchrotron shoots protons with a 26 GeV/c momentum onto an iridium target producing proton–antiproton pairs. From there the AD gets antiprotons of 3.57 GeV/c momentum and slows them down to 100 MeV/c (corresponding to 5.3 MeV kinetic energy) in four steps, in the first two steps with stochastic and then electron cooling [7]). The AD delivers $3 \ldots 4 \times 10^7$ antiprotons at 100 MeV/c momentum to several experiments, which trap them in electromagnetic fields after suitable further deceleration, and using slow positrons make antihydrogen ($\overline{\mathrm{p}}\mathrm{e}^+$) atoms [6].

The antiprotons have to slow further down to keV energies in order to facilitate trapping. The ALPHA and ATRAP experiments prepare spectroscopy on trapped antihydrogen, ASACUSA and BASE compare the properties (mass, charge and magnetic moment) of protons and antiprotons at high precision, AEGIS and GBAR plan to measure the gravitational mass of antihydrogen, and ACE studied the effects of antiprotons on living tissue. The success of the AD experiments persuaded CERN to increase their efficiency by building a small storage ring ELENA (Extreme Low Energy Antiprotons) which will supply an order of magnitude higher number of slow antiprotons for trapping than the AD with the energy absorbers of the experiments. ELENA has been constructed and it will serve all AD experiments from 2020 on.

5. Antihydrogen Production

In order to produce antihydrogen, one has to confine both antiprotons and positrons in a trap, cool them to very low temperatures and then let them interact. The radiative recombination, ($\overline{\mathrm{p}}\mathrm{e}^+\gamma$), should produce deeply bound atoms, but it is hopelessly slow. At the moment all AD experiments produce $\overline{\mathrm{H}}$ atoms using the three-body recombination reaction [8]: $\overline{\mathrm{p}}\mathrm{e}^+\mathrm{e}^+ \to \overline{\mathrm{H}}\mathrm{e}^+$ where a second positron carries away the released energy and momentum. This reaction has a quite high cross section, but it produces highly excited $\overline{\mathrm{H}}$ atoms which then should be de-excited to make spectroscopy possible.

Another method [9] is investigated at the AD: $\overline{\mathrm{H}}$ production in collisions of antiprotons with positronium, the bound state of an electron and positron. This reaction has a high rate and results in not-too-highly excited $\overline{\mathrm{H}}$, but it is more complicated to prepare.

The first cold, confined $\overline{\mathrm{H}}$ atoms were produced by the ATHENA experiment at the AD, and its successor, the ALPHA (Antimatter Laser PHysics Apparatus) Collaboration made all steps leading from $\overline{\mathrm{H}}$ atoms confined in a trap, to their de-excitation and spectroscopy. At the same time the ASACUSA (Atomic Spectroscopy And Collisions Using Slow Antiprotons) Collaboration managed to produce and extract an $\overline{\mathrm{H}}$ beam from a trap.

6. $\overline{\mathrm{H}}$ Spectroscopy by the ALPHA Experiment

The ALPHA (Antimatter Laser PHysics Apparatus) Collaboration was the first and to date the only experiment to perform $2S$–$1S$ spectroscopy on antihydrogen [12]. The measurement was quite elaborate, developed gradually step by step in ten years:

1. 90,000 antiprotons were captured and cooled in a Penning trap.

2. Mixed them with 3 million cold positrons and 50,000 $\overline{\mathrm{H}}$ atoms were produced.

3. The remaining charged particles were removed by dropping the trapping potential.

4. 20 $\overline{\mathrm{H}}$ atoms were stored in an inhomogeneous magnetic field at $T = 0.54$ K temperature.

5. The $\overline{\mathrm{H}}$ atoms were kept trapped for 10 s in order to let them to undergo de-excitation to the $1S$ ground state.

6. The excitation $1S \to 2S$ was performed with two 243 nm photons (standing wave for 300 s) tuned around the resonance (appearance measurement).

7. A microwave irradiation removed the residual $1S$ atoms (disappearance measurement).

8. The trap was flushed by dropping the confining B field measuring the number of remaining $\overline{\mathrm{H}}$ atoms.

The 10 s waiting time was necessary to let the $\overline{\mathrm{H}}$ atoms de-excite to 1S, and at the same time short enough not to lose them from the trap as demonstrated by the ALPHA experiment earlier. Half the cold $\overline{\mathrm{H}}$ atoms can be confined depending on the spin polarization of the positron, and thus they can be flushed out by a microwave irradiation on resonance with the positron spin flip. This hyperfine transition was also studied when preparing the experiment [11]. At each step the antiproton annihilations were detected with checking the vertex positions of the events to make sure that they do not come from hitting the walls of the vessel. The last three steps made both an appearance and a disappearance measurement of the same reaction, and the results agreed with each other and also with the simulation assuming CPT invariance. At laser spectroscopy the laser power affects the result: that was also measured and the results normalized to the power of 1 W. At last, ALPHA has managed also to observe the 1S–2P Lyman alpha transition in antihydrogen [12].

Using 15000 $\overline{\mathrm{H}}$ atoms the ALPHA experiment [10] yielded 2 466 061 103 079.4 $\pm$5.4 kHz for the 1S–2S transition frequency of antihydrogen. Its precision is just one order of magnitude behind that of ordinary hydrogen: 2 466 061 103 080.3 $\pm$0.6 kHz. This means a confirmation of CPT on the level of 2×10^{-12}.

7. Antimatter Gravity Measurement

The negative mass of antiparticles in the Dirac theory keeps exciting the general public, although the masses of our everyday objects are mostly (about 95%) energy-related. Of course, this is also something that has to be checked experimentally as precisely as possible. Unfortunately, gravity is so much weaker than electromagnetism that it makes a measurement with charged particles hopeless. There are nice gravity measurements made with neutrons, but the problem with antineutrons is that they cannot be slowed down without fast annihilation. That leaves antihydrogen for such studies. Of course, CPT invariance does not prescribe identical acceleration in Earth's gravitational field for protons and antiprotons: that is a result of the weak equivalence principle.

Testing antimatter gravity is the main aim of two AD experiments, AEGIS and GBAR. AEGIS (Antihydrogen Experiment: Gravity, Interferometry, Spectroscopy) is the largest AD collaboration (although still two orders of magnitude smaller than the largest LHC experiments). They are preparing to measure the gravitational falling of a beam of collimated $\overline{\mathrm{H}}$ atoms as compared to light using Moiré deflectometry. AEGIS will produce antihydrogen using the collisions of antiprotons with excited positronium atoms [13].

The GBAR (Gravitational Behaviour of Antihydrogen at Rest) Collaboration [14] plans to do an antihydrogen free-fall measurement. They plan to use such a dense positronium cloud that the antiprotons would pick up two positrons in two collisions to form an $\overline{\mathrm{H}}^{+}$ ion which then can be cooled in several steps down to the vicinity of 10 μK and they will move very slowly. Removing the excess positron via laser excitation they plan to let the neutral $\overline{\mathrm{H}}$ fall in the gravitational field of Earth and measure its acceleration. GBAR was the first AD experiment to use the slow antiprotons from ELENA in 2018. The ALPHA Collaboration has also constructed a free-fall apparatus for measuring antihydrogen gravity.

8. Antiproton Properties

The ASACUSA (Atomic Spectroscopy And Collisions Using Slow Antiprotons) Collaboration stopped antiprotons in helium gas and using laser spectroscopy measured the transition energies of antiprotons between atomic orbits determined the mass of the antiproton [15]. The method is based on the earlier observation that about 3% of antiprotons stopped in helium gas get captured in a metastable three-body bound state $[\bar{\mathrm{p}}\mathrm{He}^{+}\mathrm{e}^{-}]$. When a laser resonance excites its transition to a non-metastable state, the antiproton will immediately annihilate. The experiment managed to increase the relative precision of the measurements from year to year, reaching the order of 10^{12} (meaning a CPT-test of similar precision) using two-photon spectroscopy [16] and buffer-gas cooling [17]. The ASACUSA Collaboration has built a post-decelerator system (essentially a radio-frequency quadrupole accelerator cavity working the opposite way) which increased the trapping efficiency by orders of magnitude and made it possible to produce an extracted beam [18] of slow antihydrogen atoms.

The BASE (Baryon Antibaryon Symmetry Experiment) performed direct high-precision measurements of the charge-to-mass ratio [19] and the magnetic moment [21] of a single antiproton stored in a cryogenic Penning trap. Both of them are, of course, sensitive CPT-tests when compared to those of the proton. It is remarkable, that this method is not destructive: in all 2016 BASE used 18 antiprotons for their measurements [20]. The obtained charge-to-mass ratio agrees with the predictions of the Standard Model (i.e. CPT invariance) at the level of 10^{-10}. Moreover, assuming CPT invariance the above result helps to confirm the weak equivalence principle [20] in Earth's gravitational field on the level of 6.8×10^{-7}.

9. Antimatter in Space

To solve the problem of the lack of antimatter galaxies, CERN prepared a cosmic detector, the Alpha Magnetic Spectrometer (AMS2) with the leadership of Nobel laureate Samuel Chao-chung Ting. It has a 1200 kg permanent magnet and it was launched in 2011 from the USA. It is placed onto the International Space Station and checks antiparticles in cosmic rays and also searches for dark matter annihilation. So far it did not detect anti-helium atoms, but saw many high-energy positrons which could come from pulsars or dark matter.

10. Conclusion

The Antiproton Decelerator of CERN was built 20 years ago in order to test the validity of CPT invariance, the principle of matter-antimatter symmetry. The work of these two decades yielded many results, and the measured antiproton charge, mass, and magnetic moment, and the antihydrogen 1S–2S transition measurement all conform the validity of CPT and the Standard Model. The lack of antimatter galaxies seems to question CPT invariance, but the results of the AMS2 space detector also confirmed: no anti-helium atoms are seen in cosmic rays. Thus CPT invariance seems to be at absolute validity.

This work was supported by the National Research, Development, and Innovation Fund of Hungary under contracts K124850 and K128786.

1. F. Wilczek. In search of symmetry lost. *Nature* **433**, 239 (2005).
2. A.G. Cohen, A. De Rujula, S.L. Glashow. A matter – antimatter universe? *Astrophys. J.* **495**, 539 (1998).
3. M. Charlton, J. Eades, D. Horvath, R.J. Hughes, C. Zimmermann. Anti-hydrogen physics. *Phys. Rept.* **241**, 65 (1994).
4. G. Baur *et al.* Production of anti–hydrogen. *Phys. Lett. B* **368**, 251 (1996).
5. G. Blanford *et al.* [E862 Collaboration]. Observation of atomic anti-hydrogen. *Phys. Rev. Lett.* **80**, 3037 (1998).
6. J.S. Hangst. Fundamental physics with antihydrogen. *Springer Tracts Mod. Phys.* **256**, 203 (2014).
7. P. Beloshitsky. Report on operation of antiproton decelerator. *AIP Conf. Proc.* **821** (1), 48 (2006).
8. G. Gabrielse, S.L. Rolston, L. Haarsma, W. Kells. Antihydrogen production using trapped plasmas. *Phys. Lett. A* **129**, 38 (1988).
9. B.I. Deutch, F.M. Jacobsen, L.H. Andersen, P. Hvelplund, H. Knudsen, M.H. Holzscheiter, M. Charlton, G. Laricchia. Anti-hydrogen production by positronium anti-proton collisions in an ion trap. *Phys. Scripta T* **22**, 248 (1988).
10. M. Ahmadi *et al.* Characterization of the 1S–2S transition in antihydrogen. *Nature* **557**, 71 (2018).
11. M. Ahmadi *et al.* [ALPHA Collaboration]. Observation of the hyperfine spectrum of antihydrogen. *Nature* **548**, 66 (2017).
12. M. Ahmadi *et al.* [ALPHA Collaboration]. Observation of the 1S–2P Lyman-α transition in antihydrogen. *Nature* **561**, 211 (2018).
13. C. Amsler *et al.* [AEgIS Collaboration]. Velocity-selected production of 2^3S metastable positronium. *Phys. Rev. A* **99**, 033405 (2019).
14. B. Mansouli [GBAR Collaboration]. Status of the GBAR experiment at CERN. *Hyperfine Interact.* **240**, 11 (2019).
15. R.S. Hayano, M. Hori, D. Horvath, E. Widmann. Antiprotonic helium and CPT invariance. *Rept. Prog. Phys.* **70**, 1995 (2007).
16. M. Hori *et al.* [ASACUSA Collaboration]. Two-photon laser spectroscopy of antiprotonic helium and the

antiproton-to-electron mass ratio. *Nature* **475**, 484 (2011).
17. M. Hori *et al.* [ASACUSA Collaboration]. Buffer-gas cooling of antiprotonic helium to 1.5 to 1.7 K, and antiproton-to-electron mass ratio. *Science* **354**, 610 (2016).
18. Y. Nagata *et al.* Progress of antihydrogen beam production using a double cusp trap. *JPS Conf. Proc.* **18**, 011007 (2017).
19. S. Ulmer *et al.* [BASE Collaboration]. High-precision comparison of the antiproton-to-proton charge-to-mass ratio. *Nature* **524**, 196 (2015).
20. S. Ulmer, A. Mooser, H. Nagahama, S. Sellner, C. Smorra. Challenging the standard model by high-precision comparisons of the fundamental properties of protons and antiprotons. *Phil. Trans. Roy. Soc. Lond. A* **376**, 20170275 (2018).
21. C. Smorra *et al.* [BASE Collaboration]. A parts-per-billion measurement of the antiproton magnetic moment. *Nature* **550**, 371 (2017).

Received 08.07.19

Д. Хорват

ТЕСТИ *CPT* ІНВАРІАНТНОСТІ
НА АНТИПРОТОННОМУ УПОВІЛЬНЮВАЧІ ЦЕРНу

Р е з ю м е

Стандартна Модель теорії елементарних частинок базується на симетріях: як структура композитних частинок, так і їх взаємодія виводяться з принципів калібровної інваріантності. Деякі з них, як парність та *CP* симетрія, порушуються слабкою взаємодією, та навіть маси породжуються спонтанним порушенням симетрії. Згідно з *CPT* інваріантності – найсуттєвішої симетрії Стандартної Моделі – матерія та антиматерія еквівалентні. Проте, через відсутність антиматерії у Всесвіті, цю симетрію постійно вивчають у ЦЕРНі. Ми даємо огляд цих експериментів: вимірюємо властивості антипротонів у порівнянні з протонами на Антипротонному Уповільнювачі, а також шукаємо антиречовину в космічних променях.

https://doi.org/10.15407/ujpe64.7.595

C. VAN HULSE
on behalf of the LHCb Collaboration
University College Dublin
(Belfield, Dublin 4, Ireland; e-mail: cvanhuls@mail.cern.ch)

CENTRAL EXCLUSIVE PRODUCTION AT LHCb

The LHCb collaboration has measured central exclusive production of J/ψ, $\psi(2S)$, and Υ mesons as well as $J/\psi J/\psi$, $J/\psi\psi(2S)$, $\psi(2S)\psi(2S)$, and $\chi_c\chi_c$ meson pairs in proton-proton collisions. The analyses of Υ and charmonium pairs are performed at the centre-of-mass energies of 7 TeV and 8 TeV, and those of J/ψ and $\psi(2S)$ are done at 7 TeV and 13 TeV. The analysis at 13 TeV involves the use of new shower counters. These allow a reduction in the background by vetoing events with activity in an extended region in rapidity. The measurements of central exclusive production at LHCb are sensitive to gluon distributions for Bjorken-x values down to 2×10^{-6} (at 13 TeV). An overview of the LHCb results is presented and compared to existing measurements of other experiments and theoretical calculations.

K e y w o r d s: exclusive photoproduction, ultra-peripheral collisions, generalised parton distributions, parton distribution functions.

1. Introduction

The nucleon structure can be described in three dimensions in terms of the probability to find quarks and gluons as a function of their transverse position inside the nucleon and their longitudinal momentum fraction with respect to the nucleon momentum [1, 2]. The longitudinal direction coincides here with the direction of the probe used to investigate the nucleon. The corresponding probability distributions are called impact-parameter-dependent parton distributions. They are Fourier transforms of generalised parton distributions (GPDs) (see, e.g., Ref. [3]). These GPDs do not have a probabilistic interpretation. Instead, they represent probability amplitudes for a parton with longitudinal momentum fraction $x+\xi$ to be emitted from a nucleon and a parton with longitudinal momentum fraction $x-\xi$ to be absorbed by the nucleon. The nucleon stays intact, but receives a four-momentum transfer squared equal to $-t$. This is represented in Fig. 1, for quarks (left) and gluons (right).

Generalised parton distributions are accessible in exclusive reactions, such as the exclusive production of photons or vector mesons, involving a hard scale. The hard scale is necessary in order to factorise the process into perturbatively calculable parts and non-perturbative parts, which are the GPDs and meson distribution amplitudes in the case of exclusive meson production [4, 5]. Exclusive vector-meson production can be measured in deep-inelastic scattering, as illustrated in Fig. 1, left. The hard scale is provided here by the large virtuality, $Q^2 = -q^2 \gg 1$ GeV^2, of the photon exchanged between the lepton and the nucleon. There exists a multitude of such measurements at fixed-target experiments [6–13] and at lepton-proton colliders, by the H1 and ZEUS collaborations [14–17]. The former series of measurements are mainly sensitive to larger values of Bjorken-x, x_B, with $\xi \approx x_B/(2-x_B)$, and thus to quark GPDs, while the latter probe lower values of x_B down to 10^{-4}, where gluons dominate.

Alternatively, it is possible to use a (quasi-)real photon ($Q^2 \approx 0$ GeV^2) to investigate the nucleon, provided that the particle created in the final state has a large mass component. In the case of exclusive vector-meson production, such as J/ψ or Υ production, the large scale is then provided by the large mass of the meson valence quarks (charm or bottom quarks). The vector mesons originate, as illustrated in Fig. 1, right, from the splitting of the real photon into a quark-antiquark pair ($c\bar{c}$ or $b\bar{b}$). This pair interacts with a nucleon through the exchange of two gluons, and as a result a vector meson is formed in the final state. Quasi-real photopro-

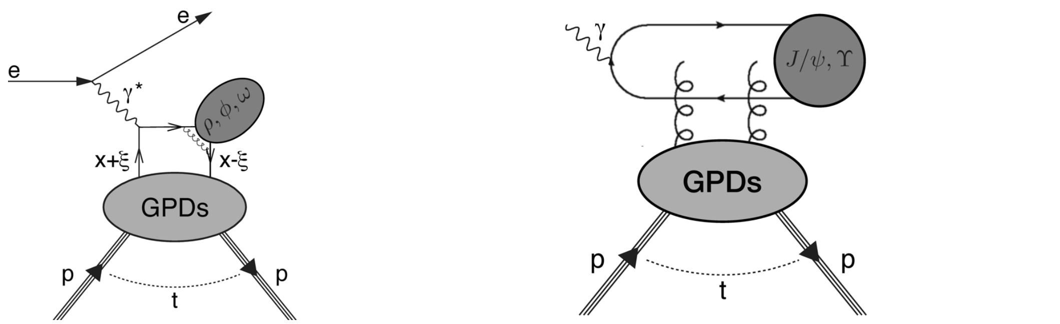

Fig. 1. Diagrams for exclusive production of vector mesons in deep-inelastic scattering (left) and in photoproduction (right). The figure on the left illustrates access to quark GPDs, while the figure on the right shows the diagram for gluon GPDs

duction of vector mesons has been measured in electron-proton collisions by the H1 and ZEUS experiments [16, 18–21]. These measurements probe a photon-nucleon centre-of-mass energy ranging from 30 GeV to 300 GeV.

It is also possible to study photoproduction in ultra-peripheral collisions of protons and ions. In such reactions, the beam particles interact at a large enough distance from each other (in practice more than the sum of their respective nuclear radii) so that they interact through the exchange of colour-neutral objects. The flux of photons emitted by a beam particle is proportional to the square of its atomic charge, and hence photon emission by heavy ions is greater than for protons. There exist measurements of exclusively produced vector mesons in gold-gold collisions by the PHENIX experiment [22], in proton-antiproton collisions by the CDF experiment [23], in lead-lead and proton-lead collisions by the ALICE experiment [24–26] and in proton-proton and lead-lead collisions by the LHCb experiment [27–31]. The covered photon-nucleon centre-of-mass energy ranges from 34 GeV, for the PHENIX experiment, to 1.5 TeV, for the measurements performed by the LHCb collaboration. The very high energy available at the LHC offers the unique possibility to probe the GPDs down to Bjorken-x values of the order of 10^{-6}, i.e., two orders of magnitude lower than for the existing measurements in electron-proton collisions. At such low values of x_{B}, one might also be sensitive to saturation effects [32]. In addition, at such low x_{B}, the exclusive cross section can be approximated in terms of standard gluon parton distribution functions (PDFs) [33–36]. This cross section has a quadratic dependence on the gluon PDFs, and thus provides a higher sensitivity than inclusive measurements, where the dependence is only linear.

2. LHCb Measurements

In central exclusive production of vector mesons in ultra-peripheral collisions, the proton (or ion) emitting the real photon is to a good approximation not altered from its original trajectory, while the proton interacting through the two gluons undergoes a small change in momentum, but remains close to the beam line. The vector meson, in turn, is produced in the central region. At LHCb, this vector meson is generally reconstructed through its decay into a $\mu^+\mu^-$ pair. Hence, the experimental signature for exclusive vector-meson production is two oppositely charged muons in the LHCb detector, with large regions of rapidity, down to close to the beam line, devoid of particle activity. There exists a different process with the same final state, but where the oppositely charged muons originate from the interaction of photons emitted by the respective beam particles. This process is called the Bethe–Heitler process. This production mode of muons forms a continuum background to the exclusive production of vector mesons, and needs to be subtracted from the measured signal. Another source of background is the production of higher-mass vector mesons that decay into the vector meson under study without detection of the other decay products. Furthermore, the production of vector mesons where one or both of the interacting protons dissociate forms another background contribution.

The LHCb detector is a forward detector, covering a rapidity range between 2 and 5. The detector is fully instrumented for particle identification, and is capa-

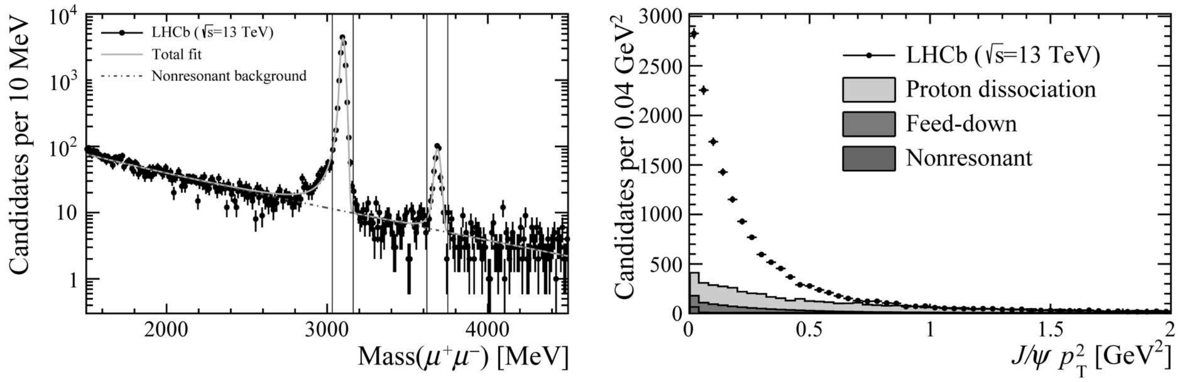

Fig. 2. Dimuon invariant-mass distribution (left) and dimuon squared-transverse-momentum distribution for muon pairs within the J/ψ invariant mass region (right) for data collected at $\sqrt{s} = 13$ TeV, and satisfying the selection requirement imposed by HeRSCheL. Different background contributions are indicated in both figures, while the vertical lines in the figure on the left indicate the selected range in invariant mass for the measurement of J/ψ and $\psi(2S)$

ble of detecting particles with transverse momenta as low as 200 MeV. The LHCb experiment is not instrumented with detectors around the beam line for the detection of protons emerging intact from the interaction or for products from proton dissociation that remain close to the beam line. However, the LHCb experiment is well suited for the measurement of exclusive processes. Firstly, the average number of interactions per beam crossing at the LHCb interaction point ranges only from 1.1 to 1.5, depending on running conditions. Secondly, besides the coverage in rapidity from 2 to 5 by the fully instrumented LHCb detector, the LHCb vertex locator is capable of detecting charged-particle activity for rapidities between –3.5 and –1.5. Also, for Run 2 of the LHC data-taking period (2015–2018), the LHCb experiment was additionally equipped with a series of five stations of scintillators, HeRSCheL [37], placed at –114 m to +114 m from the LHCb interaction point. This allowed for the detection of particle showers in a rapidity range between –10 and –5, and between +5 and +10, and hence for a supplementary reduction of the contribution from background processes.

Measurements of exclusive production of J/ψ and $\psi(2S)$ mesons have been performed by the LHCb experiment using data collected in proton-proton collisions at a centre-of-mass energy $\sqrt{s} = 7$ TeV [28], and part of the data collected at $\sqrt{s} = 13$ TeV [30], amounting to an integrated luminosity of respectively 929 ± 33 pb^{-1} and 204 ± 8 pb^{-1}. This data set allows one to access x_B down to 2×10^{-6}. Both the J/ψ meson and the $\psi(2S)$ meson are reconstructed through

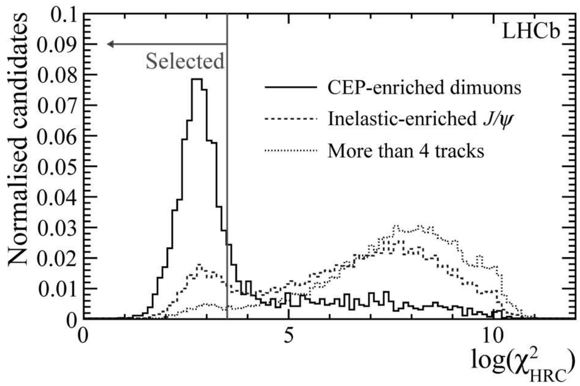

Fig. 3. The distribution, normalised to unit area, of the HeRSCheL discriminating variable χ^2_{HRC}. The continuous, black line corresponds to a sample highly enriched in exclusively produced muon pairs; the blue, dashed line represents the distribution for events enriched in inelastically produced J/ψ mesons, while the purple, short-dashed line contains events with more than four tracks

their decay into muons, which are required to lie in the LHCb detector acceptance, between 2 and 4.5 in rapidity. Furthermore, the transverse momentum squared of the dimuon pair, $p_T^2 \approx -t$, needs to be below 0.8 GeV^2. Finally, the absence of any other detector activity is required.

In Fig. 2, left, the dimuon invariant-mass distribution is shown, while in Fig. 2, right, the squared-transverse-momentum distribution of the muon pair with invariant mass in the J/ψ mass region is presented. The three sources of background contamination to the J/ψ signal are also shown. The back-

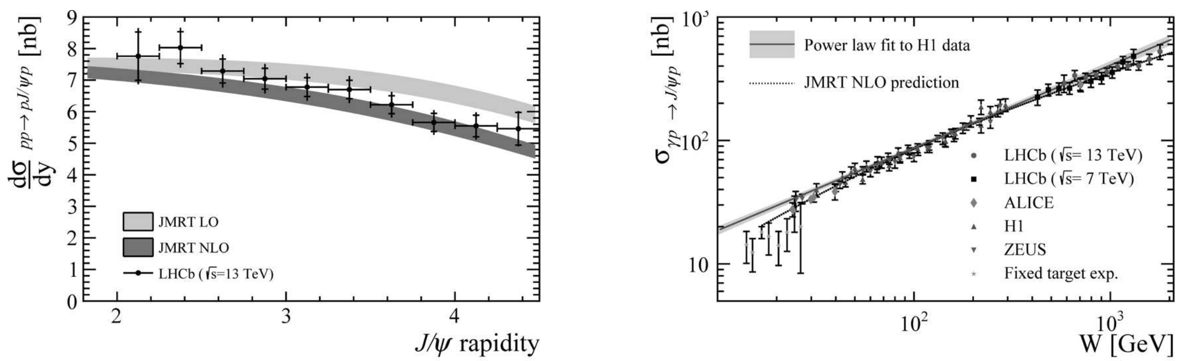

Fig. 4. Cross section differential in rapidity for exclusive J/ψ production (left) and exclusive J/ψ photoproduction cross section as a function of the photon-proton invariant mass (right). The leading-order (yellow band) and next-to-leading-order (green band and dotted line) JMRT calculations [34] are also indicated

ground contribution from the Bethe–Heitler process, labelled nonresonant background, is obtained from a fit to the dimuon mass distribution (see Fig. 2, left). The background from feed-down from exclusive production of $\psi(2S)$ and χ_c mesons is evaluated using $\psi(2S)$ and χ_c signals in experimental data and Monte-Carlo simulation. Finally, the contamination from events where at least one of the protons dissociates is evaluated for Run 1 through a fit of the dimuon transverse-momentum distribution, while for the data collected in Run 2, HeRSCheL has been used. The discriminating power of HeRSCheL is illustrated in Fig. 3. The figure represents distributions of a discriminating variable related to detector activity in HeRSCheL. The continuous, black line is the distribution for a very pure sample of exclusively produced pairs of muons, while the other lines indicate samples enriched in nonexclusive events. From the figure, it is clear that for exclusive events, the discriminating variable is located at low values, whereas for nonexclusive events, the variable extends to higher values. For the selection of exclusive events in Run 2, only events below the value indicated by the red, vertical line are selected. This results in a signal purity of 76% (73%) for J/ψ ($\psi(2S)$). For data collected in Run 1, the signal purity amounts to 62% (52%), where the contribution from proton-dissociative background is about twice as high.

The cross section differential in rapidity for exclusive production of J/ψ in proton-proton collisions at $\sqrt{s}$ = 13 TeV is shown in Fig. 4, left. It is seen to decrease at larger values of rapidity. In addition to the experimental data points, theoretical predictions (JMRT) [34], which approximate the cross section in terms of standard gluon PDFs, are shown. There are predictions at leading order in α_S (yellow band) and at next-to-leading order in α_S (green band). The leading-order predictions fail to describe the data at higher rapidities, while the next-to-leading order calculations are in reasonable agreement with the data.

The exclusive vector-meson production cross section in proton-proton collisions is related to the photoproduction cross section through

$$\sigma_{pp\to p\psi p} = r(W_+)k_+\frac{dn}{dk_+}\sigma_{\gamma p\to\psi p}(W_+) + \\ + r(W_-)k_-\frac{dn}{dk_-}\sigma_{\gamma p\to\psi p}(W_-), \quad (1)$$

where r represents the gap survival factor, $k_\pm$ the photon energy, $dn/dk_\pm$ the photon flux, and $W_\pm^2 = = 2k_\pm\sqrt{s}$ the photon-proton invariant mass squared. The subscript + (−) corresponds to the situation where the downstream-going (upstream-going) proton is the photon emitter. As can be seen from Eq. (1), the photoproduction cross section appears twice in the expression. The reason resides in the ambiguity on the identity of the proton emitting the real photon. Since the photoproduction cross section corresponding to the low-energy solution W_- only contributes about one third of the time and it has been previously measured and parametrised by the H1 collaboration, this parametrisation is used to fix the low-energy photoproduction cross section, and extract the one at high photon-proton invariant mass. The resulting photoproduction cross section is presented in Fig. 4, right. The data points represented by the red circles are the result at $\sqrt{s}$ = 13 TeV,

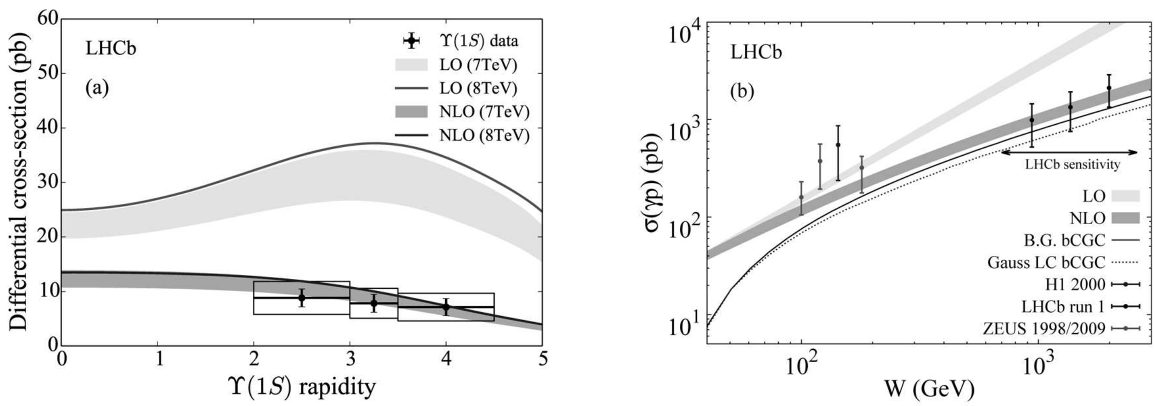

Fig. 5. Cross section differential in rapidity for exclusive $\Upsilon(1S)$ production (left) and exclusive $\Upsilon(1S)$ photoproduction cross section as a function of the photon-proton invariant mass (right). Next-to-leading-order (leading-order) JMRT calculations [34] at $\sqrt{s} = 7$ TeV are indicated by the blue (yellow) band and include uncertainties. The mean value of the next-to-leading-order (leading-order) calculations from JMRT [34] at $\sqrt{s} = 8$ TeV is indicated by the blue (red) line

while those indicated by the black squares are those at $\sqrt{s} = 7$ TeV. Also measurements from the H1 collaboration, from which the parametrisation is taken, the ZEUS and ALICE collaborations as well as from fixed-target experiments [38–40] are presented. The different data sets are in good agreement with each other. The parametrisation from the H1 collaboration is indicated in the figure by the blue band. It is seen to describe the data well at intermediate values of W, but fails at lower and higher values. Also the next-to-leading order JMRT calculations are shown, as indicated by the dotted line. They are in good agreement with the data, describing it well also at low and high values of W. Also for the proton-proton and photoproduction cross section of $\psi(2S)$ (not shown), the next-to-leading order predictions in α_S describe the data well, whereas the leading-order predictions fail to describe the data.

There exist also results from exclusive Υ production by the LHCb collaboration, using data collected in proton-proton collisions in Run 1 at $\sqrt{s} = 7$ TeV and $\sqrt{s} = 8$ TeV, corresponding to a respective luminosity of 0.9 fb^{-1} and 2.0 fb^{-1} [29]. The two data sets are combined in order to increase statistical precision. The data-selection procedure follows that of the measurement for exclusive J/ψ, with a p_T^2 restricted to below 2.0 GeV^2. Given the larger mass of the Υ meson, the lowest values in x_B reach down to 2×10^{-5}. The total proton-proton production cross section for $\Upsilon(1S)$ is determined to be $9.0 \pm 2.1 \pm 1.7$ pb, where the first uncertainty is statistical and the second systematic, while for $\Upsilon(2S)$ it is $1.3 \pm 0.8 \pm 0.3$ pb. For $\Upsilon(3S)$ production, an upper limit on the cross section of 3.4 pb at the 95% confidence level is determined. For the $\Upsilon(1S)$ resonance, the production cross section differential in rapidity and the photoproduction cross section as a function of W are also extracted. They are shown in Fig. 5. Also here, leading-order and next-to-leading order JMRT calculations are presented, and only the next-to-leading order calculations describe the data well. In the figure on the right, also results from the ZEUS and H1 collaborations are shown. These are not able to discriminate between the leading-order and next-to-leading order calculations.

The LHCb collaboration also published results of exclusive production of the charmonium pairs $J/\psi J/\psi$, $J/\psi\psi(2S)$, $\psi(2S)\psi(2S)$, $\chi_{c0}\chi_{c0}$, $\chi_{c1}\chi_{c1}$, and $\chi_{c2}\chi_{c2}$ [41]. These are potentially sensitive to glueballs and tetraquarks. In the framework of describing the exclusive cross section in terms of standard gluon PDFs, they are sensitive to the fourth power of these gluon PDFs. The measurements combine the data collected in proton-proton collisions at $\sqrt{s} = 7$ TeV and $\sqrt{s} = 8$ TeV. The production cross sections are measured to be $\sigma(J/\psi J/\psi) = 58 \pm 10 \pm 6$ pb; $\sigma(J/\psi\psi(2S)) = 63^{+27}_{-18} \pm 10$ pb; $\sigma(\psi(2S)\psi(2S)) < 237$ pb; $\sigma(\chi_{c0}\chi_{c0}) < 69$ nb; $\sigma(\chi_{c1}\chi_{c1}) < 45$ pb; $\sigma(\chi_{c2}\chi_{c2}) < 141$ pb, where only an upper limit is determined for the four last pairs. These results are not corrected for proton dissociation, due to the limited statistical precision. Only for the production of pairs of $J/\psi J/\psi$ it is possible to estimate the contribution from central exclusive production, which amounts to about 42%, and thus to determine the cross section corrected for proton dissociation, which is 24 ± 9 pb.

3. Summary

Measurements of exclusive production of J/ψ, $\psi(2S)$, and $\Upsilon(nS)$, with $n = 1, 2, 3$, have been performed by the LHCb collaboration. These measurements are sensitive to gluon GPDs and PDFs. The cross sections are measured differentially in rapidity and the photoproduction cross section is extracted as a function of the photon-proton invariant mass. Comparisons to next-to-leading order JMRT calculations show good agreement with these data. Also cross-section measurements of pairs of charmonia have been performed. They are sensitive to the fourth power of the gluon PDFs and potentially to glueballs and tetraquarks. Although not discussed here, there are also preliminary measurements of Bethe-Heitler production in proton-proton collisions [42] and on exclusive χ_c production in proton-proton collisions [42], which is sensitive to the exchange of two gluon pairs. Furthermore there are preliminary results on exclusive production of J/ψ and $\psi(2S)$ in lead-lead collisions [31], which give access to nuclear GPDs and PDFs, and are sensitive to shadowing.

1. M. Burkardt. Impact parameter dependent parton distributions and off-forward parton distributions for $\boldsymbol{\zeta}0$. *Phys. Rev. D* **62**, 071503 (2000).
2. M. Burkardt. Impact parameter space interpretation for generalized parton distributions. *Int. J. Mod. Phys. A* **18**, 173 (2003).
3. M. Diehl. Generalized parton distributions. *Phys. Rept.* **388**, 41 (2003).
4. J.C. Collins, L. Frankfurt, M.S. Strikman. Factorization for hard exclusive electroproduction of mesons in QCD. *Phys. Rev. D* **56**, 2982 (1997).
5. A.V. Radyushkin. Nonforward parton distributions. *Phys. Rev. D* **56**, 5524 (1997).
6. I. Bedlinskiy *et al.*, [CLAS]. Exclusive η electroproduction at $W > 2$ GeV with CLAS and transversity generalized parton distributions. *Phys. Rev. C* **95**, 035202 (2017).
7. P.E. Bosted *et al.*, [CLAS]. Target and beam-target spin asymmetries in exclusive pion electroproduction for $Q^2 >$ > 1 GeV^2. I $ep \to e\pi^+ n$. *Phys. Rev. C* **95**, 035207 (2017).
8. C. Adolph *et al.*, [COMPASS]. Transverse target spin asymmetries in exclusive $\rho 0$ muoproduction. *Phys. Lett. B* **731**, 19 (2014).
9. C. Adolph *et al.*, [COMPASS]. Exclusive ω meson muoproduction on transversely polarised protons *Nucl. Phys. B* **915**, 454 (2017).
10. Fuchey *et al.*, [Jefferson Lab Hall A]. Exclusive neutral pion electroproduction in the deeply virtual regime. *Phys. Rev. C* **83**, 025201 (2011).
11. A. Airapetian *et al.*, [HERMES]. Spin density matrix elements in exclusive ω electroproduction on ^{1}H and ^{2}H targets at 27.5 GeV beam energy. *Eur. Phys. J. C* **74**, 3110 (2014).
12. A. Airapetian *et al.*, [HERMES]. Transverse-target-spin asymmetry in exclusive ω-meson electroproduction. *Eur. Phys. J. C* **75**, 600 (2015).
13. A. Airapetian *et al.*, [HERMES]. Ratios of helicity amplitudes for exclusive ρ^0 electroproduction on transversely polarized protons. *Eur. Phys. J. C* **77**, 378 (2017).
14. F.D. Aaron *et al.*, [H1]. Diffractive electroproduction of ρ and φ mesons at HERA. *JHEP* **05**, 032 (2010).
15. A. Aktas *et al.*, [H1]. Measurement of F-2 (c (c) over-bar) and F-2 (b (b) over-bar) at high Q(2) using the H1 vertex detector at HERA. *Eur. Phys. J. C* **46**, 585 (2006).
16. S. Chekanov *et al.*, [ZEUS]. Exclusive electroproduction of J/ψ mesons at HERA. *Nucl. Phys. B* **695**, 3 (2004).
17. S. Chekanov *et al.*, [ZEUS]. Exclusive ρ^0 production in deep inelastic scattering at HERA. *PMC Phys. A* **1**, 6 (2007).
18. C. Adloff *et al.*, [H1]. Diffractive photoproduction of ψ(2S) mesons at HERA. *Phys. Lett. B* **541**, 251 (2002).
19. A. Aktas *et al.*, [H1]. Elastic J/ψ production at HERA. *Eur. Phys. J. C* **46**, 585 (2006).
20. C. Alexa *et al.*, [H1]. Elastic and proton-dissociative photoproduction of J/ψ mesons at HERA. *Eur. Phys. J. C* **73**, 2466 (2013).
21. S. Chekanov *et al.*, [ZEUS]. Exclusive photoproduction of γ mesons at HERA. *Phys. Lett. B* **680**, 4 (2009).
22. S. Afanasiev *et al.*, [PHENIX]. Photoproduction of J/ψ and of high mass e^+e^- in ultra-peripheral Au + Au collisions at $\sqrt{s_{NN}} = 200$ GeV. *Phys. Lett. B* **679**, 321 (2009).
23. T. Aaltonen *et al.*, [CDF]. Observation of exclusive charmonium production and $\gamma\gamma \to \mu^+\mu^-$ in $p\bar{p}$ collisions at $\sqrt{s} = 1.96$ TeV. *Phys. Rev. Lett.* **102**, 242001 (2009).
24. E. Abbas *et al.*, [ALICE]. Charmonium and e^+e^- pair photoproduction at mid-rapidity in ultra-peripheral Pb–Pb collisions at $\sqrt{s_{NN}} = 2.76$ TeV. *Eur. Phys. J. C* **73**, 2617 (2013).
25. B. Abelev *et al.*, [ALICE]. Coherent J/ψ photoproduction in ultra-peripheral Pb–Pb collisions at $\sqrt{s_{NN}} = 2.76$ TeV. *Phys. Lett. B* **718**, 1273 (2013).
26. B. Abelev *et al.*, [ALICE]. Exclusive J/ψ photoproduction off protons in ultraperipheral p-Pb collisions at $\sqrt{s_{NN}} =$ $= 5.02$ TeV. *Phys. Rev. Lett.* **113**, 232504 (2014).
27. R. Aaij *et al.*, [LHCb]. Exclusive J/ψ and ψ(2S) production in pp collisions at TeV. *J. Phys. G: Nucl. Part. Phys.* **40**, 045001 (2013).

28. R. Aaij *et al.*, [LHCb]. Updated measurements of exclusive J/ψ and ψ(2S) production cross-sections in *pp* collisions at TeV *J. Phys. G: Nucl. Part. Phys.* **41**, 055002 (2014).
29. R. Aaij *et al.*, [LHCb]. Measurement of the exclusive Y production cross-section in *pp* collisions at $\sqrt{s} = 7$ TeV and 8 TeV. *JHEP* **09**, 084 (2015).
30. R. Aaij *et al.*, [LHCb]. Central exclusive production of J/ψ and ψ(2S) mesons in *pp* collisions at $\sqrt{s} = 13$ TeV. *JHEP* **10**, 167 (2018).
31. LHCb Collaboration. Study of coherent J/ψ production in lead-lead collisions at $\sqrt{s_{NN}} = 5$ TeV with the LHCb experiment. CERN-LHCb-CONF-2018-003.
32. N. Armesto *et al.* Exclusive vector meson production at high energies and gluon saturation. *Phys. Rev. D* **90**, 054003 (2014).
33. M.G. Ryskin. Diffractive J/ψ electroproduction in LLA QCD. *Z. Phys. C* **57**, 89 (1993).
34. S.P. Jones *et al.* Probes of the small x gluon via exclusive J/ψ and Y production at HERA and the LHC. *JHEP* **11**, 085 (2013).
35. S.P. Jones *et al.* Exclusive J/ψ process Tamed to probe the low-x gluon. arXiv:1609.09738.
36. C.A. Flett *et al.* Towards a determination of the low x gluon via exclusive J/ψ production. arxiv:1907.06471.
37. K.C. Akiba *et al.* The HeRSCheL detector: High-rapidity shower counters for LHCb. *JINST* **13**, P04017 (2018).
38. M.E. Binkley *et al*, [E104]. J/ψ photoproduction from 60 to 300 GeV/c. *Phys. Rev. Lett.* **48**, 73 (1982).
39. B.H. Denby *et al.*, [E516]. Inelastic and Elastic Photoproduction of $J/\psi(3097)$. *Phys. Rev. Lett.* **52**, 795 (1984).
40. P.L. Frabetti *et al.*, [E687]. A measurement of elastic J/ψ photoproduction cross section at Fermilab E687. *Phys. Lett. B* **316**, 197 (1993).
41. R. Aaij *et al.*, [LHCb]. Observation of charmonium pairs produced exclusively in collisions. *J. Phys. G: Nucl. Part. Phys.* **41**, 115002 (2014).
42. LHCb Collaboration. Central Exclusive Production at LHCb. CERN-LHCb-CONF-2011-022.

Received 08.07.19

Ш. Ван Гулсе
від імені Колаборації LHCb

ЦЕНТРАЛЬНЕ ЕКСКЛЮЗИВНЕ
ПРОДУКУВАННЯ НА LHCb

Р е з ю м е

Колаборація LHCb вимірювала центральне ексклюзивне продукування мезонів J/ψ, $\psi(2S)$ і Υ мезонів, а також мезонних пар $J/\psi J/\psi$, $J/\psi\psi(2S)$, $\psi(2S)\psi(2S)$, $\chi_c\chi_c$ в протон-протонних зіткненнях. Аналіз пар мезонів Υ та шармонія виконано при енергіях в системі центра мас 7 та 8 ТеВ, а для J/ψ та $\psi(2S)$ – при 7 та 13 ТеВ. В аналізі при 13 ТеВ були задіяні нові лічильники, які зменшують фон, відсікаючи події з активністю в широкому інтервалі швидкостей. Виміри центрального ексклюзивного продукування на LHCb чутливі до глюонних розподілів для значень бйоркенівської змінної аж до $2 \cdot 10^{-6}$ при 13 ТеВ. Нами представлено огляд результатів LHCb та їх порівняння з існуючими вимірами в інших експериментах, а також з теоретичними розрахунками.

https://doi.org/10.15407/ujpe64.7.602

O. KOVALENKO

National Centre for Nuclear Research
(Warsaw, Poland; e-mail: oleksandr.kovalenko@ncbj.gov.pl)

NEUTRAL MESON AND DIRECT PHOTON MEASUREMENTS WITH THE ALICE EXPERIMENT

The ALICE experiment is designed to study the properties of the matter created in proton-proton and heavy-ion collisions at the LHC. Neutral mesons can be reconstructed in ALICE in a wide range of transverse momenta via two-photon decays. Neutral meson measurements in pp collisions give an opportunity to validate the NLO or NNLO pQCD calculations and to constrain the parton distribution functions and the parton fragmentation functions. Neutral meson spectra measured in pA and AA collisions allow us to test a modification of the parton distribution functions in nuclei and the parton energy loss in the hot matter created in AA collisions. The recent results from ALICE on direct photon measurements in the Pb–Pb, neutral pion and η meson productions in pp, p-Pb, and Pb–Pb collisions are presented.

Keywords: high-energy physics, neutral meson spectra, direct photons.

1. Introduction

ALICE experiment aims to explore properties of the hot ($T \sim 10^{12}$ K) and dense quark-gluon matter and to investigate the chiral symmetry restoration and the deconfinement mechanisms. The hard hadron production in pp collisions can be described by a convolution of the hard parton cross-section, parton distribution function (PDF), and fragmentation function (FF). The measurement of hadron spectra in a wide kinematic range for various collision energies provides a new input for PDF and FF parametrizations. The meson production in heavy-ion collisions allows studying several effects. The development of a collective flow can be studied at low $p_{\rm T}$ ($p_{\rm T} < 3$ GeV/c). The high-$p_{\rm T}$ ($p_{\rm T} > 5$ GeV/c) part of the spectra originates predominantly from the hard parton hadronization. At moderate $p_{\rm T}$, the π^0 and η mesons are mainly produced via the gluon fragmentation at LHC energies. As gluons show a larger energy loss in the medium than quarks, the comparison of the suppressions of the yields of light neutral mesons and heavier hadrons will provide an input for the understanding of the energy loss by the different partons. The difference in the suppression patterns of the π^0 and η meson yields can indicate the differences in the relative contributions of quarks and gluons. Neutral meson spectra also serve as an input for the direct photon analysis. Direct photons are defined as all photons that are not coming from the decays of particles. Photons do not interact strongly with the medium. They carry information on the properties of the matter at the space-time point of their emission. The high-$p_{\rm T}$ part of the direct photon spectrum is dominated by photons created in the hard scattering of the partons of incoming nucleons and can serve as a tool to constrain the models that describe the initial stage of a collision. The low-$p_{\rm T}$ part of the direct photon spectrum may contain photons from the thermal emission of the hot matter and probes its temperature and the velocity of the collective expansion.

2. Neutral Meson Measurements

The ALICE experiment is a general-purpose detector [1]. It consists of 17 separate subdetectors that are dedicated to specific goals. Neutral mesons are reconstructed via the two-photon decay channel. Photons in ALICE can be measured in an Electro-Magnetic Calorimeter (EMCal) [2] and a Photon Spectrometer (PHOS) [3] or by means of the Photon Conversion Method (PCM) based on the reconstruction of photons from e^+e^- pairs that are products of the photon conversion in the material of central barrel detectors [4].

The product the efficiency ε times the acceptance A for different methods of neutral meson reconstruction is shown in Fig. 1. The EMCal has the highest $A \cdot \varepsilon$

values, as it has a large acceptance and a high probability to measure photons. PHOS has a lower $A \cdot \varepsilon$ factor due to limited acceptance, but it has lower energy threshold for the signal and outperforms EMCal at low p_{T}. It is possible to combine the photons reconstructed with EMCal and PCM to form pairs (PCM-EMC method). In this case, the $A \cdot \varepsilon$ factor is approximately 10 times smaller than that of EMCal due to the small conversion probability of a photon. This method makes it possible to extend the measurement up to high p_{T}, because showers from different photons don't merge in a detector. The PCM efficiency is determined by the probability of the photon conversion, its $A \cdot \varepsilon$ factor is the lowest.

2.1. Transverse momentum spectra of neutral mesons in pp collisions

The ALICE experiment has measured π^0 and η meson spectra in pp collisions at several collision energies: $\sqrt{s} = 0.9, 2.76, 7, 8$ TeV [5–9], see Fig. 2. Neutral pion spectra were reconstructed up to $p_{\mathrm{T}} \sim 40$ GeV/c (for $\sqrt{s} = 2.76$ TeV). PYTHIA 8.2 [10] with Monash 2013 tune describes the data at high p_{T}, but shows a deviation from the data at moderate p_{T} at the higher energies. The NLO calculations [11–13] predict a 20–60% higher yield, and the difference increases with p_{T}. The situation with η meson is similar: PYTHIA 8.2 with Monash 2013 tune reproduces the data, whereas the NLO calculations predict a 50–100% higher yield at all colliding energies.

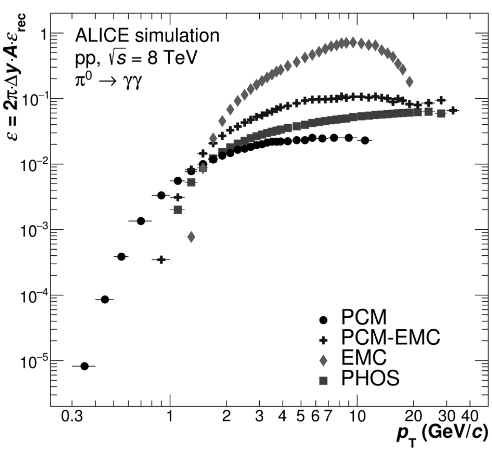

Fig. 1. Normalized correction factors ϵ for each reconstruction method for π^0 as a function of p_{T}. The factors contain the reconstruction efficiencies and the detector acceptances normalized per unit rapidity and full azimuthal angle

2.2. Transverse momentum spectra of neutral mesons in p-Pb collisions

ALICE has recently measured the π^0 and η yields in p-Pb collisions at $\sqrt{s_{\mathrm{NN}}} = 5.02$ TeV [15]. Neutral pion and η spectra are well described by the Tsallis fits [16]. The NLO pQCD calculations [11, 17] scaled

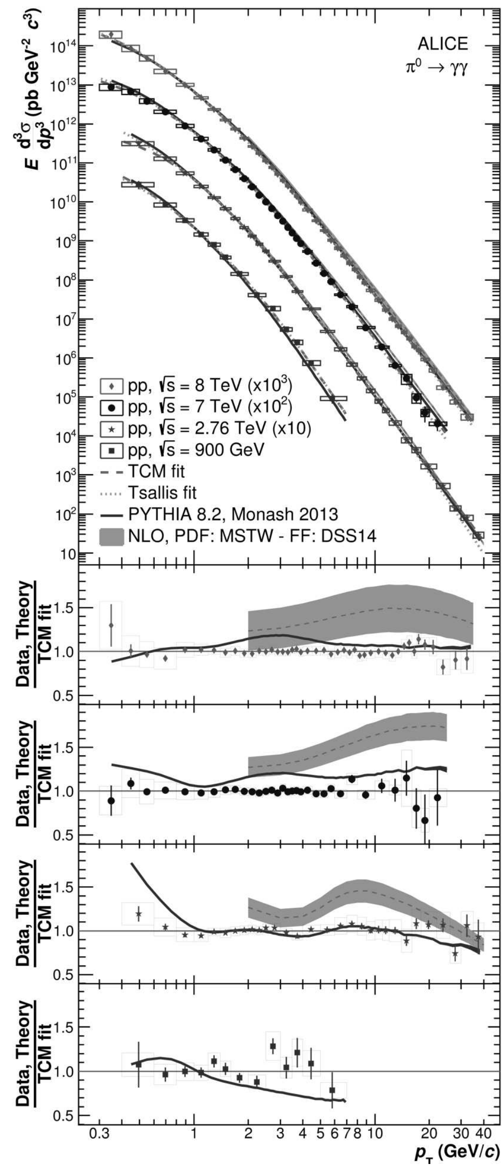

Fig. 2. Neutral pion spectrum at $\sqrt{s} = 0.9, 2.76, 7,$ and 8 TeV [5–9]. The spectrum is compared to the PYTHIA8 [10] event generator and NLO pQCD calculations. The ratios of data and predictions to the two-component model (TCM) fit [14] are shown on the bottom panels for each energy separately

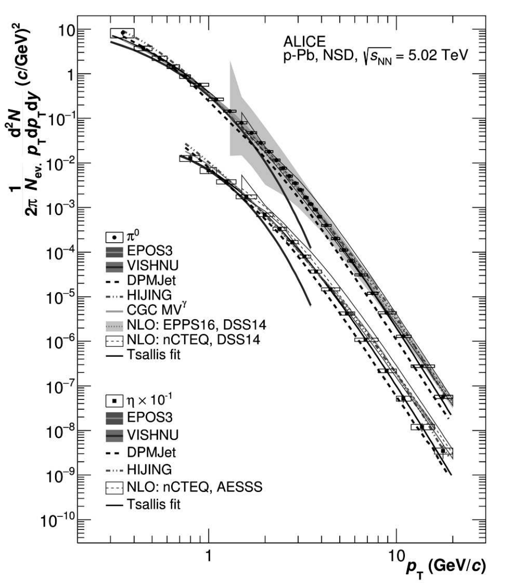

Fig. 3. Neutral pion and η spectra measured in p-Pb collisions at $\sqrt{s_{\rm NN}} = 5.02$ TeV [15]. The data are compared to the scaled NLO pQCD calculations [11, 17] and to DPMJET [19], VISHNU [20], HIJING [21], EPOS [18], CGC [22] models

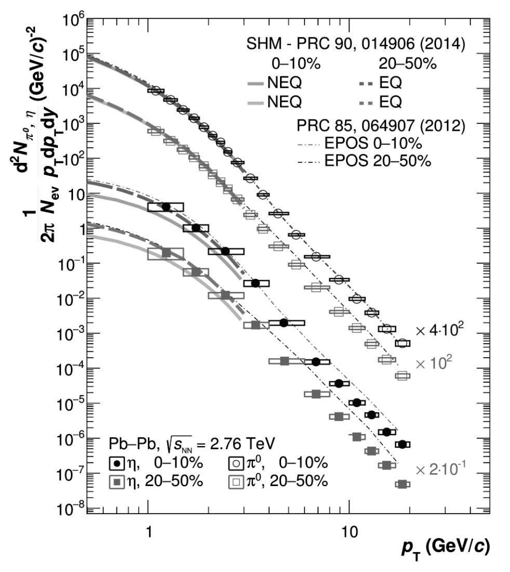

Fig. 4. Neutral pion and η spectra in two centrality classes measured in Pb–Pb collisions at $\sqrt{s_{\rm NN}} = 2.76$ TeV [6]

with the number of binary nucleon-nucleon collisions reproduce the π^0 spectrum in the entire $p_{\rm T}$ range and overpredict the η spectrum at high $p_{\rm T}$. EPOS [18] Monte-Carlo reproduces the π^0 spectrum and η spectrum below 3 GeV/c, but overpredicts it at high $p_{\rm T}$. The hydrodynamic model VISHNU[20] provides a good description at low $p_{\rm T}$. The HIJING[21] and DPMJET [19] models fail to reproduce data for $p_{\rm T}$ larger than 4 GeV/c.

2.3. Transverse momentum spectra of neutral mesons in Pb–Pb collisions

The data collected in 2010 allowed the measurement of the spectrum of π^0 in Pb–Pb collisions at $\sqrt{s_{\rm NN}} = 2.76$ TeV in the range $0.6 < p_{\rm T} < 12$ GeV/c [6]. The neutral pion yield can be described by the Tsallis fits. Combining the datasets collected in 2010 and 2011 years allowed one to extend the range of the π^0 spectrum up to 20 GeV/c and to measure also the η meson spectra in narrower centrality classes [8], see Fig. 4. Two versions of the SHM model [23] reproduce the shape of the π^0 spectrum at low $p_{\rm T}$. For the η mesons, NEQ SHM underestimates the yield at the low-$p_{\rm T}$ region.

2.4. Nuclear modification factor in Pb–Pb collisions

Figure 5 shows the nuclear modification factor defined as the meson yield in Pb–Pb collisions divided by the meson production cross-section in pp collisions at the same energy scaled with the nuclear overlap function. The value of $R_{\rm AA} = 1$ corresponds to the absence of medium effects. For Pb–Pb collisions at $\sqrt{s_{\rm NN}} = 2.76$ TeV, $R_{\rm AA} \sim 0.1$ at $p_{\rm T} \sim 7$ GeV/c was observed reflecting a strong energy loss by partons in the hot quark-gluon matter. The $R_{\rm AA}$ increases with $p_{\rm T}$. The nuclear modification factors for π^0 and η agree with those for $\pi^\pm$ and $K^\pm$. The right plot of Fig. 5 shows the centrality dependence of the nuclear modification factor in Pb–Pb collisions. The $R_{\rm AA}$ decreases, as the centrality increases, indicating that the medium effects are most prominent in the central collisions.

3. Direct Photons Measurements

Direct photons are all photons that do not originate from the hadron decays. The yield can be calculated as

$$\gamma_{\rm \,direct} = \gamma_{\rm \,inc} - \gamma_{\rm \,decay} = (1 - 1/R_\gamma)\,\gamma_{\rm \,inc},$$

where $\gamma_{\rm \,inc}$ – the inclusive photon spectrum, $\gamma_{\rm \,decay}$ – the decay photon spectrum, $\gamma_{\rm \,direct}$ – the direct photon spectrum, and $R_\gamma = \gamma_{\rm \,inc}/\gamma_{\rm \,decay}$. It turns out that the ratio R_γ expressed as a double ratio $R_\gamma =$

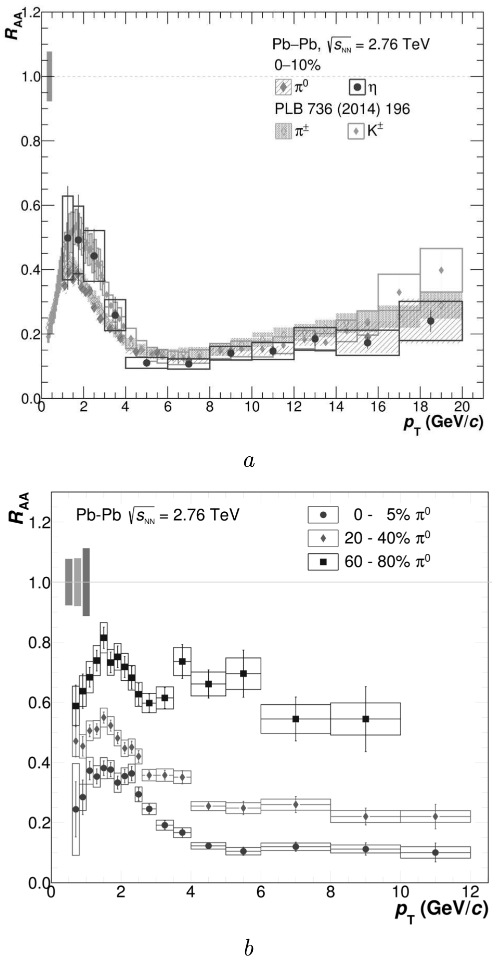

Fig. 5. Nuclear modification factor of π^0, $\pi^\pm$, η, and $K^\pm$ mesons measured in Pb–Pb collisions at $\sqrt{s_{NN}} = 2.76$ TeV in the centrality class 0–10% [8] (a). Centrality dependence of the π^0 nuclear modification factors in Pb–Pb collisions at $\sqrt{s_{NN}} = 2.76$ TeV (b)

$= \frac{(N_{\gamma,\ \mathrm{inc}}/N_{\pi^0})_{\mathrm{meas}}}{(N_{\gamma\ \mathrm{decay}}/N_{\pi^0})_{\mathrm{simulated}}}$ cancels out the significant part of systematic uncertainties of the measurement. The value of R_γ greater than unity indicates the direct photon signal. The double ratio together with the direct photon spectrum were measured for three centrality classes in Pb–Pb at $\sqrt{s_{NN}} = 2.76$ TeV [24], see Fig. 6. The pQCD calculations describe well the high p_T part [25]. There is a visible excess of direct photons compared to NLO pQCD predictions for $p_T < 4$ GeV/c in the most central collisions, which can be attributed to the thermal emission of a hot matter. The low p_T part (below 2.2 GeV/c) of the spectrum was fitted with the exponential function. The inverse slope is found to be equal to $304 \pm 11^{\mathrm{stat}} \pm 40^{\mathrm{sys}}$ MeV. To convert the slope value to the temperature, however, one has to take the expansion of the system into account.

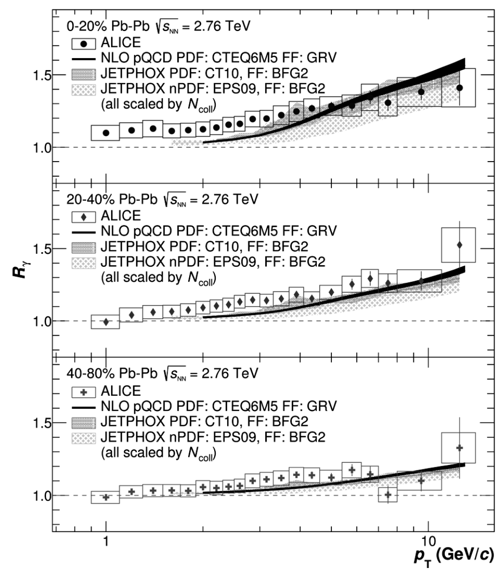

Fig. 6. The double ratio R_γ measured for three centrality classes in Pb–Pb collisions at $\sqrt{s_{NN}} = 2.76$ TeV [24] compared to NLO pQCD (for the direct photon yield in pp collisions) and JETPHOX [26] predictions with various PDFs and FFs scaled by the number of binary collisions

4. Summary

ALICE has measured the neutral meson spectra in a wide p_T range in pp collisions at $\sqrt{s} = 0.9$, 2.76, 7, and 8 TeV. The NLO calculations systematically predict a higher yield, especially at the highest collision energies. The neutral meson spectra measured in Pb–Pb collisions at $\sqrt{s_{NN}} = 2.76$ TeV were used to calculate nuclear modification factors. The nuclear modification factor measured in Pb–Pb shows the strong suppression of the π^0 yield related to the parton energy loss in a hot quark-gluon matter. That can be explained by the final-state effect, as p-Pb data are consistent with unity, showing the absence of cold nuclear matter effects. The direct photon spectrum and the double ratio R_γ were measured in Pb–Pb collisions at $\sqrt{s_{NN}} = 2.76$ TeV in three centrality classes. The double ratio R_γ in central Pb–Pb collisions exceeds the prompt photon pQCD predictions at $p_T < 4$ GeV/c. The inverse slope of the direct photon spectrum in central Pb–Pb collisions is estimated to be $304 \pm 11^{\mathrm{stat}} \pm 40^{\mathrm{sys}}$ MeV.

1. ALICE Collaboration. The ALICE experiment at the CERN LHC. *J. Instrum.* **3**, S08002 (2008).
2. ALICE Collaboration. ALICE electromagnetic calorimeter: addendum to the ALICE technical proposal. CERN-LHCC-2006-014, CERN-LHCC-96-32-ADD-3 (2006).
3. ALICE Collaboration. Technical Design Report of the Photon Spectrometer (PHOS). CERN-LHCC-99-04 (1999).
4. J. Alme *et al.* The ALICE TPC, a large 3-dimensional tracking device with fast readout for ultra-high multiplicity events. *Nucl. Instrum. Meth. A* **622**, 316 (2010).
5. ALICE Collaboration. Neutral pion and η meson production in proton-proton collisions at $\sqrt{s}$ = 0.9 TeV and $\sqrt{s} = 7$ TeV. *Phys. Lett. B* **717**, 162 (2012).
6. ALICE Collaboration. Neutral pion production at midrapidity in pp and PbPb collisions at $\sqrt{s_{\rm NN}} = 2.76$ TeV. *Eur. Phys. J. C* **74**, 3108 (2014).
7. ALICE Collaboration. Production of π^0 and η mesons up to high transverse momentum in pp collisions at 2.76 TeV. *Eur. Phys. J. C* **77**, 339 (2017).
8. ALICE Collaboration. Neutral pion and η meson production at mid-rapidity in Pb–Pb collisions at $\sqrt{s_{\rm NN}} = 2.76$ TeV. *Phys. Rev. C* **98**, 044901 (2018).
9. ALICE Collaboration. π^0 and η meson production in proton-proton collisions at $\sqrt{s} = 8$ TeV. *Eur. Phys. J. C* **78**, 263 (2018).
10. P. Skands, S. Carrazza, J. Rojo. Tuning PYTHIA 8.1: the Monash 2013 tune. *Eur. Phys. J.* **C74**, 3024 (2014).
11. D. de Florian, R. Sassot, M. Epele, R.J. Hernández-Pinto, M. Stratmann. Parton-to-pion fragmentation reloaded. *Phys. Rev. D* **91**, 014035 (2015).
12. W. Tung, H. Lai, A. Belyaev, J. Pumplin, D. Stump, C.-P. Yuan. Heavy quark mass effects in deep inelastic scattering and global QCD analysis. *JHEP* **02**, 053 (2007).
13. C.A. Aidala, F. Ellinghaus, R. Sassot, J.P. Seele, M. Stratmann. Global analysis of fragmentation functions for eta mesons. *Phys. Rev. D* **83**, 034002 (2011).
14. A. Bylinkin, N.S. Chernyavskaya, A.A. Rostovtsev. Predictions on the transverse momentum spectra for charged particle production at LHC-energies from a two component model. *Eur. Phys. J. C* **75**, 166 (2015).
15. ALICE Collaboration. Neutral pion and η meson production in p-Pb collisions at $\sqrt{s_{\rm NN}} = 5.02$ TeV. *Eur. Phys. J. C* **78**, 624 (2018).
16. C. Tsallis. Possible generalization of Boltzmann–Gibbs statistics. *J. Statist. Phys.* **52** 479 (1988).
17. B. Jäger, A. Schäfer, M. Stratmann, W. Vogelsang. Next-to-leading order QCD corrections to high-$p_{\rm T}$ pion production in longitudinally polarized pp collisions. *Phys. Rev. D* **67**, 054005 (2003).
18. K. Werner, B. Guiot, Iu. Karpenko, T. Pierog. Analyzing radial flow features in p-Pb and pp collisions at several TeV by studying identified-particle production with the event generator EPOS3. *Phys. Rev. C* **89**, 064903 (2014).
19. S. Roesler, R. Engel, J. Ranft. The Monte Carlo Event Generator DPMJET-III. arXiv:0012252 [hep-ph](2010).
20. Chun Shen, Jean-François Paquet, Gabriel S. Denicol, Sangyong Jeon, Charles Gale. Collectivity and electromagnetic radiation in small systems. *Phys. Rev. C* **95**, 014906 (2017).
21. M. Gyulassy, X.N. Wang. HIJING 1.0: A Monte Carlo program for parton and particle production in high energy hadronic and nuclear collisions. *Comput. Phys. Commun.* **83**, 307 (1994).
22. T. Lappi, H. Mäntysaari. Single inclusive particle production at high energy from HERA data to proton-nucleus collisions. *Phys. Rev. D* **88**, 114020 (2013).
23. V. Begun, W. Florkowski, M. Rybczynski. Explanation of hadron transverse-momentum spectra in heavy-ion collisions at $\sqrt{s_{\rm NN}} = 2.76$ TeV within a chemical nonequilibrium statistical hadronization model. *Phys. Rev. C* **90**, 014906 (2014).
24. ALICE Collaboration. Direct photon production in Pb–Pb collisions at $\sqrt{s_{\rm NN}} = 2.76$ TeV. *Phys. Lett. B* **235–248s**, 754 (2019).
25. S. Catani, M. Fontannaz, J.P. Guillet, E. Pilon. Cross section of isolated prompt photons in hadron-hadron collisions. *JHEP* **0205**, 028 (2002).
26. P. Aurenche, M. Fontannaz, J.P. Guillet, E. Pilon, M. Werlen. Recent critical study of photon production in hadronic collisions. *Phys. Rev. D* **73**, 094007 (2006).

Received 08.07.19

О. Коваленко, від імені Колаборації ALICE

ВИМІРЮВАННЯ НЕЙТРАЛЬНИХ МЕЗОНІВ
ТА ПРЯМИХ ФОТОНІВ В ЕКСПЕРИМЕНТАХ ALICE

Р е з ю м е

Експеримент ALICE заплановано для вивчення властивостей речовини, що народжується в зіткненнях протонів та важких іонів на LHC. Нейтральні мезони можна відтворити в ALICE в широкому інтервалі поперечних імпульсів за допомогою двофотонних розпадів. Вимірювання нейтральних мезонів у зіткненнях протонів дають можливість перевірити пертурбативну КХД в NLO та NNLO наближеннях, а також уточнити функції розподілу та фрагментації партонів. Спектри нейтральних мезонів, виміряних у pA та AA зіткненнях, дозволяють перевірити модифікацію партонної функції розподілу в ядрі і втрату енергії партонів у гарячій речовині, що утворюється в AA зіткненнях. Нами представлено останні результати ALICE стосовно вимірювання прямих фотонів у Pb–Pb зіткненнях, продукування нейтральних піонів та η мезонів у зіткненнях pp, p-Pb та Pb–Pb.

https://doi.org/10.15407/ujpe64.7.607

A. LYMANETS
for the CBM collaboration
GSI Helmholtzzentrum für Schwerionenforschung GmbH
(Planckstr. 1, 64291 Darmstadt, Germany; e-mail: a.lymanets@gsi.de)

THE SILICON TRACKING SYSTEM OF THE CBM EXPERIMENT AT FAIR

The Compressed Baryonic Matter (CBM) experiment at FAIR (Darmstadt, Germany) is designed to study the dense nuclear matter in a fixed target configuration with heavy ion beams up to kinetic energies of 11 AGeV for $Au + Au$ collision. The charged particle tracking with below 2% momentum resolution will be performed by the Silicon Tracking System (STS) located in the aperture of a dipole magnet. The detector will be able to reconstruct secondary decay vertices of rare probes, e.g., multistrange hyperons, with 50 μm spatial resolution in the heavy-ion collision environment with up to 1000 charged particle per inelastic interaction at the 10 MHz collision rate. This task requires a highly granular fast detector with radiation tolerance enough to withstand a particle fluence of up to 10^{14} n_{eq}/cm^2 1-MeV equivalent accumulated over several years of operation. The system comprises 8 tracking stations based on double-sided silicon microstrip sensors with 58 μm pitch and strips oriented at 7.5° stereo angle. The analog signals are read out via stacked microcables (up to 50 cm long) by the front-end electronics based on the STS-XYTER ASIC with self-triggering architecture. Detector modules with this structure will have a material budget between 0.3% and 1.5% radiation length increasing towards the periphery. First detector modules and ladders built from pre-final components have been operated in the demonstrator experiment mCBM at GSI-SIS18 (FAIR Phase-0) providing a test stand for the performance evaluation and system integration. The results of mSTS detector commissioning and the performance in the beam will be presented.

K e y w o r d s: low-mass tracking system, double-sided silicon microstrip sensors, self-triggering readout.

1. Introduction

A number of research centers worldwide carry out or prepare research programs to shed light on the fundamental questions of the QCD physics, e.g., the origin of the mass of hadrons, structure of neutron stars, or evolution of the early Universe. They can be addressed in high-energy collisions of heavy nuclei in which a fireball of hot and dense nuclear matter is formed prior to the hadronization. The measurement of heavy-ion collision products thus gives an experimental access to the deconfined system of quarks and gluons in a wide range of temperatures and baryon densities. The Compressed Baryonic Matter (CBM) experiment [1] at the Facility for Antiproton and Ion Research (FAIR) is a fixed target spectrometer being designed to measure multiple observables, including rare probes, with statistics high enough to build multidifferential cross-sections.

The measurement of particle yields, momentum spectra, angular distributions, as well as fluctuations and correlations of hadrons, requires a set of detectors for the vertex reconstruction and tracking, particle identification, and calorimetry. Thus, two detectors located in the aperture of a superconducting dipole magnet, a Micro-Vertex Detector (MVD) operating in the vacuum closest to the target and a Silicon Tracking System will provide the precise vertex reconstruction and the momentum determination, respectively. The detector composition further downstream implements two configurations driven by the detection of charmed or strange particles and low-mass vector mesons decaying into di-leptons. In elctron-hadron configuration, a Ring Imaging Cherenkov counter (RICH) and Transition Radiation Detector (TRD) provide the electron identification and the electron-pion separation. A time-of-flight system consisting of resistive plate chambers (RPC) and a diamond start counter will identify fast hadrons. Elect-

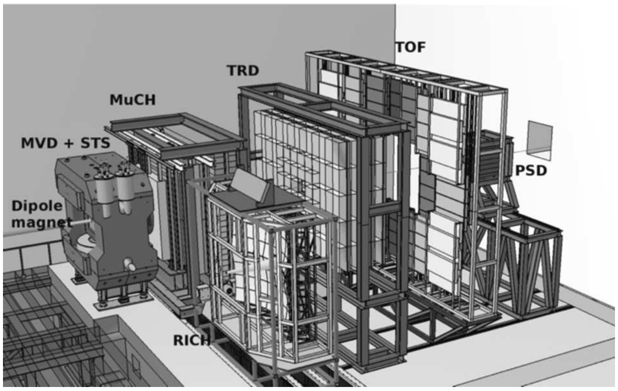

Fig. 1. CBM detector in the muon and electron-hadron configurations

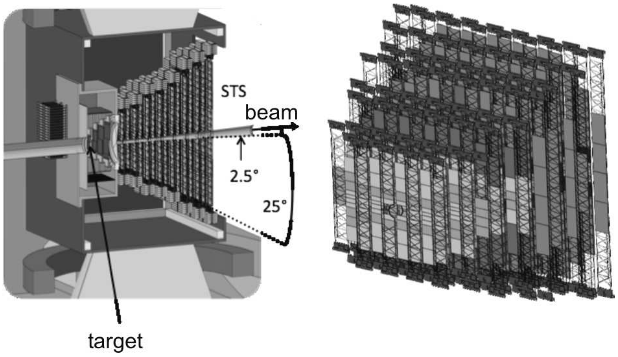

Fig. 2. Conceptual design of the STS consisting of eight tracking stations

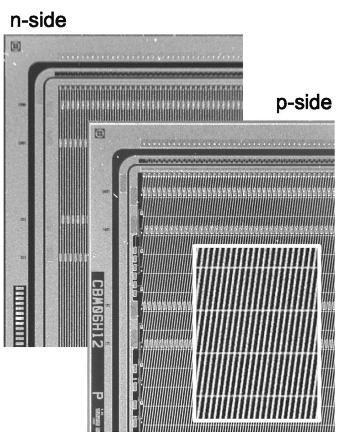

Fig. 3. Close-up of corners of a prototype sensor produced by Hamamatsu. Shown are strips on the p-side, oriented under a stereo angle with respect to the n-side strips. The horizontal lines are second-metal routing lines between short corner strips, allowing to read out the full sensor area from the staggered read-out pads at the top edge

rons and photons will be detected by the Electromagnetic Calorimeter (ECAL). The collision plane and centrality will be determined by the Projectile Spectator Detector (PSD). In the muon configuration, the RICH detector will be replaced by an instrumented absorber with muon tracking capability.

2. Silicon Tracking System

The STS consists of eight tracking stations located in the aperture of a dipole magnet with 1 T field, 30–100 cm downstream of the target. Its main mission is the momentum measurement for charged particles with a resolution of $\delta p/p < 2\%$ [2]. Therefore, a detector module must have the minimum amount of a material in the physical acceptance (polar angle 2.5–25°) with front-end electronics operating at the periphery of the stations. The system is required to have the track reconstruction efficiency >95% for tracks with momentum above 1 GeV. For this, the detector modules based on double-sided silicon microstrip sensors need to have hit the reconstruction efficiency close to 100% and the low-noise performance ensuring the operation with signal-to-noise ratio well above 10 during the whole detector lifetime.

The goal of the STS is to reconstruct up to 1000 charged particles created in the collision of gold ions with gold target at beam energies up to 11 AGeV at SIS-100 and up to 45 AGeV at a future SIS-300 synchrotron. Depending on the physics case, the interaction rate will range between 0.1 MHz and 10 MHz. In the latter case, a significant challenge is posed to the detector design and data acquisition system due to high radiation load and data rates generated by the collision products, as well as δ-electrons. The tracking stations will have to withstand radiation damage up to $10^{14}\, n_{\rm eq}/{\rm cm}^2$ within its planned operation.

In total, the STS stations will consist of 896 double-sided silicon sensors installed onto 106 carbon fibre ladders with the total area of 4 m^2 (see Fig. 2). The pre-final module components, their integration into detector modules and ladders as basic functional and structural units of the tracking stations are presented in the following sections.

3. Module Components

3.1. Sensors

Final protptypes of double-sided silicon microstrip sensors 320 μm in thickness have been produced in cooperation with Hamamatsu (Japan) [3]. The sensors

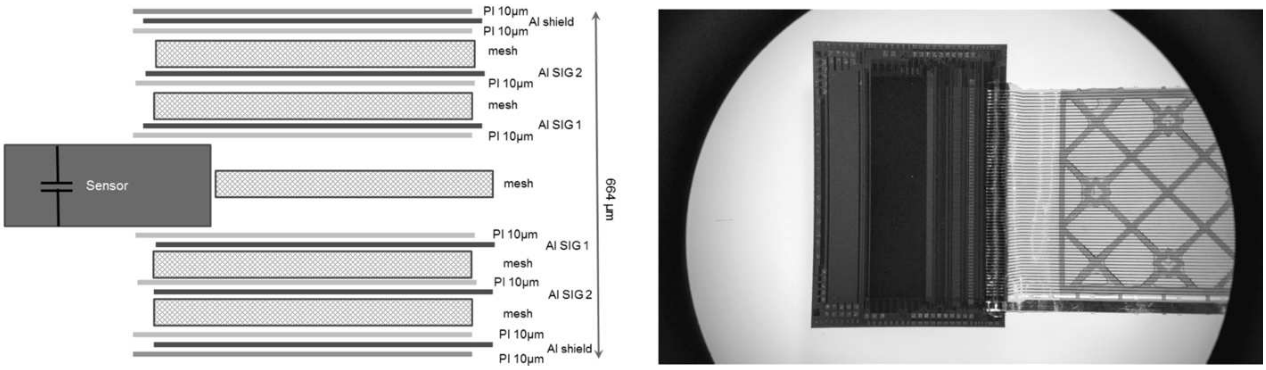

Fig. 4. Multilayer structure of microcables with two signal layers per side, shielding layers, and meshed spacers shown in the attachment to both sides of a microstrip sensor (left); photo of a single microcable layer attached to a readout chip (right)

feature four discrete sizes (62 mm width and 22, 42, 62 and 124 mm height). The wafer material is of the n-type. One prototype is shown in Fig. 3. The sensor layout has been optimized for the attachment of microcables by TAB bonding for read-out and bias connections, minimum trace resistance, and inter-strip capacitance. The sensors are segmented into 1024 strips per side at a strip pitch of 58 μm. The strips are read out through integrated AC coupling. The p-strips are arranged under a stereo angle of 7.5° with respect to the n-strips. The short corner strips are interconnected using a second metal layer in order to enable the full readout of the p-side from one sensor edge only, like with the simpler topology of the n side. The sensors are oriented with the strips vertically in the dipole magnetic field to be sensitive to the track curvature. They have been tested under the anticipated thermal operation conditions, –5 °C, and were shown to be radiation-tolerant up to twice the nominal lifetime in the experiment, 2×10^{14} 1-MeV $n_{\rm eq}$ cm^{-2}.

3.2. Microcables

In the STS module concept, the microcables are the important component to yield a low material budget. They are also central to the noise performance, because they allow one to have the readout electronics outside of the detector acceptance. A microcable is implemented as a stack of two signal layers per side with aluminum traces on a polyimide substrate with spacers inbetween and additional shielding layers on the outside (see Fig. 4). One stack is designed to read out 128 channels. Thus, 16 microcable stacks are required for the full readout of a sensor. The microcable structure aims at balancing the trace capacitance and series resistance based on the ENC contribution to the total noise seen by the preamplifier. A signal layer comprises 64 Al lines at 116 μm pitch, twice the strip pitch on the sensor. Two signal layers are stacked to match the read-out pitch. The thickness of aluminium and polyimide is 14 μm and 10 μm, respectively. Such a structure of a cable stack corresponds to 0.23% X_0 equivalent to 213 μm of silicon. The cables are produced in lengths up to 55 cm. The current pre-series production of microcables aims at maximizing the yields [4].

3.3. Front-end electronics

The readout chip STS-XYTER has been developed specifically for the STS. It is a mixed signal ASIC with data driven architecture [5]. Each channel has a fast branch for the time stamp generation with less than 5 ns resolution and a slow one for the amplitude measurement (see Fig. 5). The chip provides 128 independent channels with switchable signal polarity and two gain settings that makes it suitable for use with the STS and a further CBM sub-system, the muon detector with its GEM chambers. For the silicon detector read-out, the dynamic range of the integrated 5-bit ADC is 12 fC, which can be switched to 100 fC for the gas detectors. The design goal with STS-XYTER is to achieve a noise performance of 1000 e^{-} with a power consumption that is estimated to be <10 mW/channel. This will ensure the matching with the STS detector module structure, where significant noise contributions are expected from the capacitance and the series resistance of the microca-

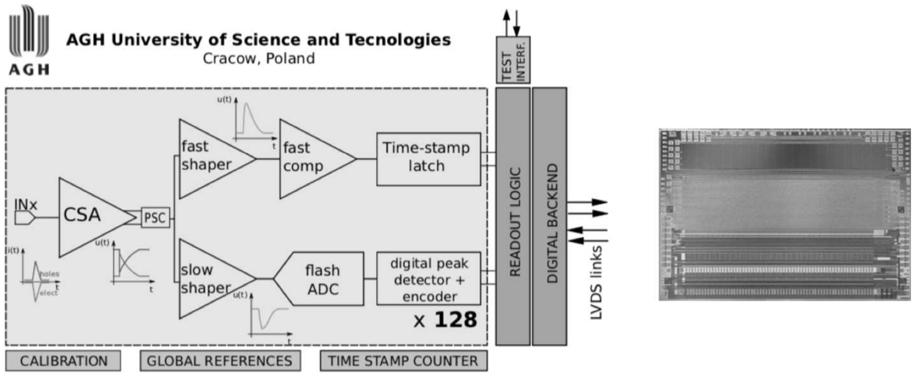

Fig. 5. Block diagram of the STS-XYTER architecture

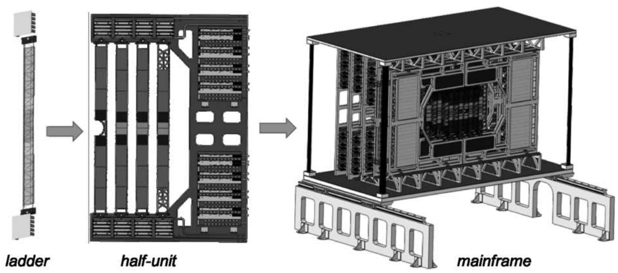

Fig. 6. System integration concept: from ladders to half-units mounted in the mainframe

Fig. 7. mSTS detector modules mounted on the C-frames. Microcables running along the ladders and integrated cooling plates are visible

ble signal traces and sensor strips. The noise performance is addressed in the chip architecture using the double-threshold technique, where triggers generated by the fast branch are vetoed if no coinciding signal peak was detected. The chip is currently under production in its second iteration, compatible with the CERN GBT read-out protocol, using a 180 nm CMOS process.

4. System Integration

The current activities on the system integration focus on devising a detailed engineering solution for the assembly of a system from individual mechanical units and its installation in the magnet aperture taking the intersection of the active volume by the beam pipe and MVD vacuum vessel into account. A thermal enclosure will have to provide numerous interfaces for services, e.g., cooling, powering, and data cables in its side walls. The integration concept foresees a hierarchical mechanical structure of the STS (see Fig. 6), where modules are mounted onto the carbon fiber ladders. The so-called half-units will carry the ladders and the necessary infrastructure so that every half of a tracking station will be formed by two such units. The stations are thus separated into two halves for the maintainability and will be movable in order to allow for the replacement of broken modules. A system [6] cooling the plates with channels for circulating the cooling liquid integrated into the C-frames of half-units is devised to remove the power dissipated by the STS front-end electronics, amounting to about 42 kW.

5. mSTS at mCBM

As a part of the FAIR Phase-0 program, a long-term beam test campaign of CBM pre-final detector systems has been started at GSI in 2018 at SIS18 synchrotron (mini-CBM or mCBM) [7] with high-rate heavy-ion collisions and followed up by a beam campaign in March 2019. The goal was to operate the full system with complex hardware and software components and to optimize their performance before the final series production. The subsystems had common free-streaming readout with the data transport to the prototype online event selection system.

At the time of the beam test, the mSTS detector shown in Fig. 7 consisted of two C-frames equipped with four detector modules mounted on carbon fiber ladders using L-legs. All modules provided the full double-sided readout of sensors with 62×62 mm^2 dimensions using about 45 cm long stacked microcable. Each sensor side is read out by a front-end board (FEB) with 8 STS-XYTER ASICS. The FEBs are mounted on the cooling plates integrated into the C-frames [8]. The plates are cooled by the chilled water circulating inside them. Apart from front-end electronics, the C-frames carry the common readout boards (C-ROBs) based on CERN GBT and Versatile Link components [9]. The functions of the C-ROB are the data aggregation from the front-end boards and the further data transport via the optical interface, control of the front-end ASICs, clock distribution, and synchronization.

In future runs, the mSTS will concentrate on optimizing the system performance towards particle tracking in combination with other detectors and increasing the number of detector modules to 13. The mCBM operation is planned till 2022.

6. Summary and Outlook

The CBM experiment will measure rare probes in the heavy-ion collision environment. This will require a tracking system with hit position resolution better than 20 μm, fast detectors compatible with operation at an interaction rate up to 10 MHz, and radiation tolerance up to 10^{14} $n_{\rm eq}$cm^{-2}. The Silicon Tracking System based on double-sided silicon microstrip detector modules compatible with these requirements will provide the charged particle tracking and measure particle momenta with a resolution of $\delta p/p < 2\%$. For this, it requires a particularly low-mass design of the system. The signals from the double-sided sensors are read out via ultra-thin analog microcables by the front-end electronics located outside of the detector acceptance. Currently, the production readiness of the system components has been achieved, and the production phase has started. The feasibility of the detector concept has been demonstrated in the mCBM beam campaign.

The author expresses his gratitude to Prof. Dr. Hans Rudolf Schmidt for his help in the preparation of this contribution and colleagues from University of Tübingen and GSI Detector Laboratory for the fruitful work presented in it.

1. B. Friman *et al. The CBM Physics Book, Compressed Baryonic Matter in Laboratory Experiments. Lecture Notes in Physics* **814** (2011) [ISBN: 978-3-642-13292-6].
2. J. Heuser *et al. Technical Design Report for the CBM. Silicon Tracking System (STS). GSI Report 2013-4, Darmstadt* (2013), 167 p.
3. J. Heuser *et al. Description of the STS microstrip sensors for series production. CBM-TN-19005 (technical note), Darmstadt* (2019).
4. V.M. Borshchov *et al. Pre-series production of microcables for STS detector modules at LTU Ltd. CBM Progress Report 2015* (2016), 36.
5. K. Kasinski, R. Kleczek, R. Szczygiel. Front-end readout electronics considerations for Silicon Tracking System and Muon Chamber. *J. Inst.* **11**, C02024 (2016).
6. K. Agarwal *et al. Conceptual Design Report of the STS Cooling System. CBM-TN-18004 (technical note), Darmstadt* (2018).
7. C. Sturm *et al. mCBM@SIS18 is on its way. CBM Progress Report 2017* (2018), p. 170.
8. O. Vasylyev *et al. Progress with the integration of the mCBM Mini Silicon Tracking System. CBM Progress Report 2017* (2018), p. 177.
9. P. Moreira *et al. The GBT Project. Topical Workshop on Electronics for Particle Physics, Paris, France, 21–25 Sep. 2009* (CERN-2009-006), p. 342.

Received 08.07.19

А. Лиманецъ, для CBM колаборації

КРЕМНІЄВА ТРЕКІНГОВА
СИСТЕМА ЕКСПЕРИМЕНТУ CBM
НА КОМПЛЕКСІ ПРИСКОРЮВАЧІВ FAIR

Р е з ю м е

Експеримент CBM на прискорювальному комплексі FAIR (Дармштадт, Німеччина) розробляється для вивчення ядерної речовини з високою густиною в експериментальній установці на фіксованій мішені із струменем важких іонів з енергіями до 11 ГеВ/нуклон у системі Au + Au. Трекінг заряджених частинок із роздільною здатністю по імпульсу краще, ніж 2%, буде проводитись Кремнієвою Трекінговою Системою (КТС), розташованою у апертурі дипольно-

го магніту. Детектор зможе реконструювати вторинні вершини розпадів рідкісних частинок, наприклад, гіперонів із кількома дивними кварками з точністю 50 мкм в оточенні продуктів зіткнення важких іонів, що породжує до 1000 заряджених частинок на кожне непружне зіткнення з частотою взаємодії до 10 МГц. Ця задача вимагає швидкого детектора із високою гранулярністю і радіаційною стійкістю, достатньою для роботи при еквівалентному флюенсі до $10^{14} n_{\rm eq}/\text{см}^2$, накопиченому за кілька років роботи. Система складається із 8 трекінгових станцій на основі двосторонніх кремнієвих мікростріпових детекторів із кроком 58 мкм і орієнтацією стріпів під стереокутом 7,5°. Аналогові сигнали із сенсорів зчитуються через багатошарові мікрокабелі довжиною до 50 см найсучаснішою електронікою на основі STS-XYTER ASIC із самозапускною архітектурою. Детекторні модулі із цією структурою матимуть кількість матеріалу від 0,3% до 1,5% радіаційної довжини, із збільшенням товщини в напрямку до периферії. Перші детекторні модулі та утворені з них "драбини" на основі компонентів, готових до серійного виробництва, тестувалися в ході демонстраційного експерименту міні-CBM на синхротроні SIS18 у GSI (Дармштадт, Німеччина) в рамках програми FAIR Phase-0. Експеримент являв собою тестовий стенд для оцінки роботи установки та системної інтеграції. Представлено результати запуску детектора та його робочі характеристики.

https://doi.org/10.15407/ujpe64.7.613

T. NOSEK
for the NOvA Collaboration
Charles University, Faculty of Mathematics and Physics, Institute of Particle and Nuclear Physics
(2, V Holesovickach, 180 00 Prague, Czech Republic; e-mail: tomas.nosek@mff.cuni.cz)

RESULTS ON NEUTRINO AND ANTINEUTRINO OSCILLATIONS FROM THE NOvA EXPERIMENT

NOvA is a two-detector long-baseline neutrino oscillation experiment using Fermilab's 700 kW NuMI muon neutrino beam. With a total exposure of 8.85 $\times$ *10*^{20} + *12.33* $\times$ *10*^{20} *protons on target delivered to NuMI in the neutrino + antineutrino beam mode (78% more antineutrino data than in 2018), the experiment has made a 4.4*σ*-significant observation of the* $\bar{\nu}_e$ *appearance in a* $\bar{\nu}_\mu$ *beam, measured oscillation parameters* $|\Delta m^2_{32}|$, $\sin^2\theta_{23}$, *and excluded most values near* $\delta_{\rm CP} = \pi/2$ *for the inverted neutrino mass hierarchy by more than 3*σ*.*

Keywords: neutrino oscillations, long-baseline experiment, NOvA, Fermilab.

1. Introduction

NOvA is a long-baseline neutrino oscillation experiment designed to make measurements of the muon neutrino (ν_μ) disappearance and the electron neutrino (ν_e) appearance in Fermilab's NuMI (Neutrinos at the Main Injector) beam. Well tuned for the first oscillation maximum around a neutrino energy of 2 GeV over 810 km baseline, the experiment studies primarily four channels of oscillations: $\nu_\mu \to \nu_\mu$ or $\nu_\mu \to \nu_e$ and $\bar{\nu}_\mu \to \bar{\nu}_\mu$ or $\bar{\nu}_\mu \to \bar{\nu}_e$. They allow us to address several concerns of neutrino oscillations:

1. mass ordering, i.e. normal (NH) or inverted hierarchy (IH) of neutrino mass eigenstates,
2. direct CP violation ($\delta_{\rm CP}$ phase) and
3. precise determination of θ_{23} and Δm^2_{32} neutrino mixing parameters.

This paper reports the 2019 NOvA combined analysis of 8.85×10^{20} POT (protons on target) neutrino data collected from Feb 2014 to Feb 2017 and 12.33×10^{20} POT antineutrino data collected from Jun 2016 to Feb 2019 [1]. Neutrino oscillation parametrization, fits, predictions, and interpretation of the results were done within the standard oscillation model of 3 active neutrino flavors of electron, muon, and tau neutrinos (ν_τ) [2].

2. The NOvA Experiment

The experiment consists of two large functionally identical detectors sitting 14.6 mrad off the beam axis 810 km apart. This off-axis configuration reduces the uncertainty on energy of incoming neutrinos and suppresses the higher-energy neutrinos background producing neutral current interactions (NC) misidentified as ν_e charged current (CC). On the other hand, it also results in a lower intensity than in the on-axis region, mitigated by the size of the detectors and beam power upgrades.

The detectors are finely grained and highly active (~65% active mass) liquid scintillator tracking calorimeters, which allow for a precise analysis of the neutrino interactions events. They are designed to be as similar as possible aside from the size: the Far Detector (FD) is 14 kt and on the surface located in Ash River, Minnesota, the Near Detector (ND) is located underground in Fermilab, close enough to the neutrinos source to see a far greater flux with only 0.3 kt of mass. Both are constructed out of extruded PVC cells (3.9×6.6 cm in cross-section and 15.5/3.8 m in length for FD/ND) filled with scintillator and equipped with a wavelength shifting fiber connected to an avalanche photodiode (APD). They collect light produced by charged particles subsequently amplified by APDs. The cells alternate in horizontal and vertical orientations to allow for a stereo readout. More information on detectors can be found in Ref. [3].

The NuMI beam is created following the decay of charged pions and kaons produced by 120 GeV protons hitting a carbon target. These parent mesons are focused by two magnetic horns and decay in flight

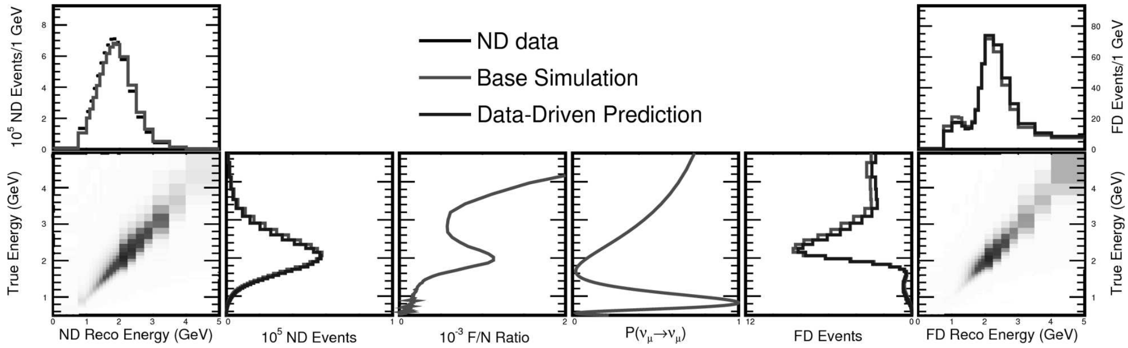

Fig. 1. Illustration of the NOvA's F/N technique. From left to right: reconstructed to true ν_μ energy translation, F/N ratio, $\nu_\mu \to \nu_\mu$ oscillation probability, true to reconstructed ν_μ energy restoration. Base simulation in red (light), ND data-driven corrected prediction in blue (dark)

through the chain $K^+, \pi^+ \to \mu^+ + \nu_\mu$, with the muon then decaying as $\mu^+ \to e^+ + \nu_e + \bar{\nu}_\mu$. By switching the polarity of the horns, the opposite charge sign particles can be focused, thus effectively selecting an antineutrino beam. The resulting neutrino events sample composition in range 1-5 GeV at ND is of 96% ν_μ, 3% $\bar{\nu}_\mu$ and 1% $\nu_e + \bar{\nu}_e$ in the case of neutrino beam and 83% $\bar{\nu}_\mu$, 16% ν_μ and 1% $\bar{\nu}_e + \nu_e$ in the case of antineutrino beam.

To identify and classify neutrino interactions, NOvA uses a method based on image recognition techniques known as Convolutional Visual Network (CVN), see Ref. [4]. CVN treats every interaction in the detector as an image, with cells being pixels and collected charge being their color. When trained with simulated events and cosmic data, CVN can extract abstract topological features of neutrino-like interactions with convolutional filters (feature maps [4]). With an input of calibrated 2D pixelmap (two views of horizontal and vertical event projections), the output is a set of normalized classification scores ranging over the hypotheses of beam neutrinos event (ν_μ CC, ν_e CC, ν_τ CC and NC), or cosmics. CVN has been used together with additional supporting PIDs: separate ν_e and ν_μ cosmic rejection boosted decision trees and muon track identification in ν_μ events.

NOvA's two identical detectors design enables us to employ data-driven predictions of FD observations. FD ν_μ and ν_e signal is predicted using ND ν_μ, whereas FD ν_e beam background is constrained using ND ν_e sample. This Far/Near (F/N) technique includes several steps (Fig. 1). First, the reconstructed neutrino energy spectrum is translated to the true energy using a simulated migration matrix. Second, the F/N ratio accounting for geometry, beam divergence, and detector acceptance is applied to create an unoscillated FD prediction. Then the FD spectrum is weighted by the oscillation probability for a given set of oscillation parameters. Finally, the true energy is smeared back again to the reconstructed energy via the migration matrix. As a reward, F/N technique significantly reduces both neutrino flux and cross section systematic uncertainties. The ND reconstructed energy spectra of ν_μ and $\bar{\nu}_\mu$ (the source of FD ν_μ and ν_e signals) can be found in Fig. 2.

3. Muon Neutrino and Antineutrino Disappearance

The muon neutrino disappearance channel is primarily sensitive to $|\Delta m^2_{32}|$ and $\sin^2 2\theta_{23}$, and the precision with which they can be measured depends on the ν_μ energy resolution. The energy of ν_μ is reconstructed as a sum of the energy of a muon and the remaining hadronic energy. The former is estimated from the range of the muon track, the latter from the sum of the calibrated hits not associated with the track. To get the best effective use of the energy resolution, the data binning is optimized in two ways. First, the energy binning has finer bins near the disappearance maximum and coarser bins elsewhere. Second, the events in each energy bin are further divided into four populations, or "quartiles", of varying reconstructed hadronic energy fraction, which correspond to different ν_μ energy resolutions. The divisions are chosen such that the quartiles are of equal size in the unoscillated FD simulation. The ν_μ ($\bar{\nu}_\mu$) energy resolution is estimated to be 5.8% (5.5%), 7.8% (6.8%), 9.9% (8.3%), and 11.7% (10.8%) for

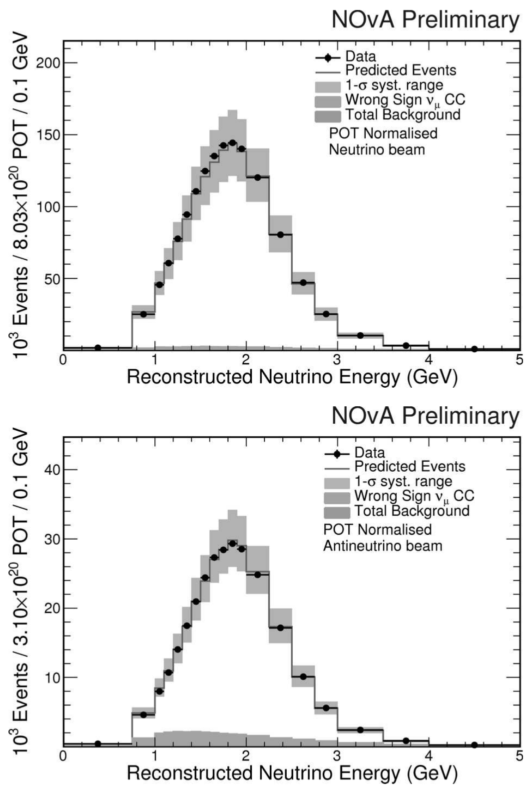

Fig. 2. ND selected ν_μ (top) and $\bar{\nu}_\mu$ (bottom) reconstructed energies in data (black dots) and simulation (band). Each bin is normalized by its width

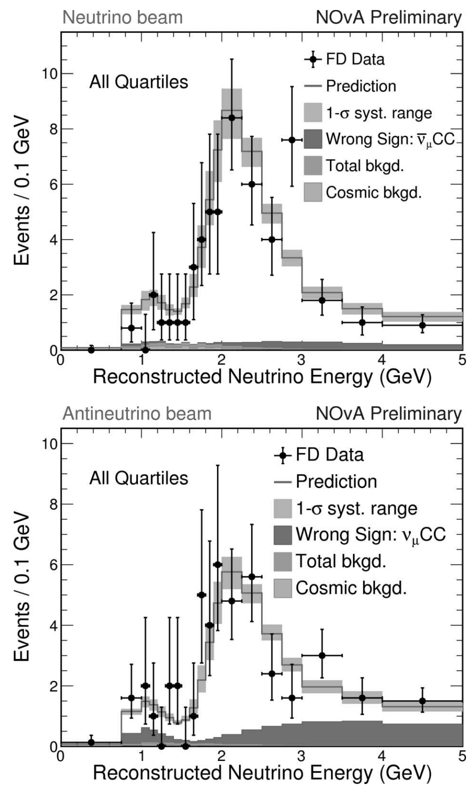

Fig. 3. FD data (black dots) selected ν_μ (top) and $\bar{\nu}_\mu$ (bottom) candidates reconstructed energies compared to the best fit prediction (line) with 1σ systematics uncertainty range. Summed over all quartiles of the hadronic energy fraction

each quartile, ordered from lower to higher hadronic energy fraction. The F/N technique is applied separately in quartiles, which has the additional advantage of isolating most of the cosmic and beam NC background events along with events of the worst energy resolution (4^{th} quartile).

The efficiency of the ν_μ ($\bar{\nu}_\mu$) CC events selection is 31.2% (33.9%) with respect to true interactions in the fiducial volume and the purity 98.6% (98.8%) in the FD samples. In total, there were 113 (102) ν_μ ($\bar{\nu}_\mu$) CC candidates observed in FD with an estimated background of $4.2^{+0.5}_{-0.6}$ ($2.2^{+0.4}_{-0.4}$). FD data and the best fit prediction can be seen in Fig. 3.

4. Electron Neutrino and Antineutrino Appearance

In order to maximize the statistical power of the ν_e selected events at FD, the sample is binned in both reconstructed energy and CVN score. There are two CVN bins of low and high purities (low and high PID), or "core" selection, and an additional "peripheral" bin. Events which fail the containment or cosmic rejection cuts, but do have a very high CVN ν_e CC score, may be added to the peripheral sample. Because the events on the periphery are not always fully contained, they are summed into a single bin instead of estimating their energy (up to reconstructed 4.5 GeV). The overall integrated selection efficiency of ν_e ($\bar{\nu}_e$) is 62% (67%). The purity of the final predicted FD samples depends on the oscillation parameters, but ranges from 57% (55%) to 78% (77%). The beam backgrounds are reduced by 95% (99%).

To estimate FD beam backgrounds, the F/N technique is used with the ND ν_e sample. It consists of the beam ν_e and ν_μ CC or NC interactions misidentified as ν_e CC. Since each of these components oscillates differently along the way to the FD, the sample needs to be broken down into them. In the case of neutrino beam, the ν_e component is constrained by inspecting the low-energy and high-energy ν_μ CC spectra to

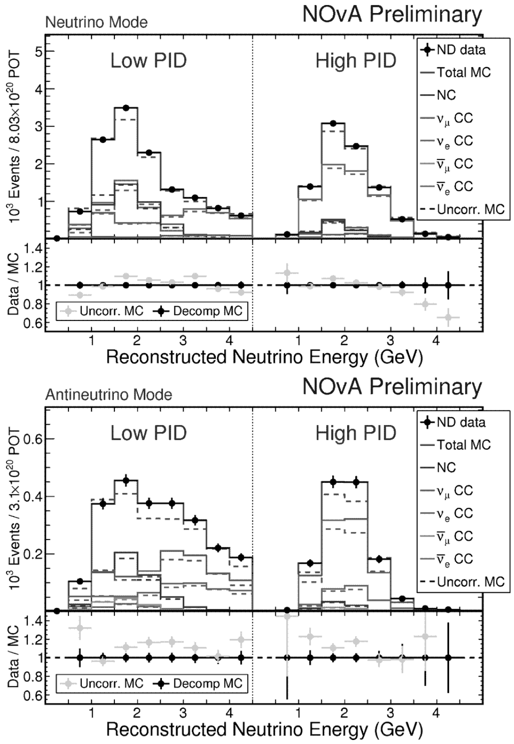

Fig. 4. ND selected ν_e (top) and $\bar{\nu}_e$ (bottom) reconstructed energy data (black dots), uncorrected simulation (dashed red) and data-driven correction (solid red). The selection is decomposed (broken down) into NC (blue), $\nu_\mu/\bar{\nu}_\mu$ CC (dark/light green) and $\nu_e/\bar{\nu}_e$ CC (light/dark magenta). Binned in two PID bins, which are correlated to lower and higher purities of $\nu_e + \bar{\nu}_e$

adjust the yields of the parent hadrons that decay into both ν_μ and ν_e (track ν_μ and ν_e to their common parents). The ν_μ component is estimated from observed distribution of time-delayed electrons from the decay of stopped μ. The rest is attributed to the NC interaction. In the case of antineutrino beam, the simulated components are evenly and proportionally scaled to match ND data in each bin. ND selections and their breakdowns, or "decomposition", can be seen in Fig. 4. The high PID bin is dominated by the beam $\nu_e+\bar{\nu}_e$, the low PID bin has a significant admixture of ν_μ ($\bar{\nu}_\mu$) CC and NC events. The beam background of the FD peripheral bin is estimated from the high PID bin of the core sample.

There were 58 (27) ν_e ($\bar{\nu}_e$) candidates in the FD data with the total expected background of $15.0^{+0.8}_{-0.9}$ ($10.3^{+0.6}_{-0.5}$) events of 7.0 (5.3) beam $\nu_e + \bar{\nu}_e$, 0.7 (0.2) $\nu_\mu+\bar{\nu}_\mu$, 3.1 (1.2) NC events, 3.3 (1.1) cosmic-

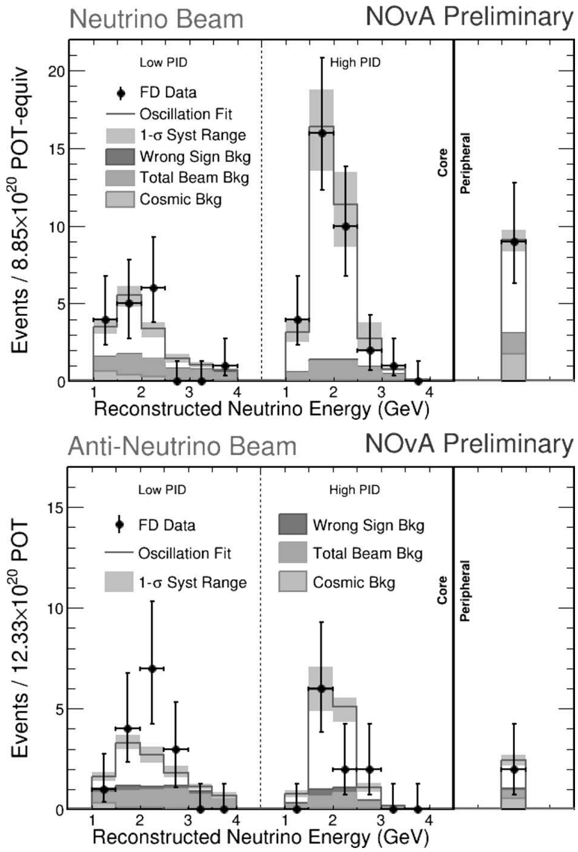

Fig. 5. FD data (black dots) selected ν_e (top) and $\bar{\nu}_e$ (bottom) candidates reconstructed energies binned in low and high PID bins and peripheral sample with energies up to 4.5 GeV. The best fit prediction (purple band) shows the expected background of wrong sign (green), other beam backgrounds (grey) and cosmics (blue) as shaded areas

ray-induced events, 0.4 (0.3) others and 0.6 $\bar{\nu}_e$ (2.2 ν_e) from the wrong sign component of the ν_μ ($\bar{\nu}_\mu$) sample. The FD data and the best fit predictions can be seen in Fig. 5. The antineutrino data give a 4.4σ evidence of the $\bar{\nu}_e$ appearance in $\bar{\nu}_\mu$ beam (an excess over predicted background).

5. Constraints on Oscillation Parameters

To obtain oscillation parameters, a simultaneous fit of joint $\nu_e + \nu_\mu$ and both the neutrino and antineutrino data was performed. Systematic uncertainties are incorporated as nuisance parameters with Gaussian penalty term, appropriately correlated between all the data sets. The leading systematics are worth a note: detector calibration (calorimetric energy scale), light production and collection model and muon energy scale (abs. + rel.) for the ν_μ disappearance; detector response and calibration, neutrino cross-sections and actual ND to FD differences for the ν_e appearance. Several oscillation parameters are taken as inputs from other measurements: solar parameters θ_{12} and Δm^2_{12}, the mixing angle θ_{13} and its uncertainty were taken from reactor experiments, all in Ref. [2]. The best fit is

$$\begin{aligned} &\Delta m^2_{32} = 2.48^{+0.11}_{-0.06} \times 10^{-3}\ \mathrm{eV}^2, \\ &\sin^2\theta_{23} = 0.56^{+0.04}_{-0.03}, \\ &\delta_{\mathrm{CP}}/\pi = 0.0^{+1.3}_{-0.4}, \end{aligned} \tag{1}$$

which corresponds to NH and the uppper θ_{23} octant (UO, $\theta_{23} > 45°$). All confidence levels (C.L.) and contours are constructed following the Feldman–Cousins approach [7].

The 90% C.L. allowed region for a combination of Δm^2_{32} versus $\sin^2\theta_{23}$ in the $\Delta m^2_{32} > 0$ half-plane, together with other results from MINOS (2014) [8], T2K (2018) [9], IceCube (2018) [10] and Super–Kamiokande (2018) [11] overlaid is shown in Fig. 5. There is a clear consistency within all experiments despite that NOvA data asymmetrically point to UO and disfavor lower θ_{23} octant (LO, $\sin^2 < 0.5$) at about 1.6σ C.L.

Fig. 7 shows the 1, 2 and 3σ C.L. allowed regions for $\sin^2\theta_{23}$ versus δ_{CP} in both cases of NH and IH (mass ordering). It is worth noticing that the values of δ_{CP} around $\pi/2$ are excluded at $> 3\sigma$ C.L. for IH, similarly to the previous NOvA neutrino only analysis [5]. On the other hand, rather weak constraints on δ_{CP} itself allow all possible values $[0,2\pi]$ for the case of NH and UO. NH is preferred with 1.9σ significance.

6. Future Prospects

NOvA is expected to run till 2025 with about an equal total exposure of neutrino and antineutrino beams. Moreover, several accelerator upgrades to enhance the beam performance are planned for the next years. Based on these prerequisities and projected 2019 analysis techniques, there is a possibility of more than 3σ sensitivity to hierarchy resolution for 30–50% of all possible δ_{CP} (up to 5σ for favorable true values of oscillation parameters: NH and $\delta_{\mathrm{CP}} = 3\pi/2$). In addition, more than 2σ sensitivity to CP violation in the case of $\delta_{\mathrm{CP}} = \pi/2$ or $3\pi/2$ (maximal violation) is expected.

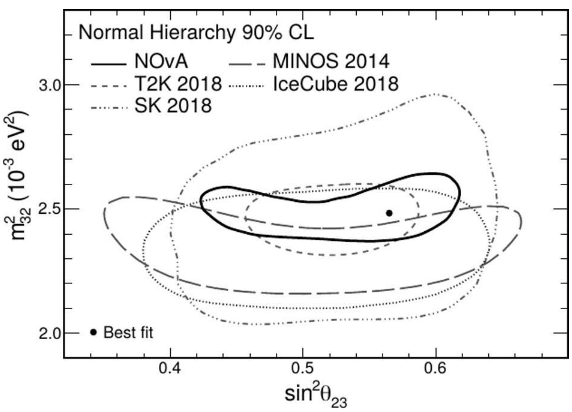

Fig. 6. Comparison of the allowed regions of Δm^2_{32} vs. $\sin^2\theta_{23}$ parameter space at the 90% confidence level as obtained by recent experiments

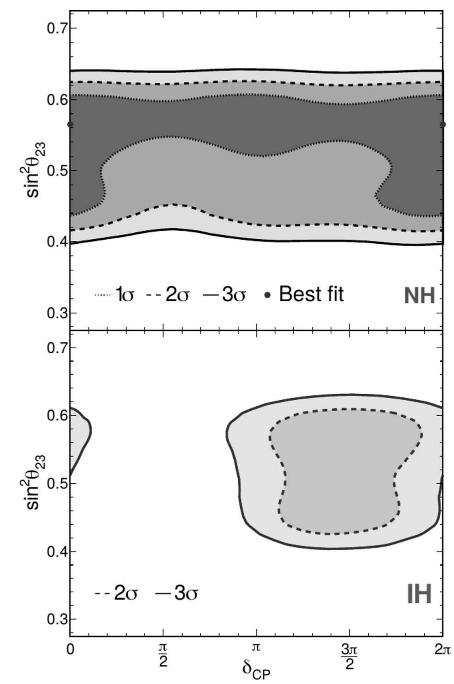

Fig. 7. 1, 2, and 3σ allowed regions of $\sin^2\theta_{23}$ vs. δ_{CP} neutrino oscillation parameter space consistent with the ν_e appearance and ν_μ disappearance data. The top panel corresponds to the case of normal hierarchy (NH) of neutrino masses ($\Delta m^2_{32} > 0$), the bottom one to the inverted hierarchy (IH, $\Delta m^2_{32} < 0$)

To further improve the neutrino oscillation analysis and to extend the reach of the experiment, NOvA started an intensive test beam program in early 2019. This should focus on the simulation tuning, systematics study and their reduction, validation and training of the reconstruction or machine learning algorithms.

7. Conclusions

New antineutrino data from NOvA (12.33×10^{20} POT in total) has been analyzed together with existing neutrino data (8.85×10^{20} POT). The measurements are well consistent with the standard oscillation model of 3 active neutrino flavors. NOvA observes 4.4σ evidence for the $\bar{\nu}_e$ appearance in $\bar{\nu}_\mu$ beam. The results of joint analysis of neutrino and antineutrino and both ν_μ disappearance and ν_e appearance channels give the parameters estimates of $\sin^2\theta_{23} = 0.56^{+0.04}_{-0.03}$ and $\Delta m^2_{32} = 2.48^{+0.11}_{-0.06}\times10^{-3}$ eV^2, which are in a good agreement with other accelerator and atmospheric oscillation experiments. The data prefer θ_{23} upper octant at 1.6σ and the normal hierarchy of neutrino masses at 1.9σ and also disfavor the inverted hierarchy for $\delta_{\rm CP}$ around $3\pi/2$ at more than 3σ. NOvA plans to continue running till 2025 in both neutrino and antineutrino beam modes.

I would like to thank the organizers for an inspiring NTIHEP2019 conference. This work was supported by MSMT CR (Ministry of Education, Youth and Sports, Czech Republic).

1. M.A. Acero *et al.*. First measurement of neutrino oscillation parameters using neutrinos and antineutrinos by NOvA. FERMILAB-PUB-19-272-ND, arXiv:1906.04907 [hep-ex].
2. M. Tanabashi *et al.* [Particle Data Group]. Review of Particle Physics. *Phys. Rev. D* **98**, 030001 (2018).
3. D.S. Ayres *et al.* [NOvA Collaboration]. The NOvA technical design report. FERMILAB-DESIGN-2007-01.
4. A. Aurisano *et al.* A convolutional neural network neutrino event classifier. *JINST* **11**, P09001 (2016), arXiv:1604.01444 [hep-ex].
5. P. Adamson *et al.* [NOvA Collaboration]. New constraints on oscillation parameters from ν_e appearance and ν_μ disappearance in the NOvA experiment. *Phys. Rev. D* **98**, 032012 (2018), arXiv:1806.00096 [hep-ex].
6. P. Adamson *et al.* [MINOS Collaboration], The NuMI neutrino beam. *Nucl. Instrum. Meth. A* **806**, 279 (2016), arXiv:1507.06690 [physics.acc-ph].
7. G.J. Feldman, R.D. Cousins. A unified approach to the classical statistical analysis of small signals. *Phys. Rev. D* **57**, 3873 (1998), arXiv:physics/9711021 [physics.data-an].
8. P. Adamson *et al.* [MINOS Collaboration]. Combined analysis of ν_μ disappearance and $\nu_\mu \to \nu_e$ appearance in MINOS using accelerator and atmospheric neutrinos. *Phys. Rev. Lett.* **112**, arXiv:1403.0867 [hep-ex].
9. K. Abe *et al.* [T2K Collaboration]. Search for CP violation in neutrino and antineutrino oscillations by the T2K experiment with 2.2×10^{21} protons on target. *Phys. Rev. Lett.* **121**, 171802 (2018), arXiv:1807.07891 [hep-ex].
10. M.G. Aartsen *et al.* [IceCube Collaboration]. Measurement of atmospheric neutrino oscillations at 656 GeV with ice cube deep core. *Phys. Rev. Lett.* **120**, 071801 (2018), arXiv:1707.07081 [hep-ex].
11. K. Abe *et al.* [Super-Kamiokande Collaboration]. Atmospheric neutrino oscillation analysis with external constraints in Super-Kamiokande I-IV. *Phys. Rev. D* **97**, 072001 (2018), arXiv:1710.09126 [hep-ex].

Received 08.07.18

Т. Носек, від Колаборації NOvA

ОСЦИЛЯЦІЇ НЕЙТРИНО
ТА АНТИНЕЙТРИНО. ЕКСПЕРИМЕНТ NOvA

Р е з ю м е

NOvA – експеримент з двома детекторами з подовженою базою для вимірювання нейтринних осциляцій за допомогою струменя мюонних нейтрино на 700 kW NuMi. З протонним струменем, спрямованим на мішень NuMi із загальною експозицією $8.85\times10^{20} + 12/33\times10^{20}$, в режимі нейтрино + антинейтрино (на 78% процентів більше антинейтрино, ніж у 2018 році), експеримент досяг достовірності 4.4σ появи $\bar{\nu}_e$ в пучку $\bar{\nu}_\mu$, було виміряно параметри осциляції $|\Delta m^2_{32}|$, $\sin^2\theta_{23}$, а також було виключено більшість значень, близьких до $\delta_{\rm CP} = \pi/2$ для зворотних нейтрино, більш ніж на 3σ.

https://doi.org/10.15407/ujpe64.7.619

V. PUGATCH
on behalf of the LHCb Collaboration
Institute for Nuclear Research, Nat. Acad. of Sci. of Ukraine
(47, Prosp. Nauky, Kyiv 03680, Ukraine; e-mail: pugatch@kinr.kiev.ua)

HEAVY-ION AND FIXED-TARGET PHYSICS IN LHCb

Selected results of the LHCb experiment on heavy ion collisions studied in the collider and fixed-target modes are presented. The clear evidence of the impact of the production mechanism (prompt/delayed, p-p or p-Pb systems) on the p_T *and rapidity distributions for* J/ψ, D^0 *and* $\Upsilon(ns)$ *species is demonstrated. The interpretation of the observations in frames of theoretical models is briefly discussed. Some original results, as well as prospects of fixed-target mode studies, are presented.*

K e y w o r d s: high-ehergy physics, heavy ions, LHCb experiment, nuclear modification factor, quark-gluon plasma.

1. Introduction

The LHCb Collaboration has started heavy ion studies in the year 2013, and many interesting observations have been reported. In this presentation, we shall discuss recent results on the charmonium and bottonium production cross-sections measured over the transverse momentum and rapidity. Physics goals include studies of the hadronic matter at high densities and temperatures, nucleon and nuclear PDFs, dynamics of the multinucleon interaction, hadronization, and QED at high electromagnetic field strengths. Charmonium and bottomonium states are considered as tools for the studies. It is assumed that their features are dependent on the properties of the QGP. One can expect their dependence on the interaction energy (collider or fixed-target mode), systems size (p-p, p-A, A-A), localization of the quarkonium production and direction of its emission (primary interaction region or displaced vertices, forward or backward emission), and different levels of a modification for the ground and excited states of the same probe, as well as on the centrality factor or multiplicity of events. To quantify the above-mentioned impacts, it is natural to compare differential production cross-sections measured in the proton proton scattering and in heavy ion collisions (p-A, A-A) at the same nucleon-nucleon cms energy. The normalized ratio of those cross-sections is defined as a Nuclear Modification Factor (NMF). The LHCb experiment operating in the collider and fixed-target modes allows one to measure the double differential production cross-sections for various hadronic probes as a function of the transverse momentum and the rapidity. The measured physical observables treated theoretically allow one to probe the structure of nuclei on the partonic scale. In this presentation, selected recent results on heavy ion collisions in the collider and fixed-target modes are presented for J/ψ, D^0, and $\Upsilon(ns)$ hadrons.

2. LHCb Detector

The LHCb detector [1] is a forward spectrometer with excellent characterisitics: accep$_T$ance $2 < \eta < 5$ (with HERSCHEL $8 < \eta < 10$), momentum resolution about 0.5%, track reconstruction efficiency >96%, impact parameter resolution $\sim$20 μm (decay time resolution: $\sim$45 fs), invariant mass resolution $\sim$15 MeV/c^2, and perfect particle identification efficiency in Ring-Imaging Cherenkov Detectors and the Muon system. LHCb is the only experiment at the LHC fully instrumented for the large-rapidity range. The proton-lead collisions were studied at two energies corresponding to the proton-nucleon center-of-mass energies $\sqrt{S_{NN}}$ = 5.02 TeV and 8.16 TeV. Protons and lead ions at fixed targets (Ar, He, Ne) were studied at energies $\sqrt{S_{NN}}$ of $\sim$0.1 TeV. The directions of proton and lead beams were swapped during the data-taking period. The configuration with the protons traveling in the direction from the Vertex detector (VELO) to the Muon system is referred to as p-Pb collisions, the inverse configuration as Pb-p ones. The positive rapidity in the proton-nucleon center-of-mass system is defined

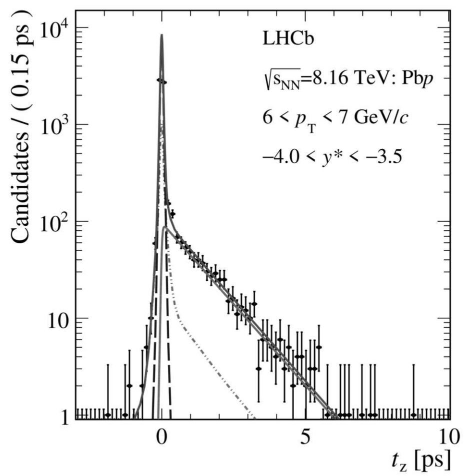

Fig. 1. Decay time distribution for J/ψ events from Pb-p collisions

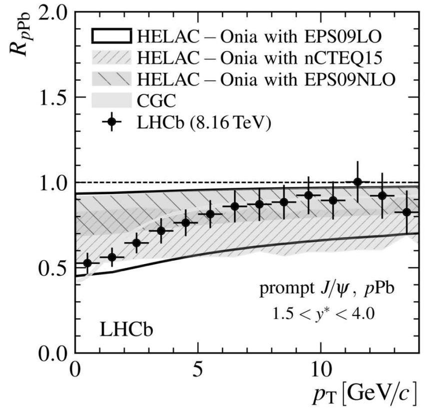

Fig. 2. NMF (experiment – black circles with error bars) as a function of p_T for prompt J/ψ in the rapidity range $1.5<y^*<4.0$

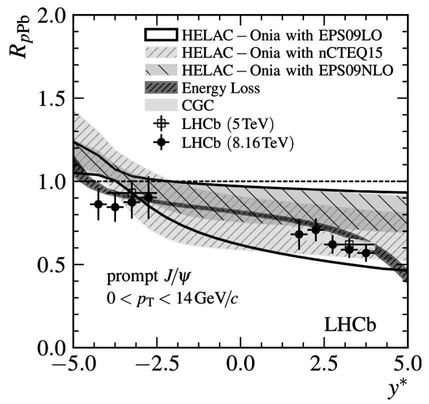

Fig. 3. Nuclear modification factor as a function of the rapidity for J/ψ from prompt events

by the direction of the proton beam. Thus, within a single experiment, the production cross-sections, forward-backward asymmetries, and nuclear modification factors were measured in a wide energy range for various hadronic states (J/ψ, D^0, $\Upsilon(ns)$, antiprotons, B mesons, and other hadrons).

3. Charmonium Production in Proton-Lead Collisions at $\sqrt{S_{NN}} = 5.02$ TeV and 8.16 TeV

Exploring the powerful vertexing tool of the detector, the double differential cross-sections were measured for prompt and delayed J/ψ mesons separated as illustrated in Fig. 1 [2]. The two components in the J/ψ decay time distribution (Fig. 1) correspond to the prompt J/ψ (narrow peak at zero time) and non-prompt J/ψ from the b-hadron falling exponentially with a time constant of beauty hadrons. The interpretation of the results in frames of different theoretical approaches is illustrated in Fig. 2, where the experimental values for the NMF (black circles with error bars) are shown as a function of p_T for prompt J/ψ in the rapidity range $1.5 < y^* < 4.0$. If there would be no impact of the media, the NMF at the level of unity should follow up the dotted line parallel to the x-axis. Instead, a strong suppression of the J/ψ production is well pronounced for p_T less than 10 GeV/c. The CGC theory [3] follows experimental points nearly ideally, while other calculations (HELAC) just reflect the general tendency with large uncertainties [2]. These results constrain nPDFs in unexplored area at low-x [4, 5]. The comparison of p_T, as well as rapidity distributions, has revealed significant differences for J/ψ mesons produced in p-p and p-Pb collisions. The data extracted from p-Pb collisions at 8.16 TeV for J/ψ originated from primary vertices (prompt events, forward rapidity region) demonstrated a reduction of the cross-section by twice for low p_T (<4 GeV/c). While, for the backward rapidity range, the cross-sections are close to be equal within statistical errors. The delayed events are characterized by a much less suppression even for the forward rapidity range y^*. These observations are consistent with data measured for J/ψ at a lower energy of 5 TeV. This is illustrated in Figs. 3 and 4 [2] which show the nuclear modification factor extracted from data measured at 5 TeV (open circles) and 8.16 TeV (filled circles) for J/ψ from prompt (Fig. 3) and from the decay of b-hadrons (Fig. 4). The remarkable dependence on the mechanism of production is clearly visible. The theoretical approach based on NLO nuclear PDFs accounting for the coherent energy-loss (black thick line) [6] follows well experimental data points for prompt J/ψ (Fig. 3). Non-prompt J/ψ are treated less satisfactorily with large uncertainties in frames of the calculations within the code FONLL with EPS09NLO [7] (Fig. 4). The production suppression at the forward rapidity for J/ψ from b-hadrons is less pronounced than for prompt J/ψ. These data allow one to constrain nPDFs at low-x [7]. Studies of the prompt D^0 meson production in pPb collisions at 5 TeV [8] have demonstrated similar observations. As an example, Figs. 5 and 6 show data for the prompt D^0 meson production in p-Pb collisions as a function of y^* (Fig. 5) and the Nuclear modification factor $R_{\text{p-Pb}}$ as a function of y^* (Fig. 6) with $p_T < 10$ GeV/c. The strong suppression in the forward-rapidity range (Fig. 6) was observed and well approximated by the theoretical description based on Nuclear PDFs and Color Glass Condensate assumptions. The data allow one to constrain nPDFs at low-Bjorken x [7].

4. Bottonium Production in Proton-Lead Collisions at 8.16 TeV

Comprehencive studies were performed for properties of bottonium states $\Upsilon(1S)$, $\Upsilon(2S)$, and $\Upsilon(3S)$ producсd in p-p and p-Pb collisions [9]. The detailed analysis of p_T, as well as rapidity distributions, demonstrates the suppression of 1S and 2S states, with the 2S state being suppressed to a larger extent. Figures 7 and 8 show an example of such analysis for the nuclear modification factors $R_{\text{p-Pb}}$ for the $\Upsilon(1S)$ and $\Upsilon(2S)$ states (black dots with error bars) compared with different theoretical calculations (bands). $R_{\text{p-Pb}}$ (1S) is consistent with unity at negative y^*, while a significant (by ∼30%) suppression is observed for positive y^*. The nuclear modification factor for $\Upsilon(2S)$ is smaller than $\Upsilon(1S)$) especially in the backward region, which is consistent with the comovers models [10] and in agreement with other experiments [11]. Calculations are based on the comovers model of $\Upsilon(nS)$ production, which implements the final state interaction of the quarkonia states and a nuclear parton distribution function modification. For the $\Upsilon(1S)$ state, the nuclear modification factor is consistent with unity for $p_T > 10$ GeV/c, as predicted by the models. It is important to point out that the measurements of B^+, B^0, and $\Lambda^0{}_b$

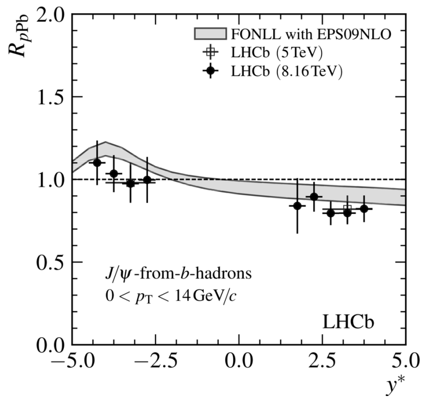

Fig. 4. Nuclear modification factor as a function of the rapidity for J/ψ from b-hadrons

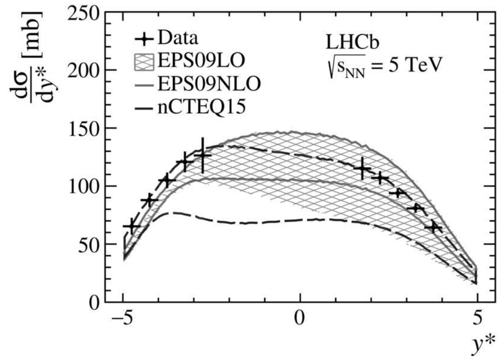

Fig. 5. Differential cross-section of the prompt D^0 meson production in p-Pb collisions as a function of y^*

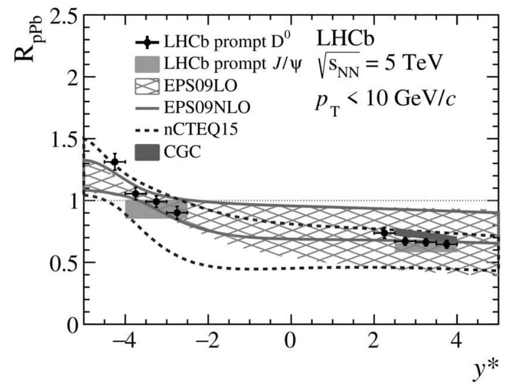

Fig. 6. Nuclear modification factor $R_{\text{p-Pb}}$ as a function of y^* for the prompt D^0 meson production with p_T<10 GeV/c

production in pPb collisions at 8.16 TeV [12] also indicated a significant nuclear suppression of the nuclear modification factors and forward-to-backward cross-section ratios at the positive rapidity.

5. Fixed-Target Mode Studies

The LHCb fixed-target program [13] includes, in particular, the study of the heavy-quark production in the large Bjorken x region, the test of the intrinsic charm content of the proton and cosmic rays physics relevant production of antiprotons. Below, some results obtained in this area are briefly presented. In particular, the antiproton production in proton-helium collisions and the charmonium production in proton-argon collisions are discussed. The prompt anti-p production in p-He collisions was thourouphly studied in a fixed-target mode at the energy $\sqrt{S_{NN}} = 110$ GeV exploring a He gas injected inside by the SMOG system [14]. These data are important for the interpretation of recent results on the antiproton fraction in cosmic rays. An increase of the antiproton fraction in cosmic rays might be a sign of the antimatter produced by the dark matter annihilation. The measured production cross-sections were interpreted in frames of the several models differing by hadronization, parton model, and dynamics. The shapes are well reproduced except at low rapidities, and the absolute yields deviate up to a factor of two [15]. The uncertainties (~10%) of experimental data are smaller than the spread of theoretical models. The results contribute to shrink background uncertainties in the dark matter searches in space [15, 16]. Among other important resuts obtained in a fixed-target mode exploring the SMOG system, the first measurement of the heavy flavor (J/ψ and D^0) production cross-section in p-He at $\sqrt{S_{NN}} = 86.6$ GeV and p-Ar at $\sqrt{S_{NN}} = 110$ GeV at the LHC were reported in [18]. The measurements were performed in the range of J/ψ and D^0 transverse momentum $p_T < 8$ GeV/c and the rapidity $2.0 < y < 4.6$. In this range, any substantial intrinsic charm contribution should be seen in the p-He results. The measurements show no strong differences between p-He data and the theoretical predictions which do not consider the intrinsic charm contribution. Future measurements with larger samples and more accurate theoretical predictions will permit one to perform more quantitative studies.

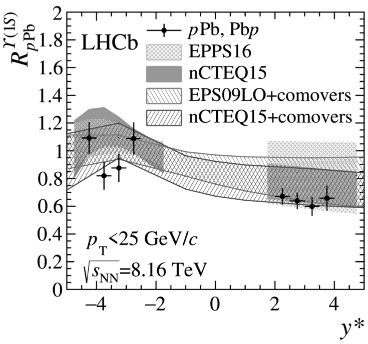

Fig. 7. Nuclear modification factor $R_{\text{p-Pb}}$ as a function of the rapidity y^* for $\Upsilon(1S)$ state

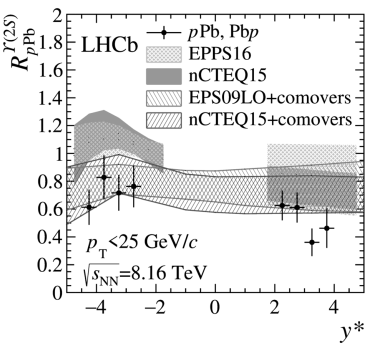

Fig. 8. Nuclear modification factor $R_{\text{p-Pb}}$ as a function of the rapidity y^* for $\Upsilon(2S)$ state

In view of the successful running in the fixed-target mode in Run2, it is decided to upgrade the system for the injection of a gas for Run3. The SMOG2 [19] will inject a gas inside a 20-cm-long storage cell (1 cm in diameter) in front of the vertex detector aiming to provide the instantaneous luminosity higher by up to two orders of magnitude. In addition to the noble gases, hydrogen and deuterium will operate as well. To extend the Heavy Ion Fixed Target program for Run4 and further, a crystal target, polarized target, and superthin wire targets were proposed and discussed. The LHCb fixed-target mode is unique for the experiments at LHC, and it is planned to extend this area of studies in the future RUN3 and Run4 data taking.

6. Summary and Outlook

Double differential cross-sections for the production of charm and beauty hadrons measured in the collider and fixed-target mode in various combinations of heavy ions collisions at 5, 8, and 0.1 TeV have been presented. The remarkable feature was observed in the collider-mode data: significant suppression of cross-sections at low transverse momenta and the forward rapidity in comparison with p-p data. The interpretation of the obtained results has been performed in frames of several theoretical approaches. The statistical and theoretical uncertainties have to be reduced for improving the extraction of nPDFs.

We express our gratitude to our colleagues in the CERN accelerator departments for the excellent performance of the LHC. We thank the technical and administrative staff at the LHCb institutes. We acknowledge the support from CERN and from the national agencies: CAPES, CNPq, FAPERJ and FINEP (Brazil); MOST and NSFC (China); CNRS/IN2P3 (France); BMBF, DFG and MPG (Germany); INFN (Italy); NWO (Netherlands); MNiSW and NCN (Poland); MEN/IFA (Romania); MSHE (Russia); MinECo (Spain); SNSF and SER (Switzerland); NASU (Ukraine); STFC (United Kingdom); NSF (USA). We acknowledge the computing resources that are provided by CERN, IN2P3 (France), KIT and DESY (Germany), INFN (Italy), SURF (Netherlands), PIC (Spain), GridPP (United Kingdom), RRCKI and Yandex LLC (Russia), CSCS (Switzerland), IFIN-HH (Romania), CBPF (Brazil), PL-GRID (Poland) and OSC (USA). We are indebted to the communities behind the multiple open-source software packages on which we depend. Individual groups or members have received the support from AvH Foundation (Germany); EPLANET, Marie Sklodowska-Curie Actions and ERC (European Union); ANR, Labex P2IO and OCEVU, and Région Auvergne-Rhône-Alpes (France); Key Research Program of Frontier Sciences of CAS, CAS PIFI, and the Thousand Talents Program (China); RFBR, RSF, and Yandex LLC (Russia); GVA, XuntaGal, and GENCAT (Spain); the Royal Society and the Leverhulme Trust (United Kingdom); Laboratory Directed Research and Development program of LANL (USA). The studies have been partially supported in frames of the Targeted research program (Fundamental research on high-energy physics and nuclear physics, international cooperation) of the NAS of Ukraine and LIA IDEATE (STCU Project P9903).

1. LHCb Collaboration. A.A. Alves Jr. *et al.* The LHCb detector at the LHC. *JINST* **3**, S08005 (2008).
2. LHCb Collaboration. R. Aaij *et al.* Prompt and nonprompt J/ψ production and nuclear modification in pPb collisions at $\sqrt{s_{NN}} = 8.16$ TeV. *Phys. Lett. B* **774**, 159 (2017).
3. B. Ducloué, T. Lappi, H. Mäntysaari. Forward J/ψ production in proton-nucleus collisions at high energy. *Phys. Rev. D* **91**, 114005 (2015).
4. J.-P. Lansberg, H.-S. Shao. Towards an automated tool to evaluate the impact of the nuclear modification of the gluon density on quarkonium, D and B meson production in proton–nucleus collisions. *Eur. Phys. J. C* **77**, 1 (2017).
5. A. Kusina, J.-P. Lansberg, I. Schienbein, H.-S. Shao. Gluon shadowing in heavy-flavor production at the LHC. *Phys. Rev. Lett.* **121**, 052004 (2018).
6. F. Arleo, S. Peigné. Heavy-quarkonium suppression in p-A collisions from parton energy loss in cold QCD matter. *JHEP* **03**, 122 (2013).
7. M. Cacciari, M. Greco, P. Nason. The p_T spectrum in heavy-flavour hadroproduction. *JHEP* **05**, 007 (1998).
8. LHCb collaboration, R. Aaij *et al.* Study of prompt D^0 meson production in pPb collisions at $\sqrt{s_{NN}} = 5$ TeV. *JHEP* **10**, 090 (2017).
9. LHCb collaboration, R. Aaij *et al.* Study of Υ production in pPb collisions at $\sqrt{s_{NN}} = 8.16$ TeV. *JHEP* **11**, 194 (2018).
10. E.G. Ferreiro, J.-P. Lansberg. Is bottomonium suppression in proton-nucleus and nucleus-nucleus collisions at LHC energies due to the same effects? *JHEP* **10**, 94 (2018).
11. ATLAS Collaboration, M. Aaboud *et al.* Measurement of quarkonium production in proton–lead and proton–proton collisions at 5.02 TeV with the ATLAS detector. *Eur. Phys. J. C* **78**, 171 (2018).
12. LHCb collaboration, R. Aaij *et al.* Measurement of B^+, B^0 and Λ_b^0 production in pPb collisions at $\sqrt{s_{NN}} = 8.16$ TeV. *Phys. Rev. D* **99**, 052011 (2019).
13. S.J. Brodsky *et al.* Physics opportunities of a fixed-target experiment using LHC beams. *Phys. Rep.* **522**, 239 (2013).
14. LHCb collaboration, R. Aaij *et al.* Precision luminosity measurements at LHCb. *JINST* **9**, P12005 (2014).
15. LHCb collaboration, R. Aaij *et al.* Measurement of antiproton production in p–He collisions at $\sqrt{s_{NN}} = 110$ GeV. *Phys. Rev. Lett.* **121**, 222001 (2018).
16. M. Korsmeier, F. Donato, Ma. Di Mauro. Production cross sections of cosmic antiprotons in the light of new data from the NA61 and LHCb experiments. *Phys. Rev. D* **97**, 103019 (2018).
17. M. Boudaud *et al.* AMS-02 antiprotons are consistent with a secondary astrophysical origin. arXiv:1906.07119 (2019).
18. LHCb collaboration, R. Aaij *et al.* First measurement of charm production in its fixed-target configuration at the LHC. *Phys. Rev. Lett.* **122**, 132002 (2019).
19. LHCb collaboration, I. Bediaga *et al. LHCb SMOG Upgrade. CERN/LHCC 2019-005. LHCb TDR 2008 May 2019.*

Received 08.07.19

В. Пугач, від імені Колаборації LHCb

ФІЗИКА ВАЖКИХ ІОНІВ
ТА ФІКСОВАНОЇ МІШЕНІ В ЕКСПЕРИМЕНТІ LHCb

Р е з ю м е

Представлено вибрані результати експерименту LHCb по зіткненням важких іонів, дослідженим в колайдерному режимі та з фіксованою мішенню. Спостережено незаперечний вплив механізму (миттєвого чи з затримкою, в p-p чи p-Pb системах) утворення мезонів J/ψ, D^0 або $\Upsilon(ns)$ на розподіли подій по p_T та бистротам. Коротко обговорюється інтерпретація спостережень у рамках теоретичних моделей. Представлено деякі оригінальні результати, а також перспективи досліджень в режимі фіксованої мішені.

https://doi.org/10.15407/ujpe64.7.624

T. ROSTOMYAN
for the MUSE Collaboration
Rutgers, The New Jersey State University
(Piscataway, New Jersey 08855, USA; e-mail: Tigran.Rostomyan@psi.ch)

STATUS OF THE MUSE EXPERIMENT

The 5.6σ difference in proton radii measured with μp atoms and with ep atoms and scattering remains an unexplained puzzle. MUSE will measure the μp and ep elastic scatterings in the same experiment at the same time. The experiment determines cross-sections, two-photon effects, form-factors, and radii and allows μp and ep to be compared with reduced systematic uncertainties. These data should provide the best test of the lepton universality in a scattering experiment to date, about an order of magnitude improvement over previous tests, a 7σ radius determination, and improved two-photon measurements.

K e y w o r d s: proton radius puzzle, MUSE, elastic scattering, muon beam, TPE.

1. Introduction

In 2010, a Paul Scherrer Institute (PSI) experiment [1] reported that the proton charge radius determined from muonic hydrogen level transitions is 0.84184 ± 0.00067 fm, about 5σ off from the nearly order-of-magnitude less precise non-muonic measurements. This "proton radius puzzle" was confirmed in 2013 by a second muonic hydrogen measurement [2] of 0.84087 ± 0.00039 fm. Subsequent *ep* scattering results of 0.879 ± 0.008 fm [3] and 0.875 ± 0.010 fm [4] confirmed the puzzle. The situation has been discussed in review papers [5], in dedicated workshops [6–8], and in many talks. It is generally agreed that new data are needed to resolve the puzzle.

The MUon Scattering Experiment (MUSE) collaboration was formed in 2012 to uniquely attempt to resolve the "Proton radius puzzle" by simultaneously measuring the μp and *ep* elastic scattering cross-sections at the sub-percent level. MUSE alternates between positive vs. negative charged beams – all previous measurements are with negative leptons. Thus, MUSE directly compares μp to *ep* cross-sections and radii, provides the first significant μp scattering radius, and measures two-photon exchange effects (TPE) at the sub-percent level, rather than using the calculated corrections.

2. PSI Beam Line and $\pi M1$ Experimental Area

The PSI High Intensity Proton Accelerator (HIPA) primary protons strike the M production target and generate secondary $e^{\pm}$, $\mu^{\pm}$, and $\pi^{\pm}$ beams that are transported through the PiM1 channel to MUSE. Particle species are identified by timing relative to beam RF (Figure 1). The beam composition delivered to $\pi M1$ is shown in the Table.

Three different beam momenta are chosen to optimize both e and μ fluxes and RF time separation and provide redundant cross-sections as a check of the systematics. Figure 1 shows that the different particle species are 3–6 ns apart, much larger than the intrinsic timing width of ≈ 300 ps.

3. MUSE Detector Setup

MUSE is implemented as a set of detectors and cryotargets mounted on a moveable platform, so that

The measured $\pi M1$ beam composition

P, MeV/c	Polarity	e, %	μ, %	π, %
115	+	96.7	2.1	0.9
153	+	63.0	12.0	25.0
210	+	12.1	8.0	79.9
115	–	98.5	0.9	0.6
153	–	89.9	3.2	6.8
210	–	47.0	4.0	49.0

the PiM1 area can be shared. Figure 2 shows the experiment as represented in a Geant4 [9] simulation. The beam strikes the Beam Hodoscope (BH) detector and three Gas Electron Multiplier (GEM) chambers, passes through a central hole in the annular Beam Veto detector, enters the cryotarget vacuum chamber, strikes one of the targets (Liquid Hydrogen, Carbon, *etc.*), and then exits the vacuum chamber. Unscattered particles go through the Beam Monitor (BM), while scattered particles are detected by two symmetric spectrometers, each with two Straw-Tube Trackers (STT-s) and two planes of Scattered Particle Scintillators (SPS). The BH identifies particles through the RF timing; triggering depends on the particle type. Reaction identification (scattering vs. decays in flight) uses GEM and STT tracking along with the time of flight (TOF) from the BH to SPS. The BM can also be used to suppress Moeller events. More details are below.

3.1. Beam hodoscope

Purpose:

The BH provides timing information that, along with the RF signal, determines beam particle species for triggering and analysis. TOF from the BH to the SPS determines the reaction type, in particular, separates the muon decay from the muon scattering. TOF from the BH to the BM identifies backgrounds and determines μ and π momenta. The BH also measures the particle-separated beam fluxes.

Requirements:

The most stringent time resolution requirement is 100 ps needed for the reaction identification at the highest beam momentum; 80 ps has been achieved. High efficiency of 99% is needed to efficiently collect data and reject backgrounds; 99.8% has been achieved. A rate capability of ≈3.3 MHz is needed to obtain the adequate statistical precision; the use of multiple paddles allows rates up to 10 MHz.

Design:

Figure 3 shows a BH plane under construction. We use BC-404 scintillator paddles that are 10 cm long and ×2 mm thick. Six central 4 mm wide paddles are flanked on each side by 5 outer 8-mm wide paddles. The paddles are read out at each end by Hamamatsu S13360-3075PE SiPMs. A 6 μm gap between the paddles suppresses cross-talk. To minimize effects on the beam and to achieve the needed performance, we use 2–4 planes of BH depending on the beam momentum.

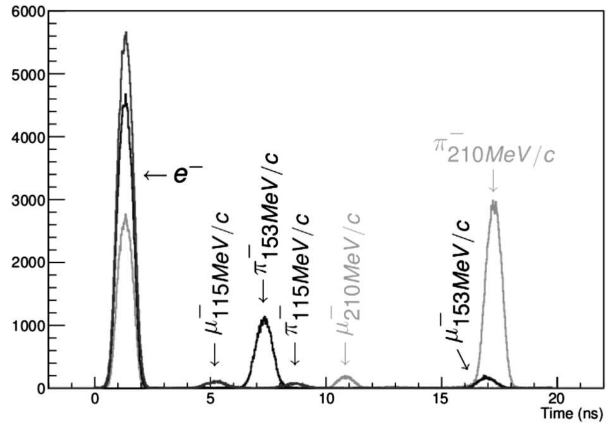

Fig. 1. Measured RF time spectrum for negative charge particles at 115, 153, and 210 MeV/c. The spectrum wraps around every ≈20 ns

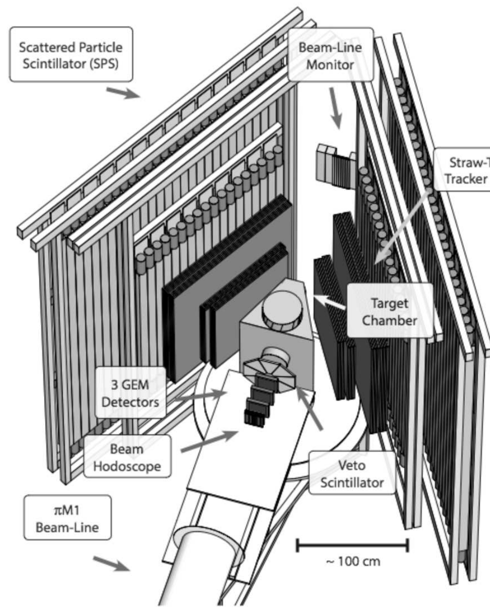

Fig. 2. MUSE detector setup implementation in GEANT4 simulation

The BH analog signal is amplified to produce a fast signal with a 1.2 (3.0) ns rise (fall) time and typically a few hundred mV peak. A Mesytec CFD sends an analog copy of the signal to a Mesytec QDC input, and the discriminated signal to a TRB3 TDC and the trigger, and an OR of all input signals to the Mesytec QDC gate.

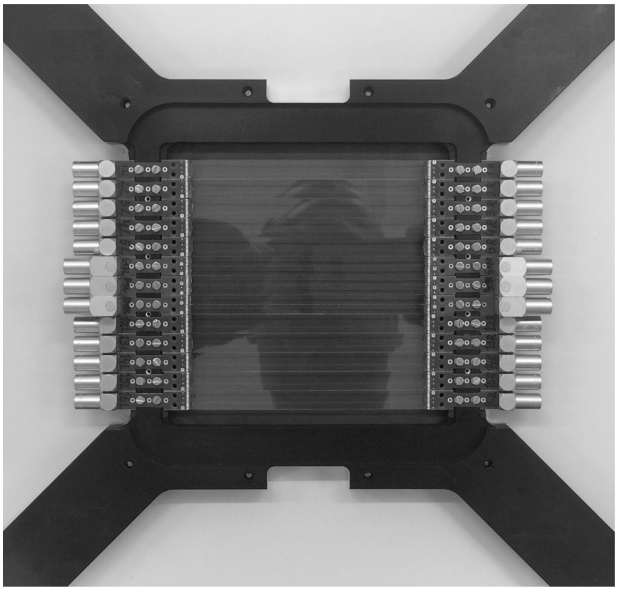

Fig. 3. BH plane with SiPM readout under construction

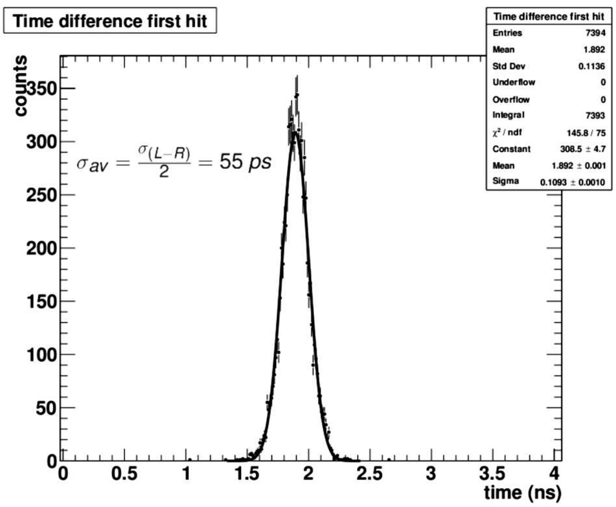

Fig. 4. The best obtained time resolution of a BH paddle

Status:

Five BH planes are built with all paddles meeting requirements. The best time resolution achieved is shown in Fig. 4.

3.2. GEM trackers

Purpose:

The GEMs measure beam trajectories so that precise scattering angles and reaction vertices can be determined. GEM chambers were chosen, as they are low-mass detectors, ≈0.5% of radiation length, which keeps the multiple scattering at a minimum, provide several MHz rate capability with <100 μm position resolution and high efficiency, >98%.

Requirements:

In addition to the performance characteristics given above, we require a read-out time <100 μs for the efficiency in obtaining data.

Detector design:

We use three 10 × 10 cm^2 GEMs, which were previously used in OLYMPUS [10]. The GEMs are read out using FPGA-controlled frontend electronics based on the APV-25 chip developed for CMS and digitized with the Multi-Purpose Digitizer (MPD) v4. There are readout strips in two directions, each with 400 μm pitch, much smaller than the amplified charge, which is distributed in a few mm wide cluster. Centroid weighting provides a resolution smaller than the pitch.

The GEM efficiency remains high at rate densities up to 2.5 MHz/cm^2. The expected rate density for MUSE is ≈3.3 MHz/5 cm^2 = 0.66 MHz/cm^2.

Current status:

The GEM system has been re-established for MUSE. We have implemented the new INFN/JLab DAQ readout software and VME controllers, which improve the read out speed along with low-noise operation and high efficiency reproduction. All requirements are now satisfed. The πM1 beam spot obtained by the GEMs is shown in Fig. 5.

3.3. Beam Veto

Purpose and requirements:

The Beam Veto detector is used to reduce the trigger rate, by vetoing some of the events that arise from beam particle decays in flight or the scattering upstream of a scattering chamber. The veto detector requires a high efficiency, >99%, and a 1-ns time resolution – 200 ps has been achieved.

Design:

The Beam Veto detector uses the same technology as the SPS (described in Section 3.7), with a modified geometry and only single-ended readout. Figure 6 shows the detector. The detector geometry is nearly annular, surrounding the beam. Four trapezoidal BC-404 scintillators are each read out with two Hamamatsu R13435 PMTs. The inner aperture roughly matches the target vacuum chamber entrance win-

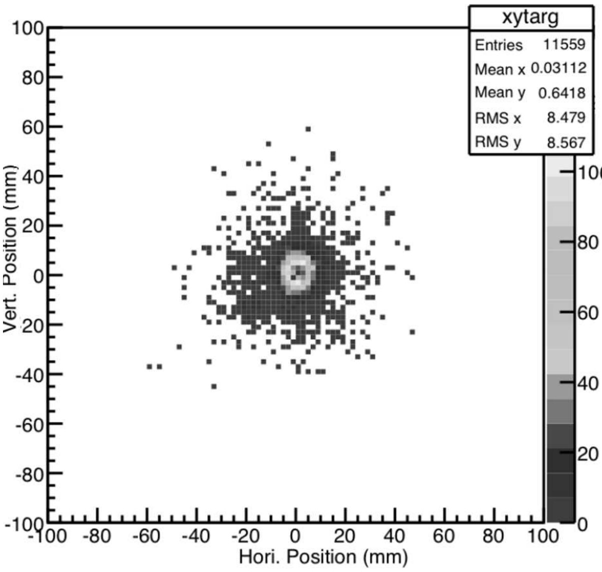

Fig. 5. The πM1 beam spot at the most upstream GEM detector

dow. The outer extent of the detector, about 16 cm radius, was determined from simulations.

Status:

The Beam Veto detector was built, installed, and commissioned. All performance requirements have been achieved.

3.4. Liquid hydrogen target

Purpose and requirements:

A Liquid Hydrogen (LH_2) target is needed for the *ep* and *μp* scatterings. In practice this requires a target ladder that includes at least a full cell, an empty cell for background subtractions, a solid target for alignment, and an empty position. The LH_2 density must be stable, <0.1%, to precisely compare cross-sections measured at different times. The geometry of the target must be uniform at the sub-mm level for precise background subtractions.

Design:

Detailed final construction designs and the actual construction were performed by CREARE Inc. working with the collaboration. The target ladder is housed in a vacuum chamber with a 7-cm diameter entrance (7.8 cm wide by 35.6 cm high exit) window, made of 125-μm thick kapton. Scattered particles with $\theta = 20°–100°$ go through side windows 33.7 cm wide and 35.6 cm high, made of Mylar laminated on aramid sailcloth fabric, with an areal density of 368 g/m^2. The main target is a 280 mL LH_2 cell made of upper and lower copper end caps connected by a side wall of 4 wraps of 25 μm thick kapton. A cryocooler cools a condenser assembly so that the resulting LH_2 drips into the target cell. A lifting mechanism switches between ladder positions, lifting as well the cryocooler cold head and the condenser assembly.

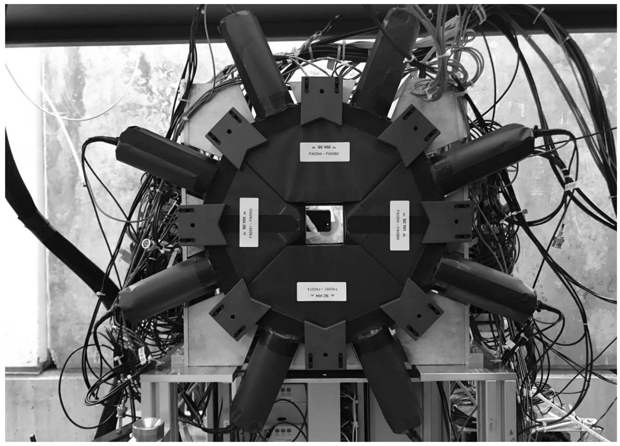

Fig. 6. Beam-Veto detector. The beam is pointing to us

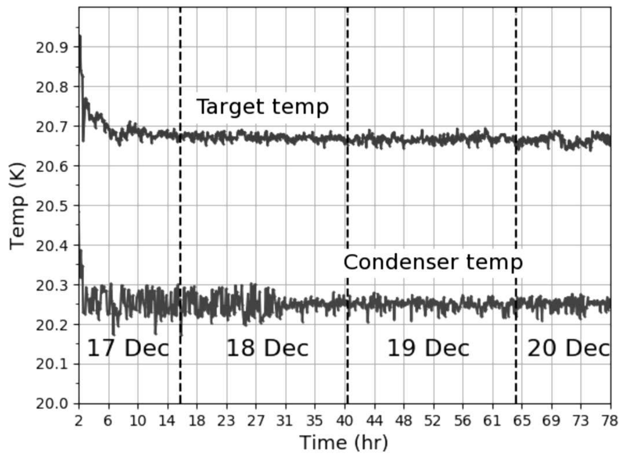

Fig. 7. Results of the first hydrogen cooldown, covering from 2 till 78 hours. Temperature stability assures the target density stability below the experimental requirements

Current status:

Filling the cryotarget with LH2 at 20.67 K takes about 2.5 h from the start of the cooldown. The target was operated steadily for over three days at a pressure of 1.1 bar with temperature constant at the 0.01 K level – see Fig. 7 – consistent with the mea-

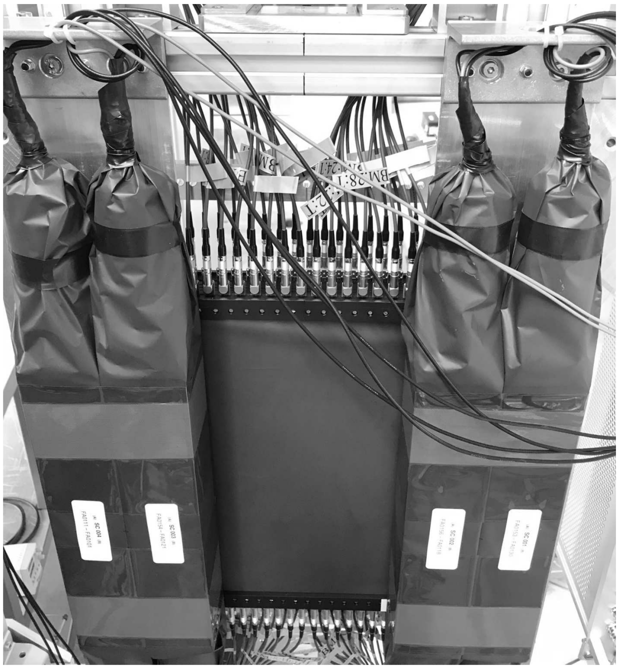

Fig. 8. Beam Monitor: The LEMO readout connectors of two offset planes are seen, continued with bigger BC-404 scintillators. The beam hits into the picture

surement uncertainty. This gives a target density of 0.070 g/cm^3 with stability <0.02%, better than experimental requirements.

3.5. Beam monitor

Purpose:

The BM provides a high-precision time measurement that determines the beam flux downstream of the target. TOF from the BH to BM determines a particle type and the background information for the RF-time only determination. TOF also determines μ and π momenta to <0.2%. The BM also detects forward Moller electrons, so it can suppress this background in the scattering data.

Requirements:

The BM comprises a central scintillator hodoscope similar to the BH of Subsection 3.1 and an outer hodoscope similar to the SPS of Subsection 3.7. The underlying technology and requirements are the same in both cases.

Design:

Figure 8 shows the BM. The central hodoscope of the BM comprises two offset planes of 16 paddles. We use 30 cm long $\times$ 12 mm wide $\times$ 3 mm thick BC-404 paddles, each read out at each end by 3 Hamamatsu S13360-3075PE SiPMs in series. The same readout electronics as for the BH is used. The outer hodoscope consists of four 30 cm long $\times$6 cm wide $\times$6 cm thick BC-404 scintillator paddles that are identical in technology to the SPS scintillators.

Status:

The BM was fully assembled, installed, and commissioned. Typical time resolutions of σ_T < 100 ps (Best: $\sigma_T = 59$ ps) were achieved, with $\geq$99.9% efficiency, exceeding performance requirements.

3.6. Straw-tube tracker

Purpose and requirements:

The STT tracks scattered particles. High resolution, <150 μm, and efficiency, >99.8%, are required for precise cross-sections.

Design:

The STT follows the PANDA straw chamber design [11] adapted to the MUSE geometry. We use the same straws, wires, end pieces, and feed-throughs as PANDA. Thin-walled, over-pressured straws allow for a significantly less straw material, while providing the mechanical stability. The straw spacing is 1.01 cm, and adjacent offset straw planes are 0.87 cm apart.

The symmetric beam left and right scattered particle detector systems include 2 chambers on each side of the beam, each with 5 vertical and 5 horizontal planes, to achieve a high tracking efficiency. The front chambers have 275 60-cm long vertical straws and 300 55-cm long horizontal straws, with an active area of 60×55 cm^2. The rear chambers have 400 90-cm long vertical straws and 450 80-cm long horizontal straws with an active area of 90×80 cm^2. The front (rear) chambers are 30 (45) cm from the target. There are 2850 straws in the system. The STT uses 90% Ar +10% CO_2 at a pressure of 2 bar. Straws operate at 1700 V. Frontend PASTTREC cards read out the straws, and are in turn read out by TRB3 TDCs.

Status:

All 4 chambers have been assembled at PSI and undergone initial performance tests. Figure 9 shows the STT being craned into the MUSE detector setup. In the initial tests, the straws operated reliably with approximately 90% efficiency, which yields ≈99% tracking efficiency for 5 planes. A preliminary analysis of

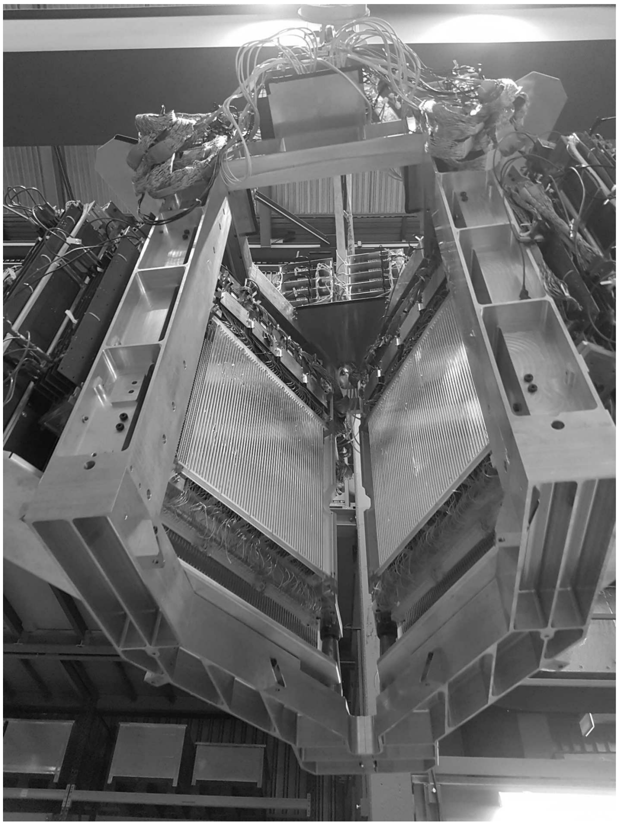

Fig. 9. Fully assembled STT detector being craned into the MUSE detector setup

the STT data yields a tracking resolution of approximately 115 μm, exceeding requirements.

3.7. Scattered particle scintillators

Purpose and requirements:

The SPS is a high-efficiency high-precision scintillator hodoscope that detects and times particles for the triggering and reaction identification. A time resolution of ≈100 ps is needed for the reaction identification. A uniform efficiency of >99% is needed so that the shape of the angular distribution is not altered.

Design:

The SPS design follows the JLab CLAS12 FTOF12 design by University of South Carolina. Symmetric left and right, front and rear hodoscope paddles are made of an Eljen Technology EJ-204 plastic scintillator, which has a high light output and a fast rise time. Hamamatsu R13435 PMTs are glued to each end of the scintillator. The front wall is roughly square and covers $\theta \approx 20°–100°$. The oversized back wall accounts for the multiple scattering in the front wall.

Status:

All 92 paddles are tested and installed. Average time resolutions of $\sigma_{\rm avg} = 52$ ps $\pm$ 4 ps for the 220-cm long rear bars and 46 ps $\pm$ 4 ps for the 110-cm long front bars were obtained. Figure 10 shows that energy deposition in the scintillators modeled with Geant4 simulations agrees nicely with measurements.

The two-plane coincidence efficiency is well above 99.5%, except for e^+ (≥99%) due to the annihilation. We expect the cross-section systematic uncertainty from the SPS efficiency to be <0.1%.

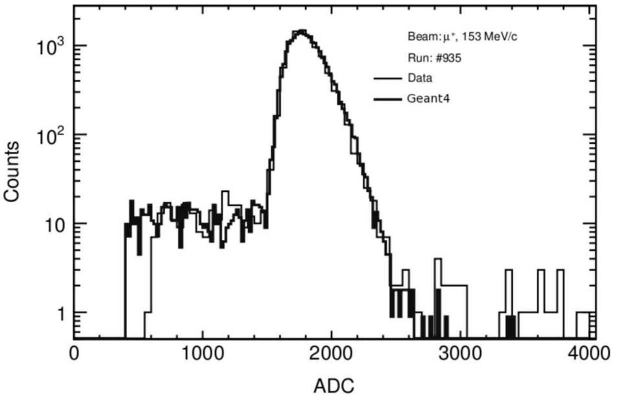

Fig. 10. SPS ADC spectra: Particles stopping or going through the bar are in peak; particles going out the side of the bar are in the low-energy tail

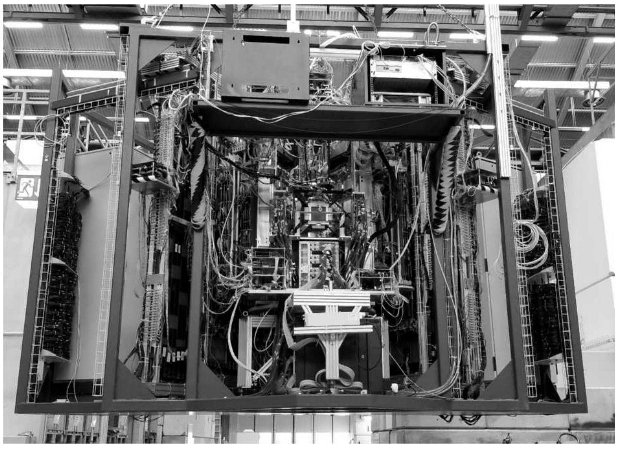

Fig. 11. MUSE Detector setup is being craned into the experimental area

3.8. Trigger, DAQ, and tracking

MUSE uses TRB3 FPGAs for the triggering. The primary scattered particle trigger logic is:

$$(e^{\pm}\ \mathrm{OR}\ \mu^{\pm})\ \mathrm{AND}\ (\mathrm{no}\ \pi^{\pm})\ \mathrm{AND}\ (\mathrm{scatter})\ \mathrm{AND}\ (\mathrm{no\ Veto}).$$

The MUSE DAQ uses a mix of VME modules for the charge determination and TRB3 TDCs for the timing. There are about 3000 TDC and 500 Q/ADC channels. Both the trigger and DAQ along with controls and basic analysis software are fully operational. The advanced analysis software development continues.

4. Conclusions

The data taken compared to simulations prove that MUSE is well suited to investigate the ($R_e - R_\mu = 0.034 \pm 0.006$ fm) 5.6σ Proton Radius Puzzle. By comparing the $p + e^{\pm}$ and $p + \mu^{\pm}$ scattering cross-sections, we will determine the absolute radius at the $\approx$0.005 fm level. All detectors are constructed and mounted on the MUSE platform. Production data runs are planned in 2019–2021.

We acknowledge the US National Science Foundation for supporting the MUSE experiment, with the additional support from the US Department of Energy, the Binational Science Foundation, and the Paul Scherrer Institute. Special thanks to Prof. Dr. Ronald Gilman for creating such a nice working atmosphere for me. Thanks to PSI for the great hospitality and the organizers of the "New Trends in High Energy Physics" for giving me opportunity to present this work.

1. R. Pohl, A. Antognini, F. Nez, F.D. Amaro, F. Biraben, *et al.* The size of the proton. *Nature* **466**, 213 (2010).
2. A. Antognini *et al.* Proton structure from the measurement of 2S-2P transition frequencies of muonic hydrogen. *Science* **339**, 417 (2013).
3. J. Bernauer *et al.* (A1 Collaboration). High-precision determination of the electric and magnetic form factors of the proton. *Phys. Rev. Lett.* **105**, 242001 (2010).
4. X. Zhan, K. Allada, D. Armstrong, J. Arrington, W. Bertozzi *et al.* High-precision measurement of the proton elastic form factor ratio μpGE/GM at low Q2. *Phys. Lett. B* **705**, 59 (2011).
5. R. Pohl, R. Gilman, G. Miller, K. Pachucki. Muonic hydrogen and the proton radius puzzle. *Annu. Rev. Nucl. Part. Sci.* **63**, 175 (2013).
6. R. Pohl, G.A. Miller, R. Gilman *et al. Workshop on the proton radius puzzle at the Trento European Center for Theory in Nuclear Physics and Related Areas* (2012) https://ectstar.fbk.eu/node/49.
7. C. Carlson, R. Hill, S. Karshenboim, M. Vanderhaeghen *et al. Workshop on the proton radius puzzle at the Mainz Institute for Theoretical Physics* (2014).
8. R. Pohl, G. A. Miller, R. Gilman *et al. Workshop on the proton radius puzzle at the Trento European Center for Theory in Nuclear Physics and Related Areas* (2016) https://ectstar.fbk.eu/node/1659.
9. S. Agostinelli *et al.* GEANT4: A Simulation toolkit. *Nucl. Instrum. Meth. A* **506**, 250 (2003).
10. R. Milner *et al.* The OLYMPUS experiment. *Nuclear Inst. and Methods in Physics Research A* **741**, 1 (2014).
11. W. Erni *et al.* Technical design report for the $\bar{P}$ ANDA (AntiProton Annihilations at Darmstadt) straw tube tracker. *Europ. Phys. J. A* **49**, 1 (2013).

Received 08.07.19

Т. Ростомян

СТАТУС ЕКСПЕРИМЕНТУ MUSE

Р е з ю м е

Різниця в 5.6σ у радіусах протона, виміряних з атомами μp і з атомами ep та в процесі розсіяння залишається нерозв'язаною головоломкою. В проекті MUSE буде вимірюватися пружне розсіяння μp і ep в тому самому експерименті одночасно. Експеримент визначає перерізи, двофотонні ефекти, форм-фактори та радіуси, і дозволяє порівнювати результати, отримані для μp і ep процесів зі зменшеною систематичною похибкою. Ці дані повинні забезпечити найкращий на сьогоднішній день тест універсальності лептона в процесі розсіяння, на порядок поліпшений у порівнянні з попередніми тестами, дати можливість визначити радіус з інтервалом надійності 7σ і забезпечити покращені двофотонні вимірювання.

https://doi.org/10.15407/ujpe64.7.631

A. RYMBEKOVA
Joint Institute for Nuclear Research
(6, Joliot-Curie Str, Dubna, Moscow Region, Russia; e-mail: aierke@jinr.ru)

STUDY OF THE POLARIZED GLUON STRUCTURE OF A PROTON VIA PROMPT-PHOTON PRODUCTION IN THE SPD EXPERIMENT AT THE NICA COLLIDER

Photons produced in the hard scattering of partons, named prompt photons, provide information about the internal structure of hadrons. The NICA collider has the possibility to provide new data to study the production of prompt photons in non-polarized and polarized proton-proton collisions, which gives an access to spin-dependent parton distribution functions for gluons. Unpolarized and polarized physics with prompt photons and capabilities of the SPD detector in such measurements is discussed.
K e y w o r d s: polarized structure of a nucleon, prompt photons, gluons, SPD.

1. Prompt Photons

Prompt photons are photons produced in the hard scattering of partons. According to the factorization theorem, the inclusive cross-section for the production of a prompt photon in collisions of h_A and h_B hadrons can be written as follows:

$$d\sigma_{AB} = \sum_{a,b=q,\bar{q},g} \int dx_a dx_b f_a^A(x_a, Q^2) f_b^B(x_b, Q^2) \times$$
$$\times\, d\sigma_{ab\to\gamma X}(x_a, x_b, Q^2). \qquad (1)$$

The function f_a^A (f_b^B) is the parton density for h_A (h_B) hadron, x_a (x_b) is the fraction of the momentum of h_A (h_B) hadron carried by parton a (b), and Q^2 is the square of the 4-momentum transferred in the hard scattering process, and $\sigma_{ab\to\gamma X}(x_a, x_b, Q^2)$ represents the cross-section for the hard scattering of partons a and b [1].

The prompt-photon production in hadron collisions is the most direct way to access the gluon structure of hadrons. There are two main hard processes for the production of prompt photons: 1) gluon Compton scattering, $gq(\bar{q}) \to \gamma q(\bar{q})$, which prevails, and 2) quark-antiquark annihilation, $q\bar{q} \to \gamma g$.

Unpolarized measurements of the differential cross-section of the prompt-photon production in proton-proton(antiproton) collisions have already been performed by the fixed-target and collider experiments. Figure 1 shows the ratio of the measured cross-sections to one predicted by theory as a function of $x_T = 2p_T/\sqrt{s}$ [2]. One can see that, for the fixed-target results corresponding to $\sqrt{s} \sim 20$ GeV, there is a significant disagreement with theoretical expectations that is absent for the high-energy collider results. A new precise measurement could clarify the problem.

2. Spin Asymmetries

A measurement of the single transverse spin asymmetry $A_\gamma^N = \frac{\sigma^\uparrow - \sigma^\downarrow}{\sigma^\uparrow + \sigma^\downarrow}$ in the prompt-photon production at high p_T in polarized p-p and d-d collisions could provide information about the gluon Sivers function which is mostly unknown at the moment. The numerator of A_γ^N can be expressed as [3]

$$\sigma^\uparrow - \sigma^\downarrow =$$
$$= \sum_i \int_{x_{\min}}^{1} dx_a \int d^2\mathbf{k}_{Ta} d^2\mathbf{k}_{Tb} \frac{x_a x_b}{x_a - (p_T/\sqrt{s})e^y} \times$$
$$\times \Big[q_i(x_a \mathbf{k}_{Ta}) \Delta_N G(x_b, \mathbf{k}_{Tb}) \times \frac{d\hat{\sigma}}{d\hat{t}}(q_i G \to q_i\gamma) +$$
$$+ G(x_a, \mathbf{k}_{Ta}) \Delta_N q_i(x_b, \mathbf{k}_{Tb}) \frac{d\hat{\sigma}}{d\hat{t}}(G q_i \to q_i\gamma) \Big]. \qquad (2)$$

Here, $\sigma^\uparrow$ and $\sigma^\downarrow$ are the cross-sections of the prompt-photon production for the opposite transverse polarizations of one of the colliding protons, $q_i(x_a, \mathbf{k}_{Ta}) \times [G(x_a, \mathbf{k}_{Ta})]$ is the quark [gluon] distribution function with specified $\mathbf{k}_T$, and $\Delta_N G(x_b, \mathbf{k}_{Tb}) \times$

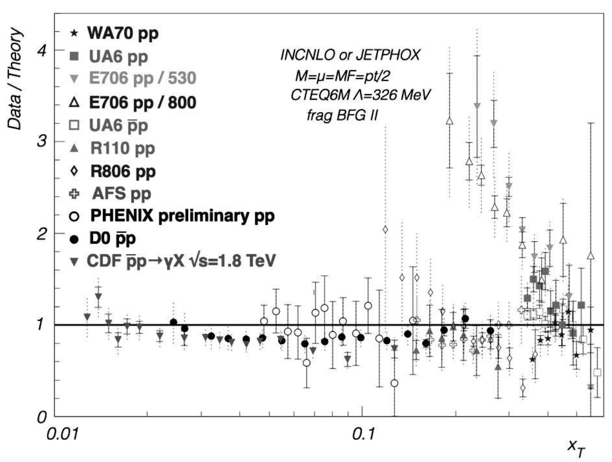

Fig. 1. Measured cross-sections of the prompt-photon production divided by those predicted by theory as a function of x_T [2]

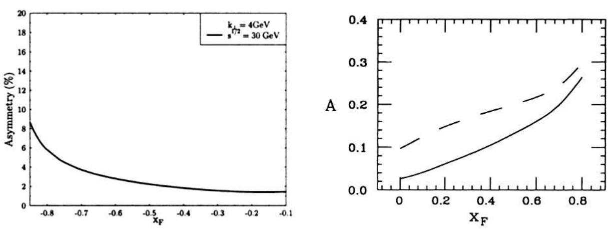

Fig. 2. Theoretical predictions for A_γ^N at $\sqrt{s} = 30$ GeV and $p_T = 4$ GeV/c for (left) positive [4] and (right) negative [5] values of x_F

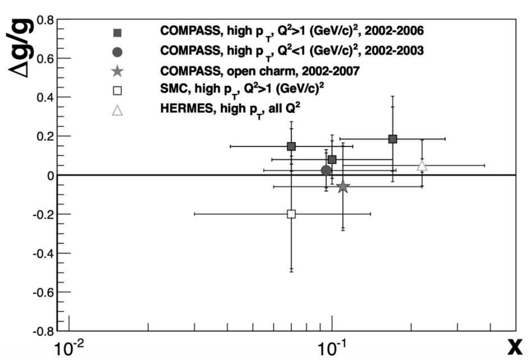

Fig. 3. A compilation of gluon polarization measurements from the open charm and high-p_T hadron production [8]

$\times\,[\Delta_N q_i(x_b, \mathbf{k}_{Tb})]$ is the gluon [quark] Sivers function, $\frac{d\widehat{\sigma}}{d\widehat{t}}$ represents the corresponding gluon Compton scattering cross-section. Figure 2 shows theoretical predictions for A_γ^N at $\sqrt{s} = 30$ GeV and $p_T = 4$ GeV/c for positive [4] (left) and negative [5] (right) values of x_F. The study of the prompt-photon production at the large transverse momentum with longitudinally polarized proton beams could provide the access to the gluon polarization Δg via the measurement of the longitudinal double spin asymmetry A_{LL}^γ [6]. Assuming the dominance of the gluon Compton scattering process, the asymmetry A_{LL}^γ can be presented as [7]

$$A_{LL} \approx \frac{\Delta g(x_a)}{g(x_a)} \left[\frac{\sum\limits_q e_q^2[\Delta q(x_b) + \Delta\bar{q}(x_b)]}{\sum\limits_q e_q^2[q(x_b) + \bar{q}(x_b)]} \right] \times$$
$$\times\, \widehat{a}_{LL}(gq \to \gamma q) + (a \leftrightarrow b). \tag{3}$$

The second factor in the equation coincides to the lowest order with the spin asymmetry A_1^p well known from polarized DIS, the partonic asymmetry $\widehat{a}_{LL}$ is calculable in perturbative QCD. Previous results for the gluon polarization show that the gluon polarization is consistent with zero: $|\Delta g/g| < \pm 0.2$ [8], while the A_1^p asymmetry is about 0.2 for $x \simeq 0.1$ [9].

Thus, under the given experimental conditions, it is possible to gain access to the gluon Sivers function, as well as to the gluon polarization (helicity).

3. The SPD Detector at NICA

The study of the gluon structure through the prompt-photon production is planned at the SPD experiment at the new accelerator complex NICA (Nuclotron-based Ion Collider fAcility) which is currently under construction at the Joint Institute for Nuclear Research (Dubna, Russia).

The possibility to have high-luminosity collisions (up to 10^{32} cm^{-2}s^{-1} at $\sqrt{s_{pp}} = 27$ GeV) of polarized protons and deuterons at the NICA collider allows studying spin- and polarization-dependent effects in hadron collisions.

The current design of the SPD setup foresees three modules: two end-caps and a barrel section. Each part has an individual magnetic system: solenoidal for the end-caps and toroidal for the barrel part of the setup. Main detector systems are the following: Range System (RS) (for muon identification), Electromagnetic calorimeter (ECal), PID/Time-of-Flight system, Main Tracker (TR), and Vertex Detector (VD).

Photons should be detected by the lead-scintillator electromagnetic calorimeter ("shashlyk"-type), which is placed inside the Range System and consists of three parts: the barrel one and two end-caps. Each part has a depth of about 12.5 X_0, which is sufficient to fully contain the highly energetic electromagnetic showers considered in this analysis. The energy resolution is planned to be about $5\%/\sqrt{E[\mathrm{GeV}]}$. The acceptance of the calorimeter in polar angle is between $2°$ and $178°$.

4. Prompt Photons at SPD

The object-oriented C++ toolkit SPDroot based on the FairRoot framework [10] was used for the Monte-Carlo simulation of the detector response. The SPD setup description is based on the ROOT geometry while the transportation of secondary particles through a material of the setup, and the simulation of the detector response is provided by the GEANT4 code. The standard multipurpose generators like PYTHIA6, PYTHIA8, FRITIOF could be used for the simulation of primary interactions.

Energy deposition in a connected area in the ECal is called a cluster. If, in the course of extrapolation, the track does not rest against a cluster, such a cluster is considered as neutral, and vice versa. The main issue of the future analysis will be the correct identification of prompt-photon clusters.

The study of background contributions and possibilities of their suppression is almost the main task. On the experience of previous experiments, the main background components are:

• decay photons. Most of them (almost 96%) are coming from the decays of π^0 and η mesons;

• fragmentation photons produced in the process of fragmentation of color partons with large transverse momenta;

• photons produced in the other parts of the facility due to the interaction of particles with a material of the setup;

• neutral hadrons like n, K^0, *etc.* and their antiparticles that are identified in the calorimeter as neutral clusters;

• ”charged” clusters in the ECal misidentified as ”neutral” ones due to the inefficiency of the track finding and reconstruction algorithms;

• the so-called “double” clusters which are a result of the overlapping of showers produced by different particles in ECal. The special case is the clusters produced by energetic π^0 decays into two photons flying at a very small angle relative to each other.

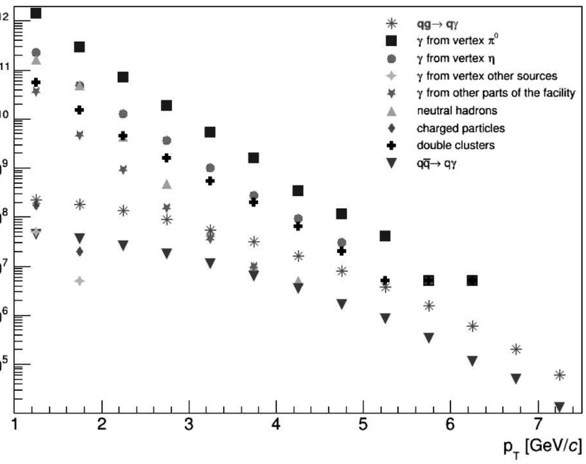

Fig. 4. Contributions of each background component for p-p collisions at $\sqrt{s} = 26$ GeV shown together with the prompt-photon production

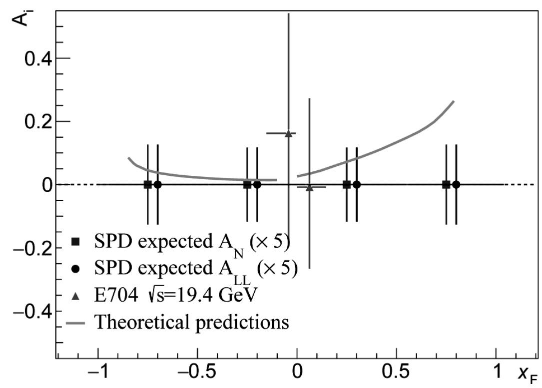

Fig. 5. Expected accuracy of A_N and A_{LL} asymmetries with $p_T > 6$ GeV/c as a function of the x_F-variable

The expected contributions of each background component mentioned above as a function of the transverse momentum p_T calculated with the use of the cluster energy and position are shown in Fig. 4 for p-p collisions at $\sqrt{s} = 26$ GeV.

As could be concluded from Fig. 4, the low p_T region is useless for any studies of prompt-photons due to a huge background. The signal-to-background ratio at $p_T = 1$ GeV/c is about 10^{-4}. Only at high values of the transverse momentum, it is possible to separate statistically the signal and the background. A reasonable cut on the transverse momentum of a photon has to be applied in order to maximize the accuracy of the planned measurements.

The background suppression process could be divided into two stages. At first, all photons from the reconstructed 2γ decays of π^0 and η mesons are rejected. After such rejection, the sample still contains an admixture of photons from 2γ decays. This residual admixture could be statistically subtracted basing on the Monte-Carlo information about properties of the SPD setup. The subtraction procedure can be illustrated by the following equation:

$$\sigma \sim N_{\rm prompt} = N_{{\rm single}\,\gamma} - N_{\pi^0,\eta} \times k, \quad (4)$$

where $N_{{\rm single}\,\gamma}$ is a number of candidates to be prompt-photons, N_{π^0} is a number of reconstructed 2γ decays of π^0 and η, and k is a factor to be determined from the Monte-Carlo procedure. The typical value of the k factor is 0.76.

To estimate the accuracy of the measurement of asymmetries, the signal and the background Monte-Carlo samples were produced. For the simulation of primary p-p collisions with $\sqrt{s} = 26$ GeV, the PYTHIA6 [11] generator with the standard settings was used. The estimation was performed for 10^7 s (one year) of data taking with an average luminosity 10^{32} s^{-1}cm^{-2}. 100% polarization of proton beams was supposed.

Using Eq. (4) and the cut $p_T > 6$ GeV$/c$ which removed most of the background and assuming that the relative accuracy $dk/k = 0.02$ could be achieved, the preliminary results on the expected accuracy of the A_N and A_{LL} asymmetries measurement in the SPD experiment were obtained. The results for four subranges of x_F-variable are shown in comparison with the E704 measurements [12] and the theoretical predictions [4, 5] in Fig. 5. The expected A_N and A_{LL} accuracies are multiplied by a factor of 5 and shown by the error bars in respect to zero values of asymmetries. The uncertainties related to polarization and luminosity measurements are not taken into account.

5. Conclusions

The study of the polarized and non-polarized gluon contents of a nucleon is one of the main physical tasks of the planned SPD experiment at the NICA collider. The prompt-photon production via the gluon Compton scattering is the most promising process for that. The precision measurement of the A_N and A_{LL} spin asymmetries with transversely and longitudinally polarized proton and deuteron beams provides the access to the gluon Sivers and helicity functions, respectively. The preliminary studies of the background conditions show that the accuracy for the asymmetries of about 2% could be achieved in the wide range of x_F.

1. Conceptual and technical design of the Spin Physics Detector (SPD) at the NICA collider. https://indico.jinr.ru/getFile.py/access?resId=11&materialId=3&confId=718 (2018).
2. P. Aurenche, M. Fontannaz, J.-P. Guillet, E. Pilon, M. Werlen. A new critical study of photon production in hadronic collisions. *Phys. Rev. D* **73**, 094007 (2006).
3. I. Schmidt, J. Soffer, J.-J. Yang. Transverse single spin asymmetries in photon production. *Phys. Lett. B* **612**, 258B (2005).
4. N. Hammon, B. Ehrnsperger, A. Schaefer. Single-transverse spin asymmetry in prompt photon production. *J. Phys. G* **24**, 991 (1998).
5. J.-W. Qiu, G.F. Sterman. Single transverse spin asymmetries in direct photon production. *Nucl. Phys. B* **378**, 52 (1992).
6. H.-Y. Cheng, S.-N. Lai. Spin asymmetry in proton proton collisions as a probe of sea and gluon polarization in a proton. *Phys. Rev. D* **41**, 91 (1990).
7. G. Bunce, N. Saito, J. Soffer, W. Vogelsang. Prospects for spin physics at RHIC, *Ann. Rev. Nucl. Part. Sci.* **50**, 525B (2000).
8. C. Adolph, *et al.* Leading and next-to-leading order gluon polarization in the nucleon and longitudinal double spin asymmetries from open charm muoproduction. *Phys. Rev. D* **87**, 052018 (2013).
9. C. Adolph, *et al.* The spin structure function $g_1^{\rm p}$ of the proton and a test of the Bjorken Sum Rule, *Phys. Rev. B* **753**, (2015).
10. M. Al-Turany, D. Bertini, R. Bertini, *et al.* The FairRoot framework, *IOP Publishing* **396**, 022001 (2012).
11. T. Sjostrand, S. Mrenna, P.Z. Skands. PYTHIA 6.4 Physics and Manual. *JHEP* **0605**, 026 (2006).
12. D.L. Adams, *et al.* Measurement of single spin asymmetry for direct photon production in pp collisions at 200-GeV$/c$. *Phys. Lett. B* **345**, 569 (1995).

Received 08.07.19

А. Римбекова

ДОСЛІДЖЕННЯ ПОЛЯРИЗОВАНОЇ СТРУКТУРИ ПРОТОНА ЗА ДОПОМОГОЮ ФОТОНАРОДЖЕННЯ В ЕКСПЕРИМЕНТІ SPD НА КОЛАЙДЕРІ NICA

Р е з ю м е

Фотони, утворені в жорсткому розсіянні партонів, так звані миттєві фотони, дають інформацію про внутрішню структуру адронів. Колайдер NICA зможе забезпечити нові дані про народження миттєвих фотонів в неполяризованих та поляризованих процесах фотонарождення, що, в свою чергу, дасть інформацію про спінові функції розподілу глюонів. В даній статті представлено фізику поляризації із миттєвими фотонами і можливості детектора SPD в таких експериментах.

https://doi.org/10.15407/ujpe64.7.635

M. SCHEVER[1, 2]
for the JUNO Collaboration

[1] Institut für Kernphysik, Forschungszentrum Jülich
(52425 Jülich, Germany; e-mail: m.schever@fz-juelich.de)
[2] III. Physikalisches Institut B, RWTH Aachen University
(52074 Aachen, Germany)

STATUS OF THE JIANGMEN UNDERGROUND NEUTRINO OBSERVATORY

The Jiangmen Underground Neutrino Observatory (JUNO) is a next generation multipurpose antineutrino detector currently under construction in Jiangmen, China. The central detector, containing 20 kton of a liquid scintillator, will be equipped with ∼18 000 20 inch and 25 600 3 inch photomultiplier tubes. Measuring the reactor antineutrinos of two powerplants at a baseline of 53 km with an unprecedented energy resolution of $3\%/\sqrt{E(MeV)}$*, the main physics goal is to determine the neutrino mass hierarchy within six years of run time with a significance of 3–4*σ*. Additional physics goals are the measurement of solar neutrinos, geoneutrinos, supernova burst neutrinos, the diffuse supernova neutrino background, and the oscillation parameters* $\sin^2\theta_{12}$, Δm^2_{12}, *and* $|\Delta m^2_{ee}|$ *with a precision <1%, as well as the search for proton decays. The construction is expected to be completed in 2021.*

Keywords: antineutrino detector, reactor antineutrinos, supernova neutrinos, proton decay, neutrino mass hierarchy.

1. Introduction

The Jiangmen Underground Neutrino Observatory (JUNO) is a 20 kton liquid scintillator (LS) detector currently under construction in the south of China close to Jiangmen. The LS is contained in a 35.4 m diameter acrylic sphere and monitored by ∼18 000 20 inch photomultiplier tubes (PMTs), allowing for an unprecedented energy resolution of $3\%/\sqrt{E(\mathrm{MeV})}$. A complementary system of 25 600 3 inch PMTs facilitates to use the concept of double calorimetry[1]. In order to reduce the external background and to track and veto cosmogenic muons, the Central Detector (CD) is submerged in a cylindrical water Cherenkov detector filled with ultra-pure water. The main goal of JUNO is to determine the neutrino mass hierarchy (MH) by measuring the oscillations of reactor antineutrinos emitted by two powerplants, Taishan and Yiangjian, with a final thermal power of 35.8 $\mathrm{GW_{th}}$ at a baseline of 53 km. Furthermore, measurements of the oscillation parameters $\sin^2\theta_{12}$, Δm^2_{12}, and $|\Delta m^2_{ee}|$ can be achieved with subpercentage precision. Numerous additional physics goals exist [2], of which measuring solar neutrinos and geoneutrinos are reviewed in the following. The Taishan Antineutrino Observatory (TAO) will be built and operated next to the Taishan power plant to reduce systematic effects in the reactor antineutrino spectrum measured by JUNO.

2. Neutrino Physics Programme at JUNO

2.1. Reactor Antineutrinos

To reach the primary goal of determining the neutrino mass hierarchy, JUNO aims at the detection of reactor antineutrinos based on the Inverse Beta Decay (IBD) of protons occuring in the LS in the CD, where the e-flavor antineutrino reacts with a proton producing a positron and a neutron according to

$$\bar{\nu}_e + p \rightarrow e^+ + n. \tag{1}$$

The IBD signature is the coincidence of a prompt and a delayed signal. The prompt signal stems from the energy loss and the subsequent annihilation of a positron taking place effectively instantaneously after its creation. Since the mass of a neutron is much larger than the mass of a positron, the energy of the

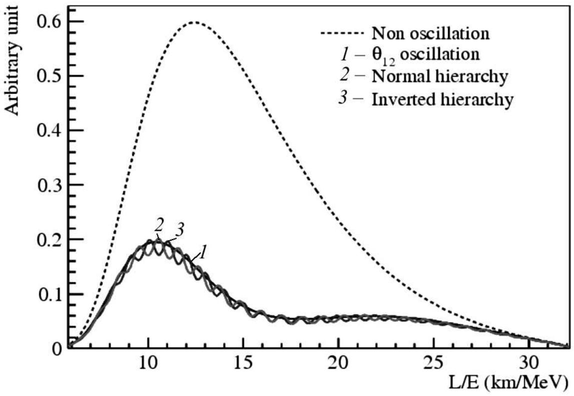

Fig. 1. Unoscillated reactor neutrino flux (dotted line) and the relative shape differences for the NH and the IH. From [2]

positron relates to the energy of an antineutrino. The delayed signal stems from the neutron being captured by hydrogen in the LS with a mean time of $\sim$200 μs after undergoing the thermalization. The neutron capture on protons emits a photon with an energy of 2.2 MeV.

The time coincidence of both the prompt and delayed signals, together with their vertex positions and the energy constraint, allows for the IBD signal detection and the background rejection. Several sources have to be considered for the background. The dominant background source is the cosmogenic isotopes ^{9}Li and ^{8}He, which are produced through the spallation by cosmogenic muons traversing through the detector. Their $(\beta^- + n)$-decay channel mimics the coincidence of the prompt and delayed signals of the IBD signature. Featuring a life time of 256 ms and

Expected signal and background rates per day with various selection cuts. From [2]

<table>
<tr><th>Section</th><th>IBD</th><th>Geo-νs</th><th>Accidental</th><th>^{9}Li/^{8}He</th><th>Fast n</th><th>(α, n)</th></tr>
<tr><td>–</td><td>83</td><td>1.5</td><td>$\sim 5.7 \times 10^4$</td><td>84</td><td>–</td><td>–</td></tr>
<tr><td>Fiducial volume</td><td>76</td><td>1.4</td><td rowspan="3">410</td><td>77</td><td rowspan="5">0.1</td><td rowspan="5">0.5</td></tr>
<tr><td>Energy cut</td><td rowspan="3">73</td><td rowspan="3">1.3</td><td rowspan="3">71</td></tr>
<tr><td>Time cut</td></tr>
<tr><td>Vertex cut</td><td>1.1</td></tr>
<tr><td>Muon Veto</td><td>60</td><td>1.1</td><td>0.9</td><td>1.6</td></tr>
<tr><td>Combined</td><td>60</td><td colspan="5">3.8</td></tr>
</table>

172 ms, respectively, 99% of the ^{9}Li and ^{8}He isotopes produce IBD-like signatures at a 3 m distance to the muon track [3, 4]. Therefore, the strategy for the muon veto includes a partial volume veto of the area of the liquid scintillator contained in a cylinder with a radius of 3 m around the muon track for a time of 1.2 s [5]. Other considerable background sources are the following:

• Accidental coincidences by natural radioactivity, mostly from the surrounding rock and the PMT glass.

• Fast neutrons produced by cosmogenic muons which travel through the surrounding rock or through the water at the corner of the detector. They can mimic the IBD signature by scattering off a proton and undergoing the subsequent neutron capture in the LS.

• Geoneutrinos produced in the radioactive decays of U and Th from inside the Earth. Causing the same signal like the reactor antineutrinos, their contribution to the reactor antineutrino energy spectrum is handled through the known β-decay spectra of U and Th.

• (α, n)-background originating from the α particles of the U and Th chain and reacting with ^{13}C in the LS and producing a neutron and ^{16}O. The IBD coincidence signature can be mimicked in the case where a neutron is fast enough or ^{16}O emits a photon during the deexcitation.

The expected rates of both the IBD reactor neutrino signal and the above-mentioned backgrounds are summarized in Table.

The neutrino MH is determined by relating the measured reactor antineutrino spectrum to the MH-dependent survival probabilities for antielectron neutrinos conditioned by neutrino oscillations. Here, the measured reactor antineutrino energy spectrum is represented by the prompt energy spectrum of the positrons produced in the IBDs. The antielectron neutrino survival probability is given by

$$P_{\bar{\nu}_e \to \bar{\nu}_e} = 1 - \sin^2 2\theta_{13} (\sin^2 \theta_{12} \sin^2 \Delta_{32} + \\ + \cos^2 \theta_{12} \sin^2 \Delta_{13}) - \sin^2 2\theta_{12} \cos^4 \theta_{13} \sin^2 \Delta_{12} \qquad (2)$$

with $\Delta_{ij} = (\Delta m^2_{ij} L)/(4E)$ and shown for both cases of the normal hierarchy (NH) and the inverted hierarchy (IH) in Fig. 1.

The χ^2-based analysis of the reactor antineutrino energy spectrum determines the neutrino mass hierarchy with a sensitivity $\Delta\chi^2$ by fitting the energy spectrum with the expected spectra both for the NH and IH. The obtained sensitivity depends both on the acquired amount of statistics and the energy resolution. Figure 2 shows the $\Delta\chi^2$-contour plot for different sensitivity levels depending on a variable energy resolution and a range of the number of IBD events included in the analysis. The latter is normalized to the expected number of events after 6 years of the data acquisition with 35.8 $\mathrm{GW_{th}}$ reactor power, corresponding to 100,000 IBD events. With this amount of detected events and the design energy resolution of $3\%/\sqrt{E(\mathrm{MeV})}$, the reachable sensitivity is expected to be 3–4σ, corresponding to 9–16$\Delta\chi^2$.

Additionally, JUNO will be able to improve the precision of the oscillation parameters $\sin^2\theta_{12}$, Δm^2_{12}, and $|\Delta m^2_{ee}|$ to the subpercentage level of 0.67%, 0.50%, and, 0.44%, respectively.

2.2. Solar neutrinos

The Sun is a powerful source of electron neutrinos. The neutrinos are produced in the nuclear fusion reactions and emitted with the energy of $\mathcal{O}$ (1 MeV). Their study yields the possibility to gain knowledge in the context of neutrino properties (e.g., the Mikheyev–Smirnov–Wolfenstein (MSW) effect [6]) as well as the Sun (e.g. the solar metallicity problem [7]).

The JUNO experiment is principally well suited for the detection of solar neutrinos via the electron scattering due to the low energy detection threshold, the high energy resolution, the high radiopurity, and the large mass. The focus lies on the neutrinos emitted from the ^{8}B and ^{7}Be chains.

Since a single energy deposition of the scattering electron is the event signature, the resulting experimental challenge is the rejection of the enormous background. Dominant background sources are natural radioactivity (^{210}Po, ^{210}Bi, ^{14}C and its pile-up, ^{85}Kr, and the ^{238}U- and ^{232}Th-chains [8]) and the cosmogenic isotopes ^{10}C and ^{11}C. The expected detection rates are $\sim10^4$ events per day for ^{7}Be and $\sim$90 events per day for ^{8}B.

2.3. Geoneutrinos

While the Earth's surface heat flow has been measured to be (46 ± 3) TW [9], the contribution of the radiogenic heat in contrast to the primordial heat remains unclear till now. Therefore, knowledge of the absolute abundance of U and Th in the Earth is required. Their abundance is accessible through the antielectron neutrino flux caused by the radioactive β-decays from the ^{238}U and ^{232}Th chains.

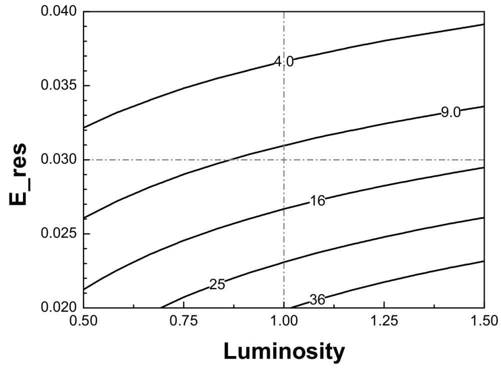

Fig. 2. Iso-$\Delta\chi^2$ contour plot as a function of the acquired statistics labeled as the luminosity and the energy resolution. The nominal luminosity marked by the vertical dotted line corresponds to a run time of 6 years and 100,000 IBD events. The design energy resolution is marked by the horizontal dotted line. From [2]

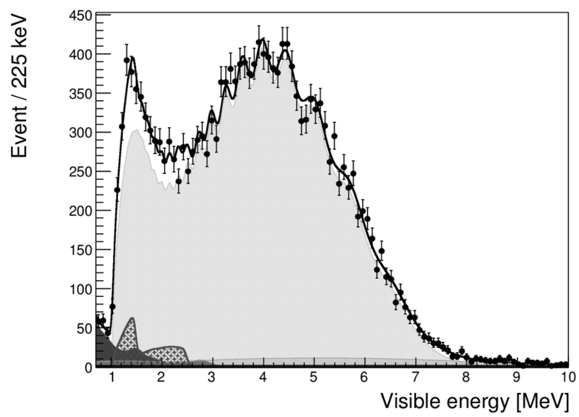

Fig. 3. Expected geoneutrino signal (grid shade) and background spectra for one year of measurement. Background contributions are the reactor antineutrinos (light grey), the cosmogenic isotopes ^{9}Li and ^{8}He (flat light grey), the accidental background (dark grey), and the (α, n)-background (small). The total sum for the best fit is indicated by the black line. From [2]

JUNO aims at measuring these so-called geoneutrinos expected with a rate of 400 events per year [2]. This would yield the world's largest sample of geoneutrinos in less than one year. The experimental challenge is the large background of reactor antineutrinos which can only be handled by the subtraction of both spectra. Further background sources are the cosmogenic isotopes ^{9}Li and ^{8}He, accidental background, and (α, n)-background. Figure 3 demonstrates the expected geoneutrino signal and background spetra for one year of measurements.

3. The JUNO Experiment

The JUNO experiment is located close to Jiangmen in China, at a distance of 53 km to both the Taishan and Yiangjian powerplants. The detector is built underground with an overburden of 700 m of a granite rock to reduce the amount of cosmogenic muons as the background source.

This section describes the following subsystems of the JUNO detector: the Central Detector (CD), the Water Pool (WP), the Top Tracker (TT), the Calibration System, activities and apparatus in the context of the LS purification, and the Taishan Antineutrino Observatory (TAO).

The central detector

The CD is an acrylic sphere with a diameter of 35.4 m containing 20 kton of LS. It is equipped with 18 000 20 inch Photo-Multiplier Tubes (PMTs) and 25 600 3 inch PMTs. The PMTs are mounted on a stainless steel truss surrounding the acrylic sphere with a distance of 1.8 m. The resulting photocoverage is 78%. A high quantum efficiency of $\sim$30% is required in order to reach the unprecedented design energy resolution of $3\%/\sqrt{E(\mathrm{MeV})}$. Out of the 18 000 20 inch PMTs, 5000 are dynode PMTs produced by *Hamamatsu Photonics K.K.*, the remaining PMTs are Micro Channel Plate PMTs and manufactured by the Chinese company *North Night Vision Technology Co. Ltd.* Shielding against the Earth's magnetic field is ensured by the compensation through electromagnetic coils.

The water pool and the top tracker

The CD is submerged into the cylindrically shaped WP containing 40 kton of ultra-pure water to provide shielding from the radioactivity of the surrounding rock and the PMT glass. The WP has a diameter of 43.5 m and is equipped with 2 400 20 inch PMTs to detect the Cherenkov light of muons traversing the JUNO detector. The TT is placed on the WP top. It was a part of the former Opera detector [10] and consists of three layers of a plastic scintillator with a spatial resolution of 2.6×2.6 cm^2 and a coverage of approximately 60% of the surface of the top of the WP. Together, the WP and the TT enable one to track cosmogenic muons providing the foundation for a partial volume muon veto.

Calibration

In order to achieve an energy scale uncertainty of less than 1%, the efficient calibration is of great importance. Four calibration systems are planned to be implemented to provide the basis for a thourough calibration. The first calibration system is the Automated Calibration Unit (ACU) which can be operated 1-dimensionally along the vertical axis in the center of the detector. The second calibration system is the Cable Loop System (CLS), and the third is the Guide Tube Calibration System (GTCS). Both CLS and GTCS can be operated 2-dimensionally, the first in a fixed vertical plane and the latter along a fixed longitude of the CD bound to a guide tube. The fourth calibration system, the Remotely Operated Vehicle (ROV), is steerable in all 3 dimensions and can move freely within the LS in the CD. Furthermore, the double calorimetry system including both the 20 inch and 3 inch PMTs provides an additional calibration strategy, especially with respect to the systematics of the large PMTs due to a multiplicity in the photo-electron detection.

LS purification

In order to prepare the mixing of the LS components and the online purification procedure for the filling of the JUNO CD, as well as to gain experience in the system cleanliness and leak-tightness, distillation, and stripping, pilot plants are currently tested at the Daya Bay Neutrino Laboratory [11].

The LS purification aims at decreasing the amount of radioimpurities primary due to ^{238}U, ^{232}Th, and ^{40}K. For ^{238}U and ^{232}Th, the abundances in the range of 10^{-15}–10^{-17} g/g are targeted. Simultaneously, the attenuation length in the wavelength interval 350–550 nm is improved to exceed 25 m for a wavelength of 430 nm. The gas stripping of the LS with steam and nitrogen extracts radioactive gases, in particular ^{85}Kr, ^{39}Ar, and ^{222}Rn.

The Taishan Antineutrino Observatory

In order to determine the neutrino MH from the oscillated reactor antineutrino spectrum measured by the JUNO detector, a precise knowledge of the unoscillated spectrum is required. The existing model for the energy-dependent reactor flux is subject, however, to both the anomalous bump observed in reactor antineutrino spectra at 5 MeV and a fine structure yet unknown [12]. Therefore, TAO will be placed in 30 m distance to a 4.6 GW_{th}-power core of the Taishan powerplant to measure the shape of the unoscillated reactor antineutrino reference spectrum for JUNO. The spherical detector will be filled with several tons of Gd–LS to detect the antineutrinos via the IBD reaction. Being equipped with Silicon Photomultipliers (SiPM) featuring a photo-electron (PE) detection efficiency of $\sim$50% at the full coverage, a light yield of 4500 PEs at an energy of 1 MeV will be reached, resulting in an energy resolution better than $3\%\sqrt{E(\mathrm{MeV})}$. The Gd-LS will be operated at –50 degree Celsius to reduce the SiPM noise [13].

4. Conclusion

JUNO is a 20 kton liquid scintillator detector currently under construction in the south of China, close to Jiangmen. The physics main goal is to determine the neutrino MH based on the detection of reactor antineutrinos at a baseline of 53 km reaching 3–4σ significance after 6 years of data taking with 35.8 GW_{th} reactor power. Therefore, an unprecedented energy resolution of $3\%/\sqrt{E(\mathrm{MeV})}$ based on a light yield of 1200 PE/MeV and an energy scale uncertainty <1% is required. Furthermore, the physics programme is extended to the detection of terrestrial and astrophysical neutrinos. The oscillation parameters $\sin^2\theta_{12}$, Δm^2_{12}, and $|\Delta m^2_{ee}|$ will be measured at a subpercentage precision level. The construction is expected to be completed in 2021.

1. Miao He on behalf of the JUNO Collaboration. Double calorimetry system in JUNO. arXiv:1706.08761 (2017).
2. F. An *et al.*, (JUNO Collaboration). Neutrino physics with JUNO. arXiv:1507.05613 (2016).
3. M. Grassi, J. Evslin, E. Ciuffoli, X. Zhang. Showering cosmogenic muons in a large liquid scintillator. *JHEP* **049**, 09 (2014).
4. M. Grassi, J. Evslin, E. Ciuffoli, X. Zhang. Vetoing cosmogenic muons in a large liquid scintillator. arXiv:1505.05609 (2015).
5. C. Genster, M. Schever, L. Ludhova, M. Soiron, A. Stahl, C. Wiebusch. Muon reconstruction with a geometrical model in JUNO. arXiv:1906.01912 (2018).
6. A.Yu. Smirnov. The MSW effect and solar neutrinos. arXiv:0305106 (2003).
7. A. Serenelli, S. Basu, J. W. Ferguson, M. Asplund. New solar composition: The problem with solar models revisited. *Astrophys. J.* **705**, L123 (2009).
8. M. Agostini *et al.*, (Borexino Collaboration). Comprehensive measurement of pp-chain solar neutrinos. *Nature* **562**, 496 (2018).
9. C. Jaupart, S. Labrosse, J.C. Mareschal. Temperatures, heat and energy in the mantle of the Earth. In *Treatise on Geophysics, vol. 7: Mantle dynamics*, Eds. by D. Bercovici, G. Schubert (Elsevier, 2007).
10. T. Adam *et. al.* The OPERA experiment Target Tracker. *Nucl. Inst. & Meth. in Phys. Res. A* **577** (3), 523 (2007).
11. P. Lombardi *et. al.* Distillation and stripping pilot plants for the JUNO neutrino detector: Design, operations and reliability. arXiv:1902.05288 (2019).
12. D.V. Forero, R. Hawkins, P. Huber. The benefits of a near detector for JUNO. arXiv:1710.07378 (2017).
13. Jun Cao (JUNO Collaboration). Measuring High Resolution Reactor Neutrino Spectrum with JUNO-TAO. Talk presented at *the Technical Meeting on Nuclear Data for Anti-neutrino Spectra and Their Applications, IAEA, Vienna, Apr. 23–26* (2019).

Received 15.08.19

М. Шевер, від імені Колаборації JUNO

СТАН ПІДЗЕМНОЇ
ОБСЕРВАТОРІЇ НЕЙТРИНО В ЖІАНГМЕНІ

Р е з ю м е

Підземна Обсерваторія Нейтрино в Жіангмені (JUNO) є багатоцільовим детектором антинейтрино нового покоління, що споруджується в Китаї. Центральний детектор, що містить 20 кілотон рідинного сцинтилятора, буде оснащено трубками фотопомножувачів, 17 571 штук по 20 дюймів та 25 600 по 3 дюйми. У процесі вимірювання антинейтрино від двох реакторів з базою 53 км при безпрецедентній роздільній здатності по енергії $3\%/\sqrt{E}$ МеВ основною метою є визначення впродовж шести років роботи ієрархії мас нейтрино з точністю 3–4σ. Додатковими фізичними цілями є вимірювання сонячних нейтрино, геонейтрино, нейтрино від вибуху супернової, нейтринного фону дифузної супернової, параметрів осциляції $\sin^2\theta_{12}$, Δm^2_{12}, $|\Delta m^2_{ee}|$ з точністю <1%, а також пошуки розпаду протона. Планується закінчити конструкцію у 2021 році.

https://doi.org/10.15407/ujpe64.7.640

M. SCHMIDT
on behalf of the PANDA collaboration
II. Physikalisches Institut, Justus Liebig University Giessen
(16, Heinrich-Buff-Ring, 35392 Giessen, Germany; e-mail: mustafa.a.schmidt@exp2.physik.uni-giessen.de)

THE PANDA DETECTOR AT FAIR

PANDA is a fixed-target experiment that is going to address a wide range of open questions in the hadron physics sector by studying the interactions between antiprotons with high momenta and a stationary proton target. The PANDA detector is currently under construction and will be situated in the HESR that is a part of the future FAIR accelerator complex on the area of the GSI Helmholtzzentrum für Schwerionenforschung in Darmstadt. The key features of the detector are: the precise tracking in strong magnetic fields, excellent particle identification, and high-resolution calorimeters.

Keywords: FAIR, PANDA, antiprotons.

1. Introduction

1.1. Antiproton Production at FAIR

The future Facility for Antiproton and Ion Research (FAIR) is designed as an extension to the existing GSI Helmholtzzentrum für Schwerionenforschung in Darmstadt, Germany. A new linear accelerator (p-LINAC) that is currently under development will accelerate protons up to a kinetic energy of 70 MeV. After being further accelerated in the two synchrotrons SIS18 and SIS100, these protons will be extracted to collide with a nickel target. The antiprotons, that are created during this process, will be collected by the Collection Ring (CR) and further injected into the High Energy Storage Ring (HESR) where the PANDA detector will be located. In addition to NUSTAR, CMB, and APPA, it is going be one of the four excellent physical experiments at FAIR [2].

1.2. HESR & PANDA

The injection momentum of the antiprotons into the HESR will be 3.8 GeV/c. Inside the HESR, the beam momentum can be modified to values between 1.5 GeV/c and 15 GeV/c. One of the key features of the HESR is the stochastic cooling that can be applied over the full momentum range. In addition to that, the HESR can run in two different modes: a high-luminosity and a high-resolution mode. The important parameters of both modes are represented in the table below. The high-luminosity mode with an interaction rate of 20 MHz will not be available in the beginning, because it requires an additional synchrotron called Recycling Energy Storage Ring (RESR). The investigation of collisions between antiprotons and protons in PANDA will be used to answer open questions in the fields of nucleon structure, hadron spectroscopy, and nuclear physics.

Because of the forward boost of the created particles, PANDA will consist of two spectrometers: a target spectrometer designed as an onion shell detector around the interaction point and a forward spectrometer covering small polar angles. Both spectrometers have redundant detector systems for the tracking, particle identification (PID), and calorimetry. The complete PANDA detector including all sub-

Different operation modes of the HESR

Parameter	High Res.	High Lum.
Momentum [GeV/c]	1.5–15	1.5–15
Antiprotons	10^{10}	10^{11}
Luminosity [$cm^2\,s^{-1}$]	2×10^{31}	2×10^{32}
Resolution $\Delta p/p$	5×10^{-5}	1×10^{-4}

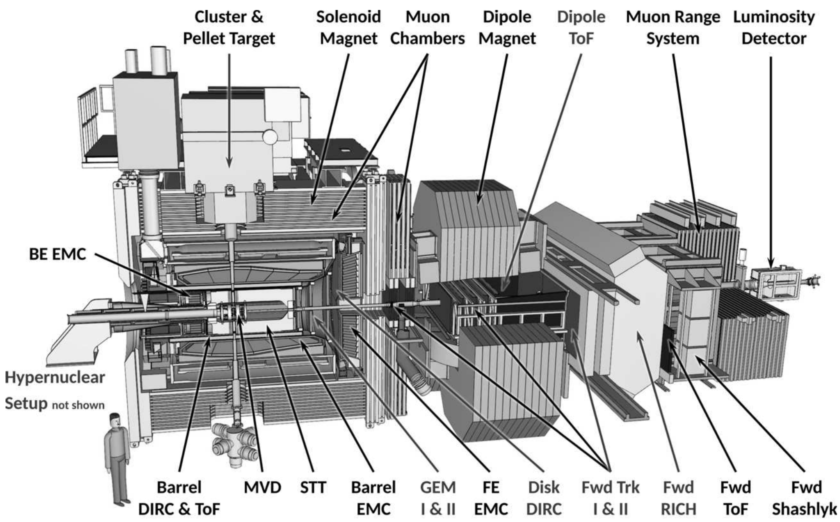

Fig. 1. The PANDA detector at FAIR including all detectors for phase *1* (black) and phase *2* (gray)

detectors is shown in Fig. 1. For most of the physical analysis, it is important to cover the full solid angle with all subdetectors.

1.3. Physics programs

The PANDA experiment is designed to cover a large amount of antiproton physics programs in order to answer many open questions related to the huge sector of hadron physics in the non-perturbative region [7]. This can be summarized as follows:

• Hadron spectroscopy: Production of exotic QCD states and exploring charm hadrons.

• Nucleon structure: Investigating the generalized parton structure and time-like form factors.

• Nuclear physics: Studying hadrons in nuclei and performing hypernuclear physics.

1.4. Time schedule

The time schedule of PANDA is divided into 3 phases. In the present phase 0, the subdetectors of PANDA are under development and tested in various other excellent High Energy Physics (HEP) experiments. With the availability of the PANDA hall in 2022, the installation of phase 1 subdetectors is going to start. In the year 2025, a proton beam will be used for commissioning the start setup of PANDA, whereas the first antiproton beam will be available in 2026. The measurements of phase 2 that includes all remaining subdetectors are going to be started around 2027. After running for a long-time period, further physical experiments with other possible setups can be performed, e.g., phase 3 that represents the high-luminosity mode. A complete overview over all phases is presented in Figure 2.

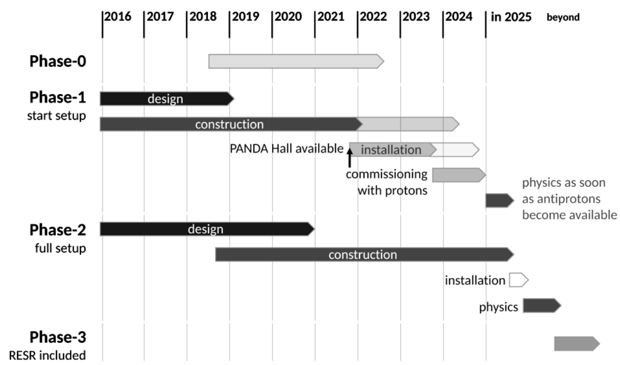

Fig. 2. The different phases of the PANDA detector

2. Proton Target

The proton target marks the interaction point (IP) and can be seen as the core component of a PANDA target spectrometer. Two targets are currently foreseen. The clusterjet target will be already installed in the first phase of PANDA. It creates small hydrogen clusters with a size of 10^3 to 10^5 atoms per cluster by expanding pre-cooled and compressed hydrogen into the vacuum of the beam pipe.

The pellet target creates small droplets of frozen hydrogen with pellet diameters between 10 and 30 μm in a triple point chamber. These pellets will be injected into the target tube with a falling speed of around 60 m/s. In total, a constant flow rate of 100,000 pellets per second can be achieved. Further targets are under development and can be installed in later phases.

3. Magnets

For the purpose of the momentum determination, two magnets will be installed in PANDA [3]. A solenoid magnet in a target spectrometer will create a field of around 2 T with a field inhomogenity of less than 2% over the full field map. Inside the iron yoke, drift tube chambers will be placed for PID and tracking of high energetic muons. The inner/outer diameter of the magnet will be 1.9 m/2.3 m. The length is given by 4.9 m, which leads to a total magnet weight of approx. 360 t.

In the forward spectrometer, a dipole magnet is going to create a magnetic field of 1 T. The length of the magnet is 2.5 m and has an overall weight of 240 t. It has a conical shape with an opening diameter of 1 m at the front- and 3 m at the backside. The key feature of this magnet is a short ramping speed of 1.25% per second and the possibility for a synchronized operation with the HESR.

4. Tracking

4.1. Micro Vertex Detector

The inner-most detector and the closest one to the target is the Micro Vertex Detector (MVD) [4]. It consists of four barrels around the interaction point and six disks in the forward direction. The inner barrel layers of the MVD contain hybrid pixels with a size of 100 μm $\times$ 100 μm, while the outer layers are made of double sided microstrips. The last two disks will be equipped with pixel and strip detectors.

A time resolution of 6 ns and a pixel resolution of 28 μm are achievable. From these values, a vertex resolution of 50 μm can be computed. This high vertex resolution is important to measure displaced vertices, e.g., to analyze different decay channels in the open charm sector.

4.2. Straw tube tracker

The Straw Tube Tracker (STT) [5] is placed in a cylindrical shape around the MVD and consists of 4,200 Al-Mylar drift tubes filled with a mixture of Ar/CO_2 gas. The readout can be done with ASICs combined with TDCs or with Flash ADCs (FADCs) instead. In total, 21 to 27 layers are planned to be installed, of which 8 layers are skewed by 3° for the purpose to reconstruct the longitudinal coordinate. The electron avalanche gain of these tubes is about 100. The inner/outer radius of the detector is 15 cm/42 cm. Each tube has a diameter of 1 cm and a length of 150 cm. Taking the spatial and time resolutions into account, a ϱ/ϕ plane resolution of 150 μm and a z resolution of 1 mm can be achieved. Currently, most of the tubes have been produced and already been mounted within an STT prototype.

4.3. Gas electron multiplier tracker

The Gas Electron Multiplier (GEM) tracker in the forward region of the target spectrometer is a combination of three stations. Two stations will be installed in phase 1 and the third one in phase 2. The foreseen large area GEMs were developed at CERN and are going to be produced in Poland. They contain a 50 μm kapton layer covered by thin copper layers with a thickness of 2 to 5 μm on both sides. The ADCs, that are planned for the readout, will allow for the cluster centroiding to calculate the precise particle position and to reach a position resolution of better than 100 μm.

4.4. Forward tracker

The forward tracker, containing similar straw tubes to the STT, assembled in three planar tracking stations, will be installed in the forward spectrometer to cover small polar angles up to $\pm 10°$ horizontally and $\pm 5°$ vertically. The momentum acceptance is larger than 3% of the beam momentum. This goal is achieved by adjusting the dipole field according to the beam momentum. For the position resolution, 0.1 mm per layer can be achieved, whereas the momentum resolution will be better than 1%.

5. Particle Identification

The envisaged physical programs of PANDA require excellent PID for all decay channels. Since PANDA does not comprise hadronic calorimeters, the PID of hadrons will be performed with four different detector methods: 2 Cherenkov detectors, a Time of Flight (ToF) system, the specific energy loss from the STT and MVD, and a muon detection system.

ISSN 2071-0186. Ukr. J. Phys. 2019. Vol. 64, No. 7

5.1. Barrel DIRC

One of the Cherenkov detectors based on the Detection of Internally Reflected Cherenkov Light (DIRC), is the Barrel DIRC [9] which will be mounted in a cylindrical shape around the STT. It is designed to separate $\pi^{\pm}$ and $K^{\pm}$ with a separation power of more than 3 s.d. in the polar angle range of 22° to 140° and the momentum range of 1.5 to 3.5 GeV/c.

The radius of the detector is 476 mm. It will consist of 16 fused silica bars and 128 Multichannel Plate Photomultiplier Tubes (MCP-PMTs), which adds up to around 10,000 channels to be read out with the DiRICH readout system. The MCP-PMT signal shape results in a time resolution of 100 ps.

5.2. Disc DIRC

Another Cherenkov detector called Disc DIRC [6] will be placed at the forward endcap of the PANDA target spectrometer, around 2 m away from the interaction point in the downstream direction. It will cover small polar angles between 5° and 22° and particle momenta of $\pi^{\pm}$ and $K^{\pm}$ between 0.5 and 4.0 GeV/c. As for the Barrel DIRC, the separation power will be larger than 3 s.d. The Disc and Barrel DIRC together will cover almost the full kaon phase space in the target region.

The Disc DIRC consists of four independent quadrants made of synthetic fused silica. The detector radius is approx. 1,200 mm. Currently, 96 MCP-PMTs are foreseen for the photon detection, which requires a readout of 30,000 channels with TOFPET ASICs from the company PETsys. The time resolution is similar to the one of the Barrel DIRC. For the reconstruction of the Cherenkov angle, the tracking information has to be taken additionally into account.

5.3. Barrel ToF

The Barrel ToF [1], also called SciTil detector, is required for the PID of low momentum particles below 1 GeV. A very good time resolution of better 100 ps is required for that purpose and can be achieved with a high photon yield. In total, 5,760 scintillator tiles with sizes around 90 mm × 30 mm × 5 mm have to be installed in the target spectrometer around the Barrel DIRC.

The scintillator material has not been finally chosen, but it will be either EJ-228 or EJ-232 from Eljen Technology. The photon signals will be detected with Silicon Photomultipliers (SiPMs) that can be read out in combination with PETsys TOFPET ASICs.

5.4. Forward ToF

In the forward spectrometer, PID is essential. Hence, a forward ToF system was developed. It does not require a start counter, but uses relative timing to the Barrel ToF. The baseline design of the Forward ToF is a wall of scintillator slabs. In the center of the detector, 20 slabs with the dimensions 1400 mm × × 5 mm × 2.5 mm will be used. On both sides, the width of each slap changes from 5 cm to 10 cm. BC-409, made by Saint-Gobain Crystals, will be used as a scintillation material. The photon detection will be done with 1-inch PMTs R4998 from Hamamatsu that are going to be mounted on both ends. The detector is going to be installed 7.5 m away from the interaction point.

5.5. Forward RICH

The PID detector with the largest distance to the interaction point is the forward Ring Imaging Cherenkov (RICH) that is placed behind the Forward ToF for phase 2. It contains two layers of aerogel with small refractive indices of $n_1 = 1.05$ and $n_2 = 1.047$ in order to obtain a better focusing of the Cherenkov ring. The setup is very simple, because it contains only one flat mirror and a Multi Anode PMT (MaPMT) array with a pixel size of 6 mm to determine the position of the photon hits. A separation of $\pi^{\pm}/K^{\pm}$ and $\mu^{\pm}/K^{\pm}$up to particle momenta of 10 GeV/c is realistic. The used MaPMTs are approx. 10 times less expensive than MCP-PMTs, but still have a long lifetime and a sufficient radiation hardness.

6. Energy Measurement

PANDA contains Electromagnetic Colorimeters (EMCs) in the target and a forward spectrometer with the goal to achieve a good energy and spatial resolution for photons from a few MeV up to 15 GeV in order to reconstruct almost all multiphoton and lepton-pair channels. Because of the hadronic interactions in PANDA, a high photon yield and the background suppression are required. For that purpose, the energy threshold of all calorimeters has to be set to a value around 10 MeV. The rate of a single crystal is given by 10^6 s^{-1}.

6.1. Target Calorimeter

The EMC in the target spectrometer [8] contains one barrel part, which will be installed around the Barrel ToF, and two flat parts at the forward and backward endcaps. It uses the 2^{nd} generation of $PbWO_4$ crystals with improved light yield and better radiation hardness. In total, 15,744 crystals have to be installed in all parts. In order to increase the photon yield by a factor of four, the crystals have to be cooled to a temperature of (-25 ± 0.1) °C. The used material has the advantage of a small radiation length around 0.9 cm and and a Molière radius of 2.1 cm. The typical size of each crystal is 2.5 mm$\times$2.5 mm with a fixed length of 20 cm. For particles with energies above 100 MeV, a time resolution of better than 1 ns and a spatial resolution of less than 1.5 mm are feasible. The energy resolution is given by

$$\frac{\sigma(E)}{E} = 1\% \oplus \frac{2\%}{\sqrt{E[\mathrm{GeV}]}}. \tag{1}$$

Currently, 75% of all required crystals have been produced.

6.2. Forward calorimeter

The EMC in the forward spectrometer [10] is a shashlyk-type sampling calorimeter consisting of interleaved scintillators and lead absorbers. The photon readout is done with PMTs and FADCs that are used for the signal digitization. The active area of the calorimeter is given as 297×154 cm^2. The total energy resolution can be calculated to

$$\frac{\sigma(E)}{E} \leq 1.3\% \oplus \frac{2.8\%}{\sqrt{E[\mathrm{GeV}]}} \oplus \frac{3.5\%}{E[\mathrm{GeV}]}. \tag{2}$$

7. Muon Detector System

In the iron yoke of the target spectrometer and in the forward spectrometer, small Muon Drift Tubes (MDTs) with a wire and cathode strip readout will be used to detect created muons. Due to the low muon momenta, a large pionic background is expected. This effect can be minimized by using a multilayer range system. In PANDA, $12+2$ layers are installed in the barrel and $5+2$ layers in the endcap part. Between the target and forward spectrometer, muon filters will be installed for the background reduction. Behind the forward EMC, $16+2$ layers of muon chambers will be installed additionally. In total, the setup will contain 3,751 MDTs in all parts.

8. Luminosity Detector

The luminosity detector of PANDA will be placed around 11 m away from the target in the forward direction behind the forward spectrometer. It is going to measure the elastic scattering of antiproton-proton interactions. The main component is a silcon pixel detector that is mounted on five Chemical Vapour Deposition (CVD) diamond wafers with a thickness of 200 μm. Each wafer contains 10 High Voltage Monolithic Active Pixel Sensors (HV MAPS) with a pixel size of 80 μm$\times$80 μm. The active pixel sensor is based on the CMOS technology which allows the digital processing directly on a chip. The detector is able to attain a very high efficiency of approx. 99.5%.

9. Hypernuclear Setup

The hypernuclear setup is an alternative setup for physical studies in phase 2. It contains two targets: one passive primary target, made of a diamond wire on piezo motored wire holders, to produce Ξ baryons and one secondary active target for capturing them together with all track products in silicon microstrips and absorbers. High-purity germanium detectors at the rear will be used for gamma spectroscopy of the related decay products.

10. Data Acquisition

One of the outstanding features of PANDA is the triggerless data acquisition [12]. Because of the absence of a hardware trigger, the data from the Front End Electronics (FEE) have to be reduced by a factor of more than 1,000. This reduction will be achieved by a daisy chain of different event building and online reconstruction levels. First, the data from the FEE will be transmitted via data concentrators to a burst building network. From there, the remaining hits will be processed further in special compute nodes to perform the 1^{st} and 2^{nd} level selections, before the reduced data will be written to the PANDA storage. The time synchronization will be done with a dedicated PANDA development called SODAnet.

11. Simulation Framework

For the simulation and analysis, a dedicated framework called PandaRoot [11], that is based on ROOT, was developed. This framework includes the geometries of all PANDA subdetectors together with the important simulation parameters and passive volumes. Different particle generators can be used in or-

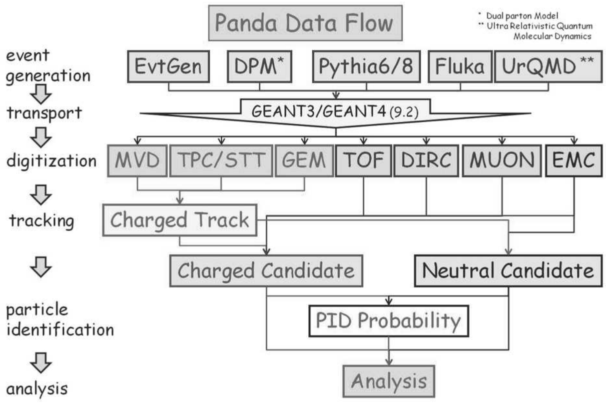

Fig. 3. The data flow in PandaRoot

der to simulate from dedicated probe tracks to specific physics channels. For the particle propagation through matter, it is possible to switch between the toolkits Geant3 and Geant4. The PandaRoot framework will additionally be used to reconstruct and analyze the acquired data of the final PANDA detector, as shown in Figure 3.

1. M. Böhm *et al.* The PANDA barrel-tof detector. *Nuclear Instruments and Methods in Physics Research Section A: Accelerators, Spectrometers, Detectors and Associated Equipment* **912**, 323 (2018).
2. M. Destefanis. The PANDA experiment at FAIR. In: *The Proceedings of the 7th Joint International Hadron Structure'13 Conference. Nucl. Phys. B – Proceedings Supplements* **245**, 199 (2013).
3. W. Erni *et al.* Technical Design Report for the PANDA Solenoid and Dipole Spectrometer Magnets. arXiv:0907.0169 [physics.ins-det] (2009).
4. W. Erni *et al.* Technical design report for the: PANDA micro vertex detector. arXiv:1207.6581 [physics.ins-det] (2012).
5. W. Erni *et al.* Technical design report for the PANDA (AntiProton Annihilations at Darmstadt) straw tube tracker. *Eur. Phys. J. A* **49**, 25 (2013).
6. K. Föhl *et al.* The PANDA Endcap Disc DIRC. *JINST* **13** (02), C02002 (2018).
7. M.F.M. Lutz *et al.* Physics performance report for PANDA: Strong interaction studies with antiprotons. arXiv:0903.3905 [hep-ex] (2009).
8. M. Moritz*et al.* The electromagnetic calorimeter for the PANDA target spectrometer. *J. Phys.: Conf. Series* **1162**, 012025 (2019).
9. B. Singh *et al.* Technical design report for the PANDA barrel Dirc detector. arXiv:1710.00684 [physics.ins-det] (2017).
10. B. Singh *et al.* Technical design report for the PANDA forward spectrometer calorimeter. arXiv:1704.02713v1 [physics.ins-det] (2017).
11. S. Spataro, the PANDA Collaboration. The pandaroot framework for simulation, reconstruction and analysis. *J. Phys.: Conf. Series* **331** (3), 032031 (2011).
12. H. Xu, Z.-A. Liu, Q.Wang, W. Kuehn, S. Lang, M. Liu. Introduction to panda data acquisition system. In: *Proceedings of the 2nd International Conference on Technology and Instrumentation in Particle Physics* (TIPP 2011). *Phys. Proc.* **37**, 1855 (2012).

Received 08.07.19

М. Шмідт

ДЕТЕКТОР PANDA НА ПРИСКОРЮВАЧІ FAIR

Р е з ю м е

PANDA – експеримент з фіксованою мішенню, в якому передбачається розглянути широкий спектр відкритих питань адронної фізики шляхом дослідження взаємодії між антипротонами з великими імпульсами та стаціонарною протонною мішенню. Детектор PANDA наразі знаходиться на стадії будівництва і буде розміщений у HESR, що є частиною майбутнього комплексу прискорювача FAIR на платформі Центру Гельмгольца для дослідження важких іонів GSI у Дармштадті. Головні характеристики детектора: треки високої точності в сильному магнітному полі, чудова ідентифікація частинок, а також калориметри високої роздільної здатності.

https://doi.org/10.15407/ujpe64.7.646

I. VALIÑO[1, 2, 3]
for the Pierre Auger Collaboration

[1] Gran Sasso Science Institute
(L'Aquila, Italy; e-mail: inesvr@gmail.com)
[2] INFN Laboratori Nazionali del Gran Sasso
(Assergi (L'Aquila), Italy)
[3] Observatorio Pierre Auger
(Av. San Martín Norte 304, 5613 Malargüe, Argentina;
Full author list: http://www.auger.org/archive/authors_2019_05.html)

THE PIERRE AUGER OBSERVATORY: STUDYING THE HIGHEST ENERGY FRONTIER

We highlight the main results obtained by the Pierre Auger Collaboration in its quest to unveil the mysteries associated with the nature and origin of the ultra-high energy cosmic rays, the highest-energy particles in the Universe. The observatory has steadily produced high-quality data for more than 15 years, which have already led to a number of major breakthroughs in the field contributing to the advance of our understanding of these extremely energetic particles. The interpretation of our measurements so far opens new questions which will be addressed by the on-going upgrade of the Pierre Auger Observatory.

K e y w o r d s: astroparticle physics, high-energy cosmic rays, multi-messenger astrophysics, hadronic interactions.

1. Introduction

Over a century after the discovery of cosmic rays, there are still a number of open, fundamental questions about their nature, especially about those with energies above 10^{17} eV, referred to as ultra-high energy cosmic rays (UHECRs). The Pierre Auger Observatory [1], the largest ultra-high energy cosmic-ray detector built so far in the world, was conceived to unveil the most important questions, namely the origin, propagation, and properties of UHECRs, and to study the interactions of these, the most energetic particles observed in Nature. To achieve the scientific goals, the Observatory was designed as an instrument for the detection of air showers initiated by the cosmic rays in Earth's atmosphere. Measured properties of the extensive air showers (EAS) allow determining the energy and arrival direction of each cosmic ray and provide a statistical determination of the distribution of primary masses.

Apart from measuring UHECRs, the Pierre Auger Observatory is a multi-purpose observatory for the extreme energy Universe with multi-messenger observations. In fact, it has shown an excellent sensitivity to EeV neutrino and photon fluxes due to its vast collecting area and its ability to efficiently discriminate between those neutral particles and hadronic cosmic rays. The Auger Observatory also offers a unique window to study particle physics at the high-energy frontier, held by UHECRs, easily reaching centre-of-mass energies ten times larger than the Large Hadron Collider (LHC) at CERN. Observables from the EAS allow improving our understanding of hadronic interactions at the higher energies.

2. The Pierre Auger Observatory

The Auger Observatory is located in a vast, high area near the small town of Malargüe in western Argentina at the latitude of about 35.2° S and the altitude of 1400 m above the sea level. Completed in 2008, it is a hybrid detector that combines an array of particle detectors, the Surface Detector array (SD), to observe the secondary shower particles that reach the ground, and Fluorescence Detector (FD) telescopes to collect the ultraviolet-light emitted by nitrogen air molecules during the shower development in the atmosphere. The SD comprises 1660 water-Cherenkov detectors (WCDs) laid out on a triangular grid with 1500 m spacing, covering an area of about 3000 km^2. Nested within this array is a low-energy extension to the SD which is comprised of 61 identical detectors with half the grid-spacing, 750 m, covering an area of 23.5 km^2. The FD comprises 24 telescopes at four perimeter buildings viewing the atmosphere over the array. A single telescope has a field of view of $30° \times 30°$ with a minimum elevation of 1.5° above the horizon. Three additional telescopes, the High Elevation Auger Telescopes (HEAT), cover an elevation up to 60° to detect the low-energy showers in coincidence with the 750 m array. The hybrid technique developed in the Auger Observatory exploits the large aperture of the SD, operating continuously, as well as the nearly calorimetric measurement of the shower energy deposited in the atmosphere obtained with the FD which, by contrast, has its on-time limited to clear moonless nights ($\sim$13%). Thanks to the combination of the FD and SD measurements, the energy scale of the Observatory is set with the FD measurement with a good control over the associated systematic uncertainties. Given the fact that the atmosphere acts as a calorimeter for the FD, a comprehensive monitoring of the atmosphere, particularly of the aerosol content and the cloud cover, is undertaken accurately with a set of high-quality monitoring devices, as described in [1].

The Observatory setup is complemented by two more detector types. The Auger Muons and Infill for the Ground Array (AMIGA) enhancement consists of coupling WCD and buried scintillation detectors deployed in two superimposed hexagon grids: the 750 m array and an even denser array with a 433 m spacing covering an area of 1.9 km^2. AMIGA provides direct measurements of the muon content in air showers. The Auger Engineering Radio Array (AERA) complements the Auger Observatory with a 17 km^2 array of more than 150 radio-antenna stations, colocated with the 750 m array, that measures EAS with energies between 10^{17} eV and several 10^{18} eV via their radio emission in the 30–80 MHz frequency band. The Auger Observatory layout is shown in Fig. 1.

3. Latest Results

Collecting scientific data since 2004, the results of the Pierre Auger Observatory have dramatically advanced our understanding of UHECRs during the last decade. In this section, a brief review of the recent highlights is given.

3.1. Energy spectrum

The measurement of the cosmic-ray energy spectrum is one of the cornerstones of astroparticle physics, since it encodes the very important information about the mechanisms of CR generation and propagation. The distribution of their sources, propagation effects, transitions over the types of particles, and classes of sources shape the spectrum.

The cosmic-ray energy spectrum above $10^{16.5}$ eV up to its very end above 10^{20} eV has been measured at the Auger Observatory with unprecedented statistics [2]. Five independent and complementary data sets collected between 1 January 2004 and 31 August 2018 have been used, with a total exposure of approximately 80000 km^2 sr yr. The method to derive the spectra is unique in this energy region, because it is entirely data-driven and nearly free of model-dependent assumptions about hadronic interactions in air showers. Two of these data sets have allowed the recent extension of the flux measurement to lower energies. An extension down to $E > 10^{17}$ eV was made possible using the 750 m array, thanks to the implementation of a new algorithm at the

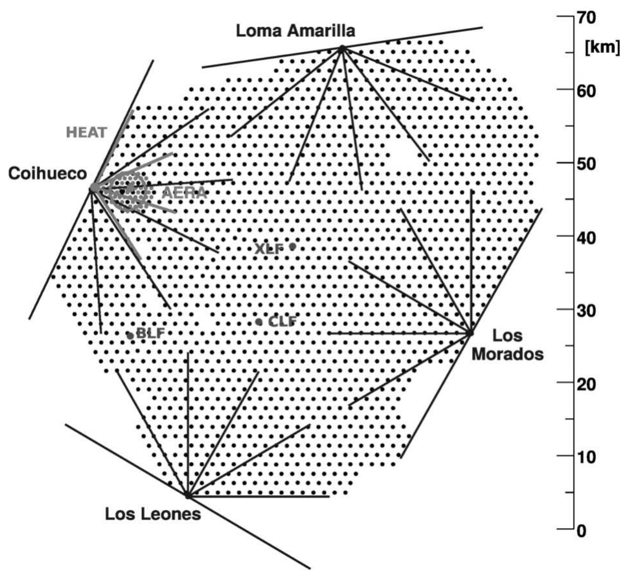

Fig. 1. Layout of the Pierre Auger Observatory. Black dots represent the WCD positions, blue and orange lines show the azimuthal field of views of the fluorescence telescopes. The location of the two laser facilities (CLF and XLF) for the monitoring of the atmospheric conditions are shown with red dots, and the area equipped with radio antennas (AERA) is marked with a light-blue circle

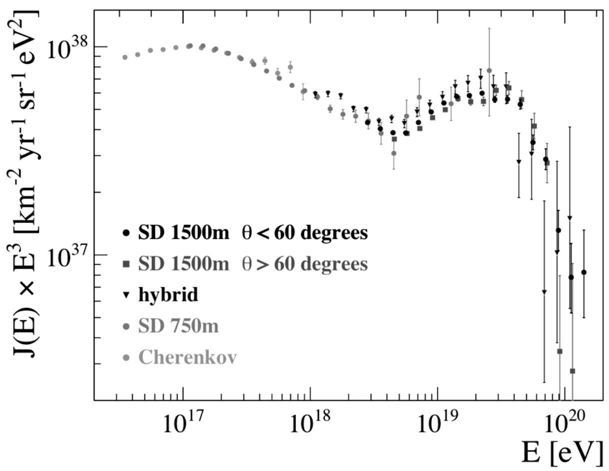

Fig. 2. Energy spectrum of cosmic rays measured using the Pierre Auger Observatory

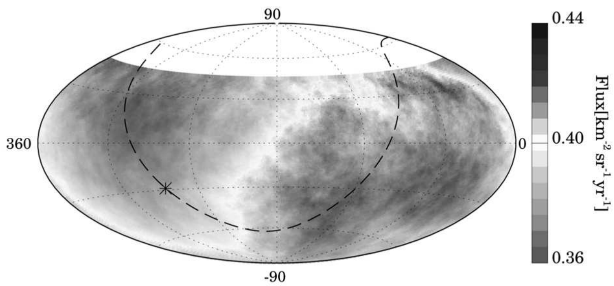

Fig. 3. Map of the CR flux above 8 EeV in equatorial coordinates, averaged on top-hat windows of 45° radius. The location of the Galactic plane is shown with a dashed line, and the Galactic centre is indicated with a star

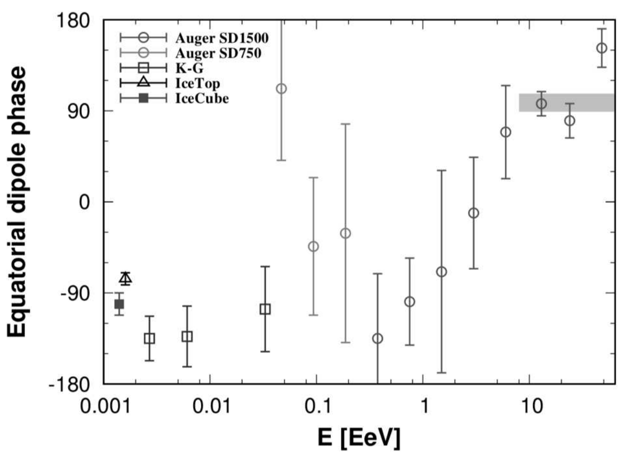

Fig. 4. Phase of the equatorial dipole amplitude determined with Auger Observatory data in different energy bins. Results from other experiments are also shown. Figure taken from [7]

WCD level [3]. This is the highest precision measurement near the region of the so-called *second-knee* or *iron-knee*, where previous experiments have shown a change in the spectral index. In addition, using for the first time events detected by HEAT in which the detected light is dominated by Cherenkov radiation, an extension of the spectrum down to $E > 10^{16.5}$ eV has been achieved [4]. Both new measurements allow studying the spectral features precisely around the *second-knee*. In total, the Auger spectrum spans over three decades in energy as shown in Fig. 2, where three relevant spectral features are observed: the softening in the spectrum at about 10^{17} eV (the *second-knee* region), the hardening at about $5{\times}10^{18}$ eV (the *ankle*), and a strong suppression of the flux at about 50×10^{18} eV.

3.2. Anisotropies

To understand the origin of UHECRs, the study of the distribution of their arrival directions has always been of capital importance, despite the difficulties that arise from the deflection they suffer due to the Galactic and extragalactic magnetic fields. Moreover, given the suggested trend towards a heavier composition with increasing energy that is inferred to happen above few EeV, only at the highest observed energies, the average deflections of CRs from an extragalactic source are expected to be smaller than a few tens of degrees, smearing point sources into *warm/hot* spots in the sky.

The Pierre Auger Collaboration has performed several anisotropy searches by using different techniques at different angular scales and by covering 85% of the celestial sphere. Among the various results, the observation of a large-scale anisotropy in the directions of CRs with energies larger than 8 EeV stands out (post-trial significance of 5.4σ) [5]. As shown in Fig. 3, the direction of the discovered dipole strongly favoured an extragalactic origin for the UHECR sources beyond the *ankle*. A new analysis was performed in [6] by splitting the events with $E > 4$ EeV into four energy bins, finding an indication at the 3.7σ level of growth of the dipolar amplitude with energy, expected from models, and consistent with the extragalactic origin in all bins. An update of this work by extending the study down to energies $\sim$0.03 EeV is presented in [7]. As shown in Fig. 4, the results suggest that the transition from the predominantly Galactic origin to the extragalactic one for the dipolar anisotropy is taking place somewhere between 1 and few EeV.

At higher energies, with more than 15 years of data and with an exposure exceeding 100000 km^2 sr yr, searches for an intrinsic anisotropy at small angular scales at energies exceeding 38 EeV have revealed an interesting possible correlation with nearby starburst galaxies, with a post-trial significance reaching 4.5σ in the most recent update [8]. A slightly weaker association (3.1σ) with active galactic nuclei emitting γ-rays is also found in events above 39 EeV. The region with the most significant flux excess is densely populated with different types of nearby extragalactic objects, with its centre at 2° away from the direction of Cen A, the nearest radio-loud active galaxy, at a distance of less than 4 Mpc.

3.3. Multi-messenger observations

The Pierre Auger Observatory has demonstrated capability to significantly contribute to Multi-messenger Astrophysics (MM) by searching for ultra-high energy (UHE) particles, particularly neutrinos and photons which, being electrically neutral, point back to their origin (see [9] for a recent review).

Given the non-observation of neutrino or photon candidates in data collected up to 31 August 2018, upper bounds on their diffuse fluxes were obtained [10, 11], allowing one to constrain the parameter space of cosmogenic neutrinos and photons. Scenarios assuming sources that accelerate only protons with a strong evolution with redshift are strongly constrained by the Auger Observatory results at more than 90% C.L.

In the MM context, the Auger Observatory can also search for neutrinos with energies above 100 PeV from point-like sources, monitoring a large fraction of the sky (from $\sim$−80° to $\sim$+60°) in the equatorial declination with peak sensitivities at declinations around −53° and +55°, unmatched for arrival directions in the northern hemisphere. An excellent sensitivity can also be obtained in the case of transient sources of order an hour or less, if they occur, when the source is in the field of view of the detection channels. The Auger Collaboration has performed several searches for UHE neutrinos following the detections of various types of transient astrophysical sources [12]. These include binary black hole (BBH) mergers, detected via gravitational waves (GWs) by the LIGO Scientific Collaboration and the Virgo Collaboration (LVC) instruments. Follow-up searches for the 21 events reported by LVC as BBH merger candidates till 2 June 2019 have been made, resulting in no candidates found in coincidence with any of them. As a consequence, the upper limit on a universal isotropic UHE neutrino luminosity as a function of the time after the merger was obtained, as shown in Fig. 5. Another source of interest is TXS $0506+056$, a powerful blazar that was found to emit an energetic neutrino candidate event correlated to a gamma-ray flare, along with a burst of events earlier in the same direction [13]. This blazar is thus the first identified source of neutrinos in the hundreds of TeV range. The Auger Collaboration performed follow-up searches for UHE neutrinos from the direction of TXS $0506+056$ during the periods of increased emission of high-energy photons and neutrinos, resulting in the non-observation of neutrino candidates. Regarding UHE photons, the search for point-like sources yielded no significant deviations from background expectations for Galactic sources and nearby extragalactic sources, the only targets accessible with photons in the EeV range.

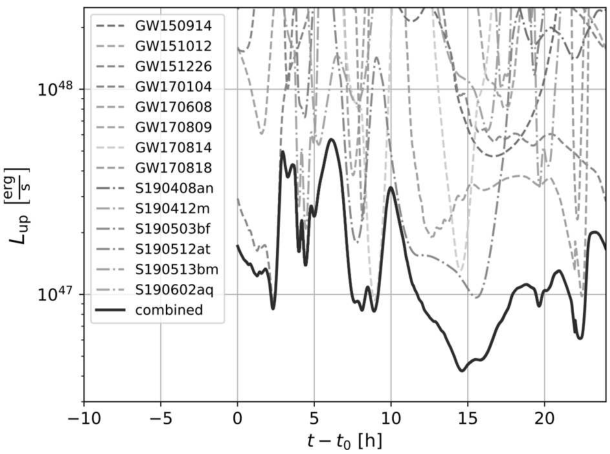

Fig. 5. A 90% C.L upper limit on the time-dependent universal isotropic luminosity (solid line), together with the contributions from the single sources (dashed lines). Sources not indicated here are above the $L_{\rm up}$-range drawn

The prominent role of the Pierre Auger Observatory as a multi-messenger observatory at the EeV range made it both a triggering and a follow-up partner in the Astrophysical Multi-messenger Observatory Network (AMON) [14], which establishes and distributes alerts for cimmediate follow-up by subscribed observatories.

3.4. Particle Physics at UHE: measurement of the muon content in cosmic-ray showers

In the quest of understanding how particles interact with another ones at energies much higher than those attainable at human-made particle accelerators, the UHECRs entering Earth's atmosphere play a key role in providing such high-energy collisions. The showers analyzed by the Auger Collaboration come from atmospheric cosmic-ray collisions with centre-of-mass energies ten times higher than the collisions produced at the LHC. Using these showers, the Auger Collaboration found, for the first time, an excess in the number of muons that arrive at the ground from cosmic-ray showers in comparison with expectations from models using LHC data as input [15–17]. One of the most direct measurements demonstrating this excess at 10^{19} eV is shown in the top panel of Fig. 6. The level of discrepancy depends on the hadronic model, and only SYBILL 2.3 c predictions are barely compatible with data within systematic uncertainties. The results of the Auger Collaboration are included in a recent meta-analysis of muon measurements in air showers with energies from PeV up to tens of EeV performed by eight air-shower leading experiments [18]. They found the muon measurements seem to be consistent with simulations based on the latest generation of hadronic interaction models up to about 10^{16} eV. Above this energy, most experimental data show a muon excess with respect to model predictions that gradually increases with energy. This result may, therefore, suggest that our understanding of hadronic interactions at the higher energies is incomplete.

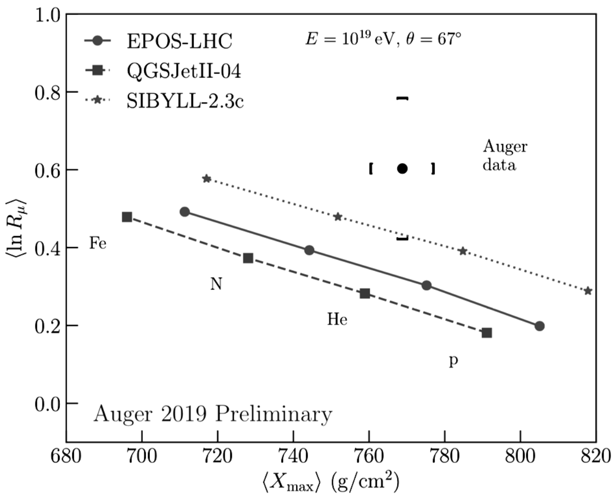

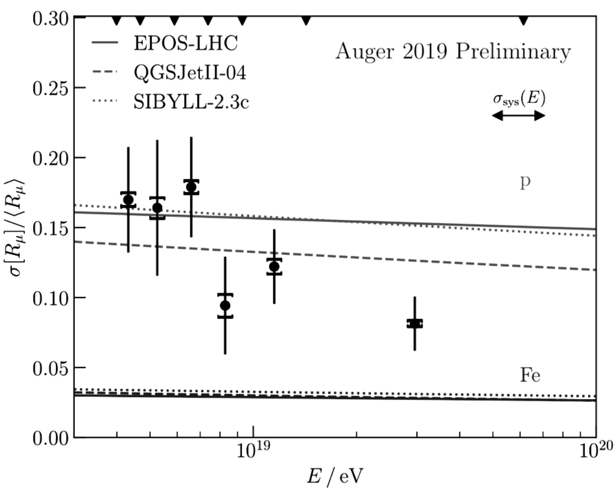

Fig. 6. Top: Average number of muons as a function of the depth of the shower maximum development. Bottom: Shower-to-shower fluctuations in the number of muons as a function of the primary cosmic-ray energy [17]

The measurement of shower-to-shower fluctuations in the number of muons in air showers allows one to constrain the available phase space for exotic explanations of the muon excess. In [17], the Pierre Auger Collaboration presents the first measurement of the fluctuations in the number of muons in inclined air showers with energies above 4×10^{18} eV. As shown in the bottom panel of Fig. 6, the observed fluctuations fall in the range of the predictions from air shower simulations with current models and, in fact, are compatible with the expectation from composition data [19]. As discussed in [17], this result suggests that the first high interaction in the shower is reasonably well described by models in this energy range. The likely explanation for the disagreement in the average value is that a small discrepancy in the particle production exists at all energies, which then is accumulated as the showers develop to create the deficit in the number of muons finally observed at the ground in simulations.

4. AugerPrime, the Observatory Upgrade

Despite a large number of valuable results as those described above, the many unknowns about UHECRs and hadronic interactions prevent the emergence of a uniquely consistent picture that would help us to understand the very complex astrophysical scenario

Fig. 7. Photograph of an upgraded station of the SD, featuring the SSD on top of the WCD

resulting from the Pierre Auger Observatory measurements. The understanding of the nature and the origin of the highest-energy cosmic rays remains an open science case that calls for an upgrade of the Observatory, called AugerPrime [20]. AugerPrime aims for the collection of a new information about the primary mass of the cosmic rays on a shower-by-shower basis from a high statistics sample of UHE events, by discriminating the electromagnetic and muonic components in air showers with SD-based observables.

The main element of the upgrade consists of 3.8 m^2 plastic scintillator detectors (SSD) on the top of each of the 1660 WCDs as illustrated in Fig. 7. The different sensitivity of the two detectors to the electromagnetic and muonic shower components is used to disentangle them. Other key elements of AugerPrime are an additional small photomultiplier (PMT) installed in the WCD for the extension of the dynamic range, and new SD electronics to process signals with higher sampling frequency and enhanced amplitude resolution. The upgrade will also be complemented by extending the FD measurements into the periods of a higher night-sky background, to increase the on-time of the FD about 50%. Finally, based on the AERA results, a new project for adding a radio antenna on the top of each WCD is now on-going [21]. The new detectors will operate together with the WCD+SSD, forming a unique setup to measure the properties of showers above $10^{17.5}$ eV.

The Engineering Array of 12 upgraded stations has been taking data in the field since late 2016. As of July 2019, over 300 SSDs have been deployed, of which 77 are operational, and the production of all the SSDs is nearing its end. The deployment of the AugerPrime should be completed in 2020. Operations and full data-taking are planned at least until 2025.

1. A. Aab *et al.* (Pierre Auger Collaboration) Nuclear instruments and methods in physics research section A: Accelerators, spectrometers, detectors and associated equipment. *Nucl. Instrum. Meth. A* **798**, 172 (2015).
2. V. Verzi, for the Pierre Auger Collab. Measurement of the energy spectrum of ultra-high energy cosmic rays using the Pierre Auger Observatory. In: *Proceedings of the 36th Int. Cosmic Ray Conf.*, PoS(ICRC2019)450.
3. A. Coleman, for the Pierre Auger Collab. Measurement of the cosmic ray flux near the second knee with the Pierre Auger Observatory. In: *Proceedings of the 36th Int. Cosmic Ray Conf.*, PoS(ICRC2019)225.
4. V. Novotny, for the Pierre Auger Collab. In: *Proceedings of the 36th Int. Cosmic Ray Conf.*, PoS(ICRC2019)374.
5. A. Aab *et al.* (Pierre Auger Collaboration). Observation of a large-scale anisotropy in the arrival directions of cosmic rays above 8×1018 eV. *Science* **357**, 1266 (2017).
6. A. Aab *et al.* (Pierre Auger Collaboration). Large-scale cosmic-ray anisotropies above 4 EeV measured by the Pierre Auger Observatory. *Astrophys. J.* **868** (1), 4 (2018).
7. E. Roulet, for the Pierre Auger Collab. Large-scale anisotropies above 0.03 EeV measuredby the Pierre Auger Observatory. In: *Proceedings of the 36th Int. Cosmic Ray Conf.*, PoS(ICRC2019)408.
8. L. Caccianiga, for the Pierre Auger Collab. Anisotropies of the highest energy cosmic-rayevents recorded by the Pierre Auger Observatory in 15 years of operation. In: *Proceedings of the 36th Int. Cosmic Ray Conf.*, PoS(ICRC2019)206.
9. A. Aab *et al.* (Pierre Auger Collaboration). Multi-messenger physics with the Pierre Auger Observatory. *Front. Astron. Space Sci.* **6**, 24 (2019).
10. F. Pedreira, for the Pierre Auger Collab. Bounds on diffuse and point source fluxes of ultra-high energy neutrinos with the Pierre Auger Observatory. In: *Proceedings of the 36th Int. Cosmic Ray Conf.*, PoS(ICRC2019)979.
11. J. Rautenberg, for the Pierre Auger Collab. Limits on ultra-high energy photons with the Pierre Auger Observatory. In: *Proceedings of the 36th Int. Cosmic Ray Conf.*, PoS(ICRC2019)398.
12. J. Rautenberg, for the Pierre Auger Collab. Follow-up searches for ultra-high energy neutrinos from transient astrophysical sources with the Pierre Auger Observatory. In: *Proceedings of the 36th Int. Cosmic Ray Conf.*, PoS(ICRC2019)415.
13. M.G. Aartsen *et al.* Neutrino emission from the direction of the blazar TXS 0506 + 056 prior to the IceCube-170922A alert. *Science* **361**, 147 (2018).

14. M.W.E. Smith *et al.* The Astrophysical Multimessenger Observatory Network (AMON). *Astropart. Phys.* **45**, 56 (2013).
15. A. Aab *et al.* (Pierre Auger Collaboration). Muons in air showers at the Pierre Auger Observatory: Mean number in highly inclined events. *Phys. Rev. D* **91**, 3 032003 (2015).
16. A. Aab *et al.* (Pierre Auger Collaboration). Testing hadronic interactions at ultrahigh energies with air showers measured by the Pierre Auger Observatory. *Phys. Rev. D* **117** (19), 192001 (2016).
17. F. Riehn, for the Pierre Auger Collab. Measurement of the fluctuations in the number of muons in inclined air showers with the Pierre Auger Observatory. In: *Proceedings of the 36th Int. Cosmic Ray Conf.*, PoS(ICRC2019)404.
18. L. Cazon *et al.* Working group report on the combined analysis of muon density measurements from eight air shower experiments. In: *Proceedings of the 36th Int. Cosmic Ray Conf.*, PoS(ICRC2019)214.
19. J. Bellido, for the Pierre Auger Collab. Depth of maximum of air-shower profiles at the Pierre Auger Observatory: Measurements above $10^{17.2}$ eV and composition implications. In: *Proceedings of the 35th Int. Cosmic Ray Conf.*, PoS(ICRC2017)506.
20. A. Aab *et al.* (Pierre Auger Collab.). The Pierre Auger Observatory upgrade – preliminary design report. arXiv:1604.03637.
21. B. Pont, for the Pierre Auger Collab. A large radio detector at the Pierre Auger Observatory – measuring the properties of cosmic rays up to the highest energies. In: *Proceedings of the 36th Int. Cosmic Ray Conf.*, PoS(ICRC2019)395.

Received 08.07.19

І. Валіно

ОБСЕРВАТОРІЯ ПЬЄРА ОЖЕ
ВИВЧАЄ ГРАНИЦІ НАЙВИЩИХ ЕНЕРГІЙ

Р е з ю м е

Ми представляємо основні результати, отримані Колаборацією Pierre Auger, метою яких є пошук загадкових джерел космічних променів надвисоких енергій – частинок з найвищою енергією у Всесвіті. Обсерваторія постійно, вже впродовж 15 років, продукує якісні дані, які привели до низки відкриттів в області фізики частинок надвисоких енергій. Інтерпретація отриманих результатів породжує також нові питання, відповідь на котрі дасть нинішня модернізація (upgrade) Обсерваторії Pierre Auger.

https://doi.org/10.15407/ujpe64.7.653

V. VOROBEL

Faculty of Mathematics and Physics, Charles University
(3, Ke Karlovu, 121 16 Praha 2, Czech Republic; e-mail: vit.vorobel@mff.cuni.cz)

LATEST RESULTS FROM NEUTRINO OSCILLATION EXPERIMENT DAYA BAY

The Daya Bay Reactor Neutrino Experiment was designed to measure θ_{13}, the smallest mixing angle in the three-neutrino mixing framework, with unprecedented precision. The experiment consists of eight identically designed detectors placed underground at different baselines from three pairs of nuclear reactors in South China. Since Dec. 2011, the experiment has been running stably for more than 7 years, and has collected the largest reactor antineutrino sample to date. Daya Bay greatly improved the precision on θ_{13} and made an independent measurement of the effective mass splitting in the electron antineutrino disappearance channel. Daya Bay also performed a number of other precise measurements such as a high-statistics determination of the absolute reactor antineutrino flux and the spectrum evolution, as well as a search for the sterile neutrino mixing, among others. The most recent results from Daya Bay are discussed in this paper, as well as the current status and future prospects of the experiment.

K e y w o r d s: neutrino oscillation, neutrino mixing, reactor, Daya Bay.

1. Daya Bay Neutrino Experiment

The Daya Bay Reactor Neutrino Experiment was designed to measure θ_{13}, the smallest mixing angle in the three-neutrino mixing framework, with unprecedented precision [1]. The experiment profits from a rare constellation of a nuclear power station complex situated near Hong Kong and adjacent mountains. The reactors serve as the source of neutrinos, while the mountains provide a sufficient overburden suppressing cosmic muons – the strongest background source (see Fig. 1). The Daya Bay and Ling Ao nuclear power plant (NPP) reactors (red circles) were situated on a narrow coastal shelf between the Daya Bay coastline and inland mountains.

At the time of the measurement, the facility consisted of six pressurized water reactors (PWRs). The electron antineutrinos are emitted in the beta-decay of fission fragments released in the chain reaction. The antineutrino flux and the energy spectrum is determined by the total thermal power of the reactor, the fraction of each fissile isotope in the fuel, the fission rate of each isotope, and the energy spectrum of neutrinos from each isotope. All the reactors have the same thermal power 2.9 GW$_{th}$ each and all together produced roughly 3.5×10^{21} $\tilde{\nu}_e$/s with energies up to 8 MeV making it one of the most intense $\tilde{\nu}_e$ sources on the Earth.

Two antineutrino detectors installed in each underground experimental hall near to the reactors (Hall 1 and Hall 2) measured the $\tilde{\nu}_e$ flux emitted by the reactors, while four detectors in the far experimental hall (Hall 3) measured a deficit in the $\tilde{\nu}_e$ flux due to oscillations in the location, where the neutrino oscillation effect is expected to be the strongest. Such configuration allows one to suppress the reactor-related uncertainty in the measured neutrino flux. The disappearance signal is most pronounced at the first oscillation minimum. Based on the existing accelerator and atmospheric neutrino oscillation measurements, this corresponded to the distance $L_f \approx 1.6$ km for the reactor $\tilde{\nu}_e$ with a mean energy of 4 MeV. The detectors were built and initially tested in a surface assembly building (SAB), transported to a liquid scintillator hall for the filling, and then installed in an experimental hall.

The detection of antineutrinos is based on the same principle as in the famous experiment of Reines and Cowan [2], who registered reactor antineutrinos in 1956. A sensitive part of the detector consists of a hydrogen-rich liquid scintillator doped with gadolinium (Reines and Cowan used Cd instead as the dopant). Antineutrino interacts via the inverse

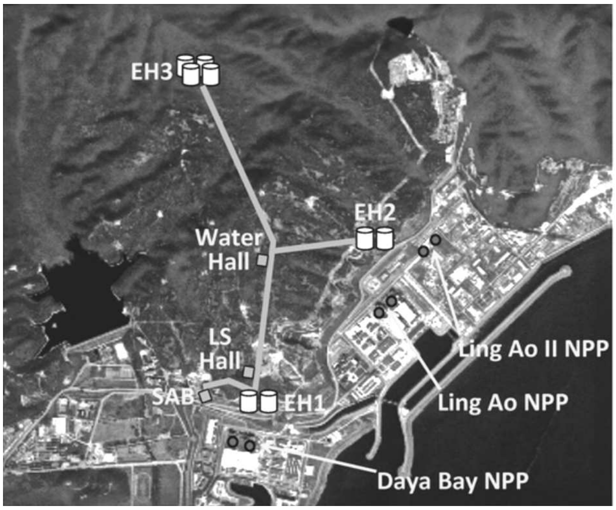

Fig. 1. Layout of the Daya Bay Neutrino Experiment

beta-decay (IBD)

$\tilde{\nu_e} + p \rightarrow e^+ + n$

with a proton (hydrogen) giving rise to a neutron and a positron. The positron deposits its kinetic energy to the scintillator, then annihilates on an electron, and generates two gamma rays, each 511 keV which together with the deposited positron kinetic energy cause a "prompt signal" within a few nanoseconds. The neutron is first moderated and then is captured on Gd typically 30 ns after the prompt signal. Consequently, a cascade of gamma quanta with a total energy of 8 MeV is emitted and generates a "delayed signal". The appearance of the two signals "prompt" and "delayed" is a signature of the antineutrino registration.

The Daya Bay antineutrino detector modules have an onion-like structure (see Fig. 2, left). The innermost volume is filled with 20 tons of the Gd-loaded liquid scintillator (GdLS) serving as the antineutrino target. The second layer – the gamma catcher – is filled with additional 20 tons of a normal liquid scintillator (LS) which can register most of the gamma energies from the neutron capture or positron annihilation. Neutrino interactions in the gamma catcher will not satisfy the trigger, since only the signal of the neutron-capture on Gd will trigger a neutrino event. The outer-most layer is normal mineral oil (MO) that shields the radiation from the PMT glass from entering the fiducial volume. The two inner vessels are fabricated of PMMA which is transparent for optical photons and chemically resistant against the used liquids, the outer-most 5 m by 5 m tank is made of a stainless steel and is equipped with 192 8-inch PMTs. Specular reflectors are located above and below the outer PMMA vessel to improve the light collection uniformity, while the vertical wall of the detector is black. Three automated calibration units are used to deploy radioactive sources (^{60}Co, ^{68}Ge, and ^{241}Am-^{13}C) and light-emitting diodes through narrow teflon-bellow penetrations into the GdLS and LS regions.

After the filling, the antineutrino detectors were installed in a 10 m deep water pool in each underground experimental hall, as shown in Fig. 2, right. The water shielded the detectors from γ-rays arising from the natural radioactivity and muon-induced neutrons, which were primarily emanated from the cavern rock walls. The pool was optically separated into two independent regions, the inner (IWS) and outer water shields (OWS). Both regions were instrumented with PMTs to detect the Cherenkov light produced by cosmogenic muons. A 4-layer resistive plate chamber (RPC) system was installed over the pool, which served in studies of muons and muon-induced backgrounds. The identification of muons which passed through the IWS, OWS, and RPC system enhanced the rejection of the background from neutrons generated by muon interactions in the immediate vicinity of the antineutrino detectors. Each detector (ADs, IWS, OWS) operated as an independently triggered system.

2. Results

2.1. Oscillation analysis based on n-Gd [3]

The presented results are from the analysis of data collected in the Daya Bay experiment with 6 detectors in 217 days (Dec/2011–Jul/2012), with 8 detectors in 1524 days (Oct/2012–Dec/2016), and with 7 detectors in 217 days (Jan/2017–Aug/2017). During 1958 days of operation, the Daya Bay experiment collected more than 3.5 millions inverse beta decays in the near halls and more than 0.5 million IBD have been detected in the far hall. The daily rate is ~2500 IBD events in the near halls and ~300 IBD in the far hall.

The distortion of the energy spectrum at the far hall relative to near halls was consistent with oscillations and allowed the measurement of $|\Delta m^2_{ee}|$. The

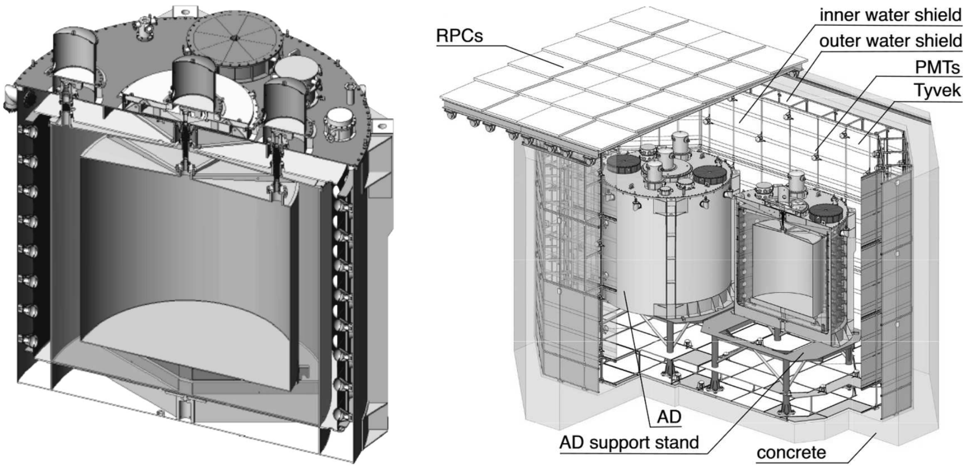

Fig. 2. Scheme of the antineutrino detector (AD) – left, and the near site detection view – right

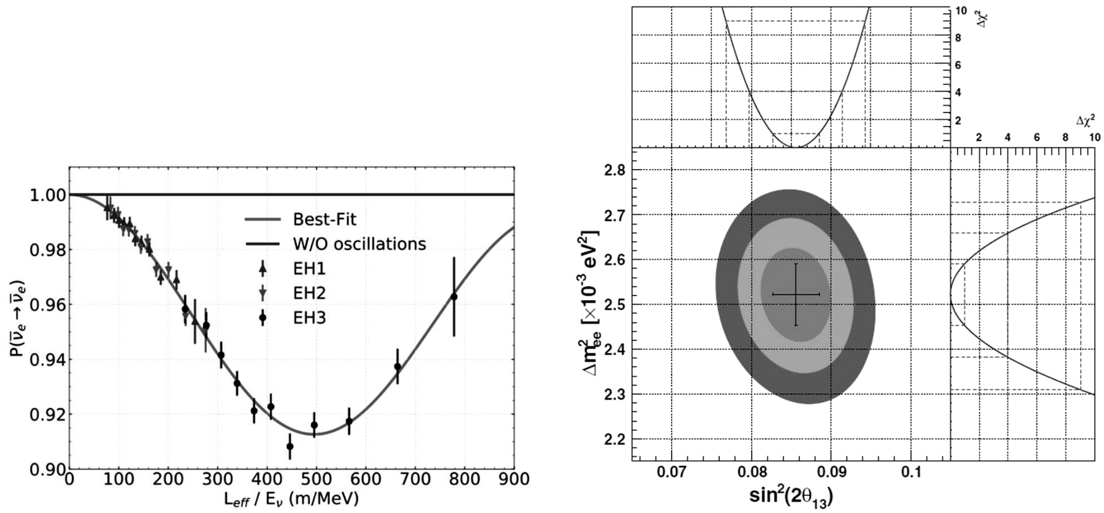

Fig. 3. Oscillation survival probability versus antineutrino proper time – left. The 68.3%, 95.5%, and 99.7% C.L. allowed regions for $\sin^2 2\theta_{13}$ and $|\Delta m^2_{ee}|$ – right

parameters of the three-flavor model in the best agreement with the observed rate and energy spectra were

$$\sin^2 2\theta_{13} = 0.0856 \pm 0.0029,$$

$$|\Delta m^2_{ee}| = [2.522^{+0.068}_{-0.070}] \times 10^{-3} \ \ \mathrm{eV}^2,$$

$$\Delta m^2_{32}(NH) = +[2.471^{+0.068}_{-0.070}] \times 10^{-3} \ \ \mathrm{eV}^2,$$

$$\Delta m^2_{32}(IH) = -[2.575^{+0.068}_{-0.070}] \times 10^{-3} \ \ \mathrm{eV}^2.$$

The Δm^2_{32} values were obtained under the assumptions of normal (NH) and inverted (IH) mass orderings.

Figure 3 – left, shows the observed electron survival probability as a function of the effective baseline L_{eff} divided by the average antineutrino energy $\langle E_\nu \rangle$. Almost one full oscillation disappearance and reappearance cycle was sampled, given the range of L/E_ν values which were measured.

The confidence intervals for Δm^2_{ee} versus $\sin^2 2\theta_{13}$ are shown in Fig. 3 – right. The 1σ, 2σ, and 3σ 2-D confidence intervals are estimated using $\Delta\chi^2$ values of 2.30 (red), 6.18 (green), and 11.83 (blue) relative to the best fit. The upper panel provides the 1-D $\Delta\chi^2$ for $\sin^2 2\theta_{13}$ obtained by profiling $|\Delta m^2_{ee}|$ (blue line), and the dash lines mark the corresponding 1σ, 2σ,

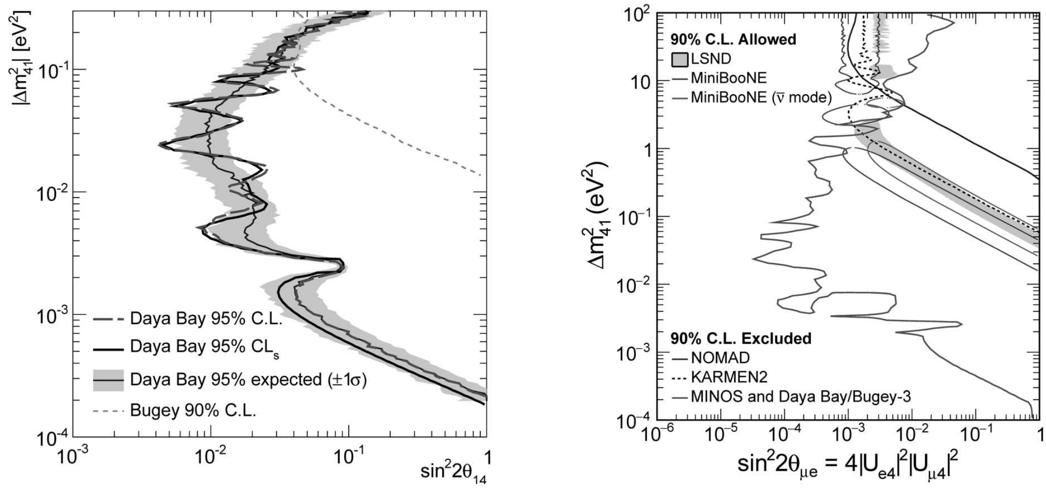

Fig. 4. Constraints for a sterile light neutrino provided by Daya Bay [13] – left, and the combined analysis of data from MINOS and Daya Bay/Bugey-3 [14] – right

and 3σ intervals. The right panel is the same, but for $|\Delta m^2_{ee}|$, with $\sin^2 2\theta_{13}$ profiled. The point marks the best estimates, and the error bars display their 1-D 1σ confidence intervals.

The Daya Bay results are compatible with the $\sin^2 2\theta_{13}$ results provided by other experiments: RENO [4], D-CHOOZ [5], T2K [6], MINOS [7], and $|\Delta m^2_{32}|$ values provided by RENO [4], T2K [6], MINOS [8], NOvA [9], Super-K [10], and IceCube [11]. While the accuracy of determination of $|\Delta m^2_{32}|$ is comparable with T2K and MINOS, the determination of $\sin^2 2\theta_{13}$ is more than twice more accurate than other results.

2.2. Oscillation analysis based on n-H [12]

The alternative analysis of data taken in 621 days and based on the events in which the neutron from IBD is captured on hydrogen results in

$$\sin^2 2\theta_{13} = 0.071 \pm 0.011.$$

The combination of the n-H and n-Gd results from 1230 days data gives the 8% improvement in precision:

$$\sin^2 2\theta_{13} = 0.082 \pm 0.004.$$

2.3. Search for Light Sterile Neutrino

The large statistics collected with the full configuration of eight detectors in the Daya Bay experiment allowed a new precise analysis with aim to search for a light sterile neutrino [13]. A relative comparison of the rate and energy spectrum of reactor antineutrinos in the three experimental halls yields no evidence of the sterile neutrino mixing in the $2 \times 10^{-4} < |\Delta m^2_{41}| < 0.3$ eV^2 mass range. The resulting limits on $\sin^2 2\theta_{14}$ shown in Fig. 4 – left, constitute the most stringent constraints to date in the $|\Delta m^2_{41}| < 0.2$ eV^2 region.

Searches for a light sterile neutrino have been independently performed by the MINOS and Daya Bay experiments using the muon (anti)neutrino and electron antineutrino disappearance channels, respectively. Results from both experiments are combined with those from the Bugey-3 reactor neutrino experiment to constrain oscillations into light sterile neutrinos [14]. The three experiments are sensitive to complementary regions of the parameter space, enabling the combined analysis to probe the regions allowed by the LSND and MiniBooNE experiments in a minimally extended four-neutrino flavor framework. Stringent limits on $\sin^2 2\theta_{\mu e}$ are set over six orders of magnitude in the sterile mass-squared splitting Δm^2_{41}. The sterile-neutrino mixing phase space allowed by the LSND and MiniBooNE experiments is excluded for $\Delta m^2_{41} < 0.8$ eV^2 at 95% CLs, see Fig. 4 – right.

2.4. Reactor antineutrino flux and spectrum anomalies [15]

Data collected in 1230 days were used to measure the IBD yield in four near detectors. The new av-

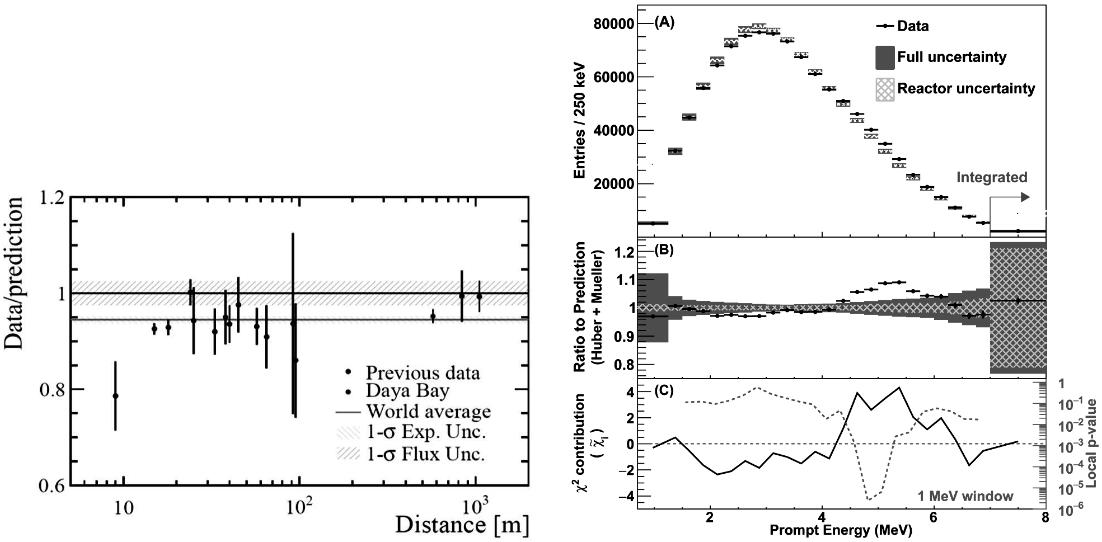

Fig. 5. Ratio of the measured antineutrino yield to the Huber–Vogel theoretical prediction vs. the distance from detector to detector – left. Comparison of the predicted and measured prompt energy spectra – right

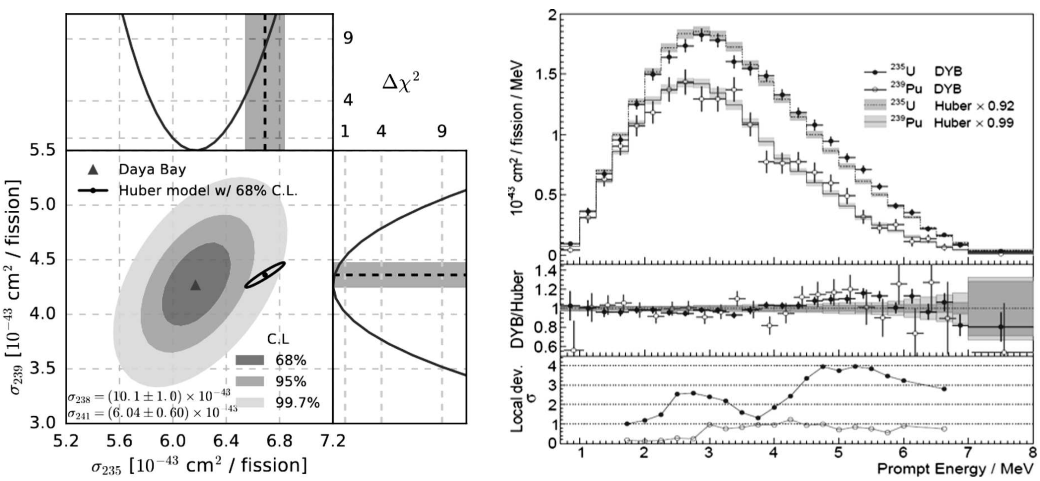

Fig. 6. Combined measurement of ^{235}U and ^{239}Pu IBD yields per fission σ_{235} and σ_{239} – left. Decomposition of the reactor anti-neutrino spectrum into two dominant contributions from ^{235}U and ^{239}Pu

erage IBD yield is determined to be $(5.91 \pm 0.09) \times \times 10^{-43}$ cm^2/fission, and the updated ratio of measured to predicted flux was found to be $0.952 \pm 0.014 \pm 0.023$ and $1.001 \pm 0.015 \pm 0.027$ for the Huber + Mueller and ILL + Vogel models, respectively, where the first and second uncertainties are experimental and theoretical model uncertainties, respectively. The tension with respect to the theoretical predictions is consistent with other experiments, see Fig. 5 – left. In particular, an excess of events in the region of 4–6 MeV was found in the measured spectrum, with a local significance of 4.4σ, see Fig. 5 – right.

2.5. Evolution of the reactor antineutrino flux and spectrum [16]

The data taken by the detectors in two near halls in 1230 days spanning multiple fuel cycles for each of the reactors were used for the investigation of the evolution of the antineutrino flux and spectrum. Weakly effective fission fractions values corresponding to the fission isotopes ^{235}U, ^{238}U, ^{239}Pu, and ^{241}Pu for each detector were calculated using thermal power and fission fraction data for each core, which were provided by the power plant.

A decrease of the total IBD yield/fission with increase of the effective fission fraction F_{239} of ^{239}Pu (larger fuel burn-up) was clearly observed. Individual yields σ_{235} and σ_{239} from the main flux contributors ^{235}U and ^{239}Pu, respectively, were fitted, see Fig. 6 – left. The discrepancy in a variation of the antineutrino flux from ^{235}U with respect to the reactor fuel composition model prediction suggests a 7.8% overestimation of the predicted antineutrino flux from ^{235}U and indicates that this isotope could be the primary contributor to the reactor antineutrino anomaly.

2.6. Reactor antineutrino spectrum decomposition [17]

The analysis of 3.5 milions of events taken during 1958 days in four near antineutrino detectors allows the partial decomposition of the antineutrino spectra – see Fig. 6 – right. The IBD yields and prompt energy spectra of ^{235}U and ^{239}Pu are obtained using the evolution of the prompt spectrum as a function of the fission fractions. The analysis confirms the discrepancy between the measured spectrum shape and the prediction. The deviation is 5.3σ and 6.3σ in the energy interval 0.7–8 MeV and in a local energy interval of 4–6 MeV, respectively.

The comparison of the measured and predicted ^{235}U and ^{239}Pu IBD yields preferes an incorrect prediction of the ^{235}U flux as the primary source of the reactor antineutrino rate anomaly. The discrepancy in the spectral shape for ^{235}U suggests the incorrect spectral shape prediction for the ^{235}U spectrum. However, no such conclusion can be drawn for the ^{239}Pu spectrum due to a larger uncertainty.

1. F.P. An *et al.* (Daya Bay Collaboration). Observation of electron-antineutrino disappearance at daya bay. *Phys. Rev. Lett.* **108**, 171803 (2012).
2. C.L. Cowan, F. Reines, F.B. Harrison, H.W. Kruse, A.D. McGuire. Detection of the free neutrino: A confirmation. *Science* **124**, 103 (1956).
3. D. Adey *et al.* (Daya Bay Collaboration). Measurement of the electron antineutrino oscillation with 1958 days of operation at daya bay. *Phys. Rev. Lett.* **121**, 241805 (2018).
4. J.H. Choi *et al.* (RENO Collaboration). Observation of energy and baseline dependent reactor antineutrino disappearance in the RENO experiment. *Phys. Rev. Lett.* **116**, 211801 (2016) (arXiv:1511.05849 [hep-ex]).
5. M. Ishitsuka. (Double Chooz Collaboration). First results with two detectors from Double Chooz. In: *Proc., 51st Rencontres de Moriond on Electroweak Interactions and Unified Theories : La Thuile, Italy, March 12–19* (2016), p. 157.
6. K. Iwamoto. (T2K Collaboration). Recent results from T2K and future prospects. *38th Int. Conf. on High Energy Physics* (2016), PoS(ICHEP2016)517.
7. P. Adamson *et al.* (MINOS Collaboration). Electron neutrino and antineutrino appearance in the full MINOS data sample.*Phys. Rev. Lett.* **110**, 171801 (2013).
8. J. Evans. (MINOS and MINOS+ Collaborations). New results from MINOS and MINOS+. *27th Int. Conf. on Neutrino Physics and Astrophysics, London, UK, July 4—9, 2016. J. Phys.: Conf. Ser.* **888**, 012017 (2017).
9. P. Vahle. (NOvA Collaboration). New results from NOvA. *27th Int. Conf. on Neutrino Physics and Astrophysics, London, UK, July 4—9, 2016.J. Phys.: Conf. Ser.* **888**, 012003 (2017).
10. S. Moriyama. (Super-Kamiokande Collaboration). New atmospheric and solar results from Super-Kamiokande. *27th Int. Conf. on Neutrino Physics and Astrophysics, London, UK, July 4—9, 2016. J. Phys.: Conf. Ser.* **888**, No. 1, 012005 (2017).
11. J. Koskinen. (Ice Cube Collaboration). Atmospheric neutrino results from IceCube-DeepCore and plans for PINGU. *27th Int. Conf. on Neutrino Physics and Astrophysics, London, UK, July 4—9, 2016. J. Phys.: Conf. Ser.* **888**, No. 1, 012023 (2017).
12. F.P. An *et al.* (Daya Bay Collaboration). New measurement of θ_{13} via neutron capture on hydrogen at Daya Bay. *Phys. Rev. D* **93**, 072011 (2016).
13. F.P. An *et al.* (Daya Bay Collaboration). Improved search for a light sterile neutrino with the full configuration of the Daya Bay experiment. *Phys. Rev. Lett.* **117**, No. 15, 151802 (2016).
14. F.P. An *et al.* (Daya Bay Collaboration, MINOS Collaboration). Limits on active to sterile neutrino oscillations from disappearance searches in the MINOS, Daya Bay, and Bugey-3 experiments. *Phys. Rev. Lett.* **117**, No. 15, 151801 (2016).
15. D. Adey. *et al.* (Daya Bay Collaboration). Improved measurement of the reactor antineutrino flux at Daya Bay. arXiv:1808.10836 (2018).
16. F.P. An *et al.* (Daya Bay Collaboration). Evolution of the reactor antineutrino flux and spectrum at Daya Bay. arXiv:1704.01082 (2017).
17. D. Adey *et al.* (Daya Bay Collaboration). Measurement of individual antineutrino spectra from ^{235}U and ^{239}Pu at Daya Bay. arXiv:1904.07812 (2019).

Received 08.07.19

В. Воробел
від імені Колаборації Daya Bay

НОВІТНІ РЕЗУЛЬТАТИ
З ЕКСПЕРИМЕНТУ НЕЙТРИННИХ
ОСЦИЛЯЦІЙ DAYA BAY

Р е з ю м е

Експеримент з реакторними нейтрино DAYA BAY задумано для вимірювання Θ_{13} – найменшого кута в рамках тринейтринного змішування – з безпрецедентною точністю. Експериментальна система складається з восьми однакових детекторів, розміщених під землею на різних базових відстанях від трьох пар ядерних реакторів Південного Китаю. Починаючи від 2011 року, експериментальна система працює стабільно впродовж більш ніж 7 років та накопичила найбільше як на сьогодні даних про реакторні антинейтрино. DAYA BAY значно покращив точність Θ_{13} і виконав незалежні вимірювання ефективного розщеплення мас в каналі зникнення електронного нейтрино. DAYA BAY провів також інші точні експерименти, такі як вимірювання з високою точністю абсолютного потоку реакторних нейтрино і їхнього спектра, а також пошук змішування стерильних нейтрино. В даній роботі обговорюються новітні результати з DAYA BAY, а також сучасний стан та перспективи експерименту.

https://doi.org/10.15407/ujpe64.8.665

A. AYALA,[1,2] M. HENTSCHINSKI,[3] L.A. HERNÁNDEZ,[1] M. LOEWE,[4,2,5]
R. ZAMORA [6]

[1] Instituto de Ciencias Nucleares, Universidad Nacional Autónoma de México
(Apartado Postal 70-543, CdMx 04510, Mexico)

[2] Centre for Theoretical and Mathematical Physics, and Department of Physics,
University of Cape Town
(Rondebosch 7700, South Africa)

[3] Departamento de Actuaría, Física y Matemáticas, Universidad de las Américas Puebla
(Santa Catarina Mártir, San Andrés Cholula, 72820 Puebla, Mexico)

[4] Instituto de Física, Pontificia Universidad Católica de Chile
(Casilla 306, Santiago 22, Chile)

[5] Centro Científico-Tecnológico de Valparaíso CCTVAL,
Universidad Técnica Federico Santa María
(Casilla 110-V, Valaparaíso, Chile)

[6] Instituto de Ciencias Básicas, Universidad Diego Portales
(Casilla 298-V, Santiago, Chile)

EFFECTS OF SUPERSTATISTICS ON THE LOCATION OF THE EFFECTIVE QCD CRITICAL END POINT

Effects of the partial thermalization during the chiral symmetry restoration at the finite temperature and quark chemical potential are considered for the position of the critical end point in an effective description of the QCD phase diagram. We find that these effects cause the critical end point to be displaced toward larger values of the temperature and lower values of the quark chemical potential, as compared to the case where the system can be regarded as completely thermalized. These effects may be important for relativistic heavy ion collisions, where the number of subsystems making up the whole interaction volume can be linked to the finite number of participants in the reaction.

Keywords: superstatistics, QCD phase diagram, critical end point, relativistic heavy-ion collisions.

The usual thermal description of a relativistic heavy-ion collision assumes that the produced matter reaches equilibrium, characterized by values of the temperature T and the baryon chemical potential μ, common within the whole interaction volume, after some time from the beginning of the reaction. The system evolution is subsequently described by the time evolution of the temperature down to a kinetic freeze-out, where particle spectra are established. This implicitly assumes the validity of the Gibbs–Boltzmann statistics and system's adiabatic evolution.

For expansion rates not too large compared to the interaction rate, the adiabatic evolution can perhaps be safely assumed. However, the Gibbs–Boltzmann statistics can be applied only to systems in the thermodynamical limit, namely, long after the relaxation time has elapsed and the randomization has been achieved within system's volume. In the case of a relativistic heavy-ion collision, the reaction starts off from nucleon-nucleon interactions. This means that the entire reaction volume is made, at the beginning, of a superposition of interacting pairs of nucleons. If the thermalization is achieved, it seems natural to assume that it starts off in each of the interacting nucleon pair subsystems and later spreads to the entire volume. In this scenario, the temperature and chemical potential within each subsystem may not be the same for other subsystems. Thus, a superposition of statistics, one in the usual Gibbs–Boltzmann sense for particles in each subsystem and another one, for the probability to find particular values for T and μ for different subsystem, seems appropriate. This is described by the so-called superstatistics scenario which describes a nonextensive behavior that naturally arises due to fluctuations in T or μ over the system's volume. This feature could be of particular relevance, when studying the position of the critical end point (CEP) in the QCD phase diagram, where one resorts to measuring ratios of fluctuations in conserved charges with the expectation that the volume factor cancels out in the ratio. If the thermalization is not complete, this expectation cannot hold, and a more sophisticated treatment is called for.

From the theoretical side, efforts to locate the CEP employing several techniques [1–20] were recently carried out. In all of these cases, the full thermalization over the whole reaction volume has been assumed. From the experimental side, the STAR BES-I program has recently studied heavy-ion collisions in the energy range 200 GeV $> \sqrt{s_{NN}} >$ 7.7 GeV [21]. Future experiments [22–24] will continue to thoroughly explore the QCD phase diagram, using different system sizes and varying the temperature and baryon density using different collision energies down to about $\sqrt{s_{NN}} \simeq 5$ GeV.

The superstatistics scenario has been explored in the context of relativistic heavy-ion collisions in many papers, *e.g.* Refs. [25–41] and references therein, with a particular focus on the study of imprints of the superstatistics on the particle production, using a particular version, the so-called Tsallis statistics [42]. Its use in the context of the computation of the rapidity distribution profile for the stopping in heavy ion collisions has been recently questioned in Ref. [43]. It has also been implemented to study generalized entropies and generalized Newton's law in Refs. [44–47]. The superstatistics concept has been nicely described in Refs. [48, 49]. In this work, we summarize the findings of Ref. [50] describing the implications of the superstatistics, when applied to temperature fluctuations for the location of the CEP in the QCD phase diagram.

For a system that has not yet reached a full equilibrium and contains space-time fluctuations of an intensive parameter β, such as the inverse temperature or chemical potential, one can still think of dividing the full volume into spatial subsystems, where β is approximately constant. Within each subsystem, one can apply the ordinary Gibbs–Boltzmann statistics, namely, one can use the ordinary density matrix giving rise to the Boltzmann factor $e^{-\beta\hat{H}}$, where $\hat{H}$ corresponds to the Hamiltonian for the states in each subsystem. The whole system can thus be described in terms of a space-time average over the different values that β could take for the different subsystems. In this way, one obtains a superposition of two statistics, one referring to the Boltzmann factor $e^{-\beta\hat{H}}$ and the other for β, hence, the name superstatistics.

To implement the scenario, one defines an averaged Boltzmann factor

$$B(\hat{H}) = \int\limits_0^\infty f(\beta) e^{-\beta\hat{H}} d\beta, \tag{1}$$

where $f(\beta)$ is the probability distribution of β. The partition function then becomes

$$Z = \mathrm{Tr}[B(\hat{H})] = \int\limits_0^\infty B(E) dE, \tag{2}$$

where the last equality holds for a suitably chosen set of eigenstates of the Hamiltonian.

When all the subsystems can be described with the same probability distribution [44], a possible choice to distribute the random variable β is the χ^2 distribution,

$$f(\beta) = \frac{1}{\Gamma(N/2)} \left(\frac{N}{2\beta_0}\right)^{N/2} \beta^{N/2-1} e^{-N\beta/2\beta_0}, \tag{3}$$

where Γ is the Gamma function, N represents the number of subsystems that make up the whole system, and

$$\beta_0 \equiv \int\limits_0^\infty \beta f(\beta) d\beta = \langle\beta\rangle \tag{4}$$

is the average of the distribution. The χ^2 is the distribution that emerges for a random variable that is made up of the sum of the squares of random variables X_i, each of which is distributed with a Gaussian probability distribution with vanishing average and unit variance. This means that if we take

$$\beta = \sum_{i=1}^{N} X_i^2, \tag{5}$$

then β is distributed according to Eq. (3). Moreover, its variance is given by

$$\langle \beta^2 \rangle - \beta_0^2 = \frac{2}{N}\beta_0^2. \tag{6}$$

Given that β is a positive definite quantity, thinking of it as being the sum of positive definite random variables is an adequate model. Note, however, that these variables do not necessarily correspond to the inverse temperature in each of the subsystems. Nevertheless, since the use of the χ^2 distribution allows for an analytical treatment, we hereby take this as the distribution to model the possible values of β.

To add superstatistics effects to the dynamics of a given system, we first find the effective Boltzmann factor. This is achieved by taking Eq. (3) and substituting it into Eq. (1). The integration over β leads to

$$B(\hat{H}) = \left(1 + \frac{2}{N}\beta_0 \hat{H}\right)^{-\frac{N}{2}}. \tag{7}$$

Note that, in the limit as $N \to \infty$, Eq. (7) becomes the ordinary Boltzmann factor. For large, but finite N, Eq. (7) can be expanded as

$$B(\hat{H}) = \left[1 + \frac{1}{2}\left(\frac{2}{N}\right)\beta_0^2 \hat{H}^2 - \frac{1}{3}\left(\frac{2}{N}\right)^2 \beta_0^3 \hat{H}^3 + \ldots\right] e^{-\beta_0 \hat{H}}. \tag{8}$$

Working up to first order in $1/N$, Eq. (8) can be written as [48]

$$B(\hat{H}) = e^{-\beta \hat{H}}\left(1 + \frac{\beta^2 H^2}{N} + \ldots\right) = \\ = \left[1 + \frac{\beta_0^2}{N}\left(\frac{\partial}{\partial \beta_0}\right)^2 + \ldots\right] e^{-\beta_0 \hat{H}}. \tag{9}$$

Therefore, the partition function to the first order in $1/N$ is given by

$$Z = \left[1 + \frac{\beta_0^2}{N}\left(\frac{\partial}{\partial \beta_0}\right)^2 + \ldots\right] Z_0 \tag{10}$$

with

$$Z_0 = e^{-\mathtt{V}\beta_0 V^{\text{eff}}}, \tag{11}$$

where $\mathtt{V}$ and V^{eff} are the system's volume and effective potential, respectively. After a bit of a straightforward algebra, we write the expression for the partition function in terms of $T_0 = 1/\beta_0$ as

$$Z = \left[1 + \frac{\beta_0^2}{N}\left(\frac{\partial}{\partial \beta_0}\right)^2 + \ldots\right] Z_0 = \\ = Z_0\left[1 + \frac{2T_0}{NZ_0}\left(\frac{\partial Z_0}{\partial T_0} + \frac{T_0}{2}\frac{\partial^2 Z_0}{\partial T_0^2}\right)\right], \tag{12}$$

and, therefore,

$$\ln[Z] = \ln[Z_0] + \ln\left[1 + \frac{2T_0}{NZ_0}\left(\frac{\partial Z_0}{\partial T_0} + \frac{T_0}{2}\frac{\partial^2 Z_0}{\partial T_0^2}\right)\right]. \tag{13}$$

To explore the QCD phase diagram from the point of view of chiral symmetry restoration, we use an effective model that accounts for the physics of spontaneous symmetry breaking at finite temperature and density: the linear sigma model. In order to account for the fermion degrees of freedom around the phase transition, we also include quarks in this model and work with the linear sigma model with quarks. The Lagrangian in the case where only the two lightest quark flavors are included is given by

$$\mathcal{L} = \frac{1}{2}(\partial_\mu \sigma)^2 + \frac{1}{2}(\partial_\mu \boldsymbol{\pi})^2 + \frac{a^2}{2}(\sigma^2 + \boldsymbol{\pi}^2) + \\ + \frac{\lambda}{4}(\sigma^2 + \boldsymbol{\pi}^2)^2 + i\bar{\psi}\gamma^\mu \partial_\mu \psi - g\bar{\psi}(\sigma + i\gamma_5 \boldsymbol{\tau}\,\boldsymbol{\pi})\psi, \tag{14}$$

where ψ is an SU(2) isospin doublet, $\boldsymbol{\pi} = (\pi_1, \pi_2, \pi_3)$ is an isospin triplet, σ is an isospin singlet, λ is the boson's self-coupling, g is the fermion-boson coupling, and $a^2 > 0$ is the squared mass parameter.

To allow for an spontaneous symmetry breaking, we let the σ field develop a vacuum expectation value v

$$\sigma \to \sigma + v, \tag{15}$$

which serves as the order parameter to identify the phase transitions. After this shift, the Lagrangian can be rewritten as

$$\mathcal{L} = \frac{1}{2}(\partial_\mu \sigma)^2 - \frac{1}{2}\left(3\lambda v^2 - a^2\right)\sigma^2 +$$

$$+\frac{1}{2}(\partial_\mu \boldsymbol{\pi})^2 - \frac{1}{2}\left(\lambda v^2 - a^2\right)\boldsymbol{\pi}^2 + \frac{a^2}{2}v^2 + \\ -\frac{\lambda}{4}v^4 + i\bar{\psi}\gamma^\mu\partial_\mu\psi - gv\bar{\psi}\psi + \mathcal{L}_I^b + \mathcal{L}_I^f, \tag{16}$$

where the sigma, three pions, and the quarks have masses given by

$$m_\sigma^2 = 3\lambda v^2 - a^2, \\ m_\pi^2 = \lambda v^2 - a^2, \\ m_f = gv, \tag{17}$$

respectively, and $\mathcal{L}_I^b$ and $\mathcal{L}_I^f$ are given by

$$\mathcal{L}_I^b = -\frac{\lambda}{4}(\sigma^2 + \boldsymbol{\pi}^2)^2 \\ \mathcal{L}_I^f = -g\bar{\psi}(\sigma + i\gamma_5 \boldsymbol{\tau}\,\boldsymbol{\pi})\psi. \tag{18}$$

Equation (18) describes the interactions among the σ, $\boldsymbol{\pi}$, and ψ fields after the symmetry breaking.

In order to analyze the chiral symmetry restoration, we compute the effective potential at finite temperature and density. In order to account for plasma screening effects, we also work up to the contribution of ring diagrams. All matter terms are computed in the high-temperature approximation. The effective potential is given by [20]

$$V^{\rm eff}(v, T_0, \mu_q) = -\frac{(a^2 + \delta a^2)}{2}v^2 + \frac{(\lambda + \delta\lambda)}{4}v^4 + \\ + \sum_{b=\sigma,\bar{\pi}}\left\{-\frac{m_b^4}{64\pi^2}\left[\ln\left(\frac{a^2}{4\pi T_0^2}\right) - \gamma_E + \frac{1}{2}\right] - \right. \\ \left. -\frac{\pi^2 T_0^4}{90} + \frac{m_b^2 T_0^2}{24} - \frac{(m_b^2 + \Pi(T_0, \mu_q))^{3/2} T_0}{12\pi}\right\} + \\ + \sum_{f=u,d}\left\{\frac{m_f^4}{16\pi^2}\left[\ln\left(\frac{a^2}{4\pi T_0^2}\right) - \gamma_E + \frac{1}{2} - \right.\right. \\ \left. - \psi^0\left(\frac{1}{2} + \frac{\mathrm{i}\mu_q}{2\pi T_0}\right) - \psi^0\left(\frac{1}{2} - \frac{\mathrm{i}\mu_q}{2\pi T_0}\right)\right] - \\ - 8m_f^2 T_0^2\left[\mathrm{Li}_2(-e^{\mu_q/T_0}) + \mathrm{Li}_2(-e^{-\mu_q/T_0})\right] + \\ \left. + 32T_0^4\left[\mathrm{Li}_4(-e^{\mu_q/T_0}) + \mathrm{Li}_4(-e^{-\mu_q/T_0})\right]\right\}, \tag{19}$$

where μ_q is the quark chemical potential, and δa^2 and $\delta\lambda$ represent the counterterms which ensure that the one-loop vacuum corrections do not shift the position of the minimum or the vacuum mass of the sigma. These counterterms are given by

$$\delta a^2 = -a^2\frac{(8g^4 - 12\lambda^2 - 3\lambda^2\ln[2])}{32\pi\lambda}, \\ \delta\lambda = \frac{(16 + 8\ln[g^2/\lambda])g^4 - (18 + 9\ln[2])\lambda^2}{64\pi^2}. \tag{20}$$

The self-energy at finite temperature and quark chemical potential, $\Pi(T_0, \mu_q)$, includes the contribution from both bosons and fermions. In the high temperature approximation, it is given by [20]

$$\Pi(T_0, \mu_q) = -N_f N_c g^2\frac{T_0^2}{\pi^2}\left[\mathrm{Li}_2(-e^{\mu_q/T_0}) + \right. \\ \left. + \mathrm{Li}_2(-e^{-\mu_q/T_0})\right] + \frac{\lambda T_0^2}{2}. \tag{21}$$

To implement superstatistics corrections, we substitute Eq. (19) into Eq. (11). The partition function is obtained from Eq. (12) and the effective potential including superstatistics effects is obtained from the logarithm of this partition function,

$$V_{\rm sup}^{\rm eff} = -\frac{1}{\mathsf{V}\beta}\ln[Z]. \tag{22}$$

As a consequence, the effective potential of Eq. (22) has four free parameters. Three of them come from the original model, namely, λ, g and a. The remaining one corresponds to the superstatistics correction, N. In the absence of superstatistics, the effective potential in Eq. (19) allows for the second- and first-order phase transitions, depending on the values of λ, g and a, as well as of T_0 and μ_q. For given values of λ, g, and a, we now proceed to analyze the phase structure that emerges, when varying N, paying particular attention to the displacement of the CEP location in the T_0, μ_q plane.

The figure shows the effective QCD phase diagram calculated with $a = 133$ MeV, $g = 0.51$, and $\lambda = 0.36$ for different values of the number of subsystems making up the whole system, N. For the different curves, the star shows the position of the CEP. Note that this position moves to larger values of T and lower values of μ_q, with respect to the CEP position for $N = \infty$, that is, without superstatistics effects, as N decreases. Note also that, for these findings, we have not considered fluctuations in the chemical potential. Those have been included to study the CEP position in the Nambu–Jona-Lasinio model in Ref. [53].

Our findings show that fermions become more relevant for lower values of the baryon chemical potential, than they do in the case of the homogeneous system. To picture this result, as above, let (μ_c^0, T_c^0) and (μ_c, T_c) be the critical values for the baryon chemical potential and temperature at the onset of first-order phase transitions for the homogeneous and fluctuating systems, respectively. The parameter that determines, when fermions become relevant, is the combination μ_c^0/T_c^0. Since our calculation for a single-boson degrees of freedom shows that the critical temperature decreases with decreasing the number of subsystems (see Ref. [50]), this means that, for the boson-fermion fluctuating system, fermions become relevant for $\mu_c/T_c \simeq \mu_c^0/T_c^0$ and, thus, for $\mu_c < \mu_c^0$.

To apply these considerations to the context of relativistic heavy-ion collisions, we recall that temperature fluctuations are related to the system's heat capacity by

$$\frac{(1-\xi)}{C_v} = \frac{\langle (T-T_0)^2 \rangle}{T_0^2}, \tag{23}$$

where the factor $(1-\xi)$ accounts for deviations [54] from the Gaussian [55] distribution for the random variable T. The right-hand side of Eq. (23) can be written in terms of fluctuations in β as

$$\frac{\langle (T-T_0)^2 \rangle}{T_0^2} \frac{\langle T^2 \rangle - T_0^2}{T_0^2} = \frac{\beta_0^2 - \langle \beta^2 \rangle}{\langle \beta^2 \rangle} = = \frac{\left(\frac{\beta_0^2}{\langle \beta^2 \rangle}\right)^2 \langle \beta^2 \rangle - \beta_0^2}{\beta_0^2}. \tag{24}$$

Note that, according to Eq. (6),

$$\left(\frac{\beta_0^2}{\langle \beta^2 \rangle}\right)^2 = \left(\frac{1}{1+2/N}\right)^2 \simeq 1 - 4/N. \tag{25}$$

Therefore, for N finite, but large,

$$\frac{\langle (T-T_0)^2 \rangle}{T_0^2} \simeq \frac{\langle \beta^2 \rangle - \beta_0^2}{\beta_0^2}. \tag{26}$$

Using Eqs. (6) and (26), we obtain

$$\frac{\langle (T-T_0)^2 \rangle}{T_0^2} = \frac{2}{N}. \tag{27}$$

This means that the heat capacity is related to the number of subsystems by

$$\frac{(1-\xi)}{C_v} = \frac{2}{N}. \tag{28}$$

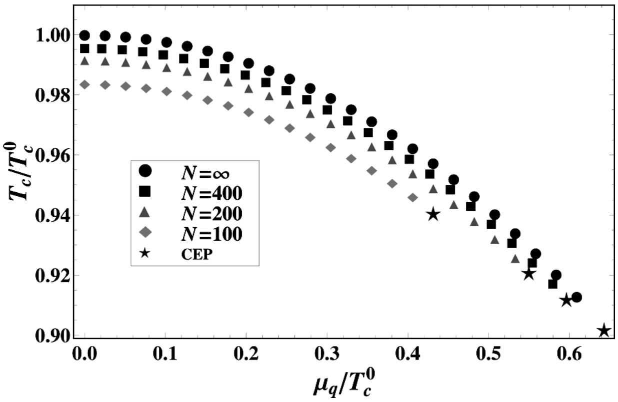

Effective QCD phase diagram calculated with $a = 133$ MeV, $g = 0.51$, and $\lambda = 0.36$ for different values of N. The star shows the position of the CEP which moves toward larger values of T and lower values of μ_q, as N decreases

To introduce the specific heat c_v for a relativistic heavy-ion collision, it is natural to divide C_v by the number of participants N_p in the reaction. Therefore, Eq. (28) can be written as

$$\frac{2}{N} = \frac{(1-\xi)}{N_p c_v}. \tag{29}$$

In Ref. [54], ξ is estimated as $\xi = N_p/A$, where A is the smallest mass number of the colliding nuclei. Equation (29) provides the link between the number of subsystems in a general superstatistics framework and a relativistic heavy-ion collision. It has been shown [56] that, at least for Gaussian fluctuations, c_v is a function of the collision energy. Therefore, in order to make a thorough exploration of the phase diagram, as the collision energy changes, we need to account for this dependence, as well as to work with values of the model parameters λ, g, and a, appropriate to the description of the QCD phase transition. Work along these lines is currently underway and will be reported elsewhere.

M.H., M.L., and R.Z. would like to thank Instituto de Ciencias Nucleares, Universidad Nacional Autónoma de México for their warm hospitality during a visit in June-July 2018. A.A. and L.A.H. would like to thank the Physics Derpartment, PUC and CIDCA for their warm hospitality during a visit in July 2018. This work was supported by UNAM-DGPA-PAPIIT grant number IG100219, by Consejo Nacional de Ciencia y Tecnología grant num-

ber 256494, by Fondecyt (Chile) grant numbers 1170107, 1150471, 11508427, Conicyt/PIA/Basal (Chile) grant number FB0821. R.Z. would like to acknowledge the support from CONICYT FONDECYT Iniciación under grant number 11160234.

1. A. Ayala, C. A. Dominguez, M. Loewe. For a recent review on the QCD sum rules technique at finite temperature. *Adv. High Energy Phys.* **2017**, 9291623 (2017).
2. P. Costa, M.C. Ruivo, C.A. de Sousa. Thermodynamics and critical behavior in the Nambu–Jona-Lasinio model of QCD. *Phys. Rev. D* **77**, 096001 (2008).
3. G.A. Contrera, D. Gomez-Dumm, N.N. Scoccola. Nonlocal SU(3) chiral quark models at finite temperature: The role of the Polyakov loop. *Phys. Lett. B* **661**, 113 (2008).
4. A. Ayala, A. Bashir, C. A. Dominguez, E. Gutierrez, M. Loewe, A. Raya. QCD phase diagram from finite energy sum rules. *Phys. Rev. D* **84**, 056004 (2011).
5. X.-Y. Xin, S.-X. Qin, Y.-X. Liu. Quark number fluctuations at finite temperature and finite chemical potential via the Dyson–Schwinger equation approach. *Phys. Rev. D* **90**, 076006 (2014).
6. C.S. Fischer, J. Luecker, C.A. Welzbacher. Phase structure of three and four flavor QCD. *Phys. Rev. D* **90**, 034022 (2014).
7. Y. Lu, Y.-L. Du, Z.-F. Cui, H.-S. Zong. Critical behaviors near the (tri-) critical end point of QCD within the NJL model. *Eur. Phys. J. C* **75**, 495 (2015).
8. A. Ayala, M. Loewe, R. Zamora. Inverse magnetic catalysis in the linear sigma model with quarks. *Phys. Rev. D* **91**, 016002 (2015).
9. A. Ayala, M. Loewe, A.J. Mizher, R. Zamora. Inverse magnetic catalysis for the chiral transition induced by thermomagnetic effects on the coupling constant. *Phys. Rev. D* **90**, 036001 (2014).
10. A. Ayala, C.A. Dominguez, L.A. Hernández, M. Loewe, R. Zamora. Magnetized effective QCD phase diagram. *Phys. Rev. D* **92**, 096011 (2015).
11. C. Shi, Y.-L. Du, S.-S. Xu, X.-J. Liu, H.-S. Zong. Continuum study of the QCD phase diagram through an OPE-modified gluon propagator. *Phys. Rev. D* **93**, 036006 (2016).
12. G.A. Contrera, A.G. Grunfeld, D. Blaschke. Supporting the search for the CEP location with nonlocal PNJL models constrained by lattice QCD. *Eur. Phys. J. A* **52**, 231 (2016).
13. A. Ayala, C.A. Dominguez, L.A. Hernández, M. Loewe, A. Raya, J.C. Rojas, C. Villavicencio. Thermomagnetic properties of the strong coupling in the local Nambu–Jona-Lasinio model. *Phys. Rev. D* **94**, 054019 (2016).
14. Z.-F. Cui, J.-L. Zhang, H.-S. Zong. Proper time regularization and the QCD chiral phase transition. *Sci. Rep.* **7**, 45937 (2017).
15. S. Datta, R.V. Gavai, S. Gupta. Quark number susceptibilities and equation of state at finite chemical potential in staggered QCD with $N_t = 8$. *Phys. Rev. D* **95**, 054512 (2017).
16. J.P. Carlomagno, M. Loewe. Comparison between the continuum threshold and the Polyakov loop as deconfinement order parameters. *Phys. Rev. D* **95**, 036003 (2017).
17. J. Knaute, R. Yaresko, B. Kämpfer. Holographic QCD phase diagram with critical point from Einstein–Maxwell-dilaton dynamics. *Phys. Lett. B* **778**, 419 (2018).
18. N.G. Antoniou, F.K. Diakonos, X.N. Maintas. C.E. Tsagkarakis. Locating the QCD critical endpoint through finite-size scaling. *Phys. Rev. D* **97**, 034015 (2018).
19. R. Rougemont, R. Critelli, J. Noronha-Hostler, J. Noronha, C. Ratti. Dynamical versus equilibrium properties of the QCD phase transition: A holographic perspective. *Phys. Rev. D* **96**, 014032 (2017).
20. A. Ayala, S. Hernández-Ortiz, L.A. Hernández. QCD phase diagram from chiral symmetry restoration: analytic approach at high and low temperature using the linear sigma model with quarks. *Rev. Mex. Fis.* **64**, 302 (2018).
21. L. Adamczyk *et al.*, [STAR Collaboration]. Energy dependence of moments of net-proton multiplicity distributions at RHIC. *Phys. Rev. Lett.* **112**, 032302 (2014); Beam energy dependence of moments of the net-charge multiplicity distributions in Au + Au collisions at RHIC. *Phys. Rev. Lett.* **113**, 092301 (2014).
22. C. Yang, [for the STAR Collaboration]. The STAR beam energy scan phase II physics and upgrades. *Nucl. Phys. A* **967**, 800 (2017).
23. P. Senger. The heavy-ion program of the future FAIR facility. *J. Phys. Conf. Ser.* **798**, 012062 (2017).
24. V. Kekelidze, A. Kovalenko, R. Lednicky, V. Matveev, I. Meshkov, A. Sorin, G. Trubnikov. Feasibility study of heavy-ion collision physics at NICA JINR. *Nucl. Phys. A* **967**, 884 (2017).
25. G. Wilk, Z. Wlodarczyk. Multiplicity fluctuations due to the temperature fluctuations in high-energy nuclear collisions. *Phys. Rev. C* **79**, 054903 (2009).
26. G. Wilk, Z. Wlodarczyk. Power laws in elementary and heavy-ion collisions. *Eur. Phys. J. A* **40**, 299 (2009).
27. G. Wilk, Z. Wlodarczyk. The imprints of superstatistics in multiparticle production processes. *Cent. Eur. J. Phys.* **10**, 568 (2012).
28. M. Rybczynski, Z. Wlodarczyk. Tsallis statistics approach to the transverse momentum distributions in p-p collisions. *Eur. Phys. J. C* **74**, 2785 (2014).
29. C.Y. Wong, G. Wilk, L.J.L. Cirto, C. Tsallis. From QCD-based hard-scattering to nonextensive statistical mechanical descriptions of transverse momentum spectra in high-energy pp and $p\bar{p}$ collisions. *Phys. Rev. D* **91**, 114027 (2015).
30. G. Wilk, Z. Wlodarczyk. Superstatistical cluster decay. *Phys. Lett. A* **379**, 2941 (2015).
31. A. Bialas. Tsallis $p_\perp$ distribution from statistical clusters. *Phys. Lett. B* **747**, 190 (2015).
32. T. Bhattacharyya, J. Cleymans, A. Khuntia, P. Pareek, R. Sahoo. Radial flow in non-extensive thermodynamics

and study of particle spectra at LHC in the limit of small $(q-1)$. *Eur. Phys. J. A* **52**, 30 (2016).
33. A. Bialas, A. Bzdak. Short-range two-particle correlations from statistical clusters. *Phys. Rev. D* **93**, 094015 (2016).
34. J. Rozynek, G. Wilk. An example of the interplay of nonextensivity and dynamics in the description of QCD matter. *Eur. Phys. J. A* **52**, 294 (2016).
35. S. Tripathy, T. Bhattacharyya, P. Garg, P. Kumar, R. Sahoo, J. Cleymans. Nuclear modification factor using Tsallis non-extensive statistics. *Eur. Phys. J. A* **52**, 289 (2016).
36. S. Grigoryan. Using the Tsallis distribution for hadron spectra in *pp* collisions: Pions and quarkonia at $\sqrt{s}$ = 5–13000 GeV. *Phys. Rev. D* **95**, 056021 (2017).
37. A. Khuntia, S. Tripathy, R. Sahoo, J. Cleymans. Multiplicity dependence of non-extensive parameters for strange and multi-strange particles in proton-proton collisions at $\sqrt{s}$ = 7 TeV at the LHC. *Eur. Phys. J. A* **53**, 103 (2017).
38. T. Bhattacharyya, J. Cleymans, L. Marques, S. Mogliacci, M.W. Paradza. On the precise determination of the Tsallis parameters in proton-proton collisions at LHC energies. *J. Phys. G* **45**, 055001 (2018).
39. S. Tripathy, S.K. Tiwari, M. Younus, R. Sahoo. Elliptic flow in Pb+Pb collisions at $\sqrt{s_{\rm NN}} = 2.76$ TeV at the LHC using Boltzmann transport equation with non-extensive statistics. *Eur. Phys. J. A* **54**, 38 (2018).
40. M. Ishihara. Phase transition for the system of finite volume in the ϕ^4 theory in the Tsallis nonextensive statistics. *Int. J. Mod. Phys. A* **33**, 1850067 (2018).
41. G. Wilk, Z. Wlodarczyk. Some intriguing aspects of multiparticle production processes. *Int. J. Mod. Phys. A* **33**, 1830008 (2018).
42. C. Tsallis. Possible generalization of Boltzmann–Gibbs statistics. *J. Stat. Phys.* **52**, 479 (1988).
43. A. Simon, G. Wolschin. Examining nonextensive statistics in relativistic heavy-ion collisions. *Phys. Rev. C* **97**, 044913 (2018).
44. O. Obregón, A. Gil-Villegas. Generalized information entropies depending only on the probability distribution. *Phys. Rev. E* **88**, 062146 (2013).
45. A. Martínez-Merino, O. Obregón, M.P. Ryan, jr. Modified entropies, their corresponding Newtonian forces, potentials, and temperatures. *Phys. Rev. D* **95**, 124031 (2017).
46. O. Obregón. Superstatistics and gravitation. *Entropy 2010* **12**, 2067 (2010).
47. O. Obregón. Superstatistics and gravitation. *Entropy 2010* **12**, 2067 (2010).
48. C. Beck, E.G.D. Cohen. Superstatistics. *Phys. A* **322**, 267 (2003).
49. C. Beck. Superstatistics: theory and applications. *Continuum Mech. Thermodyn.* **16**, 293 (2004); C. Beck. Recent developments in superstatistics. *Braz. J. Phys.* **39**, 2A, 357 (2009).
50. Al. Ayala, M. Hentschinski, L.A. Hernandez, M. Loewe, R. Zamora. Superstatistics and the effective QCD phase diagram. *Phys. Rev. D* **98**, 114002 (2018).
51. A. Ayala, A. Sanchez, G. Piccinelli, S. Sahu. Effective potential at finite temperature in a constant magnetic field. I. Ring diagrams in a scalar theory. *Phys. Rev. D* **71**, 023004 (2005).
52. M.E. Carrington. The effective potential at finite temperature in the Standard Model. *Phys. Rev. D* **45**, 2933 (1992).
53. J. Rozynek, G. Wilk. An example of the interplay of nonextensivity and dynamics in the description of QCD matter. *Eur. Phys. J. A* **52**, 294 (2016).
54. G. Wilk, Z. Wlodarczyk. Multiplicity fluctuations due to the temperature fluctuations in high-energy nuclear collisions. *Phys. Rev. C* **79**, 054903 (2009).
55. L.D. Landau, E.M. Lifshitz. *Statistical Physics* (Elsevier, 2013), ISBN 9780080570464.
56. S. Basu, S. Chatterjee, R. Chatterjee, T.K. Nayak, B.K. Nandi. Specific heat of matter formed in relativistic nuclear collisions. *Phys. Rev. C* **94**, 044901 (2016).

Received 08.07.19

А. Аяла, М. Хентшинскі,
Л.А. Гернандез, М. Леве, Р. Замора

ВПЛИВ СУПЕРСТАТИСТИКИ
НА ПОЛОЖЕННЯ КРИТИЧНОЇ КІНЦЕВОЇ
ТОЧКИ В ЕФЕКТИВНІЙ КХД

Р е з ю м е

В рамках ефективної моделі фазової діаграми КХД розглядається вплив часткової термалізації під час відновлення кіральної симетрії при скінченних температурі і хімічному потенціалі кварків на положення критичної кінцевої точки. Ми показали, що ці ефекти спричиняють зміщення критичної точки в бік більших температур та менших значень хімічного потенціалу кварків по відношенню до повністю термалізованої системи. Ці ефекти можуть бути важливими для зіткнень релятивістських важких іонів, де число підсистем, що заповнюють весь об’єм, можна пов’язати зі скінченним числом частинок в реакції.

https://doi.org/10.15407/ujpe64.8.672

S. CATTO,[1,2] Y. GÜRCAN,[3] A. KHALFAN,[4] L. KURT,[3] B. NICOLESCU,[5] E. YU[5]

[1] CUNY Graduate School and University Center
(365, Fifth Avenue, New York, NY 10016-4309; e-mail: scatto@gc.cuny.edu)
[2] The Rockefeller University
(1230, York Avenue, New York, NY10021-6399)
[3] Department of Science, Borough of Manhattan CC
(The City University of New York, NY 10007)
[4] Physics Department, LaGuardia CC
(The City University of New York, NY 11101)
[5] Baruch College, City University of New York
(17, Lexington Ave, New York, NY 10010)

HADRONIC SUPERSYMMETRY FROM QCD

The evolution of hadronic mass formulae with special emphasis on group theoretical descriptions and supersymmetry suggested by QCD and based on quark-antidiquark symmetry is shown, with further comments on possible applications to a Skyrme-type models that may compete with the potential quark models in the future.

Keywords: supersymmetry, quark models, skyrmions.

1. Introduction

The quark model with potentials derived from QCD, including the quark-diquark model for excited hadrons gives mass formulae in a very good agreement with experiments and goes a long way in explaining the approximate symmetries and supersymmetries of the hadronic spectrum, including the symmetry breaking mechanism.

The mathematical expression of supersymmetry arises through a generalization of Lie algebras to superalgebras. When a Lie algebra is $su(n)$ it can be extended to a graded algebra (superalgebra) $su(n/m)$ with even and odd generators, the even generators being paired with commuting (bosonic) parameters and the odd generator with the Grassmann (fermionic) parameters. The algebra can then be exponentiated to the supergroup SU(n/m). This was done by Miyazawa [1] who derived the correct commutation and anticommutation relations for such a superalgebra, as well as the generalized Jacobi identity. This discovery predates the supersymmetry in dual resonance models or supersymmetry in quantum field theories invariant under the super-Poincaré group that generalizes special relativity. Miyazawa looked for a supergroup that would contain SU(6) and settled on broken SU(6/21). He showed that an SU(3) singlet-octet of this supergroup leads to a new kind of mass formulae relating fermionic and bosonic mass splittings.

2. Quark-Diquark Model

We shall first discuss the validity domain of SU(6/21) supersymmetry [2, 3, 6]. The diquark structure with spins $s = 0$ and $s = 1$ emerges in inelastic inclusive lepton-baryon collisions with high impact parameters that excite the baryon rotationally, resulting in inelastic structure functions based on point-like quarks and diquarks instead of three point-like quarks. In this case, both mesons and baryons are bilocal with large separation of constituents.

In addition, there is a symmetry between color antitriplet diquarks with $s = 0$ and $s = 1$ and color antitriplet antiquarks with $s = \frac{1}{2}$. This is only possible, if the force between quark q and antiquark $\bar{q}$, and between q and diquark D is mediated by a zero spin object that sees no difference between the spins of $\bar{q}$ and D. The object can be in color states that are either singlet or octet since q and D are both triplets. Such an object is provided by scalar flux tubes of gluons that dominate over the one gluon exchange at large distances. Various strong coupling approximations to QCD, like lattice gauge theory [4, 5], 't Hooft's $\frac{1}{N}$ approximation [7], when N, the number of colors, is very large, or the elongated bag model [8] all give a linear potential between widely separated quarks and an effective string that approximates the gluon flux tube. In such a theory, it is energetically favorable for the three quarks in a baryon to form a linear structure with a quark in the middle and two at the ends or, for a high rotational excitation, a bilocal linear structure (diquark) at one end and a quark at the other end. In order to illustrate these points, we start with the suggestion of Johnson and Thorn [8] that the string-like hadrons may be pictured as the vortices of color flux lines which terminate on the concentration of color at the end points. The color flux connecting opposite ends is the same for mesons and baryons giving an explanation for the same slope of meson and baryon trajectories [3].

To construct a solution, which yields a maximal angular momentum for a fixed mass, we consider a bag with elongated shape rotating about the center of mass with an angular frequency ω. Its ends have the maximal velocity allowed, which is the speed of light ($c = 1$). Thus, a given point inside the bag, at a distance r from the axis of rotation moves with a velocity

$$v = |\boldsymbol{\omega} \times \mathbf{r}| = \frac{2r}{L}, \tag{1}$$

where L is the length of the string. In this picture, the bag surface will be fixed by balancing the gluon field pressure against the confining vacuum pressure B, which (in analogy to electrodynamics) can be written in the form

$$\frac{1}{2}\sum_{\alpha=1}^{8}(E_\alpha^2 - B_\alpha^2) = B. \tag{2}$$

Using Gauss' law, the color electric field E through the flux tube connecting the color charges at the ends of the string is given by

$$\int \mathbf{E}_\alpha \, d\mathbf{S} = E_\alpha A = g\frac{1}{2}\lambda_\alpha, \tag{3}$$

where $A(r)$ is the cross-section of the flux tube at distance r from the center and $g\frac{1}{2}\lambda_\alpha$ is the color electric charge, which is the source of E_α. By analogy with classical electrodynamics, the color magnetic field $\mathbf{B}_\alpha(r)$ associated with the rotation of the color electric field is

$$\mathbf{B}_\alpha(r) = \mathbf{v}(r) \times \mathbf{E}_\alpha(r), \tag{4}$$

at a point moving with a velocity $\mathbf{v}(r)$. For the absolute values, this yields

$$B_\alpha = v \; E_\alpha, \tag{5}$$

because $\mathbf{v}(r)$ is perpendicular to $\mathbf{E}_\alpha(r)$. Using last three equations together with

$$\left\langle \sum_{\alpha=1}^{8} \left(\frac{1}{2}\lambda_\alpha\right)^2 \right\rangle = \frac{4}{3} \tag{6}$$

for the $SU(3)^c$ triplet in Eq. (2), we obtain that the cross-section of the bag

$$A(r) = \sqrt{\frac{2}{3B}} \; g \; \sqrt{1 - v^2}, \tag{7}$$

which shows the expected Lorentz contraction.

The total energy E of the bag

$$E = E_q + E_G + BV \tag{8}$$

is the sum of the quark energy E_q, the gluon field energy E_G, and the volume energy of the bag, BV. Because the quarks at the ends move with the a speed close to the speed of light, their energy is simply given by

$$E_q = 2p, \tag{9}$$

where p is the momentum of a quark, a diquark, or an antiquark, respectively. By analogy with electrodynamics, Eqs. (3)–(5) yield

$$E_G = \frac{1}{2}\int d^3x \sum_{\alpha=1}^{8}(E_\alpha^2 + B_\alpha^2) = \\ = \sqrt{\frac{2}{3}}\, g\sqrt{B}\, L \int_0^1 dv \frac{1+v^2}{\sqrt{1-v^2}} = \sqrt{\frac{2}{3}}\, g\sqrt{B}\, L\frac{3\pi}{4} \tag{10}$$

for the gluon energy and

$$BV = 2B \int_0^{\frac{L}{2}} A(r) \; dr = \\ = 2B \int_0^1 \sqrt{\frac{2}{3B}}\, g\sqrt{1-v^2}\frac{L}{2}\, dv = \\ = \sqrt{\frac{2}{3}}\, g\sqrt{B} L\frac{\pi}{4} = \frac{BA(0)L\pi}{4} \tag{11}$$

for the volume energy. It is obvious from Eq. (10) that the gluon field energy is proportional to the length L of the bag. The gluon field energy and the volume energy of the bag together correspond to a linear rising potential of the form

$$V(L) = E_G + BV = bL, \tag{12}$$

where

$$b = \sqrt{\frac{2B}{3}}\, g\pi. \tag{13}$$

The total angular momentum J of this classical bag is the sum of the angular momenta of the quarks at the two ends

$$J_q = pL \tag{14}$$

and the angular momentum J_G of the gluon field. From Eq. (4), we get

$$\mathbf{E}_\alpha \times \mathbf{B}_\alpha = \mathbf{v} E_\alpha^2, \tag{15}$$

for the momentum of the gluon field. Hence,

$$J_G = \left| \int\limits_{\text{bag}} d^3\mathbf{r} \sum_{\alpha=1}^{8} \mathbf{r} \times (\mathbf{E}_\alpha \times \mathbf{B}_\alpha) \right| =$$
$$= 2\int\limits_0^{\frac{L}{2}} dr A(r) r v E_\alpha^2 = \frac{16}{3L} g^2 \int\limits_0^{\frac{L}{2}} \frac{r^2 dr}{A(r)} = \sqrt{\frac{2}{3}} g\sqrt{B} L^2 \frac{\pi}{4}, \tag{16}$$

where we have used Eq. (1) and Eq. (3) in the third step. We can now express the total energy of the bag in terms of angular momenta. Putting these results back into the formulae for E_q and E_G, we arrive at

$$E_q = \frac{2J_q}{L}, \quad E_G = \frac{3J_G}{L}, \tag{17}$$

so that the bag energy now becomes

$$E = \frac{2J_q}{L} + \frac{3J_G}{L} + \sqrt{\frac{2B}{3}} L g \frac{\pi}{L} =$$
$$= \frac{2J_q + 4J_G}{L} = \frac{2(J + J_G)}{L} =$$
$$= \frac{1}{L}\left(2J + \sqrt{\frac{2}{3}} g\sqrt{B} L^2 \frac{\pi}{2}\right). \tag{18}$$

Minimizing the total energy for a fixed angular momentum with respect to the length of the bag, $\frac{\partial E}{\partial L} = 0$ gives the relation

$$-\frac{2J}{L^2} + \sqrt{\frac{2}{3}} g\sqrt{B}\frac{\pi}{2} = 0 \tag{19}$$

so that

$$L^2 = \frac{4J}{g\pi}\sqrt{\frac{3}{2B}}. \tag{20}$$

Re-inserting this into Eq. (18), we arrive at

$$E = 2\sqrt{Jg\pi}\left(\frac{2B}{3}\right)^{\frac{1}{4}}, \tag{21}$$

or

$$J = \left(\sqrt{\frac{3}{2B}} \frac{1}{4\pi g}\right) E^2 =$$
$$= \left(\sqrt{\frac{3}{2B}} \frac{1}{8\pi^{\frac{3}{2}}} \frac{1}{\sqrt{\alpha_s}}\right) E^2 = \alpha'(0) M^2, \tag{22}$$

where $M = E$, and $\alpha_s = \frac{g^2}{4\pi}$ is the unrationalized color gluon coupling constant. We can now let $\alpha'(0)$ defined by the last equation, which is the slope of the Regge trajectory, be expressed as

$$\alpha'(0) = \sqrt{\frac{3}{2B}} \frac{1}{8\pi^{\frac{3}{2}}} \frac{1}{\sqrt{\alpha_s}} = \frac{1}{4b}, \tag{23}$$

where b was defined in Eq. (12).

The parameters B and α_s have been determined [9, 10] using the experimental information from the low lying hadron states: $B^{\frac{1}{4}} = 0.146$ GeV and $\alpha_s = 0.55$ GeV. If we use these values in Eq. (23), we find

$$\alpha'(0) = 0.88\ (\text{GeV})^{-2} \tag{24}$$

in the remarkable agreement with the slope determined from experimental data, which is about $0.9\ (\text{GeV})^{-2}$.

Then the total phenomenological non-relativistic potential is the well-known superposition of the Coulomb-like and confining potentials $V(r) = \frac{a}{r} + br$, where $r = |\mathbf{r}_1 - \mathbf{r}_2|$ is the distance between q and $\bar{q}$ in a meson or between q and D in a baryon with high angular momentum. This was verified in lattice QCD to a high degree of accuracy [11] ($a = \frac{-c\alpha_c}{r}$, where

c is the color factor, and α_c is the strong coupling strength).

It is interesting to know that all this is related very closely to the dual strings. Indeed, we can show that the slope given in Eq. (23) is equivalent to the dual string model formula for the slope, if we associate the "proper tension" in the string with the proper energy per unit length of the color flux tube and the volume. By the proper energy per unit length, we mean the energy per unit length at a point in the bag evaluated in the rest system of that point. This will be

$$T_0 = \frac{1}{2}\sum_\alpha E_\alpha^2 A_0 + BA_0. \tag{25}$$

The relation $\frac{1}{2}\sum_\alpha E_\alpha^2 = B$ in the rest system gives

$$T_0 = 2BA_0, \tag{26}$$

where A_0 is the cross-sectional area of the bag. Let $A = A_0$ in Eq. (7), when $v = 0$. Then, using

$$A_0 = \sqrt{\frac{2}{3B}}\, g, \tag{27}$$

we find

$$T_0 = 2\sqrt{\frac{2}{3}}\, g\sqrt{B} = 4\sqrt{\frac{2\pi}{3}}\,\sqrt{\alpha_s}\sqrt{B} \tag{28}$$

for the proper tension. In the dual string, the slope and the proper tension are related by the formula [12]

$$T_0 = \frac{1}{2\pi\alpha'}, \tag{29}$$

so that the slope is

$$\alpha' = \frac{1}{8}\sqrt{\frac{3}{2}}\,\frac{1}{\pi^{\frac{3}{2}}}\,\frac{1}{\sqrt{\alpha_s}}\,\frac{1}{\sqrt{B}}, \tag{30}$$

which is identical to the earlier formula we produced in Eq. (23).

It would appear from Eq. (28) that the ratio of volume to field energy would be one-to-one in one space dimension in contrast to the result one-to-three, which holds for a three-dimensional bag [13]. However, the ratio one-to-one is true only in the rest system at a point in the bag, and each position along the x-axis is, of course, moving with a different velocity. Indeed, we see from Eq. (10) and Eq. (11) that the ratio of the total volume energy to the total field energy is given by one-to-three in conformity with the virial theorem [13].

In the string model of hadrons, we have $E^2 \sim J$ between the energy and the angular momentum of the rotating string. If we denote, by $\rho(r)$, the mass density of a string, and, by v and ω, its linear and angular velocities, respectively, the energy and the angular momentum of the rotating string are given by

$$E = 2\int \frac{\rho(r)}{\sqrt{1-\omega^2 r^2}}\, dr = \frac{2}{\omega}\int_0^1 \frac{\rho(v)}{\sqrt{1-v^2}} dv \tag{31}$$

and

$$J = 2\int \frac{\rho(r)}{\sqrt{1-\omega^2 r^2}}\, r^2\omega dr = \frac{2}{\omega^2}\int_0^1 \frac{\rho(v)}{\sqrt{1-v^2}} v^2 dv. \tag{32}$$

Hence, the relation

$$E^2 \propto J \tag{33}$$

holds. If the string is loaded with mass points at its ends, they no longer move with the speed of light. However, the above relation still holds approximately for the total energy and angular momentum of the loaded string.

We now look at various ways of the partitioning of the total angular momentum into two subsystems. Figures *a*, *b*, and *c* show the possible configurations of three quarks in a baryon. If we put the proportionality constant in Eq. (33) equal to unity, then the naive evaluation of energies yield

$$E^2 = J_1 + J_2 = E_1^2 + E_2^2 \le (E_1 + E_2)^2 = E'^2, \tag{34}$$

where E and E' denote the energies corresponding to Figures *a* or *c*. In the case of Figure *b*, J_1 and J_2 are the angular momenta corresponding to the energies E_1 and E_2 of the subsystems. The equality in Eq. (34) holds, only if E_1 or E_2 is zero. Therefore, for each fixed total angular momentum, its most unfair partition into two subsystems gives us the lowest energy levels, and its more or less fair partition gives rise to energy levels on daughter trajectories. Hence, on the leading baryonic trajectory, we have a quark-diquark structure (Fig. *a*) or a linear molecule structure (Fig. *c*). On the other hand, on low-lying trajectories, we have more or less symmetric ($J_1 \sim J_2$) configuration of quarks.

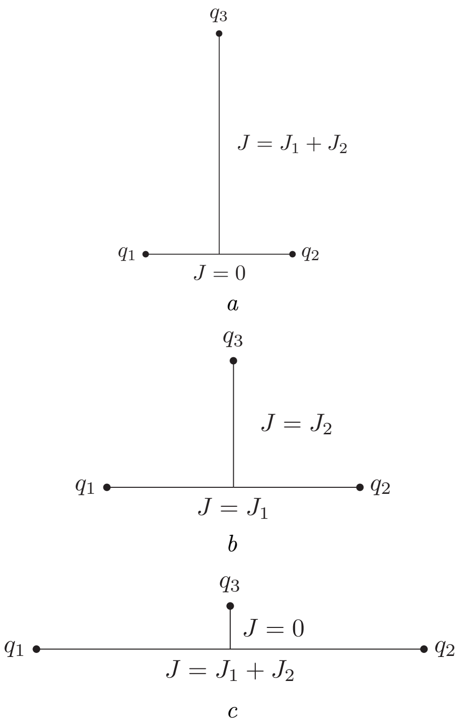

Since the high-J hadronic states on leading Regge trajectories tend to be bilocal with large separation of their constituents, they fulfill all the conditions for supersymmetry between $\bar{q}$ and D. Then the only difference between the energies of $(q\bar{q})$ mesons and (qD) baryons comes from the different masses of their constituents, namely, $m_q = m_{\bar{q}} = m$, and $m_D \sim 2m$. For high J, this is the main source of symmetry breaking, which is spin-independent. We will show how we can obtain sum rules from this breaking. The part of the mass operator that gives rise to this splitting is a diagonal element of U(6/21) that commutes with SU(6).

Let us now consider the spin-dependent breaking of SU(6/21). For low J states, the (qD) system becomes trilocal(qqq), and the flux tube degenerates to a single gluon propagator that gives spin-dependent forces in addition to the Coulomb term $\frac{a}{r}$. In this case, we have the regime studied by de Rujula, Georgi, and Glashow, where the breaking is due to the hyperfine splitting caused by the exchange of single gluons that have spin 1. These mass splittings give rise to different intercepts of the Regge trajectories given by

$$\Delta m_{12} = k\frac{\mathbf{S}_1\,\mathbf{S}_2}{m_1 m_2}, \quad k = |\psi(0)|^2, \tag{35}$$

both for baryons and mesons at high energies. But, at low energies, the baryon becomes a trilocal object (with three quarks), and the mass splitting is given by

$$\Delta m_{123} = \frac{1}{2}k\left(\frac{\mathbf{S_1}\,\mathbf{S_2}}{m_1 m_2} + \frac{\mathbf{S}_2\,\mathbf{S}_3}{m_2 m_3} + \frac{\mathbf{S}_3\,\mathbf{S}_1}{m_3 m_1}\right), \tag{36}$$

where m_1, m_2, and m_3 are the masses of the three different quark constituents.

The element of SU(6/21) that gives rise to such splittings is a diagonal element of its U(21) subgroup and gives rise to $s(s+1)$ terms that behave like an element of the (405) representation of SU(6) in the SU(6) mass formulae. The splitting of isospin multiplets is due to a symmetry breaking element in the (35) representation of SU(6). Hence, all symmetry breaking terms are in the adjoint representation of SU(6/21). If we restrict ourselves to the non-strange sector of hadrons with approximate SU(4) symmetry, the effective supersymmetry will relate the splitting in m^2 between Δ $(s = \frac{3}{2}, I = \frac{3}{2})$, and N $(s = \frac{1}{2}, I = \frac{1}{2})$ to the splitting between ω $(s = 1, I = 0)$ and π $(s = 0, I = 1)$, so that

$$m_\Delta^2 - m_N^2 = m_\omega^2 - m_\pi^2, \tag{37}$$

which is satisfied to within 5%. Our potential model gives a more accurate symmetry breaking

$$\frac{9}{8}(m_\Delta^2 - m_N^2) = m_\omega^2 - m_\pi^2 \tag{38}$$

to within 1%, where the $\frac{8}{9}$ arises from $\frac{1}{2}(\frac{4}{3}\alpha_s)^2 = \frac{8}{9}\alpha_s^2$. For a classification of supergroups including SU(m/n), we refer to the paper by Viktor Kac [14].

3. Conclusions and Future Prospects

Effective Hamiltonians and new mass relations including quark and diquark masses were worked out in our previous works that included the complete understanding of hadronic color algebras as well. In the case of heavy quarks, one can also use the nonrelativistic approximation, so that the potential models for the spectrum of charmonium and the $b\bar{b}$ system can be worked out. In such an approach, gluons can be eliminated leaving quarks interacting through potentials.

It is also possible to take an opposite approach by eliminating quarks as well as gluons, leaving only an effective theory that involves mesons and baryons as

ISSN 2071-0186. Ukr. J. Phys. 2019. Vol. 64, No. 8

collective excitations (solitons) in a way by Skyrme. A Skyrme model that can compete with the potential model is not yet realized.

It is a pleasure to acknowledge helpful conversations with Professors Vladimir Akulov, Cestmir Burdik, and Francesco Iachello.

The work is supported in part by DOE contracts Nos. DE-AC-0276-ER 03074 and 03075; NSF Grant No. DMS-8917754; and several PSC-CUNY research grants.

1. H. Miyazawa. Baryon number changing currents. *Prog. Theor. Phys.* **36**, 1266 (1966); Spinor currents and symmetries of baryons and mesons. *Phys. Rev.* **170**, 1586 (1968).
2. S. Catto, F. Gürsey. New realizations of hadronic supersymmetry. *Nuovo Cimento A* **99**, 685 (1988).
3. S. Catto, F. Gürsey. Algebraic treatment of effective supersymmetry. *Nuovo Cimento A* **86**, 201 (1985).
4. K.N. Wilson. Confinement of quarks. *Phys. Rev. D* **10**, 2445 (1974).
5. R.L. Jaffe. Multiquark hadrons. II. Methods. *Phys. Rev. D* **15**, 281 (1977).
6. S. Catto. Exceptional projective geometries and internal symmetries. ArXiv: Hep-th/0302079.
7. G. 't Hooft. A planar diagram theory for strong interactions. *Nucl. Phys. B* **72**, 461 (1974).
8. K. Johnson, C.B. Thorn. Stringlike solutions of the bag model. *Phys. Rev. D* **13**, 1934 (1976).
9. A. Chodos, R.L. Jaffe, K. Johnson, C.B. Thorn. Baryon structure in the bag theory. *Phys. Rev. D* **10**, 2599 (1974).
10. T. De Grand, R.L. Jaffe, K. Johnson, J. Kiskis. Masses and other parameters of the light hadrons. *Phys. Rev. D* **12**, 2060 (1975).
11. S.W. Otto, J.D. Stark. SU(3) heavy-quark potential with high statistics. *Phys. Rev. Lett.* **52**, 2328 (1984).
12. P. Goddard, J. Goldstone, C. Rebbi, C.B. Thorn. Quantum dynamics of a massless relativistic string. *Nucl. Phys. B* **56**, 109 (1973).
13. A. Chodos *et al.* New extended model of hadrons. *Phys. Rev. D* **9**, 3471 (1974).
14. V.G. Kac. A sketch of Lie superalgebra theory. *Comm. Math. Phys.* **53**, 31 (1977).

Received 08.07.19

С. Катто, І. Гюркан,
Ф. Хальфан, Д. Курт, Б. Ніколеску, Е. Ю

ГАДРОННА СУПЕРСИМЕТРІЯ З КХД

Р е з ю м е

Запропоновано модифікацію масових формул для гадронів, з наголосом на теоретико-груповий опис і суперсиметрію, яка відповідає КХД і базується на кварк-антикварковій симетрії, із подальшими коментарями щодо можливих застосувань до моделей типу Скірма, які в майбутньому можуть конкурувати з потенціальними кварковими моделями.

https://doi.org/10.15407/ujpe64.8.678

V.S. FADIN[1,2]

[1] G.I. Budker Institute of Nuclear Physics of SD RAS
(630090 Novosibirsk Russia; e-mail: fadin@inp.nsk.su)
[2] Novosibirsk State University
(630090 Novosibirsk, Russia; e-mail: fadin@inp.nsk.su)

REGGE CUTS AND NNLLA BFKL

In the leading and next-to-leading logarithmic approximations, QCD amplitudes with gluon quantum numbers in cross-channels and negative signature have the pole form corresponding to a reggeized gluon. The famous BFKL equation was derived using this form. In the next-to-next-to-leading approximation (NNLLA), the pole form is violated by contributions of Regge cuts. We discuss these contributions and their impact on the derivation of the BFKL equation in the NNLLA.
K e y w o r d s: gluon Reggeization, BFKL equation, Regge cuts.

1. Introduction

The equation, which is called now BFKL (Balitskii–Fadin–Kuraev–Lipatov), was first derived in non-Abelian gauge theories with spontaneously broken symmetry [1–3]. Then its applicability to QCD was shown in [4]. The derivation of the equation was based on the Reggeization of gauge bosons in non-Abelian gauge theories (gluons in QCD). The Reggeization determines the high-energy behavior of cross-sections non-decreasing, as the energy increases. In the Regge and multi-Regge kinematics in each order of perturbation theory, dominant (having the largest $\ln s$ degrees) are the amplitudes with gluon quantum numbers and negative signatures in cross-channels. They determine the s-channel discontinuites of amplitudes with the same and all other possible quantum numbers.

It is extremely important that, both in the leading logarithmic approximation (LLA) and in the next-to-leading one (NLLA), the amplitudes used in the unitarity relations are determined by the Regge pole contributions and have a simple factorized form (pole Regge form). Due to this, the Reggeization provides a simple derivation of the BFKL equation in the LLA and in the NLLA. The s-channel discontinuities are presented by Fig. 1 and symbolically can be written as $\Phi_{A'A} \otimes G \otimes \Phi_{B'B}$, where the impact factors $\Phi_{A'A}$ and $\Phi_{B'B}$ describe the transitions $A \to A'$ and $B \to B'$, G is Green's function for two interacting Reggeized gluons, $\hat{\mathcal{G}} = e^{Y\hat{\mathcal{K}}}$, $Y = \ln(s/s_0)$, $\hat{\mathcal{K}}$ is the universal (process-independent) BFKL kernel, which determines the energy dependence of scattering amplitudes and is expressed through the gluon trajectory and the Reggeon vertices. Validity of the pole Regge form is proved now in all orders of perturbation theory in the coupling constant g both in the LLA [5], and in the NLLA (see [6, 7] and references therein).

The first observation of the violation of the pole Regge form was done [8] in the high-energy limit of the results of direct two-loop calculations of the two-loop amplitudes for gg, gq, and qq scattering. Then the terms breaking the pole Regge form in two- and three-loop amplitudes of the elastic scattering were found in [9–11] using the techniques of infrared factorization.

It is worth to say that, in general, the breaking of the pole Regge form is not a surprise. It is well known that Regge poles in the complex angular momenta plane generate Regge cuts. Moreover, in amplitudes with positive signature, the Regge cuts appear already in the LLA. In particular, the BFKL Pomeron is the two-Reggeon cut in the complex angular momenta plane. But, in amplitudes with negative signature due to the signature conservation, a cut must be at least three-Reggeon one and can appear only in the NNLLA. It is natural to expect that the observed violation of the pole Regge form can be explained by their contributions.

Indeed, all known cases of breaking the pole Regge form are now explained by the three-Reggeon cuts

[12, 13]. Unfortunately, the approaches used and the explanations given in these papers are different. Their results coincide in the three-loop approach, but may diverge for more loops. It requires a further investigation.

Here, we consider the contributions of a three-Reggeon cut to the amplitudes of elastic scattering of partons (quarks and gluons) with negative signature up to four loops.

2. Three-Reggeon Cut

Since our Reggeon is the Reggeized gluon, the three-Reggeon cut first contributes to the amplitudes corresponding to the diagrams shown in Fig. 2. In contrast to the Reggeon which contribute only to amplitudes with the adjoint representation of the color group (color octet in QCD) in the t-channel, the cut can contribute to various representations. Possible representations for the quark-quark and quark-gluon scatterings are only singlet (**1**) and octet (**8**), whereas, for the gluon-gluon scattering, there are also **10**, **10***, and **27**. The account for the Bose statistics for gluons, symmetry of the representations **1** and **27**, antisymmetry **10** and **10***, and the existence of both symmetric $\mathbf{8_s}$ and antisymmetric $\mathbf{8_a}$ representations for them, gives that, in addition to the Reggeon channel, the amplitudes with negative signature are in the representations **1** for the quark-quark-scattering and in the representation **10** and **10*** for the gluon-gluon scattering. The amplitude of the process $\mathcal{A}_{AB}^{A'B'}$ depicted by the diagrams in Fig. 2 can be written as the sum over the permutations σ of products of color factors and color-independent matrix elements:

$$\mathcal{A}_{AB}^{A'B'} = \sum_{\sigma} \left(C_{AB}^{(0)\sigma}\right)^{\alpha\beta}_{\alpha'\beta'} M_{AB}^{(0)\sigma}(s,t), \tag{1}$$

where α and β (α' and β') are the color indices of an incoming (outgoing) projectile A and a target B, respectively. We use the same letters for the quark and gluon color indices; it should be remembered, however, that there is no difference between upper and lower indices (running from 1 to N_c^2-1) for gluons, whereas, for quarks, lower and upper indices (running from 1 to N_c) refer to mutually related representations.

The color factors can be decomposed into irreducible representations $\mathcal{R}$ of the color group in the t-channel:

$$\left(C_{AB}^{(0)\sigma}\right)^{\alpha\beta}_{\alpha'\beta'} = \sum_{R} [\mathcal{P}_{AB}^{R}]^{\alpha\beta}_{\alpha'\beta'} \sum_{\sigma} \mathcal{G}(R)_{AB}^{(0)\sigma}, \tag{2}$$

where

$$[\mathcal{P}_{AB}^{R}]^{\alpha\beta}_{\alpha'\beta'} = \sum_{n} [\mathcal{P}_{A}^{R,n}]^{\alpha}{}_{\alpha'} [\mathcal{P}_{B}^{R,n}]^{\beta}{}_{\beta'}, \tag{3}$$

$\hat{\mathcal{P}}^{R,n}$ is the projection operator on the state n in the representation $\mathcal{R}$,

$$\mathcal{G}(R)_{AB}^{(0)\sigma} = \frac{1}{N_R\, T_A\, T_B} \left(\mathcal{T}_A^{c_1}\mathcal{T}_A^{c_2}\mathcal{T}_A^{c_3}\right)^{\alpha'}{}_{\alpha} \times$$
$$\times \left(\mathcal{T}_B^{c_1^\sigma}\mathcal{T}_B^{c_2^\sigma}\mathcal{T}_B^{c_3^\sigma}\right)^{\beta'}{}_{\beta} [\mathcal{P}_{AB}^{R}]^{\alpha\beta}_{\alpha'\beta'}, \tag{4}$$

N_R is the dimension of the representation R, $\mathcal{T}^a$ are the color group generators in the corresponding representations, $[\mathcal{T}^a, \mathcal{T}^b] = i f_{abc}\mathcal{T}^c$; $(\mathcal{T}^a)^{\alpha'}{}_{\alpha} = -i f_{\alpha'\alpha}$ for

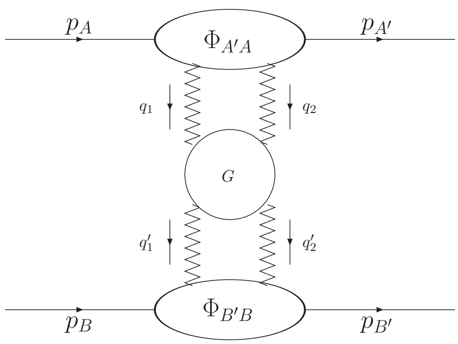

Fig. 1. Schematic representation of the s-channel discontinuities of amplitudes $A + B \to A' + B'$

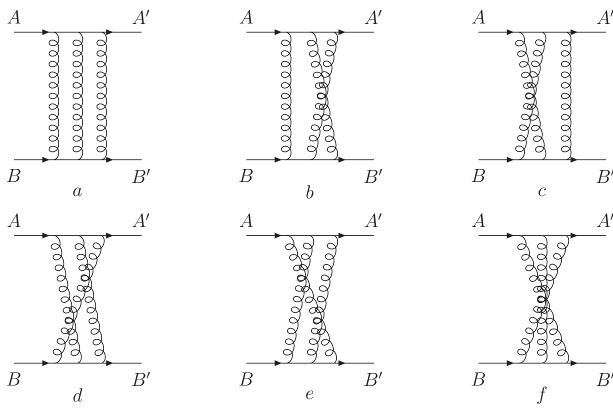

Fig. 2. Feynman diagrams of the process $A + B \to A' + B'$ with three-gluon exchanges

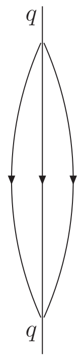

Fig. 3. Schematic representation of $A_2(q_\perp)$

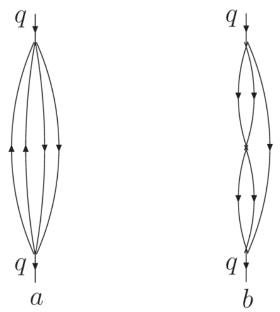

Fig. 4. Schematic representation of $A^a_3(q_\perp)$ and $A^b_3(q_\perp)$

gluons and $(\mathcal{T}^a)^{\alpha'}_{\alpha} = (t^a)^{\alpha'}_{\alpha}$ for quarks; $\mathrm{Tr}(\mathcal{T}^a_i \mathcal{T}^b_i) = T_i\delta_{ab}$, $T_q = 1/2$, $T_g = N_c$.

In [12] the Reggeon channel (R=8) was considered. It was discovered that that the terms violating the pole factorization in $\mathcal{G}(8)^{(0)\sigma}_{AB}$ do not depend on σ (let us call them $\mathcal{G}(8)^{(0)}_{AB}$), so that the momentum-dependent factors for them are summed up to the eikonal amplitude

$$\sum_\sigma M^{(0)\sigma}_{AB} = A^{eik} = g^6 \frac{s}{t}\left(\frac{-4\pi^2}{3}\right)\mathbf{q}^{\,2} A_2(q_\perp), \tag{5}$$

where $A_2(q_\perp)$ is depicted by the diagram presented in Fig. 3 and is written as

$$A_2(q_\perp) = \int \frac{d^{2+2\epsilon}l_1 d^{2+2\epsilon}l_2}{(2\pi)^{2(3+2\epsilon)}\mathbf{l}_1^2\mathbf{l}_2^2(\mathbf{q}-\mathbf{l}_1-\mathbf{l}_2)^2}. \tag{6}$$

Note that we use the "infrared" ϵ, $\epsilon = (D-4)/2$, D is the space-time dimension.

This result is very important, because the contribution of the cut must be gauge-invariant, whereas $M^{(0)\sigma}_{AB}$ taken separately are gauge-dependent.

In [14], other channels with possible cut contributions were considered. It was shown that, for them, the color coefficients $\mathcal{G}(R)^{(0)\sigma}_{AB}$ do not depend on σ,

$$\mathcal{G}(10+\bar{1}0)^{(0)}_{gg} = \frac{-3}{4}N_c, \;\; \mathcal{G}(1)^{(0)}_{qq} = \frac{(N_c^2-4)(N_c^2-1)}{16N_c^3}, \tag{7}$$

so that the momentum-dependent factors for them are also summed up to the eikonal amplitude (5).

The separation of the pole and cut contributions in the octet channel is impossible in the two-loop approximation, because of the ambiguity of the allocation of parts of the amplitudes violating the factorization. The separation becomes possible for higher loops, due to the different energy dependences of the pole and cut contributions. The energy dependence of the pole contribution is determined by the Regge factor of a Reggeized gluon $\exp(\omega(t)\ln s)$, where $\omega(t)$ is the gluon trajectory, whereas, for the three-Reggeon cut, it is

$$e^{[(\hat{\omega}_1+\hat{\omega}_2+\hat{\omega}_3+\hat{\mathcal{K}}_r(1,2)+\hat{\mathcal{K}}_r(1,3)+\hat{\mathcal{K}}_r(2,3))\ln s]}, \tag{8}$$

where $\hat{\mathcal{K}}_r(m,n)$ is the real part of the BFKL kernel describing the interaction between Reggeons m and n.

The calculations of the first logarithmic correction to the cut contribution in the octet channel was performed in [12, 14, 15] and, in the other channels, in [14]. In the latter case, the correction is

$$\mathcal{G}(10+\bar{1}0)^{(0)}_{gg}\; g^6\frac{s}{t}\left(\frac{-4\pi^2}{3}\right)\mathbf{q}^{\,2} g^2 N_c \times$$
$$\times \ln s\left(-\frac{1}{2}A^a_3(q_\perp) - \frac{1}{2}A^b_3(q_\perp)\right), \tag{9}$$

$$\mathcal{G}(1)^{(0)}_{qq}\; g^6\frac{s}{t}\left(\frac{-4\pi^2}{3}\right)\mathbf{q}^{\,2} g^2 N_c \times$$
$$\times \ln s\left(\frac{3}{2}A^a_3(q_\perp) - \frac{3}{2}A^b_3(q_\perp)\right), \tag{10}$$

and in the first case as

$$\mathcal{G}(8)^{(0)}_{AB}\; g^6\frac{s}{t}\left(\frac{-4\pi^2}{3}\right)\mathbf{q}^{\,2} g^2 N_c \times$$
$$\times \ln s\left(\frac{1}{2}A^a_3(q_\perp) - A^b_3(q_\perp)\right), \tag{11}$$

where $A^a_3(q_\perp)$ and $A^b_3(q_\perp)$ are depicted by the diagrams presented in Figs. 4, a and 4, b, respectively,

$$A^a_3(q_\perp) = \int \frac{d^{2+2\epsilon}l_1\, d^{2+2\epsilon}l_2 d^{2+2\epsilon}l_3}{(2\pi)^{3(3+2\epsilon)}\mathbf{l}_1^2\mathbf{l}_2^2\mathbf{l}_3^2(\mathbf{q}-\mathbf{l}_1-\mathbf{l}_2-\mathbf{l}_3)^2}, \tag{12}$$

$$A_3^b(q_\perp) = \\ = \int \frac{d^{2+2\epsilon}l_1\, d^{2+2\epsilon}l_2 d^{2+2\epsilon}l_3(\mathbf{q}-l_1)^2}{(2\pi)^{3(3+2\epsilon)}\mathbf{l}_1^2\mathbf{l}_2^2\mathbf{l}_3^2(\mathbf{q}-\mathbf{l}_1-\mathbf{l}_2)^2(\mathbf{q}-\mathbf{l}_1-\mathbf{l}_3)^2}. \tag{13}$$

It was shown in [12, 14, 15] that the violation of the pole Regge form, analyzed in this approximation in [9]–[11] with the help of the infrared factorization, can be explained by the pole and cut contributions. In other words, the restrictions imposed by the infrared factorization on the parton scattering amplitudes with the adjoint representation of the color group in the t-channel and negative signature can be fulfilled in the NNLLA with two and three loops, if, in addition to the Regge pole contribution, there is the Regge cut contribution. It should be noted that this result is limited to three loops and cannot be considered as a proof that, in the NNLLA, the only singularities in the J plane are the Regge pole and the three-Reggeon cut. Moreover, the explanation of the violation of the pole Regge form given in [13] differs from that described above. In this paper, in addition to the cut with the vertex of interaction with particles i having the color structure

$$(C^{(0)c})^{\alpha}_{\alpha'} = (\mathcal{T}^c)^{\alpha}_{\alpha'}\frac{1}{3!}\ \mathrm{Tr}\sum_\sigma \left(\mathcal{T}_i^{c_1^\sigma}\mathcal{T}_i^{c_2^\sigma}\mathcal{T}_i^{c_3^\sigma}\mathcal{T}_i^{c}\right), \tag{14}$$

the Reggeon-cut mixing is introduced. Actually, in the three-loop approximation, the mixing is not required.

Whether the mixing is necessary can be verified in the four-loop approximation.

The four-loop calculations should answer the questions whether the existence of a pole and a cut is sufficient in this approximation, with or without mixing.

In the four-loop approximation, there are three types of corrections. The first (simplest) ones come from the account for the Regge factors of each of three Reggeons. The second type of the corrections is given by the products of the trajectories and real parts of the BFKL kernels, and the third one comes from the account for Reggeon–Reggeon interactions. All types of corrections are expressed through the integrals over the transverse momentum space corresponding to the diagrams in Fig. 5:

$$I_i = \int \frac{d^{2+2\epsilon}l_1\, d^{2+2\epsilon}l_2\, d^{2+2\epsilon}l_3}{(2\pi)^{3(3+2\epsilon)}\mathbf{l}_1^2\mathbf{l}_2^2\mathbf{l}_3^2} F_i\delta^{2+2\epsilon}(\mathbf{q}-\mathbf{l}_1-\mathbf{l}_2-\mathbf{l}_3), \tag{15}$$

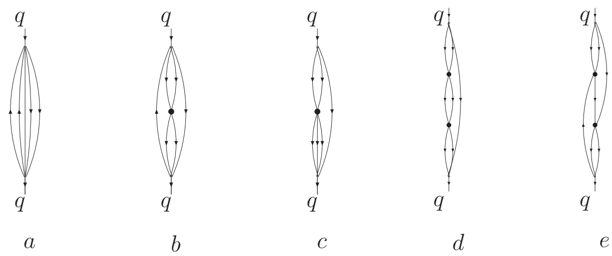

Fig. 5. Four-loop diagrams

$$F_a = f_1(\mathbf{l}_1)f_1(\mathbf{l}_2),\quad F_b = f_1(\mathbf{l}_1)f_1(\mathbf{l}_1),\quad F_c = f_2(\mathbf{l}_1+\mathbf{l}_2),$$
$$F_d = f_1(\mathbf{l}_1+\mathbf{l}_2)f_1(\mathbf{l}_1+\mathbf{l}_2),\quad F_e = f_1(\mathbf{q}-\mathbf{l}_1)f_1(\mathbf{q}-\mathbf{l}_3), \tag{16}$$

$$f_1(\mathbf{k}) = \mathbf{k}^{\,2}\int \frac{d^{2+2\epsilon}l}{(2\pi)^{(3+2\epsilon)}\mathbf{l}^{\,2}(\mathbf{l}-\mathbf{k})^2},$$
$$f_2(\mathbf{k}) = \int \frac{d^{2+2\epsilon}l f_1(\mathbf{l})}{(2\pi)^{(3+2\epsilon)}\mathbf{l}^{\,2}(\mathbf{l}-\mathbf{k})^2}. \tag{17}$$

These integrals enter the total four-loop correction with different color factors in the approaches with or without Reggeon-cut mixing. The question of whether the four-loop amplitudes of the elastic scattering in QCD are given by the Regge pole and cut contributions, with or without mixing, can be solved by comparing these corrections with the result obtained with the use of the infrared factorization.

3. Discussion

The gluon Reggeization is the basis of the BFKL approach. The BFKL equation was derived assuming the pole Regge form of amplitudes with gluon quantum numbers in cross channels and negative signature. It is proved now in all orders of perturbation theory that this form is valid both in the leading and in the next-to-leading logarithmic approximations. However, this form is violated in the NNLLA.

Currently, there are two evidences of the violation. First, it was discovered, using the results of direct calculations of parton (gg, gq and qq) scattering amplitudes in the two-loop approximation, that the non-logarithmic terms (the lowest terms of the NNLLA) do not agree with the pole Regge form of the amplitudes. Second, it was shown using the techniques of infrared factorization that there are single-logarithmic terms with three loops wihich can not be attributed to the Regge pole contribution.

It was shown that the observed violation can be explained by the three-Reggeon cuts [12, 13]. But the assertion that the QCD amplitudes with gluon quantum numbers in cross-channels and negative signature are given in the NNLLA by the contributions of the Regge pole and the three-Reggeon cut is only a hypotheses. Since there is no general proof of it, it should be checked in each order of perturbation theory. In addition, the approaches used and the explanations given in [12] and [13] are different. Their results coincide in the three-loop case but may diverge for more loops.

The calculations of the cut contributions presented here aim to prove this hypothesis in the four-loop case. Unfortunately, direct calculations in that order in the NNLLA do not exist, and there is no hope for that they will be done in the foreseeable future. But it seems possible to obtain the corresponding results using the infrared factorization. The comparison of the results should answer the questions whether the existence of a pole and a cut is sufficient with or without mixing.

Work supported in part by the Ministry of Science and Higher Education of the Russian Federation, in part by RFBR, grant 19-02-00690.

1. V.S. Fadin, E.A. Kuraev, L.N. Lipatov. On the Pomeranchuk singularity in asymptotically free theories. *Phys. Lett. B* **60**, 50 (1975).
2. E.A. Kuraev, L.N. Lipatov, V.S. Fadin. Multi-reggeon processes in the Yang–Mills theory. *Sov. Phys. JETP* **44**, 443 (1976).
3. E.A. Kuraev, L.N. Lipatov, V.S. Fadin. The Pomeranchuk singularity in non-Abelian gauge theories. *Sov. Phys. JETP* **45**, 199 (1977).
4. I.I. Balitsky, L.N. Lipatov. The Pomeranchuk singularity in quantum chromodynamics. *Sov. J. Nucl. Phys.* **28**, 822 (1978).
5. Ya.Ya. Balitskii, L.N. Lipatov, V.S. Fadin. Regge processes in non-Abelian gauge theories. In: *Materials of IV Winter School of LNPI* (1979), p. 109.
6. B.L. Ioffe, V.S. Fadin, L.N. Lipatov. *Quantum Chromodynamics: Perturbative and Nonperturbative Aspects* (Cambridge Univ. Press, 2010).
7. V.S. Fadin, M.G. Kozlov, A.V. Reznichenko. Gluon reggeization in Yang–Mills theories. *Phys. Rev. D.* **92**, 085044 (2015).
8. V. Del Duca, E.W.N. Glover. The high-energy limit of QCD at two loops. *JHEP* **0110** 035 (2001).
9. V. Del Duca, G. Falcioni, L. Magnea, L. Vernazza. High-energy QCD amplitudes at two loops and beyond. *Phys. Lett. B.* **732**, 233 (2014).
10. V. Del Duca, G. Falcioni, L. Magnea, L. Vernazza. Beyond reggeization for two- and three-loop QCD amplitudes. PoS RADCOR **2013**, 046 (2013).
11. V. Del Duca, G. Falcioni, L. Magnea, L. Vernazza. Analyzing high-energy factorization beyond next-to-leading logarithmic accuracy. *JHEP* **1502**, 029 (2015).
12. V.S. Fadin. Particularities of the NNLLA BFKL. *AIP Conf. Proc.* **1819**, 060003 (2017).
13. S. Caron-Huot, E. Gardi, L. Vernazza. Two-parton scattering in the high-energy limit. *JHEP* **1706**, 016 (2017).
14. V.S. Fadin. Violation of a simple factorized form of QCD amplitudes and Regge cuts. *PoS DIS* **2017**, 042 (2018).
15. V.S. Fadin, L.N. Lipatov. Reggeon cuts in QCD amplitudes with negative signature. *Eur. Phys. J. C* **78**, 439 (2018).

Received 08.07.19

В.С. Фадін

РЕДЖЕВСЬКІ РОЗРІЗИ
І BFKL У НАБЛИЖЕННІ NNLLA

Р е з ю м е

У головному та наступному логарифмічному наближеннях КХД амплітуди з глюонними квантовими числами в крос-каналі та від'ємною сигнатурою мають полюсну форму, яка відповідає реджезованому глюону. За допомогою цієї форми виводиться знамените рівняння BFKL. В наближенні NNLLA полюсна форма порушена внесками реджевських розрізів. Ми обговорюємо ці внески та їх вплив на отримання рівняння BFKL у наближенні NNLLA.

https://doi.org/10.15407/ujpe64.8.683

I. GKIGKITZIS,[1] I. HARANAS,[2] E. CAVAN[2]

[1] NOVA, Department of Mathematics
(8333 Little River Turnpike, Annandale, VA 22003, USA; e-mail: igkigkitzis@nvcc.edu)
[2] Wilfrid Laurier University
(Waterloo, ON, Canada; e-mail: iharanas@wlu.ca, cava0920@mylaurier.ca)

BLACK HOLE TORSION EFFECT AND ITS RELATION TO INFORMATION

In order to study the effects of the torsion on the gravitation in space-time and its relation to information, we use the Schwarzschild metric, where the torsion is naturally introduced through the spin particle density. In the black hole scenario, we derive an analytic solution for the black hole gravitational radius with the spin included. Then we calculate its entropy in the cases of parallel and antiparallel spins. Moreover, four analytical solutions for the spin density as a function of the number of information are found. Using these solutions in the case of parallel spin, we obtain expressions for the Ricci scalar as a function of the information number N, and the cosmological constant λ is also revealed.

Keywords: gravitation, quantization, torsion, spin, black holes.

1. Introduction

A natural way to talk about spin effects in gravitation is through torsion. Its introduction becomes significant for the understanding of the last stage in the black hole evaporation. It could be the case of an evaporating black hole of mass M_H that disappears via an explosion burst, which can last for the time $t_p = 10^{-44}$ s, when it reaches a mass of the order of Planck's mass

$$m_p = \sqrt{\frac{\hbar c}{G}} = 10^{-15} \text{ s.} \tag{1}$$

If this happens, there might be three distinct possibilities for the fate of the evaporating black hole [3]: The black hole may evaporate completely leaving no residue, in which case it would give rise to a serious problem of quantum consistency. If the final state of evaporation leaves a naked singularity behind, then it might violate the cosmic censorship at the quantum level. If a stable remnant of the residue with approximately Planck's mass remains, the emission process might stop.

If somebody tries to quantize the gravitational field, he must know that the quantization has to be directed with the unique structure of the space-time itself. The quantization will also imply that somebody might try to discretize the space and, probably, the time. Progress in this direction will also be related to the introduction of a spin in the theory of general relativity. The general relativity (GR) is the simplest theory of gravity which agrees with all present-day data. A major recent success is the detection of the lensed emission near the event horizon in the center of M-87 supergiant elliptic galaxy in the constellation Virgo. All the data obtained are consistent with the presence of a central Kerr black hole, as predicted by the general theory of relativity [1]. Somebody might want to formulate a generalized theory of general relativity to compare GR with various theories that explain other physical interactions. As an example, we say that the electromagnetic forces, strong interactions, and weak interactions are described with the help of quantum relativistic fields interacting in a flat Minkowski space. Furthermore, the fields that represent the interactions are defined over the space-time. But, at the same time, they are distinguished from the space-time which, we must say, is not affected by them. On the other hand, the gravitational interactions can modify the space-time geometry, but they are not represented by a new field. They are just represented by their effect on the geometry of the space itself. Thus, we can say that most parts of the modern physics are successful in being described in a flat rigid space-time geometry. But a small fraction of the remaining physics, i.e., macroscopic gravitational physics, requires the use of a curved dynamical geometric background. To overcome this difficulty, somebody might try to extend the geometric principles of GR into microphysics in order to establish a direct comparison and possibly some connection between gravity and other interactions. In GR theory, the matter is represented by the energy-momentum tensor, which essentially gives description of the mass density distribution in space-time. Therefore, the idea of mass-energy in GR is enough to define the properties of classical macroscopic bodies.

Looking at the microscopic level, we know that the matter is composed of elementary particles that obey the laws of special relativity and quantum mechanics. Each particle is characterized not only by its mass, but also by a spin measured in units of $\hbar$. At the microscopic level, the mass and the spin are two independent quantities. The mass distributions in space-time are described by the energy-momentum tensor, whereas the spin distribution is described, in field theory, by the spin density tensor. Inside any microscopic body, the spins of elementary particles are, in general, randomly oriented with the total average spin equal to zero. Therefore, the spin density tensor of a macroscopic body is zero. This explains why the energy-momentum tensor is adequate to dynamically characterize a macroscopic matter. Thus, the gravitational interactions can be sufficiently described by the Riemannian geometry. Another point that should be stressed is that the spin density tensor represents the intrinsic angular momentum of particles, and not the classical orbital angular momentum due to the macroscopic rotation. A fundamental difference is that the latter can be eliminated by an appropriate coordinate transformation. On the other hand, the spin density can be eliminated at a point only. The spin density tensor is a non-vanishing quantity, if the spins inside a body are oriented at least partially along a preferred direction and, at the same time, are not affected by the rotation of the macroscopic body. At the macroscopic level, the energy-momentum tensor is not enough to characterize the dynamics of the matter sources, because the spin density tensor is also needed, unless we are considering scalar fields that correspond to spineless particles. In the case where GR must be extended to include microphysics, the matter must be considered and described, by using the mass and the spin density. On the other hand, the mass is related to a curvature in a generalized theory of GR, and the spin should be related to the spin density tensor or, probably, to a different property of the space-time. The geometric property of the space-time in relation to spin in the U4 theory is the torsion.

The torsion, thus, can be described by the antisymmetric part of Christoffel symbols of the second kind. Therefore, the torsion tensor reads [5]:

$$Q^{\mu}_{\nu\lambda} = \frac{1}{2}\left(\Gamma^{\mu}_{\nu\lambda} - \Gamma^{\mu}_{\lambda\nu}\right) = \Gamma^{\mu}_{[\nu\lambda]}. \tag{2}$$

The torsion is characterized by a third-rank tensor that is antisymmetric in the first two indices and has 24 independent components. If the torsion does not vanish, the affine connection is not coincident with the Christoffel connection. Therefore, the geometry is not any longer the Riemannian, but rather Riemann–Cartan space-time with a non-symmetric connection. To introduce the torsion simply represents a very natural way of modifying GR. The relation of the torsion and the spin allows one to modify the GR theory and Riemannian geometry resulting in a more natural and complete description of the matter at the microscopical level as well. Finally, the early Universe is the place, where GR must be applied together with quantum theory. On the other hand, GR is a classical field theory. So far, the quantization of the gravity has been a problem in our effort to develop a consistent and coherent theory in understanding the physics of the early Universe.

In the presence of a torsion, the space-time is called a Riemann–Cartan manifold and is denoted by U4. When the torsion is taken into consideration, one can define distances in the following way. Supposing that we consider a small close circuit, we can write [5] the non-closure property given by the integral:

$$\ell^{\mu} = \oint Q^{\mu}_{\nu\lambda} dx^{\nu} \wedge dx^{\mu} \neq 0, \tag{3}$$

where $dx^{\nu}dx^{\mu}$ is the area element enclosed by the loop, ι^{μ} represents the so-called closure failure, and the torsion tensor $Q^{\mu}_{\nu\lambda}$ is a true tensorial quantity. In other words, the geometric meaning of the torsion can be represented by the failure of the loop closure. It has now the dimension of length, andn the torsion tensor itself has the dimension of L^{-1} .

2. Quantum Gravity and Torsion

The inclusion of the torsion into GR might constitute a way to the quantization of gravity, by considering the effect of the spin and connecting the torsion to the defects in the topology of space-time. For that, we can define a minimal unit of length l, as well as a minimal unit of time t. In GR and quantum field theory, there are now, indeed, difficulties due to the existence of infinities and singularities. One of the reasons is the consideration of point mass particles, which results in the divergence of the energy integrals going to infinity. In the case of collapsing bodies in GR, we have singularities. All these difficulties can disappear, if, together with the introduction of a torsion, we introduce the minimal time and length or, in other words, if we consider a discretized space-time. If we want to quantize the gravity, we cannot exactly follow the same procedure of quantization used in other fields. Indeed, the gravity is not a force, but the curvature and torsion of the space-time. The inclusion of the torsion in the space-time gives rise to space-time topology defects. The problem may be avoided, if the torsion is included. In this case, the asymmetric part of the connection $\Gamma^{\mu}_{[\nu\lambda]}$ or, in other words, the torsion tensor $Q^{\mu}_{\nu\lambda}$ is a true tensorial quantity. Since the torsion is related to the intrinsic spin, we see that the intrinsic spin $\hbar$ and, hence, the spin are quantized. We can conclude that the space-time defect in topology should occur in multiples of Planck's length $l_p = \sqrt{\frac{G\hbar}{c^3}}$. In other words, we can write [5]

$$\oint Q^{\mu}_{\nu\lambda} dx^{\nu} \wedge dx^{\lambda} = n\sqrt{\frac{\hbar G}{c^3}} n^{\mu}, \tag{4}$$

where n is an integer, and n^{μ} is a unit point vector. This is a relation analogous to the Bohr–Sommerfeld relation in quantum mechanics. The torsion tensor $Q^{\mu}_{\nu\lambda}$ plays the role of a field strength, which is analogous to that of the electromagnetic field tensor $F_{\mu\nu}$. Equation (4) defines the minimal fundamental length, a minimal length that enters the picture through the unit of action $\hbar$. In other words, $\hbar$ represents the intrinsic defect that is built in the torsion structure of space-time, in quantized units of $\hbar$ related to a quantized time like-vector with the dimension of length. This vector is related to the intrinsic geometric structure, when the torsion is considered. The intrinsic spin in units of $\hbar$ characterizes all the matter, and, therefore, the torsion is now entering the geometry. Thus, the Einstein–Cartan theory of gravitation can provide the corresponding quantum gravity effects. At the same time, we can also define the time at the quantum geometric level again through the torsion according to the equation:

$$t = \frac{1}{c}\oint Q^{\mu}_{\nu\lambda} dx^{\nu} \wedge dx^{\lambda} = n\sqrt{\frac{\hbar G}{c^5}}. \tag{5}$$

So, when the torsion is included, it is important that a minimal time interval given by Eq. (5) exists and is different from zero. This is the smallest unit of time $t_p = 5.391 \times 10^{-44}$ s. In the limit as $\hbar \to 0$, we recover the classical geometry of GR and, if $c \to \infty$, the Newtonian case. Finally, the geodesic equations in the case of a nonzero spin turn to

$$\frac{d^2x^{\mu}}{dp^2} + \Gamma^{\mu}_{\nu\lambda}\frac{dx^{\mu}}{dp}\frac{dx^{\nu}}{dp} = -2Q^{\mu}_{\nu\lambda}\frac{dx^{\nu}}{dp}\frac{dx^{\lambda}}{dp}, \tag{6}$$

where p is an affine parameter. To understand the spin effects in gravitation, we can use the torsion. Consequently, let us first write a Schwarzschild metric that includes torsion effects [4]:

$$ds^2 = c^2\left(1 - \frac{2GM}{c^2r} \pm \frac{3G^2s^2}{2r^4c^6}\right)dt^2 - \\ - \left(1 - \frac{2GM}{c^2r} \pm \frac{3G^2s^2}{2r^4c^6}\right)^{-1} dr^2 - r^2\left(d\theta^2 + \sin^2\theta d\phi^2\right), \tag{7}$$

where s is the torsion. We can write $s = \sigma r^3$, where σ is the spin density [4]. So, the Schwarzschild metric is modified by the inclusion of torsion effects. The torsion gives a natural way to understand the spin effects in gravitation. Making use of an expression that relates the torsion to the spin density, we can eliminate s and include σ in Eq. (7). Our primary goal is to establish a possible relation between the spin density σ and the information number N and between the Ricci scalar, as derived from Eq. (7), and information. This is an effort to understand why information plays an important role in the space-time structure in the case wherethe torsion effects are included in gravitation.

3. Analysis

Consider the case of a Schwarzschild metric with the torsion. Substituting $s = \sigma r^3$ [4], we get the gravitational radius:

$$\left(1 - \frac{2GM}{c^2 r} \pm \frac{3G^2\sigma^2}{2c^6} r^2\right) = 0. \tag{8}$$

In the case of a spin parallel to the gravitation (plus sign), we have

$$\left(1 - \frac{2GM}{c^2 r} + \frac{3G^2\sigma^2}{2c^6} r^2\right) = 0. \tag{9}$$

From whence, we obtain

$$r_{H_{\uparrow\downarrow}} = \frac{1}{3}\big[-\big(2^{2/3}c^6\big)/\big(\big(9c^4G^5M\sigma^4 + \\ + \sqrt{c^8G^6\sigma^6\left(2c^{10} + 81G^4M^2\sigma^2\right)}\big)^{1/3}\big)\big] \pm \\ \pm \frac{1}{3}\big[\big(2^{1/3}\big(9c^4G^5M\sigma^4 + \\ + \sqrt{c^8G^6\sigma^6(2c^{10} + 81G^4M^2\sigma^2)}^{1/3}\big)\big)/\big(G^2\sigma^2\big)\big], \tag{10}$$

where the plus sign in Eq. (10) corresponds to the plus sign of the second term in Eq. (8). The negative sign in Eq. (10) corresponds to the negative sign in the second term of Eq. (8). In other words, we deal with parallel and antiparallel spins. Let us write the entropy formula as [6]

$$S = \frac{k_{\rm B}}{4\ell_p^2} A_H, \tag{11}$$

where k_B is the Boltzmann constant, $l_p^2 = \frac{G\hbar}{c^3}$ is Planck's length, and A_H is horizon area [2]. This is the Bekenstein–Hawking area-entropy law. This is a macroscopic formula, and it should be viewed in the same light as the classical macroscopic thermodynamic formulae. It describes how the properties of event horizons in general relativity change as their parameters are varied. Substituting Eq. (10) in Eq. (12), we obtain

$$S = \frac{\pi k_{\rm B}}{\ell_p^2}(r_{H_{\uparrow\downarrow}})^2 = \\ = \frac{\pi k_{\rm B}}{\ell_p^2}\left[\frac{1}{3}\left[-\left(2^{2/3}c^6\right)/\left(\left(9c^4G^5M\sigma^4 + \\ + \sqrt{c^8G^6\sigma^6\left(2c^{10} + 81G^4M^2\sigma^2\right)}\right)^{1/3}\right) \pm \\ \pm \left(2^{1/3}\left(9c^4G^5M\sigma^4 + \\ + \sqrt{c^8G^6\sigma^6(2c^{10} + 81G^4M^2\sigma^2)}\right)^{1/3}\right)/(G^2\sigma^2)\right]\right]^2, \tag{12}$$

where the minus sign in the root stands for the parallel torsion and plus stands for the antiparallel one. We note that the information number in nats is given by [8]

$$N = \frac{S}{k_{\rm B}\ln 2}. \tag{13}$$

Using the positive sign, equating Eqs. (12) and (13), and solving for the spin density as a function of information in nat N, we obtain the following solutions:

$$\sigma_{1_\uparrow} = \sigma_{2_\uparrow} = \pm i\left(\frac{4c^4M}{G\ell_p^3N^{\frac{3}{2}}}\left(\frac{\pi}{\ln 2}\right)^{3/2} + \frac{\pi c^6}{G\ell_p^2 N\ln 2}\right)^{1/2}, \tag{14}$$

$$\sigma_{3_\uparrow} = \sigma_{4_\uparrow} = \pm i\left(\frac{4c^4M}{G\ell_p^3N^{\frac{3}{2}}}\left(\frac{\pi}{\ln 2}\right)^{3/2} - \frac{\pi c^6}{G\ell_p^2 N\ln 2}\right)^{1/2}. \tag{15}$$

Similarly, the negative sign (or antiparallel spin) gives the only real solution:

$$\sigma_{1_\downarrow} = \left[\frac{8\pi^3c^8M^2}{3G^2\ell_p^6\left(\Phi_0 + \frac{6\sqrt{\Gamma_0}}{G^5\ell_p^9}\right)^{1/3}} + \frac{2\left(\Phi_0 + \frac{6\sqrt{\Gamma_0}}{G^5\ell_p^9}\right)^{1/3}}{9N^3\ln 2^3} + \\ + \frac{4\pi c^6}{9G^2\ell_p^2N\ln 2} + \frac{2\pi^2c^{12}N\ln 2}{9G^4\ell_p^6(\Phi_0 + \frac{6\sqrt{\Gamma_0}}{G^5\ell_p^9})^{1/3}}\right]^{1/2}, \tag{16}$$

where the quantities Γ_0 and Φ_0 are defined as follows:

$$\Gamma_0 = -48\pi^9c^{24}\ln 2^9M^6N^9 + \\ + 24\pi^8c^{28}G^2\ell_p^2M^4\ln 2^{10}N^{10} + \\ + \pi^7c^{32}\ell_p^4M^2N^{11}\ln 2^{11}, \tag{17}$$

$$\Phi_0 = \frac{36\pi^4c^{14}M^2N^5\ln 2^5}{G^4\ell_p^8} + \frac{\pi^3c^{18}N^6\ln 2^6}{G^6\ell_p^6}. \tag{18}$$

4. Calculation of the Ricci Scalar and Its Relation to Information

Next, we are going to calculate the Ricci scalar in the cases of parallel and antiparallel spins. So, we define the metric coefficients to be

$$A(r) = c^2\left[1 - \frac{2GM}{rc^2} \pm \frac{3G^2\sigma^2}{2c^6}r^2\right], \tag{19}$$

and

$$B(r) = \left[1 - \frac{2GM}{rc^2} \pm \frac{3G^2\sigma^2}{2c^6} r^2\right]^{-1}. \quad (20)$$

The correspondent Ricci scalar is given by [9]

$$R = -\frac{2}{r^2 B(r)}\left[1 - B(r) + \frac{r^2 A''(r)}{2A(r)} + \right.$$

$$\left. + \frac{A'(r)}{A(r)}\left(r - \frac{r^2 A'(r)}{4A(r)}\right) - \frac{B'(r)}{B(r)}\left(r + \frac{r^2 A'(r)}{4A(r)}\right)\right]. \quad (21)$$

In the case of the torsion parallel to the gravity, we get

$$R = -\frac{18G^2\sigma^2}{c^6} = -\frac{9}{2}\left(\frac{R_{\rm Sch}}{M}\right)^2 \left(\frac{\sigma}{c}\right)^2. \quad (22)$$

Similarly, in the case of the torsion antiparallel to the gravity, we obtain

$$R = \frac{18G^2\sigma^2}{c^6} = \frac{9}{2}\left(\frac{R_{\rm Sch}}{M}\right)^2 \left(\frac{\sigma}{c}\right)^2. \quad (23)$$

Next, we proceed in writing the Ricci scalar as a function of the information number in nats N. In this calculation, we will only deal with a parallel spin. Therefore, we use Eqs. (22) and (15) and obtain

$$R\left(\sigma_1/\sigma_2\right)_\uparrow =$$

$$= \frac{18G^2}{c^6}\left[\left(\frac{\pi}{\ln 2}\right)^{3/2} \frac{4c^4 M}{3G\ell_p^3 N^{3/2}} + \frac{2\pi c^6}{3G^2\ell_p^2 N \ln 2}\right]^2, \quad (24)$$

$$R\left(\sigma_3/\sigma_4\right)_\uparrow =$$

$$= -\frac{18G^2}{c^6}\left[\left(\frac{\pi}{\ln 2}\right)^{3/2} \frac{4c^4 M}{3G\ell_p^3 N^{\frac{3}{2}}} - \frac{2\pi c^6}{3G^2\ell_p^2 N \ln 2}\right]^2, \quad (25)$$

which simplifies to

$$R\left(\sigma_1/\sigma_2\right)_\uparrow = 12\left(\frac{\pi}{\ln 2}\right)^{3/2}\left(\frac{R_{\rm Sch}}{\ell_p^3 N^{\frac{3}{2}}}\right) + \frac{12\pi}{N\ell_p^2 \ln 2}, \quad (26)$$

$$R\left(\sigma_3/\sigma_4\right)_\uparrow = 12\left(\frac{\pi}{\ln 2}\right)^{3/2}\left(\frac{R_{\rm Sch}}{\ell_p^3 N^{\frac{3}{2}}}\right) + \frac{12\pi}{N\ell_p^2 \ln 2}. \quad (27)$$

With reference to [6] and [7], we note that

$$\Lambda = \frac{3\pi}{N\ell_p^2 \ln 2}. \quad (28)$$

Equation (28) gives the cosmological constant as a function of the information number N. Therefore, Eqs. (26) and (27) for the Ricci scalar become

$$R\left(\sigma_1/\sigma_2\right)_\uparrow = 12\left(\frac{\pi}{\ln 2}\right)^{3/2}\left(\frac{R_{\rm Sch}}{\ell_p^3 N^{3/2}}\right) + 4\Lambda, \quad (29)$$

$$R\left(\sigma_3/\sigma_4\right)_\uparrow = 12\left(\frac{\pi}{\ln 2}\right)^{3/2}\left(\frac{R_{\rm Sch}}{\ell_p^3 N^{3/2}}\right) + 4\Lambda. \quad (30)$$

5. Conclusion

We have examined the effect of a torsion in the Schwarzschild metric corrected for torsion effects and its relation to information. In this case, the torsion effects can be represented by the spin density. We start by calculating the entropy at the horizon of such a black hole, and then we equate the entropy to a known expression that gives the entropy in terms of the information number N. Thus, we obtain analytical expressions for the spin density as a function of the information number N. We obtain two spin density solutions. One of them is real, and another one is imaginary. Moreover, we have found that, for the spin density, both real and imaginary roots scale proportionally to the information number N according to the relation $\sigma \propto \frac{1}{N^{\frac{3}{2}}} - \frac{1}{N}$. In the case of parallel spin, we find that Ricci scalar also depends on the information number according to the relation $R \propto N^{\frac{3}{2}} + N^{-1}$ for both parallel and antiparallel spins. This comes from an extra term that is equal to the cosmological constant λ expressed as a function of the information number N adds the information dependence to the Ricci scalar via the cosmological constant λ. In this aspect, we can perceive the cosmological constant as a cosmological depository of information that affects the space-time structure or is included as an important parameter in the space-time structure and in the geometry of the Universe. Therefore, we conclude that information enters this torsion-corrected metric via the dependence of the spin density on the information number N, as well as the cosmological constant itself.

1. K. Akiyama *et al*. First M 87 event horizon telescope results. I. The shadow of the supermassive black hole. *Astrophys. J. Lett.* **875**, L1 (2019).
2. J.D. Bekenstein . Black holes and entropy. *Phys. Rev. D* **7**, 2333 (1973).
3. V. De Sabbata, D. Wang, C. Sivaram. Torsion effects in black hole evaporation. *Ann. Phys.* **47**, 508 (1990).

4. *Black Hole Physics.* Edited by V. De Sabbata, Z. Zhang (Kluwer Academic, 1992).
5. *The Early Universe*, edited by V.B. Johri (Hadronic Press, 1996).
6. I. Haranas, I. Gkigkitzis. The number of information bits related to the minimum quantum and gravitational masses in a vacuum dominated universe. *Astrophys. Space-Sci.* **346**, No. 1, 213 (2013).
7. I. Haranas, I. Gkigkitzis. Bekenstein bound of information number N and its relation to cosmological parameters in a universe with and without cosmological constant. *Modern Phys. Lett. A* **28**, No.19, Article ID1350077 (2013).
8. S. Lloyd. *Ultimate physical limits to computation. Nature* **406**, 1047 31 (2000).
9. M. Sharif, H. Kausar, R. *Dust Static Spherically Symmetric Solution in f(R) Gravity,*, arXiv:1102.4124v1 [physics.gen-ph] (2011).

Received 08.07.19

Й. Ґікіціс, Й. Харанас, Е. Praванз

ЕФЕКТ КРУЧЕННЯ ЧОРНОЇ ДІРИ
ТА ЇЇ ВІДНОШЕННЯ ДО ІНФОРМАЦІЇ

Р е з ю м е

Для вивчення впливу кручення на гравітацію в просторі-часі та його відношення до інформації ми користуємося метрикою Шварцшільда, де кручення природно вводиться через спінову щільність частинки. В сценарії чорної діри ми отримали аналітичний розв'язок для гравітаційного радіуса чорної діри з включенням спіну, звідки ми обчислили ентропію для випадків паралельних та антипаралельних спінів. Більше того, ми знайшли чотири аналітичні розв'язки для спінової щільності в залежності від числа інформації. Користуючись цими розв'язками, ми отримали вирази для коефіцієнтів Річчі як функції числа інформації N; отримано також значення для космологічної константи.

https://doi.org/10.15407/ujpe64.8.689

V.M. GORKAVENKO

Taras Shevchenko National University of Kyiv, Ukraine
(64, Volodymyrs'ka Str., Kyiv 01601, Ukraine; e-mail: gorkavol@gmail.com)

SEARCH FOR HIDDEN PARTICLES IN INTENSITY FRONTIER EXPERIMENT SHiP

*Despite the undeniable success of the Standard Model of particle physics (SM), there are some phenomena (neutrino oscillations, baryon asymmetry of the Universe, dark matter, etc.) that SM cannot explain. This phenomena indicate that the SM have to be modified. Most likely, there are new particles beyond the SM. There are many experiments to search for new physics that can be can divided into two types: energy and intensity frontiers. In experiments of the first type, one tries to directly produce and detect new heavy particles. In experiments of the second type, one tries to directly produce and detect new light particles that feebly interact with SM particles. The future intensity frontier SHiP experiment (**S**earch for **Hi**dden **P**articles) at the CERN SPS is discussed. Its advantages and technical characteristics are given.*

K e y w o r d s: physics beyond the Standard Model, hidden particles, hidden sectors, renormalizable portals, intensity frontier experiment, SHiP, SPS.

1. Introduction

The Standard Model of particle physics (SM) [1–3] was developed in the mid-1970s. It is one of the greatest successes of physics. It is experimentally tested with high precision for the processes of electroweak and strong interactions with the participation of elementary particles up to the energy scale ~100 GeV and for individual processes up to several TeV. It predicted a number of particles, last of them (Higgs boson) has been observed in 2012. However, the SM cannot explain several phenomena in particle physics, astrophysics, and cosmology. Namely: the SM does not provide the dark matter candidate; the SM does not explain neutrino oscillations and the baryon asymmetry of the Universe; the SM cannot solve the strong CP problem in particle physics, the primordial perturbations problem and the horizon problem in cosmology, *etc.*

The presence of the problems in the SM indicates the incompleteness of the Standard Model and the existence of as yet "hidden" sectors with particles of a new physics. Although it may seem surprising, but some of the above-mentioned SM problems really can be solved with help either heavy or light new particles. Neutrino oscillations and the smallness of the active neutrino mass can be explained as with help of a new particle with sub-eV mass, as well as with help of heavy particles of the GUT scale, see, e.g., [4]. The same can be said about the problem of baryon asymmetry of the Universe and dark matter problem: physics on the very different scales can be responsible for it, see, e.g., [5].

Can the new light particles exist in the SM extensions? The answer is positive. There are many theories beyond SM that have light particles in the spectrum (e.g., GUT, SUSY, theories with extra dimensions), see, e.g., [6]. Light particles in those theories can be, e.g., (pseudo)-Goldstone bosons that were produced as a result of the spontaneous breaking of some not exact symmetry. Alternatively, a particle can be massless at the tree level, but it can obtain a light mass as a result of loops-involving corrections.

So, two answers on the question "why do we not observe particles of the new physics?" are possible. First, the new particles can be very heavy (e.g., with the mass $M_X \gtrsim 100$ TeV), so they cannot be directly produced at the present-day powerful accelerators like LHC. On other hand, the new particles can be light (with mass below or of order of the electroweak scale) and can feebly interact with particles of the SM (otherwise, we would have already seen them in the experiments). In this case, the light new particles can be produced at many high-energy experiments, but it were not still observed due to the

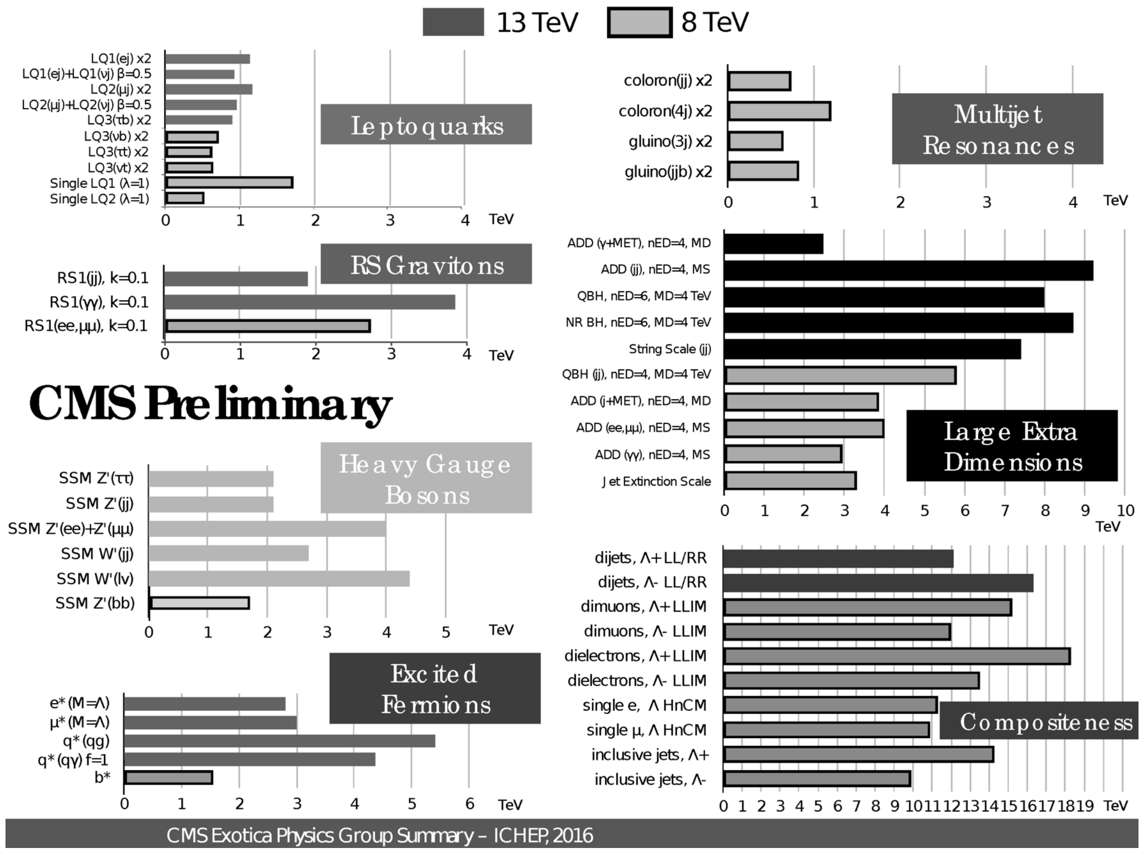

Fig. 1. Search for new particles beyond SM with mass at the TeV region at CERN CMS

extreme rarity of events with their production and to the complexity of their detection.

Based on the above, there are two types of particle search experiments.

First of them is energy frontier experiments like those at LHC or Fermilab. In these experiments, one tries to directly produce and detect new heavy particles assuming that the coupling of new particles to the SM particles is not very small. The new particles with mass of several TeV are actively searched in such experiments, see Fig. 1. Last decades, a lot of attention were paid to the energy frontier experiments.

Second of them is intensity frontier experiments. In this experiments, we try to search for the particles that feebly interact with the SM particles. So, in the intensity frontier experiments, we search for very rare events. For the successful production of hidden particles (to compensate their feeble interaction), those experiments must have the largest possible luminosity. In this sense, the beam-dump experiments are good as the intensity frontier experiments to seek the GeV-scale hidden particles, because of their luminosities is several orders of magnitude larger than those at colliders. The detection of hidden particles is possible only due to observing their decays into the SM particles. So, these experiments must be background-free. Because of the feeble interaction with the SM particles, one can expect their small decay width and long lifetime (here, we suppose that a hidden particle does not decay in non-SM channels, or the corresponding partial decay width is very small). So, the detector have to be placed as far as possible from the point of the production of hidden particles.

The intensity frontier experiments have been paid much less attention in the recent years. These experiments include PS 191 (early 1980s), CHARM (1980s), NuTeV (1990s), DONUT (late 1990s – early 2000). However, as was shown in [7, 9], the search for the new physics in the region of masses below the electroweak scale is not sufficiently investigated.

The difference between the energy and intensity frontier experiments for seeking the hidden particles can be schematically illustrated with the help of Fig. 2.

In this paper, we consider the future intensity frontier SHiP (**S**earch for **Hi**dden **P**articles) beam-dump experiment at the CERN Super Proton Synchrotron (SPS) accelerator. Its advantages and technical characteristics will be considered, and the class of theories that can be tested on SHiP will be discussed.

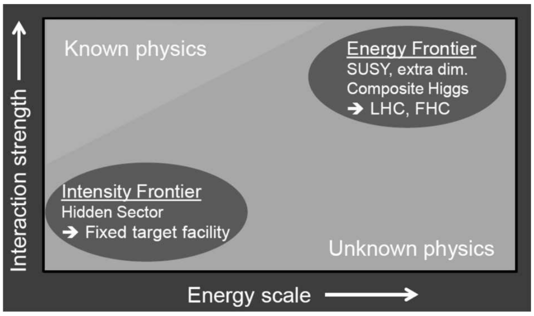

Fig. 2. Different strategies for the search for hidden particles in the energy and intensity frontier experiments

2. Interaction of New Particles with the SM Particles. Portals

If we will focused on detecting a new light particle, we have understand that this particle can originate from the large number of beyond-SM theories that predict different parameters for it (masses of new particles and their coupling to the SM particles). In particular, such relatively light particles can be mediators due to the interaction with particles of the SM and very heavy particles of "hidden sectors". Those light particles can be coupled to the Standard Model sectors either via renormalizable interactions with small dimensionless couplings ("portals") or by higher-dimensional operators suppressed by the dimensionful couplings Λ^{-n} corresponding to a new energy scale of the hidden sector [7].

Because of a limited number of possible types of particles (scalar, pseudoscalar, vector, pseudovector, fermion), there is limited number of possible effective Lagrangians of interaction of such particles with the SM particles that satisfy the Lorentz conditions and gauge invariance ones.

Renormalizable portals can be classified into the following 3 types:

Vector portal: new particles are vector Abelian fields (A'_μ) with the field strength $F'_{\mu\nu}$ that couple to the hypercharge field $F_Y^{\mu\nu}$ of the SM as

$$\mathcal{L}_{\text{Vectorportal}} = \epsilon F'_{\mu\nu} F_Y^{\mu\nu}, \tag{1}$$

where ϵ is a dimensionless coupling characterising the mixing between a new vector field with the fields of Z-bosons and photons.

Scalar portal: new particles are neutral singlet scalars, S_i, that couple to the Higgs field

$$\mathcal{L}_{\text{Scalarportal}} = (\lambda_i S_i + g_i S_i^2)(H^\dagger H), \tag{2}$$

where λ_i are dimensionless couplings, and g_i are the couplings with a dimension of mass.

Neutrino portal: new particles are neutral singlet fermions N_I

$$\mathcal{L}_{\text{Neutrinoportal}} = F_{\alpha I} \bar{L}_\alpha \tilde{H} N_I, \tag{3}$$

where index $\alpha = e, \mu, \tau$ corresponds to the lepton flavors, L_α is for the lepton doublet, $F_{\alpha I}$ is for the new matrix of the Yukawa constants, and $\tilde{H} = i\sigma_2 H^*$.

Non-renormalizable couplings of new particles to the SM operators are also possible. For example, pseudo-scalar axion-like particles A couple to SM as

$$\mathcal{L}_{\text{A}} = \sum_f \frac{C_{Af}}{2\, f_a} \bar{f} \gamma^\mu \gamma^5 f\, \partial_\mu A -$$
$$- \frac{\alpha}{8\pi} \frac{C_{A\gamma}}{f_a} F_{\mu\nu} \tilde{F}^{\mu\nu} A - \frac{\alpha_3}{8\pi} \frac{C_{A3}}{f_a} G^b_{\mu\nu} \tilde{G}^{b\,\mu\nu} A, \tag{4}$$

where $f = \{\text{quarks, leptons, neutrinos}\}$, $F_{\mu\nu}$ is the electromagnetic field strength tensor, $G^b_{\mu\nu}$ the field strength for a strong force, and the dual field strength tensors are defined as $\tilde{Q}^{\mu\nu} = \frac{1}{2}\epsilon^{\mu\nu\rho\sigma} Q_{\rho\sigma}$.

Another important example is a Chern–Simons-like gauge interaction [8] of a new pseudo-vector X_μ particle

$$\mathcal{L}_1 = \frac{C_Y}{\Lambda_Y^2} \cdot X_\mu (\mathfrak{D}_\nu H)^\dagger H B_{\lambda\rho} \cdot \epsilon^{\mu\nu\lambda\rho} + \text{h.c.} \tag{5}$$

$$\mathcal{L}_2 = \frac{C_{SU(2)}}{\Lambda_{SU(2)}^2} \cdot X_\mu (\mathfrak{D}_\nu H)^\dagger F_{\lambda\rho} H \cdot \epsilon^{\mu\nu\lambda\rho} + \text{h.c.}, \tag{6}$$

where the Λ_Y, $\Lambda_{SU(2)}$ are new scales of the theory, C_Y, $C_{SU(2)}$ are new dimensionless coupling constants, and $B_{\mu\nu}$, $F_{\mu\nu}$ are the field strength tensors of the

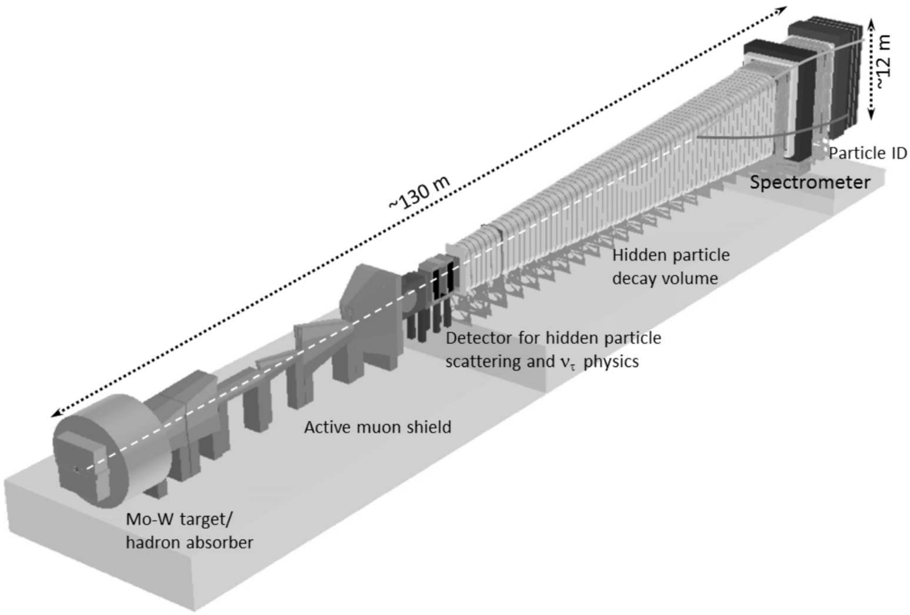

Fig. 3. General scheme of the SHiP facility

$U_Y(1)$ and $SU_W(2)$ gauge fields. After the spontaneous symmetry breaking of the Higgs field, this interaction is effectively reduced to a renormalizable interaction of the form

$$\mathcal{L}_{\rm CS} = c_z \epsilon^{\mu\nu\lambda\rho} X_\mu Z_\nu \partial_\lambda Z_\rho + c_\gamma \epsilon^{\mu\nu\lambda\rho} X_\mu Z_\nu \partial_\lambda A_\rho + \\ + c_w \epsilon^{\mu\nu\lambda\rho} X_\mu W^-_\nu \partial_\lambda W^+_\rho. \quad (7)$$

So, from the experimental point of view, one has to test all of the above-mentioned possible new interactions in the wide range of new particle masses and couplings.

3. SHiP Experiment

The SHiP experiment was first proposed in 2013 [10]. The technical proposal was presented in 2015 [11]. The theoretical background, main channels of production and decay of new particles, and preliminary estimations of the sensitivity region for different portals for the SHiP experiment were considered in 2016 [7]. Somewhat later, the clarifying complementary works were published [12–15]. Currently, the SHiP collaboration [16] includes nearly 250 scientists from 53 institutions. The experiment will begin its work allegedly in 2026 year [17].

The main goal of the future SHiP beam-dump experiment at the CERN SPS accelerator is to search for the new physics in the region of feebly interacting long-lived light particles including Heavy Neutral Leptons (HNL), vector, scalar, axion portals to the Hidden Sector, and light supersymmetric particles. The experiment provides great opportunities for the study of neutrino physics as well.

Now, we describe the work of the SHiP experiment, see Fig. 3. A beam line from the CERN SPS accelerator will transmit 400-GeV protons at the SHiP. The proton beam will strike in a Molybdenum and Tungsten fixed target at a center-of-mass energy $E_{\rm CM} \approx 27$ GeV. Approximately 2×10^{20} proton-target collisions are expected in 5 years of the SHiP operation. The great number of the SM particles and hadrons will be produced under such collisions. Hidden particles are expected to be predominantly produced in the decays of the hadrons.

The main concept of the SHiP functioning is following. Almost all the produced SM particles should be either absorbed or deflected in a magnetic field (muons). Remaining events with SM particles can be rejected using specially developed cuts. If the hidden particles will decay into SM particles inside the decay volume, the last will be detected. This will mean the existence of hidden particles.

So, the target will be followed by a 5-m-long iron hadron absorber. It will absorb the hadrons and the electromagnetic radiation from the target, but the decays of mesons result in a large flux of muons and neutrinos. After the hadron stopper, a system of shielding magnets (which extends over a length of $\sim$40 m) is located to deflect muons away from the fiducial decay volume [12].

Despite the aim to search for the long-lived particles, the sensitive volume should be situated as close as possible to the proton target due to relatively large transverse momenta of the hidden particles with respect to the beam axis. The minimum distance is determined by the necessity for the system to absorb the electromagnetic radiation and hadrons produced in the proton-target collisions and to reduce the beam-induced muon flux.

The system of detectors of the SHiP consists of two parts. Just after the hadron absorber and muon shield, the detector system for recoil signatures of hidden-sector particle scattering and for neutrino physics is located. The neutrino detector has mass of nearly 10 tons. The study of neutrino physics is based on a hybrid detector similar to the detector of the OPERA Collaboration [18]. In addition, this system allows one to detect and veto charged particles produced outside the main decay volume.

The second detector system consist of the fiducial decay volume that is contained in a nearly 50-m-long rectangular vacuum tank. In order to suppress the background from neutrinos interacting in the fiducial volume, it is maintained at a pressure of $O(10^{-3})$ bar. The decay volume is surrounded by background taggers to tag the neutrino and muon inelastic scatterings in the surrounding structures, which may produce long-lived neutral Standard Model particles whose decay can mimic signal events. The vacuum tank is followed by a large spectrometer with a rectangular acceptance of 5 m in width and 10 m in height and a calorimeter. The system is constructed in such a way to detect as many final states as possible in order to be sensitive to a very wide range of models that can be tested. With the help of Table, one can see what modification of the SM is tested depending on final states of the hidden particles decay.

Modification of the SM that can be tested on SHiP depending on final states of the hidden particles decay

Decay modes	Final states	Models tested
Meson and lepton	πl, Kl, l ($l = e, \mu, \tau$)	ν portal, HNL, SUSY neutralino
Two leptons	$e^+ e^-$, $\mu^+ \mu^-$	V, S and A portals, SUSY s-goldstino
Two mesons	$\pi^+ \pi^-$, $K^+ K^-$	V, S and A portals, SUSY s-goldstino
3 bodies	$l^+ l^- \nu$	HNL, neutralino

It should be noted that the SHiP experiment gives great opportunities for the study of neutrino physics. As a result of nearly 2×10^{20} proton-target collisions, $N_{\nu_\tau} = 5.7 \times 10^{15}$ ν_τ and $\nu_{\bar{\tau}}$ neutrino, $N_{\nu_e} = 5.7 \times 10^{18}$ electron neutrino, and $N_{\nu_\mu} = 3.7 \times 10^{17}$ muon neutrino will be produced. It is expected to detect nearly 10^4 τ-neutrino and at first to detect anti τ-neutrino. It is very important, because only 14 τ-neutrino candidates by the experiment DONUT in Fermilab and 10 τ-neutrino candidates by the experiment OPERA in CERN were found till now. No event with anti τ-neutrino was still observed.

4. Conclusions

There are some indisputable phenomena that point to the fact that SM has to be modified and complemented by a new particle (particles). We are sure that there is a new physics, but we do not know where to search for it. There are many theoretical possibilities to modify the SM by scalar, pseudoscalar, vector, pseudovector, or fermion particles of the new physics. These particles may be sufficiently heavy on the electroweak scale and the scale of energy of the present colliders. But these particles may be light (with masses less than that on the electroweak scale) and may feebly interact with the SM particles. The main task now is to experimentally observe particles of the new physics.

Since the possibilities for increasing the energies of the present colliders are limited by high costs, and the heavy new particles are difficult to be produced, it seems reasonable to check another variant and to find light particles of the new physics in intensity frontier experiments.

The goal of the SHiP experiment is to search for the new physics in the region of feebly interacting long-lived light particles including HNL, vector, scalar, axion particles with mass $\leq$10 GeV. There are theoretical predictions for the sensitivity region of the SHiP experiment for each type of new-physics particles (in the mass versus coupling constant coordinates). The experiment will provide great opportunities for the study of neutrino physics as well.

Since the idea of searching for new light feebly interacting particles is very tempting and promising, there are another projects such as REDTOP at the PS beam lines, NA64++, NA62++, LDMX, AWAKE, KLEVER at the SPS beam lines, and FASER, MATHUSLA, CODEX-b at the LHC. All these experiments are compared and summarized in [17]. It is possible that great discoveries in particle physics are right ahead.

The work was presented on the conference "New trends in high-energy physics", May 12-18, Odessa, Ukraine. I also thank Kyrylo Bondarenko for the useful discussion and helpful comments.

1. S.L. Glashow. Partial symmetries of weak interactions. *Nucl. Phys.* **22**, 579 (1961).
2. S. Weinberg. A Model of leptons. *Phys. Rev. Lett.* **19**, 1264 (1967).
3. A. Salam. Weak and electromagnetic interactions. In: *Proc. of 8th Nobel Symposium.* Edit. by N. Svartholm (Almquist and Wiksells, 1968), p. 367.
4. A. Strumia, F. Vissani. Neutrino masses and mixings and... arXiv:hep-ph/0606054 (2010).
5. D.S. Gorbunov, V.A. Rubakov. *Introduction to the Theory of the Early Universe: Hot Big Bang Theory* (World Scientific, 2011).
6. W. de Boer. Grand unified theories and supersymmetry in particle physics and cosmology. *Prog. Part. Nucl. Phys.* **33**, 201 (1994).
7. S. Alekhin. *et al.* A facility to search for hidden particles at the CERN SPS: the SHiP physics case. *Rept. Prog. Phys.* **79**, 124201 (2016).
8. I. Antoniadis, A. Boyarsky, S. Espahbodi, O. Ruchayskiy, J.D. Wells. Anomaly driven signatures of new invisible physics at the Large Hadron Collider. *Nucl. Phys. B* **824**, 296 (2010).
9. J. Alexander *et al.* Dark Sectors 2016 Workshop: Community report. arXiv:1608.08632, FERMILAB-CONF-16-421 (2016).
10. W. Bonivento *et al.* Proposal to search for Heavy Neutral Leptons at the SPS. arXiv:1310.1762 (2013).
11. M. Anelli *et al.* A facility to Search for Hidden Particles (SHiP) at the CERN SPS. arXiv:1504.04956, CERN-SPSC-2015-016, SPSC-P-350 (2015).
12. A. Akmete *et al.* The active muon shield in the SHiP experiment. *JINST* **12**, P05011 (2017).
13. C. Ahdida *et al.* Sensitivity of the SHiP experiment to Heavy Neutral Leptons. *J. High Energ. Phys.* **2019**, 77 (2019).
14. C. Ahdida *et al.* The experimental facility for the Search for Hidden Particles at the CERN SPS. *JINST* **14**, P03025 (2019).
15. I. Boiarska, K. Bondarenko, A. Boyarsky, V. Gorkavenko, M. Ovchynnikov, A. Sokolenko. Phenomenology of GeV-scale scalar portal. arXiv:1904.10447v2 (2019).
16. https://ship.web.cern.ch/ship.
17. J. Beacham *et al.* Physics Beyond Colliders at CERN: Beyond the Standard Model Working Group Report. arXiv:1901.09966, CERN-PBC-REPORT-2018-007 (2019).
18. R. Acquafredda *et al.* OPERA collaboration. The OPERA experiment in the CERN to Gran Sasso neutrino beam. *JINST* **4**, P04018 (2009).

Received 08.07.19

В.М. Горкавенко

ПОШУК ЧАСТИНОК НОВОЇ
ФІЗИКИ В ЕКСПЕРИМЕНТІ SHiP

Р е з ю м е

Незважаючи на величезні успіхи Стандартної Моделі фізики елементарних частинок (СМ), існують окремі явища (нейтринні осциляції, баріонна асиметрія Всесвіту, темна матерія тощо), які СМ пояснити не в змозі. Дані явища вказують на необхідність модифікації СМ та введення нових частинок. Експерименти з пошуку частинок нової фізики можна розділити на два типи: експерименти, в яких намагаються досягти найбільшої енергії частинок, що зіштовхуються, та експерименти, в яких намагаються досягти найбільшої кількості необхідних реакцій. В експериментах першого типу намагаються безпосередньо утворити та зареєструвати нові важкі частинки. В експериментах другого типу намагаються безпосередньо утворити та зареєструвати нові легкі частинки, що слабко взаємодіють з частинками СМ. В роботі обговорюється майбутній експеримент з високою інтенсивністю подій SHiP, що проводитиметься на прискорювачі SPS CERN, його технічні характеристики та переваги.

https://doi.org/10.15407/ujpe64.8.695

P. LEBIEDOWICZ,[1] A. SZCZUREK,[1] O. NACHTMANN [2]

[1] Institute of Nuclear Physics, Polish Academy of Sciences
(Radzikowskiego 152, PL-31342 Cracow, Poland; e-mail: Piotr.Lebiedowicz@ifj.edu.pl)
[2] Institut fur Theoretische Physik, Universitat Heidelberg
(Philosophenweg 16, D-69120 Heidelberg, Germany)

SEARCHING FOR ODDERON IN EXCLUSIVE REACTIONS

We discuss the possibility to use the $pp \to pp\phi\phi$ process in identifying the odderon exchange. So far, there is no unambiguous experimental evidence for the odderon, the charge conjugation $C = -1$ counterpart of the $C = +1$ pomeron. Last year, the results of the TOTEM collaboration suggest that the odderon exchange can be responsible for a disagreement of theoretical calculations and the TOTEM data for the elastic proton-proton scattering. Here, we present recent studies for the central exclusive production (CEP) of $\phi\phi$ pairs in proton-proton collisions. We consider the pomeron-pomeron fusion to $\phi\phi$ ($\mathbb{PP} \to \phi\phi$) through the continuum processes, due to the $\hat{t}$- and $\hat{u}$-channel reggeized ϕ-meson, photon, and odderon exchanges, as well as through the s-channel resonance process ($\mathbb{PP} \to f_2(2340) \to \phi\phi$). This f_2 state is a candidate for a tensor glueball. The amplitudes for the processes are formulated within the tensor-pomeron and vector-odderon approach. Some model parameters are determined from the comparison to the WA102 experimental data. The odderon exchange is not excluded by the WA102 data for high $\phi\phi$ invariant masses. The measurement of large $M_{\phi\phi}$ or $Y_{\rm diff}$ events at the LHC would therefore suggest the presence of the odderon exchange. The process is advantageous, as here the odderon does not couple to protons.

Keywords: exclusive reactions, meson, Regge physics, pomeron, odderon, LHC.

1. Introduction

Diffractive studies are one of the important parts of the physics program for the RHIC and LHC experiments. A particularly interesting class is the central-exclusive-production (CEP) processes, where all centrally produced particles are detected.

In recent years, there has been a renewed interest in the exclusive production of $\pi^+\pi^-$ pairs at high energies related to successful experiments by the CDF [1] and the CMS [2] collaborations. These measurements are important in the context of the resonance production, in particular, in searches for glueballs. In the CDF and CMS experiments, the large rapidity gaps around the centrally produced dimeson system were checked, but the forward- and backward-going (anti)protons were not detected. Preliminary results of similar CEP studies have been presented by the ALICE and LHCb collaborations at the LHC. Although such results will have a diffractive nature, further efforts are needed to ensure their exclusivity. Ongoing and planned experiments at the RHIC (see, e.g., [3]) and future experiments at the LHC will be able to detect all particles produced in central exclusive processes, including the forward- and backward-going protons. The feasibility studies for the $pp \to pp\pi^+\pi^-$ process with the tagging of scattered protons, as carried out for the ATLAS and ALFA detectors, are in [4]. Similar possibilities exist using the CMS and TOTEM detectors.

In [21], the tensor-pomeron and vector-odderon concepts were introduced for soft reactions. In this approach, the $C = +1$ pomeron and the reggeons $\mathbb{R}_+ = f_{2\mathbb{R}}, a_{2\mathbb{R}}$ are treated as effective rank-2 symmetric tensor exchanges, while the $C = -1$ odderon and the reggeons $\mathbb{R}_- = \omega_\mathbb{R}, \rho_\mathbb{R}$ are treated as effective vector exchanges. For these effective exchanges, a number of propagators and vertices, respecting the standard rules of quantum field theory, were derived from comparisons with experiments. This allows for an easy construction of amplitudes for specific processes. In [22], the helicity structure of a

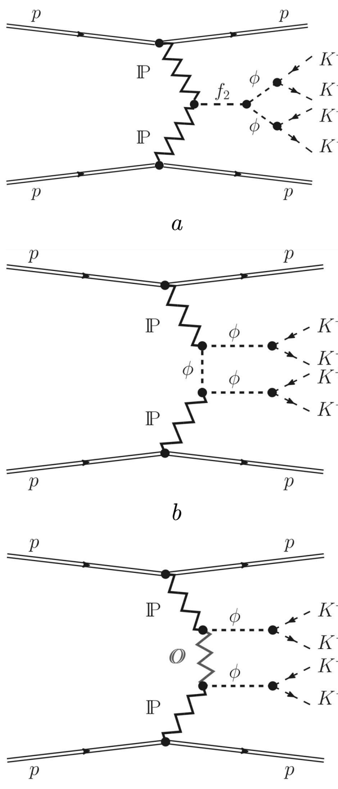

Fig. 1. Born-level diagrams for the double pomeron central exclusive $\phi\phi$ production and their decays into $K^+K^-K^+K^-$: $\phi\phi$ production via an f_2 resonance (a). Other resonances, e.g., of f_0- and η-type, can also contribute here. The continuum $\phi\phi$ production via an intermediate ϕ and odderon ($\mathbb{O}$) exchanges, respectively, (b) and (c). $\mathbb{P}$-γ-$\mathbb{P}$ and $\mathbb{O}$-$\mathbb{P}$-$\mathbb{O}$ contributions are also possible, but negligibly small

small-$|t|$ proton-proton elastic scattering was considered in three models for the pomeron: tensor, vector, and scalar ones. Only the tensor ansatz for the pomeron was found to be compatible with the high-energy experiment on the polarized pp elastic scattering [10].

Applications of the tensor-pomeron and vector-odderon ans'atze were given for the photoproduction of pion pairs in [11] and for a number of central-exclusive-production (CEP) reactions in pp collisions in [12–20]. In addition, contributions from the subleading exchanges, $\mathbb{R}_+$ and $\mathbb{R}_-$, were discussed in these works. As an example, for the $pp \to ppp\bar{p}$ reaction [17], the contributions involving an odderon are expected to be small since its coupling to a proton is very small. We have predicted asymmetries in the (pseudo)rapidity distributions of the centrally produced antiproton and proton. The asymmetry is caused by interference effects of the dominant $(\mathbb{P}, \mathbb{P})$ with the subdominant $(\mathbb{O}+\mathbb{R}_-, \mathbb{P}+\mathbb{R}_+)$ and $(\mathbb{P}+\mathbb{R}_+, \mathbb{O}+\mathbb{R}_-)$ exchanges. We find only very small effects for the odderon, roughly a factor of 10 smaller than the effects due to reggeons.

So far, there is no unambiguous experimental evidence of the odderon, the charge conjugation $C = -1$ counterpart of the $C = +1$ pomeron, introduced on theoretical grounds in [5]. A hint of the odderon was seen in ISR results [6] as a small difference between the differential cross-sections of elastic proton-proton (pp) and proton-antiproton ($p\bar{p}$) scatterings in the diffractive dip region at $\sqrt{s} = 53$ GeV. Recently, the TOTEM Collaboration has published data from high-energy elastic pp scattering experiments at the LHC. In [7], results were given for the ρ parameter, the ratio of the real part to the imaginary one of the forward scattering amplitude. The interpretation of these results is controversial at the moment.

As was discussed in [8], the exclusive diffractive J/ψ and ϕ productions from the pomeron-odderon fusion in high-energy pp and $p\bar{p}$ collisions are a direct probe for a possible odderon exchange. For a nice review of the odderon physics, see [9]. In the diffractive production of ϕ meson pairs, it is possible to have the pomeron-pomeron fusion with intermediate $\hat{t}/\hat{u}$-channel odderon exchange [20]; see the corresponding diagram in Fig. 1, c. Thus, the $pp \to pp\phi\phi$ reaction is a good candidate for the odderon-exchange searches, as it does not involve the coupling of the odderon to the proton.

Studies of different decay channels in the central exclusive production would be very valuable also in the context of identification of glueballs. One of the promising reactions is $pp \to pp\phi\phi$ with both $\phi \equiv \phi(1020)$ mesons decaying into the K^+K^- channel. Structures in the $\phi\phi$ invariant-mass spectrum were observed by several experiments, e.g., in the exclusive $\pi^-p \to \phi\phi n$ [23] and $K^-p \to \phi\phi\Lambda$ [24] reactions, and in the central production [25]. Three tensor states, $f_2(2010)$, $f_2(2300)$, and $f_2(2340)$, observed previously in [23], were also observed in the radiative decay $J/\psi \to \gamma\phi\phi$ [26]. The nature of these resonances is not understood at present and a tensor glueball has still not been clearly identified. According to lattice-QCD simulations, the lightest tensor glueball has a mass between 2.2 and 2.4 GeV, see, e.g. [27]. The $f_2(2300)$ and $f_2(2340)$ states are good candidates to be tensor glueballs.

For an interesting approach to the exclusive diffractive resonance production in pp collisions at high energies, see also Ref. [28, 29].

2. A Sketch of Formalism

In [20], we considered the CEP of four charged kaons via the intermediate $\phi\phi$ state. Explicit expressions for the $pp \to pp\phi\phi$ amplitudes involving the pomeron-pomeron fusion to $\phi\phi$ ($\mathbb{P}\mathbb{P} \to \phi\phi$) through the continuum processes, due to the $\hat{t}$- and $\hat{u}$-channel reggeized ϕ-meson, photon, and odderon exchanges, as well as through the s-channel resonance reaction ($\mathbb{P}\mathbb{P} \to f_2(2340) \to \phi\phi$) were given there. Here, we discuss briefly the continuum processes for the $pp \to pp\phi\phi$ reaction.

The "Born-level" amplitude for the $pp \to pp\phi\phi$ reaction is

$$\mathcal{M}^{\mathrm{Born}} = \mathcal{M}^{(f_2-\mathrm{exchange})} + \mathcal{M}^{(\phi-\mathrm{exchange})} + \\ + \mathcal{M}^{(\mathbb{O}-\mathrm{exchange})}. \tag{1}$$

For the continuum process with the odderon exchange (Fig. 1, c), the amplitude is a sum of $\hat{t}$- and $\hat{u}$-channel amplitudes. The $\hat{t}$-channel term can be written as

$$\begin{aligned}\mathcal{M}^{(\hat{t})} &= (-i)\bar{u}(p_1,\lambda_1) i\Gamma^{(\mathbb{P}pp)}_{\mu_1\nu_1}(p_1,p_a)u(p_a,\lambda_a) \times \\ &\times i\Delta^{(\mathbb{P})\,\mu_1\nu_1,\alpha_1\beta_1}(s_{13},t_1) \times \\ &\times i\Gamma^{(\mathbb{P}\mathbb{O}\phi)}_{\rho_1\rho_3\alpha_1\beta_1}(\hat{p}_t,-p_3)\left(\epsilon^{(\phi)\,\rho_3}(\lambda_3)\right)^* \times \\ &\times i\Delta^{(\mathbb{O})\,\rho_1\rho_2}(s_{34},\hat{p}_t) \times \\ &\times i\Gamma^{(\mathbb{P}\mathbb{O}\phi)}_{\rho_4\rho_2\alpha_2\beta_2}(p_4,\hat{p}_t)\left(\epsilon^{(\phi)\,\rho_4}(\lambda_4)\right)^* \times \\ &\times i\Delta^{(\mathbb{P})\,\alpha_2\beta_2,\mu_2\nu_2}(s_{24},t_2) \times \\ &\times \bar{u}(p_2,\lambda_2) i\Gamma^{(\mathbb{P}pp)}_{\mu_2\nu_2}(p_2,p_b)u(p_b,\lambda_b),\end{aligned} \tag{2}$$

where $p_{a,b}$, $p_{1,2}$ and $\lambda_{a,b}, \lambda_{1,2} = \pm\frac{1}{2}$ denote the four-momenta and helicities of the protons and $p_{3,4}$ and $\lambda_{3,4} = 0, \pm1$ denote the four-momenta and helicities of the ϕ mesons, respectively. $\hat{p}_t = p_a - p_1 - p_3$, $\hat{p}_u = p_4 - p_a + p_1$, $s_{ij} = (p_i + p_j)^2$, $t_1 = (p_1 - p_a)^2$, $t_2 = (p_2 - p_b)^2$. $\Gamma^{(\mathbb{P}pp)}$ and $\Delta^{(\mathbb{P})}$ denote the proton vertex function and the effective propagator, respectively, for the tensorial pomeron. The corresponding expressions are as follows [21]:

$$\begin{aligned} i\Gamma^{(\mathbb{P}pp)}_{\mu\nu}(p',p) &= -i3\beta_{\mathbb{P}NN}F_1(t) \times \\ &\times \left\{\frac{1}{2}\left[\gamma_\mu(p'+p)_\nu + \gamma_\nu(p'+p)_\mu\right] - \frac{1}{4}g_{\mu\nu}(\not{p}'+\not{p})\right\}, \end{aligned} \tag{3}$$

$$\begin{aligned} i\Delta^{(\mathbb{P})}_{\mu\nu,\kappa\lambda}(s,t) &= \frac{1}{4s}\left(g_{\mu\kappa}g_{\nu\lambda} + g_{\mu\lambda}g_{\nu\kappa} - \frac{1}{2}g_{\mu\nu}g_{\kappa\lambda}\right) \times \\ &\times (-is\alpha'_{\mathbb{P}})^{\alpha_{\mathbb{P}}(t)-1}, \end{aligned} \tag{4}$$

where $\beta_{\mathbb{P}NN} = 1.87\ \mathrm{GeV}^{-1}$. The pomeron trajectory $\alpha_{\mathbb{P}}(t)$ is assumed to be of the standard linear form (see, e.g., [30]): $\alpha_{\mathbb{P}}(t) = \alpha_{\mathbb{P}}(0) + \alpha'_{\mathbb{P}}\,t$, $\alpha_{\mathbb{P}}(0) = 1.0808$, $\alpha'_{\mathbb{P}} = 0.25\ \mathrm{GeV}^{-2}$.

Our ansatz for the effective propagator of the $C = -1$ odderon is [21]

$$i\Delta^{(\mathbb{O})}_{\mu\nu}(s,t) = -ig_{\mu\nu}\frac{\eta_{\mathbb{O}}}{M_0^2}(-is\alpha'_{\mathbb{O}})^{\alpha_{\mathbb{O}}(t)-1}$$

with

$$M_0 = 1\ \mathrm{GeV}, \quad \eta_{\mathbb{O}} = \pm1. \tag{5}$$

Here, $\alpha_{\mathbb{O}}(t) = \alpha_{\mathbb{O}}(0) + \alpha'_{\mathbb{O}}\,t$ and we choose, as an example, $\alpha'_{\mathbb{O}} = 0.25\ \mathrm{GeV}^{-2}$, $\alpha_{\mathbb{O}}(0) = 1.05$.

For the $\mathbb{P}\mathbb{O}\phi$ vertex, we use an ansatz with two rank-four tensor functions [20]:

$$\begin{aligned} i\Gamma^{(\mathbb{P}\mathbb{O}\phi)}_{\mu\nu\kappa\lambda}(k',k) &= iF^{(\mathbb{P}\mathbb{O}\phi)}((k+k')^2, k'^2, k^2) \times \\ &\times \left[2\,a_{\mathbb{P}\mathbb{O}\phi}\,\Gamma^{(0)}_{\mu\nu\kappa\lambda}(k',k) - b_{\mathbb{P}\mathbb{O}\phi}\,\Gamma^{(2)}_{\mu\nu\kappa\lambda}(k',k)\right]. \end{aligned} \tag{6}$$

We take the factorized form for the $\mathbb{P}\mathbb{O}\phi$ form factor:

$$\begin{aligned} F^{(\mathbb{P}\mathbb{O}\phi)}((k+k')^2, k'^2, k^2) &= \\ &= F((k+k')^2)\,F(k'^2)\,F^{(\mathbb{P}\mathbb{O}\phi)}(k^2), \end{aligned} \tag{7}$$

where $F(k^2) = (1 - k^2/\Lambda^2)^{-1}$ and $F^{(\mathbb{P}\mathbb{O}\phi)}(m_\phi^2) = 1$. The coupling parameters $a_{\mathbb{P}\mathbb{O}\phi}$, $b_{\mathbb{P}\mathbb{O}\phi}$ and the cutoff parameter Λ^2 could be adjusted to the WA102 experimental data [25].

At low $\sqrt{s_{34}} = \mathrm{M}_{\phi\phi}$, the Regge type of interaction is not realistic and should be switched off. To achieve this, we multiplied the $\mathbb{O}$-exchange amplitude by a purely phenomenological factor: $F_{\mathrm{thr}}(s_{34}) = 1 - \exp[(s_{\mathrm{thr}} - s_{34})/s_{\mathrm{thr}}]$ with $s_{\mathrm{thr}} = 4m_\phi^2$.

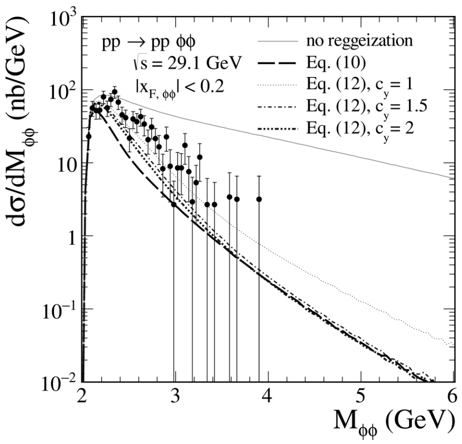

a

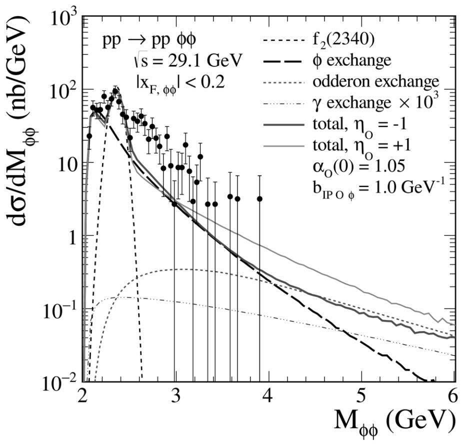

b

Fig. 2. Distributions in the $\phi\phi$ invariant mass. The calculations were done for $\sqrt{s} = 29.1$ GeV and $|x_{F,\phi\phi}| \leqslant 0.2$. The WA102 experimental data from [25] are shown. In the top panel, the green solid line corresponds to the non-reggeized ϕ-exchange contribution. The results for two prescriptions of the reggeization, (10) and (12), are shown by the black and blue lines, respectively. In the bottom panel, we show the complete results including the $f_2(2340)$-resonance contribution and the continuum processes due to the reggeized-ϕ, odderon, and photon exchanges. The black long-dashed line corresponds to the ϕ-exchange contribution and the black dashed line corresponds to the $f_2(2340)$ contribution. The red dotted line represents the odderon-exchange contribution for $a_{\mathbb{P}\mathbb{O}\phi} = 0$ and $b_{\mathbb{P}\mathbb{O}\phi} = 1.0$ GeV^{-1} in (6)

The amplitude for the process shown in Fig. 1, *b* has the same form as the amplitude with the $\mathbb{O}$ exchange, but we have to make the following replacements:

$$i\Gamma^{(\mathbb{P}\mathbb{O}\phi)}_{\mu\nu\kappa\lambda}(k', k) \to i\Gamma^{(\mathbb{P}\phi\phi)}_{\mu\nu\kappa\lambda}(k', k), \tag{8}$$

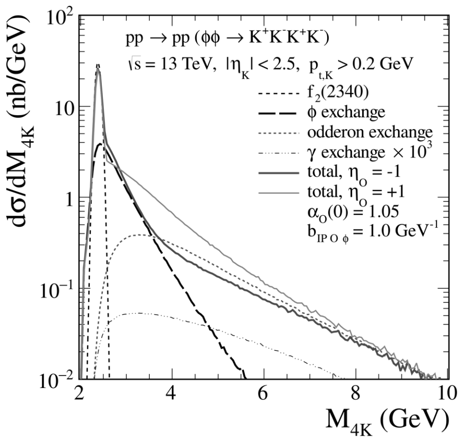

a

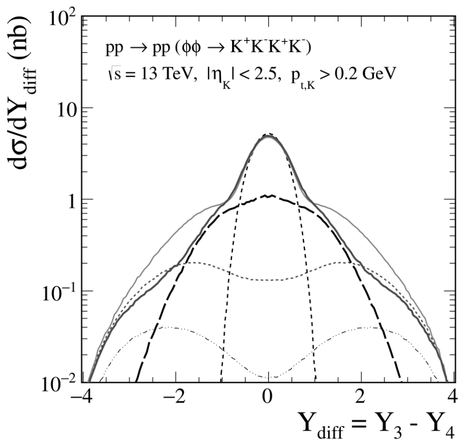

b

Fig. 3. Distributions in M_{4K} (left) and in $\mathrm{Y}_{\mathrm{diff}}$ (right) for the $pp \to pp(\phi\phi \to K^+K^-K^+K^-)$ reaction calculated for $\sqrt{s} = 13$ TeV and $|\eta_K| < 2.5$, $p_{t,K} > 0.2$ GeV. The coherent sum of all terms is shown by the red and blue solid lines for $\eta_{\mathbb{O}} = -1$ and $\eta_{\mathbb{O}} = +1$, respectively. Here, we take $\alpha_{\mathbb{O}}(0) = 1.05$. The absorption effects are included in the calculations

$$i\Delta^{(\mathbb{O})}_{\mu\nu}(s_{34}, \hat{p}^2) \to i\Delta^{(\phi)}_{\mu\nu}(\hat{p}). \tag{9}$$

We have fixed the coupling parameters of the tensor pomeron to the ϕ meson, based on the HERA experimental data for the $\gamma p \to \phi p$ reaction; see [18].

We should take the reggeization of the intermediate ϕ meson into account. We consider two prescriptions of the reggeization (only expected to hold in the $|\hat{p}^2|/s_{34} \ll 1$ regime):

$$\Delta^{(\phi)}_{\mu\nu}(\hat{p}) \to \Delta^{(\phi)}_{\mu\nu}(\hat{p}) \left(\exp(i\phi(s_{34}))\,\frac{s_{34}}{s_{\mathrm{thr}}}\right)^{\alpha_\phi(\hat{p}^2)-1} \tag{10}$$

$$\phi(s_{34}) = \frac{\pi}{2}\exp\left(\frac{s_{\rm thr}-s_{34}}{s_{\rm thr}}\right) - \frac{\pi}{2}, \tag{11}$$

where $s_{\rm thr} = 4m_\phi^2$. Alternatively, we use

$$\Delta^{(\phi)}_{\rho_1\rho_2}(\hat{p}) \to \Delta^{(\phi)}_{\rho_1\rho_2}(\hat{p})\, F(\mathrm{Y_{diff}}) + \\ + \Delta^{(\phi)}_{\rho_1\rho_2}(\hat{p})\,[1 - F(\mathrm{Y_{diff}})] \times \\ \times \left(\exp(i\phi(s_{34}))\,\frac{s_{34}}{s_{\rm thr}}\right)^{\alpha_\phi(\hat{p}^2)-1}, \tag{12}$$

where $F(\mathrm{Y_{diff}}) = \exp\left(-\mathrm{c_y}|\mathrm{Y_{diff}}|\right)$. Here, $\mathrm{c_y}$ is an unknown parameter which measures, how rapidly one approaches the Regge regime. This gives the proper Regge behavior for $s_{34} - 4m_\phi^2 \gg 1$ GeV^2; whereas, for smaller s_{34}, we have the mesonic behavior. We take $\alpha_\phi(\hat{p}^2) = \alpha_\phi(0) + \alpha'_\phi\,\hat{p}^2$, $\alpha_\phi(0) = 0.1$ [31], and $\alpha'_\phi = 0.9$ GeV^{-2}.

In order to give realistic predictions, we shall include the absorption effects calculated at the amplitude level and related to the pp nonperturbative interactions. The full amplitude includes the pp-rescattering corrections (absorption effects)

$$\mathcal{M}_{pp\to pp\phi\phi} = \mathcal{M}^{\rm Born} + \mathcal{M}^{\rm absorption},$$

$$\mathcal{M}^{\rm absorption}(s, \boldsymbol{p}_{1t}, \boldsymbol{p}_{2t}) = \\ = \frac{i}{8\pi^2 s}\int d^2\boldsymbol{k}_t\, \mathcal{M}^{\rm Born}(s, \tilde{\boldsymbol{p}}_{1t}, \tilde{\boldsymbol{p}}_{2t})\, \mathcal{M}^{(\mathbb{P})}_{\rm el}(s, -\boldsymbol{k}_t^2), \tag{13}$$

where $\tilde{\boldsymbol{p}}_{1t} = \boldsymbol{p}_{1t} - \boldsymbol{k}_t$ and $\tilde{\boldsymbol{p}}_{2t} = \boldsymbol{p}_{2t} + \boldsymbol{k}_t$. $\mathcal{M}^{(\mathbb{P})}_{\rm el}$ is the elastic pp-scattering amplitude with the momentum transfer $t = -\boldsymbol{k}_t^2$.

3. Results

It is very difficult to describe the WA102 data for the $pp \to pp\phi\phi$ reaction including resonances and the ϕ-exchange mechanism only [20]. Inclusion of the odderon exchange improves the description of the WA102 data [25]. The result of our analysis is shown in Fig. 2.

Having fixed the parameters of our quasifit to the WA102 data, we wish to show our predictions for the LHC. In Fig. 3, we show the results for the ATLAS experimental conditions ($|\eta_K| < 2.5$, $p_{t,K} > 0.2$ GeV). The distribution in the four-kaon invariant mass is shown in the top panel, and the difference in rapidities between the two ϕ mesons in the bottom panel. The small intercept of the ϕ-reggeon exchange, $\alpha_\phi(0) = 0.1$, makes the ϕ-exchange contribution steeply falling with increasing M_{4K} and $|\mathrm{Y_{diff}}|$. Therefore, an odderon with an intercept $\alpha_{\mathbb{O}}(0)$ around 1.0 should be clearly visible in the region of large four-kaon invariant masses and for large rapidity distance between the ϕ mesons.

4. Conclusions

By confronting our model results, including the odderon, the reggeized ϕ exchange, and the $f_2(2340)$ resonance exchange contributions, with the WA102 data from [25], we derived an upper limit for the $\mathbb{P}\mathbb{O}\phi$ coupling. advantage of this process for experimental studies is the following. With regard for the typical kinematic cuts for LHC experiments in the $pp \to pp\phi\phi \to ppK^+K^-K^+K^-$ reaction, we have found that the odderon exchange contribution should be distinguishable from other contributions for a large rapidity distance between the outgoing ϕ mesons and in the region of large four-kaon invariant masses. At least, it should be possible to derive an upper limit on the odderon contribution in this reaction.

Our results can be summarized in the following way:

• CEP is a particularly interesting class of processes which provides insight to the unexplored soft QCD phenomena. The fully differential studies of the exclusive $pp \to pp\phi\phi$ reaction within the tensor-pomeron and vector-odderon approaches were executed; for more details, see [20].

• Integrated cross-sections of order of a few nb are obtained, including the experimental cuts relevant for the LHC experiments. The distribution in the rapidity difference of both ϕ-mesons could shed light on the $f_2(2340) \to \phi\phi$ coupling, not known at present. Here, we used only one type of $\mathbb{P}\mathbb{P}f_2$ coupling (out of 7 possible; see [14]). We have checked that, for the distributions studied here, the choice of $\mathbb{P}\mathbb{P}f_2$ coupling is not important. This is a different situation compared to the one observed by us for the $pp \to pp(\mathbb{P}\mathbb{P} \to f_2(1270) \to \pi^+\pi^-)$ reaction [14].

• From our model, we have found that the odderon-exchange contribution should be distinguishable from other contributions for a relatively large rapidity separation between the ϕ mesons.

Hence, to study this type of mechanism, one should investigate events with rather large four-kaon invariant masses, outside of the region of resonances. These events are then "three-gap events": proton–gap–ϕ–gap–ϕ–gap–proton. Experimentally, this should be a clear signature.

• Clearly, an experimental study of CEP of a ϕ-meson pair should be very valuable for clarifying the status of the odderon. At least, it should be possible to derive an upper limit on the odderon contribution to this reaction.

I thank the Organizers of the New Trends in High-Energy Physics conference in Odessa, Ukraine for the hospitality and good organization. P.L. was partially supported by the Polish Scientific Center of the PAS in Kiev.

1. T. Aaltonen *et al.* (CDF Collaboration). Measurement of central exclusive $\pi^+\pi^-$ production in pp collisions at $\sqrt{s} = 0.9$ and 1.96 TeV at CDF. *Phys. Rev. D* **91**, 091101 (2015).
2. CMS Collaboration. Measurement of total and differential cross sections of central exclusive $\pi^+\pi^-$ production in proton-proton collisions at 5.02 and 13 TeV. CMS-PAS-FSQ-16-006.
3. R. Sikora (STAR Collaboration). Recent results on Central Exclusive Production with the STAR detector at RHIC. arXiv:1811.03315 [hep-ex].
4. R. Staszewski, P. Lebiedowicz, M. Trzebinski, J. Chwastowski, A. Szczurek. Exclusive $\pi^+\pi^-$ production at the LHC with forward proton tagging. *Acta Phys. Polon. B* **42**, 1861 (2011).
5. L. Łukaszuk, B. Nicolescu. A possible interpretation of pp rising total cross-sections. *Lett. Nuovo Cim.* **8**, 405 (1973).
6. A. Breakstone. Measurement of $\bar{p}p$ and pp elastic scattering in the dip region at $\sqrt{s} = 53$ GeV. *Phys. Rev. Lett.* **54**, 2180 (1985).
7. TOTEM Collaboration. First determination of the ρ parameter at $\sqrt{s} = 13$ TeV – probing the existence of a colourless three-gluon bound state. arXiv:1812.04732 [hep-ex]; arXiv:1812.08610 [hep-ex].
8. A. Schäfer, L. Mankiewicz, O. Nachtmann. Double-diffractive J/ψ and φ production as a probe for the odderon. *Phys. Lett. B* **272**, 419 (1991).
9. C. Ewerz. The odderon in quantum chromodynamics. arXiv:0306137 [hep-ph].
10. L. Adamczyk *et al.* (STAR Collaboration). Single spin asymmetry AN in polarized proton–proton elastic scattering at $\sqrt{s} = 200$ GeV. *Phys. Lett. B* **719**, 62 (2013).
11. A. Bolz, C. Ewerz, M. Maniatis, O. Nachtmann, M. Sauter, A. Schoning. Photoproduction of $\pi^+\pi^-$ pairs in a model with tensor-pomeron and vector-odderon exchange. *JHEP* **1501**, 151 (2015).
12. P. Lebiedowicz, O. Nachtmann, A. Szczurek. Exclusive central diffractive production of scalar and pseudoscalar mesons; tensorial vs. vectorial pomeron. *Annals Phys.* **344**, 301 (2014).
13. P. Lebiedowicz, O. Nachtmann, A. Szczurek. ρ^0 and Drell–Soding contributions to central exclusive production of $\pi^+\pi^-$ pairs in proton-proton collisions at high energies. *Phys. Rev. D* **91**, 074023 (2015).
14. P. Lebiedowicz, O. Nachtmann, A. Szczurek. Central exclusive diffractive production of the $\pi^+\pi^-$ continuum, scalar, and tensor resonances in pp and $p\bar{p}$ scattering within the tensor Pomeron approach. *Phys. Rev. D* **93**, 054015 (2016).
15. P. Lebiedowicz, O. Nachtmann, A. Szczurek. Exclusive diffractive production of $\pi^+\pi^-\pi^+\pi^-$ via the intermediate $\sigma\sigma$ and $\rho\rho$ states in proton-proton collisions within tensor Pomeron approach. *Phys. Rev. D* **94**, 034017 (2016).
16. P. Lebiedowicz, O. Nachtmann, A. Szczurek. Central production of ρ^0 in pp collisions with single proton diffractive dissociation at the LHC. *Phys. Rev. D* **95**, 034036 (2017).
17. P. Lebiedowicz, O. Nachtmann, A. Szczurek. Central exclusive diffractive production of $p\bar{p}$ pairs in proton-proton collisions at high energies. *Phys. Rev. D* **97**, 094027 (2018).
18. P. Lebiedowicz, O. Nachtmann, A. Szczurek. Towards a complete study of central exclusive production of K^+K^- pairs in proton-proton collisions within the tensor Pomeron approach. *Phys. Phys. D* **98**, 014001 (2018).
19. P. Lebiedowicz, O. Nachtmann, A. Szczurek. Extracting the pomeron-pomeron-$f_2(1270)$ coupling in the $pp \to pp\pi^+\pi^-$ reaction through angular distributions of the pions. arXiv:1901.07788 [hep-ph].
20. P. Lebiedowicz, O. Nachtmann, A. Szczurek. Central exclusive diffractive production of $K^+K^-K^+K^-$ via the intermediate $\phi\phi$ state in proton-proton collisions. *Phys. Rev. D* **99**, 094034 (2019).
21. C. Ewerz, M. Maniatis, O. Nachtmann. A model for soft high-energy scattering: Tensor pomeron and vector odderon. *Annals Phys.* **342**, 31 (2014).
22. C. Ewerz, P. Lebiedowicz, O. Nachtmann, A. Szczurek. Helicity in proton–proton elastic scattering and the spin structure of the pomeron. *Phys. Lett. B* **763**, 382 (2016).
23. A. Etkin *et al.* Increased statistics and observation of the g_T, $g_{T'}$, and $g_{T''}$ 2^{++} resonances in the Glueball enhanced channel $\pi^- p \to \varphi\varphi n$. *Phys. Lett. B* **201**, 568 (1988).
24. D. Aston *et al.* Strangeonium production from LASS. *Nucl. Phys. Proc. Suppl.* **21**, 5 (1991).
25. D. Barberis *et al.* (WA102 Collaboration). A Study of the centrally produced phi phi system in pp interactions at 450-GeV/c. *Phys. Lett. B* **432**, 436 (1998).
26. M. Ablikim *et al.* (BESIII Collaboration). Observation of pseudoscalar and tensor resonances in $J/\psi \to \gamma\phi\phi$. *Phys. Rev. D* **93**, 112011 (2016).
27. C.J. Morningstar, M.J. Peardon. Glueball spectrum from an anisotropic lattice study. *Phys. Rev. D* **60**, 034509 (1999).
28. R. Fiore, L. Jenkovszky, R. Schicker. Resonance production in Pomeron–Pomeron collisions at the LHC. *Eur. Phys. J. C* **76**, 38 (2016).

29. R. Fiore, L. Jenkovszky, R. Schicker. Exclusive diffractive resonance production in proton–proton collisions at high energies. *Eur. Phys. J. C* **78**, 468 (2018).
30. A. Donnachie, H.G. Dosch, P.V. Landshoff, O. Nachtmann. *Pomeron Physics and QCD* (Cambridge Univ. Press, 2002).
31. P.D.B. Collins. *Regge Theory and Particle Physics* (Univ. of Durham, 1970).

Received 08.07.19

П. Лебедович

ПОШУКИ ОДДЕРОНА
В ЕКСКЛЮЗИВНИХ РЕАКЦІЯХ

Р е з ю м е

Обговорюємо можливість користуватися процесом $pp \to$ $\to pp\phi\phi$ для ідентифікації обміну оддероном. До цього часу немає однозначного експериментального доказу існування оддерона – партнера померона з негативним зарядовим спряженням, $C = -1$. Минулорічні результати Колаборації TOTEM вказують на те, що оддерон може спричиняти розбіжність між теоретичними розрахунками та даними TOTEM про пружне розсіяння протонів. Ми презентуємо нові результати досліджень центрального ексклюзивного народження (CEP) пар $\phi\phi$ в протонних зіткненнях. Ми разглядаємо фузію померонів у $\phi\phi$ ($\mathbb{PP} \to \phi\phi$) через континуум завдяки обміну в $\hat{t}$- і $\hat{u}$-каналах реджезованого ϕ-мезона, фотона та оддерона, а також резонансного процесу в s-каналі ($\mathbb{PP} \to f_2(2340) \to \phi\phi$). Частинка f_2 є кандидатом на тензорний глюбол. Амплітуда процесу формулюється в рамках підходу, де померон є тензором, а оддерон є вектором. Деякі з параметрів моделі визначаються з порівняння з експериментальними даними WA102. Дані WA102 не виключають обмін оддероном для великих інваріантних мас $\phi\phi$. Сигнал з великими значеннями $M_{\phi\phi}$ або $Y_{\rm diff}$ на LHC буде таким чином вказувати на присутність обміну оддероном. Цей процес привабливий ще тим, що в ньому оддерон не прив'язується до протона.

https://doi.org/10.15407/ujpe64.8.702

S.A. LUKASHEVICH, N.V. MAKSIMENKO
Francisk Skorina Gomel State University
(98, Sovetskaya Str., Gomel 246019, Belarus; e-mail: lukashevich@gsu.by)

THE CONSTRUCTION OF RELATIVISTICALLY INVARIANT EQUATIONS OF MOTION AND THE MOMENTUM ENERGY TENSOR FOR SPIN-1/2 PARTICLES WITH POLARIZABILITIES IN AN ELECTROMAGNETIC FIELD

Within the covariant Lagrangian formalism, the equations of motion for spin-1/2 particles with polarizabilities in an electromagnetic field have been obtained. We have analyzed the phenomenological tensor constant quantities as well.

Keywords: covariant Lagrangian, equations of motion, energy-momentum tensor.

1. Introduction

The interaction of an electromagnetic field with structural particles in the electrodynamics of hadrons is based on the main principles of relativistic quantum field theory. In the model conceptions, where basically the diagram technique is used, a number of features for the interaction of photons with hadrons have been determined [1, 2]. However, the diagram technique is mainly employed for the description of electromagnetic processes in the simplest quark systems. In the case of interaction for the electromagnetic field with complex quark-gluon systems in the low-energy region, the perturbative methods of QCD are nonapplicable. That is why, the low-energy theorems and sum rules were widely used lately [3–6]. In the present time, the low-energy electromagnetic characteristics which are connected with a hadron structure, such as the formfactor and polarizabilities, can be obtained from nonrelativistic theory [5]. Passing from the nonrelativistic electrodynamics to the relativistic field theory, one can use the correspondence principle. But it is necessary to investigate, step-by-step, a transition from the covariant Lagrangian formalism to the Hamiltonian one [7–9].

The determination of the interaction vertex of γ-photons with protons taking the polarizabilities into account [10] has recently been used to fit experimental data on the Compton scattering on a proton in the energy neighborhood of a birth of the $\Delta(1232)$-resonance [11].

This work is a continuation of the researches which have been presented in our previous articles [6–8]. Using the covariant Lagrangian of interaction of the electromagnetic field with a structural polarizable particle, the equations of motion and the canonical and metric energy-momentum tensors have been obtained.

2. Total Lagrangian

The total Lagrangian of the interaction of spin-1/2 particles with the electromagnetic field consists of the Lagrangian for the free electromagnetic field L_{e-m}, the spinor or Dirac field L_D, the Lagrangian of the interaction of the free electromagnetic field with the Dirac field $L_{\text{int}-D}$, and the Lagrangian which considers electric and magnetic polarizabilities of particles $L_{\alpha_0\beta_0-D}$:

$$L_{\text{total}-D} = L_{e-m} + L_D + L_{\text{int}-D} + L_{\alpha_0\beta_0-D},$$

thus,

$$L_{\text{total}-D} = -\frac{1}{4}F_{\alpha\beta}F^{\alpha\beta} + \overline{\psi}\left(\frac{1}{2}i\gamma_\alpha \overset{\leftrightarrow}{\partial^\alpha} - m\right)\psi - \\ - e(\overline{\psi}\gamma_\alpha\psi)A^\alpha + K_{\sigma\nu}\Theta^{\sigma\nu}, \tag{1}$$

where

$$K_{\sigma\nu} = \frac{2\pi}{m}\left(\alpha_0 F_{\sigma\mu}F^{\mu}_{\nu} + \beta_0 \tilde{F}_{\sigma\mu}\tilde{F}^{\mu}_{\nu}\right),$$

$$\overset{\leftrightarrow}{\partial_\nu} = \overset{\leftarrow}{\partial_\nu} - \overset{\rightarrow}{\partial_\nu},$$

$$\Theta^{\sigma\nu} = \frac{i}{2}\left(\bar{\psi}\,\gamma^{\sigma}\,\overleftrightarrow{\partial}^{\nu}\,\psi\right),$$

ψ is the wave function of spin-1/2 particles.

In this expression $\tilde{F}_{\mu\nu} = \frac{1}{2}\varepsilon_{\mu\nu\rho\sigma}F^{\rho\sigma}$, where $F_{\mu\nu}$ and $\tilde{F}_{\mu\nu}$ are the tensors of the electromagnetic field, α_0 and β_0 are electric and magnetic polarizabilities, and $\varepsilon_{\mu\nu\rho\sigma}$–Levi-Civita antisymmetric tensor ($\varepsilon^{0123} = 1$).

The part of the Lagrangian with polarizabilities can be rewritten as

$$L^{(\alpha\beta)} = -\frac{1}{4}F_{\mu\nu}G^{\mu\nu} = K_{\sigma\nu}\Theta^{\sigma\nu}, \tag{2}$$

where $G^{\mu\nu}$ is the antisymmetric tensor $G^{\mu\nu} = -G^{\nu\mu}$ and is equal to

$$G^{\mu\nu} = -\frac{\partial L^{(\alpha\beta)}}{\partial(\partial_\mu A_\nu)} = \frac{4\pi}{m}\big((\alpha_0+\beta_0)(F^{\mu}_{\sigma}\widetilde{\Theta}^{\rho\nu} - $$
$$- F^{\nu}_{\rho}\widetilde{\Theta}^{\rho\mu}) - \beta_0\Theta^{\rho}_{\rho}F^{\mu\nu}\big), \tag{3}$$

where
$\widetilde{\Theta}^{\rho\nu} = 1/2(\Theta^{\rho\nu} + \Theta^{\nu\rho})$.

3. Equations of Motion

For the interaction of the spinor and electromagnetic fields, the following system of equations is used:

$$-\frac{\partial L}{\partial A_\mu} + \partial_\gamma\frac{\partial L}{\partial(\partial_\gamma A_\mu)} = 0, \tag{4}$$
$$-\frac{\partial L}{\partial\overline{\psi}} + \partial_\gamma\frac{\partial L}{\partial(\partial_\gamma\overline{\psi})} = 0, \tag{5}$$
$$-\frac{\partial L}{\partial\psi} + \partial_\gamma\frac{\partial L}{\partial(\partial_\gamma\psi)} = 0, \tag{6}$$

where A_μ is the vector-potential of the electromagnetic field.

From Lagrangian (1) and expressions (4–6), we get the equations of motion for a charged spin-1/2 particle with α_0-electric and β_0-magnetic polarizabilities:

$$\partial_\mu F^{\mu\nu} = e\overline{\psi}\gamma^\nu\psi - \partial_\mu G^{\mu\nu}, \tag{7}$$
$$(i\gamma^\nu\,\overrightarrow{\partial}_\nu - m)\psi = eA_\nu\gamma^\nu\psi - \frac{i}{2}(\partial^\nu K_{\sigma\nu}\gamma^\sigma)\psi - $$
$$- iK_{\sigma\nu}\gamma^\sigma\partial^\nu\psi, \tag{8}$$
$$\bar{\psi}\,(i\,\overleftarrow{\partial}_\nu\,\gamma^\nu + m) = -e\,\bar{\psi}\,A_\nu\gamma^\nu - $$
$$-\frac{i}{2}\,\bar{\psi}\,(\partial^\nu K_{\sigma\nu}\gamma^\sigma) - i(\partial^\nu\,\bar{\psi})\gamma^\sigma K_{\sigma\nu}. \tag{9}$$

In expression (7), $e\overline{\psi}\gamma^\nu\psi$ is the current associated with a charge, $-\partial_\mu G^{\mu\nu}$ is the current associated with the polarizabilities of the particle.

Following work [12], we perform a relativistic generalization of the phenomenological energy-momentum tensor of the interaction of the electromagnetic field with a polarizable particle as

$$T^{\mu\nu} = T^{\mu\nu}_0 + T^{\mu\nu}_{(\alpha\beta)\mathrm{int}}. \tag{10}$$

Lagrangian (1) takes the form

$$L_{\mathrm{total}-D} = L_0 + L_{\mathrm{int}}, \tag{11}$$

where
$$L_0 = -\frac{1}{4}F_{\alpha\beta}F^{\alpha\beta} + \overline{\psi}\left(\frac{1}{2}i\gamma_\alpha\,\overleftrightarrow{\partial}^{\alpha} - m\right)\psi$$

is the usual Lagrangian, and

$$L_{\mathrm{int}} = -e(\overline{\psi}\gamma_\alpha\psi)A^\alpha + K_{\sigma\nu}\Theta^{\sigma\nu}$$

is the interaction Lagrangian of the electromagnetic field and a particle with polarizabilities.

With the help of Lagrangian (11), the canonical energy-momentum tensor looks like

$$T^{\mu\nu}_{\mathrm{can}} = \frac{\partial L_0}{\partial(\partial_\mu A_\rho)}(\partial^\nu A_\rho) + \partial^\nu\bar{\psi}\frac{\partial L_0}{\partial(\partial_\mu\bar{\psi})} + \frac{\partial L_0}{\partial(\partial_\mu\psi)}\partial^\nu\psi - $$
$$- g^{\mu\nu}\left(-\frac{1}{4}F_{\alpha\beta}F^{\alpha\beta} - \frac{1}{4}F_{\alpha\beta}G^{\alpha\beta}\right).$$

As a result, we get

$$T^{\mu\nu}_{\mathrm{can}} = T^{\mu\nu}_{\mathrm{can}(0)} + \frac{g^{\mu\nu}}{4}G_{\rho\sigma}F^{\rho\sigma}, \tag{12}$$

where $\frac{g^{\mu\nu}}{4}G_{\rho\sigma}F^{\rho\sigma}$ is the energy-momentum tensor of the interaction of the electromagnetic field with regard for the polarizabilities of the particle, and

$$T^{\mu\nu}_{\mathrm{can}(0)} = -F^{\mu\rho}\partial^\nu A_\rho + \frac{g^{\mu\nu}}{4}F_{\rho\sigma}F^{\rho\sigma} + \Theta^{\mu\nu}.$$

Using the unambigious definition of a energy-momentum tensor for $T^{\mu\nu}_{\mathrm{can}}$, we construct the metric energy-momentum tensor:

$$T^{\mu\nu}_{\mathrm{metr}} = T^{\mu\nu}_{\mathrm{can}(0)} + \partial_\rho(F^{\mu\rho}A^\nu) + \frac{g^{\mu\nu}}{4}G_{\rho\sigma}F^{\rho\sigma}. \tag{13}$$

Thus, $T^{\mu\nu}_{\mathrm{metr}}$ reads

$$T^{\mu\nu}_{\mathrm{metr}} = F^{\mu\rho}F^{\nu}_{\rho} + \frac{g^{\mu\nu}}{4}F_{\rho\sigma}F^{\rho\sigma} + \Theta^{\mu\nu} - $$

$$-j^\mu A^\nu + \frac{g^{\mu\nu}}{4} G_{\rho\sigma} F^{\rho\sigma}, \quad (14)$$

where j^μ is the current density of the charged particle.

In the rest frame of the particle, we obtain the energy density of interaction for the particle with polarizabilities and the electromagnetic field:

$$\mathcal{E} = -\frac{2\pi}{m}\Theta^{00}(\alpha_0 \mathbf{E}^2 + \beta_0 \mathrm{H}^2),$$

where Θ^{00} is the energy density of the spin-1/2 particle.

4. Conclusion

Taking the covariant Lagrangian of interaction of the electromagnetic field with a polarizable spin-1/2 particle as a basis in the Lagrangian covariant formalism, the equations of motion have been found. The correlations between the covariant Lagrangian and the canonical and metric energy-momentum tensors have been obtained. In the rest frame of the particle, the energy density of interaction for the particle with polarizabilities and the electromagnetic field has been determined.

1. S.J. Brodsky, J.R. Primack. The electromagnetic interaction of composite systems. *Annals of Physics* **52**, 315 (1969).
2. S. Scherer, A. Yu. Korchin, J.H. Koch. Virtual Compton scattering off the nucleon at low energies. *Phys. Rev. C* **54**, 904 (1996).
3. M.I. Levchuk, L.G. Moroz. Gyration nucleon as one of the characteristics of its electromagnetic structure. *Vesti AN BSSR Ser.: fiz.-mat. nauk* **1**, 49 (1985).
4. A.J. L'vov, V.A. Petrun'kin. Dispersion theory of proton Compton scattering in the first and second resonance regions. *Phys. Rev. C* **55**, 359 (1997).
5. M.-Th. Hutt, A.J. L'vov, A.J. Milstein, M. Schumacher. Compton scattering by nuclei. *Phys. Reports* **323**, No. 6, 458 (2000).
6. N.V. Maksimenko, L.G. Moroz. Phenomenological description polarizabilities of elementary particles in a field-theory. In: *Proc. 11 Intern. School on High Energy Physics and Relativistic Nucl. Phys. Dubna JINR* **D2-11707**, 533 (1979).
7. S.A. Belousova, N.V. Maksimenko. The description for spin polarizabilities based on the covariant Lagrangian. In *Proc. of "OFTHEP'2000". Tver, Russia*, 305 (2000), hep-ph/0009334.
8. N.V. Maksimenko, O.M. Deruzhkova, S.A. Lukashevich. The electromagnetic characteristics of hadrons in the covariant Lagrangian approach. In *Proc. of Intern. School-Seminar "Actual Problems of Particles Physics", Gomel, 2001. JINR* **2**, 145 (2002).
9. D. Babusci, J. Jiordano, A.J. L'vov, J. Matone, A.N. Nathan. Low-energy Compton scattering of polarized photons on polarized nucleons. *Phys. Rev. C* **58**, 1013 (1998).
10. A. Ilyichev, S. Lukashevich, N. Maksimenko. Static polarizability vertex and its application. arXiv: hep-ph/0611327v1.
11. Y. Zhang, K. Savvidy. Proton Compton scattering in a unified proton Δ^+ model. *Phys. Rev. C* **88**, No. 6, 064614 (2013). arXiv:1305.3847 [hep-ph] NITS-PHY-2013002.
12. C. Itzykson, J.B. Zuber. *Quantum Field Theory* (McGraw-Hill, 1980).

Received 08.07.19

С.А. Лукашевич, Н.В. Максименко

ПОБУДОВА РЕЛЯТИВІСТСЬКО-ІНВАРІАНТНИХ РІВНЯНЬ РУХУ ТА ТЕНЗОР ЕНЕРГІЇ-ІМПУЛЬСУ ДЛЯ ЧАСТИНОК ЗІ СПІНОМ 1/2 З ПОЛЯРИЗОВНІСТЮ В ЕЛЕКТРОМАГНІТНОМУ ПОЛІ

Р е з ю м е

В рамках коваріантного лагранжового формалізму отримано рівняння руху для частинок зі спіном 1/2 з поляризовністю в електромагнітному полі. Нами також проаналізовано феноменологічні тензорні константи.

https://doi.org/10.15407/ujpe64.8.705

M.V.T. MACHADO

High Energy Physics Phenomenology Group, GFPAE IF-UFRGS
Caixa Postal 15051, CEP 91501-970
(Av. Bento Goncalves 9500, Porto Alegre, RS, Brazil; e-mail: magnus@if.ufrgs.br)

INVESTIGATING THE SOFT PROCESSES WITHIN THE QCD COLOR DIPOLE PICTURE

We consider the QCD parton saturation models to describe the soft interactions at the high-energy limit. The total and elastic cross-sections, as well as the elastic slope parameter, are obtained for proton-proton and pion-proton collisions and compared to recent experimental results.

K e y w o r d s: color dipole picture, QCD parton saturation, Regge theory.

1. Introduction

Describing the soft processes with the use of the QCD degrees of freedom is a quite difficult task, since they are dominated by a long distance (non-perturbative) physics. It has been shown that the soft observables as the total and elastic cross-sections depend on the transition region between the high parton density system (saturation domain) and the perturbative QCD region [1–3]. The parton saturation phenomenon [4–6] is a well-established property of high-energy systems and gives a high-quality description of inclusive and exclusive deep inelastic scattering (DIS) data. As evidences of the successfulness of such approach, we quote the description of the light meson photoproduction cross-section [7–12] and diffractive DIS (DDIS) [13, 14]. Both are semihard processes, where an important contribution to the cross-section comes from the kinematic region in a vicinity of the saturation momentum, Q_s. This dimensional scale increases in the high-energy region. A well-known formalism, which is intuitive, and where the saturation physics can be easily implemented, is the QCD color dipole picture. It is expected [1] that the soft processes measured, for instance, at the Large Hadron Collider (LHC) in hadron-hadron collisions probe the distances about $r \sim 1/Q_s \ll R_h$, with R_h being the hadron radius. In this context, the hadron scattering at the LHC could be described by color dipoles as the correct degrees of freedom even at large transverse distances. Moreover, it has been shown that the cross-sections for soft hadron-hadron collisions within saturation approaches satisfy the Froissart–Martin bound [2,3]. In this context, the role played by the unitarized hard Pomeron contribution to the soft observables has been carefully discussed in Refs. [15, 16].

Here, we will investigate the soft observable in the small-t regime within the color dipole picture and parton saturation approaches. The paper is organized as follows. In the next section, we summarize the theoretical information to compute the cross-section for hadron-hadron collisions in two color dipole approaches. First, we consider the asymptotic cross-section following Ref. [3], where the pp cross-section is assumed to be dominated by the two-gluon production in the final state, $pp \to gg + X$. There, the main ingredients are the gluon distribution of a projectile and the partonic cross-section associates to the interaction $gN \to gg + X$. We also consider the model presented in Ref. [1], where the virtual photon wave-function is replaced by the corresponding wave-function for the hadron projectile. The hadron-proton interaction is computed using the dipole-proton amplitude constrained from DIS data. The numerical results from both models are compared to experimental measurements focusing in the LHC kinematic regime. Finally, we discuss the main theoretical uncertainties and present the main conclusions.

2. Theoretical Frameworks and Their Phenomenological Applications

Our first investigation will consider the color dipole approach applied to hadron-hadron collisions proposed in Refs. [3]. For simplicity, we address initially the case for proton-proton collisions in colliders. The formalism is able to provide us the production cross-section of (heavy or light) quark pairs or gluons at the final state. Namely, similarly to photon-hadron interactions, the total quark production cross-section is given by [17, 18]

$$\sigma(pp \to q\bar{q}X) = 2 \int_0^{-\ln\left(\frac{2m_q}{\sqrt{s}}\right)} dy\, x_1 G\left(x_1, \mu_F^2\right) \times$$
$$\times\, \sigma(GN \to q\bar{q}X), \tag{1}$$

where $y = \frac{1}{2}\ln(x_1/x_2)$ is the rapidity of the pair, $\mu_F \sim m_Q$ is the factorization scale. The quantity $x_1 G(x_1, \mu_F^2)$ is the projectile gluon density on the scale μ_F, and the partonic cross-section $\sigma(GN \to \to q\bar{q}X)$ is given by [17]

$$\sigma(GN \to q\bar{q}X) = \int dz\, d^2 \left|\Psi_{G\to q\bar{q}}(z,)\right|^2 \sigma_{q\bar{q}G}(z,),$$

with $\Psi_{G\to q\bar{q}}$ being the pQCD calculated distribution amplitude, which describes the dependence of the $|q\bar{q}\rangle$ Fock component on the transverse separation and the fractional momentum. It is given by,

$$|\Psi_{G\to q\bar{q}}(z,\mathbf{R})|^2 = \frac{\alpha_s(\mu_R)}{(2\pi)^2}\Big\{m_q^2 k_0^2(m_q r) +$$
$$+\left[z^2 + (1-z)^2\right] m_q^2 k_1^2(m_q r)\Big\}, \tag{2}$$

where $\alpha_s(\mu_R)$ is the strong coupling constant, which is probed on a renormalization scale $\mu_R \sim m_Q$. We note that the wavefunction will lead to a dominance of dipole sizes around $r \sim 1/m_q$ in the corresponding r-integration. Therefore, for the heavy quark production, the color transparency behavior from the dipole cross-section, $\sigma_{\mathrm{dip}}(r) \propto r^2$, will be the main contribution (pQCD). In the charm case, an important contribution should come from the saturation region, since the typical dipole size, $r \simeq 1$ GeV^{-1}, can reach an order of magnitude similar to the saturation radius, $R_s(x) = 1/Q_s(x) \propto (\sqrt{s})^{-\lambda/2}$ (with $\lambda \simeq \simeq 0.3$). On the other hand, for light quarks, $m_q \simeq \simeq 0.14$ GeV, we are deep in the parton saturation (very low-x_2 and a small scale of the probe) and non-perturbative regions. This will be the case in the following calculation.

In the partonic cross-section, $\sigma_{q\bar{q}G}$ is the cross-section for the scattering of a color neutral quark-antiquark-gluon system on the target and is directly connected with the dipole cross-section:

$$\sigma_{q\bar{q}G} = \frac{9}{8}\left[\sigma_{\mathrm{dip}}(x_2, z\mathbf{R}) + \sigma_{\mathrm{dip}}(x_2, \bar{z}\mathbf{R})\right] -$$
$$-\frac{1}{8}\sigma_{\mathrm{dip}}(x_2, \mathbf{R}). \tag{3}$$

Here, the main idea is that, at high energies, a gluon G from the projectile hadron can develop a fluctuation which contains a $Q\bar{Q}$ pair. Interaction with the color field of a target then may release these heavy quarks. Such an approach is valid for high energies, where the coherence length $l_c \approx 1/x_2$ is larger than the target radius. Therefore, it is natural to include the parton saturation effects and to use the fact the dipole cross-section is universal, i.e., it is process-independent. For the sake of completeness, the parton momentum fractions are written in terms of the quark pair rapidity and masses, $x_{1,2} = \frac{2m_Q}{\sqrt{s}}\exp(\pm y)$.

Following Ref. [3], we obtain the asymptotic hadron-hadron cross-section within the color dipole approach considering the dominant process, $pp \to \to GGX$, at high energies. Now, the gluon G from the projectile hadron develops a fluctuation which contains a two-gluon (GG) pair further interacting with target's color field. Accordingly, the expression for the total cross-section for the gluon production at the final state is given by [19],

$$\sigma(pp \to GGX) = 2 \int_0^{-\ln\left(\frac{2m_G}{\sqrt{s}}\right)} dy\, x_1 G\left(x_1, \mu_F^2\right) \times$$
$$\times\, \sigma(GN \to GGX), \tag{4}$$

where the effective gluon mass, m_G, was introduced in order to regularize the calculation. Thus, in this case, one has $x_{1,2} = \frac{2m_G}{\sqrt{s}}\exp(\pm y)$.

The new partonic cross-section $\sigma(GN \to GGX)$ is given by

$$\sigma(GN \to GGX) =$$
$$= \int dz\, d^2\mathbf{R}\, \left|\Psi_{G\to GG}(z,\mathbf{R})\right|^2 \sigma_{GGG}(z,\mathbf{R}), \tag{5}$$

with $\Psi_{G\to GG}$ being the corresponding distribution amplitude associated with the $|GG\rangle$ Fock state. It is obtained from Eq. (2) in the following way: $|\Psi_{G\to GG}|^2 = 2(N_c - 1)|\Psi_{G\to q\bar{q}}|^2$. The partonic cross-section σ_{GGG} is the cross-section for the scattering a a color neutral three-gluon system on the target and is directly related to the dipole cross-section in the following way [19]:

$$\sigma_{GGG} = \frac{1}{2}\left[\sigma_{\rm dip}(x_2, z\mathbf{R}) + \sigma_{\rm dip}(x_2, \bar{z}\mathbf{R}) + \sigma_{\rm dip}(x_2, \mathbf{R})\right]. \tag{6}$$

Now, we will present the corresponding phenomenology using Eq. (4). From Ref. [3], we identify basically two main shortcomings: a very low value for the effective gluon mass, $m_G = 154$ MeV $< \Lambda_{QCD}$ and the identification of the scale μ with the starting evolution scale in the gluon PDFs considered, $\mu^2 = Q_0^2$. Here, we will use the value $m_G = 400$ MeV. Moreover, for the gluon PDF probed on the low scale, $\mu^2 = m_G^2 = 0.16$ GeV^2 will be given for a prediction from the parton saturation physics,

$$x\,G(x, Q^2) = \frac{3\,\sigma_0 Q_s^2}{4\pi^2\alpha_s}\left[1 - \left(1 + \frac{Q^2}{Q_s^2}\right)\, e^{-\frac{Q^2}{Q_s^2}}\right], \tag{7}$$

where the updated values for the GBW model parameters have been used [20]. Consistently, for the dipole cross-section, we have used the GBW parametrization. It should be noted that the result is parameter-free and corresponds to the soft Pomeron contribution to the cross-section.

In Fig. 1, the result for the total cross-section in proton-proton collisions is presented. Both the low-energy and cosmic rays data are presented. Experimental measurements from colliders are properly identified [21], especially the recent LHC data. The asymptotic model is in a quite good agreement compared to accelerator data, despite no further adjustment has been done. There is some room for fitting the reggeon contribution at low energies.

We have also considered another color dipole approach addressing the soft scattering processes. In such a case, other observables can be described as the elastic cross-section and the elastic slope parameter. We follow Ref. [1] and compute the total cross-section in following way:

$$\sigma_{\rm tot}^{hp}(\sqrt{s}) = 2\int d^2b \int_0^1 dz \int d^2r\, |\Psi_h(r,z)|^2\; N(s,r,b). \tag{8}$$

It depends on the color dipole amplitude, $N(s,r,b)$, and on the hadron wavefunction, $\Psi_h(r,z)$. The expressions resembles the same equation for the DIS description within the color dipole approach. In other words, the photon wavefunction is replaced by the hadron one. Here, in the meson-proton scattering, a meson is treated as a $q\bar{q}$ pair: the calculation implies that DIS, i.e., the interaction of a color dipole with a proton target and the saturation physics can be embedded in the dipole amplitude. A similar approach has been considered also in Refs. [22–24], where the Pomeron dynamics is written in terms of the dipole-dipole cross-section. For instance, in Ref. [22], the large dipoles are dominated by a soft Pomeron contribution, whereas small dipoles are driven by a hard Pomeron piece (two-Pomeron model with hard and soft Pomerons). On the other hand, in Ref. [23, 24] based on Mueller's cascade model, the authors discussed several contributions including the effect of Pomeron loops.

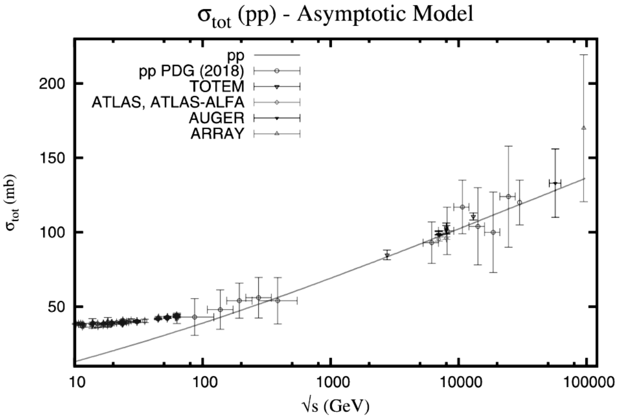

Fig. 1. (pp total cross-section as a function of the center-of-mass-energy, including low-energy and cosmic rays data. The LHC data are explicitly identified (TOTEM and ATLAS Collaborations)

To characterize mesons and baryons, we use the phenomenological ansatz from Wirbel–Stech–Bauer (WSB) [22] which gives

$$\psi_h(z, \mathbf{r}) = \sqrt{\frac{z(1-z)}{2\pi S_h^2 N_h}}\; e^{-(z-\frac{1}{2})^2/(4\Delta z_h^2)}\; e^{-|\mathbf{r}|^2/(4S_h^2)}, \tag{9}$$

where the hadron wave function normalization to unity, $\int dz d^2r\, |\psi_h(z,\mathbf{r})|^2 = 1$, requires the following normalization constant:

$$N_h = \int_0^1 dz\; z(1-z)\; e^{-(z-\frac{1}{2})^2/(2\Delta z_h^2)}. \tag{10}$$

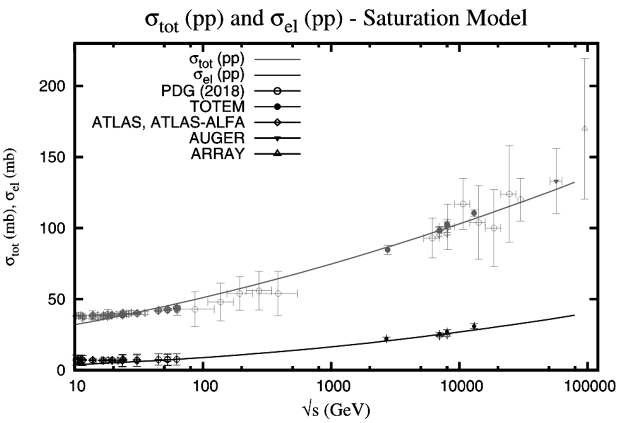

Fig. 2. The total and elastic cross-sections for *pp* collisions. The upper cross-sections are total cross-sections, while the lower ones are the elastic cross-sections. Tevatron, SPS, LHC, and cosmic rays data are presented [21]. The lines are the results from the eikonal-type (saturation) model

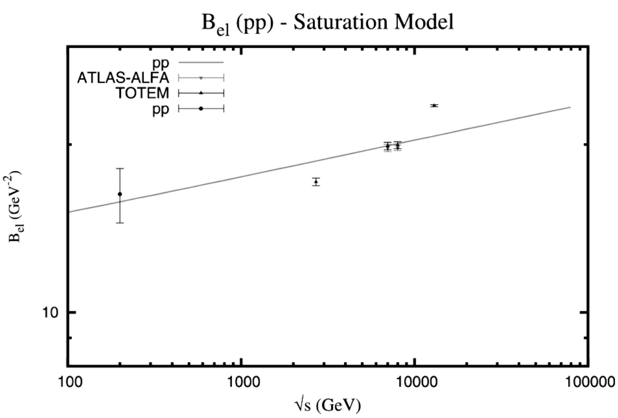

Fig. 3. Slope $B_{\rm el}(s)$ for the *pp* elastic scattering as a function of $\sqrt{s}$. The recent LHC data from TOTEM and ATLAS-ALFA are presented

Therefore, mesons and baryons are assumed to have a $q\bar{q}$ and quark–diquark valence structure. Since quark–diquark systems are equivalent to $q\bar{q}$ systems, this allows us to model not only mesons but also baryons as color-dipoles. The values of the parameters in our case are the following: $\Delta z_h = 0.3\,(2)$ and $S_h = 0.86\,(0.607)$ fm, for $p/\bar{p}\,(\pi^{\pm})$, respectively [22].

Before discussing an impact-parameter dipole amplitude extracted from DIS data, we would need to rewrite the energy dependence from the photon-hadron scattering in terms of the appropriate Bjorken scaling variable-x. In this work, the following ansatz has been considered:

$$\frac{1}{x} = \frac{sr^2}{(s_0\,R_c^2)}, \tag{11}$$

which has been successfully considered in Ref. [25]. Here, $s_0^2 \sim m_h^2$ and $R_c = 0.2$ fm. Such an ansatz is numerically equivalent to the proposal $\frac{1}{x} = \frac{s}{Q_0^2}$, with $Q_0^2 \sim (2m_q)^2 \simeq m_h^2$, done in Ref. [1]. For simplicity and faster numerical calculations, we consider the last relation, where the Q_0^2 parameter will be extracted from the total cross-section data.

We tested an eikonal-like expression for the dipole amplitude, where the impact parameter dependence is factorized from the energy dependence. The function $S(b)$ is described by the dipole profile function. Namely, the amplitude has the following form:

$$N(x,r,b) = 1 - \exp\left(-\frac{1}{2}\hat{\sigma}(x,r)S(b)\right),$$
$$\hat{\sigma}(x,r) = \sigma_0\frac{(rQ_s(x))^2}{4}, \quad S(b) = \frac{2\beta b}{\pi R^2}K_1(\beta b), \tag{12}$$

where we have considered the parameters for $\hat{\sigma}$ from the GBW saturation model [20] and the value $R^2 =$ $= 4.5$ GeV^{-2}. Here, the parameter β was defined as $\beta = \frac{\sqrt{8}}{R}$. In Fig. 2, we present the results associated with the application of the model for the b-dependent color dipole amplitude to the *pp* scattering at the accelerator energy regime. Accordingly, we can say that the model adequately describes the proton-proton cross-section data, and we extend it to higher energies to make predictions for cosmic-ray energies. Moreover, in Fig. 3, we present the slope parameter, $B_{\rm el}(s)$ as a function of the center-of-mass energy. We present the comparison against the recent LHC data, and it was found that the description of data is quite reasonable.

In summary, we have applied the color dipole picture to the soft hadron-hadron scattering, by including the parton saturation phenomenon as the transition region between the soft and hard domains. We have shown that the inclusive process is mainly driven for dipole sizes near the saturation radius in the high-energy regime. The main advantage is that the corresponding phenomenology is almost free of parameters, as they are completely constrained from DIS data in *ep* interactions. The models rely on the dipole cross-section or b-dependent dipole amplitude and indicate that the impact parameter profile is crucial for a good data description. The advent of the

LHC opened a new window for the studies of the diffraction and the elastic and inelastic scatterings, as they are not strongly contaminated by non-diffractive events. This is translated in the Regge-theory language saying that the scattering amplitude is completely determined by a Pomeron exchange. The current measurements on these soft observables at the LHC in proton-proton collisions are in a very good shape, covering the energies of 0.9, 2.76, 7, 8, and 13 TeV [21]. In the context of the saturation physics, the soft Pomeron may be understood as an unitarized perturbation Pomeron [26]. It can be shown that the trajectory of a soft Pomeron could emerge as a result of the interplay between perturbative physics of a hard Pormeron and the confining properties of the QCD vacuum. Specifically, the local unitarization in the impact parameter plane can lead to a reasonable description of the intercept and the slope of a soft Pomeron [26]. Our work corroborates those statements, once the soft observable in the small-t regime is correctly described within the color dipole picture and the parton saturation approach.

The author thanks the conference organizers and other presenters for making this valuable opportunity available to all of us. Thank you for your gracious hospitality and professionalism. This work was partially financed by the Brazilian funding agencies CNPq and CAPES.

1. J. Bartels, E. Gotsman, E. Levin, M. Lublinsky, U. Maor. The Dipole picture and saturation in soft processes. *Phys. Lett. B* **556**, 114 (2003).
2. F. Carvalho, F. O. Duraes, V. P. Goncalves, F.S. Navarra. Gluon saturation and the Froissart bound: A Simple approach. *Mod. Phys. Lett. A* **23**, 2847 (2008).
3. C.A. Argueelles, F. Halzen, L. Wille, M. Kroll, M.H. Reno. High-energy behavior of photon, neutrino, and proton cross sections. *Phys. Rev. D* **92**, 074040 (2015).
4. F. Gelis, E. Iancu, J. Jalilian-Marian, R. Venugopalan. *Ann. Rev. Nucl. Part. Sci.* **60**, 463 (2010).
5. H. Weigert. Evolution at small x_bj: The color glass condensate. *Prog. Part. Nucl. Phys.* **55**, 461 (2005).
6. J. Jalilian-Marian, Y.V. Kovchegov. Saturation physics and deuteron–gold collisions at RHIC *Prog. Part. Nucl. Phys.* **56**, 104 (2006).
7. A.C. Caldwell, M.S. Soares. Vector meson production in the Golec-Biernat Wuesthoff model. *Nucl. Phys. A* **696**, 125 (2001);
8. H. Kowalski, D. Teaney. An impact parameter dipole saturation model. *Phys. Rev. D* **68**, 114005 (2003).
9. J.R. Forshaw, R. Sandapen, G. Shaw. Color dipoles and ρ, φ electroproduction. *Phys. Rev. D* **69**, 094013 (2004).
10. C. Marquet, R. Peschanski, G. Soyez. Exclusive vector meson production at HERA from QCD with saturation. *Phys. Rev. D* **76**, 034011 (2007).
11. H. Kowalski, L. Motyka, G. Watt. Exclusive diffractive processes at HERA within the dipole picture. *Phys. Rev. D* **74**, 074016 (2006).
12. N. Armesto, A.H. Rezaeain. *Phys. Rev. D* **90**, 054003 (2014).
13. J.R. Forshaw, R. Sandapen, G. Shaw. Further success of the colour dipole model. *JHEP* **0611**, 025 (2006).
14. K. Golec-Biernat, M.Wüsthoff. Saturation in diffractive deep inelastic scattering. *Phys. Rev. D* **60**, 114023 (1999).
15. J.-R. Cudell, O. V. Selyugin. Unitarisation and black-disk limit at the LHC in the presence of a hard pomeron. *Phys. Lett. B* **662**, 417 (2008).
16. J.-R. Cudell, E. Predazzi, O.V. Selyugin. New analytic unitarisation schemes. *Phys. Rev. D* **79**, 034033 (2009).
17. N.N. Nikolaev, G. Piller, B.G. Zakharov. Inclusive heavy-flavor production from nuclei. *Z. Phys. A* **354**, 99 (1996).
18. B.Z. Kopeliovich, A.V. Tarasov. Gluon shadowing in heavy flavor production off nuclei. *Nucl. Phys. A* **710**, 180 (2002).
19. N.N. Nikolaev, W. Schafer, B.G. Zakharov. Nonlinear $k \perp$ factorization for gluon-gluon dijets produced off nuclear targets *Phys. Rev. D* **72**, 114018 (2005).
20. K. Golec-Biernat, S. Sapeta. Saturation model of DIS: An update. *JHEP* **1803**, 102 (2018).
21. M. Tanabashi *et al.*, (Particle Data Group). Review of Particle Physics. *Phys. Rev. D* **98**, 030001 (2018).
22. A.I. Shoshi, F.D. Steffen, H.J. Pirner. S-matrix unitarity, impact parameter profiles, gluon saturation and high-energy scattering. *Nucl. Phys. A* **709**, 131 (2002).
23. C. Flensburg, G. Gustafson, L. Lonnblad. Elastic and quasi-elastic pp and y^*p scattering in the dipole model. *Eur. Phys. J. C* **60**, 233 (2009)
24. G. Gustafson, L. Lonnblad, A. Ster, T. Csorgo. Total, inelastic and (quasi-)elastic cross sections of high energy pA and γ^* A reactions with the dipole formalism. *JHEP* **1510**, 022 (2015).
25. A. Donnachie, H.G. Dosch. Comprehensive approach to structure functions. *Phys. Rev. D* **65**, 014019 (2002).
26. L. Motyka. Soft pomeron trajectory from a saturation model. *Acta Phys. Polon. B* **34**, 3069 (2003).

Received 08.07.19

М.В.Т. Машадо

ДОСЛІДЖЕННЯ М'ЯКИХ
ПРОЦЕСІВ В РАМКАХ КОЛЬОРОВОГО
ДИПОЛЬНОГО ПІДХОДУ КХД

Р е з ю м е

В роботі ми розглядаємо КХД-партонну модель насичення для опису м'яких процесів при високих енергіях. Отримано повний та пружний перерізи, а також параметр нахилу для розсіяння протонів на протонах та піонів на протонах. Ці результати порівнюються з експеримельними даними.

https://doi.org/10.15407/ujpe64.8.710

P. MINAIEV, V. SKALOZUB
Oles Honchar Dnipro National University
(72, Gagarin Ave., Dnipro 49010, Ukraine; e-mail: minaevp9595@gmail.com)

THE ELECTROWEAK PHASE TRANSITION IN A SPONTANEOUSLY MAGNETIZED PLASMA

We investigate the electroweak phase transition (EWPT) in the Minimal (One Higgs doublet) Standard Model (SM) with account for the spontaneous generation of magnetic and chromomagnetic fields. As it is known, in the SM for the mass of a Higgs boson greater than 75 GeV, this phase transition is of the second order. But, according to Sakharov's conditions for the formation of the baryon asymmetry in the early Universe, it has to be strongly of the first order. In the Two Higgs doublets SM, there is a parametric space, where the first-order phase transition is realized for the realistic Higgs boson mass $m_{\rm H} = 125$ GeV. On the other hand, in the hot Universe, the spontaneous magnetization of a plasma had happened. The spontaneously generated (chromo) magnetic fields are temperature-dependent. They influence the EWPT. The color chromomagnetic fields B_3 and B_8 are created spontaneously in the gluon sector of QCD at a temperature $T > T_d$ higher the deconfinement temperature T_d. The usual magnetic field H has also to be spontaneously generated. For T close to the T_{EWPT}, these magnetic fields could change the kind of the phase transition.

Keywords: electroweak phase transition, standard model, deconfinement.

1. Introduction

In the Early Universe, there are many phase transitions. The most important is EWPT, when particles acquired masses. Other important problem is baryogenesis.

As is well known, in the Minimal Standard Model (MSM) of elementary particles, EWPT is of the first order for the mass of a Higgs boson less than 75 GeV. For greater masses, it is of the second order. Experiments give $m_{\rm H} = 125$ GeV. Sakharov [1] proposed the conditions for generation of the asymmetry between baryons and antibaryons. Today, they are formulated as three baryogenesis conditions. According to them, the phase transition should be strongly of the first order. So, Sakharov's conditions are violated.

Another important property of non-Abelian gauge fields at high temperatures is a spontaneous vacuum magnetization. It is closely related to the asymptotic freedom, which happens due to a large magnetic moment of charged color gluons (gyromagnetic ratio $\gamma = 2$).

In fact, the asymptotic freedom at high temperatures is always accompanied by the background stable, temperature-dependent, and long-range chromomagnetic fields [2].

The magnetization phenomenon was investigated in the SU(3) gluodynamics in detail [3], and the supersymmetric theories [4, 5] were developed by analytic methods and in the SU(2) gluodynamics [6, 7] by Monte-Carlo simulations on a lattice. In all these cases, the spontaneous creation of magnetic fields was bdetected. Within the application to the early Universe, the spontaneous vacuum magnetization in the electroweak sector of the standard model was described in [8].

At the LHC experiments, a new matter, namely, phase–quark–gluon plasma (QGP), has to be produced in heavy ion collisions. The deconfinement phase transition (DPT) temperature is expected to be of the order of T_d ∼180–200 MeV. In theory, the investigation of the DPT and QGP properties were carried out by different method – analytic perturbative and nonperturbative.

In papers [9, 10], we have shown that, due to the vacuum polarization of quark fields by the color magnetic fields B_3 and B_8 existing in the QGP after DPT, the usual magnetic field H can be generated for temperatures $T_d < T < T_{\rm EWPT}$. The field H is temperature-dependent and occupies a large plasma volume as the fields B_3 and B_8 [3].

In the present paper, we will investigate the influence of the magnetic and chromomagnetic fields spontaneously created after DPT on EWPT. The magnetic fields could realize Sakharov's conditions in MSM and change the behavior of phase transitions as in the superconductivity. The proper time representation is used. The effective potential of the external fields $V(\phi, B_3, B_8, H, T)$ with one-loop plus daisy diagrams accounting for the gluons and all quark flavors at finite temperatures is calculated. This field configuration is stable due to the daisy diagram contributions, which cancel the imaginary terms presenting in the one-loop effective potential of charged gluons $V^{(1)}(B_3, B_8, T)$. To estimate the field strengths, the asymptotic high temperature expansion derived by Mellin's transformation technique is applied [2, 11].

2. Effective Potential of MSM with Magnetic Fields at Finite Temperatures

The spontaneous vacuum magnetization has been derived from the investigation of the effective potential (EP) of covariantly constant(soursless) chromomagnetic fields $H^a = H\delta^{a3}$, which is a solution to the classical Yang–Mills field equation, where $H = \text{const}$, and a is an isotopic index,

$$V(H,T) = \frac{H^2}{2} + V^{(1)}(H,T). \tag{1}$$

It includes the tree-level and one-loop parts. The minimum of the EP at a high temperature T corresponds to the nonzero magnetic field.

The Lagrangian of the boson sector of the Salam–Weinberg model is

$$L = -\frac{1}{4}F^a_{\mu\nu}F^{\mu\nu}_a - \frac{1}{4}G_{\mu\nu}G^{\mu\nu} + (D_\mu\Phi)^+(D^\mu\Phi) + \\ + \frac{m^2}{2}(\Phi^2 + \Phi) - \frac{\lambda}{4}(\Phi^2 + \Phi)^2, \tag{2}$$

where the following standard notations are introduced:

$$F^a_{\mu\nu} = \partial_\mu A^a_\nu - \partial_\nu A^a_\mu + g\varepsilon^{abc}A^b_\mu A^c_\nu, \\ G^a_{\mu\nu} = \partial_\mu B_\nu - \partial_\nu B_\mu, \\ D_\mu = \partial_\mu + \frac{1}{2}igA^a_\mu\tau^a + \frac{1}{2}ig'B_\mu. \tag{3}$$

The vacuum expectation value of the field Φ is

$$\langle\Phi\rangle = \frac{1}{\sqrt{2}}\begin{pmatrix}0\\ \phi_c\end{pmatrix}. \tag{4}$$

The fields of Z-, $W^\pm$-bosons, and photons are

$$W^\pm_\mu = \frac{1}{\sqrt{2}}(A^1_\mu \pm iA^2_\mu), \\ Z_\mu = \frac{1}{\sqrt{g^2+g'^2}}(gA^3_\mu - g'B_\mu), \\ A_\mu = \frac{1}{\sqrt{g^2+g'^2}}(g'A^3_\mu + g'B_\mu). \tag{5}$$

For the investigation of EWPT, according to [9, 13], the EP is

$$V(H,T,\phi_c) = \frac{H_8^2}{2} + \frac{H_3^2}{2} + \frac{H^2}{2} + \\ + V^{(0)}(\phi_c) + V^{(1)}(H,T,\phi_c) + V^{(\text{Ring})}(H,T,\phi_c). \tag{6}$$

To compute the EP $V^{(1)}$ in the background magnetic fields, let us introduce the proper time, and s-representation for the Green functions:

$$G^{ab} = -i\int \exp(-is(G^{-1})^{ab})ds. \tag{7}$$

To incorporate the temperature into this formalism, the connection between the Matsubara Green function and the Green function at the zero temperature is needed:

$$G^{ab}_k(x,x';T) = \\ = \sum_{-\infty}^{+\infty}(-1)^{(n+[x])\sigma_k}G^{ab}_k(x-[x]\beta u, x'-n\beta u), \tag{8}$$

where G^{ab}_k is the corresponding function at $T = 0$, $\beta = 1/T$, $u = (0,0,0,1)$, $[x]$ denotes an integer part of $x_4/\beta, \sigma_k = 1$ in the case of physical fermions, and $\sigma_k = 0$ for bosons and ghost fields.

The one-loop contribution to EP is given by the expression

$$V^{(1)} = -\frac{1}{2}\text{Tr}\ \ln G^{ab}, \tag{9}$$

where G^{ab} stands for the propagators of all the quantum fields $W^\pm, Z, ...$ in the background magnetic field H.

The term with $n = 0$ in Eqs. (8) and (9) gives the zero-temperature expression for the Green function and EP, respectively.

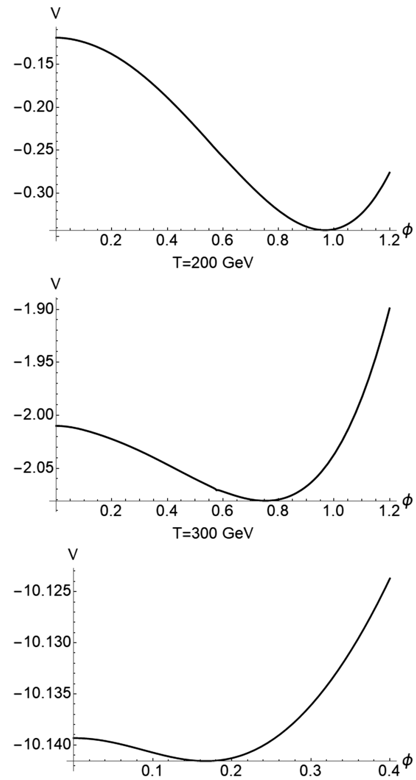

Fig. 1. Effective potential view at different temperatures; the symmetry is broken

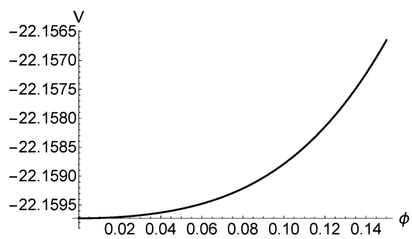

Fig. 2. Effective potential view at a temperature of 365 GeV; the symmetry is restored

Strengths of generated fields

T, GeV	ϕ	V	$H, 10^{21}$ G	$H_3, 10^{23}$ G	$H_8, 10^{23}$ G
100	0.96	-0.35	0.436	0.131	1.092
200	0.75	-2.1	1.97	0.601	3.17
260	0.4	-4.9	3.28	0.928	4.91
300	0.26	-10.14	4.70	1.20	6.66
350	0.11	-18.77	6.66	2.13	9.28
363	0.01	-21.68	6.69	2.18	9.51

In the quark sector of EP, we have the mixing of external magnetic and chromomagnetic fields, according to [9]. The next linear combinations are appear

$$\begin{cases} \mathcal{H}_f^1 = q_f H + g\left(\dfrac{H_3}{2} + \dfrac{H_8}{2\sqrt{3}}\right); \\ \mathcal{H}_f^2 = q_f H + g\left(\dfrac{H_8}{2\sqrt{3}} - \dfrac{H_3}{2}\right); \\ \mathcal{H}_f^3 = q_f H - g\dfrac{H_8}{\sqrt{3}}. \end{cases} \tag{10}$$

They are included in the quark part of EP

$$V_{\text{quark}} = \frac{1}{8\pi^2}\sum_f \sum_{a=1}^{3} \sum_{l=-\infty}^{\infty} (-1)^l \times$$
$$\times \int_0^\infty \frac{ds}{s^3}\, e^{-m_f^2 s - \frac{\beta^2 l^2}{4s}} \left(s\mathcal{H}_f^a \coth\left(s\mathcal{H}_f^a\right) - 1\right). \tag{11}$$

In our calculations, H, H_3, and H_8 are parameters. To investigate EWPT, we need to calculate EP as a function of ϕ_c at some constant temperature and for different temperatures, to look after the behavior of the symmetry, and to find the values of parameters, which minimize EP.

3. Numerical Results

For numerical calculations, we use the following dimensionless parameters:

$$\begin{gathered} V^0 = \frac{V^{(0)}e^2}{M_W^4}; \quad V^T = \frac{V^{(T)}e^2}{M_W^4}; \quad \phi = \frac{\phi_c}{\delta(0)}; \\ \mu_f = \frac{m_f}{M_W}; \quad h_{f,a} = \frac{e\mathcal{H}_f^a}{M_W^2}; \quad \beta_p = M_W\beta. \end{gathered} \tag{12}$$

After the calculation, we should find the minimum value depending on ϕ, H_3, H_8, and H for a fixed temperature.

The strength of generated fields at the energy minimum is shown in Table. The most important point is the next one – we have nonzero chromomagnetic and magnetic fields and a negative value of EP. The magnetic field is two orders less than the chromomagnetic one.

In Figs. 1 and 2, the behavior of the symmetry is shown. We have minimum of EP with a nonzero scalar field. The symmetry is restored at high temperatures. The critical temperature is obtained near $T_{\text{EWPT}} = 365$ GeV.

4. Conclusions

In our calculations, we applied the consistent approximation for the effective potential accounting for the one-loop plus daisy diagrams. It includes the terms of the order $\sim g^2$ and $\sim g^3$ and makes the potential real due to the cancellation of the imaginary terms. That is sufficient at high temperatures because of small couplings.

The most interesting observation of the above investigation is twofold. First, as the temperature grows, the magnetic field strengths are increased. Second, simultaneously, the value of the effective potential at the minimum is negative.

Really, as we have noted already, the asymptotic freedom at high temperatures has always to be accompanied by the temperature-dependent background magnetic fields [2].

As it follows from the obtained results, the strong chromo(magnetic) fields of the order $H_{3,8} \sim 10^{18}$–10^{19} G and $H \sim 10^{16}$–10^{17} G must be present in QGP [9]. This influences all the processes happening and may serve as the distinguishable signals of DPT. Due to the magnetization, in particular, all the initial states of charged particles have to be discrete ones. These fields are present at higher temperatures, as the deconfinement appears. At temperatures close to T_{EWPH}, the strengths are 5 order higher than for the deconfinement temperature.

We have demonstrated that EWPT in MSM has the critical temperature near 360 GeV, and the nonzero magnetic and chromomagnetic fields should be spontaneously generated as well. In Fig. 1, we see that there is no reheating phase. This illustrates that the phase transition is of the second type, and Sakharov's conditions are not satisfied. So, even with magnetic and chromomagnetic fields, the phase transition is of the second order.

As was shown in [12], the Sakharov conditions can be satisfied in the parametric space of the Two Higgs doublet Standard Model without background magnetic fields.

This work is partially supported by the ICTP through AF-06.

1. A.D. Sakharov. Violation of CP Invariance, C asymmetry, and baryon asymmetry of the universe. *JETP Lett.* **5**, 32 (1967).
2. V. Skalozub. Effective coupling constants in gauge theories at high temperature. *Int. J. Mod. Phys. A* **11** 5643 (1996).
3. V. Skalozub, A. Strelchenko. On the generation of Abelian magnetic fields in SU(3) gluodynamics at high temperature. *Eur. Phys. J. C* **33**, 105 (2004).
4. M.D. Pollock. Magnetic fields and vacuum polarization at the Planck era. *Int. J. Mod. Phys. D* **12**, 1289 (2003).
5. V.I. Demchik, V.V. Skalozub. The spontaneous generation of magnetic fields at high temperature in a supersymmetric theory. *Eur. Phys. J. C* **27**, 601 (2003).
6. V. Demchik, V. Skalozub. The spontaneous creation of a chromomagnetic field and A_0-condensate at high temperature on a lattice. *J. Phys. A* **41**, 164051 (2008).
7. S. Antropov, M. Bordag, V. Demchik, V. Skalozub. Long range chromomagnetic fields at high temperature. *Intern. J. Mod. Phys. A* **26**, 4831 (2011).
8. V. Demchik, V. Skalozub. Spontaneous magnetization of a vacuum in the hot Universe and intergalactic magnetic fields. *Phys. Part. Nucl.* **46**, 1 (2015).
9. V. Skalozub, P. Minaiev. Magnetized quark-gluon plasma at the LHC. *Phys. Part. Nucl. Lett.* **15**, 568 (2018).
10. V. Skalozub, P. Minaiev. On magnetization of quark-gluon plasma at the LHC experiment energies. *Visnyk Dnipropetr. Univ. Fiz. Radioel.* **24**, (2016).
11. H.E. Haber, H.A. Weldon. On the relativistic Bose–Einstein integrals. *J. Math. Phys.* **23**, 1852 (1982).
12. V. Skalozub, A. Kozhushko. The parametric space of the two-Higgs-doublet model and Sakharov's baryogenesis conditions. *Ukr. J. Phys.* **56**, 431 (2011).
13. V. Skalozub, V. Demchik. Electroweak phase transition in strong magnetic fields in the standard model of elementary particles. arXiv:hep-th/9912071v1 (1999).

Received 08.07.19

П. Мінаєв, В. Скалозуб

ЕЛЕКТРОСЛАБКИЙ ФАЗОВИЙ
ПЕРЕХІД В СПОНТАННО НАМАГНІЧЕНІЙ ПЛАЗМІ

Р е з ю м е

Досліджується електрослабкий фазовий перехід в мінімальній (один дуплет хіггсівських бозонів) Стандартній Моделі (СМ) з урахуванням спонтанного народження магнітних та хромомагнітних полів при високій температурі. Як відомо, в СМ для маси бозона Хіггса, більшій за 75 ГеВ, цей фазовий перехід є переходом другого роду. Але відповідно до критеріїв Сахарова для формування баріонної асиметрії на ранніх етапах еволюції Всесвіту, він повинен бути жорстким переходом першого роду. В параметричному просторі дводуплетної СМ без магнітних полів можливий перехід першого роду. В ранньому Всесвіті існували спонтанно народжені температурозалежні магнітні та хромомагнітні поля. Хромомагнітні поля B_3 і B_8 народжувались в глюонному секторі КХД за температури $T > T_d$, більшої за температуру деконфайменту T_d. Звичайне магнітне поле народжувалось за рахунок кваркових петель. Як результат, для температур T, близьких до критичної температури T_{EWPT}, ці поля можуть змінити характер фазового переходу.

https://doi.org/10.15407/ujpe64.8.714

T.V. OBIKHOD, I.A. PETRENKO

Institute for Nuclear Research, Nat. Acad. of Sci. of Ukraine
(47, Prosp. Nauky, Kyiv 03680, Ukraine; e-mail: obikhod@kinr.kiev.ua)

MASS RECONSTRUCTION OF MSSM HIGGS BOSON

The problems of the Standard Model, as well as questions related to Higgs boson properties led to the need to model the ttH associated production and the Higgs boson decay to a top quark pair within the MSSM model. With the help of computer programs MadGraph, Pythia, and Delphes and using the latest kinematic cuts taken from experimental data obtained at the LHC, we have predicted the masses of MSSM Higgs bosons, A and H.

Keywords: MSSM Higgs boson, top quark, b-tagging, computer modeling, the mass of a Higgs boson.

1. Introduction

The study of the properties of a Higgs boson discovered in 2012 is one of the main objectives of the LHC [1]. The importance of the experiments is related to the refinement of the channels of formation and decay of the Higgs boson, which shows that there are deviations of more than 2σ from the Standard Model (SM). Such data, together with the theoretical predictions of new physics, such as supersymmetry and the theory of extra dimensions, lead to the need to model the properties of the Higgs boson beyond the SM (BSM) such as production cross sections, angular distributions, and masses of supersymmetric Higgs bosons.

The existence of SM problems related to the impossibility of combining gravity with the other three types of interactions, the problem of radiative corrections to the Higgs boson mass, neutrino oscillations, and dark matter and dark energy problems lead to the introduction of new theories, one of which is supersymmetry. There are many supersymmetric theories. We will further use Minimal Supersymmetric Standard Model (MSSM) for the prediction of new supersymmetric particles – superpartners of the Higgs boson. The advantage of such a search lies not only in the possibility of going beyond the framework of the SM, but also in the small mass of the Higgs superparticles provided by the new theories. Such searches could be implemented both at the existing LHC collider, and at future accelerators of the type ILC or FCC. To establish a deviation from the SM behavior, the next goal is to identify the nature of the electro-weak symmetry breaking (EWSB), which is connected with properties of the top quark and Higgs boson interactions. Predictions for the coupling of the Higgs boson to top quarks directly influence the measurements of the production and decay rates and angular correlations. Therefore, this information can be used to study whether the data are compatible with the SM predictions for the Higgs boson. Since the QCD and electroweak gauge interactions of top quarks have been well established, the top Yukawa coupling might differ from the SM value. Therefore, the measurement of the ttH production rate and the tt decay of an A boson can provide a direct information about the top-Higgs Yukawa coupling, probably the most crucial coupling to fermions. The anomalous interaction of the Higgs boson with the top quark, has been experimentally studied through the measurement of the Higgs boson production in association with a top quark, [2]. According to the combined analysis of the experimental data at the LHC, the constrain on the top quark Yukawa coupling, y_t, within $[-0.9, -0.5]$ and $[1.0, 2.1] \times y_t^{\rm SM}$ were obtained. Recent ATLAS Higgs results using Run-2 data at a center-of-mass energy of 13 TeV with up to an integrated luminosity of 80 fb^{-1} to probe BSM coupling for the $tH + ttH$ processes [3] showed that the Higgs boson will continue to provide an important probe for new physics and beyond.

To implement the searches for the MSSM Higgs bosons and to facilitate their findings, we chose a specific search channels and the methods by which the corresponding superparticles were identified. Using the latest experimental data for the ttH production of a Higgs boson [4], b-tagging algorithm, MadGraph, Pythia, and Delphes programs, and latest kinematic cuts we predicted the masses of superparticles, A and H.

2. B-Tagging Identification and Reconstruction of MSSM Higgs Boson Masses

The top-quark Yukawa coupling y_t is parametrized as

$$L_{Htt} = -\frac{m_t}{v} H\bar{t}(a_t + ib_t\gamma_5)\, t,$$

where m_t is the top-quark mass, $v = 174$ GeV is the vacuum expectation value, and the coefficient a (b) denotes the CP-even (CP-odd) coupling, respectively.

Examples of Feynman diagrams for the considered tt and ttH processes are presented in Fig. 1.

It is necessary to reconstruct as many final particles as possible for the disentanglement of decay products of the exotic particles from the SM background. The B-tagging identification connected with b-quark signatures has following features and benefits for the experimental determination of primary particles:

- hadrons containing b-quarks have sufficient lifetime;
- presence of a secondary vertex (SV);
- tracks with large impact parameter (IP);
- the bottom quark is much more massive, with mass about 5 GeV, and thus its decay products have higher transverse momentum;
- b-jets have higher multiplicities and invariant masses;
- the B-decay produces often leptons.

We carried out a comprehensive computer modeling of the MSSM Higgs boson mass using MadGraph, Pythia, and Delphes programs. With the help of the program MadGraph, we carried out a calculation of the production cross-sections of the processes under consideration. The simulation of further developments, i.e. all information on decomposition products and their kinematic data, was produced using the Pythia program. In our calculations with the Pythia program, we used the latest experimental constraints on the low $\tan\beta$ region covered by the ttH, $H \to tt$ processes [5]. The calculation of the response of a detector to the resulting array of events was carried out using the Delphes program. We made a selection of events on the basis of additional kinematic restrictions associated with the peculiarities of the reactions under consideration and the b-tagging method.

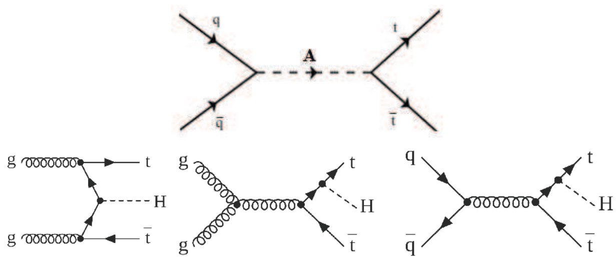

Fig. 1. Examples of Feynman diagrams for the $pp \to A$ (up) and $pp \to ttH$ (down) production process from [4]

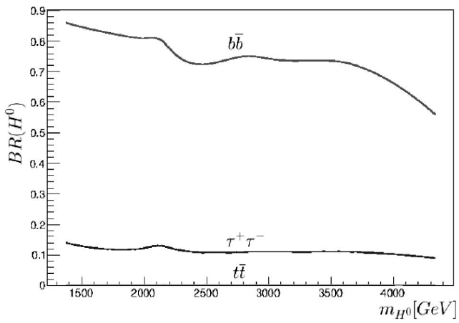

Fig. 2. Branching ratios of H to bb (red), $\tau^+\tau^-$ (blue), and tt (green)

Let us consider these processes separately and in more details.

2.1. $pp \to A \to tt$ process

The importance of the formation of a top quark pair is associated both with the possibility of a good identification of top quarks using the b-tagging algorithm and with the search for new physics due to the Yukawa constants of the top-quark and Higgs boson interaction [6]. The SM makes predictions for the coupling of the Higgs boson to a top quark. Therefore, the measurement of the decay rates of the observed state yields the information which can be used to probe whether data are compatible with the SM predictions for the Higgs boson. Loop-induced vertices allow probing for BSM contributions of new particles in the loops. In addition, it must be said that the the measuring of the properties of top pair quarks also sheds light on the stability of the electroweak vacuum [7]. The importance of this section is connected with the improvement of the searches for $H \to tt$ by studying the fully leptonic and semileptonic final states [8]. The results of our calculations presented in [9] are shown in Fig. 2.

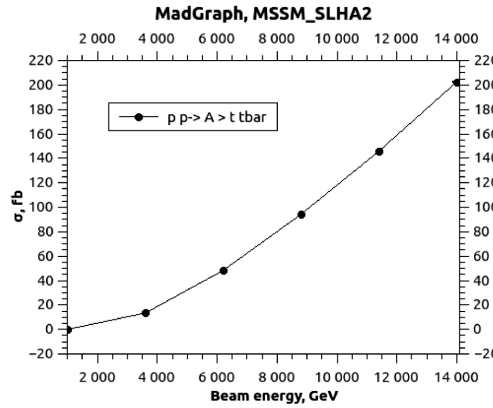

Fig. 3. Production cross section of the $pp \to A \to t\bar{t}$ process

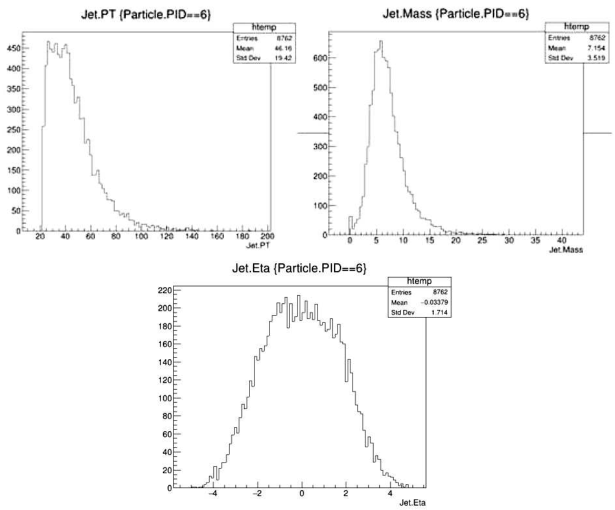

Fig. 4. Modeling of kinematic properties of jets from the reaction $pp \to A \to tt$: jet p_T distribution (left) and jet mass (right) (a); jet η distribution (b)

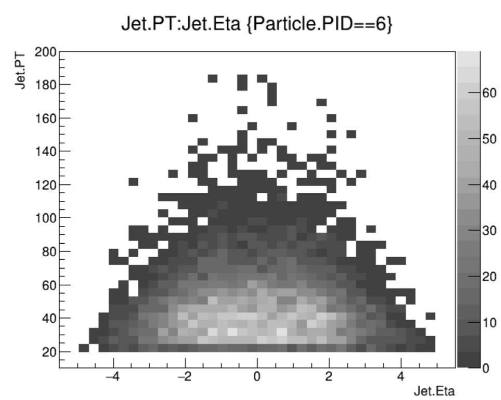

Fig. 5. Distribution for jets over the momenta and angles for the reaction $pp \to A \to tt$

The most probable decay channels for a CP-even boson, H, are the following:

- bb;
- $\tau^+\tau^-$;
- $t\bar{t}$.

We are dealing with massive MSSM particles which prefer to decay into the most massive decay products, for example, into a top-anti-top quark pair. So, we will consider the decay of the CP-odd Higgs boson into a top-anti-top quark pair, $A \to t\bar{t}$. With the help of the program MadGraph, we calculated the production cross-section of the $pp \to A \to t\bar{t}$ process presented in Fig. 3.

The increase of the production cross-section with the energy at the LHC and its large value for the formation of an A boson, about 0.2 pb at the energy of 14 TeV, lead to the conclusion about the importance of the consideration of this channel of formation and decay of the MSSM Higgs boson. Kinematic properties of decay products of A boson at the energy 14 TeV were modeled and presented in Fig. 4.

From Fig. 4, we see that jet p_T is maximal in the region of 30–50 GeV/c and then sharply decreases in the region of 120–140 GeV/c. The average jet mass is about 5–7 GeV/c, which is in accordance with the mass of the b-quark, into which the top quark decays with a probability of 99.8%. The angular distribution of the decay products shown in Fig. 4, b indicates the predominant direction of the decay products in the direction of angles from 35° to 90° to the axis of the proton-proton collision. In Fig. 5, we present the distribution for jets over the momenta and angles.

Using the distribution of Fig. 5, we can pick out the most high-energetic jets and present their separation in Fig. 6.

Using the data of Fig. 6, we can predict the mass of the A boson, which is about 360 GeV/c, since the momentum is equal to the mass at high energies.

2.2. ttH production process

We considered a combined analysis of proton-proton collision data at center-of-mass energies of $\sqrt{s} = 7$, 8, and 13 TeV, corresponding to integrated luminosities up to 5.1, 19.7, and 35.9 fb^{-1}, respectively. In this experiment, the observation of the ttH production with a significance of 5.2 standard deviations above the background-only hypothesis, at a Higgs boson mass of 125.09 GeV was reported in [4]. Then we consid-

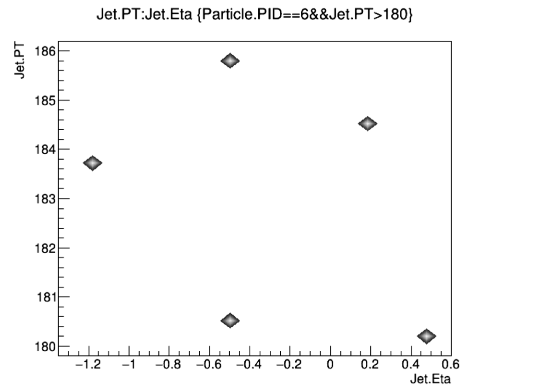

Fig. 6. The most energetic jets in the p_T range 180–186 GeV/c and the jet $\eta > |1.2|$ for the reaction $pp \to A \to tt$

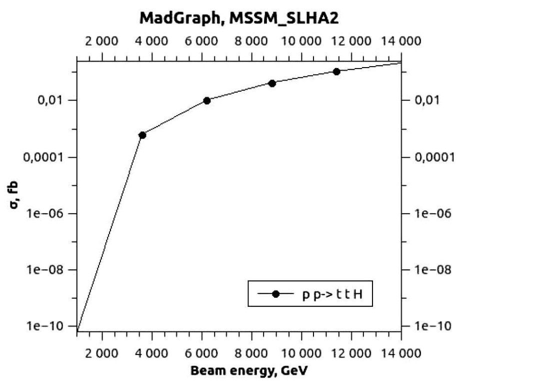

Fig. 7. Production cross-section of the $pp \to Htt$ process as a function of the energy range at the LHC

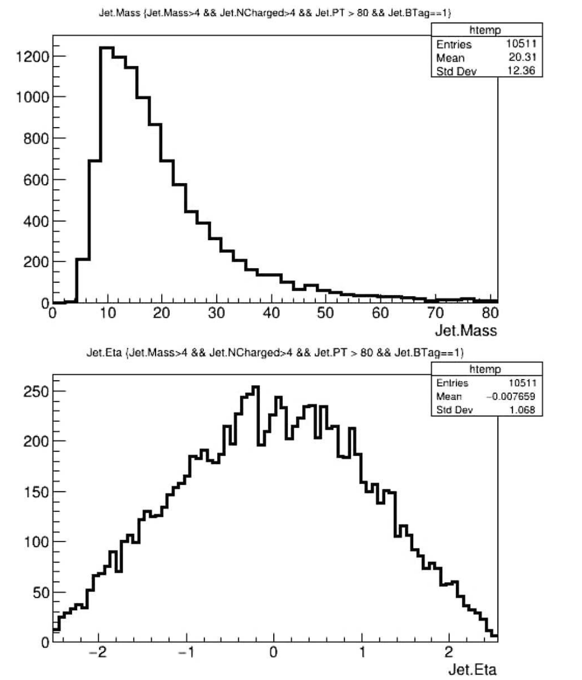

Fig. 8. Modeling of the jet mass range (a) and the angular distribution of jets (b)

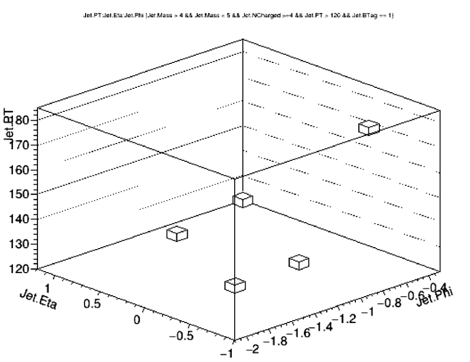

Fig. 9. Modeled angular and p_T jet distributions

ered the decay process of the Higgs boson, $H \to bb$, as the most probable [9].

Using the program MadGraph, we calculated the production cross-sections $pp \to Htt$ of a Higgs boson via the proton-proton interaction. Our calculations for the range of 2–14 TeV at the LHC are presented in Fig. 7.

With the program Pythia, we simulated a further development of events. The detector response to the received array of events was modeled by the program Delphes. Thus, our simulation was maximally close to the experimental conditions.

The results of calculations of the jet mass range and the eta distribution of jets are presented in Fig. 8. The events were selected with the following cuts: the number of jets, $N_{\text{charged}} >$ or ~ 4, transverse momentum, $p_T > 80$ GeV, $B_{\text{tag}} = 1$, mass of one b-jet, $M > 4$ GeV. From the jet distribution in Fig. 4, we conclude that the mass of jets of about 16–20 GeV for the minimal number of jets equal to 4 corresponds to the b-jet distribution and to the corresponding angular distribution of jet flux signals about the selected distribution of the jet flow in the direction perpendicular to the proton collision axis with $\theta \sim 40°$–$90°$.

As a result of the detector response calculations for the process $pp \to Htt \to Hbbbb$ with $N = 5000$ initial events and corresponding cross section of about 0.517 fb at 14 TeV at the LHC, we get the angular and p_T jet distributions presented in Fig. 9.

We have used together the following kinematic constraints: rapidity $-0.5 < y < 0.5$, mass of jets of about $4 < M < 5$ GeV, number of charge jets, $N_{\text{charged}} > 4$, transverse momentum, $p_T > 120$ GeV, parameter of the MSSM model, $M_H \sim 500$ GeV. Thus, we selected the toughest and most massive jets that can be formed from the decay process of the CP-even Higgs boson of the MSSM model. As we can see from Fig. 9, the approximate mass of one jet is about 150–170 GeV/c. We used the fact that each of the protons has an energy of 7 TeV, giving a total collision energy of 14 TeV. At this energy, the protons move at about 0.999999990 of the speed of light. Knowing the most probable Higgs boson decay channel, $H \to bb$, we conclude that the mass of the CP-even Higgs boson is about 300–340 GeV/c.

3. Conclusions

We have considered the most important channels of the MSSM Higgs boson production and decay. Since these channels are associated with the formation and decay of top quarks, whose properties shed light on the instability of the electroweak vacuum, the study of such reactions seems the most relevant to us. In addition, the MSSM Higgs bosons are the lightest supersymmetric particles predicted by supersymmetry. Therefore, finding their masses at the LHC collider is possible in the near future, which would remove a lot of theoretical questions related to the symmetries and unification of interactions. Using the programs MadGraph, Pythia, and Delphes to simulate the processes and to model the response of a detector, as well as strict kinematic cuts on the angles and momenta of particles taken from the experimental data, we have calculated the masses of the A boson equal to 360 GeV/c and H boson equal approximately to 320 GeV/c.

Our thanks to the organizers of the conference "New Trends in High-Energy Physics," Odessa, Ukraine May 12–18, 2019 and, in particular, to Laszlo L. Jenkovszky for organizing an important scientific event on topical issues of high-energy physics.

1. Y. Liu, S. Moretti. Probing anomalous top-Higgs couplings at the HL-LHC via $H \to WW^*$ decay channels. *Chin. Phys. C* **43** (1), 013102 (2019).
2. R. Goncalo. Recent highlights in top quark and Higgs boson physics from the LHC. *J. Phys.: Conf. Series* **1137**, 012012 (2019).
3. W. Leight. Studies of the SM Higgs Boson and Searches for BSM Higgs Bosons with the ATLAS Detector. *Acta Phys. Polon. B Proc. Sup.* **9** (3), 561 (2016).
4. CMS Collaboration. Observation of ttH production. *Phys. Rev. Lett.* **120**, 231801 (2018).
5. C. Gao, M. Luty, M. Mulhearn, N. Neill, Z. Wang. Searching for additional Higgs bosons via Higgs cascades. *Phys. Rev. D* **97** (7), 075040 (2018).
6. LHC Higgs Cross Section Working Group. Handbook of LHC Higgs Cross Sections: 3. Higgs Properties. arXiv:1307.1347 [hep-ph].
7. S. Alekhin, A. Djouadi, S. Moch. The top quark and Higgs boson masses and the stability of the electroweak vacuum. *Phys. Lett. B* **716**, 214 (2012).
8. M. Guchait, A. Vijay. Probing heavy charged Higgs boson at the LHC. *Phys. Rev. D* **98** (11), 115028 (2018).
9. T.V. Obikhod. Experimental searches for the extended Higgs sector at the LHC. *Prob. Atom. Sci. Technol. Series: Nucl. Phys. Invest.* **67**, 3 (2016).

Received 08.07.19

Т.В. Обіход, Е.О. Петренко

РЕКОНСТРУКЦІЯ МАСИ MSSM БОЗОНА ХІГГСА

Р е з ю м е

Проблеми Стандартної Моделі, а також питання, пов'язані з властивостями бозона Хіггса, призвели до необхідності моделювання ttH асоційованого утворення і розпаду бозона Хіггса на топ кваркову пару в рамках MSSM моделі. За допомогою комп'ютерних програм MadGraph5, Pythia8 і Delphes3 та використання останніх кінематичних обмежень, взятих з експериментальних даних, отриманих на LHC, ми передбачили маси MSSM бозонів Хіггса, A і H.

https://doi.org/10.15407/ujpe64.8.719

G.X.A. PETRONILO, S.C. ULHOA, A.E. SANTANA

Centro Internacional de Física, Universidade de Brasília
(70910-900, Brasília, DF, Brazil; e-mail: gustavopetronilo@gmail.com)

SYMPLECTIC FIELD THEORY OF THE GALILEAN COVARIANT SCALAR AND SPINOR REPRESENTATIONS

We explore the concept of the extended Galilei group, a representation for the symplectic quantum mechanics in the manifold $\mathcal{G}$, written in the light-cone of a five-dimensional de Sitter space-time in the phase space. The Hilbert space is constructed endowed with a symplectic structure. We study the unitary operators describing rotations and translations, whose generators satisfy the Lie algebra of $\mathcal{G}$. This representation gives rise to the Schrödinger (Klein–Gordon-like) equation for the wave function in the phase space such that the dependent variables have the position and linear momentum contents. The wave functions are associated to the Wigner function through the Moyal product such that the wave functions represent a quasiamplitude of probability. We construct the Pauli–Schrödinger (Dirac-like) equation in the phase space in its explicitly covariant form. Finally, we show the equivalence between the five-dimensional formalism of the phase space with the usual formalism, proposing a solution that recovers the non-covariant form of the Pauli–Schrödinger equation in the phase space.

K e y w o r d s: Galilean covariance, star-product, phase space, symplectic structure.

1. Introduction

In 1988, Takahashi *et. al.* [1] began a study of the Galilean covariance, where it was possible to develop an explicitly covariant non-relativistic field theory. With this formalism, the Schrödinger equation takes a similar form as the Klein–Gordon equation in the light-cone of a (4,1) de Sitter space [2, 3]. With the advent of the Galilean covariance, it was possible to derive the non-relativistic version of the Dirac theory, which is known in its usual form as the Pauli–Schrödinger equation. The goal in the present work is to derive a Wigner representation for such covariant theory.

The Wigner quasiprobability distribution (also called the Wigner function or the Wigner–Ville distribution in honor of Eugene Wigner and Jean–André Ville) was introduced by Eugene Wigner in 1932 [4] in order to study quantum corrections to classical statistical mechanics. The aim was to relate the wave function that appears in the Schrödinger equation to a probability distribution in the phase space. It is a generating function for all the spatial autocorrelation functions of a given quantum mechanical function $\psi(x)$. Thus, it maps the quantum density matrix onto the real phase space functions and operators introduced by Hermann Weyl in 1927 [5] in a context related to the theory of representations in mathematics (Weyl quantization in physics). Indeed, this is the Wigner–Weyl transformation of the density matrix; i.e., the realization of that operator in the phase space. It was later re-derived by Jean Ville in 1948 [6] as a quadratic representation (in sign) of the local time frequency energy of a signal, effectively a spectrogram. In 1949, José Enrique Moyal [7], who independently derived the Wigner function, as the functional generator of the quantum momentum, as a basis for an elegant codification of all expected values and, therefore, of quantum mechanics in the phase-space formulation (phase-space representation). This representation has been applied to a number of areas such as statistical mechanics, quantum chemistry, quantum optics, classical optics, signal analysis, electrical engineering, seismology, time-frequency analysis for music signals, spectrograms in biology and speech processing, and motor design. In order to derive a phase-space representation for the Galilean-covariant spin 1/2 particles, we use a symplectic representation for the Galilei group, which is associated with the Wigner approach [8–11].

This article is organized as follows. In Section 2, the construction of the Galilean covariance is presented. The Schrödinger (Klein–Gordon-like) equation and the Pauli–Schrödinger (Dirac-like) equation are derived showing the equivalence between our formalism and the usual non-relativistic formalism. In Section 4, a symplectic structure is constructed in the Galilean manifold. Using the commutation relations, the Schrödinger equation in five dimensions in the phase space is constructed. With a proposed solution, the Schrödinger equation in the phase space is restored to its non-covariant form in $(3+1)$ dimensions. The explicitly covariant Pauli–Schrödinger equation is derived in Section 5. We study a Galilean spin $1/2$ particle in a external potential, and the solutions are proposed and discussed. In Section 6, the final concluding remarks are presented.

2. Galilean Covariance

The Galilei transformations are given by

$$\mathbf{x}' = R\mathbf{x} + \mathbf{v}t + \mathbf{a}, \tag{1}$$

$$t' = t + b, \tag{2}$$

where R stands for the three-dimensional Euclidian rotations, v is the relative velocity defining the Galilean boosts, $\mathbf{a}$ and $\mathbf{b}$ stand for spatial and time translations, respectively. Consider a free particle with mass m; the mass shell relation is given by $\widehat{P}^2 - 2mE = 0$. Then we can define a 5-vector, $p^\mu = (p_x, p_y, p_z, m, E) = (p^i, m, E)$, with $i = 1, 2, 3$.

Thus, we can define a scalar product of the type

$$p_\mu p_\nu g^{\mu\nu} = p_i p_i - p_5 p_4 - p_4 p_5 = \widehat{P}^2 - 2mE = k, \tag{3}$$

where $g^{\mu\nu}$ is the metric of the space-time to be constructed, e $p_\nu g^{\mu\nu} = p^\mu$.

Let us define a set of canonical coordinates q^μ associated with p^μ, by writing a five-vector in M, $q^\mu = (\mathbf{q}, q^4, q^5)$, $\mathbf{q}$ is the canonical coordinate associated with $\widehat{P}$; q^4 is the canonical coordinate associated with E, and thus can be considered as the time coordinate; q^5 is the canonical coordinate associated with m explicitly given in terms of $\mathbf{q}$ and q^4, $q^\mu q_\mu = q^\mu q^\nu \eta_{\mu\nu} = \mathbf{q}^2 - q^4 q^5 = s^2 = 0$. From this $q^5 = \frac{\mathbf{q}^2}{2t}$, or infinitesimally, we obtain $\delta q^5 = \mathbf{v}\,\delta\frac{\mathbf{q}}{2}$. Therefore, the fifth component is basically defined by the velocity.

That can be seen as a special case of scalar product in G denoted as

$$(x|y) = g^{\mu\nu} x_\mu y_\nu = \sum_{i=1}^{3} x_i y_i - x_4 y_5 - x_5 y_4, \tag{4}$$

where $x^4 = y^4 = t$, $x^5 = \frac{x^2}{2t}$ e $y^5 = \frac{y^2}{2t}$. Hence, the following metric can be introduced:

$$(g_{\mu\nu}) = \begin{pmatrix} 1 & 0 & 0 & 0 & 0 \\ 0 & 1 & 0 & 0 & 0 \\ 0 & 0 & 1 & 0 & 0 \\ 0 & 0 & 0 & 0 & -1 \\ 0 & 0 & 0 & -1 & 0 \end{pmatrix}. \tag{5}$$

This is the metric of a Galilean manifold $\mathcal{G}$. In the sequence, this structure is explored in order to study unitary representations.

3. Hilbert Space and Sympletic Structure

Consider an analytical manifold $\mathcal{G}$, where each point is specified by the coordinates q_μ, with $\mu = 1, 2, 3, 4, 5$ and the metric specified by (5). The coordinates of every point in the cotangent-bundle $T^*\mathcal{G}$ will be denoted by (q_μ, p_μ). The space $T^*\mathcal{G}$ is equipped with a symplectic structure via the 2-form

$$\omega = dq^\mu \wedge dp_\mu \tag{6}$$

called the symplectic form (sum over repeated indices is assumed). We consider the following bidifferential operator on $C^\infty(T^*\mathcal{G})$ functions,

$$\Lambda = \frac{\overleftarrow{\partial}}{\partial q^\mu}\frac{\overrightarrow{\partial}}{\partial p_\mu} - \frac{\overleftarrow{\partial}}{\partial p^\mu}\frac{\overrightarrow{\partial}}{\partial q_\mu}, \tag{7}$$

such that, for C^∞ functions, $f(q,p)$ and $g(q,p)$, we have

$$\omega(f\Lambda, g\Lambda) = f\Lambda g = \{f, g\} \tag{8}$$

where

$$\{f, g\} = \frac{\partial f}{\partial q^\mu}\frac{\partial g}{\partial p_\mu} - \frac{\partial f}{\partial p^\mu}\frac{\partial g}{\partial q_\mu}. \tag{9}$$

It is the Poisson bracket, and $f\Lambda$ and $g\Lambda$ are two vector fields given by $h\Lambda = X_h = -\{h, \}$.

The space $T^*\mathcal{G}$ endowed with this symplectic structure is called the phase space and will be denoted by Γ. In order to associate the Hilbert space with the phase space Γ, we will consider the set of square-integrable complex functions, $\phi(q,p)$ in Γ such that

$$\int dpdq\ \phi^\dagger(q,p)\phi(q,p) < \infty \tag{10}$$

is a real bilinear form. In this case, $\phi(q,p) = \langle q,p|\phi\rangle$ is written with the aid of

$$\int dpdq|q,p\rangle\langle q,p| = 1, \tag{11}$$

where $\langle\phi|$ is the dual vector of $|\phi\rangle$. This symplectic Hilbert space is denoted by $H(\Gamma)$.

4. Symplectic Quantum Mechanics and the Galilei Group

In this section, we will study the Galilei group considering $H(\Gamma)$ as the space of representation. To do so, consider the unit transformations $U:\mathcal{H}(\Gamma) \rightarrow \mathcal{H}(\Gamma)$ such that $\langle\psi_1|\psi_2\rangle$ is invariant. Using the Λ operator, we define a mapping $e^{i\frac{\Lambda}{2}} = \star:\Gamma\times\Gamma \rightarrow \Gamma$ called a Moyal (or star) product and defined by

$$f\star g = f(q,p)\exp\left[\frac{i}{2}\left(\frac{\overleftarrow{\partial}}{\partial q^\mu}\frac{\overrightarrow{\partial}}{\partial p_\mu} - \frac{\overleftarrow{\partial}}{\partial p^\mu}\frac{\overrightarrow{\partial}}{\partial q_\mu}\right)\right] g(q,p),$$

it should be noted that we used $\hbar = 1$. The generators of U can be introduced by the following (Moyal–Weyl) star-operators:

$$\widehat{F} = f(q,p)\star = f\left(q^\mu + \frac{i}{2}\frac{\partial}{\partial p_\mu}, p^\mu - \frac{i}{2}\frac{\partial}{\partial q_\mu}\right).$$

To construct a representation of the Galilei algebra in $\mathcal{H}$, we define the operators

$$\widehat{P}^\mu = p^\mu\star = p^\mu - \frac{i}{2}\frac{\partial}{\partial q_\mu}, \tag{12a}$$

$$\widehat{Q}^\mu = q\star = q^\mu + \frac{i}{2}\frac{\partial}{\partial p_\mu}. \tag{12b}$$

and

$$\widehat{M}_{\nu\sigma} = M_{\nu\sigma}\star = \widehat{Q}_\nu\widehat{P}_\sigma - \widehat{Q}_\sigma\widehat{P}_\nu, \tag{12c}$$

where $\widehat{M}_{\nu\sigma}$ and $\widehat{P}_\mu$ are the generators of homogeneous and inhomogeneous transformations, respectively. From this set of unitary operators, we obtain, after some simple calculations, the following set of commutations relations:

$$\left[\widehat{P}_\mu, \widehat{M}_{\rho\sigma}\right] = -i(g_{\mu\rho}\widehat{P}^\sigma - g_{\mu\sigma}\widehat{P}^\rho),$$
$$\left[\widehat{P}_\mu, \widehat{P}_\sigma\right] = 0,$$

and

$$\left[\widehat{M}_{\mu\nu}, \widehat{M}_{\rho\sigma}\right] =$$
$$= -i(g_{\nu\rho}\widehat{M}_{\mu\sigma} - g_{\mu\rho}\widehat{M}_{\nu\sigma} + g_{\mu\sigma}\widehat{M}_{\nu\rho} - g_{\mu\sigma}\widehat{M}_{\nu\rho}).$$

Consider a vector $q^\mu \in G$ that obeys the set of linear transformations of the type

$$\bar{q}^\mu = G^\mu{}_\nu q^\nu + a^\mu. \tag{13}$$

A particular case of interest in these transformations is given by

$$\bar{q}^i = R^i_j q^j + v^i q^4 + a^i \tag{14}$$

$$\bar{q}^4 = q^4 + a^4 \tag{15}$$

$$\bar{q}^5 = q^5 - (R^i_j q^j)v_i + \frac{1}{2}\mathbf{v}^2 q^4. \tag{16}$$

In the matrix form, the homogeneous transformations are written as

$$G^\mu{}_\nu = \begin{pmatrix} R^1{}_1 & R^1{}_2 & R^1{}_3 & v^i & 0 \\ R^2{}_1 & R^2{}_2 & R^2{}_3 & v^2 & 0 \\ R^3{}_1 & R^3{}_2 & R^3{}_3 & v^3 & 0 \\ 0 & 0 & 0 & 1 & 0 \\ v_i R^i{}_j & v_i R^i{}_2 & v_i R^i{}_3 & \frac{\mathbf{v}^2}{2} & 1 \end{pmatrix}. \tag{17}$$

We can write the generators as

$$\begin{aligned} &\widehat{J}_i = \frac{1}{2}\epsilon_{ijk}\widehat{M}_{jk}, \quad \widehat{C}_i = \widehat{M}_{4i}, \\ &\widehat{K}_i = \widehat{M}_{5i}, \quad \widehat{D} = \widehat{M}_{54}. \end{aligned} \tag{18}$$

Hence, the non-vanishing commutation relations can be rewritten as

$$\begin{aligned}
&\left[\widehat{J}_i, \widehat{J}_j\right] = i\epsilon_{ijk}\widehat{J}_k, && \left[\widehat{J}_i, \widehat{K}_j\right] = i\epsilon_{ijk}\widehat{K}_k, \\
&\left[\widehat{J}_i, \widehat{C}_j\right] = i\epsilon_{ijk}\widehat{C}_k, && \left[\widehat{K}_i, \widehat{C}_j\right] = i\delta_{ij}\widehat{D} + i\epsilon_{ijk}J_k, \\
&\left[\widehat{D}, \widehat{K}_i\right] = i\widehat{K}_i, && \left[\widehat{C}_i, \widehat{D}\right] = i\widehat{C}_i, \\
&\left[\widehat{P}_4, \widehat{D}\right] = i\widehat{P}_4, && \left[\widehat{J}_i, \widehat{P}_j\right] = i\epsilon_{ijk}\widehat{P}_k, \\
&\left[\widehat{P}_i, \widehat{K}_j\right] = i\delta_{ij}\widehat{P}_5, && \left[\widehat{P}_i, \widehat{C}_j\right] = i\delta_{ij}\widehat{P}_4, \\
&\left[\widehat{P}_4, \widehat{K}_i\right] = i\widehat{P}_i, && \left[\widehat{P}_5, \widehat{C}_i\right] = i\widehat{P}_i. \\
&\left[\widehat{D}, \widehat{P}_5\right] = i\widehat{P}_5, &&
\end{aligned} \tag{19}$$

These relations have the Lie algebra of the Galilei group as a subalgebra in the case of $\mathcal{R}^3 \times \mathcal{R}$, considering J_i the generators of rotations K_i of the pure Galilei transformations, P_μ the spatial and temporal translations. In fact, we can observe that Eqs. (14) and (15) are the Galilei transformations given by

Eq. (1) and (2) with $x^4 = t$. Equation (16) is the compatibility condition which represents the embedding

$$\mathcal{I} : \mathbf{A} \to A = \left(\mathbf{A}, A_4, \frac{\mathbf{A}^2}{2A_4}\right); \quad \mathbf{A} \in \mathcal{E}_3, A \in \mathcal{G}.$$

The commutation of K_i and P_i is naturally nonzero in this context, so P_5 will be related to the mass, which is the extension parameter of the Galilei group or an invariant of the extended Galilei–Lie algebra. So, the invariants of this algebra in the light cone of the de Sitter space-time are

$$I_1 = \widehat{P}_\mu \widehat{P}^\mu \tag{20}$$

$$I_2 = \widehat{P}_5 = -mI \tag{21}$$

$$I_3 = \widehat{W}_{5\mu} \widehat{W}_5^\mu, \tag{22}$$

where I is the identity operator, m is the mass, $W_{\mu\nu} = \frac{1}{2}\epsilon_{\mu\alpha\beta\rho\nu} P^\alpha M^{\beta\rho}$ is the 5-dimensional Pauli–Lubanski tensor, and $\epsilon_{\mu\nu\alpha\beta\rho}$ is the totally antisymmetric tensor in five dimensions. In the scalar represantation, we can defined $I_3 = 0$. Using the Casimir invariants I_1 and I_2 and applying them to Ψ, we have

$$\widehat{P}_\mu \widehat{P}^\mu \Psi = k^2 \Psi,$$

$$\widehat{P}_5 \Psi = -m\Psi.$$

We obtain

$$\left(p^2 - i\mathrm{p}\,\nabla - \frac{1}{4}\nabla^2 - k^2\right)\Psi = $$
$$= 2\left(p_4 - \frac{i}{2}\partial_t\right)\left(p_5 - \frac{i}{2}\partial_5\right)\Psi,$$

and a solution of this equation is

$$\Psi = e^{-i2p_5q^5}\rho(q^5)e^{-2ip_4t}\chi(t)\Phi(\mathbf{q},\mathbf{p}). \tag{23}$$

Thus,

$$\left(p^2\Phi - i\mathrm{p}\,\nabla\Phi - \frac{1}{4}\nabla^2\Phi - k^2\right)\frac{1}{\Phi} =$$
$$= \frac{1}{2}\left(i\partial_t\chi\right)\left(i\partial_5\rho\right)\frac{1}{\chi\rho},$$

which yields

$$i\partial_t\chi = \alpha\chi, \quad \text{and} \quad i\partial_5\rho = \beta\rho.$$

Thus, our solution for χ and ρ is

$$\chi = e^{-i\alpha t}, \quad \rho = e^{-i\beta q^5}. \tag{24}$$

Using the fact that

$$\widehat{P}_4\Psi = \left(p_4 - \frac{i}{2}\partial_t\right)e^{-i(2p_4+\alpha)t} = -E\,e^{-i(2p_4+\alpha)t}$$

and

$$\widehat{P}_5\Psi = \left(p_5 - \frac{i}{2}\partial_5\right)e^{-i(2p_5+\beta)q^5} = -m\,e^{-i(2p_5+\beta)q^5},$$

we can conclude that

$$\alpha = 2E, \quad \beta = 2m. \tag{25}$$

So, we have

$$\frac{1}{2m}\left(p^2 - i\boldsymbol{p}\,\nabla - \frac{1}{4}\nabla^2\right)\Phi = \left(E + \frac{k^2}{2m}\right)\Phi,$$

which is the usual form of the Schrödinger equation in the phase space for a free particle with mass m and with an additional kinetic energy of $\frac{k^2}{2m}$, that we can always set as the zero of energy.

This equation and its complex conjugate can also be obtained by using the Lagrangian density in the phase space (we use $d^\mu = d/dq_\mu$)

$$\mathcal{L} = \partial^\mu\Psi(q,p)\partial\Psi^*(q,p) + \frac{i}{2}p^\mu[\Psi(q,p)\partial^\mu\Psi^*(q,p) -$$
$$-\Psi^*(q,p)\partial^\mu\Psi(q,p)] + \left[\frac{p^\mu p_\mu}{4} - k^2\right]\Psi.$$

The association of this representation with the Wigner formalism is given by

$$f_w(q,p) = \Psi(q,p) \star \Psi^\dagger(q,p),$$

where $f_w(q,p)$ is the Wigner function. To prove this, we recall that Eq. (23) can be written as

$$\widehat{P}_\mu\widehat{P}^\mu\Psi = p^2 \star \Psi(q,p).$$

Multiplying the right-hand side of the above equation by $\Psi^\dagger$, we obtain

$$(p^2 \star \Psi) \star \Psi^\dagger = k^2\Psi \star \Psi^\dagger. \tag{26}$$

But $\Psi^\dagger \star p^2 = k^2\Psi^\dagger$. Thus,

$$\Psi \star (\Psi^\dagger \star p^2) = k^2\Psi \star \Psi^\dagger. \tag{27}$$

Subtracting (27) from (26), we have

$$p^2 \star f_w(q,p) - p^2 \star f_w(q,p) = 0, \tag{28}$$

which is the Moyal brackets $\{p^2, f_w\}_M$. In view of Eq. (12a), Eq. (28) becomes

$$p_\mu \partial_{q_\mu} f_w(q,p) = 0, \tag{29}$$

where the Wigner function in the Galilean manifold is a solution of this equation.

5. Spin 1/2 Symplectic Represenatio n

In order to study the representations of spin-1/2 particles, we introduce $\gamma^\mu \widehat{P}_\mu$, where $\widehat{P}_\mu = p_\mu - \frac{i}{2}\partial_\mu$ in such a way that, acting on the 5-spinor in the phase space $\Psi(q,p)$, we have

$$\gamma^\mu \left(p_\mu - \frac{i}{2}\partial_\mu\right)\Psi(p,q) = k\Psi(p,q), \tag{30}$$

which is the Galilean-covariant Pauli–Schrödinger equation. Consequently, the mass shell condition is obtained by the usual steps:

$$(\gamma^\mu \widehat{P}_\mu)(\gamma^\nu \widehat{P}_\nu)\Psi(q,p) = k^2\Psi(q,p). \tag{31}$$

Therefore,

$$\gamma^\mu\gamma^\nu(\widehat{P}_\mu\widehat{P}_\nu) = k^2 = \widehat{P}^\mu\widehat{P}_\nu. \tag{32}$$

Since $\widehat{P}_\mu\widehat{P}_\nu = \widehat{P}_\nu\widehat{P}_\mu$, we have

$$\frac{1}{2}(\gamma^\mu\gamma^\nu + \gamma^\nu\gamma^\mu)\widehat{P}_\mu\widehat{P}_\nu = \widehat{P}^\mu\widehat{P}_\nu, \tag{33}$$

so

$$\{\gamma^\mu, \gamma^\nu\} = 2g^{\mu\nu}. \tag{34}$$

Equation (30) can be derived from the Lagrangian density for spin-1/2 particles in the phase space, which is given by

$$\mathcal{L} = -\frac{i}{4}\Big((\partial_\mu\bar{\Psi})\gamma^\mu\Psi - \bar{\Psi}(\gamma^\mu\partial_\mu\Psi)\Big) - (k - \gamma^\mu p_\mu)\Psi\bar{\Psi},$$

where $\bar{\Psi} = \zeta\Psi^\dagger$, with$\zeta = -\frac{i}{\sqrt{2}}\{\gamma^4 + \gamma^5\} = \begin{pmatrix} 0 & -i \\ i & 0\end{pmatrix}$. In the Galilean-covariant Pauli–Schrödinger equation case, the association to the Wigner function is given by $f_w = \Psi \star \bar{\Psi}$, with each component satisfying Eq. (29).

Let us now examine the gauge symmetries in the phase space demanding the invariance of the Lagrangian under a local gauge transformation given by $e^{\Lambda(q,p)}\Psi$. This leads to the minimum coupling,

$$\widehat{P}_\mu\Psi \to (\widehat{P}_\mu - eA_\mu)\Psi = \left(p_\mu - \frac{i}{2}\partial_\mu - eA_\mu\right)\Psi.$$

This describes an electron in an external field with the Pauli–Schrödinger equation given by

$$\left[\gamma^\mu\left(p_\mu - \frac{i}{2}\partial_\mu - eA_\mu\right) - k\right]\Psi = 0. \tag{35}$$

In order to illustrate such result, let us consider a electron in an external field given by $A_\mu(\mathbf{A}, A_4, A_5)$, with $A_4 = -\phi$ and $A_5 = 0$. Considering the representation of the γ^μ matrices

$$\gamma^i = \begin{pmatrix}\sigma^i & 0 \\ 0 & -\sigma^i\end{pmatrix},\ \gamma^4 = \begin{pmatrix}0 & 0 \\ \sqrt{2} & 0\end{pmatrix},\ \gamma^5 = \begin{pmatrix}0 & -\sqrt{2} \\ 0 & 0\end{pmatrix}.$$

where σ^i are the Pauli matrices, and $\sqrt{2}$ is the identity 2×2 matrix multiplied by $\sqrt{2}$. We can rewrite the object Ψ, as $\Psi = \binom{\varphi}{\chi}$, where φ and χ are 2-spinors dependent on $x^\mu; \mu = 1, ..., 5$. Thus, in the representation where $k = 0$, the Eq. (35) becomes

$$\begin{aligned} &\sigma\left(\mathbf{p} - \frac{i}{2}\partial_q - e\mathbf{A}\right)\varphi - \sqrt{2}\left(p_5 - \frac{i}{2}\partial_5\right)\chi = 0, \\ &\sqrt{2}\left(p_4 - \frac{i}{2}\partial_t - e\phi\right)\varphi - \boldsymbol{\sigma}\left(\mathbf{p} - \frac{i}{2}\partial_q - e\mathbf{A}\right)\chi = 0. \end{aligned} \tag{36}$$

Solving the coupled equations, we get an equation for φ and χ. Replacing the eigenvalues of $\widehat{P}_4$ and $\widehat{P}_5$, we have

$$\left[\frac{1}{2m}\left(\boldsymbol{\sigma}\left(\mathbf{p} - \frac{i}{2}\partial_q - e\mathbf{A}\right)\right)^2 + e\phi\right]\varphi = E\varphi,$$

$$\left[\frac{1}{2m}\left(\boldsymbol{\sigma}\left(\mathbf{p} - \frac{i}{2}\partial_q - e\mathbf{A}\right)\right)^2 + e\phi\right]\chi = E\chi.$$

These are the non-covariant form of the Pauli–Schrödinger equation in the phase space independent of the time with

$$f_w = \Psi \star \bar{\Psi} = i\varphi \star \chi^\dagger - i\chi \star \varphi^\dagger.$$

This leads to

$$E_n = \frac{eB}{m}\left(n + \frac{1}{2} - \frac{s}{2}\right) - \frac{k^2}{2m},$$

where $s = \pm1$. It should be noted that the above expression represents the Landau levels which show the spin-splitting feature.

The above Figures 1 and 2 show the Wigner functions for the ground and first excited states, respec-

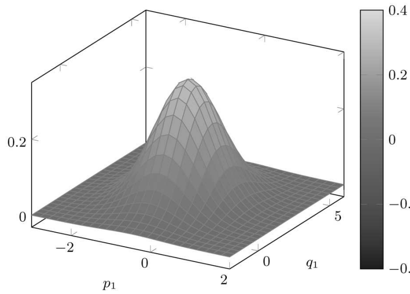

Fig. 1. Wigner Function (cut in q_1,p_1),Ground State

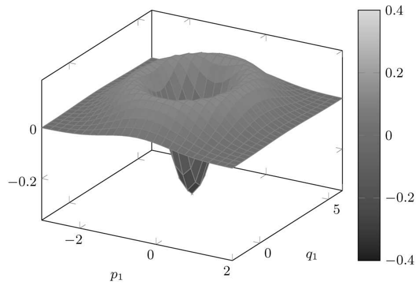

Fig. 2. Wigner Function (cut in q_1,p_1), First Excited State

tively, in the cut (q_1, p_1). These are the same solutions known in the literature using the usual Wigner method.

6. Concluding Remarks

We study the spin-1/2 particle equation, the Pauli–Schrödinger equation, in the context of the Galilean covariance, considering a symplectic Hilbert space. We begin with a presentation on the Galilean manifold which is used to review the construction of the Galilean covariance and the representations of quantum mechanics in this formalism, namely, the spin-1/2 and scalar representations and the Schrödinger (Klein–Gordon-like) and Pauli–Schrödinger (Dirac-like) equations, respectively.

The quantum mechanics formalism in the phase space is derived in this context of the Galilean covariance giving rise to the representations of spin-0 and spin-1/2 equations. For the spin-1/2 equation (the Dirac-like equation), we study the electron in an external field. Solving it, we were able to recover the non-covariant Pauli–Schrödinger equation in phase space and to analyze, in this context, the Landau levels.

This work was supported by CAPES and CNPq of Brazil.

1. Y. Takahashi. Towards the many-body theory with the Galilei invariance as a guide: Part I. *Fortschr. Phys.* **36**, 63 (1988).
2. M. Omote, S. Kamefuchi, Y. Takahashi, Y. Ohnuki. Galilean covariance and the Schrödinger equation. *Fortschr. Phys.* **37**, 933 (1989).
3. A.E. Santana, F.C. Khanna, Y. Takahashi. Galilei covariance and (4,1) de Sitter space. *Prog. Theor. Phys.* **99**, 327 (1998).
4. E. Wigner. Über das überschreiten von potentialschwellen bei chemischen reaktionen. *Z. Phys. Chem.* **19**, 203 (1932).
5. H. Weyl. Quantenmechanik und gruppentheorie. *Z. Phys.* **46**, 1 (1927).
6. J. Ville. Theorie et application de la notion de signal analytique. *Cables et Transmissions* **2**, 61 (1948).
7. J.E. Moyal. Quantum mechanics as a statistical theory. *Math. Proc. Cambr. Phil. Soc.* **45**, 99 (1949).
8. M.D. Oliveira, M.C.B. Fernandes, F.C. Khanna, A.E. Santana, J.D.M. Vianna. Symplectic quantum mechanics. *Ann. Phys.* **312**, 492 (2004).
9. R.G.G. Amorim, F.C. Khanna, A.P.C. Malbouisson, J.M.C. Malbouisson, A.E. Santana. Quantum field theory in phase space. *Int. J. Mod. Phys. A* 1950037 (2019).
10. R.A.S. Paiva, R.G.G. Amorim. Quantum physics in phase space: An analysis of simple pendulum. *Adv. Theor. Comp. Phys.* **1**, 1 (2018).
11. H. Dessano, R.A.S. Paiva, R.G.G. Amorim, S.C. Ulhoa, A.E. Santana. Wigner function and non-classicality for oscillator systems. *Brazilian J. Phys.* 1 (2019).

Received 08.07.19

Г. Петроніло, С. Уйоа, А. Сантана

СИМПЛЕКТИЧНА ТЕОРІЯ ПОЛЯ
ГАЛІЛЕЄВО-КОВАРІАНТНИХ СКАЛЯРНОГО
І СПІНОРНОГО ПРЕДСТАВЛЕНЬ

Р е з ю м е

Ми досліджуємо концепцію розширеної групи Галілея, деякого представлення для симплектичної квантової механіки на многовиді $\mathcal{G}$, заданого на світловому конусі п'ятивимірного простору-часу де Сіттера у фазовому просторі. Побудувано Гільбертів простір, наділений симплектичною структурою. Ми вивчаємо унітарні оператори, що описують повороти і трансляції, генератори яких утворюють алгебру Лі в $\mathcal{G}$. Це представлення породжує рівняння Шредінгера (типу Кляйна–Гордона) для хвильової функції у фазовому просторі, так що змінні мають зміст положення і лінійного імпульсу. Хвильові функції пов'язані з функцією Вігнера через добуток Мойала, так що хвильові функції репрезентують квазіамплітуду ймовірності. Ми будуємо рівняння Паулі–Шредінгера (типу рівняння Дірака) у фазовому просторі в явно коваріантній формі. На завершення ми показуємо еквівалентність між п'ятивимірним формалізмом фазового простору і звичайним формалізмом, пропонуючи розв'язок, що відновлює нековаріантну форму рівняння Паулі–Шредінгера у фазовому просторі.

https://doi.org/10.15407/ujpe64.8.725

J. PROCHÁZKA, V. KUNDRÁT, M.V. LOKAJÍČEK

The Czech Academy of Sciences, Institute of Physics
(18221 Prague 8, Czech Republic; e-mail: jiri.prochazka@fzu.cz, kundrat@fzu.cz, lokaj@fzu.cz)

MODELS OF ELASTIC pp SCATTERING AT HIGH ENERGIES – POSSIBILITIES, LIMITATIONS, ASSUMPTIONS, AND OPEN QUESTIONS

The simplest collision process, the elastic scattering of protons, has been measured at various energies and in a broad interval of scattering angles. Its theoretical description is, however, much more delicate, than it may seem at first glance. The widely used eikonal model allowed one to analyze the pp elastic scattering data at an ISR energy of 52.8 GeV and the TOTEM data at a much higher LHC energy of 8 TeV. The results represent the most detailed elaborated impact parameter analysis of pp data which has ever been performed. They have helped to identify several deeper open questions and problems concerning all widely used theoretical frameworks used for the description of the elastic pp scattering. The problems should be further studied and solved to derive some important proton characteristics which may be obtained with the help of the elastic scattering.

Keywords: proton-proton collisions, elastic scattering of hadrons, eikonal model, Coulomb-hadronic interference, central or peripheral scattering, impact parameter, WY approach.

1. Introduction

The elastic differential cross-section $\mathrm{d}\sigma/\mathrm{d}t$ represents a basic experimental characteristic established in the elastic collisions of hadrons. If the influence of spins is not considered then the t (four momentum transfer squared) dependence exhibits a very similar structure in all cases of elastic scattering of charged hadrons at contemporary high energies: there is a peak at very low values of $|t|$, followed by a (nearly) exponential region, and then there is a dip-bump or shoulder structure at even higher values of $|t|$ practically for all colliding hadrons [1].

The measured differential elastic cross-section of two charged hadrons (protons) is standardly described with the help of the complete elastic scattering amplitude $F^{\mathrm{C+N}}(s,t)$ as

$$\frac{\mathrm{d}\sigma}{\mathrm{d}t} = \frac{\pi}{sp^2}\left|F(s,t)\right|^2. \tag{1}$$

Here, s is the square of the total collision energy, and p is the value of the momentum of one incident proton in the center-of-mass system. The Coulomb amplitude $F^{\mathrm{C}}(s,t)$ is widely assumed to be well-known from QED (except from electromagnetic form factors). However, the t-dependence of the elastic hadronic amplitude $F^{\mathrm{N}}(s,t)$ is yet not fully known. The elastic scattering of two protons is kinematically the simplest collision process, but its description is not satisfactory in many aspects.

The description of the Coulomb-hadronic interference proposed by West and Yennie (WY) [2] in 1968 was widely used for the analysis of experimental data in the era of the ISR. However, several problems and limitations in the given model were identified later. This approach is discussed in sect. 2. The description is not usable for a reliable data analysis. It has, however, negatively influenced many recent models of elastic hadronic scattering. To overcome these problems, another approach based on the eikonal model framework has been developed. The results of analysis of experimental data using the eikonal model (under different assumptions) are summarized in sect. 3. The list of deeper open questions and problems identified in *all* contemporary descriptions of the elastic scattering is presented in sect. 4. Concluding remarks may be found in sect. 5. This paper very briefly summarizes the results obtained and discussed in more details in [3, 4].

2. Approach of West and Yennie

In 1968, West and Yennie [2] derived for the complete amplitude the following simplified formula:

$$F^{\mathrm{C+N}}_{\mathrm{WY}}(s,t) = \pm\frac{\alpha s}{t} G_1(t) G_2(t)\, \mathrm{e}^{\mathrm{i}\alpha\phi(s,t)} + \\ + \frac{\sigma^{\mathrm{tot,N}}(s)}{4\pi} p\sqrt{s}(\rho(s)+\mathrm{i})\, \mathrm{e}^{B(s)t/2}, \tag{2}$$

where (see also Locher 1967 [5])

$$\alpha\phi(s,t) = \mp\alpha\left[\ln\left(\frac{-B(s)t}{2}\right)+\gamma\right]. \tag{3}$$

Here, $\alpha = 1/137.036$ is the fine structure constant, $\gamma = 0.577215...$ is the Euler constant, $G_1(t)$ and $G_2(t)$ are the electric dipole form factors (being put into formula (2) by hand at the very end of the whole derivation for point-like particles). The quantity $\sigma^{\mathrm{tot,N}}$ is the total cross-section given by the optical theorem:

$$\sigma^{\mathrm{tot,N}}(s) = \frac{4\pi}{p\sqrt{s}} \operatorname{Im} F^{\mathrm{N}}(s,t=0). \tag{4}$$

The simplified formula (2) was used widely mainly in the era of the ISR for the determination (often very misleadingly called a measurement) of three free parameters: $\sigma^{\mathrm{tot,N}}$, quantity $\rho(t=0)$, and diffractive slope $B(t=0)$. However, in the derivation of Eq. (2), two very strong assumptions concerning the t-dependence of the elastic hadronic amplitude were assumed to be valid at *all* kinematically allowed values of t:

1. t-independence of the phase of $F^{\mathrm{N}}(s,t)$, i.e., the quantity

$$\rho(s,t) = \frac{\operatorname{Re} F^{\mathrm{N}}(s,t)}{\operatorname{Im} F^{\mathrm{N}}(s,t)} \tag{5}$$

was assumed to be t-independent;

2. purely exponential t-dependence of $\left|F^{\mathrm{N}}(s,t)\right|$, i.e., the diffractive slope defined as

$$B(s,t) = \frac{\mathrm{d}}{\mathrm{d}t}\left[\ln\frac{\mathrm{d}\sigma^{\mathrm{N}}}{\mathrm{d}t}(s,t)\right] = \frac{2}{|F^{\mathrm{N}}(s,t)|}\frac{\mathrm{d}}{\mathrm{d}t}\left|F^{\mathrm{N}}(s,t)\right| \tag{6}$$

was assumed to be t-independent.

It has been shown in [6] that the first assumption must be valid otherwise the relative phase $\phi(s,t)$ becomes a complex function, which would lead to a contradiction (the relative phase has been defined as a real function [2]). The second assumption is in contradiction to the observed dip-bump structure in measured $\mathrm{d}\sigma/\mathrm{d}t$ data. Several other limitations and problems in the derivation of the simplified formula (2) or its application in the forward region were identified later, see [3, 7] for corresponding details and further references. The approach of WY is inapplicable for the reliable analysis of experimental data. Many recent models of elastic hadronic amplitude have been negatively influenced by the simplified formula (2). The models have been typically constrained by the values of $\sigma^{\mathrm{tot,N}}$, quantity $\rho(t=0)$, and $B(t=0)$ determined on the basis of the simplified formula, even though they have corresponded to the strongly t-dependent quantities $B(t)$ and $\rho(t)$. The measured differential cross-section data have been, therefore, described inconsistently.

3. Eikonal Model Approach

3.1. Theoretical background

In order to avoid (some of) the discrepancies and limitations related to the simplified WY formula, another approach to the description of the Coulomb-hadronic interference based on the eikonal model was proposed in 1994 by Kundrát and Lokajíček [8]. This widely used theoretical framework allowed one to derive a more general formula for the complete elastic scattering amplitude valid for *any* t-dependence of the phase and modulus of $F^{\mathrm{N}}(s,t)$ at a given (high) collision energy $\sqrt{s}$ and *any* value of t:

$$F^{\mathrm{C+N}}(s,t) = \pm\frac{\alpha s}{t} G^2_{\mathrm{eff}}(t) + F^{\mathrm{N}}(s,t)[1\mp\mathrm{i}\alpha\bar{G}(s,t)], \tag{7}$$

where

$$\bar{G}(s,t) = \int\limits_{t_{\min}}^{0} \mathrm{d}t' \left\{\ln\left(\frac{t'}{t}\right)\frac{\mathrm{d}}{\mathrm{d}t'}\left[G^2_{\mathrm{eff}}(t')\right] - \\ - \frac{1}{2\pi}\left[\frac{F^{\mathrm{N}}(s,t')}{F^{\mathrm{N}}(s,t)}-1\right] I(t,t')\right\}, \tag{8}$$

and

$$I(t,t') = \int\limits_0^{2\pi} \mathrm{d}\Phi'' \frac{G^2_{\mathrm{eff}}(t'')}{t''}; \tag{9}$$

here, $t'' = t + t' + 2\sqrt{tt'}\cos\Phi''$. The upper (lower) sign corresponds to the scattering of particles with the same (opposite) charges. G^2_{eff} is the effective form factor squared reflecting the electromagnetic structure of colliding protons and was introduced in [9] as

$$G^2_{\mathrm{eff}}(t) = \frac{1}{1+\tau}\left[G^2_{\mathrm{E}}(t) + \tau\, G^2_{\mathrm{M}}(t)\right], \quad \tau = -\frac{t}{4m^2}, \tag{10}$$

where G_{E} and G_{M} stand for the electric and magnetic form factors, and m is the proton mass. The interference formula given by Eq. (7) allows one to study the t-dependence of the elastic hadronic amplitude and corresponding b-dependent properties consistently in the whole measured t range.

The b-dependent characteristics of *pp* collisions are standardly analyzed with the help of the Fourier–Bessel transform. It should be, however, consistent with a *finite* allowed region of the variable t and *finite* collision energies [10] (which is often not respected at all)

$$h_{\mathrm{el}}(s,b) = h_1(s,b) + h_2(s,b) = \\ = \frac{1}{4p\sqrt{s}}\int\limits_{-\infty}^{t_{\min}} F^{\mathrm{N}}(s,t) J_0(b\sqrt{-t})\mathrm{d}t + \\ + \frac{1}{4p\sqrt{s}}\int\limits_{t_{\min}}^{0} F^{\mathrm{N}}(s,t) J_0(b\sqrt{-t})\mathrm{d}t. \tag{11}$$

In this case, the unitarity equation in the b-space is

$$\mathrm{Im}\, h_1(s,b) = |h_1(s,b)|^2 + g_1(s,b) + K(s,b). \tag{12}$$

Here, $g_1(s,b)$ is a real inelastic overlap function which has been introduced in a similar way as the complex elastic amplitude in Eq. (11). The complex function $h_1(s,b)$ and real functions $g_1(s,b)$ oscillate at finite energies. The oscillations can be removed, if a real function $c(s,b) = -\,\mathrm{Im}\, h_2(s,b)$ fulfilling some mathematical conditions is added to both sides of the unitarity equation (12) [3]. It is then possible to define, at finite energies, the total, elastic, and inelastic profile functions $D^{\mathrm{X}}(s,b)$ (X=tot, el, inel)

$$D^{\mathrm{el}}(s,b) \equiv 4\,|h_1(s,b)|^2, \tag{13}$$

$$D^{\mathrm{tot}}(s,b) \equiv 4\,(\mathrm{Im}\, h_1(s,b) + c(s,b)), \tag{14}$$

$$D^{\mathrm{inel}}(s,b) \equiv 4\,(g_1(s,b) + K(s,b) + c(s,b)) \tag{15}$$

and rewrite the unitarity condition in the b-space as

$$D^{\mathrm{tot}}(s,b) = D^{\mathrm{el}}(s,b) + D^{\mathrm{inel}}(s,b). \tag{16}$$

These profile functions (sometimes called overlap functions) represent main b-dependent characteristics. They are used to define the root-mean-squared impact parameter $\sqrt{\langle b^2\rangle^{\mathrm{X}}}$ corresponding to the total, elastic, or inelastic hadron collisions.

Nearly all contemporary models of elastic hadron scattering a priori strongly constrain the elastic hadronic amplitude $F^{\mathrm{N}}(s,t)$ from the very beginning without sufficient reasoning, by requiring

1. dominance of the imaginary part of $F^{\mathrm{N}}(s,t)$ in a quite broad interval of t in the forward region close to $t = 0$;

2. vanishing of the imaginary part of $F^{\mathrm{N}}(s,t)$ at (or around) the dip $t = t_{\mathrm{dip}}$ (wrongly reasoned as a consequence of the minimum of $\mathrm{d}\sigma/\mathrm{d}t$ at t_{dip});

3.values of $\sigma^{\mathrm{tot,N}}]$, $B(t = 0)$ and $\rho(t = 0)$ (often misleadingly denoted as “measurement”) obtained from the simplified WY formula;

4. change of a sign of the real part of $F^{\mathrm{N}}(s,t)$ at “low” values of $|t|$ (motivated by Martin’s theorem [11] derived under certain (asymptotic) conditions).

The corresponding t-dependence of $F^{\mathrm{N}}(s,t)$ (its phase) is strongly constrained by these requirements. It may be shown that mainly the first requirement leads to the *central* behavior of elastic collisions corresponding to $\sqrt{\langle b^2\rangle^{\mathrm{el}}} < \sqrt{\langle b^2\rangle^{\mathrm{inel}}}$. The structure of protons which would correspond to this behavior has never been sufficiently explained.

One may, therefore, ask if it is possible to obtain a description of data which would lead to the *peripheral* behavior of elastic collisions $\sqrt{\langle b^2\rangle^{\mathrm{el}}} > \sqrt{\langle b^2\rangle^{\mathrm{inel}}}$ (without imposing the unreasoned constrains above). It was shown in 1981 [12] that the peripheral solution of the scattering problem may be obtained, if the hadronic phase has specific t-dependence.

3.2. Analysis of Measured Data

One may try to determine $F^{\mathrm{N}}(s,t)$ on the basis of experimental data under a given set of assumptions (constraints) and to study their impact on values of determined hadronic quantities. The eikonal interference formula given by Eqs. (7) to (9) may be used to subtract the Coulomb effect from the measured elastic pp $\mathrm{d}\sigma/\mathrm{d}t$ data at a given energy. The analysis of experimental elastic data in the full measured region of t values with the help of Eqs. (7) to (9) (with either effective electric or effective electromagnetic proton form factors determined from the ep scattering)

Comparison of several hadronic quantities characterizing the pp elastic scattering at energies of 52.8 GeV and 8 TeV

Particle types $\sqrt{s}$ [GeV] Fit Case	pp 52.8 1 central	pp 52.8 2 peripheral	pp 8000 1 central	pp 8000 2 peripheral
$\rho(t=0)$	0.0763 ± 0.0017	0.0827 ± 0.0016	0.122 ± 0.018	0.149 ± 0.016
$B(t=0)$ [GeV^{-2}]	13.515 ± 0.035	13.444 ± 0.036	21.021 ± 0.085	20.829 ± 0.055
$\sigma^{\mathrm{tot,N}}$ [mb]	42.694 ± 0.033	42.861 ± 0.034	103.44 ± 0.35	104.12 ± 0.31
$\sigma^{\mathrm{el,N}}$ [mb]	7.469	7.539	27.6	28.0
σ^{inel} [mb]	35.22	35.32	75.9	76.1
$\sigma^{\mathrm{el,N}}/\sigma^{\mathrm{tot,N}}$	0.1750	0.1759	0.267	0.269
$\mathrm{d}\sigma^{\mathrm{N}}/\mathrm{d}t(t=0)$ [mb.GeV^{-2}]	93.67	94.51	555	566
$\sqrt{\langle b^2\rangle^{\mathrm{tot}}}$ [fm]	1.026	1.023	1.28	1.27
$\sqrt{\langle b^2\rangle^{\mathrm{el}}}$ [fm]	0.6778	1.959	0.896	1.86
$\sqrt{\langle b^2\rangle^{\mathrm{inel}}}$ [fm]	1.085	0.671	1.39	0.970
$D^{\mathrm{tot}}(b=0)$	1.29	1.30	2.01	2.04
$D^{\mathrm{el}}(b=0)$	0.530	0.0342	0.980	0.205
$D^{\mathrm{inel}}(b=0)$	0.762	1.27	1.03	1.84

requires a convenient parametrization of the complex elastic hadronic amplitude, i.e., of its modulus and phase:

$$F^{\mathrm{N}}(s,t) = \mathrm{i}\left|F^{\mathrm{N}}(s,t)\right| \mathrm{e}^{-\mathrm{i}\zeta^{\mathrm{N}}(s,t)} . \tag{17}$$

The modulus can be parametrized as

$$\left|F^{\mathrm{N}}(s,t)\right| = (a_1 + a_2 t)\,\mathrm{e}^{b_1 t + b_2 t^2 + b_3 t^3} + \\ + (c_1 + c_2 t)\,\mathrm{e}^{d_1 t + d_2 t^2 + d_3 t^3}, \tag{18}$$

and the phase can be parametrized as

$$\zeta^{\mathrm{N}}(s,t) = \zeta_0 + \zeta_1 \left|\frac{t}{t_0}\right|^{\kappa} \mathrm{e}^{\nu t}, \quad t_0 = 1\ \ \mathrm{GeV}^2. \tag{19}$$

This parametrization of the phase allows very different t-dependences according to the values of free parameters. It allows a rather fast increase of $\zeta^{\mathrm{N}}(s,t)$ with $|t|$, which is inevitable for increasing the value of $\sqrt{\langle b^2\rangle^{\mathrm{el}}}$ (for details, see, e.g., [3, 7, 8, 12, 13]). All parameters specifying the modulus and phase of the elastic hadronic amplitude $F^{\mathrm{N}}(s,t)$ may be energy-dependent. The parameter κ needs to be chosen as a positive integer to keep the analyticity of $F^{\mathrm{N}}(s,t)$.

Many fits of measured differential cross-section at 52.8 GeV [14] and 8 TeV data [15] under different additional constraints have been recently performed in [3] (see also [7]). Table shows two fits at each energy. Fit 1 corresponds to the widely imposed requirements on $F^{\mathrm{N}}(s,t)$ in many models of elastic scattering discussed in sect. 3.1. This leads to the *central* behavior of elastic collisions. Fit 2 corresponds to the *peripheral* picture of elastic collisions, and it has been obtained without imposing the strong and unreasoned constraints. The b-dependent profile functions given by Eqs. (13) to (15) corresponding to Fit 1 (central) and Fit 2 (peripheral) at an energy of 52.8 GeV are plotted in Figure.

The impact of a choice of the form factor (effective electric or effective electromagnetic one) has been found to be negligible or very small. The t-dependence of the hadronic phase $\zeta^{\mathrm{N}}(s,t)$ has, however, a fundamental impact on the character of collisions in the b-space. In a central case, relation $\sqrt{\langle b^2\rangle^{\mathrm{el}}} < \sqrt{\langle b^2\rangle^{\mathrm{tot}}}$ holds. But, in the peripheral alternative, the relation is reversed. It may be also interesting to note that Martin's theorem [11] is fulfilled in the central, as well as peripheral, alternative (at both energies).

4. Open Questions and Problems

We have reviewed many (all widely discussed) historical and contemporary models concerning the de-

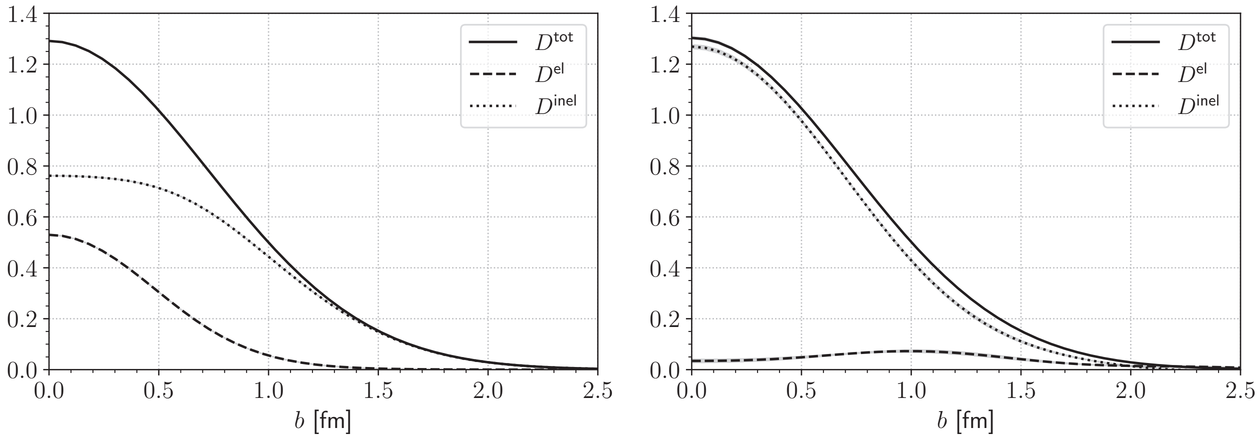

(a) central case – Fit 1 (b) peripheral case – Fit 2

Proton-proton profile functions $D(b)$ at an energy of 52.8 GeV. Full line corresponds to the total profile function, dashed line to the elastic one, and dotted line to the inelastic one

scription of elastic collisions and performed various fits of data under different conditions in order to better understand the processes with strongly interacting particles. On the basis of these studies, we have identified some deeper problems and open questions in *all* models and theoretical frameworks used in the description of the elastic scattering:

1. Coulomb interaction and experimental conditions;

a) (non-)divergence at $t = 0$

b) multiple collisions

c) electromagnetic form factors

2. Different mechanisms of Coulomb and strong forces;

3. Different types of short-ranged (contact) interactions;

4. Properties of the S matrix and the structure of a Hilbert space;

5. Optical theorem;

6. Determination of the b-dependent probability functions of hadron collisions;

7. Distribution of elastic scattering angles for a given value of the impact parameter;

8. Increase in the integrated total, elastic, and inelastic cross-sections and the dimensions of colliding particles in dependence on the collision energy;

9. extrapolations outside measured regions.

The identified open problems 1–7 were published in [4]. One may find there also the historical context concerning the dependence of proton collisions on the impact parameter, which is not widely known. Problems related specifically to the derivation of the optical theorem in particle physics are discussed in [16]. Open questions 8 and 9 are discussed in [3].

5. Conclusion

The simplified WY formula given by Eq. (2) and (3) was used widely in the era of the ISR for the analysis of experimental data. Determined values of $\sigma^{\mathrm{tot,N}}$], $B(t = 0)$, and $\rho(t = 0)$ (at a given collision energy) on the basis of this model have often been denoted misleadingly as "measurement". Many problems and limitations in the derivation of the formula, as well as in its application to data, have been identified, see sect. 2. The WY approach should be, therefore, abandoned in the era of the LHC, as it may lead to wrong physical conclusions. It should not be used for constraining the hadronic models based on assumptions inconsistent with the assumptions used in the derivation of a simplified WY model. One should look for the other description of the elastic scattering of (charged) hadrons.

The eikonal model approach is more general and relevant for the analysis of elastic scattering data at the present time, than the (over)simplified WY model. The former allows one to study the t-dependence of the elastic hadronic amplitude and corresponding hadronic quantities. It is more fundamental than the other contemporary models of elastic scattering as it may be used for the description of the Coulomb-hadronic interference *and* to consider the dependence of collisions on the impact parameter (in order not to mix collisions corresponding to different values of the impact parameter). We have analyzed elastic scattering data at 52.8 GeV and 8 TeV with the help of the eikonal model under different assumptions consistently in the whole measured t-range to see the impact on values of different physical quantities, see sect. 3.

This analysis of elastic scattering data with the use of the eikonal model approach has been prepared for the analysis of TOTEM data at the LHC. The first measurement of elastic differential pp data at the LHC energy of 8 TeV in the Coulomb-hadronic region published by TOTEM [15] contains the first analysis of the 8 TeV data using the eikonal model approach.

The results of our analysis (see sect. 3 and [3, 7] for more details and further references) represent the most elaborated impact parameter analysis of elastic pp collision data which has ever been performed. On the basis of our results, it may be concluded that the transparency of protons during elastic collisions (derived in widely used models of elastic pp scattering) has been based on unreasoned and unnecessary assumptions; the corresponding structure of protons has never been sufficiently explained in the literature. It is possible to say that there is no argument against the more realistic interpretation of elastic processes being peripheral and the protons regarded as rather compact (non-transparent) objects during elastic collisions.

We have reviewed basically all publicly available descriptions (models) of elastic hadron scattering over many years. Several deeper problems and open questions in *all* contemporary theoretical approaches (this includes WY model, eikonal model, Regge-based approaches, QCD-inspired approaches, ...) have been identified, see sect. 4. The proper analysis of hadron collisions in dependence on the impact parameter may provide an important insight concerning the shapes and dimensions (and other properties) of colliding particles, which can be hardly obtained in a different way. However, one should carefully study the assumptions involved in any collision model and test the consequences. It is also necessary to solve all the known fundamental problems and open questions in *any* contemporary description of the elastic pp scattering before making the far-reaching conclusions concerning the structure and properties of collided particles.

Further comments and new ideas how to move forward may be found in [4, 17]. The more fundamental analysis of the whole contemporary state of fundamental physical researches has been recently summarized in [18]. It has been argued that, to make progress in physics, one needs to return to *causal ontology* and *falsification approach* (i.e., the logic and systematic analysis of involved assumptions). In our opinion, our results may be important for new trends not only in high-energy physics, but in physics in general.

We would like to thank to the organizers, especially to L. Jenkovszky, of the "New Trends in High-Energy Physics" conference which took place in Odessa (Ukraine) in May 12–18 (2019) for the opportunity to present and discuss the achieved results.

1. M.K. Carter, P.D.B. Collins, M.R. Whalley. Compilation of nucleon-nucleon and nucleon-antinucleon elastic scattering data. Preprint RAL-86-002 (1986).
2. G.B. West, D.R. Yennie. Coulomb interference in high-energy scattering. *Phys. Rev.* **172**, 1413 (1968).
3. J. Procházka, V. Kundrát. Eikonal model analysis of elastic proton-proton collisions at 52.8 GeV and 8 TeV. *arXiv:1606.09479* (2019).
4. J. Procházka, M. V. Lokajíček, V. Kundrát. Dependence of elastic hadron collisions on impact parameter. *Eur. Phys. J. Plus* **131**, 147 (2016).
5. M.P. Locher. Relativistic treatment of structure in the Coulomb interference problem. *Nucl. Phys. B* **2**, 525 (1967).
6. V. Kundrát, M. Lokajíček, I. Vrkoč. Limited validity of West and Yennie interference formula for elastic scattering of hadrons. *Phys. Lett. B* **656**, 182 (2007).
7. J. Procházka. *Elastic Proton-Proton Collisions at High Energies*, PhD thesis (Charles University, 2018).
8. V. Kundrát, M. Lokajíček. High-energy scattering amplitude of unpolarized and charged hadrons. *Z. Phys. C* **63**, 619 (1994).
9. M.M. Block. Are we really measuring the phase of the nuclear scattering amplitude? *Phys. Rev. D* **54**, 4337 (1996).
10. M.M. Islam. *Lectures in theoretical Physics*. Edited by A.O. Barut and W.E. Brittin (Gordon and Breach, 1968), Vol. 10, B, 97.
11. A. Martin. A theorem on the real part of the high-energy scattering amplitude near the forward direction. *Phys. Lett. B* **404**, 137 (1997).
12. V. Kundrát, M. Lokajíček, jr., M. Lokajíček. Can quantum-mechanical description of physical reality be considered complete? *Czech. J. Phys. B* **31**, 1334 (1981).

13. V. Kundrát, M. Lokajíček, D. Krupa. Impact parameter structure derived from elastic collisions. *Phys. Lett. B* **544**, 132 (2002).
14. J. Bystricky *et al.* Nucleon-Nucleon and Kaon-Nucleon Scattering. In *Landolt–Bornstein, Numerical Data and Functional Relationships in Science and Technology, New Series.* Edited by H. Schopper (Springer, 1980), Vol. 9.
15. TOTEM Collaboration. Measurement of elastic pp scattering at $\sqrt{s} = 8$ TeV in the Coulomb-nuclear interference region – determination of the ρ-parameter and the total cross-section. *Eur. Phys. J. C* **76**, 661 (2016).
16. J. Procházka, V. Kundrát, M.V. Lokajíček. Elastic scattering of hadrons without optical theorem. arXiv:1502.00468 (2015).
17. M. V. Lokajíček, V. Kundrát, J. Procházka. Schrödinger equation and (future) quantum physics. In *Advances in Quantum Mechanics*, Edited by Paul Bracken (Intech, 2013).
18. M. V. Lokajíček, J. Procházka. The Contemporary State of Fundamental Physical Research and the Future Path to Scientific Knowledge. arXiv:1610.08331 (2019).

Received 08.07.19

Ї. Прохазка, В. Кундрат, М.В. Локаїчек

МОДЕЛІ ПРУЖНОГО pp-РОЗСІЯННЯ – МОЖЛИВОСТІ, ОБМЕЖЕННЯ ТА ПИТАННЯ

Р е з ю м е

Найпростіший процес зіткнень, а саме пружне розсіяння протонів вимірювалось при різних енергіях та широкому інтервалі кутів розсіяння. Відповідний теоретичний опис, однак, набагато делікатніший, ніж може здаватися. Широко відома ейкональна модель дозволила провести аналіз пружних pp-даних при енергіях прискорювачів ISR, 52,8 ГеВ та LHC 8 ТеВ. Наші результати представляють найдетальніший та ретельно опрацьований прицільний аналіз pp-даних. Вони допомогли прояснити ряд питань та проблем опису пружного розсіяння протонів. Цю програму потрібно продовжити.

https://doi.org/10.15407/ujpe64.8.732

D.A. PTASHYNSKIY, T.M. ZELENTSOVA, N.O. CHUDAK, K.K. MERKOTAN,
O.S. POTIIENKO, V.V. VOITENKO, O.D. BEREZOVSKIY, V.V. OPYATYUK,
O.V. ZHAROVA, T.V. YUSHKEVICH, I.V. SHARPH, V.D. RUSOV

Odessa National Polytechnic University
(1, Shevchenko Ave., Odessa, 65044, Ukraine; e-mail: sharph@ukr.net)

MULTIPARTICLE FIELDS ON THE SUBSET OF SIMULTANEITY

We propose a model describing the scattering of hadrons as bound states of their constituent quarks. We build the dynamic equations for the multiparticle fields on the subset of simultaneity, using the Lagrange method, similarly to the case of "usual" single-particle fields. We then consider the gauge fields restoring the local internal symmetry on the subset of simultaneity. Since the multiparticle fields, which describe mesons as bound states of a quark and an antiquark, are two-index tensors relative to the local gauge group, it is possible to consider a model with two different gauge fields, each one associated with its own index. Such fields would be transformed by the same laws during a local gauge transformation and satisfy the same dynamic equations, but with different boundary conditions. The dynamic equations for the multiparticle gauge fields describe such phenomena as the confinement and the asymptotic freedom of colored objects under certain boundary conditions and the spontaneous symmetry breaking under another ones. With these dynamic equations, we are able to describe the quark confinement in hadrons within a single model and their interaction during the hadron scattering through the exchange of the bound states of gluons – the glueballs.

Keywords: multiparticle fields, problem of simultaneity in relativistic quantum theory, confinement of quarks and gluons, Higgs mechanism, energy-momentum conservation law in hadron processes.

1. Introduction

Probably for the first time, the idea of multiparticle fields was proposed by H. Yukawa [1–3]. H. Yukawa called these fields "nonlocal" fields. We use another term "multiparticle fields" to show the differences between our model from the model proposed by H. Yukawa. The most essential difference between the proposed model from not only the Yukawa model, but also from models on the light cone [4, 5], quasipotential models [6–8], and models with multitime probability amplitudes [9–11] is that, in our opinion, the internal variables of such fields in different inertial reference systems cannot be related to each other, whereas these variables are connected by Lorentz transformations in the said models. We have already partially explained our viewpoint in the previous article [12]. The use of multitime probability amplitudes in [9–11, 13–15], other works of this direction, and the above-mentioned works contradicts the principles of quantum theory, because it does not consider, in our opinion, the measuring instrument influence on the state of a microsystem. In more details, we explain it in work [16], where we proposed an alternative approach to ensuring the simultaneity of quantum-mechanical measurements in different reference systems, and introduce a subset of simultaneity of the Cartesian product of several Minkowski spaces. On the other hand, the existing field theories are considered in such a way that all interaction effects are reduced only to changes in the occupation numbers of the single-particle states of free particles. This leads to the fact that, in such models, when the dynamics of processes is described, the sum of energy-momenta of these one-particle states is conserved. At the same time, the energy-momentum of hadrons, but not of constituent particles, must be conserved for the processes with hadrons. The model of multiparticle fields on the subset of simultaneity proposed in this article allows us to construct a dynamic description, which is free of the mentioned problems.

2. Scalar Product on a Subset of Simultaneity

Let us consider a meson as a two-particle system consisting of the constituent quark and antiquark. The time and coordinates of the Minkowski space of the first particle will be denoted $\left(x^0_{(1)}, x^1_{(1)}, x^2_{(1)}, x^3_{(1)}\right)$, for the second particle $\left(x^0_{(2)}, x^1_{(2)}, x^2_{(2)}, x^3_{(2)}\right)$. Here, as usual, the index 0 denotes the time coordinate of the event, and 1,2,3 are the spatial coordinates. The lower indices in parentheses identify the first and second particles. The parentheses are used to distinguish these indices from the covariant coordinates of the event. The upper indices are used to denote contravariant coordinates. The Cartesian product of Minkowski spaces for two particles is an eight-dimensional linear space. Its elements can be considered as columns

$$z^a = \begin{pmatrix} x^0_{(1)} \\ x^1_{(1)} \\ x^2_{(1)} \\ x^3_{(1)} \\ x^0_{(2)} \\ x^1_{(2)} \\ x^2_{(2)} \\ x^3_{(2)} \end{pmatrix}. \tag{1}$$

We introduce a scalar product in this eight-dimensional space by the following expression:

$$\langle z|z\rangle = \frac{1}{2}\left(g^{\mathrm{Minc}}_{ab} x^a_{(1)} x^b_{(1)} + g^{\mathrm{Minc}}_{ab} x^a_{(2)} x^b_{(2)}\right). \tag{2}$$

Here, g^{Minc}_{ab} is the Minkowski tensor. The indices a and b are repeated and summed up, and each of these indices takes the value of 0,1,2,3. Then it is convenient to use the Jacobi coordinates

$$X^a = \frac{1}{2}\left(x^a_{(1)} + x^a_{(2)}\right), \quad y^a = x^a_{(2)} - x^a_{(1)}. \tag{3}$$

In view of (3), the expression for a scalar product (2) takes the form

$$\langle z|z\rangle = g^{\mathrm{Minc}}_{ab}\left(X^a X^b + \frac{1}{4} y^a y^b\right). \tag{4}$$

A condition for the subset of simultaneity in coordinates (3) reads

$$y^0 = 0. \tag{5}$$

The coordinates of a point on a subset of simultaneity are denoted by a seven-component column

$$q^a = \begin{pmatrix} X^0 \\ X^1 \\ X^2 \\ X^3 \\ y^1 \\ y^2 \\ y^3 \end{pmatrix}. \tag{6}$$

We define the scalar product on a subset of simultaneity so that it coincides with product (4) with regard for condition (5):

$$\langle q|q\rangle = g_{ab} q^a q^b, \tag{7}$$

where the metric tensor is

$$g^{ab} = \begin{pmatrix} 1 & 0 & 0 & 0 & 0 & 0 & 0 \\ 0 & -1 & 0 & 0 & 0 & 0 & 0 \\ 0 & 0 & -1 & 0 & 0 & 0 & 0 \\ 0 & 0 & 0 & -1 & 0 & 0 & 0 \\ 0 & 0 & 0 & 0 & -4 & 0 & 0 \\ 0 & 0 & 0 & 0 & 0 & -4 & 0 \\ 0 & 0 & 0 & 0 & 0 & 0 & -4 \end{pmatrix}. \tag{8}$$

The multiparticle field will be described by a set of field functions $\Psi_a(q) = \Psi_a(X, \mathbf{y})$. Here, X is a set of coordinates X^0, X^1, X^2, X^3, and $\mathbf{y}$ is a set of internal variables y^1, y^2, y^3. The index a enumerates different components of the field, and its range space is determined by the representation of a transformation group, which describes the transition from field functions relative to one reference system to field functions relative to another reference system. The group of matrices acts on a subset of simultaneity as follows:

$$\hat{G} = \begin{pmatrix} \Lambda^0_0 & \Lambda^0_1 & \Lambda^0_2 & \Lambda^0_3 & 0 & 0 & 0 \\ \Lambda^1_0 & \Lambda^1_1 & \Lambda^1_2 & \Lambda^1_3 & 0 & 0 & 0 \\ \Lambda^2_0 & \Lambda^2_1 & \Lambda^2_2 & \Lambda^2_3 & 0 & 0 & 0 \\ \Lambda^3_0 & \Lambda^3_1 & \Lambda^3_2 & \Lambda^3_3 & 0 & 0 & 0 \\ 0 & 0 & 0 & 0 & R^1_1 & R^1_2 & R^1_3 \\ 0 & 0 & 0 & 0 & R^2_1 & R^2_2 & R^2_3 \\ 0 & 0 & 0 & 0 & R^3_1 & R^3_2 & R^3_3 \end{pmatrix}. \tag{9}$$

The indices of the G^a_b matrix take the values from 0 to 6. $\Lambda^a_b, a, b = 0, 1, 2, 3$ are the elements of the Lorentz transformation matrix, and $R^a_b, a, b = 1, 2, 3$ are the elements of the rotation matrix.

The scalar product (7) with the metric tensor (8) is invariant relative to the group transformations (9).

Hence, our further aim will be to construct a quantum field theory not on the Minkowski space with the Lorentz group, but on the above subset of simultaneity with group (9). In work [16], we show that if the Minkowski space is replaced by a subset of simultaneity and the Lorentz group is group (9), then such a theory can be constructed in the same way as a "usual" one-particle field theory. At the same time, such a model conforms to the principle of relativity.

3. Lagrangian of a Two-Particle Meson Field

We use the notation $\psi_{c_1c_2,f_1,f_2}(q)$ for a two-particle meson field, which describes, after the quantization, the processes of creation and annihilation of bound states of a quark and an antiquark. Here, q is a set of seven variables (6). Indices with subindices 1 and 2 correspond to an antiquark and a quark, respectively, c_1 is the color of an antiquark, and c_2 is the color of a quark, f_1 is the flavor of an antiquark, and f_2 is a flavor of a quark. Accordingly, the field $\psi_{c_1c_2,f_1,f_2}(q)$ takes the value, for which the mixed tensor representations of the $SU_c(3)$ and $SU_f(3)$ groups are realized:

$$\begin{aligned}&{\psi'}_{c_1c_2,f_1,f_2}(q) =\\&= u^{(c)\dagger}_{c_1c_3}\, u^{(c)}_{c_2c_4}\, u^{(f)\dagger}_{f_1f_3}\, u^{(f)}_{f_2f_4}\, \psi_{c_3c_4,f_3,f_4}(q).\end{aligned} \tag{10}$$

Here, $u^{(c)}_{c_2c_4}$ are the elements of an arbitrary matrix of the $SU_c(3)$ group and $u^{(f)}_{f_2f_4}$ are elements of an independent matrix of the $SU_f(3)$ group. A sign † is used to denote the elements of the adjoint matrix. Duplicate indices usually mean the summation. The dynamic equations for the field $\psi_{c_1c_2,f_1,f_2}(q)$ must be symmetric relative to transformations (10).

Moreover, the dynamic equations must be symmetric relative to group (9). The simplest Lagrangian that generates such equations can be written in the form

$$\begin{aligned}&L^{(0)} = g^{ab}\,\frac{\partial\psi^*_{c_1c_2,f_1,f_2}(q)}{\partial q^a}\,\frac{\partial\psi_{c_1c_2,f_1,f_2}(q)}{\partial q^b} -\\&- M^2_\mu\psi^*_{c_1c_2,f_1,f_2}(q)\,\psi_{c_1c_2,f_1,f_2}(q).\end{aligned} \tag{11}$$

Here, g^{ab} are the tensor components (8), and the term M_μ will be considered as the "bare" meson mass. The "real" meson mass was considered in [16].

Since the field $\psi_{c_1c_2,f_1,f_2}(q)$ must describe the dynamics of the bound states of a quark and an antiquark, Lagrangian (11) is obviously incomplete, because it does not involve the interaction between a quark and an antiquark, which ensures the existence of a bound state. As usual, such an interaction can be introduced, if we demand the symmetry of the Lagrangian relative to the local transformations of the internal symmetry in the form (10). Since the existence of a meson as a bound state of the quark and the antiquark is due to the strong interaction, we choose the symmetry relative to the local $SU_c(3)$-transformations. This symmetry can also be achieved in the usual way, if we will replace the "ordinary" derivatives in Lagrangian (11) by the covariant derivatives and will introduce the corresponding compensating fields $A^{(1)}_{a,g_1}(q)$ and $A^{(2)}_{a,g_1}(q)$.

Further, instead of these fields, it would be convenient to consider their linear combinations, similarly to Jacobi variables,

$$\begin{aligned}&A^{(+)}_{a,g_1}(q) = \frac{1}{2}\Big(A^{(1)}_{a,g_1}(q) + A^{(2)}_{a,g_1}(q)\Big),\\&A^{(-)}_{a,g_1}(q) = A^{(2)}_{a,g_1}(q) - A^{(1)}_{a,g_1}(q).\end{aligned} \tag{12}$$

A local $SU_c(3)$ group representation is given for the domain of values of the field functions $\psi_{c_1c_2,f_1,f_2}(q)$. So, this domain may be decomposed into a direct sum of subspaces which are invariant relative to transformations of this representation. Since the hadron is colorless, we will be interested in a field that has a nonzero projection only on a subspace, on which a scalar irreducible representation is realized. This means that the field $\psi_{c_1c_2,f_1,f_2}(q)$ can be given as

$$\psi_{c_1c_2,f_1,f_2}(q) = \delta_{c_1c_2}\psi_{f_1,f_2}(q), \tag{13}$$

where $\psi_{f_1,f_2}(q)$ are the new field functions for the dynamical equations, which should describe, after the quantization, the processes of creation and annihilation of mesons. These dynamic equations can be obtained from the Lagrangian with covariant derivatives that is formed, if we substitute (13) with regard for notation (12). After these transformations, this Lagrangian takes the form

$$\begin{aligned}&L_\mu = 3g^{ab}\left(\partial\psi^*_{f_1,f_2}(q)/\partial q^a\right)\left(\partial\psi_{f_1,f_2}(q)/\partial q^b\right) +\\&+ V(q)\psi^*_{f_1,f_2}(q)\psi_{f_1,f_2}(q) -\\&- 3M^2_\mu\psi^*_{f_1,f_2}(q)\psi_{f_1,f_2}(q),\end{aligned} \tag{14}$$

where

$$V(q) = 2g^2 g^{ab} A^{(-)}_{a,g_1}(q)\, A^{(-)}_{b,g_1}(q). \tag{15}$$

4. Dynamic Equation for the Field $V(q)$

In order to obtain the dynamic equations for a two-gluon field, we consider the simplest tensor that can be formed from single-gluon fields

$$A_{ab,g_1g_2}(q) = g^2 \left(A^{(-)}_{a,g_1}(q)\, A^{(-)}_{b,g_2}(q)\right), \quad a,b = 4,5,6. \tag{16}$$

Extending the linear space of the tensors $A_{ab,g_1g_2}(q)$ relative to group (9) into the direct sum of invariant subspaces, we pick a term corresponding to the projection on a scalar subspace

$$A_{ab,g_1g_2}(q) = -A_{g_1g_2}(q)\, g_{ab} + \ldots . \tag{17}$$

Convolving both sides of equality (17) with the metric tensor g^{ab}, we obtain

$$A_{g_1g_2}(q) = \frac{4}{7} g^2 \sum_{b=4}^{6} \left(A^{(-)}_{b,g_1}(q)\, A^{(-)}_{b,g_2}(q)\right). \tag{18}$$

Then we apply a similar procedure for internal indices. Considering the coupling equations obtained in [16] and definition (15), we get

$$\begin{aligned} &A_{g_1g_2}(q) = A(q)\,\delta_{g_1g_2} + \ldots, \\ &A(q) = \frac{1}{14} g^2 \sum_{b=4}^{6} \left(A^{(-)}_{b,g_1}(q)\, A^{(-)}_{b,g_1}(q)\right) = \frac{1}{14} V(q). \end{aligned} \tag{19}$$

The kinetic part of the Lagrangian for the $A_{g_1g_2}(q)$ field can be given as

$$\begin{aligned} L^{(0)}_G &= \frac{1}{2} g^{ab} \frac{\partial A_{g_1g_2}(q)}{\partial q^a} \frac{\partial A_{g_1g_2}(q)}{\partial q^b} - \\ &- \frac{1}{2} M_G^2 A_{g_1g_2}(q)\, A_{g_1g_2}(q). \end{aligned} \tag{20}$$

Replacing ordinary derivatives by covariant ones and performing some calculations described in [16], we obtain the Lagrangian

$$\begin{aligned} L_V &= \frac{1}{2} g^{ab} \frac{\partial V(q)}{\partial q^a} \frac{\partial V(q)}{\partial q^b} + \\ &+ \frac{3}{2} (V(q))^3 - \frac{1}{2} M_G^2 (V(q))^2. \end{aligned} \tag{21}$$

Having a Lagrangian for the field $V(q)$, we can obtain a dynamic equation for this field such as the Euler–Lagrange equation:

$$-g^{ca} \frac{\partial^2 V(q)}{\partial q^c \partial q^a} - M_G^2 V(q) + \frac{9}{2}(V(q))^2 = 0. \tag{22}$$

We introduce the function $V(q) = V(X, \mathbf{y})$ (with regard for (6)) in the form

$$\begin{aligned} &V(X,\mathbf{y}) = V_0(\mathbf{y}) + V_1(X,\mathbf{y}), \\ &V_1(X,\mathbf{y}) \equiv V(X,\mathbf{y}) - V_0(\mathbf{y}). \end{aligned} \tag{23}$$

Then the function $V_0(\mathbf{y})$, will enter the complete Lagrangian as the potential energy of interaction of nonrelativistic constituent quarks. At the same time, it will satisfy the equation

$$4\Delta_{\mathbf{y}} V_0(\mathbf{y}) - M_G^2 V_0(\mathbf{y}) - \frac{9}{2}(V_0(\mathbf{y}))^2 = 0. \tag{24}$$

Analyzing the properties of the solutions of Eq. (24), we can obtain information about the interaction potential for quarks. Before analyzing these properties, we will make this equation to be dimensionless.

Let us introduce the dimensionless internal coordinates $\mathbf{r}$, dimensionless glueball mass m_G, and dimensionless potential energy $u(\mathbf{r})$:

$$\begin{aligned} &\mathbf{y} = l\mathbf{r}, M_G = l^{-1} m_G, \\ &V_0(\mathbf{y}) = V_0(l\mathbf{r}) = l^{-2} u(\mathbf{r}). \end{aligned} \tag{25}$$

Then, instead of Eq. (24), we obtain

$$4\Delta_{\mathbf{r}} u(\mathbf{r}) - m_G^2 u(\mathbf{r}) - \frac{9}{2}(u(\mathbf{r}))^2 = 0. \tag{26}$$

Here, $\Delta_{\mathbf{r}} \equiv \sum_{b=1}^{3} \frac{\partial^2}{\partial (r^b)^2}$ is the Laplace operator in dimensionless variables $\mathbf{r}$.

We now consider the properties of a spherically symmetric solution of Eq. (26). In order to transform the variables $\mathbf{r}\left(r^1, r^2, r^3\right)$, we pass to spherical coordinates and make the standard replacement

$$u(r) = \frac{\chi(r)}{r}. \tag{27}$$

Finally,we obtain

$$\frac{d^2\chi(r)}{dr^2} = \frac{9}{8} \frac{\chi(r)\left(\chi(r) + \left(m_G^2/9\right) r\right)}{r}. \tag{28}$$

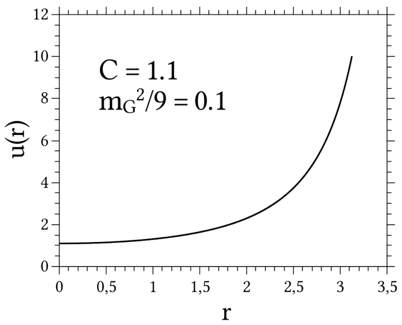

Fig. 1. Results of the numerical calculation of the dimensionless inter-quark potential $u(r)$ as a function of the dimensionless distance r for $C = 1.1$, $m_G^2/9 = 0.1$

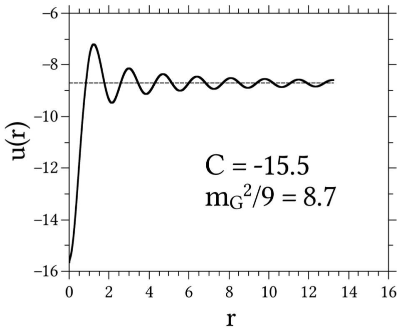

Fig. 2. Results of numerical calculations of the dimensionless inter-quark potential $u(r)$ as a function of the dimensionless distance r for $C = -15.5$, $m_G^2/9 = 8.7$

In order to analyze the properties of solutions of Eq. (28), we use an analogy with classical mechanics. We will consider the independent variable r as an analog of the time. We will call the quantity χ a "coordinate". Let its first derivative $d\chi/dr$ be a "velocity," and let the second derivative $d^2\chi/dr^2$ be an "acceleration". The dependence of "acceleration" on "coordinate", which is determined by the right part of Eq. (28), leads to the fact that, on the coordinate plane (r, χ), there are three domains [16]. Inside each of them, the "acceleration" has a constant sign. So, if the graph $\chi(r)$ gets into one of these three selected domains, then the following path of this graph is determined by the corresponding sign of the "acceleration".

Let us establish the boundary conditions for the function $\chi(r)$. We can see from Eq. (27) that if we want to obtain the finite potential energy $u(r)$ for all finite values r, we should fulfill the condition

$$\chi(r)|_{r=0} = 0. \tag{29}$$

At that, the "initial velocity" should not be equal to zero, and we can set it to a certain real number:

$$\left.\frac{d\chi(r)}{dr}\right|_{r=0} = C, \quad C \in \mathbb{R}. \tag{30}$$

We now consider the properties of a solution of Eq. (28) depending on the selection of the value C.

Let the solution satisfy the boundary conditions (29) and (30) with $C > 0$.

In Fig. 1, we see that, as r increases, the inter-quark potential $u(r)$ tends to infinity. Consequently, the considered model describes the quark confinement.

If $C < 0$, the potential $u(r)$ tends to some negative constant value. Thus, the eigenvalue of the squared internal Hamiltonian will definitely be negative. Since this eigenvalue is a coefficient at the squared field describing the bound state of two gauge bosons, this corresponds to the mechanism of spontaneous symmetry breaking. In this case, the result of numerical calculations of the $u(r)$ dependence on r is presented in Fig. 2.

5. Conclusions

In the proposed model, the strong interaction between the quarks in hadrons can be caused by the exchange of the bound states of gluons – the glueballs. The field $V(X, \mathbf{y})$, according to glueballs, can be represented as a sum of two terms, $V_0(\mathbf{y})$ and $V_1(X, \mathbf{y})$. The field $V_0(\mathbf{y})$ is not quantized and describes the strong interaction of quarks and gluons inside mesons and glueballs. This field satisfies the dynamic equation which describes the confiment of quarks and gluons under certain boundary conditions and spontaneous symmetry breaking – under another ones. When the bare mass of a glueball has a zero value, all solutions of this equation, irrespective of the boundary conditions, will lead to the confiment. The field $V_1(X, \mathbf{y})$ can be quantized. Though we did not consider the quantization procedure for multiparticle fields in this work, it is not different from the procedure described in work [17]. The operators obtained after the quantization will describe the processes of creation and annihilation of glueballs, as shown in [17]. Accordingly, the considered meson field quantization leads to the operators of creation and annihilation of the mesons. The meson interaction due to the interaction of constituent quarks can be described as the exchange by scalar glueballs. This approach differs from the one-particle field approach, because, in our model, the energy-momentum conservation law holds true precisely for hadrons, and not for the constituent particles.

1. H. Yukawa. On the radius of the elementary particle. *Phys. Rev.* **76**, 300 (1949).
2. H. Yukawa. Quantum theory of non-local fields. Part I. Free fields. *Phys. Rev.* **77**, 219 (1950).
3. H. Yukawa. Quantum theory of non-local fields. Part II. Irreducible fields and their interaction. *Phys. Rev.* **80**, 1047 (1950).
4. P. Dirac. Forms of relativistic dynamics. *Rev. Mod. Phys.* **21**, 392 (1949).
5. T. Heinzl. Light cone quantization: Foundations and applications. *Lect. Notes Phys.* **572**, 55 (2001).
6. A. Logunov, A. Tavkhelidze. Quasi-optical approach in quantum field theory. *Il Nuovo Cim. Ser. 10* **29**, 380 (1963).
7. A. Logunov, A. Tavkhelidze, I. Todorov, O. Khrustalev. Quasi-potential character of the scattering amplitude. *Il Nuovo Cim. Ser. 10* **30**, 134 (1963).
8. R. Faustov. Relativistic wavefunction and form factors of the bound system. *Ann. Phys.* **78**, 176 (1973).
9. S. Tomonaga. On a relativistically invariant formulation of the quantum theory of wave fields. *Prog. Theor. Phys.* **1**, 27 (1946).
10. P. Dirac, W. Fock, B. Podolsky. On quantum electrodynamics. *Phys. Zs. Sowjet.* **2**, 468 (1932).
11. S. Petrat, R. Tumulka. Multi-time wave functions for quantum field theory. *Ann. Phys.* **345**, 17 (2014).
12. N.O. Chudak, K.K. Merkotan, D.A. Ptashynskiy *et al.* Internal states of hadrons in relativistic reference systems. *Ukr. Fiz. Zh.* **61**, 1039 (2016).
13. E. Marx. Generalized relativistic Fock space. *Int. J. Theor. Phys.* **6**, 359 (1972).
14. H. Sazdjian. Relativistic wave equations for the dynamics of two interacting particles. *Phys. Rev. D* **33**, 3401 (1986).
15. S. Petrat, R. Tumulka. Multi-time equations, classical and quantum. *Proc. Royal Soc. of London A: Math., Phys. Eng. Sci.* **470**, 1364 (2014).
16. D.A. Ptashynskiy, T.M. Zelentsova, N.O. Chudak *et al.* Multiparticle fields on the subset of simultaneity. *arXiv:1905.07233* [physics.gen-ph].
17. N. Chudak, M. Deliyergiyev, K. Merkotan *et al.* Multiparticle quantum fields. *Phys. J.* **2**, 181 (2016).

Received 08.07.19

Д.А. Пташинський, Т.М. Зеленцова, Н.О. Чудак, К.К. Меркотан, О.С. Потієнко, В.В. Войтенко, О.Д. Березовський, В.В. Опятюк, О.В. Жарова, Т.В. Юшкевич, І.В. Шарф, В.Д. Русов

БАГАТОЧАСТИНКОВІ ПОЛЯ
НА ПІДМНОЖИНІ ОДНОЧАСНОСТІ

Р е з ю м е

В роботі пропонується модель для опису процесів розсіяння гадронів як зв'язаних станів конституентних кварків. На підмножині одночасності розглядається побудова динамічних рівнянь для багаточастинкових полів за допомогою методу Лагранжа, аналогічно тому, як це робиться для "звичайних" одночастинкових полів. Розглянуто калібрувальні поля, які відновлюють локальну внутрішню симетрію на підмножині одночасності. Для багаточастинкових полів, що описують мезони як зв'язані стани кварка і антикварка і є двоіндексними тензорами відносно локальної калібрувальної групи, запропоновано модель з двома різними калібрувальними полями, кожне з яких пов'язане зі своїм індексом. Такі поля перетворюються за однаковим законом при локальному калібрувальному перетворенні і задовольняють однаковим динамічним рівнянням, але на них накладаються різні крайові умови. При певних крайових умовах ці рівняння описують такі фізичні явища, як конфайнмент і асимптотичну свободу кольорових об'єктів, а при інших крайових умовах – механізм спонтанного порушення симетрії. Ці динамічні рівняння дозволяють в межах однієї й тієї ж моделі описати як утримання кварків всередині гадронів, так і їх взаємодію в процесах розсіяння гадронів, шляхом обміну зв'язаними станами глюонів – глюболами.

https://doi.org/10.15407/ujpe64.8.738

M. RYBCZYŃSKI,[1] G. WILK,[2] Z. WŁODARCZYK[1]
[1] Institute of Physics, Jan Kochanowski University
(25-406 Kielce, Poland; e-mail: maciej.rybczynski@ujk.edu.pl, zbigniew.wlodarczyk@ujk.edu.pl)
[2] National Centre for Nuclear Research
(02-093 Warsaw, Poland; e-mail: grzegorz.wilk@ncbj.gov.pl)

A LOOK AT MULTIPLICITY DISTRIBUTIONS VIA MODIFIED COMBINANTS

The experimentally measured multiplicity distributions exhibit, after a closer inspection, the peculiarly enhanced void probability and the oscillatory behavior of modified combinants. We show that both these features can be used as additional sources of information, not yet fully explored, on the mechanism of multiparticle production. We provide their theoretical understanding within the class of compound distributions.

Keywords: multiplicity distributions, combinants, void probabilities, compound distributions.

1. Introduction

The experimentally measured (non-single diffractive (NSD) charged) multiplicity distributions, $P(N)$ (which are one of the most thoroughly investigated and discussed sources of information on the mechanism of the production process [1]), exhibit, after a closer inspection, the peculiarly enhanced void probability, $P(0) > P(1)$ [2, 3], and the oscillatory behavior of the so-called modified combinants, C_j, introduced by us in [4, 5] (and thoroughly discussed in [6, 7]; they are closely connected with the combinants $C^\star_j$ introduced in [8] and discussed occasionally for some time [9–14]). Both features were only rarely used as a source of information. We demonstrate that the modified combinants can be extracted experimentally from the measured $P(N)$ by means of a recurrence relation involving all $P(N < j)$, and that new information is hidden in their specific distinct oscillatory behavior, which, in most cases, is not observed in the C_j obtained from the $P(N)$ commonly used to fit experimental results [4–7]. We discuss the possible sources of such behavior and the connection of C_j with the enhancement of void probabilities, and their impact on our understanding of the multiparticle production mechanism, with emphasis on understanding both phenomena within the class of compound distributions.

2. Recurence Relation and Modified Combinants

The dynamics of the multiparticle production process is hidden in the way, in which the consecutive measured multiplicities N are connected. There are two ways of characterizing the multiplicity distributions: by means of generating functions, $G(z) = \sum_{N=0}^{\infty} P(N) z^N$, or by some form of a recurrence relation between $P(N)$. In the first case, one uses the Poisson distribution as a reference and characterizes deviations from it by means of combinants $C^\star_N$ defined as [8]

$$C^\star_j = \frac{1}{j!} \frac{d^j \ln G(z)}{dz^j}\bigg|_{z=0}, \tag{1}$$

or by the expansion

$$\ln G(z) = \ln P(0) + \sum_{j=1}^{\infty} C^\star_j z^j. \tag{2}$$

For the Poisson distribution, $C^*_1 = \langle N \rangle$ and $C^*_{j>1} = 0$. The combinants were used in the analysis of experimental data in [9–14]. In [10,13], it was demonstrated that they are particularly useful in identifying the nature of the emitting source. It turns out that, in the case of S sources emitting particles without any restrictions concerning their number, the multiplicity $P^S(N)$ is a completely symmetric function of degree N of the probabilities of emission, p_i, the generating function of which reduces for $p_i \to 0$ to the generating function of the Poisson Distribution (PD). For all probabilities remaining the same, $p_i = p$, it reduces to the generating function of the Negative Binomial Distribution (NBD). In this case, the combinants are given by a power series

$$C_j^\star = \frac{1}{j}\sum_{i=1}^{S} p_i^j \tag{3}$$

and are always positive. However, when each of the sources can emit only a given number of particles (let us assume, for definiteness, that at most only one particle), then $P^S(N)$ is an elementary symmetric function of degree N in the arguments, and the corresponding combinants are given by

$$C_j^\star = (-1)^{j+1}\frac{1}{j}\sum_{i=1}^{S}\left(\frac{p_i}{1-p_i}\right)^j, \tag{4}$$

and alternate in sign for different j's. For all probabilities remaining the same, $p_i = p$, a generating function in this scenario reduces to the generating function of the Binomial Distribution (BD) and the combinants oscillate rapidly with period equal to 2.

Note that, in both cases, we were working with probabilities p_i, which were not extracted from experiment, but their values were taken such that the measured multiplicity distributions are reproduced. They are then usually represented by one of the known theoretical formulae for multiplicity distributions, $P(N)$, which can be defined either by the generating functions mentioned above or by some recurrence relations connecting different $P(N)$. In the simplest (and most popular) case, one assumes that the multiplicity N is directly influenced only by its neighboring multiplicities, $(N \pm 1)$, i.e., we have

$$(N+1)P(N+1) = g(N)P(N), \quad g(N) = \alpha + \beta N. \tag{5}$$

This recurrence relation yields BD (when $\alpha = Kp/(1-p)$ and $\beta = -\alpha/K$), PD (when $\alpha = \lambda$ and $\beta = 0$), and NBD (when $\alpha = kp$ and $\beta = \alpha/k$, where p denotes the particle emission probability). Usually, the first choice of $P(N)$ in fitting the data is a single NBD [15] or two- [16, 17], three- [18], or multicomponent NBDs [19] (or some other forms of $P(N)$ [1,15,20]). However, such a procedure only improves the agreement at large N, whereas the ratio R = data/fit still deviates dramatically from unity at small N for all fits [4, 5]. This means that the measured $P(N)$ contains information which is not yet captured by the rather restrictive recurrence relation (5). Therefore, in [4], we proposed to use a more general form of the recurrence relation (used, e.g., in counting statistics when dealing with multiplication effects in point processes [21]):

$$(N+1)P(N+1) = \langle N\rangle \sum_{j=0}^{N} C_j P(N-j). \tag{6}$$

This relation connects multiplicities N by means of some coefficients C_j, which contain the memory of particle $N+1$ about all the $N-j$ previously produced particles. The most important feature of this recurrence relation is that C_j can be directly calculated from the experimentally measured $P(N)$ by reversing Eq. (6) [4–7]:

$$\langle N\rangle C_j = (j+1)\left[\frac{P(j+1)}{P(0)}\right] - \langle N\rangle \sum_{i=0}^{j-1} C_i \left[\frac{P(j-i)}{P(0)}\right]. \tag{7}$$

The modified combinants C_j defined by the recurrence relation (7) are closely related to the combinants $C_j^\star$ defined by Eq. (1), namely,

$$C_j = \frac{j+1}{\langle N\rangle} C_{j+1}^\star. \tag{8}$$

Using Leibnitz's formula for the j^{th} derivative of the quotient of two functions $x = G'(z)/G(z)$,

$$x^{(j)} = \frac{1}{G}\left(G'^{(j)} - j!\sum_{k=1}^{j}\frac{G'^{(j+1-k)}}{(j+1-k)!}\frac{x^{(k-1)}}{(k-1)!}\right), \tag{9}$$

where $G'(z)/G(z) = [\ln G(z)]'$ and $G(z)^{(N)}/N!|_{z=0} = P(N)$, we immediately obtain the recurrence relation (7).

The modified combinants, C_j, share with the combinants $C_j^\star$ the apparent ability of identifying the nature of the emitting source mentioned above (with, respectively, Eq. (3) corresponding to the NBD case with no oscillations, and Eq. (4) corresponding to the rapidly oscillating case of BD). This also means that C_j can be calculated from the generating function $G(z)$ of $P(N)$,

$$\langle N\rangle C_j = \frac{1}{j!}\frac{d^{j+1}\ln G(z)}{dz^{j+1}}\bigg|_{z=0}. \tag{10}$$

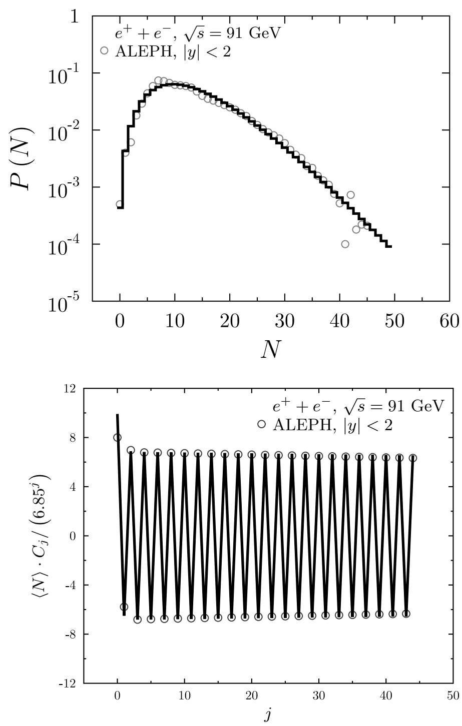

Fig. 1. Upper panel: Data on $P(N)$ measured in e^+e^- collisions by the ALEPH experiment at 91 GeV [23] are fitted by the distribution obtained from the generating function given by the product $G(z) = G_{\mathrm{BD}}(z) G_{\mathrm{NBD}}(z)$ with the parameters: $k' = 1$ and $p' = 0.8725$ for BD and $k = 4.2$ and $p = 0.75$ for NBD. Lower panel: the modified combinants C_j deduced from these data on $P(N)$. They can be fitted by C_j obtained from the same generating function with the same parameters, as used for fitting $P(N)$

Thus, whereas the recurrence relation, Eq. (7), allows us to obtain the C_j from the experimental data on $P(N)$, Eq. (10) allows for their calculation from the distribution defined by the generating function $G(z)$.

Note that C_j provide a similar measure of fluctuations as the set of cumulant factorial moments, K_q, which are very sensitive to the details of the multiplicity distribution and are frequently used in phenomenological analyses of data (cf., [1, 22]),

$$K_q = F_q - \sum_{i=1}^{q-1} \binom{q-1}{i-1} K_{q-i} F_i, \tag{11}$$

where $F_q = \langle N(N-1)(N-2) \dots (N-q+1) \rangle$ are the factorial moments, and K_q can be expressed as an infinite series in C_j,

$$K_q = \sum_{j=q}^{\infty} \frac{(j-1)!}{(j-q)!} \langle N \rangle C_{j-1}. \tag{12}$$

However, while the cumulants are best suited to study densely populated regions of the phase space, combinants are better suited for the study of sparsely populated regions, because, according to Eq. (7), the calculation of C_j requires only a finite number of probabilities $P(N < j)$ (which may be advantageous in applications).

The modified combinants share with the cumulants the property of additivity. For a random variable composed of independent random variables, with its generating function given by the product of their generating functions, $G(x) = \prod_j G_j(x)$, the corresponding modified combinants are given by the sum of the independent components. To illustrate this property, let us consider the e^+e^- data and use the generating function $G(z)$ formally treated as a generating function of the multiplicity distribution $P(N)$, in which N consists of both the particles from BD (N_{BD}) and from NBD (N_{NBD}):

$$N = N_{\mathrm{BD}} + N_{\mathrm{NBD}}. \tag{13}$$

In this case, the multiplicity distribution can be written as

$$P(N) = \sum_{i=0}^{\min\{N,k'\}} P_{\mathrm{BD}}(i) P_{\mathrm{NBD}}(N-i), \tag{14}$$

and the respective modified combinants as

$$\langle N \rangle C_j = \langle N_{\mathrm{BD}} \rangle C_j^{(\mathrm{BD})} + \langle N_{\mathrm{NBD}} \rangle C_j^{(\mathrm{NBD})}. \tag{15}$$

Figure 1 shows the results of attempts to fit both the experimentally measured [23] multiplicity distributions and the corresponding modified combinants C_j calculated from these data (cf. [24] for details). The fits shown in Fig. 1 correspond to the parameters: $k' = 1$ and $p' = 0.8725$ for BD and $k = 4.2$ and $p = 0.75$ for NBD.

Concerning the void probabilities at all energies of interest, one observes that $P(0) > P(1)$, a feature which cannot be reproduced by any composition of NBD used to fit the data [7]. To visualize the importance of this result, we note firstly that $P(0)$ is strongly connected with the modified combinants C_j, in fact:

$$P(0) = \exp\left(-\sum_{j=0}^{\infty} \frac{\langle N\rangle}{j+1} C_j\right). \tag{16}$$

From Eq. (7), one can deduce that the $P(0) > P(1)$ property is possible only when $\langle N\rangle C_0 < 1$. For most multiplicity distributions, $P(2) > P(1)$, which results in an additional condition, $C_1 > C_0(2-\langle N\rangle C_0)$; taken togethe,r this means that $C_1 > C_0$. However, because of the normalization condition $\sum_{j=0}^{\infty} C_j = 1$, such an initial increase of C_j cannot continue for all ranks j, and we should observe some kind of nonmonotonic behavior of C_j with rank j in this case. This means that all multiplicity distributions, for which the modified combinants C_j decrease monotonically with rank j, do not exhibit the enhanced void probability.

3. Compound Distributions

To continue, we use the idea of *compound distributions* (CD), which are applicable, when (as in our case) the production process consists of a number M of some objects (clusters/fireballs/etc.) produced according to a distribution $f(M)$ (defined by a generating function $F(z)$), which subsequently decay independently into a number of secondaries, $n_{i=1,\dots,M}$, following some other (always the same for all M) distribution, $g(n)$ (defined by a generating function $G(z)$). The resultant multiplicity distribution,

$$h\left(N = \sum_{i=0}^{M} n_i\right) = f(M) \otimes g(n), \tag{17}$$

is a compound distribution of f and g with the generating function

$$H(z) = F[G(z)]. \tag{18}$$

Equation (18) means that, in the case where $f(M)$ is a Poisson distribution with the generating function

$$F(z) = \exp[\lambda(z-1)], \tag{19}$$

the combinants for any other distribution $g(n)$ with a generating function $G(z)$, which are obtained from the compound distribution $h(N) = P_{\rm PD} \otimes g(n)$ and calculated with the use of Eq. (10), do not oscillate and are equal to

$$C_j = \frac{\lambda(j+1)}{\langle N\rangle} g(j+1). \tag{20}$$

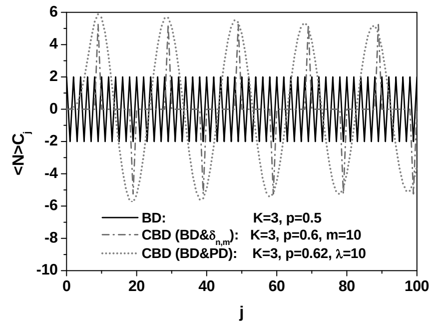

Fig. 2. C_j for BD, BD compounded with $\delta_{n,m}$ with $m = 10$ and compounded with the Poisson distribution with $\lambda = 10$

This fact explains why C_j from NBDs do not oscillate. This is because NBD is a compound distribution of the Poisson and logarithmic distributions. This means that $g(n) = -p^n/[n\ln(1-p)]$, and $h(N)$ is NBD with $k = -\lambda/\ln(1-p)$. In this case, C_j coincide with those derived before and given by Eq. (3). Actually, this reasoning applies to all more complicated compound distributions, with any distribution itself being a compound Poisson distribution. This property limits the set of distributions $P(N)$ leading to oscillating C_j, to BD, and to all compound distributions based on it. In this case, the period of oscillations is determined by the number of particles emitted from the source. For the compound distributions based on BD with $P(n) = \delta_{n,m}$, we have

$$C_j = (-1)^{j/m+1} \frac{K}{\langle N\rangle} \left(\frac{p}{1-p}\right)^{j/m+1}, \tag{21}$$

(for $j = mk$ and $C_j = 0$ for $j \neq mk$, where $k = 1, 2, 3, \dots$). For broader distributions $P(n)$, we get a smoother C_j dependence on rank j. For example, for $P(n)$ given by the Poisson distribution (with expected value λ), we obtain a Compound Binomial Distribution (CBD) with the generating function

$$H(z) = \{p\exp[\lambda(z-1)] + 1 - p\}^K, \tag{22}$$

and the modified combinants are given by

$$C_j = \frac{(-1)^{j+1} K e^{\lambda} \lambda^{j+1} \frac{1-p}{p}}{\langle N\rangle \left(e^{\lambda}\frac{1-p}{p} + 1\right)^{j+1}} A_j\left(e^{\lambda}\frac{p-1}{p}\right), \tag{23}$$

where $A_j(x)$ are the Eulerian polynomials. As an illustration, we show in Fig. 2 that, by compounding

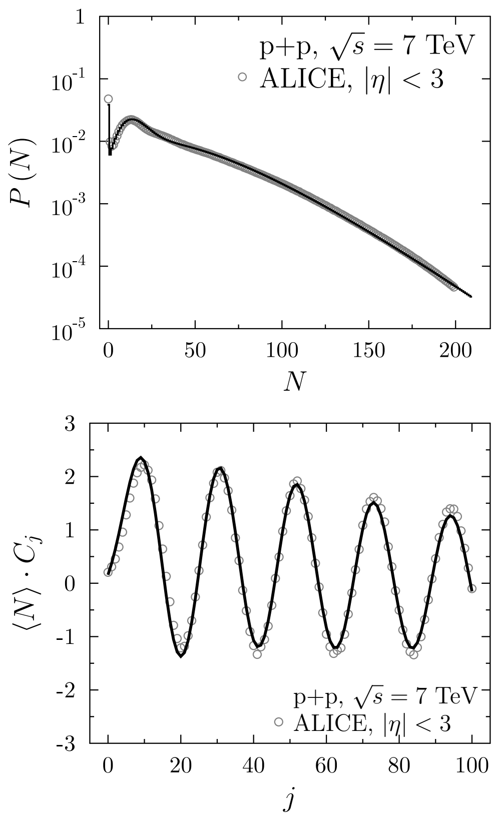

Fig. 3. Multiplicity distributions $P(N)$ measured in pp collisions by ALICE [25] (upper panel) and the corresponding modified combinants C_j (lower panel). Data are fitted using a two compound distribution (BD+NBD) given by Eqs. (25) and (24) with the parameters: $K_1 = K_2 = 3$, $p_1 = 0.9$, $p_2 = 0.645$, $k_1 = 2.8$, $k_2 = 1.34$, $m_1 = 5.75$, $m_2 = 23.5$, $w_1 = 0.24$ and $w_2 = 0.76$

BD with a Poisson distribution, one gains control over the period of oscillations (now equal to 2λ) and their amplitude. However, it turns out that such a combination does not allow us to fit data.

4. Multicomponent

The situation improves substantially, when one uses a multi-CBD based on Eq. (22). But the agreement is not yet satisfactory. It turns out that the situation improves dramatically, if one replaces the Poisson distribution by NBD and, additionally, uses a two-component version of such CBD with

$$P(N) = \sum_{i=1,2} w_i h\left(N; p_i, K_i, k_i, m_i\right) \tag{24}$$

with the generating function of each component equal to

$$H(z) = \left[p\left(\frac{1-p'}{1-p'z}\right)^k + 1 - p\right]^K. \tag{25}$$

In such a case, as can be seen in Fig. 3, one gains a satisfactory control over the periods of oscillations, their amplitudes, and their behavior as a function of the rank j. Moreover, one can nicely fit $P(N)$ and C_j. Of special importance is the fact that the enhancement $P(0) > P(1)$ is also reproduced in this approach.

The above result also explains the apparent success in fitting the experimentally observed oscillations of C_j by using a weighted sum of the three NBD used in [26]. Such a distribution uses freely selected weights and parameters (p, k) of NBDs and, therefore, resembles the compound distribution of BD with NBD. However, we note that the sum of M variables (with $M = 0,\ 1,\ 2, ...$), each from NBD characterized by parameters (p, k), is described by NBD characterized by (p, Mk). Therefore, as discussed before, it cannot reproduce the void probability $P(0)$. This can be reproduced only in the case where $M = 0,\ 1, ..., K$ is distributed according to BD, and we have a K-component NBD (where the consecutive NBDs have precisely defined parameters k),

$$P(N) = \sum_{M=0}^{K} P_{\mathrm{BD}}(M) P_{\mathrm{NBD}}(N; p, Mk). \tag{26}$$

In this case, one also has the $M = 0$ component, which is lacking in the previous multi-NBD case used in [26]. This is the reason for that, whereas the compound (BD&NBD) distribution reproduces the void probability, $P(0)$, the single NBD (or any combination of NBDs) do not. This means that the observation of the peculiar behavior of the void probability discussed above signals the necessity of using some compound distribution based onBD to fit data for $P(N)$ (and the C_j obtained from it).

5. Summary and Conclusions

Since the time of Ref. [8], one encounters essentially no detailed experimental studies of the combinants and only rather sporadic attempts at their phenomenological use to describe the multiparticle production processes. We demonstrate that the modified combinants C_j are a valuable tool for the in-

ISSN 2071-0186. Ukr. J. Phys. 2019. Vol. 64, No. 8

vestigations of multiplicity distributions, and C_j deduced from the measured multiplicity distributions, P(N), could provide additional information on the dynamics of the particle production. This, in turn, could allow us to reduce the number of possible interpretations presented so far and, perhaps, answer some of the many still open fundamental questions (that this is possible, despite experimental errors, has been shown in [7, 26]). Finally, let us note that a large number of papers suggest some kind of universality in the mechanisms of hadron production in e^+e^- anihilations and in pp and $p\bar{p}$ collisions. This arises from observations of the average multiplicities and relative dispersions in both types of processes (cf., e.g., [27, 28]). However, as we have shown here, the modified combinant analysis reveals differences between these processes. Namely, while, in e^+e^- annihilations, we observe oscillations of C_j with period 2, the period of oscillations in pp collisions is ~ 10 times longer, and the amplitude of oscillations in both types of processes differs dramatically. At the moment, this problem remains open and awaits a further investigation.

This research was supported in part by the Polish Ministry of Science and Higher Education (Contract No. DIR/WK/2016/2010/17-1), by the National Science Centre (NCN) (Contract No. DEC-2016/22/M/ST/00176) (G.W.), and by the NCN grant 2016/23/B/ST2/00692 (M.R.). We would like to thank Dr. Nicholas Keeley for reading the manuscript.

1. W. Kittel, E.A. De Wolf. *Soft Multihadron Dynamics* (World Scientific, 2005).
2. Ding-wei Huang. Multiplicity distribution with enhanced void probability. *J. Phys. G* **23**, 895 (1997).
3. S. Dutta, A.H. Chan, C.H. Oh. Mod. Void probability enhanced multiplicity distribution of produced hadrons in p–p collision at lhc energies. *Phys. Lett. A* **27**, 1250145 (2012).
4. G. Wilk, Z. Włodarczyk. How to retrieve additional information from the multiplicity distributions. *J. Phys. G* **44**, 015002 (2017).
5. G. Wilk, Z. Włodarczyk. Some intriguing aspects of multiparticle production processes. *Int. J. Mod. Phys. A* **33**, 1830008 (2018).
6. M. Rybczyński, G. Wilk, Z. Włodarczyk. Intriguing feature of multiplicity distributions. *Eur. Phys. J. Web Conf.* **206**, 03002 (2019).
7. M. Rybczyński, G. Wilk, Z. Włodarczyk. Intriguing properties of multiplicity distributions. *Phys. Rev. D* **99**, 094045 (2019).
8. S.K. Kauffmann, M. Gyulassy. Multiplicity distribution. *J. Phys. A* **11**, 1715 (1978).
9. J. Bartke. On the description of multiplicity distributions in multiple production processes in terms of combinants. *Phys. Scripta* **27**, 226 (1983).
10. A.B. Balantekin, J.E. Seger. Description of pion multiplicities using combinants. *Phys. Lett. B* **266**, 231 (1991).
11. Bao-An Li. Pion multiplicity distributions and combinants in relativistic heavy ion collisions. *Phys. Lett. B* **300**, 14 (1993).
12. S. Hegyi. Correlation studies in quark jets using combinants. *Phys. Lett. B* **463**, 126 (1999).
13. A.B. Balantekin. Combinant analysis of multiplicity distributions. *AIP Conf. Proc.* **276**, 346 (1993).
14. A.Z. Mekjian, T. Csörgö, S. Hegyi. A Bose–Einstein model of particle multiplicity distributions. *Nucl. Phys. A* **784**, 515 (2007).
15. J.F. Fiete Grosse-Oetringhaus, K. Reygers. Charged-particle multiplicity in proton–proton collisions. *J. Phys. G* **37**, 083001 (2010).
16. P. Ghosh. Negative binomial multiplicity distribution in proton-proton collisions in limited pseudorapidity intervals at LHC up to $\sqrt{s} = 7$ TeV and the clan model. *Phys. Rev. D* **85**, 0541017 (2012).
17. A. Giovannini, R. Ugoccioni. Signals of new physics in global event properties in pp collisions in the TeV energy domain. *Phys. Rev. D* **68**, 034009 (2003).
18. I.J. Zborovsky. A three-component description of multiplicity distributions in pp collisions at the LHC. *J. Phys. G* **40**, 055005 (2013).
19. I.M. Dremin, V.A. Nechitailo. Independent pair parton interactions model of hadron interactions. *Phys. Rev. D* **70**, 034005 (2004).
20. S.V. Chekanov, V.I. Kuvshinow. Multifractal multiplicity distribution in bunching parameter analysis. *J. Phys. G* **22**, 601 (1996).
21. B.E.A.Saleh, M.K. Teich. Multiplied-Poisson noise in pulse, particle, and photon detection. *Proc. IEEE* **70**, 229 (1982).
22. R. Botet, M. Płoszajczak. *Universal Fluctuations. The Phenomenology of Hadronic Matter*, (World Scientific, 2002).
23. D. Buskulic *et al.* (ALEPH Collaboration). Measurements of the charged particle multiplicity distribution in restricted rapidity intervals. *Z. Phys. C* **69**, 15 (1995).
24. H.W. Ang, A.H. Chan, M. Ghaffar, Q. Leong, M. Rybczyński, G. Wilk, Z. Włodarczyk. Modified combinant analysis of the e^+e^- multiplicity distributions. *Modern Phys. Lett. A* **34**, 1950324 (2019).

25. J. Adam *et al.* (ALICE Collaboration). Measurement of D-meson production versus multiplicity in p-Pb collisions at $\sqrt{s_{NN}} = 5.02$ TeV. *J. High Energy Phys.* **78**, 1608 (2016).
26. I. Zborovsky. Three-component multiplicity distribution, oscillation of combinants and properties of clans in pp collisions at the LHC. *Eur. Phys. J. C* **78**, 816 (2018).
27. A. Biswas. Charged multiplicity distributions in e^+e^- annihilation and pp collision. *J. Phys. G* **12**, 1 (1986).
28. J.F. Grosse-Oetringhaus, K. Reygers. Charged-particle multiplicity in proton–proton collisions. *J. Phys. G* **37** 083001 (2010).

Received 08.07.19

М. Рибчинські, Г. Вілк, З. Влодарчик

ПОГЛЯД НА МНОЖИННІ РОЗПОДІЛИ ЧЕРЕЗ МОДИФІКОВАНІ КОМБІНАНТИ

Р е з ю м е

Експериментально виміряні розподіли по множинності після їх ретельного аналізу демонструють незвично підвищену ймовірність порожнечі і осциляторну поведінку модифікованих комбінантів. Ми показуємо, що обидві ці риси можна використати як додаткові джерела інформації, ще не використані в повній мірі в механізмах багаточастинкового народження. Ми надаємо їх теоретичну інтерпретацію в термінах компаундних розподілів.

https://doi.org/10.15407/ujpe64.8.745

L.M. SATAROV,[1,2] I.N. MISHUSTIN,[1,2] A. MOTORNENKO,[1,3] V. VOVCHENKO,[1,3]
M.I. GORENSTEIN,[1,4] H. STOECKER [1,3,5]

[1] Frankfurt Institute for Advanced Studies
(1, Ruth-Moufang-Str., D-60438 Frankfurt am Main, Germany; e-mail: satarov@fias.uni-frankfurt.de)
[2] National Research Center "Kurchatov Institute"
(1, Kurchatov Sq., 123182 Moscow, Russia)
[3] Institut für Theoretische Physik, Goethe Universität Frankfurt
(1, Max-von-Laue-Str., D-60438 Frankfurt am Main, Germany)
[4] Bogolyubov Institute for Theoretical Physics, Nat. Acad. of Sci. of Ukraine
(14b, Metrologichna Str., 03143 Kyiv, Ukraine)
[5] GSI Helmholtzzentrum für Schwerionenforschung GmbH
(1, Planck-Str., D-64291 Darmstadt, Germany)

PHASE TRANSITIONS AND BOSE–EINSTEIN CONDENSATION IN ALPHA-NUCLEON MATTER

The equation of state and the phase diagram of an isospin-symmetric chemically equilibrated mixture of α particles and nucleons (N) are studied in the mean-field approximation. We use a Skyrme-like parametrization of mean-field potentials as functions of the partial densities of particles. The parameters of these potentials are chosen by fitting the known properties of pure N- and pure α-matters at zero temperature. The sensitivity of results to the choice of the αN attraction strength is investigated. The phase diagram of the $\alpha - N$ mixture is studied with a special attention paid to the liquid-gas phase transitions and the Bose–Einstein condensation of α particles. We have found two first-order phase transitions, stable and metastable, which differ significantly by the fractions of α's. It is shown that the states with α condensate are metastable.

K e y w o r d s: phase transitions, mean-field model, Bose–Einstein condensation, chemical equilibrium.

1. Introduction

At subsaturation densities and low temperatures, the nuclear matter has a tendency to the clusterization, when small and big nucleon clusters are formed under the conditions of thermal and chemical equilibrium. This state of excited nuclear matter is realized in nuclear reactions at intermediate energies known as the multifragmentation of nuclei [1, 2]. It is believed that the clusterized nuclear matter is also formed in outer regions of neutron-stars and in supernova explosions [3].

In our recent paper [4], we studied the equation of state (EoS) of an idealized system composed entirely of α-particles. Their interaction was described by a Skyrme-like mean-field potential. We have found that such a system exhibits two interesting phenomena, namely, the Bose–Einstein condensation (BEC) and the liquid-gas phase transition (LGPT). Earlier, the cold alpha matter was considered microscopically, by using phenomenological $\alpha\alpha$ potentials in Ref. [5].

However, by introducing such one-component system, one disregards a possible dissociation of alphas into lighter clusters and nucleons. The binary $\alpha - N$ matter in chemical equilibrium with respect to the reactions $\alpha \leftrightarrow 4N$ was considered in [6], by using the virial approach. Due to the neglect of quantum statistics and three-body forces, such approach may be justified only at small baryon densities.

In this paper, we briefly discuss the results of our recent article [7], where we studied the isospin-symmetric $\alpha - N$ matter under the conditions of chemical equilibrium. The EoS of such matter was calculated in the mean-field approach, by using Skyrme-like mean-field potentials. In our study, we simultaneously take into account the LGPT and BEC effects.

2. Mean-Field Model for Interacting $\alpha - N$ Matter

Let us consider the iso-symmetric system (with equal numbers of protons and neutrons) composed of nucleons (N) and alpha-particles (α). A small difference between the proton and neutron masses and the Coulomb interaction effects will be neglected. Our consideration will be restricted to small temperatures $T \lesssim 30$ MeV. In this case, the production of pions and other mesons, as well as the excitation of baryonic resonances, become negligible. In addition, the masses $m_N \simeq 938.9$ MeV and $m_\alpha \simeq 3727.3$ MeV are much larger than the system temperature. Thus, a non-relativistic approximation can be used in the lowest order in T/m_N.

In the grand canonical ensemble, the pressure $p\,(T,\mu)$ is a function of the temperature T and baryon chemical potential μ. The latter is responsible for the conservation of the baryon charge. The chemical potentials of N and α satisfy the relations

$$\mu_N = \mu, \quad \mu_\alpha = 4\mu, \tag{1}$$

which correspond to the condition of chemical equilibrium in the $N-\alpha$ mixture due to the reactions $\alpha \leftrightarrow 4N$.

Let us denote, by n_N and n_α, the partial number densities of N and α, respectively. The baryonic density $n_B\,(T,\mu) = n_N + 4n_\alpha$, entropy density s, and energy density ε can be calculated from $p\,(T,\mu)$, by using the equations

$$n_B = \left(\frac{\partial p}{\partial \mu}\right)_T, \quad s = \left(\frac{\partial p}{\partial T}\right)_\mu, \quad \varepsilon = Ts + \mu n_B - p. \tag{2}$$

To characterize the relative abundances of α's, we introduce their mass concentration $\chi = 4n_\alpha/n_B$.

In our mean-field model, we consider multiparticle interactions in the $\alpha - N$ matter, by introducing a temperature-independent "excess part" of the pressure Δp

$$p = p_N^{\rm id}(T,n_N) + p_\alpha^{\rm id}(T,n_\alpha) + \Delta p\,(n_N,n_\alpha), \tag{3}$$

where the first and second terms on the right-hand side (RHS) are, respectively, the pressure of the ideal gas of nucleons and α's. At known Δp, one can calculate the chemical potentials of N and α as functions of T, n_N, n_α. Solving further Eqs. (1), we get all thermodynamic quantities at given T,μ.

Earlier, we suggested a similar scheme to describe the particle interactions in one-component α [4] and nucleon [8] matters. This corresponds, respectively, to the limiting cases $n_N \to 0$ and $n_\alpha \to 0$. In the case of binary $\alpha - N$ mixture, we use a generalized Skyrme-like parametrization [7] for the excess pressure

$$\Delta p\,(n_N,n_\alpha) = -(a_N n_N^2 + 2a_{N\alpha} n_N n_\alpha + a_\alpha n_\alpha^2) + \\ + b_N\,(n_N + \xi\, n_\alpha)^{\gamma+2}. \tag{4}$$

Using Eqs. (3) and (4) and applying the thermodynamic relations, we get the expressions

$$\mu_N = \widetilde{\mu}_N(T,n_N) - 2\,(a_N n_N + a_{N\alpha} n_\alpha) + \\ + \frac{\gamma+2}{\gamma+1}\, b_N (n_N + \xi\, n_\alpha)^{\gamma+1}, \tag{5}$$

$$\mu_\alpha = \widetilde{\mu}_\alpha(T,n_\alpha) - 2\,(a_{N\alpha} n_N + a_\alpha n_\alpha) + \\ + \frac{\gamma+2}{\gamma+1}\, b_N\, \xi\,(n_N + \xi\, n_\alpha)^{\gamma+1}. \tag{6}$$

Here, $\widetilde{\mu}_i(T,n_i)$ is the chemical potential of the ideal gas of ith particles with the density n_i ($i = N,\alpha$). The second and third terms on RHS correspond to the attractive and repulsive parts of mean-field potentials for N ans α. Note that, in the region of BEC, $\widetilde{\mu}_\alpha$ reaches its maximum possible value $\widetilde{\mu}_\alpha = m_\alpha$, and n_α contains the contribution of Bose-condensed α's. In our calculations, we separate the states which are (meta)stable with respect to fluctuations of particle densities [1].

To choose the model parameters a_N, b_N, γ, we fit the ground-state (GS) properties of the cold ($T = 0$) iso-symmetric nuclear matter. This is the state with zero pressure and minimal energy per baryon. We assume the GS-values $\mu_N = 923$ MeV, $n_N = 0.15$ fm^{-3} [8] and choose $\gamma = 1/6$ [2]. The parameters a_α, ξ are estimated, by using the properties of a cold α matter. We fit the values of density ($n_\alpha = 0.036$ fm^{-3}) and binding energy per baryon ($E/B = -12$ MeV) obtained in Ref. [5] for the GS of this matter.

The cross-term coefficient $a_{N\alpha}$ determines the attractive part of the $N\alpha$ mean-field potential. It is

[1] For such states, the matrix $||\partial\mu_i/\partial n_j||$ is positive definite.

[2] As shown in Refs. [7, 8], such γ gives reasonable values of nuclear compressibility.

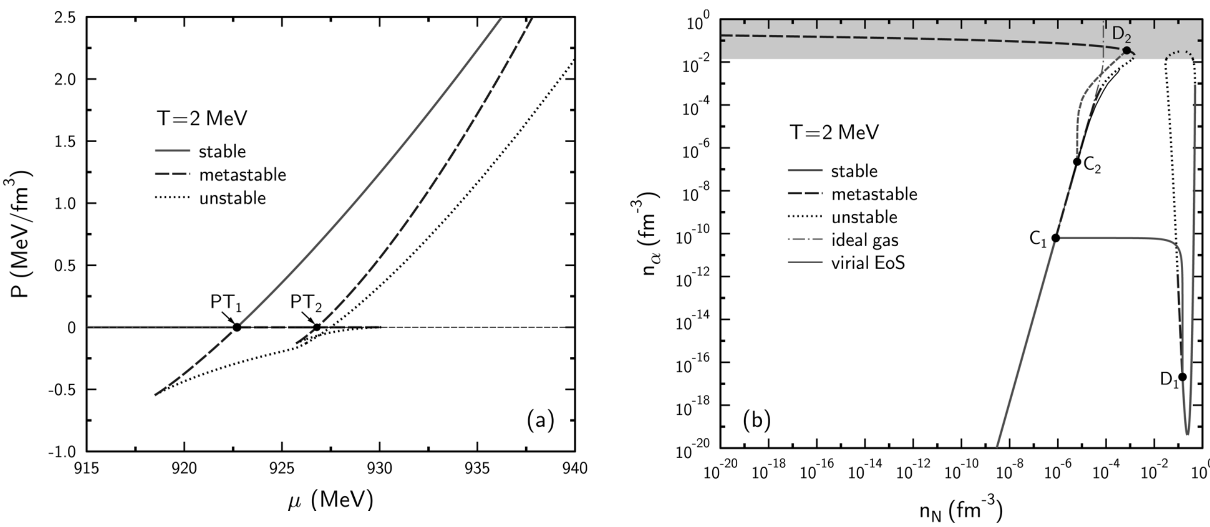

Fig. 1. Isotherm $T = 2$ MeV of $\alpha - N$ matter on the (μ, p) (a) and (n_N, n_α) (b) planes. The stable, metastable, and unstable parts of the isotherm are shown, respectively, by the solid, dashed, and dotted lines. The dots PT$_1$ and PT$_2$ in (a) show the positions of stable and metastable LGPT, respectively. The dash-dotted line in (b) is calculated for the ideal $\alpha - N$ gas. Lines C_1D_1 and C_2D_2 correspond to the mixed–phase states of PT$_1$ and PT$_2$, respectively. The thin solid line represents the isotherm $T = 2$ MeV from Ref. [6]

the only model parameter which is not fixed in our approach. To constrain this coefficient, we consider contours of the energy per baryon for the cold $\alpha - N$ matter on the (n_B, χ) plane. Our calculations show [7] that the properties of GS of such matter change drastically at some critical value $a_{N\alpha} = a_* \simeq 2.1$ GeVfm^3. In the overcritical region $a_{N\alpha} > a_*$, the model predicts nonzero fractions of α in the GS of the $\alpha - N$ matter. In this case, the GS is stronger bound as compared to the pure nucleon matter. Apparently, this is in contradiction with phenomenological properties of the nuclear matter. Therefore, we consider only subcritical values of $a_{N\alpha}$. To probe the sensitivity to this coefficient, we made calculations for $a_{N\alpha} = 1$ and 1.9 GeVfm^3. From the comparison with results of Ref. [6], we found that the latter value is more reasonable. Our "preferred" values of model parameters are given in Table 1.

3. Phase Diagram of $\alpha - N$ Matter

By substituting (5) and (6) into (1) and solving the resulting equations, we get the isotherms of the $\alpha - N$ matter for different μ. At low enough temperatures, one obtains, in general, several solutions for the pressure at given T, μ. Solutions with the largest (smallest) pressure correspond to stable (unstable) states. This is a typical situation for LGPT.

Figure 1, a represents the isotherm $T = 2$ MeV on the (μ, p) plane. According to the Gibbs rule, the intersection points of (meta)stable branches of the pressure as functions of μ correspond to phase transitions (PTs). As one can see from Fig. 1, a, there are two PTs at $T = 2$ MeV. The first transition, PT$_1$, occurs at a smaller baryon chemical potential than for PT$_2$. The states on the dashed lines have smaller pressure as compared to states with the same μ on the solid lines. Therefore, the second transition PT$_2$ is metastable.

Figure 1, b shows the same isotherm $T = 2$ MeV, but on the (n_N, n_α) plane. The shading represents the region of BEC. The states between C_1 and D_1 (C_2 and D_2) are mixed-phase states for the stable (metastable) PT. As compared to PT$_1$, the concentrations of α are much larger for the mixed-phase states of PT$_2$. A strong suppression of α is predicted at large nucleon densities. According to our calculation, BEC states are metastable (see the dashed line in the shaded domain).

Table 1. **Model parameters**

γ	a_N, GeV fm^3	b_N, GeV fm$^{3.5}$	a_α, GeV fm^3	ξ	$a_{N\alpha}$, GeV fm^3
1/6	1.17	1.48	3.83	2.006	1.9

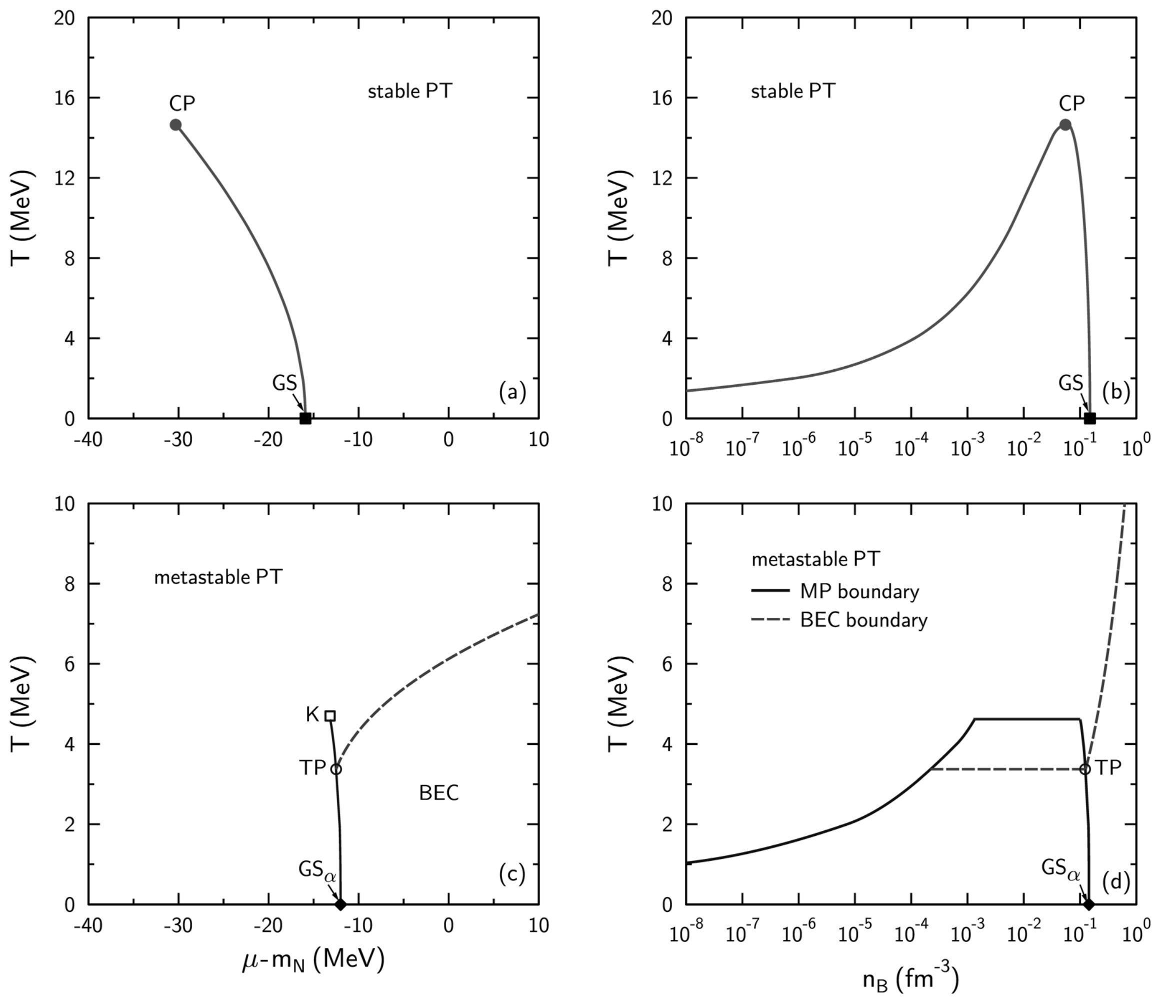

Fig. 2. Left panels: critical lines of stable (*a*) and metastable (*c*) PT of the $\alpha - N$ matter on the (μ, T) plane. Right panels: boundaries of the mixed phase for stable (*b*) and metastable (*d*) PT of the $\alpha - N$ mixture on the (n_B, T) plane. Full circles in (*a*) and (*b*) show positions of the critical point. The dashed lines in (*c*) and (*d*) represent boundaries of the BEC region. The open square (circle) marks the end (triple) point of the metastable PT. The full squares and diamonds show, respectively, the GS positions for the pure nucleon and pure alpha matters, respectively

Table 2. **Characteristics of phase transitions in $\alpha - N$ matter**

Stable PT				Metastable PT			
T_{CP}, MeV	μ_{CP}, MeV	$n_{B\mathrm{CP}}$, fm^{-3}	χ_{CP}	T_K, MeV	μ_K, MeV	χ_K	T_{TP}, MeV
14.7	908.6	5.3×10^{-2}	6.9×10^{-2}	4.6	925.7	0.46–0.86	3.4

Analyzing the results at different T, we get the phase diagram of the $\alpha - N$ matter. The stable and metastable parts of this diagram are shown in the upper and low panels of Fig. 2. Characteristics of PT$_1$ and PT$_2$ are shown in Table 2. Note that the metastable PT disappears at the temperature $T_K \simeq$ $\simeq 5$ MeV which is much less than the critical temperature $T_{\mathrm{CP}} \simeq 15$ MeV of the stable PT.

4. Conclusions

Our model describes both the phase transitions and BEC of the $\alpha - N$ matter. The results of this paper may be used for studying the nuclear cluster production in heavy-ion reactions, as well as in astrophysics. We think that the present formalism can be also used for the binary mixtures of fermionic atoms and bosonic molecules, like $H + H_2$ or $D + D_2$.

1. J.P. Bondorf. Heavy ion reactions between 30 and a few hundred MeV/nucleon. *J. Phys. Colloq.* **37**, 5 (1976).
2. J.P. Bondorf, A.S. Botvina, A.S. Illjinov, I.N. Mishustin, K. Sneppen. Statistical multifragmentation of nuclei. *Phys. Rep.* **257**, 133 (1995).
3. J.M. Lattimer, F.D. Swesty. A generalized equation of state for hot, dense matter. *Nucl. Phys. A* **535**, 331 (1991).
4. L.M Satarov, M.I. Gorenstein, A. Motornenko, V. Vovchenko, I.N. Mishustin, H. Stoecker. Bose-Einstein condensation and liquid-gas phase transition in strongly-interacting matter composed of α particles. *J. Phys. G* **44**, 125102 (2017).
5. J.W. Clark, T.-P. Wang. Theory of α matter. *Ann. Phys.* **40**, 127 (1966).
6. C.J. Horowitz, A. Schwenk. Cluster formation and the virial equation of state of low-density nuclear matter. *Nucl. Phys. A* **776**, 55 (2006).
7. L.M. Satarov, I.N. Mishustin, A. Motornenko, V. Vovchenko, M.I. Gorenstein, H. Stoecker. Phase transitions and Bose–Einstein condensation in alpha-nucleon matter. *Phys. Rev. C* **99**, 024909 (2019).
8. L.M. Satarov, M.N. Dmitriev, I.N. Mishustin. Equation of state of hadron resonance gas and the phase diagram of strongly interacting matter. *Phys. At. Nucl.* **72**, 1390 (2009).

Received 08.07.19

Л.М. Сатаров, І.Н. Мішустін, А. Моторненко, В. Вовченко, М.І. Горенштейн, Х. Штокер

ФАЗОВІ ПЕРЕТВОРЕННЯ
ТА КОНДЕНСАЦІЯ БОЗЕ–ЕЙНШТЕЙНА
В АЛЬФА-НУКЛОННІЙ МАТЕРІЇ

Р е з ю м е

Рівняння стану та фазова діаграма ізоспін-симетричної хімічно рівноважної суміші α частинок та нуклонів (N) вивчається в наближенні середнього поля. Ми застосовуємо параметризацію Скірма для потенціалів середнього поля як функцій парціальних густин частинок. Параметри цих потенціалів знайдені як результат підгонки відомих властивостей чистої N- та чистої α-матерії при нульовій температурі. Вивчена чутливість результатів до вибору величини αN притягання. Фазова діаграма $\alpha - N$ суміші вивчається з особливою увагою до процесів фазового перетворення рідина-газ та конденсації Бозе–Ейнштейна для α-частинок. Ми знаходимо два фазові перетворення, стабільний та метастабільний, які значно відрізняються концентраціями α-частинок. Показано, що стани з α-конденсатом є метастабільними.

https://doi.org/10.15407/ujpe64.8.750

W. SCHÄFER,[1] I. BABIARZ,[1] A. CISEK,[2] A. SZCZUREK[1]

[1] Institute of Nuclear Physics, Polish Academy of Sciences
(152, Ul. Radzikowskiego, PL-31-142 Kraków, Poland; e-mail: wolfgang.schafer@ifj.edu.pl)
[2] Faculty of Mathematics and Natural Sciences, University of Rzeszów,
(1, Ul. Pigonia, PL-35-310 Rzeszów, Poland)

RECENT RESULTS ON INCLUSIVE QUARKONIUM PAIR PRODUCTION IN PROTON-PROTON COLLISIONS

Recently, there has been much interest in the pair production of charmonia. One of the main motivations behind these studies is that the production of quarkonium pairs is expected to receive an important contribution from the double parton scattering (DPS) production mode. A large effective cross-section $\sigma_{\rm eff}$ is found from the empirical analysis of the J/ψ-pair production – about a factor 2.5 smaller than the usually accepted $\sigma_{\rm eff}$ = 15 mb. Here, we present the recent results of our calculations of the χ_c pair production, mainly in the single parton scattering (SPS) mode. An important feature is that the single-gluon exchange mechanism can to some extent mimic the behavior of the DPS production.

Keywords: perturbative QCD, quarkonia, multiparton processes.

1. Introduction

The production of J/ψ-pairs has been suggested as a probe of the double-parton scattering (DPS) processes [1]. More generally, the DPS production mode is expected to be especially important in the charm sector [2]. Therefore, recently, there has been much interest in the quarkonium pair production in proton-proton collisions also from the experimental side. Among others, the cross-sections for the production of J/ψ-pairs were measured at the Tevatron [3] and the LHC [4–7].

A number of puzzles remain with these data, however. For example, the single parton scattering (SPS) leading order of $\mathcal{O}(\alpha_S^4)$ (see, e.g., [8, 9]) does not describe well all the kinematic distributions in the case of the ATLAS and CMS data. Especially, when the rapidity distance Δy between two J/ψ mesons is large, it falls short of experimental data. If one ascribes the whole discrepancy to DPS processes, the normalization of DPS comes out a factor ~ 2.5 larger than in other hard processes. It is still an open issue at the moment whether this points to a nonuniversality of DPS effects or whether there are additional single parton scattering mechanisms not taken into account up to now.

This problem motivated our recent studies of the χ_c-pair production in the k_T-factorization [10] and of the production of χ_c-pairs associated with a gluon (jet) in the collinear factorization [11]. We summarize these works in this contribution.

2. Production of χ_c-Pairs

In the standard hard scattering approach, the cross-section of the production of a pair of quarkonia a, b is calculated from a convolution of parton densities with a parton-level cross-section (see the left diagram in Fig. 1). However, at high energies, favored by a rise of the gluon distribution at small x, there is a sizable contribution from processes in which two or more hard processes proceed in the same proton-proton collision (see the right diagram in Fig. 1).

One commonly assumes the factorized ansatz for the production cross- section in the DPS mode:

$$\frac{d\sigma_{\rm DPS}(pp\to abX)}{dy_a dy_b d^2\mathbf{p}_{aT} d^2\mathbf{p}_{bT}} = \\ = \frac{1}{1+\delta_{ab}}\,\frac{1}{\sigma_{\rm eff}}\,\frac{d\sigma(pp\to aX)}{dy_a d^2\mathbf{p}_{aT}}\,\frac{d\sigma(pp\to bX)}{dy_b d^2\mathbf{p}_{bT}}. \quad (1)$$

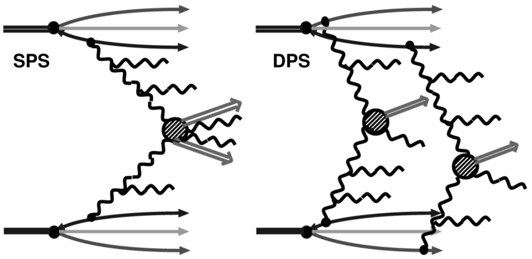

Fig. 1. Sketch of the single parton scattering (SPS) and double parton scattering (DPS) production modes

The DPS cross-section is written as a product of the inclusive single-particle spectra, and the cross-section is normalized by the "effective cross-section" σ_{eff}. The latter is not the cross-section for a specific process – the real parameter is rather its inverse, which is related in the simplest model to the overlap of parton densities in the transverse plane, $t_N(\mathbf{b})$:

$$\frac{1}{\sigma_{\text{eff}}} = \int d^2\mathbf{b}\, T^2_{NN}(\mathbf{b}),$$
$$T_{NN}(\mathbf{b}) = \int d^2\mathbf{s}\, t_N(\mathbf{s}) t_N(\mathbf{b}-\mathbf{s}). \tag{2}$$

The salient features of DPS are obvious from Eq. (1). Important for us is the observation that each of the single particle spectra is a fairly broad function of $y_{a,b}$. Thus, the DPS distribution in rapidity distance $\Delta y = y_b - y_a$ will be very broad as well. As far as the effective cross-section is concerned, it is usually taken in the ballpark of $\sigma_{\text{eff}} = 15$ mb, which is within the line of a fair amount of hard processes, see, e.g., a table in [5].

In the case of J/ψ-pair production, the lowest-order "box-diagram" mechanism suggests a very clean separation of SPS versus DPS modes. Indeed, the explicit calculations performed in the k_T-factorization [9] show that the J/ψ-pair distribution is sharply peaked around $\Delta y = 0$.

A main point of this presentation is the fact that the situation looks completely different in the case of production of a pair of χ_c mesons. Indeed, the χ_{cJ} states, which come in three different spins $J = 0, 1, 2$ have positive C-parity and thus couple to two gluons in a color singlet state. Hence, the mechanism of Fig. 2 with the t-channel exchange of a single gluon is possible. It is well understood that it will lead to a $gg \to \chi\chi$ cross-section independent of the cm-energy in the high-energy limit. The matrix element for this

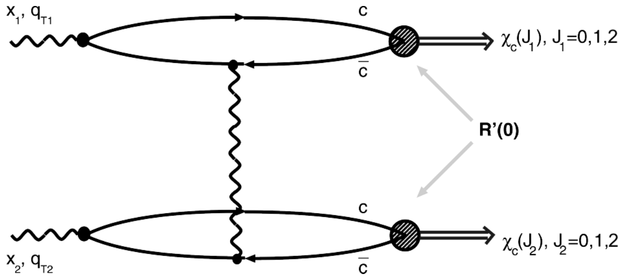

Fig. 2. Gluon t-channel exchange mechanism for the production of $\chi_c\chi_c$ pairs

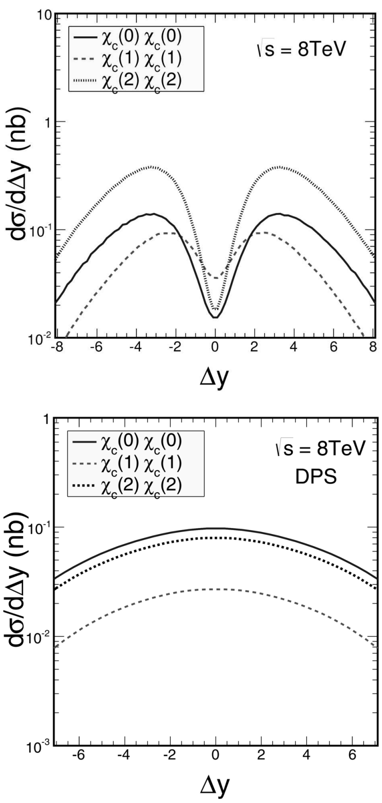

Fig. 3. Distribution of χ_c-pairs in the rapidity difference between mesons. Top panel: SPS mode, lower panel: DPS mode

process thus puts no penalty on a large rapidity distance Δy between the χ_c-mesons.

The relevant amplitudes can be obtained from effective $g^*g^* \to \chi_{cJ}$ vertices for the fusion of two spacelike off-shell gluons. These have been obtained in Ref. [10] for all possible spin-states of the χ_c family. We also performed calculations in the k_T-factorization including the transverse momenta of incoming gluons. In the upper panel of Fig. 3, we

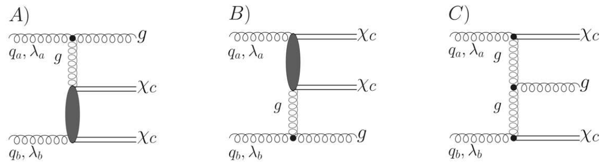

Fig. 4. Feynman diagrams for the production of a χ_c-pair associated with a gluon

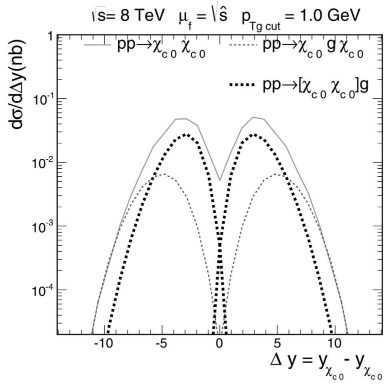

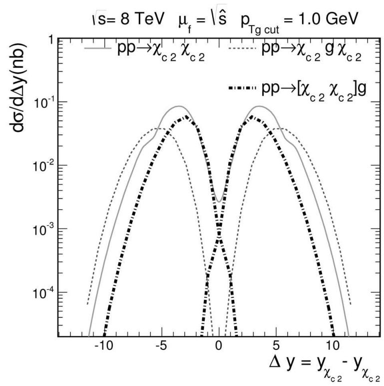

Fig. 5. Distribution in rapidity between χ_0 mesons (top panel) and χ_{c2} mesons for the following different processes: Born-level production of χ_c-pairs, production of χ_c pairs with a leading gluon, and production of χ_c-pairs with a central gluon

show the distribution in rapidity distance Δy between mesons. Note that we only show, as an example, the production of pairs of identical mesons, the full array of all possible combinations can be found in Ref. [10]. In the lower panel of Fig. 3, we show distributions in Δy for the DPS mode, by using $\sigma_{\rm eff} = 15$ mb. We see that these distributions are very broad and in the same ballpark as the SPS contribution. Of course, there is no minimum at $\Delta y = 0$ for the DPS distributions. Thus, we observe rather similar distributions in Δy for single and double parton scattering productions of different χ_c-quarkonia states. This shows that both contributions must be included in the analysis of future data on the $\chi_{cJ_i}\chi_{cJ_j}$ production. Now, one would observe that the large rapidity distance between mesons means a large phase space for the emission of additional gluons. To investigate this situation, we studied the associated production of χ_c pairs with a gluon in the standard collinear factorization in Ref. [11]. There are two main contributions shown in the diagrams of Fig. 4: first, the emission of a "leading gluon", where the gluon jet carries a large fraction of the momentum carried by one of the incoming gluons, and, second, the production of "central" gluons, which are emitted in the rapidity space between two mesons with a large difference in rapidity from either one. Some distributions, again in rapidity distance Δy between mesons, are shown in Fig. 5. The production of leading gluons adds to the Born-result to recover the k_T-factorization result, while the production of central gluons gives rise to an about 20% enhancement of the cross-section. Here, one may think of $\alpha_S\,\Delta y$ as a large parameter which could be resummed in the future using the BFKL formalism.

3. Conclusions

The pair production of quarkonia is a topic that still poses puzzles to theorists. The quantitative understanding of DPS contributions requires not only a reliable formalism for its calculation but also a good understanding of SPS processes that can show a similar behavior as DPS in many kinematic variables.

For the theoretically simplest case, the production of χ_c-pairs, we have shown that the cross-sections for different combinations of χ_c quarkonia, the SPS and DPS cross-sections, are of the similar size, and both involve very broad distributions in the rapidity distance Δy.

We have also shown that an enhancement of the pair production cross-section for χ_c-pairs can be expected from the higher-order corrections, due to the large phase space of the gluon emission.

However, it turns out that the feed-down from χ-pairs into the J/ψ-pair channel does not resolve the discrepancy between different determinations of $\sigma_{\rm eff}$.

It might be necessary to look deeper into the fundamentals of the DPS theory (see, e.g., [13]) to understand the peculiar behavior of the charmonium pair production.

 ISSN 2071-0186. Ukr. J. Phys. 2019. Vol. 64, No. 8

The participation of W.S. in the conference New Trends in High Energy Physics 2019 has been partially supported by the Polish Academy of Sciences.

1. C. H. Kom, A. Kulesza, W. J. Stirling. Pair production of J/ψ as a probe of double parton scattering at LHCb. *Phys. Rev. Lett.* **107**, 082002 (2011).
2. M. Łuszczak, R. Maciuła, A. Szczurek. Production of two $c\bar{c}$ pairs in double-parton scattering. *Phys. Rev. D* **85**, 094034 (2012).
3. V.M. Abazov *et al.*, [D0 Collaboration]. Observation and studies of double J/ψ production at the Tevatron. *Phys. Rev. D* **90**, 111101 (2014).
4. V. Khachatryan *et al.*, [CMS Collaboration]. Measurement of prompt J/ψ pair production in pp collisions at $\sqrt{s} = 7$ Tev. *JHEP* **1409**, 094 (2014).
5. M. Aaboud *et al.*, [ATLAS Collaboration]. Measurement of the prompt J/ ψ pair production cross-section in pp collisions at $\sqrt{s} = 8$ TeV with the ATLAS detector. *Eur. Phys. J. C* **77**, 76 (2017).
6. R. Aaij *et al.*, [LHCb Collaboration]. Observation of J/ψ pair production in *pp* collisions at $\sqrt{s} = 7$ TeV. *Phys. Lett. B* **707**, 52 (2012).
7. R. Aaij *et al.*, [LHCb Collaboration]. Measurement of the J/ψ pair production cross-section in pp collisions at $\sqrt{s} = 13$ TeV. *JHEP* **1706**, 047 (2017); Erratum: *JHEP* **1710**, 068 (2017).
8. S.P. Baranov. Pair production of J/ψ mesons in the k_t-factorization approach. *Phys. Rev. D* **84**, 054012 (2011).
9. S.P. Baranov, A.M. Snigirev, N.P. Zotov, A. Szczurek, W. Schäfer. Interparticle correlations in the production of J/ψ pairs in proton-proton collisions. *Phys. Rev. D* **87**, 034035 (2013).
10. A. Cisek, W. Schäfer, A. Szczurek. Production of χ_c pairs with large rapidity separation in k_T factorization. *Phys. Rev. D* **97**, 114018 (2018).
11. I. Babiarz, W. Schäfer, A. Szczurek. Associated production of χ_c pairs with a gluon in the collinear-factorization approach. *Phys. Rev. D* **99**, 074014 (2019).
12. W. Schäfer. Production of quarkonium pairs in high-energy proton-proton collisions. *EPJ Web Conf.* **199**, 01021 (2019).
13. J. R. Gaunt, R. Maciuła, A. Szczurek. Conventional versus single-ladder-splitting contributions to double parton scattering production of two quarkonia, two Higgs bosons and $c\bar{c}c\bar{c}$. *Phys. Rev. D* **90**, 054017 (2014).

Received 26.01.18

В. Шефер, І. Бабяж, А. Чішек, А. Щурек

НОВІ РЕЗУЛЬТАТИ
ПРО ІНКЛЮЗИВНЕ НАРОДЖЕННЯ
ПАР КВАРКОНІУМУ
В ПРОТОН-ПРОТОННИХ ЗІТКНЕННЯХ

Р е з ю м е

Останнім часом спостерігається значний інтерес до процесів парного народження шармонія. Однією з причин інтересу є те, що продукування пар кварконіуму в значній мірі зумовлене подвійним розсіянням партонів (DPS). З емпіричного аналізу народження пар J/ψ знайдено велике значення ефективного перерізу $\sigma_{\rm eff} = 15$ мб. Ми представляємо нові результати наших розрахунків продукування пар χ_c в моді одинарного партонного розсіяння (SPS). Важливим моментом є те, що однопіонний обмін в деякій мірі може симулювати ефект подвійного партонного обміну (DPE).

https://doi.org/10.15407/ujpe64.8.754

V. SKALOZUB

Oles Honchar Dnipro National University

(72, Gagarin Ave., Dnipro 49010, Ukraine; e-mail: Skalozubv@daad-alumni.de)

INDUCED COLOR CHARGES, EFFECTIVE $\gamma\gamma G$ VERTEX IN QGP. APPLICATIONS TO HEAVY-ION COLLISIONS

We calculate the induced color charges $Q^3_{\rm ind}, Q^8_{\rm ind}$ and the effective vertex $\gamma-\gamma$-gluon generated in a quark-gluon plasma with the A_0 condensate because of the color C-parity violation at this background. To imitate the case of heavy-ion collisions, we consider the model of the plasma confined in the narrow infinite plate and derive the classical gluon potentials $\bar\phi^3$ and $\bar\phi^8$ produced by these charges. Two applications – the scattering of photons on a plasma and the conversion of gluon fields in two photons radiated from the plasma – are discussed.

Keywords: quark-gluon plasma, heavy-ion collision, Polyakov's loop, effective vertex.

1. Introduction

Investigations of the deconfinement phase transition (DPT) and the quark-gluon plasma (QGP) are in the center of modern high energy physics. These phenomena happen at high temperature due to the asymptotic freedom of strong interactions. The researches are carried out either in experiments on hadron collisions or in quantum field theory. The order parameter for DPT is Polyakov's loop (PL), which is zero at low temperatures and nonzero at high temperatures $T > T_d$, where $T_d \sim 160$–180 MeV [1] is the phase transition temperature. The standard information on DPT is adduced, in particular, in [2].

The PL is defined as [3]:

$$PL = \int\limits_C dx_4\ A_0(x_4, \mathbf{x}). \tag{1}$$

Here, $A_0(x_4, \mathbf{x})$ is the zero component of the gauge field potential, the integration contour is going along the fourth direction and back to an initial point in the lattice Euclidean space-time. The PL was introduced in pure gluodynamics. It violates the center of the color group symmetry $Z(3)$ that results in the nonconservation of the color charges Q^3 and Q^8.

The QGP state consists of quarks and gluons liberated from hadrons. Polyakov's loop is not a solution to the local Yang–Mills equations. The local order parameter for DPT is the A_0 condensate, which is a constant at $T > T_d$. It can be calculated, in particular, from a two-loop effective potential. More details on different calculations carried out in analytic quantum field theory can be seen in [4]. Taking these results into consideration, we have to consider QGP as a state at the A_0 background, which breaks the color C-parity symmetry. So, new type phenomena may happen.

In the SU(2) gluodynamics, the gluon spectra at A_0 were calculated and investigated in Ref. [5, 6]. In particular, the induced color charge $Q^3_{\rm ind}$ was also computed. It was shown that the state with a condensate is free of infrared instabilities existing in a gluon plasma in the empty space. Thus, the ground state with A_0 is a good approximation to the plasma after DPT.

In Ref. [7], the induced charges $Q^3_{\rm ind}, Q^8_{\rm ind}$ generated by quark loops in QCD were calculated. In what follows, we consider the QCD case, but the precise values of the induced charges will not be specified.

The paper is organized as follows. In Sect. 2, the color induced charges $Q^3_{\rm ind}$ and $Q^8_{\rm ind}$ generated by tadpole quark loops with one gluon lines, which are nonzero due to Furry's theorem violation, are calculated. In Sect. 3, we consider a simple model of the plasma confined in a plate narrow in one dimension and infinite in two other dimensions with the A_0 condensate and induced charges. We compute the classical gluon potentials $\bar\phi^3$ and $\bar\phi^8$ generated by the induced charges $Q^3_{\rm ind}$ and $Q^8_{\rm ind}$. In Sect. 4, the effective $\gamma\gamma G$ vertex generated in the plasma is calculated in the high-temperature approximation. In Sect. 5, the processes of photon scattering on these potentials and the conversion of gluons in two photons are considered as the application. These new phenomena have to happen due to the three-linear effective vertices.

2. Induced Color Charges and Quark Propagator

In what follows, we consider the case of A_0^3 background field and present the color field potential in the form $Q_\mu^a \to A_0\delta^{a3}\delta_{\mu 4} + Q_\mu^a$, where Q_μ^a is a quantum field. The calculation of $Q_{\rm ind}^8$ is similar (see [7]), and the final results will be adduced only.

The explicit expression is given by the form $Q_\mu^a Q_{\rm ind}^3 \delta_{\mu 4}\delta_{a3} = Q_4^3 Q_{\rm ind}^3$, where

$$Q_{\rm ind}^3 = \frac{g}{\beta}\sum_{p_4}\int\frac{d^3p}{(2\pi)^3}{\rm Tr}\left[\gamma^4\frac{\lambda_{ij}^3}{2}G^{ij}(p_4,\mathbf{p},A_0)\right]. \quad (2)$$

Here, λ^3 is the Gell-Mann matrix, and $\beta = 1/T$ is the inverse temperature. The expressions for the propagators are

$$G^{11} = \frac{\gamma^4(p_4 - A_0) + \mathbf{p}\,\boldsymbol{\gamma} + m}{(p_4 - A_0)^2 + \mathbf{p}^2 + m^2},$$
$$G^{22} = \frac{\gamma^4(p_4 + A_0) + \mathbf{p}\,\boldsymbol{\gamma} + m}{(p_4 + A_0)^2 + \mathbf{p}^2 + m^2}. \quad (3)$$

For brevity, we denoted $A_0 = gA_0/2$ entering the interaction Lagrangian. Accounting for the trace ${\rm Tr}[(\gamma^4)^2] = -4$, the diagonal values of λ^3, and ${\rm Tr}[\gamma^4\boldsymbol{\gamma}] = 0$, we get

$$Q_{\rm ind}^3 = \frac{4g}{\beta}\sum_{p_4}\int\frac{d^3p}{(2\pi)^3}\frac{p_4 + A_0}{(p_4 + A_0)^2 + \mathbf{p}^2 + m^2}. \quad (4)$$

The sum over $p_4 = \frac{\pi(2n+1)}{2\beta}$ can be calculated, by using the formula

$$\frac{1}{\beta}\sum_{p_4} f(p_4) = -\frac{1}{4\pi i}\int\limits_C \tan\left[\frac{\beta\omega}{2}\right] f(\omega), \quad (5)$$

where the contour C encloses clockwise the real axis in the complex plane ω.

The calculations (after transformation to the spherical coordinates and angular integrations) give

$$Q_{\rm ind}^3 = \frac{g\sin(A_0\beta)}{\pi^2}\int\limits_0^\infty p^2 dp\frac{1}{\cos(A_0\beta) + \cosh(\epsilon_p\beta)}, \quad (6)$$

where $\epsilon_p^2 = p^2 + m^2$.

Considering the high-temperature limit $\beta \to \infty$, we obtain

$$Q_{\rm ind}^3 = gA_0\left[\frac{4}{3}\beta^{-2} - \frac{2m^2}{3\pi^2}\beta + O(\beta^3)\right]. \quad (7)$$

Hence, we see that the first term is independent of the mass and dominant at high temperatures.

Now, for completeness, we calculate the temperature sum in Eq. (4).

The integrand in Eq. (4) has the form

$$f(p_4) = \frac{p_4 + A_0}{(p_4 - p_4^{(1)})(p_4 - p_4^{(2)})}, \quad (8)$$

where $p_4^{(1)} = -A_0 + i\epsilon_p$, $p_4^{(2)} = -A_0 - i\epsilon_p$. The sum in Eq. (5) after computing the simple residues equals

$$S_1 = \frac{1}{\beta}\sum_{p_4} f(p_4) = -\frac{1}{2}\left[\frac{i\epsilon_p}{p_4^{(1)} - p_4^{(2)}}\tan\left(\frac{\beta}{2}p_4^{(1)}\right) + \right.$$
$$\left. + \frac{-i\epsilon_p}{p_4^{(2)} - p_4^{(1)}}\tan\left(\frac{\beta}{2}p_4^{(2)}\right)\right]. \quad (9)$$

Substituting the corresponding parameters and fulfilling elementary transformations, we find

$$S_1 = \frac{1}{2}\frac{\sin(A_0\beta)}{\cos(A_0\beta) + \cosh(\epsilon_p\beta)}. \quad (10)$$

By substituting S_1 in Eq. (4), we obtain Eq. (6).

Performing similar calculations for $Q_{\rm ind}^8$, we get [7]

$$Q_{\rm ind}^8 = gA_0^8\left[\frac{16}{3\sqrt{3}}\beta^{-2} - \frac{8m^2}{3\sqrt{3}\pi^2}\beta + O(\beta^3)\right]. \quad (11)$$

Here, A_0^8 is the background field generated in the plasma. For our problem, it is a given number.

Now, we calculate the quark propagator accounting for the induced charge by means of Schwinger–Dyson's equation. In the Euclidean space-time, it reads

$$S^{-1}(p) = -\left(\gamma^4\left(p_4 - \frac{\lambda^3}{2}gA_0\right) + \boldsymbol{\gamma}\mathbf{p}\right) + m - \Sigma(p), \quad (12)$$

where $\Sigma(p)$ is a quark mass operator. In our problem, to consider the presence of the induced charge, we separate the part of radiation corrections $\Sigma^{(\rm tp.)}$ equaling to the sum of the tadpole diagrams with one gluon line G_4^3, which relates the quark bubble to a quark line. In Eq. (12), we also substitute the A_0 expression explicitly. In the rest frame of the plasma, where the actual calculations are carried out, the velocity vector is $u_\mu = (u_4 = 1,\ \mathbf{u} = 0)$.

Next, we have to consider the gluon field propagator $G^3_{44}(k)$. For that, we use the generalized Green's function of neutral gluons. It reads (in the Lorentz–Feynman gauge) [5, 6]

$$(G^3_{44})^{-1} = k^2 - \Pi_{44}(k_4, \mathbf{k}), \tag{13}$$

where $\Pi_{44}(k^2)$ is the $4-4$ component of a polarization tensor. For $k_4 = 0$, $\mathbf{k} \to 0$, it defines Debye's temperature mass having the order $m_D^2 \sim g^2T^2$. This mass is responsible for the screening of the Coulomb color fields.

The component of interest G^3_{44} taken at zero momenta reads [5, 6]

$$G^3_{44}(p = 0) = \frac{1}{m_D^2}. \tag{14}$$

Using the vertex of interactions in Eq. (12) and Eqs. (6), (14), we obtain

$$\Sigma^{(\mathrm{tp.})} = -\frac{\lambda^3}{2}\gamma^4 \frac{gQ^3_{\mathrm{ind}}}{m_D^2}. \tag{15}$$

Substituting this result in Eq. (12), we conclude that the resummation of tadpole insertions results in the replacement $gA_0 \to gA_0 + g\frac{Q^3_{\mathrm{ind}}}{m_D^2}$ in the initial propagator.

3. Potentials of Classical Color Fields

The presence of the induced color charges in the plasma leads to the generation of classical gluon potentials. To describe this phenomenon, we introduce a simple model motivated by heavy-ion collisions. In this case, the plasma is created for a short period of time in a finite space volume which has a much smaller size in the direction of collisions compared to the transversal ones.

We consider the QGP confined in the plate of the size L in the z-axis direction and infinite in the x-, y-directions. For this geometry, we calculate the classical potentials $\bar{\phi}^3 = G^3_4, \bar{\phi}^8 = G^8_4$ by solving the classical field equations for the gluon fields G^3_4, G^8_4 generated by the induced charges $Q^3_{\mathrm{ind}}, Q^8_{\mathrm{ind}}$. In doing so, we account for the results of Refs. [5, 6], where the gluon modes at the A_0 background were calculated. For our problem, we are interested in the longitudinal modes of the fields G^3_4, G^8_4 that have temperature masses $\sim g^2T^2$.

The classical potential $\bar{\phi}^3$ is calculated from the equation

$$\left[\frac{\partial^2}{\partial x_\mu^2} - m_D^2\right]\bar{\phi}^3 = -Q^3_{\mathrm{ind}}. \tag{16}$$

Making Fourier's transformation to the momentum k-space, we derive the spectrum of modes – $k_4^2 = = k_x^2 + k_y^2 + k_z^2 + m_D^2$, where $k_z^2 = (\frac{2\pi}{L})^2 l^2$ and $l = = 0, \pm1, \pm2, \ldots$. The discreteness of k_z is due to the periodic boundary condition for the plane: $\bar{\phi}^3(z) = = \bar{\phi}^3(z + L)$. The general solution to Eq. (16) is

$$\bar{\phi}^3(x_4, \mathbf{x}) = d + a\ e^{-i(k_4x_4 - \mathbf{k}\,\mathbf{x})} + b\ e^{i(k_4x_4 - \mathbf{k}\,\mathbf{x})}. \tag{17}$$

In the case of zero induced charge, $d = 0$, and we have two well-known plasmon modes. In the case of $Q^3_{\mathrm{ind}} \neq = 0$, the values a, b, d calculated from the confinement boundary condition

$$\bar{\phi}^3\left(z = -\frac{L}{2}\right) = \bar{\phi}^3\left(z = \frac{L}{2}\right) = 0 \tag{18}$$

result in the expression

$$\bar{\phi}^3(z)\frac{Q^3_{\mathrm{ind}}}{m_D^2}\left[1 - \frac{\cos(k_z z)}{\cos(k_z L/2)}\right]. \tag{19}$$

The generated potential depends on the z-variable only. There are no dynamical plasmon states at all. The same result follows for the potential $\bar{\phi}^8(z)$. This is the main observation. In the presence of the induced charges, the static classical color potentials have to be realized in the plasma.

For applications, it is also necessary to get the Fourier transform $\bar{\phi}^3(k)$ of potential (19). Fulfilling that for the interval of $z[-\frac{L}{2}, \frac{L}{2}]$, we obtain

$$\bar{\phi}^3(k) = \frac{Q^3_{\mathrm{ind}}L}{m_D^2}\ \frac{\sin(kL/2)}{(kL/2)}\frac{k_z^2}{k_z^2 - k^2}, \tag{20}$$

where the values of k_z are given by Eq. (16).

The energy for a mode with momentum k_z is positive and equals

$$E_l = \frac{(Q^3_{\mathrm{ind}})^2}{m_D^4}\frac{k_z^2}{2}L = \frac{(Q^3_{\mathrm{ind}})^2}{m_D^4}\frac{2\pi^2}{L}l^2. \tag{21}$$

ISSN 2071-0186. Ukr. J. Phys. 2019. Vol. 64, No. 8

The total energy is given by the sum over l of energies (21). Similar results hold for the potential $\bar{\phi}^8$.

Thus, in the presence of the induced charges, the static gluon potentials with positive energy should be generated. This is a consequence of condition Eq. (18). Obviously, such a situation is independent of the specific form of the bag, where the plasma is confined. In general, we have to expect that the color static potentials $\bar{\phi}^3$, $\bar{\phi}^8$ should be present in the QGP that results in a new type of processes.

4. Effective $\gamma\gamma G$ vertices in QGP

Other interesting objects, which have to be generated in QGP with the A_0 condensate, are the effective three-line vertices $\gamma\gamma G^3, \gamma\gamma G^8$. They also should exist due to Furry's theorem violation and relate the colored and white states. These vertices, in particular, lead to observable processes such as the inelastic scattering of photons, splitting (or conversion) of gluon $\bar{\phi}^3$, $\bar{\phi}^8$ potentials in two photons.

In this and next sections, we calculate the vertex $\gamma\gamma G^3$ and investigate the mentioned processes.

Let us consider the vertex $\Gamma^{\nu}_{\mu\lambda}$ corresponding to the diagram depicted in the plot. The second diagram is obtained by changing the direction of the quark line. We set that all the momenta are ingoing, the first photon is $\gamma_1(k^1_\mu)$, the second photon is $\gamma_2(k^3_\lambda)$, a color $a = 3$ gluon – $Q^3(k^2_\nu)$, and $k^1 + k^2 + k^3 = 0$. $k^{1,2,3}$ are the momenta of external fields.

We consider the contributions coming from the traces of four γ-matrices, which are proportional to the quark mass and dominant for small photon momenta $k^1, k^3 \ll m$. The analytic expression (common factor is $e^2 g m$) is

$$\Gamma^{\nu}_{\mu\lambda}(k^1,k^3) = \Gamma^{\nu,(1)}_{\mu\lambda}(k^1,k^3) + \Gamma^{\nu,(2)}_{\mu\lambda}(k^1,k^3), \tag{22}$$

where

$$\Gamma^{\nu,(1)}_{\mu\lambda}(k^1,k^3) = \\ = \frac{1}{\beta}\sum_{p_4}\int \frac{d^3p}{(2\pi)^3}\frac{N_1}{D(\tilde{P})D(\tilde{P}-k^1)D(\tilde{P}+k^3)}. \tag{23}$$

Here, the summation is over $p_4 = \frac{2\pi}{\beta}(l+1/2), l = 0, \pm1, \pm2, ...$, the integration is over three-dimensional momentum space p, N_1 denotes the numerator coming from the first diagram, $\tilde{P} = (\tilde{P}_4 = p_4 - A_0, \mathbf{p})$, $D(\tilde{P}) = (p_4 - A_0)^2 + \mathbf{p}^2 + m^2 = \tilde{P}_4^2 + \epsilon_p^2$, and $\epsilon_p^2 =$

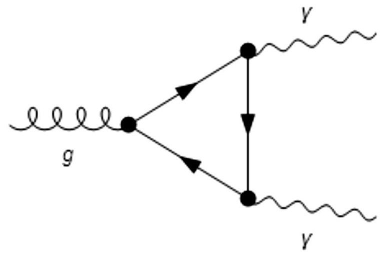

$= \mathbf{p}^2 + m^2$ is the squared energy of a free quark. The functions $D(\tilde{P}-k^1), D(\tilde{P}+k^3)$ assume a corresponding shift in the momentum. The numerator N_1 is

$$(N_1)_{\mu\nu\lambda} = \delta_{\mu\nu}(\tilde{P}-k^2)_\lambda + \\ + \delta_{\lambda\nu}(\tilde{P}-k^2)_\mu + \delta_{\mu\lambda}(\tilde{P}-q)_\nu, \tag{24}$$

where $q = k^3 - k^1$ is the photon momentum transferred.

The expression for the second term in (22) comes from the second diagram and can be obtained from (23), (24) by the substitutions $k^1 \to -k^1$, $k^2 \to -k^2$, $q \to -q$. We denote the second numerator by N_2. In what follows, we carry out actual calculations for the first term in (22) and adduce the results for the second one.

Now, we consider the fact that, in the high temperature limit, the large values of the integration momentum p give the leading contribution. Therefore, we can present the functions

$$D(\tilde{P}), \quad D(\tilde{P}-k^1), \quad D(\tilde{P}+k^3)$$

in the form:

$$\begin{aligned} D(\tilde{P}) &= \tilde{P}_4^2 + \epsilon_p^2 = \tilde{P}^2, \\ D(\tilde{P}-k^1) &= \tilde{P}^2\Big(1 - \frac{2\tilde{P}\,k^1 - k_1^2}{\tilde{P}^2}\Big), \\ D(\tilde{P}+k^3) &= \tilde{P}^2\Big(1 + \frac{2\tilde{P}\,k^3 + k_3^2}{\tilde{P}^2}\Big) \end{aligned} \tag{25}$$

with $k_1^2 = (k_4^1)^2 + \mathbf{k}_1^2, k_3^2 = (k_4^3)^2 + \mathbf{k}_3^2$. At high temperature and $\tilde{P}^2 \to \infty$, the k-dependent terms are small. So, we can expand in these parameters. Now, the integrand in Eq. (23) reads

$$\text{Intd.} = \frac{N_1}{(\tilde{P}^2)^3}\left[1 + \sum_{i=1}^{4} A_i\right], \tag{26}$$

where

$$A_1 = -2\frac{(\tilde{P}\,q)}{\tilde{P}^2}, \quad A_2 = -\frac{k_3^2 - k_1^2}{\tilde{P}^2},$$

$$A_3 = -4\frac{(\tilde{P}\,k^1)(\tilde{P}\,k^3)}{\tilde{P}^2}, \quad A_4 = 4\frac{(\tilde{P}\,k^1)^2 + (\tilde{P}\,k^3)^2}{\tilde{P}^2}, \tag{27}$$

and the vector $q_\mu = (q_4, \mathbf{q})$.

For the second diagram, we have to substitute $q \to \to -q$, other terms are even and do not change.

Further, we concentrate on the scattering of photons on the potential Q_4^3 in the medium rest frame and set the thermostat velocity $u_\nu = (1, \mathbf{0}), \nu = 4$. The corresponding terms in the numerators are

$$N_1 \to \delta_{\mu\lambda}(\tilde{P} + q)_4, \quad N_2 \to \delta_{\mu\lambda}(\tilde{P} - q)_4. \tag{28}$$

In this case, $\tilde{P}_4 = p_4 - A_0$ and $\tilde{P}^2 = (p_4 - A_0)^2 + \epsilon_p^2$.

We have to calculate, in general, the series of two types corresponding to these numerators:

$$S_1^{(n)} = \frac{1}{\beta}\sum_{p_4}\frac{p_4 - A_0}{(\tilde{P}^2)^n}, \quad S_2^{(n)} = \frac{1}{\beta}\sum_{p_4}\frac{q_4}{(\tilde{P}^2)^n}, \tag{29}$$

$n = 3, 4, 5$.

These functions can be calculated from the $S_1^{(1)}$ and $S_2^{(1)}$, by computing a number of derivatives with respect to ϵ_p^2. The latter series result in simple expressions. First is the one calculated already for the tadpole diagram Eq. (10). But now, we have to change the sign $A_0 \to -A_0$. The function $S_2^{(1)}$ is

$$S_2^{(1)} = \frac{1}{\beta}\sum_{p_4}\frac{q_4}{\tilde{P}^2} = -\frac{q_4}{2\epsilon_p}\frac{\sinh(\epsilon_p\beta)}{\cos(A_0\beta) + \cosh(\epsilon_p\beta)}. \tag{30}$$

Let us adduce the expressions for A_i obtained after some simplifying algebraic transformations:

$$A_1 = -2\frac{(p_4 - A_0)q_4}{\tilde{P}^2}, \tag{31}$$

$$A_3 = -\frac{4}{\tilde{P}^2}\left[\left(1 - \frac{\epsilon_p^2}{\tilde{P}^2}\right)k_4^1 k_4^3 + \frac{(\mathbf{p}\,\mathbf{k}_1)(\mathbf{p}\,\mathbf{k}_3)}{\tilde{P}^2}\right], \tag{32}$$

$$A_4 = \frac{4}{\tilde{P}^2}\left[\left(1 - \frac{\epsilon_p^2}{\tilde{P}^2}\right)((k_4^1)^2 + (k_4^3)^2) + \right.$$
$$\left. + \frac{(\mathbf{p}\,\mathbf{k}_1)^2 + (\mathbf{p}\,\mathbf{k}_3)^2}{\tilde{P}^2}\right]. \tag{33}$$

Finally, the resulting amplitude consists of the terms

$$M_1 = 2\delta_{\mu\lambda}\frac{p_4 - A_0}{(\tilde{P}^2)^3}(1 + A_1 + A_3 + A_4) \tag{34}$$

and

$$M_2 = -4\delta_{\mu\lambda}\frac{(p_4 - A_0)q_4^2}{(\tilde{P}^2)^4}. \tag{35}$$

Thus, all the contributions of the $S_2^{(n)}$ series are cancelled in the total. Now, we turn to the d^3p integration.

We present calculation of high temperature asymptotic considering the first term in Eq. (34) which is calculated as the second derivative of $S_1^{(1)}$ over ϵ_p^2 and equals to

$$S_3 = -A_0\beta\,\frac{\mathrm{sech}(\beta\epsilon_p/2)^4}{64p^3}(-2\beta\epsilon_p +$$
$$+ \beta\epsilon_p\cosh(\beta\epsilon_p) + \sinh(\beta\epsilon_p)). \tag{36}$$

Performing integration in the spherical coordinates and taking the leading order approximation, $\epsilon_p\beta = = p\beta$, we get

$$I_3 = \int\limits_{-\infty}^{\infty} d^3p\, S_3 = -A_0\pi\beta\ (0.3348). \tag{37}$$

In such a way all the other integrations in Eqs. (34), (35) can be carried out.

5. Scattering of Photons on the Potentials

Relations (19), (20) give the calculated expressions for the potential $\bar{Q}_4^3 = \bar{\phi}^3$ in the plasma plate. Here, we consider the scattering of photons on potential (20). Let us denote the momenta of ingoing and outgoing photons as k_μ^1 and k_λ^3, respectively. The matrix element of the process is

$$M = (2\pi)^4\delta(k^1 + k^2 - k^3)\ \frac{e_\mu^{\sigma_1}}{\sqrt{2\omega_1}}\ \bar{\phi}^3\ \Gamma_{\mu\lambda}^4\ \frac{e_\lambda^{\sigma_3}}{\sqrt{2\omega_3}}. \tag{38}$$

Here, $e^{\sigma_1}{}_\mu, e^{\sigma_2}{}_\lambda$ are polarization amplitudes of photons, and ω_1, ω_3 are the corresponding energies, $\Gamma_{\mu\lambda}^4(k^1, k^3)$ is the effective vertex calculated in the previous section.

We assume that the beams are not polarized, $\sum_{\sigma_3} e_\mu^{\sigma_1} e_{\mu'}^{\sigma_1} = = \delta_{\mu\mu'}$, $\sum_{\sigma_3} e_\lambda^{\sigma_3} e_{\lambda'}^{\sigma_3} = \delta_{\lambda\lambda'}$. Then the probability

$$P = MM^+ = (\bar{\phi}^3(k))^2\ \Gamma_{\mu\lambda}^4\Gamma_{\mu\lambda}^4\frac{C}{4\omega_1\omega_3}\ \delta(k^1 + k^2 - k^3), \tag{39}$$

where C is some nonrelevant number. In this expression (accounting for the momentum conservation),

ISSN 2071-0186. Ukr. J. Phys. 2019. Vol. 64, No. 8

$\omega_3 = [(\omega_x^1)^2 + (\omega_y^1)^2 + (\omega_z^1 + k_z^2)^2]^{1/2}$. The value of k_z^2 is a free parameter of the problem. It indicates the point, at which the actual scattering happens in the z-plane. Since this is not known, we have to sum up the probability over k_z^2, i.e., over l. In this expression, all the parameters and functions are known. So, the scattering on the induced color potentials can be calculated. Analogous process has to happen for the classical field $\bar{\phi}^8(k)$. This kind of scattering drastically differs from that for the plasma consisting of free chaotically moving particles.

Another related process is the conversion of classical gluon fields $\bar{\phi}^3(k), \bar{\phi}^8(k)$ in two photons coming out from the QGP due to the effective vertex $\Gamma^{\nu}_{\mu\lambda}(k^1, k^3)$. In the rest frame of the plasma, two photons moving in opposite directions and having specific energies, which correspond to the energy levels E_l Eq. (21), have to be observed. The amplitude is described by Eq. (38) with corresponding changes of momenta.

6. Conclusions

We have demonstrated that, in QGP with the A_0 condensates, the induced color charges $Q^3_{\rm ind}, Q^8_{\rm ind}$ and the static classical gluon fields $\bar{\phi}^3, \bar{\phi}^8$ have to be present. This results in specific new phenomena. In particular, the conversion of gluons in photons happened due to the effective $\Gamma^{\nu}_{\mu\lambda}$ vertex could influence the exit of direct photons from the plasma.

1. Y. Aoki, *et al.* The QCD transition temperature: results with physical masses in the continuum limit II. arxiV: 0903.4155 (2009).
2. H. Satz. Extreme states of matter in strong interaction physics: An introduction. *Lect. Notes Phys.* **841**, 237 (2012).
3. M. Srednicki, I. Susskin. Colored monopoles on the lattice. *Nucl. Phys. B* **179**, 239 (1981).
4. O.A. Borisenko, J. Bohacik, V.V. Skalozub. A_0 condensate in QCD. *Fortschr. Phys.* **43**, 301 (1995).
5. O.K. Kalashnikov. Infrared properties of the hot gauge theory after symmetry breaking. *Progr. Theor. Phys.* **92**, 1207 (1994).
6. O.K. Kalashnikov. Self-energy peculiarities of the hot gauge theory after symmetry breaking. *Mod. Phys. Lett. A* **11**, 1825 (1996).
7. I.A. Baranov, V.V. Skalozub. Induced charges and quark polarization operator at A0 background. *J. Phys. Electron.* **26 (1)**, 3 (2018).

Received 26.07.19

В. Скалозуб

ІНДУКОВАНІ КОЛЬОРОВІ ЗАРЯДИ,
ЕФЕКТИВНА $\gamma\gamma G$-ВЕРШИНА У КВАРК-ГЛЮОННІЙ
ПЛАЗМІ. ЗАСТОСУВАННЯ ДО ЗІТКНЕНЬ
ВАЖКИХ ІОНІВ

Р е з ю м е

Ми обчислюємо індуковані кольорові заряди $Q^3_{\rm ind}, Q^8_{\rm ind}$ та ефективну $\gamma - \gamma$-глюон вершину, які генеруються у кварк-глюонній плазмі в присутності A_0 конденсату внаслідок порушення кольорової C-парності в таких умовах. Для імітації зіткнення важких ядер ми розглядаємо модель плазми, що знаходиться всередені вузької пластини необмежених поперечних розмірів. Для таких умов ми отримуємо потенціали класичних глюонних полів $\bar{\phi}^3, \bar{\phi}^8$, що виникають у присутності індукованих зарядів. У якості застосування розглядаються два процеси – розсіювання фотонів на плазмі та конвертація класичних глюонів у два фотони, що випромінюються із плазми.

https://doi.org/10.15407/ujpe64.8.760

I. SZANYI,[1] V. SVINTOZELSKYI[2]

[1] Eötvös Loránd University
(1/A, Pázmány Péter Walkway, 1117 Budapest, Hungary; e-mail: istvan.szanyi@cern.ch)
[2] Taras Shevchenko National University of Kyiv
(64/13, Volodymyrska Str., Kyiv 01601, Ukraine; e-mail: 1vladimirsw@gmail.com)

POMERON-POMERON SCATTERING

The central exclusive diffractive (CED) production of meson resonances potentially is a factory producing new particles, in particular, a glueball. The produced resonances lie on trajectories with vacuum quantum numbers, essentially on the pomeron trajectory. A tower of resonance recurrences, the production cross-section, and the resonances widths are predicted. A new feature is the form of a non-linear pomeron trajectory, producing resonances (glueballs) with increasing widths. At LHC energies, in the nearly forward direction, the t-channel both in elastic, single, or double diffraction dissociations, as well as in CED, is dominated by the pomeron exchange (the role of secondary trajectories is negligible, however a small contribution from the odderon may be present).

K e y w o r d s: Regge trajectory, pomeron, glueball, CED, LHC.

1. Introduction

The central exclusive diffractive (CED) production continues attracting attention of both theorists and experimentalists (see, e.g., [1] and references therein). Interest in this subject is triggered by LHC's high energies, where even the subenergies at an equal partition is sufficient to neglect the contribution from secondary Regge trajectories. Consequently, CED can be considered as a gluon factory to produce exotic particles such as glueballs.

Below, we will study CED shown in Fig. 1 with topology 4. Its knowledge is essential in studies with diffractive excited protons, topologies 5 and 6.

In the single-diffraction dissociation or single dissociation (SD), one of the incoming protons dissociates (topology 2 in Fig. 1), in double-diffraction dissociation or double dissociation (DD), both protons dissociate (topology 3), and, in central dissociation (CD) or double-Pomeron exchange (DPE), none of the protons dissociates (topology 4). These processes are tabulated below as

SD $pp \to Xp$
or $pp \to pY$
DD $pp \to XY$
CD (DPE) $pp \to pXp$,

where X and Y represent diffractive dissociated protons.

2. Pomeron/Glueball Trajectory

Regge trajectories $\alpha(s)$ connect the scattering region, $s < 0$, with that of particle spectroscopy, $s > 0$. In this way, they realize the crossing symmetry and anticipate the duality, *i.e.*, the dynamics of two kinematically disconnected regions is intimately related: the trajectory at $s < 0$ should "know" its behavior in the cross channel and vice versa. Most of the familiar meson and baryon trajectories follow the above regularity: with their parameters fitted in the scattering region, they fit the masses and spins of relevant resonances, see, e.g., [2]. The behavior of trajectories both in the scattering and particle regions is close to linear, which is an approximation to reality. Resonances on real and linear trajectories imply unrealistic infinitely narrow resonances. Analyticity and unitarity also require that the trajectories be non-linear complex functions [3, 4]. Constraints on the threshold and asymptotic behaviors of Regge trajectories were derived from dual amplitudes with Mandelstam analyticity [4]. Accordingly, near the threshold (see also [5–7])

$$\Im m\alpha(s)_{s\to s_0} \sim (s - s_0)^{\alpha(s_0)+1/2}, \quad (1)$$

while the trajectories are constrained asymptotically by [4]

$$\left|\frac{\alpha(s)}{\sqrt{s}\ln s}\right|_{s\to\infty} \le \mathrm{const.} \tag{2}$$

The above asymptotic constrain can be still lowered to a logarithm by imposing (see [8] and earlier references) the wide-angle power behavior for the amplitude.

The above constrains are restrictive, but still leave much room for the model building. In Refs. [9, 10], the imaginary part of the trajectories (resonances' widths) was recovered from the nearly linear real part of the trajectory by means of dispersion relations and fits to the data.

While the parameters of meson and baryon trajectories can be determined both from the scattering data and from the particle spectra, this is not true for the pomeron (and odderon) trajectory, known from fits to scattering data only (negative values of its argument). An obvious task is to extrapolate the pomeron trajectory from negative to positive values to predict glueball states at $J = 2, 4, ...$ was not solved. Given the nearly linear form of the pomeron trajectory, known from the fits to the (exponential) diffraction cone, little room is left for variations in the region of particles ($s > 0$.) The non-observability of any glueball state in the expected values of spins and masses may have two explanations: 1. glueballs appear as hybrid states mixed with quarks, which makes their identification difficult; 2. their production cross-section is low and their widths is large. To resolve these problems, one needs a reliable model to predict cross-sections and decay widths of the expected glueballs, in which the pomeron trajectory plays a crucial role.

Models for the pomeron/glueball trajectories were proposed and discussed in quite a number of papers [11–14]. They range from simple phenomenological (also linear) models to quite sophisticated ones, involving QCD, lattice calculations, extra dimensions, etc. The basic problem of the production cross-sections and the decay widths of produced glueballs in the cited papers remains open. Close to the spirit of the present approach are papers [12–14], where the pomeron/glueball trajectory, including the threshold singularities is manifestly non-linear, and the real part terminates.

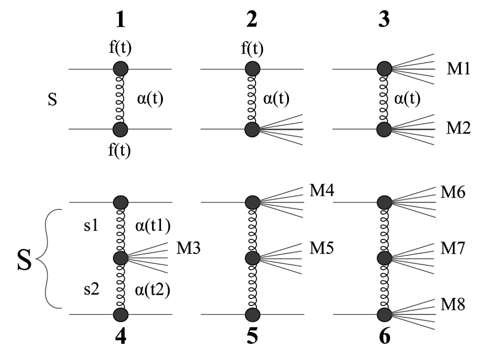

Fig. 1. Regge-pole factorization

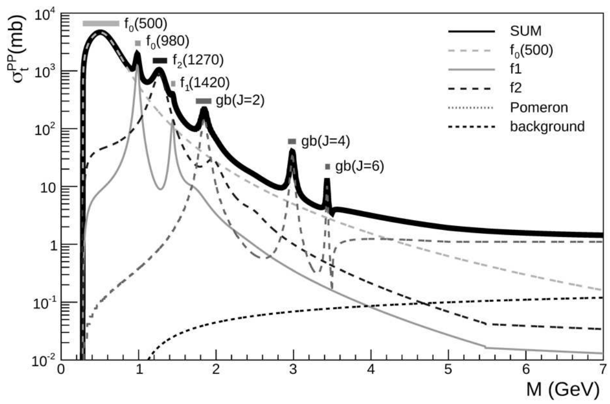

Fig. 2. Pomeron-pomeron total cross-section in CED calculated in Ref. [1]

We continue the lines of researches initiated in Refs. [1, 15] in which an analytic pomeron trajectory was used to calculate the pomeron-pomeron cross-section in the central exclusive production measurable in the proton-proton scattering, e.g., at the LHC. The basic idea in that approach is the use of a non-linear complex Regge trajectory for the pomeron satisfying the requirements of the analytic S-matrix theory and fitting the data. Fits imply high-energy elastic proton-proton scattering data. For the scattering amplitude, the simple and efficient Donnachie–Landshoff model [16] was used. The essential difference with respect to many similar studies lies in the non-linear behavior of the trajectories. They affect crucially the predicted properties of the resonances. Our previous papers [1, 15] contain more than that: the fitted trajectories are used to calculate pomeron-pomeron scattering cross-sections in the central exclusive diffraction at the LHC. Figure 2 shows the result of those calculations.

Papers [1, 15] contain detailed analyses and fits of both the pomeron and non-leading (also complex!) Regge trajectories, the emphases being on the pomeron/gluon one. In the present study, we revise the basic object, namely the model of a pomeron trajectory, postponing other details (secondary reggeons, CED, *etc.*) to a forthcoming study.

2.1. Scattering amplitude, cross-sections, resonances

In Ref. [1], the contribution of resonances to the pomeron-pomeron (PP) cross-section was calculated from the imaginary part of the amplitude with the use of the optical theorem:

$$\sigma_t^{PP}(M^2) = \Im m\, A(M^2, t=0) =$$

$$= a \sum_{i=f,P} \sum_J \frac{[f_i(0)]^{J+2}\, \Im m\, \alpha_i(M^2)}{(J - \Re e\, \alpha_i(M^2))^2 + (\Im m\, \alpha_i(M^2))^2}. \tag{3}$$

In this section, we concentrate on the pomeron. In this case, Eq. (3) reduces to

$$\sigma_t^{PP}(M^2) = a \sum_J \frac{k^{J+2}\, \Im m\, \alpha(M^2)}{(J - \Re e\, \alpha(M^2))^2 + (\Im m\, \alpha(M^2))^2}, \tag{4}$$

where $k = f_i(0)$, and, for simplicity, we set $k = 1$.

We start by comparing the resulting glueball spectra in two ways: first, we plot the real and imaginary parts of the trajectory (Chew–Frautchi plot) and calculate the resonances' widths by using the relation (see, e.g., Eq. (18) in [15])

$$\Gamma(s = M^2) = \frac{2\Im m \alpha(s)}{|\alpha'(s)|}, \tag{5}$$

where $\alpha'(s) = d\Re e\alpha(\sqrt{s})/d\sqrt{s}$.

2.2. Analytic Regge trajectories

In the previous studies [1, 15, 18], the following two types of trajectories were considered:

$$\alpha(s) = \alpha_0 + \alpha_1 s + \alpha_2(\sqrt{s_0 - s} - \sqrt{s_0}), \tag{6}$$

and

$$\alpha(s) = \alpha_0 + \alpha_2(\sqrt{s_0 - s} - \sqrt{s_0}) + \alpha_3(\sqrt{s_1 - s} - \sqrt{s_1}), \tag{7}$$

In trajectory Eq. (7), the second, heavy threshold was introduced to mimic the nearly linear rise of the trajectory for $s < s_1$, avoiding an indefinite rise as in Eq. (6), thus securing the asymptotic square-root upper bound (2). As realized in Refs. [1, 15], these trajectories result in "narrowing" the resonances (here, a glueball) whose widths decrease, as their masses increase. Below, we show that this deficiency is remedied in a trajectory that satisfies the constraint of the analytic S-matrix theory, namely, the threshold behavior and asymptotic boundedness, and produces fading resonances (glueballs), whose widths are rising with mass.

The trajectory is:

$$\alpha(s) = \frac{a + bs}{1 + c(\sqrt{s_0 - s} - \sqrt{s_0})}, \tag{8}$$

where $s_0 = 4m_\pi^2$, and a, b, c are adjustable parameters, to be fitted to scattering ($s < 0$) data with the obvious constraints: $\alpha(0) \approx 1.08$ and $\alpha'(0) \approx 0.3$. Trajectory Eq. (8) has square-root asymptotic behavior, in accord with the requirements of the analytic S-matrix theory.

With the parameters fitted in the scattering region, we continue trajectory Eq. (8) to positive values of s. When approaching the branch cut at $s = s_0$, one has to choose the right Riemann sheet, For the $s > s_0$ trajectory Eq. (8) may be rewritten as

$$\alpha(s) = \frac{a + bs}{1 - c(i\sqrt{s - s_0} + \sqrt{s_0})} \tag{9}$$

with the sign "minus" in front of c, according to the definition of the physical sheet.

For $s \gg s_0, |\alpha(s)| \to \frac{b}{c}\sqrt{|s|}$. For $s > s_0$ (on the upper edge of the cut), $\Im m\, \alpha > 0$.

The intercept is $\alpha(0) = a$, and the slope at $s = 0$ is

$$\alpha'(0) = b + \frac{ac}{2\sqrt{s_0}}. \tag{10}$$

To anticipate subsequent fits and discussions, we note that the presence of the light threshold $s_0 = 4m_\pi^2$ (required by unitarity and the observed "break" in the data) results in the increasing, compared with the "standard" value of ≈ 0.25 GeV^{-2}, intercept.

2.3. Simple Regge-pole fits to high-energy elastic scattering data

High-energy elastic proton-proton and proton-antiproton scatterings, including ISR and LHC energies, were successfully fitted with non-linear pomeron trajectories Eqs. (6) and (7) in a number of papers, see [17] and references therein. Here, we are interested in the parametrization of the pomeron (and odderon) trajectories, dominating the LHC energy region, and concentrate on the LHC data, where the secondary trajectories can be completely ignored in the near forward direction.

At lower energies (e.g., at the ISR), the diffraction cone shows the almost perfect exponential behavior corresponding to a linear pomeron trajectory in a wide span of $0 < -t < 1.3$ GeV^2, which is violated only by the "break" near $t \approx -0.1$ GeV^2. At the LCH, it is almost immediately followed by another structure, namely, by the dip at $t \approx -0.6$ GeV^2. The dynamics of the dip (diffraction minimum) has been treated fully and successfully [18]. However, those details are irrelevant to the behavior of the pomeron trajectory in the resonance (positive s) region and the expected glueballs there, that depend largely on the imaginary part of the trajectory and basically on the threshold singularity in Eq. (8).

In Fig. 3, we show a fit to the low-$|t|$ elastic proton-proton differential cross-section data [19] at 13 TeV with a simple model:

$$A_P(s,t) = a_P e^{b_P t} e^{-i\pi\alpha_P(t)/2} (s/s_{0P})^{\alpha_P(t)}, \tag{11}$$

where $\alpha_P(t)$ is given by Eq. (8) (changing the variable s to the variable t).

We used the norm

$$\frac{d\sigma}{dt} = \frac{\pi}{s^2} |A_P(s,t)|^2. \tag{12}$$

Figure 4 shows the normalized form of the differential cross-section (used by TOTEM [19]) illustrating the low-$|t|$ "break" phenomenon [17] related to the non-linear square-root term in the pomeron trajectory. However, it should be also noted that the "break" may be resulted from the two-pion threshold both in the trajectory and the non-exponential residue, as discussed in [17].

2.4. Extrapolating the pomeron trajectory to the resonance region, $s > 0$

Fitting to the measured pp scattering data, the values of the pomeron trajectory parameters became known. Changing back the variable t to the variable s (crossing symmetry), we can extrapolate now the

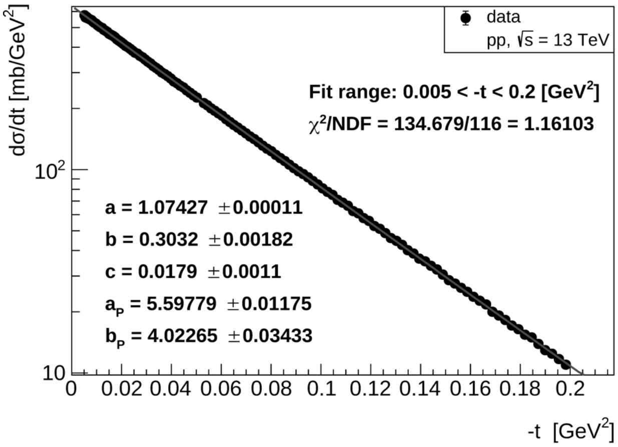

Fig. 3. Fitted pp differential cross-section at 13 TeV using amplitude Eq. (11) and trajectory Eq. (8)

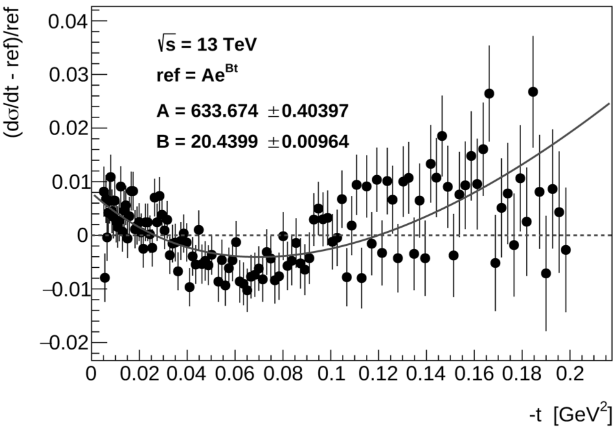

Fig. 4. Normalized form of the fitted pp differential cross-section at 13 TeV using amplitude Eq. (11) and trajectory Eq. (8)

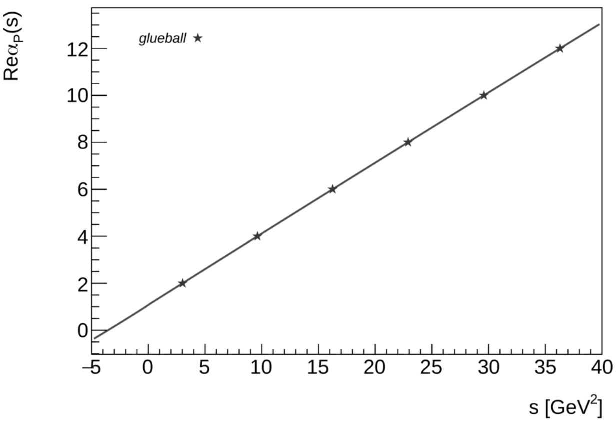

Fig. 5. Real part of the pomeron trajectory Eq. (8) as a function of s

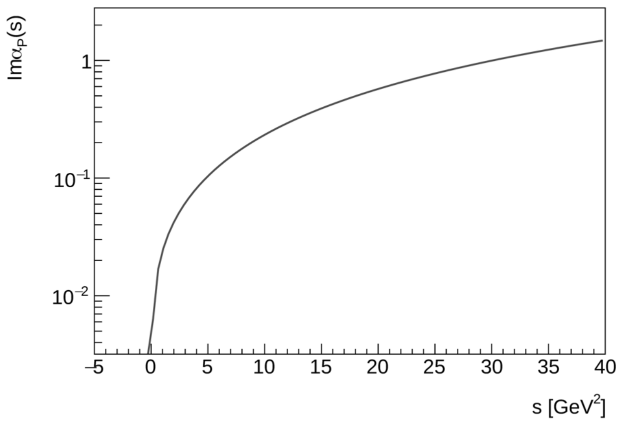

Fig. 6. Imaginary part of the pomeron trajectory Eq. (8) as a function of s

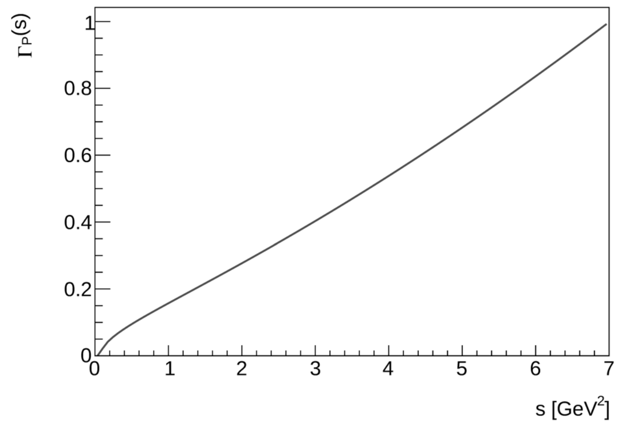

Fig. 7. Resonance width Eq. (5) calculated with trajectory Eq. (8)

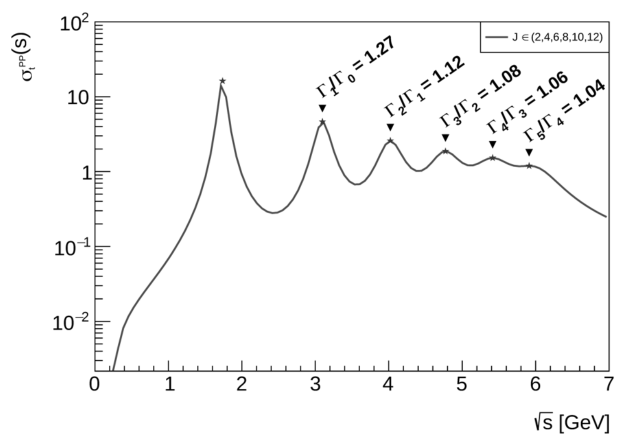

Fig. 8. Pomeron-pomeron total cross-section Eq. (4) (setting $a = 1$ and $J \in (2, 4, 6, 8, 10, 12)$) calculated with trajectory Eq. (8) showing also the ratios of neighboring resonances' widths

pomeron trajectory to the resonance region, $s > 0$. Figures 5 and 6 show, respectively, the real and imaginary parts of the trajectories (during the calculations, the trajectory parameter values are taken from the fit shown in Fig. 3). Figure 5 shows the glueball spectra lying on the pomeron trajectory. Such glueballs have even integer spins ($J \equiv \mathrm{Re}\,\alpha_P(s) = 2, 4, 6, ...$) and mass square $M^2 = s$.

In Figs. 8 and 7, we can see, respectively, the resonance width and the pomeron-pomeron total cross section.

3. Summary

Using a simple pomeron pole model fit to the 13-TeV pp low-$|t|$ differential cross-section data, we have extrapolated the pomeron trajectory from negative to positive values to predict glueball states at $J = 2$, 4, 6, 8, 10, and 12. We have predicted also the cross-sections and decay widths of the expected glueballs. Applying the pomeron trajectory Eq. (8), we have obtained such resonances (glueballs) whose widths increase with their masses.

We thank the organizers of the New Trends in High-Energy Physics 2019 for their support and the inspiring discussions provided by the Conference. We thank also László Jenkovszky for his guidance during the preparation of the manuscript. The work of I. Szanyi was supported by the "Márton Áron Szakkollégium" program.

1. R. Fiore, L. Jenkovszky, R. Schicker. Exclusive diffractive resonance production in proton-proton collisions at high energies. *Eur. Phys. J. C* **78**, 468 (2018).
2. P.D.B. Collins. *An Introduction to Regge Theory and High Energy Physics* (Cambridge Univ. Press, 1977).
3. A. Degasperis, E. Predazzi. Dynamical calculation of Regge trajectories. *Nuovo Cimento A* **65**, 764 (1970).
4. A.I. Bugrij, G. Cohen-Tannoudji, L.L. Jenkovszky, N.A. Kobylinsky. Dual amplitudes with Mandelstam analyticity. *Fortschritte der Physik* **21**, 427 (1973).
5. A.O. Barut, D.E. Zwanziger. Complex angular momentum in relativistic S-matrix theory. *Phys. Rev.* **127**, 974 (1962).
6. V.N. Gribov, Ya.I. Pomeranchuk. Properties of the elastic scattering amplitude at high energies. *Nucl. Phys.* **38**, 516 (1962).
7. R. Oehme. Complex angular momentum in elementary particle scattering, in *Proceedings of the Scottish Universities Summer School* Edinburgh 1963, edited by R. G. Moorhouse, p.129 (1964).

8. L.L. Jenkovszky. High-energy elastic hadron scattering. *La Rivista del Nuovo Cimento* **10**, 1 (1987).
9. R. Fiore, L.L. Jenkovszky, F. Paccanoni, A. Prokudin. Baryonic Regge trajectories with analyticity constraints. *Phys. Rev. D* **70**, 054003 (2004).
10. R. Fiore, L.L. Jenkovszky, V. Magas, F. Paccanoni, A. Papa. Analytic model of Regge trajectories. *Eur. Phys. J. A* **10**, 217 (2001).
11. M.N. Sergeenko. Gluonium states and the Pomeron trajectory. arXiv:0807.0911.
12. M.M. Brisudova, L. Burakovsky, T. Goldman, A. Szczepaniak. Nonlinear Regge trajectories and glueballs. arXiv:nucl-th/0303012.
13. T. Goldman, A. Szczepaniak. Nonlinear Regge trajectories and glueballs. arXiv:hep-ph/0009126.
14. M.M. Brisudova, L. Burakovsky, T. Goldman. Spectroscopy "windows" of quark-antiquark mesons and glueballs with effective Regge trajectories. arXiv:hep-ph/0008212.
15. R. Fiore, L. Jenkovszky, R. Schicker. Resonance production in Pomeron–Pomeron collisions at the LHC. *Eur. Phys. J. C* **76**, 38 (2016).
16. A. Donnachie, P.V. Landshoff. Hard diffraction: Production of high pT jets, W or Z, and Drell–Yan pairs. *Nucl. Phys. B* **303**, 634 (1988).
17. L. Jenkovszky, I. Szanyi, CI. Tan. Shape of proton and the pion cloud. *Eur. Phys. J. A* **54**, 116 (2018).
18. I. Szanyi, N. Bence, L. Jenkovszky. New physics from TOTEM's recent measurements of elastic and total cross-sections. *J. Phys. G: Nucl. Part. Phys.* **46**, 055002 (2019).
19. The TOTEM collaboration. First determination of the ρ parameter at $\sqrt{s} = 13$ TeV – probing the existence of a colourless three-gluon bound state. arXiv:1812.04732.

Received 08.07.19

I. Сані, В. Свінтозельський

ПОМЕРОН-ПОМЕРОННЕ РОЗСІЮВАННЯ

Р е з ю м е

Центральне ексклюзивне дифракційне (ЦЕД) народження мезонних резонансів потенційно може бути фабрикою нових частинок, зокрема глюболів. Отримані резонанси лягають на траєкторії з вакуумними квантовими числами, переважно на траєкторію померона. Отримано ширини резонансів та їхній поперечний переріз. Новою особливістю є використання нелінійної траєкторії для померона, що продукує резонанси (глюболи) зі зростаючою шириною. При енергіях ВАК, у майже прямому напрямку в t-каналі як при пружних – одинарної чи подвійної дифракційної дисоціації, так і в ЦЕД домінує обмін померонами (вплив вторинних траєкторій нехтовний, хоча можливе врахування невеликого внеску оддерона).

https://doi.org/10.15407/ujpe64.8.766

M. SZYMAŃSKI,[1] M. BLUHM,[1,2,3] K. REDLICH,[1,3] C. SASAKI[1]
[1] Institute of Theoretical Physics, University of Wrocław
(PL-50204 Wrocław, Poland; e-mail: michal.szymanski@ift.uni.wroc.pl)
[2] SUBATECH UMR 6457 (IMT Atlantique, Université de Nantes, IN2P3/CNRS)
(4 rue Alfred Kastler, 44307 Nantes, France)
[3] Extreme Matter Institute EMMI, GSI
(Planckstr. 1, D-64291 Darmstadt, Germany)

SEARCHING FOR THE QCD CRITICAL POINT WITH NET-PROTON NUMBER FLUCTUATIONS

Net-proton number fluctuations can be measured experimentally and, hence, provide a source of important information about the matter created during relativistic heavy ion collisions. Particularly, they may give us clues about the conjectured QCD critical point. In this work, the beam-energy dependence of ratios of the first four cumulants of the net-proton number is discussed. These quantities are calculated using a phenomenologically motivated model in which critical mode fluctuations couple to protons and antiprotons. Our model qualitatively captures both the monotonic behavior of the lowest-order ratio, as well as the non-monotonic behavior of higher-order ratios, as seen in the experimental data from the STAR Collaboration. We also discuss the dependence of our results on the coupling strength and the location of the critical point.

Keywords: net-proton number fluctuations, QCD critical point, heavy-ion collisions.

1. Introduction

The theoretical and experimental investigations of the phase diagram of strongly interacting matter are an important subject of modern high-energy physics. One of the unresolved questions concerns the existence and location of the QCD critical point (CP) in the T and μ planes. Strong fluctuations of the critical mode, σ, in the vicinity of CP, although not directly observable, are expected to couple to physically measurable quantities such as fluctuations of conserved charges [1, 2].

Fluctuations of the net-proton number serve as an experimental probe of baryon number fluctuations. Recent, but still preliminary results of the STAR Collaboration [3–5] show a non-monotonic beam energy dependence of the ratios of higher-order net-proton number cumulants. However, the interpretation of the data is still unclear [6–9]. Therefore, effective models are needed to improve our understanding of these quantities.

One of such models was developed in [10], where the impact of resonance decays on net-proton number cumulant ratios was studied. This model could qualitatively describe the non-monotonic behavior of the C_3/C_2 and C_4/C_2 ratios. However, it also showed a strong non-monotonic behavior of the C_2/C_1 ratio which is not observed experimentally. Recently, this model was re-examined [11] to account for the scaling properties of the baryon number and chiral susceptibilities obtained within effective models [12, 13]. This reduces the effect of critical fluctuations in the net-proton number variance and, thus, allows for a better description of the STAR data.

Here, we discuss the beam energy dependence of the ratios of net-proton number cumulants obtained using the refined model from Ref. [11] and study their dependence on the coupling strength between the critical mode and (anti)protons, as well as their dependence on the location of the critical point.

2. Model Setup

As a baseline model to calculate the net-proton number cumulants, we choose the hadron resonance gas (HRG) model in which the number density of each particle species is given by the ideal gas formula,

$$n_i(T, \mu_i) = d_i \int \frac{d^3k}{(2\pi)^3} f_i^0(T, \mu_i). \qquad (1)$$

Here, d_i is the degeneracy factor, and

$$f_i^0 = \frac{1}{(-1)^{B_i} + e^{(E_i - \mu_i)/T}} \tag{2}$$

is the equilibrium distribution function, where $E_i = \sqrt{\mathbf{p}^2 + m_i^2}$ is the dispersion relation, and $\mu_i = B_i\mu_B + S_i\mu_S + Q_i\mu_Q$ is the chemical potential of a particle with mass m_i, baryon number B_i, strangeness S_i, and electric charge Q_i; μ_B, μ_Q and μ_S denote the baryon, strangeness and charge chemical potentials.

Since the QCD pressure is approximated in the HRG model by a sum of partial ideal gas pressures corresponding to different particles, there are only thermal fluctuations in this approximation. To include critical fluctuations on the top of thermal ones, we follow the phenomenological approach employed in Ref. [10]. In this approach, the particle mass is assumed to be composed of critical and non-critical parts as suggested in linear sigma models,

$$m_i \sim m_0 + g_i\sigma, \tag{3}$$

where m_0 is a non-critical contribution, and g_i is the coupling strength between the critical mode and the particle of type i. Critical mode fluctuations modify the distribution function into $f_i = f_i^0 + \delta f_i$, where a change of the distribution function due to critical mode fluctuations reads

$$\delta f_i = \frac{\partial f_i}{\partial m_i}\delta m_i = -\frac{g_i}{T}\frac{v_i^2}{\gamma_i}\delta\sigma, \tag{4}$$

with $v_i^2 = f_i^0((-1)^{B_i} f_i^0 + 1)$ and $\gamma_i = E_i/m_i$.

Fluctuations of the particle number in the thermal medium can be quantified in terms of cumulants. The n-th order cumulant of the i-th particle species reads

$$C_n^i = VT^3 \frac{\partial^{n-1}(n_i/T^3)}{\partial(\mu_i/T)^{n-1}}\bigg|_T, \tag{5}$$

where the temperature T is kept constant. In this work, we consider the first four cumulants of the net-proton number, $N_{p-\bar{p}} = N_p - N_{\bar{p}}$, which are given by [10]

$$C_n = C_n^p + (-1)^n C_n^{\bar{p}} +$$
$$+ (-1)^n \langle (V\delta\sigma)^n\rangle_c (m_p)^n (J_p - J_{\bar{p}})^n, \tag{6}$$

where C_n^p and $C_n^{\bar{p}}$ are the n-th order proton and antiproton cumulants obtained within the baseline model, respectively, $\langle (V\delta\sigma)^n\rangle_c$ is the n-th critical mode cumulant, and

$$J_i = \frac{gd}{T}\int \frac{d^3k}{(2\pi)^3}\frac{1}{E} f_i^0(1 - f_i^0). \tag{7}$$

Moreover, the contributions of other particles and resonance decays are neglected.

In general, cumulants of the critical mode cannot be calculated analytically. Following the approach introduced in Ref. [10], we model them using the universality class arguments which state that different physical systems belonging to the same universality class exhibit the same critical behavior close to the critical point [14]. Under the assumption that QCD belongs to the same universality class, as the three-dimensional Ising model [16–18], we can identify the QCD order parameter, σ, with the magnetization, M_I, the order parameter of the spin model. Hence, the critical mode cumulants can be written as [10]

$$\langle (V\delta\sigma)^n\rangle_c = \left(\frac{T}{VH_0}\right)^{n-1} \frac{\partial^{n-1} M_I}{\partial h^{n-1}}\bigg|_r, \tag{8}$$

where $r = (T - T_c)/T_c$ is the reduced temperature, and $h = H/H_0$ is the reduced magnetic field. The critical point is located at $r = h = 0$.

In the net-proton number cumulants, the singular part of the second cumulant receives a contribution from the first derivative of the order parameter with respect to the reduced magnetic field,

$$C_2^{\text{sing.}} \propto \frac{\partial M_I}{\partial h}. \tag{9}$$

The right-hand side of this equation is the magnetic susceptibility of the Ising model which, due to universality, can be identified with the chiral susceptibility of QCD. However, C_2 is related to the baryon number susceptibility which is known to diverge weaker than the chiral one [12, 13, 19]. Therefore, the model introduced in Ref. [10] requires some modifications [11]. This can be done using the following relation obtained by calculations within the effective model on the mean field level [12, 13]:

$$\chi_{\mu\mu} \simeq \chi_{\mu\mu}^{\text{reg}} + \sigma^2\chi_{\text{chiral}}, \tag{10}$$

in which the singular contribution to the baryon number susceptibility is proportional to the chiral susceptibility times the squared order parameter, and $\chi_{\mu\mu}^{\text{reg}}$

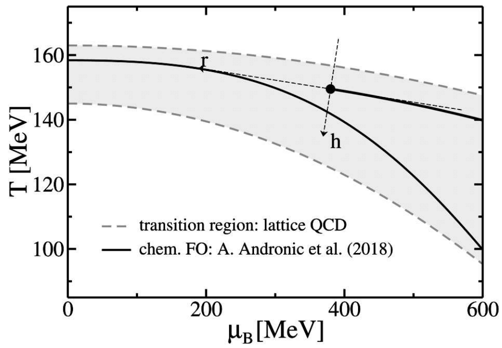

Fig. 1. The model setup used in this work. The filled band between two dashed curves shows the lattice QCD constraints for the chiral crossover transition. The green dot denotes the critical point with the spin model coordinate system attached to it and the first-order phase transition line for a larger baryon chemical potential. The solid blue line corresponds to the chemical freeze-out curve from [15]

is the regular part of the baryon number susceptibility. To obtain such a form of the second cumulant, the proton mass in Eq. (6) should be replaced by the order parameter, σ, such that the new C_2 reads

$$C_2 = C_2^p + C_2^{\bar{p}} + g^2\sigma^2\langle(V\delta\sigma)^n\rangle(J_p - J_{\bar{p}})^2. \quad (11)$$

The modified higher-order cumulants are

$$C_3 = C_3^p - C_3^{\bar{p}} - g^3\sigma^3\langle(V\delta\sigma)^n\rangle(J_p - J_{\bar{p}})^3 \quad (12)$$

and

$$C_4 = C_4^p + C_4^{\bar{p}} + g^4\sigma^4\langle(V\delta\sigma)^n\rangle(J_p - J_{\bar{p}})^4. \quad (13)$$

Since the cumulants are volume-dependent, it is convenient to consider their ratios in which this dependence cancels out,

$$\frac{C_2}{C_1} = \frac{\sigma^2}{M}, \quad \frac{C_3}{C_2} = S\sigma, \quad \frac{C_4}{C_2} = \kappa\sigma^2, \quad (14)$$

where $M = C_1$ is the mean, $\sigma^2 = C_2$ the variance, $\kappa = C_4/C_2^2$ the kurtosis, and $S = C_3/C_2^{3/2}$ the skewness.

To use the universality class arguments discussed above, a mapping between the QCD phase diagram and the reduced temperature and a magnetic field of the spin model is needed. Such a mapping is non-universal and has to be modeled for each system separately. In this work, we use a linear mapping [20, 21] in which the critical point is located at $r = h = 0$, the r axis is tangential to the QCD first-order phase transition line, and the positive direction of the h axis points toward the hadronic phase. Schematically, this is shown in Fig. 1, where the green line denotes the first-order phase transition, and the filled band shows lattice QCD constraints on the location of the chiral crossover region.

To calculate the order parameter and its cumulants, we use the parametric representation of the magnetic equation of state [22]. For a more detailed discussion of the mapping, lattice limits, and the magnetic equation of state, we refer the reader to the papers [10, 11].

Finally, assuming that the matter created during a heavy ion collision forms a thermal medium characterized by the temperature and chemical potentials, experimental data on event-by-event multiplicity fluctuations can be compared with model results. To this end, we calculate the net-proton number cumulants at the chemical freeze-out. The chemical freeze-out conditions used in this work were obtained by the analysis of hadron yields [23–28]. The blue line in Fig. 1 shows the recently obtained parametrization [15].

3. Numerical Results

In this section, we discuss numerical results on net-proton number cumulant ratios obtained within the current model. The set of model parameters includes the coupling strength g between (anti)protons and the critical mode, the parameters of the magnetic equation of state, as well as the size of a critical region in the (T, μ) plane. Their values and a detailed discussion can be found in Refs. [10, 11]. Moreover, the location of the QCD critical point is unknown. To study the effect of its position in the QCD phase diagram on the refined model results, we consider three different locations of the CP listed in Table and shown in Fig. 2, where the distance to the freeze-out curve is the farthest for CP_1 and closest for CP_3.

The first step of our discussion is the comparison between the C_2/C_1 ratio obtained using the model from Ref. [10], where the n-th net-proton number cumulant is given by Eq. (6), and the refined model [11] for the critical point location CP_1. This is shown in Fig. 3. Results obtained using the original model exhibit a clear non-monotonic behavior and deviate strongly from the non-critical baseline (the black-dotted line) even for the small coupling, $g = 3$, which becomes more pronounced for $g = 5$ (the red solid and dashed lines, respectively). Using the current approach, we find a substantial reduction of the criti-

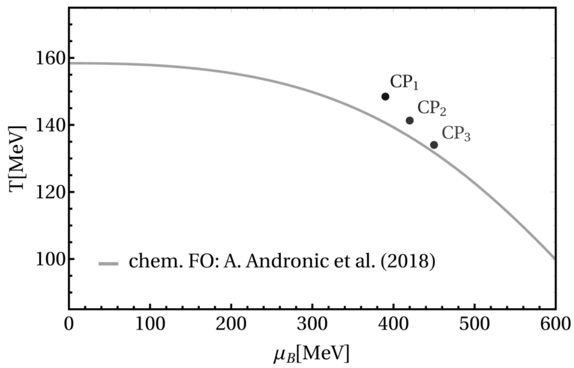

Fig. 2. QCD critical point locations from Table plotted with the chemical freeze-out curve [15] used in this work

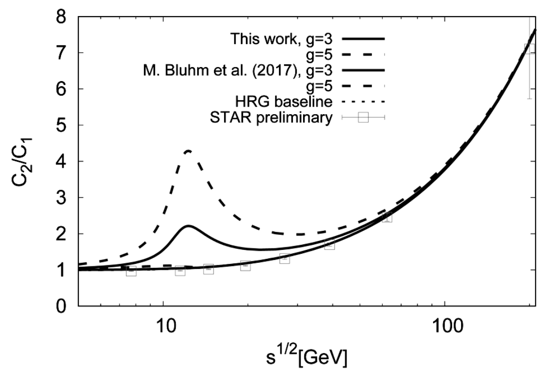

Fig. 3. Second to first net-proton number cumulant ratio for $g = 3$ and 5 calculated following Ref. [10] (red solid and dashed lines, respectively) compared to the refined model results [11] (blue solid and dashed lines, respectively). The preliminary STAR data on the net-proton number fluctuations [5] (squares with the error bars containing both statistical and systematic errors) and HRG baseline result (black dotted line) are also shown for comparison

Locations of the QCD critical point in the (μ_B, T)-plane considered in this work. These locations in the QCD phase diagram are shown in Fig. 2

CP_i	μ_{cp} [MeV]	T_{cp} [MeV]
1	390	149
2	420	141
3	450	134

cality in the C_2/C_1 ratio even for larger values of g (see the blue curves in Fig. 3). The refined model results for the C_2/C_1 ratio agree with the experimental data from the STAR Collaboration [5]. On the other hand, the original model would require an exceptionally small coupling strength in order to capture the experimentally observed behavior.

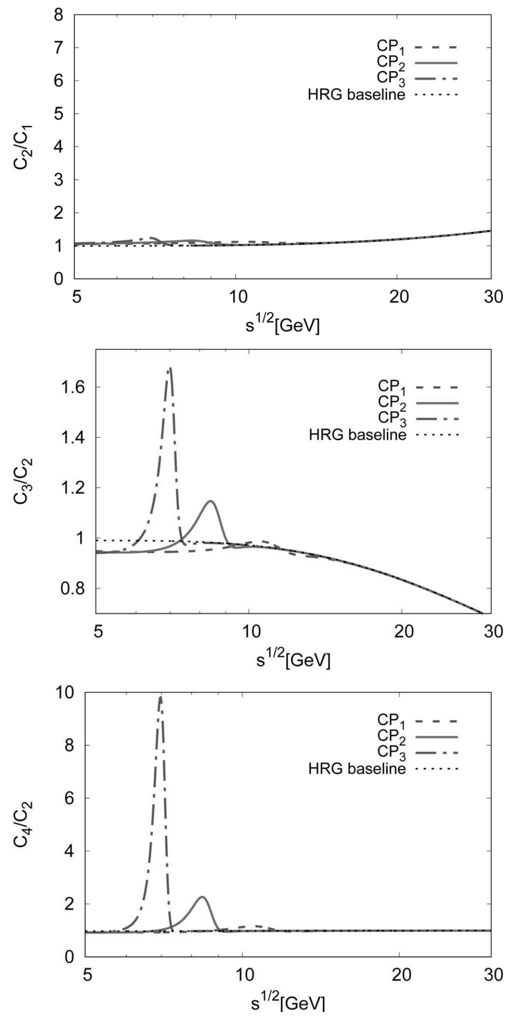

Fig. 4. Ratios of net-proton number cumulants calculated in the refined model [11] for the fixed coupling $g = 5$ and for different locations of the QCD critical point (listed in Table)

The net-proton cumulant ratios obtained in the refined model for different locations of the critical point (as listed in Table) and with a fixed value of the coupling, $g = 5$, are shown in Fig. 4. We find that a non-monotonic behavior of the cumulant ratios becomes more pronounced, when the critical point is closer to the freeze-out line. Moreover, the deviation from the non-critical HRG baseline becomes larger for higher-order cumulant ratios.

Finally, Fig. 5 shows the coupling strength dependence of the net-proton number cumulant ratios ob-

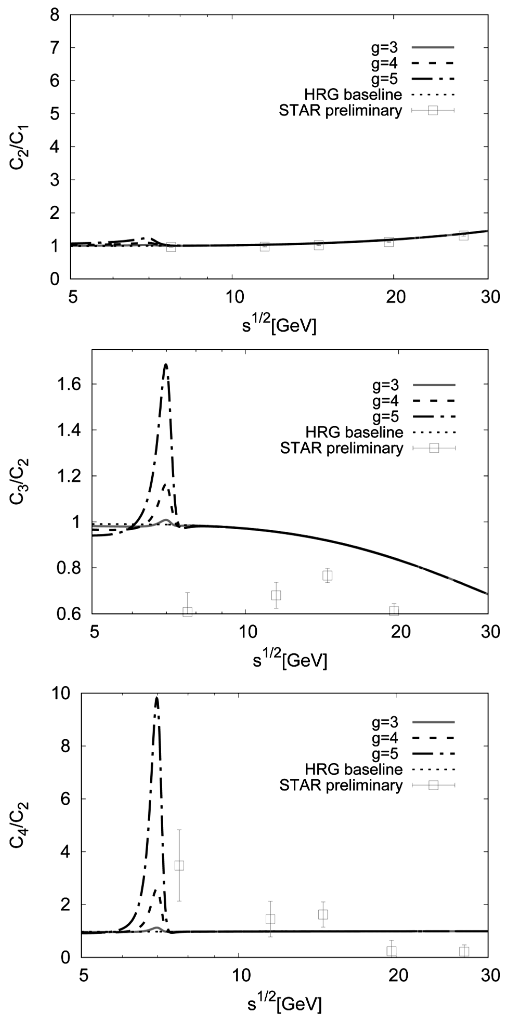

Fig. 5. Ratios of net-proton number cumulants calculated in the refined model [11] with CP_3 and for the coupling strengths, $g = 3$, 4 and 5 (orange solid, green long-dashed, and red dash-dotted lines, respectively). The preliminary STAR data on the net-proton number fluctuations [5] (squares with the error bars containing both statistical and systematic errors) and HRG baseline results (black dotted lines) are also shown for comparison

tained for CP_3. We find a strong g dependence of all ratios. This is expected, since, in our refined model, the n-th cumulant scales as g^{2n}, according to Eqs. (7) and (11)–(13). When our model results are compared to the STAR data [5], we find a qualitative agreement with the C_2/C_1 and C_4/C_2 ratios. On the other hand, the C_3/C_2 ratio does not follow the systematics seen in the data, i.e., our model results overshoot the HRG baseline, while the data stay below.

Our results suggest that the appropriate choice of model parameters, as well as the location of the QCD critical point, allows us to describe some of the experimentally observed cumulant ratios. Especially, the smooth dependence of C_2/C_1 and the strong increase of C_4/C_2 at low beam energies, $\sqrt{s} < 20$ GeV, seen by the STAR Collaboration, suggest that the QCD critical point may be located close to the freeze-out curve. However, in this case, the C_3/C_2 ratio should increase beyond the non-critical baseline, which is not seen in the experimental data. Therefore, it seems unlikely that the QCD critical point is close to the freeze-out curve. This conclusion requires, however, additional theoretical and experimental justifications due to uncertainties in the model parameters as well as in the experimental data.

4. Conclusions

We have presented the ratios of net-proton number cumulants obtained within an effective model in which the coupling between (anti)protons and critical mode fluctuations is introduced by connecting the particle masses to the order parameter. We have modified the existing approach [10] to account for the correct scaling properties of the baryon number susceptibility, as dictated by the universality hypothesis.

Model results were compared with the recent experimental data on net-proton number fluctuations from the STAR Collaboration. We find a substantial reduction of the signal coming from the presence of the QCD critical point in the C_2/C_1 ratio which stays in agreement with the experimental data. Moreover, we find that the model discussed in the present work allows us to describe some of the experimentally observed features in the net-proton number cumulant ratios. Particularly, the smooth dependence of C_2/C_1 and an increase in C_4/C_2 at lower beam energies ($\sqrt{s} < 20$ GeV) suggest that the critical point may be located close to the freeze-out curve. However, the experimentally observed C_3/C_2 ratio does not follow the behavior expected from such a scenario.

Therefore, it seems unlikely that the QCD critical point is located close to the phenomenological freeze-out curve. However, because of uncertainties on both theoretical and experimental sides, this statement requires a further investigation.

M.S. and M.B. acknowledge the support of the Polish National Science Center (NCN) under grant Po-

lonez UMO-2016/21/P/ST2/04035. M.B. was partly supported by the program "Etoiles montantes en Pays de la Loire 2017". This work is partly supported by the Polish National Science Center (NCN) under Maestro grant No. DEC-2013/10/A/ST2/00106 and Opus grant No. 2018/31/B/ST2/01663. K.R. also acknowledges the partial support of the Polish Ministry of Science and Higher Education. We thank F. Geurts and J. Thäder for providing the preliminary STAR data [5] shown in Figs. 3 and 5.

1. M.A. Stephanov, K. Rajagopal, E.V. Shuryak. Signatures of the tricritical point in QCD. *Phys. Rev. Lett.* **81**, 4816 (1998).
2. M.A. Stephanov, K. Rajagopal, E.V. Shuryak. Event-by-event fluctuations in heavy ion collisions and the QCD critical point. *Phys. Rev. D* **60**, 114028 (1999).
3. X. Luo, [STAR Collaboration]. Energy dependence of moments of net-proton and net-charge multiplicity distributions at STAR. *PoS CPOD* **2014**, 019 (2015).
4. X. Luo. Exploring the QCD phase structure with beam energy scan in heavy-ion collisions. *Nucl. Phys. A* **956**, 75 (2016).
5. J. Thäder [STAR Collaboration]. Higher moments of net-particle multiplicity distributions. *Nucl. Phys. A* **956**, 320 (2016).
6. G.A. Almasi, B. Friman, K. Redlich. Baryon number fluctuations in chiral effective models and their phenomenological implications. *Phys. Rev. D* **96**, 014027 (2017).
7. F. Karsch. Lattice QCD results on cumulant ratios at freeze-out. *J. Phys. Conf. Ser.* **779**, 012015 (2017).
8. A. Bzdak, V. Koch. Net-baryon multiplicity distribution consistent with lattice QCD. *Phys. Rev. C* **99**, 024913 (2019).
9. V. Koch, A. Bzdak. Fluctuations and the QCD phase diagram. *Acta Phys. Polon. B* **47**, 1867 (2016).
10. M. Bluhm, M. Nahrgang, S.A. Bass, T. Schäfer. Impact of resonance decays on critical point signals in net-proton fluctuations. *Eur. Phys. J. C* **77**, 210 (2017).
11. M. Szymański, M. Bluhm, K. Redlich, C. Sasaki. Net-proton number fluctuations in the presence of the QCD critical point. *arXiv*:1905.00667 [nucl-th].
12. C. Sasaki, B. Friman, K. Redlich. Quark number fluctuations in a chiral model at finite baryon chemical potential. *Phys. Rev. D* **75**, 054026 (2007).
13. C. Sasaki, B. Friman, K. Redlich. Chiral phase transition in the presence of spinodal decomposition. *Phys. Rev. D* **77**, 034024 (2008).
14. J. Zinn-Justin. *Quantum Field Theory and Critical Phenomena* (Clarendon Press, 2002).
15. A. Andronic, P. Braun-Munzinger, K. Redlich, J. Stachel. Decoding the phase structure of QCD via particle production at high energy. *Nature* **561**, 321 (2018).
16. F. Wilczek. Application of the renormalization group to a second-order QCD phase transition. *Int. J. Mod. Phys. A* **07**, 3911 (1992).
17. A.M. Halasz, A.D. Jackson, R.E. Shrock, M.A. Stephanov, J.J.M. Verbaarschot. Phase diagram of QCD. *Phys. Rev. D* **58**, 096007 (1998).
18. H.-T. Ding, F. Karsch, S. Mukherjee. Thermodynamics of strong-interaction matter from Lattice QCD. *Int. J. Mod. Phys. E* **24**, 1530007 (2015).
19. Y. Hatta, T. Ikeda. Universality, the QCD critical/tricritical point and the quark number susceptibility. *Phys. Rev. D* **67**, 014028 (2003).
20. S. Mukherjee, R. Venugopalan, Y. Yin. Real time evolution of non-Gaussian cumulants in the QCD critical regime. *Phys. Rev. C* **92**, 034912 (2015).
21. C. Nonaka, M. Asakawa. Hydrodynamical evolution near the QCD critical end point. *Phys. Rev. C* **71**, 044904 (2005).
22. R. Guida, J. Zinn-Justin. 3-D Ising model: The scaling equation of state. *Nucl. Phys. B* **489**, 626 (1997).
23. B. Abelev *et al.*, [ALICE Collaboration]. Centrality dependence of π, K, p production in Pb–Pb collisions at $\sqrt{s_{NN}} = 2.76$ TeV. *Phys. Rev. C* **88**, 044910 (2013).
24. B.B. Abelev *et al.*, [ALICE Collaboration]. K^0_S and Λ production in Pb–Pb collisions at $\sqrt{s_{NN}} = 2.76$ TeV. *Phys. Rev. Lett.* **111**, 222301 (2013).
25. B.B. Abelev *et al.*, [ALICE Collaboration]. Multi-strange baryon production at mid-rapidity in Pb–Pb collisions at $\sqrt{s_{NN}} = 2.76$ TeV. *Phys. Lett. B* **728**, 216 (2014), Erratum: [*Phys. Lett. B* **734**, 409 (2014)].
26. B.B. Abelev *et al.*, [ALICE Collaboration]. $K^*(892)^0$ and ffl(1020) production in Pb–Pb collisions at $\sqrt{sNN} = 2.76$ TeV. *Phys. Rev. C* **91**, 024609 (2015).
27. J. Adam *et al.*, [ALICE Collaboration]. ${}^3_\Lambda\mathrm{H}$ and ${}^3_{\overline{\Lambda}}\overline{\mathrm{H}}$ production in Pb–Pb collisions at $\sqrt{s_{\mathrm{NN}}} = 2.76$ TeV. *Phys. Lett. B* **754**, 360 (2016).
28. J. Adam *et al.*, [ALICE Collaboration]. Production of light nuclei and anti-nuclei in *pp* and Pb–Pb collisions at energies available at the CERN large hadron collider. *Phys. Rev. C* **93**, 024917 (2016).

Received 18.07.19

М. Шиманскі, М. Блум, К. Редліх, К. Сасакі

ПОШУКИ КРИТИЧНОЇ ТОЧКИ
КХД З ФЛУКТУАЦІЄЮ ЧИСЛА ПРОТОНІВ

Р е з ю м е

Флуктуації повного числа протонів можна вимірювати експериментально, отримуючи таким чином важливу інформацію про речовину, що народжується під час зіткнень релятивістських іонів. Зокрема вона може містити інформацію про критичну точку КХД. В даній роботі ми обговорюємо залежність відношень перших чотирьох кумулянтів числа протонів від енергії струменя частинок. Ці величини розраховані за допомогою феноменологічної моделі, в якій флуктуації з критичною модою пов'язані з протонами та антипротонами. Наша модель якісно відтворює як монотонну поведінку відношення найнижчих порядків, так і немонотонну поведінку відношень високих порядків, як це спостерігається в результатах колаборації STAR. Ми обговорюємо також залежність наших результатів від сили зв'язку і місцезнаходження критичної точки.

https://doi.org/10.15407/ujpe64.8.772

M. TRZEBIŃSKI
Institute of Nuclear Physics Polish Academy of Sciences
(152, Radzikowskiego Str., 31-342 Cracow, Poland; e-mail: maciej.trzebinski@ifj.edu.pl)

DIFFRACTIVE PHYSICS AT THE LHC

Diffractive processes possible to be measured at the LHC are listed and briefly discussed. This includes soft (elastic scattering, exclusive meson pair production, diffractive bremsstrahlung) and hard (single and double Pomeron exchange jets, γ + jet, W/Z, jet-gap-jet, exclusive jets) processes as well as Beyond Standard Model phenomena (anomalous gauge couplings, magnetic monopoles).

Keywords: LHC, AFP, ALFA, TOTEM, pomeron, diffraction, exclusive processes, beyond standard model.

1. Introduction

About a half of collisions at the LHC are of diffractive nature. In such events, a rapidity gap [1] between the centrally produced system and scattered protons is present. Due to the exchange of a colorless object – photon (electromagnetic) or Pomeron (strong interaction) – one or both outgoing protons may stay intact.

Studies of diffractive events are an important part of the physics program of the LHC experiments. The diffractive production could be recognized by the search for a rapidity gap in the forward direction or by the measurement of scattered protons. The first method is historically a standard one for the diffractive pattern recognition. It uses the usual detector infrastructure: *i.e.* tracker and forward calorimeters. Unfortunately, the rapidity gap may be destroyed by *e.g.* particles coming from the pile-up – parallel, independent collisions happening in the same bunch crossing. In addition, the gap may be outside the acceptance of a detector. In the second method, protons are directly measured. This solves the problems of gap recognition in the very forward region and a presence of a pile-up. However, since protons are scattered at small angles (few hundreds microradians), additional devices called "forward detectors" are needed to be installed.

At the LHC, the so-called Roman pot technology is used. In ATLAS [1], two systems of such detectors were installed: ALFA [2, 3] and AFP [4]. At the LHC interaction point 5, Roman pots are used by CMS [5] and TOTEM [6,7] groups. Since protons are scattered at small angles, there are several LHC elements (*i.e.*, magnets and collimators) between them and the IP which influence their trajectory. The settings of these elements, commonly called machine optics, determine the acceptance of forward detectors. The detailed description of the properties of optics sets used at the LHC can be found in [8].

In both experiments, a large community works on both phenomenological and experimental aspects of diffraction. In this paper, the diffractive processes possible to be measured will be briefly described.

2. Soft Diffraction

Collisions at hadron accelerators are dominated by soft processes. The absence of a hard scale in these events prevents one from using perturbation theory. Instead, in order to calculate the properties of the produced particles such as the energy or angular distributions, one has to use approximative methods.

The elastic scattering process has the simplest signature that can be imagined: two protons exchange their momentum and are scattered at small angles. At the LHC, the measurement of protons scattered elastically requires a special settings commonly named the high-β^* optics. Properties of the elastic scattering were measured by both ATLAS and TOTEM Collaborations for center-of-mass energies of 7 [9, 10], 8 [11, 12], and 13 TeV [13].

Another soft process is a diffractive bremsstrahlung. It is typically of electromagnetic nature. However, high-energy photons can be radiated in the elastic

[1] A space in the rapidity devoid of particles.

proton-proton scattering as postulated in [14]. This idea was further extended in [15] by introducing the proton form-factor into the calculations and by considering other mechanisms such as a virtual photon re-scattering. The feasibility studies presented in [16] suggest that such measurement should be possible at the LHC. The requirements are high-β^* optics, proton measurement in ALFA/TOTEM and photon measurement in Zero Degree Calorimeter.

Last of the processes described in this section is the exclusive meson pair production, a $2 \to 4$ process in which two colliding protons result in two charged mesons and two scattered protons present in the final state. In the non-resonant pion pair production (also called continuum), a Pomeron is "emitted" from each proton resulting in four particles present in the final state: scattered protons and (central) pions [17]. The object exchanged in the t-channel is an off-shell pion. Exclusive pions can also be produced via resonances, *e.g.*, f_0 [18]. Although the dominant diagram of the exclusive pion pair continuum production is a Pomeron-induced one, the production of a photon-induced continuum is also possible. On the top of that, a resonant ρ^0 photo-production process may occur [19].

Recently, the models of elastic scattering, exclusive meson production, and diffractive bremsstrahlung were added to the GenEx Monte-Carlo generator [20–22].

3. Hard Diffraction

Hard diffractive events can be divided into the single diffractive and double Pomeron exchange classes. In the first case, one proton stays intact, whereas the other one dissociates. In the second case, both interacting protons "survive". In addition, the sub-case of the exclusive production can be considered – a processes in which all final-state particles can be measured by ATLAS and CMS/TOTEM detectors.

Depending on the momentum lost during the interaction, the emitting proton may remain intact and be detected by a forward proton detector. However, it may happen that the soft interactions between the protons or the proton and the final-state particles can destroy the diffractive signature. Such effect is called the gap survival probability. For the LHC energies, the gap survival is estimated to be of about 0.03–0.1 depending on the process [23].

From all hard events, the diffractive jets have the highest cross-section [2]. By studying the single diffractive and double Pomeron exchange jet productions, a Pomeron universality between ep and pp colliders can be probed. As was discussed in [24], the tagging of diffractive protons will allow the QCD evolution of gluon and quark densities in the Pomeron to be tested and compared to the ones extracted from the HERA measurements. Another interesting measurement is the estimation of the gap survival probability. A good experimental precision will allow for comparison to theoretical predictions and differential measurements of the dependence of the survival factor on, *e.g.*, the mass of the central system.

An interesting class of jet events is one with a rapidity gap is present between jets – the so-called jet-gap-jet production. In such events, an object exchanged in the t-channel is a color singlet and carries a large momentum transfer. When the gap size is sufficiently large, the perturbative QCD description of jet-gap-jet events is usually performed in terms of the Balitsky–Fadin–Kuraev–Lipatov (BFKL) model [27–29]. The jet-gap-jet topology can be produced also in the single diffractive and double Pomeron exchange processes. Properties of such events were never measured – the determination of the cross-section should enable the tests of the BFKL model [30].

Jets produced in the processes described above are typically of gluonic nature. In order to study the quark composition of a Pomeron, diffractive photon + + jet productions should be considered. In such cases, one Pomeron emits a gluon, whereas the other one delivers a quark. A measurement of the photon + jet production in the DPE mode can be used to test the Pomeron universality between HERA and LHC. Moreover, HERA was not sensitive to the difference between the quark components in a Pomeron. This means that the fits assumed the equal amounts of light quarks, $u = d = s = \bar{u} = \bar{d} = \bar{s}$. The LHC data should allow more precise measurements [25].

Another interesting process is the diffractive production of W and Z bosons. Similarly to γ + jet, it is sensitive to the quark component, since many of the observed production modes can originate from a quark fusion. As was discussed in [26], by measuring the ratio of the W production cross-section to the Z one, the d/u and s/u quark density values in the

[2] Depends on the jet transverse momentum.

Pomeron can be estimated. In addition, a study of the DPE W asymmetry can be performed [26]. Such measurement can be used to validate theoretical models.

The feasibility studies of all measurements described above in this section are described in Ref. [31].

Diffractive jets can be produced in the exclusive mode. Usually, it is assumed that one gluon is hard, whereas the other one is soft [32, 33]. The role of the soft gluon is to provide the color screening in order to keep the net color exchange between protons equal to zero. The exclusivity of the event is assured via the Sudakov form factor [34], which prohibits an additional radiation of gluons in higher orders of perturbative QCD. In [35], a discussion about the feasibility of such measurement in the case of the ATLAS detector and both tagged protons is held. A semiexclusive measurement, when one of the protons is tagged, is discussed in [36, 37].

4. Anomalous Couplings and Beyond Standard Model Physics

The presence of an intact proton can be used to search for a new phenomena. The Beyond Standard Model (BSM) processes are usually expected to be on a high mass, which makes them visible in forward detectors.

One example of the BSM physics is anomalous couplings: $\gamma\gamma WW$, $\gamma\gamma ZZ$, $\gamma\gamma\gamma\gamma$ or $WW\gamma$. As was shown in [38, 39], the possibility of the forward proton tagging provides a much cleaner experimental environment which improves the discovery potential. Authors expect that, with 30–300 fb^{-1}, the data collected with the ATLAS detector with information about scattered protons tagged in AFP should result in a gain in the sensitivity of about two orders of magnitude over a standard ATLAS analysis.

Finally, the presence of protons with a high energy loss and a lack of energy registered in the central detector might be a sign of a new physics, for example, magnetic monopoles [31].

5. Conclusions

The Large Hadron Collider gives possibility to study the properties of diffractive physics in a new kinematic domain. Diffractive events can be identified in all major LHC experiments using the rapidity gap recognition method. In addition, as ATLAS and CMS/TOTEM are equipped with the set of forward detectors, it is possible to use the proton tagging technique.

In this paper, a brief summary of the diffractive processes measurable at the LHC was done. Using special settings of the LHC – high-β^* optics – the processes of elastic scattering, exclusive meson pair production, and diffractive bremsstrahlung can be studied. Hard diffractive events, due to smaller cross-sections, should be measured with the standard LHC optics. The studies of properties of the diffractive dijet, photon+jets, and the W/Z boson production processes should lead *i.a.* to the determination of a gap survival probability and a Pomeron structure. Studies of diffractive jet-gap-jet events should bring more insight into the description of the Pomeron, *i.a.* to verify predictions of the BFKL model. On the top of that, the measurement of the jet production in the exclusive (double proton tag) and semiexclusive (single tag) modes can be performed. Finally, the additional information about a scattered proton may improve the searches for a New Physics including such phenomena as anomalous gauge couplings or magnetic monopoles.

Development of the GenEx Monte Carlo generator was partially supported by the Polish National Science Center grant: UMO-2015/17/D/ST2/03530.

1. ATLAS Collaboration. The ATLAS experiment at the CERN Large Hadron Collider. *JINST* **3**, S08003 (2008).
2. ATLAS Luminosity and Forward Physics Community. *Technical Design Report*, CERN-LHCC-2008-004.
3. S. Abdel Khalek *et al.* The ALFA Roman Pot Detectors of ATLAS. *JINST* **11**, P11013 (2016).
4. ATLAS Collaboration. *Technical Design Report for the ATLAS Forward Proton Detector*, CERN-LHCC-2015-009, ATLAS-TDR-024.
5. CMS Collaboration. The CMS experiment at the CERN large hadron collider. *JINST* **3**, S08004 (2008).
6. TOTEM Collaboration. *Technical Design Report* CERN-LHCC-2004-002.
7. TOTEM Collaboration. *TOTEM Upgrade Proposal* CERN-LHCC-2013-009.
8. M. Trzebinski. Machine optics studies for the LHC measurements. In *Proceedings of XXXIV-th IEEE-SPIE Joint Symposium*, SPIE 0277-786X, vol. 9290, (2014), p. 26.
9. ATLAS Collaboration. Measurement of the total cross section from elastic scattering in pp collisions at $\sqrt{s} = 7$ TeV with the ATLAS detector. *Nucl. Phys. B* **889**, 486 (2014).
10. TOTEM Collaboration. Proton-proton elastic scattering at the LHC energy of $\sqrt{s} = 7$ TeV. *EPL* **95**, (2011).
11. ATLAS Collaboration. Measurement of the total cross section from elastic scattering in pp collisions at $\sqrt{s} = 8$ TeV with the ATLAS detector. *Phys. Lett. B* **761**, 158 (2016).

12. TOTEM Collaboration. Measurement of elastic pp scattering at $\sqrt{s} = 8$ TeV in the coulomb-nuclear interference region – determination of the ρ parameter and the total cross-section. *Eur. Phys. J. C* **76**, 661 (2016).
13. TOTEM Collaboration. First measurement of elastic, inelastic and total cross-section at $\sqrt{s} = 13$ TeV by TOTEM and overview of cross-section data at LHC energies. *Eur. Phys. J. C* **79**, 103 (2019).
14. V.A. Khoze, J.W. Lamsa, R. Orava, M.G. Ryskin. Forward physics at the LHC: Detecting elastic *pp* scattering by radiative photons. *JINST* **6**, P01005 (2011).
15. P. Lebiedowicz, A. Szczurek. Exclusive diffractive photon bremsstrahlung at the LHC. *Phys. Rev. D* **87**, 114013 (2013).
16. J.J. Chwastowski, S. Czekierda, R. Staszewski, M. Trzebinski. Diffractive bremsstrahlung at high-β^* LHC case study. *Eur. Phys. J. C* **77**, 216 (2017).
17. P. Lebiedowicz, O. Nachtmann, A. Szczurek. Central exclusive diffractive production of $\pi^+\pi^-$ continuum, scalar and tensor resonances in *pp* and *pp* scattering within tensor pomeron approach. *Phys. Rev. D* **93**, 054015 (2016).
18. P. Lebiedowicz, O. Nachtmann, A. Szczurek. Exclusive central diffractive production of scalar and pseudoscalar mesons tensorial vs. vectorial pomeron. *Annals Phys.* **344**, 301 (2014).
19. P. Lebiedowicz, O. Nachtmann, A. Szczurek. The ρ^0 and Drell–Soding contributions to central exclusive production of $\pi^+\pi^-$ pairs in proton-proton collisions at high energies. *Phys. Rev. D* **91**, 074023 (2015).
20. R.A. Kycia, J. Chwastowski, R. Staszewski, J. Turnau. GenEx: A simple generator structure for exclusive processes in high energy collisions. *Commun. Comput. Phys.* **24**, 860 (2018).
21. P. Erland, R. Staszewski, M. Trzebinski, R. Kycia. Elastic hadron scattering in various Pomeron models. *Acta Phys. Pol. B* **48**, 981 (2017).
22. R.A. Kycia, J. Turnau, J.J. Chwastowski, R. Staszewski, M. Trzebinski. The adaptive Monte Carlo toolbox for phase space integration and generation. *Commun. Comput. Phys.* **25**, 1547 (2019).
23. A.B. Kaidalov, V.A. Khoze, A.D. Martin, M.G. Ryskin. Probabilities of rapidity gaps in high energy interactions. *Eur. Phys. J. C* **21**, 521 (2001).
24. C. Royon. Forward physics with tagged protons at the LHC: QCD and anomalous couplings. In *Proceedings of the Low x 2013 workshop* (Weizmann Institute of Sci., 2013).
25. C. Marquet, C. Royon, M. Saimpert, D. Werder. Probing the Pomeron structure using dijets and γ+jet events at the LHC. *Phys.Rev. D* **88**, 074029 (2013).
26. K. Golec-Biernat, C. Royon, L. Schoeffel, R. Staszewski. Electroweak vector boson production at the LHC as a probe of mechanisms of diffraction. *Phys. Rev. D* **84**, 114006 (2011).
27. L.N. Lipatov. Reggeization of the vector meson and the vacuum singularity in non-Abelian Gauge theories. *Sov. J. Nucl. Phys.* **23**, 338 (1976).
28. E.A Kuraev, L.N. Lipatov, V.S. Fadin. The pomeranchuk singularity in non-Abelian Gauge theories. *Sov. Phys. JETP* **45**, 199 (1977).
29. I.I. Balitsky, L.N. Lipatov. The Pomeranchuk singularity in quantum chromodynamics. *Sov. J. Nucl. Phys.* **28**, 822 (1978).
30. C. Marquet, C. Royon, M. Trzebinski, R. Zlebcik. Gaps between jets in double-Pomeron-exchange processes at the LHC. *Phys. Rev. D* **87**, 034010 (2013).
31. K. Akiba *et al. LHC Forward Physics*, SLAC-PUB-16364, DESY 15-167.
32. V.A. Khoze, A.D. Martin, M.G. Ryskin. Central jet production as a probe of the perturbative formalism for exclusive diffraction. *Eur. Phys. J. C* **48**, 467 (2006).
33. M.G. Albrow, T.D. Coughlin, J.R. Forshaw. Central exclusive particle production at high energy hadron colliders. *Prog. Part. Nucl. Phys.* **65**, 149 (2010).
34. V.V. Sudakov. Vertex parts at very high energies in quantum electrodynamics. *Sov. Phys. J. E. T. P.* **30**, 65 (1956).
35. ATLAS Collaboration. *Exclusive jet production with forward proton tagging feasibility studies for the AFP project*, ATL-PHYS-PUB-2015-003.
36. M. Trzebinski, R. Staszewski, J. Chwastowski. On the possibility of measuring the single-tagged exclusive jets at the LHC. *Eur. Phys. J. C* **75**, 320 (2015).
37. M. Trzebinski. Exclusive jet measurement in special LHC runs – feasibility studies. *Acta Phys. Pol. B* **47**, 1745 (2016).
38. E. Chapon *et al.* Anomalous quartic $\gamma\gamma WW$, $\gamma\gamma ZZ$, and trilinear $WW\gamma$ couplings in two-photon processes at high luminosity at the LHC. *Phys. Rev. D* **81**, 074003 (2010).
39. S. Fichet *et al.* Probing new physics in diphoton production with proton tagging at the Large Hadron Collider. *Phys. Rev. D* **89**, 114004 (2014).

Received 08.07.19

М. Тшебіньскі

ДИФРАКЦІЯ НА LHC

Р е з ю м е

Перераховано і коротко обговорено дифракційні процеси, які можна вимірювати на LHC. Список включає м'які (пружне розсіяння, ексклюзивне продукування мезонних пар, дифракційне гальмівне випромінювання) та жорсткі (струмені з обміном одного або двох померонів, фотон + струмінь, W/Z, струмінь-розрив-струмінь, ексклюзивні струмені) процеси, а також явища поза рамок Стандартної Моделі (аномальні калібрувальні зв'язки, магнітні монополі).

AUTHOR'S INDEX

Надруковано в друкарні “Аутдор-Шарк”
Ужгород, пл. Жупанська, 15/1, 15.12.2020
Накладом 300 екз.

Printed in Uzhhorod (Ungvár) on Dec. 15, 2020
by “Outdoor-Shark”, Zhupanskaya str. 15/1
Edition: 300 copies